EFFECTS OF EDGE CONFIGURATION ON THE RESPONSE OF TALL BUILDINGS UNDER WIND LOADS

A THESIS

SUBMITTED IN PARTIAL FULFILMENT OF THE REQUIREMENTS

FOR THE AWARD OF THE DEGREE

OF

DOCTOR OF PHILOSOPHY

IN

CIVIL ENGINEERING

Submitted by:

ARUN KUMAR
(2K13/PHD/CE/05)

Under the supervision of

DR RITU RAJ

DEPARTMENT OF CIVIL ENGINEERING
DELHI TECHNOLOGICAL UNIVERSITY
(Formerly Delhi College of Engineering)
Bawana Road, DELHI – 110042

Nov, 2023

DELHI TECHNOLOGICAL UNIVERSITY
(Formerly Delhi College of Engineering)
Bawana Road, DELHI – 110042

CANDIDATE’S DECLARATION

I, Arun Kumar, 2K13/PhD/CE/05, a research scholar in the Department of Civil Engineering, hereby declare that the Thesis titled “EFFECTS OF EDGE CONFIGURATION ON THE RESPONSE OF TALL BUILDINGS UNDER WIND LOADS” which is submitted by me to the Department of Civil Engineering, Delhi Technological University, Delhi in partial fulfilment of the requirement for the award of the degree of Doctor of Philosophy, is original and not copied from any source without proper citation. This work has not previously formed the basis for the award of any Degree, Diploma, Associateship, Fellowship, or other similar title or recognition.

Place: Delhi (ARUN KUMAR)
Date: 09.11.2023

DELHI TECHNOLOGICAL UNIVERSITY
(Formerly Delhi College of Engineering)
Bawana Road, DELHI – 110042

CERTIFICATE

I hereby certify that the Thesis titled "EFFECTS OF EDGE CONFIGURATION ON THE RESPONSE OF TALL BUILDINGS UNDER WIND LOADS" which is submitted by Arun Kumar, 2K13/PhD/CE/05, Research Scholar, Department of Civil Engineering, Delhi Technological University, Delhi in partial fulfilment of the requirement for the award of the Degree of Doctor of Philosophy, is a record of the original research work carried out by the scholar under my supervision. To the best of my knowledge this research work has not been submitted in part or full for any Degree or Diploma to this University or elsewhere.

Ritu Raj

Place: Delhi (DR RITU RAJ)
Date: 09.11.2023 SUPERVISOR

ABSTRACT

Wind flow is horizontal motion of air column in atmosphere. The pressure gradient, Coriolis effect, and earth’s frictional resistance are three basic factors which influences wind speed and direction.

In building engineering wind pressure is an important factor governing the natural ventilation, pedestrian comfort, safety from the failure of cladding units, and design of the buildings for structural resistance and stability. With increase in height of buildings and; the complex architectural shapes, analysis of wind loads has become an integral part for building serviceability requirements and comfort of users. As of now, wind load analysis is done with the help of wind codes and/or wind tunnel experiments. However, with increasing developments in computer facilities and precise software, Computational Fluid Dynamics (CFD) is, now-a-days, being commonly used for the purpose.

Computational Fluid Dynamics (CFD) is a convenient, economic, and faster solution to access the behaviour and wind pressure on tall buildings of complex architectural shapes, especially during the preliminary stage of finalization of the geometry of the building and its orientation. Through CFD, wind response on tall buildings for structural variables like moments, loads, pressure, etc. can be calculated up to a level of acceptable accuracy.

ANSYS (CFX) is one of the CFD tools used to analyse wind pressure on any bluff body. It is suitable for low Mack number fluid flows on sharp-edged bluff bodies. In ANSYS (CFX) complex geometry of buildings can be easily modelled and discretized into smaller elements for numerical analysis. Good quality meshing can be achieved with full control. Changes in geometry and meshing can also be easily done for parametric studies. The Present study is an approach to quantitatively find out the pressure developed by the wind on the facades of the building and; the force and moment (base shear, base moment, and torsional moment) generated on the building and qualitatively understand the wind flow pattern and its effects on various building plan models having the equal plan area and height.

The building models have been tested in a boundary layer flow using power-law corresponding to terrain category - II, as defined in IS: 875 (Part-3): 2015. Steady-state flow with 5 % turbulence at a wind speed of 0.63 m/s at the model top for stand-alone has been adopted. Verification and validation have been done with wind standard codes and previous experimental data on rectangular model. The results for varied wind incidence angles have been presented in the form of contour plots and graphs. Structural parameters (base shear force/drag and lift, base moments and twisting moments have also been taken from the study.

The results of the study will be of great use to architects while planning the cross-sectional shapes and deciding their critical orientations for good ventilation. Structural designers will be able to design tall buildings having similar cross-sections under wind loads with greater confidence without going for wind tunnel tests.

ACKNOWLEDGEMENTS

I wish to express my sincere appreciation and thanks to the entire staff of DTU for their help in this endeavour. Special thanks are extended to the Department of Civil engineering staff for their support and encouragement for the thesis.

I am indebted to my supervisor Dr Ritu Raj who reviewed various portions of the manuscripts and provided valuable comments. Additionally, my special thanks to Prof. A. K. Ahuja, the then HOD, Department of Civil Engineering, IIT Roorkee, and guest faculty in the Department of Civil Engineering, IIT Jammu whom I met at IIT Roorkee during the ACMS 2018 summit and get strong motivation for doing this study.

Appreciation is acknowledged to Dr S. K. Nagar and Dr R. K. Meena, both my Co-Scholars, Department of Civil Engineering, DTU who were helpful during my simulation study and my thesis writing.

Most deserving of special gratitude is my wife, Smt. Smriti Sinha. My source of inspiration, she helped in all aspects of this venture – from the very beginning of joining my Ph.D. program to the thesis writing. Her companionship made the arduous task a less formidable activity. My profound admiration and appreciation are extended to her for her unconditional love, encouragement, support, and, devotion. Without her patience and absolute commitment to spare me from the domestic and family responsibilities, it would have been difficult to come to this stage of thesis writing. Special thanks to my lovely & caring children - Dr Swasti Sinha, Dr Aadya Sinha & Er Amartya Sinha.

(ARUN KUMAR)

DEDICATION

I am indebted to my parents. My father didn’t say much, but I felt his love. While I was finishing this journey, I remembered his silent presence behind my table to see what I was involved in when I was writing one of my papers. Without his blessings, I could not have reached to the end of this journey. My mother always encouraged me to enhance my academic qualification and knowledge. I miss you both Maa - Pita Jee.

The thesis is dedicated to my parents.

(ARUN KUMAR)

TABLE OF CONTENTS

LIST OF TABLES

LIST OF FIGURES

LIST OF SYMBOLS AND ABBREVIATIONS

p_z = Wind pressure in at height $'z'$.

V_z = Design wind velocity in at height $'z'$.

V_b= Basic wind speed.

k_1= Probability Factor (risk coefficient) based on probable design life of structure.

k_2 = Terrain roughness (terrain category) and height of structure factor.

k_3= Topography factor above sea level for upwind slope of ground.

k_4= Importance factor for cyclonic region.

K_d = Wind directionality factor (a factor for randomness in the directionality of wind).

K_a= Area averaging factor (area average pressure values decrease with increase in area and vice-versa).

K_c = Combination factor for frames of clad buildings.

F_d = Design wind load in at any height $'z'$.

p_d= Design wind pressure in at any height $'z'$.

C_{P_e}= Area average pressure coefficient on the building in wind direction

C_f = Force coefficient for clad building

A= Area normal to wind direction contributing load at height $'z'\ m$

P = Total pressure (atmospheric pressure + velocity pressure) at any point on the surface

P_o = Reference pressure (atmospheric pressure in natural wind condition) at any point on the surface

ρ = Density of air

u = Time averaged uniform velocity at height $'z'$ above ground.

F_x = Shear force in wind direction.

F_y = Shear force in across wind direction.

M_x = Base moment about wind direction.

M_y = Base moment about across wind direction.

M_Z = Twisting moment of Building

u_{Ref} = Reference free stream time averaged uniform velocity at Z_{Ref}

Z_{Ref} = Reference height (taken as 10 m).

α = Terrain roughness coefficient

u_0 = Friction Velocity

τ_w = Wall Shear Stress

Z_0 = Aerodynamic roughness length which is a surface roughness parameter.

Z_d = Zero plane displacement i.e., the height of zero wind speed achieved above the ground

N-S = Navier Stokes equations

RANS = Reynolds Averaged Navier Stokes

k = Turbulence Kinetic Energy (TKE)

ε = Dissipation of Turbulence Kinetic Energy

S_M = Sum of body forces

μ_{eff} = Effective viscosity

p' = Modified pressure

μ_t = Turbulent viscosity

$$\left.\begin{array}{l} C_\mu = 0.09 \\ C_{\varepsilon 1} = 1.44 \\ C_{\varepsilon 2} = 1.92 \\ \sigma_k = 1.0 \text{ and} \\ \sigma_\varepsilon = 1.3 \end{array}\right\} \text{are } \mathrm{k}-\varepsilon \text{ turbulence model constants}$$

u_{wall} = Velocity normal to the wall

C_{fx} = Base Force Coefficient along wind direction/Drag Coefficient

C_{fy} = Base Force Coefficient across wind direction/Lift Coefficient

F_x = Base Forces in along wind direction at CG of the model

F_y = Base Forces in across wind direction at CG of the model

L_x = Projected width of model across wind direction

L_y = Projected length of model along wind direction

$A_x = L_x H$, is projected area on plane ⊥ to wind direction.

$A_y = L_y H$, is projected area on plane || to wind direction.

H = Height of model

u_H = Velocity at roof height of model

C_{mx} = Overturning Moment Coefficient about wind direction

C_{my} = Overturning Moment Coefficient across wind direction

C_{tm} = Twisting Moment Coefficient

M_x = Overturning Moments about wind direction taken at CG of the model

M_y = Overturning Moments across direction taken at CG of the model

M_z = Twisting Moments taken at CG of the model

CFD = Computational Fluid Dynamics

CWE = Computational Wind Engineering

LES = Large Eddy Simulation

IF = Interference Factor

EIF = Envelop Interference Factor

PEIF = Peak Envelop Interference Factor

RMS = Root Mean Square

CAARC = Commonwealth Advisory Aeronautical Research Council

AEP = Area Extreme Pressure

TTU = Texas Tech University

EPS = Electronic Pressure Scanner

CHAPTER 1 INTRODUCTION

1.1 GENERAL

Buildings are manmade objects/structures for safe and comfortable occupation and their intended use. Until the first half of 20th century sufficient land was available for the construction of buildings. In those days single or low-rise buildings were constructed with rigid, stiff, and dense characteristics of building materials available in those days. Now-a- days, due to rapid urbanization and shortage of land in urban areas, vertical expansion for more dwelling units is being made in the shape of tall and complex buildings. Innovations of construction materials; flexible with reduced stiffness but high strength and lightweight materials have invented super tall building and mega tall building technologies. This has necessitated study of the effect of wind on tall and high-rise buildings.

Wind is a natural phenomenon and may be defined as flow of air. Near the surface of the earth, it is three-dimensional. The horizontal motion of wind and its turbulence is much greater than the vertical motion near the surface of the earth. This horizontal motion and turbulence of wind are predominant up to about 400 meters from the surface of the earth. It is the impact of the horizontal motion of wind and its turbulence on buildings that is of concern to civil engineers.

Wind in general has two main effects on the tall buildings:

- Firstly, it exerts forces and moments on the structure and its cladding units.
- Secondly, it distributes the air in and around the building termed wind pressure.

Sometimes, because of the unpredictable nature of wind, it becomes so devastating during high wind storms that it can upset the internal ventilation system when it passes into the building. For these reasons, the study of airflow is becoming an integral part while planning a building and its environment.

1.2 TYPES OF BUILDING:

Ministry of Housing and Urban Affairs (MoHUA), GOI has defined types of buildings depending upon their usages, designs, heights, safety standards, and other features. Since we are intended to study the effect of edge configuration on tall buildings under wind loads, we will categorize buildings in terms of height. In "Model Building Bye-Laws – 2016" [1] of Town and Country Planning Organization, the Ministry of Urban Development categories building height as the vertical distance measured

i. in the case of flat roofs, from the average level of the front road to the highest point of the building.
ii. in the case of pitched roofs, up to the point where the external surface of the outer wall intersects the finished surface of the sloping roof and
iii. in the case of gables, facing the road midpoint between the eaves level and the ridge.

Architectural features serving no other function except aesthetic appearance is excluded for the purpose of measuring heights. The height of the building is taken up to the terrace level for the purpose of fire safety requirements.

On the basis of above discussions, categorization of building type may be done as:

1.2.1 Low Rise Buildings

Present days low rise buildings have been classified in IS 875 (Part 3): 2015 as buildings having a height less than 20 m. Low-rise buildings are generally made of rigid construction material. They provide more privacy to the occupants in the walk-up range through stairs. For example, single-family detached houses, and apartment buildings of one to three/four stories, may be considered low-rise buildings.

1.2.2 High Rise Buildings (Tall Buildings)

IS 875 (Part 3): 2015 has defined high rise building (tall building) which is constructed with a height of more than or equal to 50 m or having a ratio of height to smaller dimension more than 6.

According to the Council on Tall Buildings and Urban Habitat (CTBUH), which is an international body, tallness of a building is a subjective matter [2] in the context of the relative height of the adjoining buildings agglomeration, for example, a 14-story building may not be considered a tall building in a high-rise city such as Chicago or Hong Kong, but in a provincial European city or a suburb this may be distinctly taller than the urban norm (Figure 1.1); slenderness & appearance of the buildings, for example, there are numerous buildings that are not particularly high, but are slender enough to give the appearance of a tall building. Conversely, there are numerous big/large footprint buildings that are quite high, but their size/floor area rules them out of being classed as a tall building (Figure 1.2) and execution of relevant technologies such as structural wind bracing (Figure 1.3 a) and vertical transport system (Figure 1.3 b), etc. used in the construction of the building. According to the council, a building of 14 or more stories or more than 50 meters in height can normally be used as a threshold for a "tall building". Such buildings are equipped with lifts for the vertical transport system of the occupants. Tall buildings are constructed as mixed developments due to the limited urban land area and all the services (residences, office work, etc.) are accommodated within the building.

Tall buildings that achieve considerable heights may be classified into two additional sub-groups.

1.2.2.1 Super-Tall Buildings

Categorization in this range of buildings in terms of fixed height cannot be acclaimed but, buildings taller than 300 meters or more may be considered in this range.

1.2.2.2 Mega Tall Buildings

A tall building that achieves a height of more than 600 meters or more is classified in this category. As of today, there are 115 super-tall and only five mega-tall buildings completed globally. Jeddah Tower (Figure 1.4) was targeted for completion in the year 2020 but, due to Covid-19 pandemic, it is delayed.

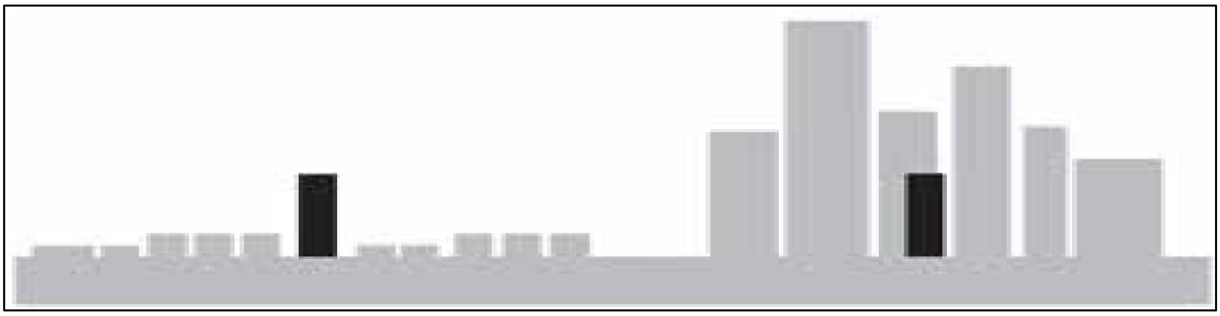

Figure 1. 1: High Rise Building According to Relative Height of the Adjoining Buildings (Source: CTBUH)

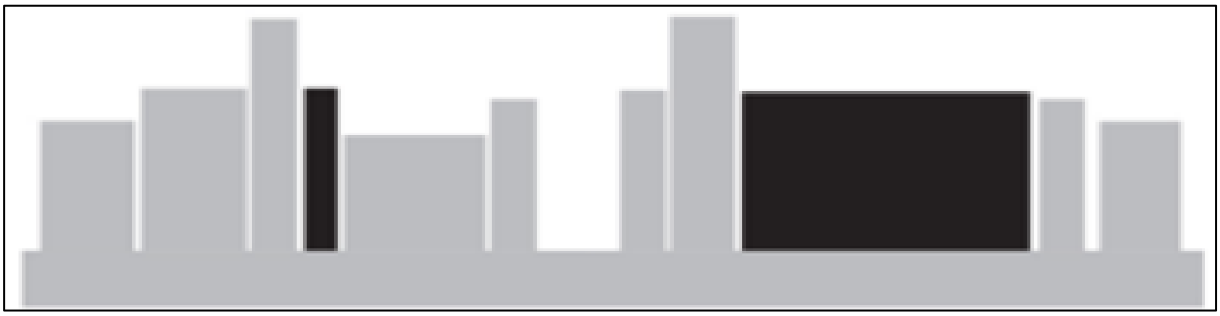

Figure 1. 2: High Rise Building According to Slenderness & Appearance of the Buildings (Source: CTBUH)

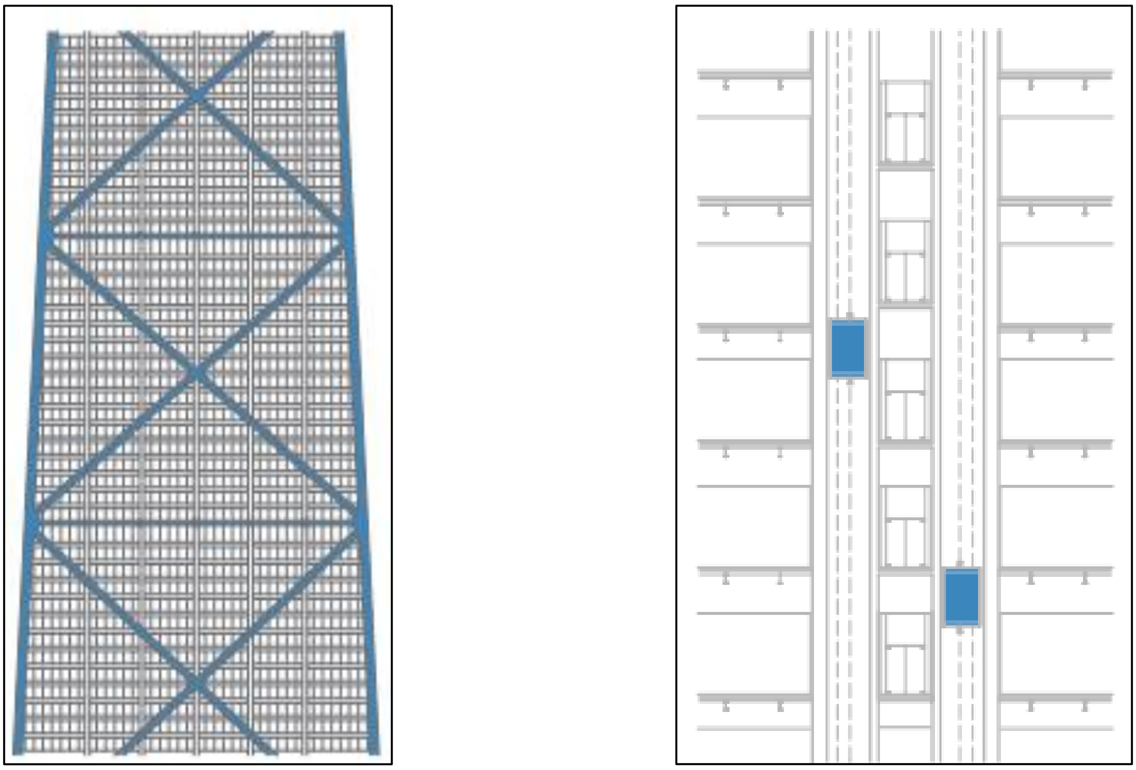

(a) Structural Wind Bracing

(b) Vertical Transport Technology

Figure 1. 3: High Rise Buildings According to Execution of Technologies (Source: CTBUH).

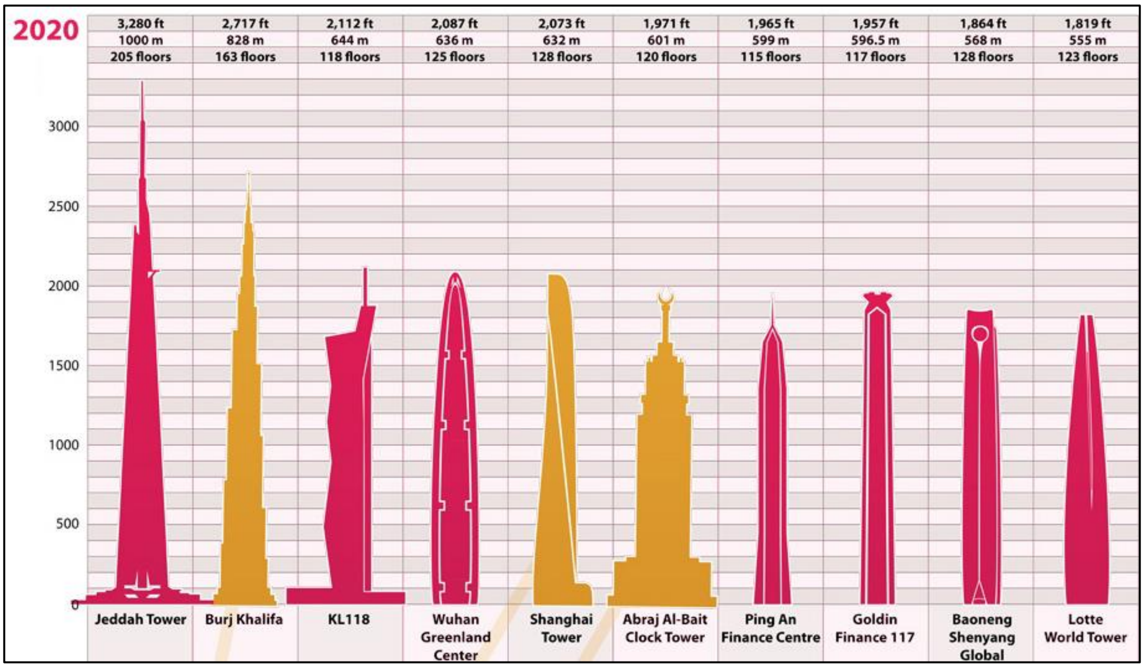

Figure 1. 4: World's Tallest Building
(Source: Visual Capitalist)

Jeddah Tower, Saudi Arabia *Burj Khalifa, Dubai* *Shanghai Tower, China*
(Courtesy: Internet Resource)

Figure 1. 5: Tall Buildings Across World (Contd.)

High Cliff, Hong Kong
(Courtesy: Lauri Silvennoinen)

Taipei 101, Taiwan
(Courtesy: Dfenix)

Figure 1. 5: Tall Buildings Across World.

1.3 GENERATION AND TYPES OF WIND

1.3.1 Generation of Wind

Circulation of wind around the globe occurs due to the following physical phenomenon.

1.3.1.1 Thermal radiation & pressure difference

The Earth's surface becomes warmer due to radiation effect of the Sun. The effect of the Sun's radiation is more near the equator than at the poles. The air surrounding the Earth's surface absorbs heat from the Earth's surface and becomes lighter; rises above into the atmosphere. At the poles, the cooler air settles down to the surface of the Earth and moves toward the equator to fill the gap created by the rising up of lighter air. This unequal heating of the Earth's surface creates large global wind patterns.

1.3.1.2 Earth's rotation

Because Earth rotates on its axis, circulating air is deflected towards right in the Northern Hemisphere and towards left in the Southern Hemisphere.

1.3.2 Types of Global Wind

1.3.2.1 Trade winds

At the latitude of about 30° north and south of the equator, the warm, moist air that rise vertically, cools and begins to sink. Some of the sinking air travels back towards the equator. The air moving back towards the equator forms warm, steady winds, known as the trade winds. In the northern hemisphere this trade wind is deflected by the rotation of the earth and is called as the northeast trade wind. Similarly, in the southern hemisphere it is called as the southeast trade wind.

1.3.2.2 Prevailing westerlies

Some of the cool, sinking air continues to move towards the North and South Poles. These winds are called the westerlies and are located between 40° to 60° latitude in both hemispheres.

1.3.2.3 Polar easterlies

In both hemispheres, the westerlies start rising and cooling between 50° and 60° latitude as they approach the poles. They meet extremely cold air flowing toward the equator from the poles and form the polar easterlies.

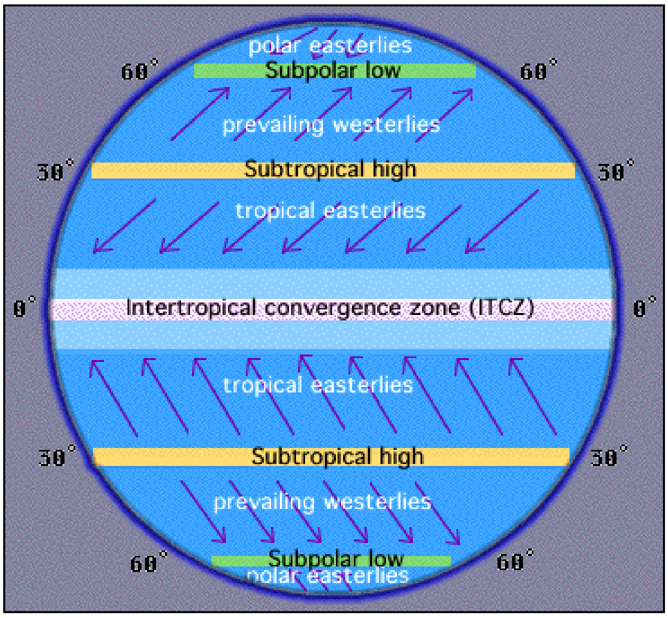

Figure 1. 6: Pattern of Global Wind

(Courtesy: Internet Resource)

1.3.3 Types of Wind

1.3.3.1 Trade/Prevailing winds

The global circulation of wind as explained in para 1.3.2.1 is called trade wind or prevailing wind.

1.3.3.2 Seasonal winds

Such wind flow occurs due to pressure differences between the vertical air strips over the oceans and the land. The air movement from the oceans towards the land during summer and from the land to oceans during the winter are termed as seasonal wind. The monsoon from the Indian ocean and China sea come in this category. Seasonal wind brings cyclones in the region of Australia and India, hurricanes in Atlantic, Caribbean and eastern Pacific and typhoons in the western Pacific. During cyclones/hurricanes wind speed may exceed 120 km/h.

1.3.3.3 Local winds

This type of wind is generated due to local changes in temperature and pressure and is associated with the regional phenomenon. Some of the local wind types are described below.

(a) Tornadoes/Cyclones/Hurricanes/Typhoons

A tornado is a narrow, twisting, funnel-shaped violently rotating column of air originating from rotating thunderstorms. Tornadoes occur in many parts of the world, including Australia, Europe, Africa, Asia, and South America, New Zealand, Argentina and Bangladesh. It is an intense spin in the atmosphere with very strong winds circulating around it in anti-clockwise and clockwise direction in the Northern and Southern Hemisphere respectively. In the Australian region and Indian Ocean, it is called cyclone (Figure 1.7). In Atlantic, Caribbean and eastern Pacific, it is called hurricanes and in the western Pacific, it is called typhoons. They usually rotate with wind speeds of 175 km/h or less, but can have tangential wind speeds up to 350 km/h. Tornadoes can occur at any time of day or night, but most tornadoes occur between 4 PM –9 PM local time.

Figure 1. 7: Cyclone

(Courtesy: Pixabay)

Amid the second wave of the COVID-19 pandemic, India witnessed two cyclones, Tauktae and Yaas, leaving behind a trail of destruction across several Indian states. The year 2020 marked the first pre-monsoon cyclone in a century-- Cyclone Amphan. Another Cyclone, Nisarga, hit the financial capital of India and was the second pre-monsoon cyclone after Amphan. As per IMD, India could witness many other pre-monsoon cyclones in the coming years. (Source: https://www.jagranjosh.com/general-knowledge/list-of-cyclones-in-india-1591178815-1).

(b) Foehn winds

Foehn winds develop when dry and warm wind passing over Rocky Mountains descends downslope on the lee side of the mountains. When moist air encounters the rocky mountain, condensation occurs resulting in precipitation on the upwind side of the mountain losing its moisture content. While passing through the hot rocky mountain peak, the dry wind gets heated up. This dry & warm wind passing through the downslope grassland attains high speed. Though, it is not disastrous, but causes soil erosion along the slope. This type of wind generally occurs in New Zealand, Zonda (South America), Central Asia and South Africa.

(c) Bora winds

Bora wind is similar to Foehn winds. It is cold wind and generally originates in low mountain range areas along the coast of a sea. The Bora wind speed can exceed 200 km/h and is disastrous. It occurs in Italy, Slovenia, and Croatia.

(d) Land and sea breezes

During the day time land mass gets heated and low-pressure zone is developed above the land mass. Cool air from sea (sea breeze) flow towards land mass. During night the process is reversed as land mass gets cooler quickly than the sea water due to higher specific heat of water. Air flow occurs from land to sea (land breeze). Such air movement is localized along the coastal area and are responsible for temperate climate in the region. Wind speed during sea breeze is approximately 10 km/h and during land breeze it is about 5 km/h up to fetch length of 15 to 30 km.

(e) Thunderstorms

A thunderstorm is a violent short-lived storm accompanied by lightning and thunder with strong gusty winds. Some thunderstorms are accompanied by swirling vortices of air that become concentrated and powerful to bring tornadoes and/or hail. During thunderstorm winds gusting speed can go up to 90 km/h.

(f) Whirlwinds

Whirlwinds are similar to a tornado but are characterized by smaller diameter columnlike vortex of rapidly swirling air with eddies greater than macrolevel eddies. Sometimes dust and debris are also drawn into the whirlwind. Wind speed during a whirlwind can exceed 55 km/h.

(g) Canalized winds

Wind while passing through a deep narrow valley (canyon) with steep sides or through streets of high-rise buildings flow with high speed through the gaps. The high speed of flow of wind is experienced by the pedestrians. This type of flow around the building is termed as canalized wind.

1.4 DESIGN LOADS:

Tall buildings are designed for dead loads, live loads and occasional loads from earthquake and wind. The earthquake and wind load act laterally on the building. In tall buildings lateral load resisting system is suitably provided by the design engineer for lateral stability of the building depending upon type of construction (steel or concrete) and height of the building. Wind load may be classified as overall design load and local cladding load. The overall wind load along wind and across wind directions is summation of total pressure exerted by wind in along wind and across wind directions respectively. Design of structural members of building is made taking consideration of the overall wind load. When air flows around the building there are locations, edges and roofs, where separation of flow and formation of eddies generates high negative pressure, much in excess of the positive pressure on the center of elevation. This local pressure fluctuation varies from point to point of the surface of building. The cladding design, therefore, is strongly influenced by local pressure. Failure of exterior glass cladding and curtain walls is because of improper design for local cladding pressure. Importance of both types of wind loads in design of a building is quite obvious. It has been observed that building collapses seldom occurs due to wind forces. However, breaking of glass units from the cladding is an unpredictable occurrence due to wind. It is very hazardous for pedestrian safety. The repairing of broken glass panels in high-rise buildings poses great challenge to the maintenance workers too. As such, careful examination and assessment of both types of loads is important.

1.4.1 Method of Evaluation of Wind Load For Structural Design

Building and its structural parts are designed for wind load for the life time of the buildings envisaged. Wind load on a tall building can be determined by:

a) Analytical method

IS 875 (Part 3): 2015 provides method for evaluation of pressure force on buildings with regular shape and size and is based on the geometric properties of the building in standalone condition. Interreference effect on the principal building by nearby agglomeration of developments and topography has been taken in the code for the purpose of preliminary design only, by introducing interference factor (IF) with the advice to the designers to ascertain the IF for final design of tall buildings from literature or wind tunnel/CFD studies. [Clause 8.1, IS 875 (Part 3): 2015]

For standalone clad buildings of regular shape and size, two methods are given in IS 875 (Part 3): 2015 for determination of total wind load - Pressure Coefficient Method & Force Coefficient Method.

Design wind pressure [Clause 7.2, IS 875 (Part 3): 2015]

Wind pressure at any height $'z'\ m$ above mean ground level is obtained by

$$p_z = 0.6\, V_z^2 \qquad (Eq. 1.1)$$

where p_z = Wind pressure in N/m^2 at height $'z'\ m$.

V_z= Design wind velocity in m/s at height $'z'\ m$ and is modified from the basic wind speed for any site as

$$V_z = V_b . k_1 . k_2 . k_3 . k_4 \qquad (Eq. 1.2)$$

Where,

V_b= Basic wind speed in m/s.

k_1= Probability Factor (risk coefficient) based on probable design life of structure.

k_2= Terrain roughness (terrain category) and height of structure factor.

k_3= Topography factor above sea level for upwind slope of ground.

k_4= Importance factor for cyclonic region.

The design wind pressure in N/m^2 is obtained from

$$p_d = K_d . K_a . K_c . p_z \ (\geq 0.7 p_z) \qquad (Eq. 1.3)$$

K_d = Wind directionality factor (a factor for randomness in the directionality of wind).

K_a= Area averaging factor (area average pressure values decrease with increase in area and vice-versa).

K_c = Combination factor for frames of clad buildings.

(i) Pressure coefficient method

This is also called peak wind approach method which is a static method.

Design wind load in kN at any height $'z'm$,

$$F_d = p_d . C_{P_e} . A \qquad (Eq. 1.4)$$

Where, p_d= Design wind pressure in N/m^2 at any height $'z'\ m$

C_{P_e}= Resultant pressure coefficient on the building in wind direction as given in table 5 (Clause 7.3.3.1) of IS 875 (Part 3): 2015

A= Area normal to wind direction contributing load at height $'z'\ m.$

(ii) Force coefficient method.

Design wind load in kN at any height $'z'm,$

$$F_d = p_d.C_f.A \qquad (Eq.1.5)$$

Where, C_f is the force coefficient for clad building as per clause 7.4.2.1 of IS 875 (Part 3): 2015.

1.4.2 Prediction of Wind Load Through Model Analysis

Now a days, architectural designs of high-rise buildings, non-prismatic and irregular shapes with unique topography of each site, are innovated for different economic and aesthetic reasons making the wind load analysis difficult through analytical method. For such buildings, prediction of air flow around buildings and the resulting pressure distribution around them to find out overall total design loads and the local cladding loads are estimated experimentally on scaled down model in either wind tunnel or through CFD techniques. Full scale measurements are also conducted on the existing buildings for comparison with modeled experiments in the wind tunnel or through CFD for improvements in the practices and techniques involved in the model analysis.

Although wind tunnels are useful tools for analysis of wind induced pressure distribution for design of buildings many researchers and designers do not have access of it. In the past decades, with the development of computer hardware and software CFD has undergone a successful transition from an emerging field into a gradually recognized field for study of wind environment on structures. CFD study can be performed economically with much more speed than wind tunnel testing. It is also possible to simulate full scale model in CFD. However, the accuracy and reliability of CFD simulations are of concern and solution verification and validation studies are essential. Therefore, wind tunnel experiments remain indispensable compared to computational wind engineering (CWE).

Nevertheless, with the recent advancement in the algorithm in software like ANSYS, computational study has now become widely accepted, especially for the preliminary investigation and conceptual finalization of geometry and orientation of the building.

1.4.3 Evaluation of Wind Load For Cladding Units

Most of the earlier building designs were carried out for structural stability of buildings on the basis of overall peak pressure and base bending moments. However, now-a-days higher and higher buildings are coming up. As such, local peak suction pressures have also gained significance as they are important from the view point of cladding/glazing design.

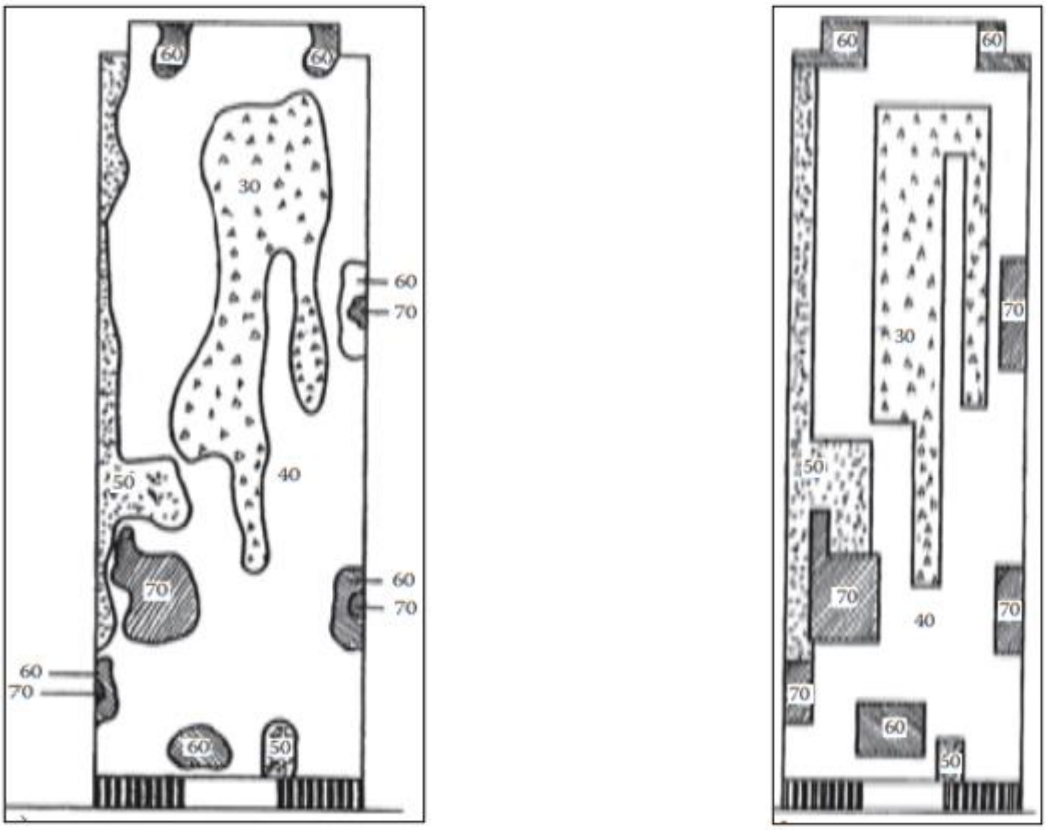

(a) Pressure Contour Diagram

(b) Block Pressure Diagram

Figure 1. 8 : Pressure Contour Diagram and Block Pressure Diagram

(Source: CRC Press, Tall Building Design)

It is important to mention that most of the cladding/glazing materials are manufactured with good quality control to resist peak wind load. They generally fail due to local peak suction pressure. Their repair/maintenance becomes a challenging task in tall buildings. As such appropriate and economical design of cladding/glazing units and their support systems are a point of concern to the designers. This can be achieved by preparing block pressure diagrams on the basis of pressure contour diagrams for equivalent static loads (Figure 1.8).

1.5 STRUCTURAL SYSTEMS

The function of structural system or systems in a tall building is to resist load acting on the structure. The structural systems are the combinations of elements which resist the load together and behaves as integrated part with each other. For lateral loads such as wind load and earthquake load the structural systems are provided with such system which resist the lateral sway of the building. This can be achieved through various systems depending upon the need and requirement. Some of them are discussed herein.

1.5.1 Braced Frame Structures

Braced frame structural system is provided in steel buildings as they relatively lack in lateral stiffness compared to concrete building. The steel frames are braced between the frames to carry the lateral loads in the form of axial tension or compression and eventually transfer them to foundation. Different types of lateral bracing systems are:

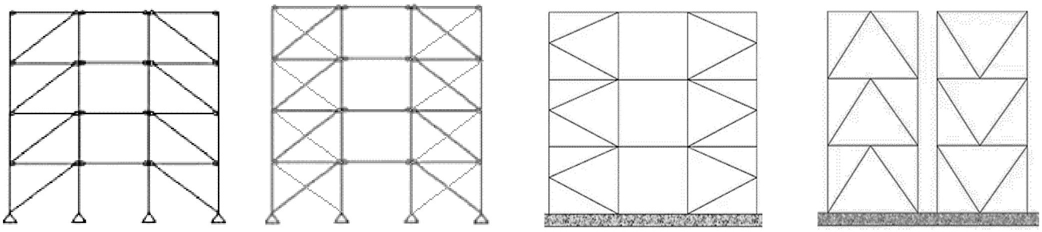

Single Diagonals *Cross Bracing* *K Bracing* *V Bracing*

Figure 1. 9: Different Types of Braced Framed Structures

1.5.2 Rigid Frame Structures

This type of frame structure provides stability to the building and is one of the most widely used structural forms. Beams and columns are connected with rigid joints as moment-resisting connections in this structural system. In rigid frame rectangular structures, more clear space at floor levels is achieved, providing more freedom to plan the floor layouts.

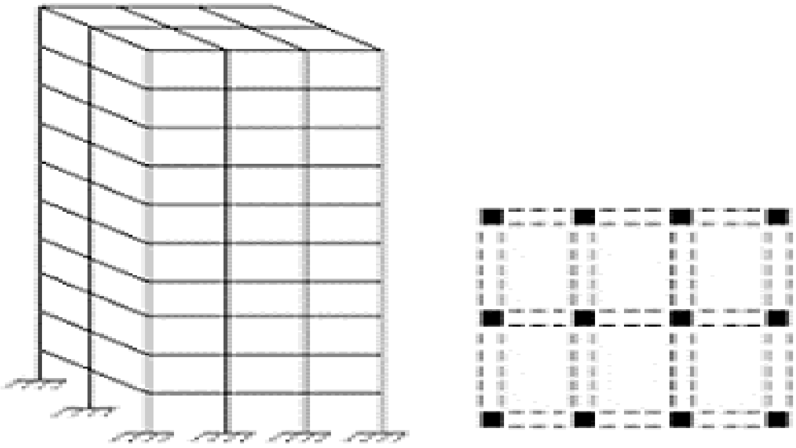

Figure 1. 10: Rigid Framed Structure

1.5.3 Shear Wall Structures

A shear wall is a vertical concrete wall in tall buildings with fixity at the base that can resist lateral forces acting on it. Adequate cross-sectional area is given to provide required stiffness to resist the lateral forces. Shear walls are constructed as lift walls, staircase core walls, partition walls, etc where it can be continued from base to roof.

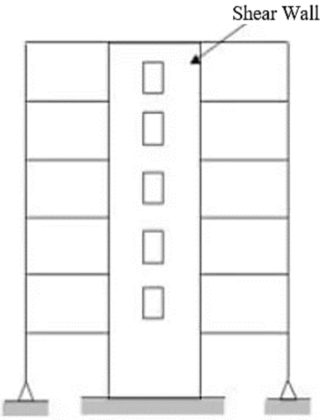

Figure 1. 11: Shear Wall Structure

1.5.4 Framed Tube Structures

Framed tube structure is a system where a building is designed to act like a cantilever hollow system perpendicular to the ground. Columns at a spacing of 2 - 4 m with deep beams along the perimeter create a tube structure. Fazlur Rahman Khan, an

American- Bangladeshi architect and structural engineer, defined the framed tube structure as "*a three-dimensional space structure composed of three, four, or possibly more frames, braced frames, or shear walls, joined at or near their edges to form a vertical tube-like structural system capable of resisting lateral forces in any direction by cantilevering from the foundation".*

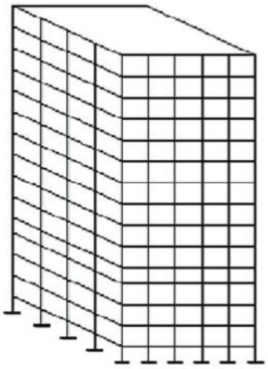

Figure 1. 12: Framed Tube Structure

1.5.5 Tube-in-Tube or Hull-Core Structures

This type of structure consists of a core tube inside the main exterior structural system for utilities such as lifts and staircases. The inner and outer tube act horizontally to withstand lateral loads. This system is one step forward from the frame tube structure discussed above.

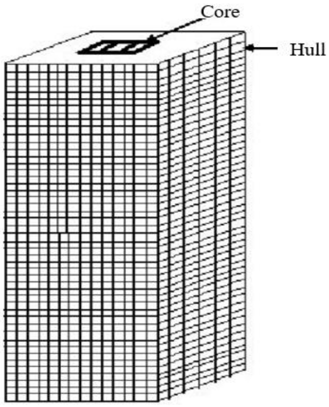

Figure 1. 13: Hull- Core Structure

1.5.6 Bundled Tube Structures

In this type of structural system several individual tubes are connected with each other to resist lateral loads. This structural form can be used in tallest structures.

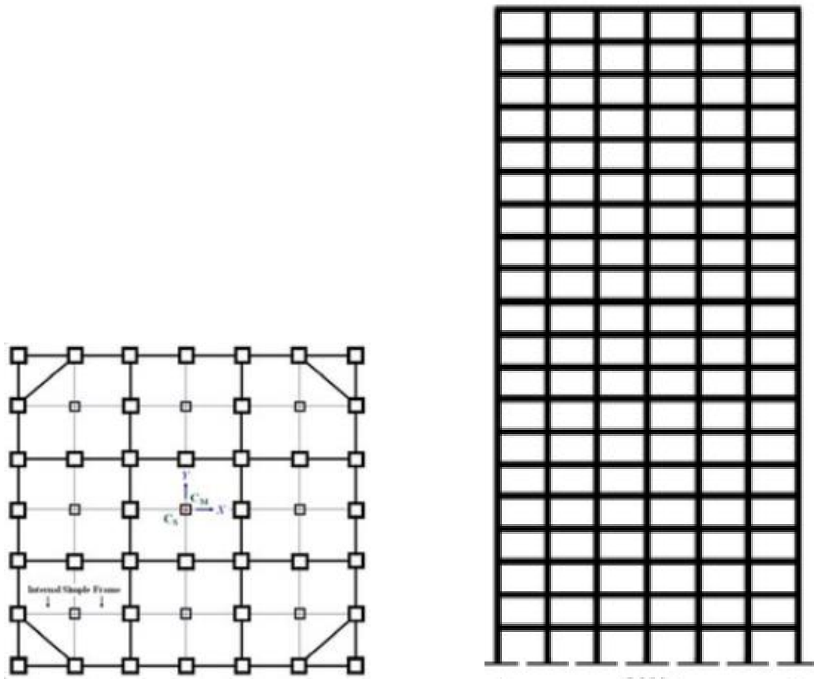

Figure 1. 14: Bundled Tube Structure

(Plan by Masoud Azhdarifar)

1.5.7 Braced Tube Structures

They are similar to the framed tube structure but, the columns are spaced farther apart and the lateral load resisting capability is compensated with tying the columns with steel bracing in steel structure and concrete shear walls in concrete structures. The internal space arrangements are not affected in such structural system. However, it could affect the arrangement of the facade and windows.

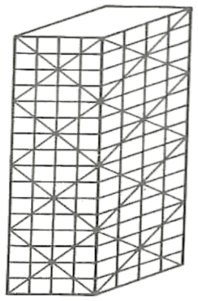

Figure 1. 15: Braced Tube Structure

1.5.8 Outrigger Braced Structures

A deep beam or a concrete wall constructed between the successive levels or steel trusses constructed between successive levels can be considered as an outrigger braced structure. It connects the core and the perimeter. This system is more commonly used in buildings having repetitive floors.

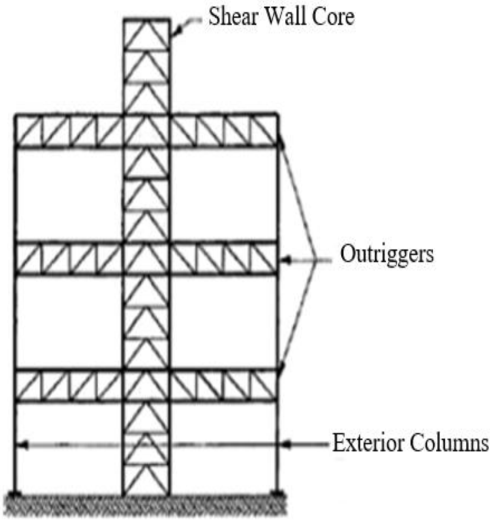

Figure 1. 16: Outrigger-Braced Structures

1.5.9 Hybrid Structures

Hybrid structures are different combinations, discussed above, in different part of the structure. A hybrid system is used for slender buildings where single structural system cannot provide adequate strength and stiffness.

1.6 CLASSIFICATION OF STRUCTURAL SYSTEM:

Fazlur Rahman Khan (1973), a structural engineer and an architect, who initiated important structural systems for skyscrapers and is considered the "father of tubular designs" for high-rises buildings, classified structural systems for tall building as shown in Figure 1.18 (a) and (b) [https://structille.com/2020/12/structural-systems-for-tall-buildings.html].

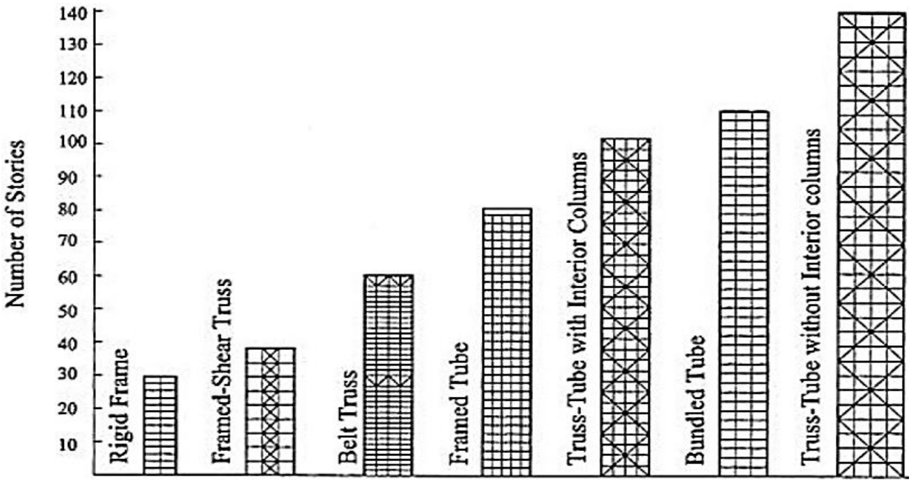

(a): Steel Building Structural Systems

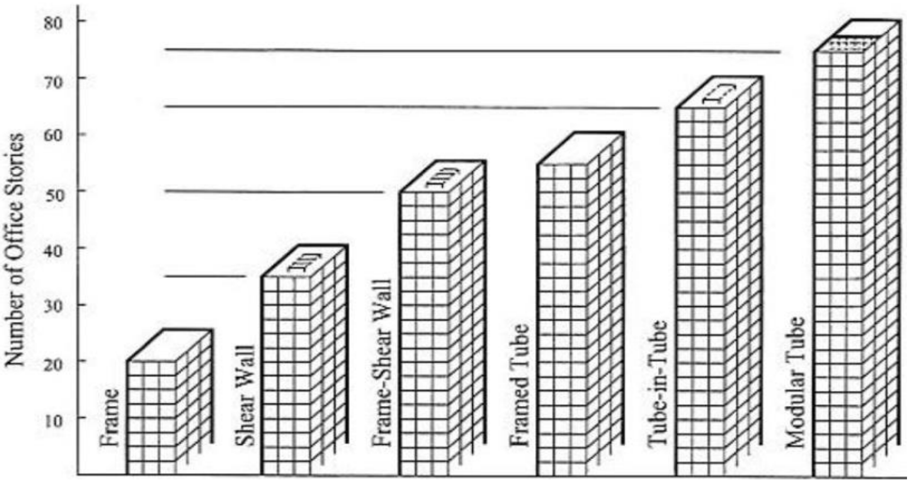

(b): Concrete Building Structural Systems

Figure 1. 17: Classification of tall Building Structural systems

1.7 FLOW AROUND BUILDING

As wind impinges on the windward face of a building, airflow separates from the leading edges generating recirculation zones over side and downwind surfaces extending into downwind wake. On the windward wall, surface flow patterns are largely influenced by approach wind characteristics. In the ABL condition the mean wind speed approaching the building increases with height above ground level. Higher wind speed at roof level causes a larger pressure on the upper part of the wall than near the ground. This leads to downwash on the lower one half to two-third of the building height. On the upper one quarter to one third of the building height, wind flow is directed upward (upwash) over the roof. For a building of height Z, three or more times width W of the upwind face, an intermediate stagnation zone can exist between upwash and downwash region where surface streamlines pass horizontally around the building. Downwash on the lower surface of the upwind face separates from the surface before it reaches the ground level and moves upwind to form a vortex. This generates high velocity near the ground. This ground level upwind vortex is carried around the sides of the model in U-shape. Part of the downwash on the lower surface of the upwind face exhibits a region of low average velocity and high turbulence and creates a flow recirculation region extending to some distance downwind. If the building has sufficient length L in the downwind direction, flow reattaches to the building and may generate two distinct regions of separated recirculation of flow of the building and its wake. A typical diagram of flow separation and recirculation of wind is shown in Figure 1.19 and that of the wind flow pattern around the building in Figure 1.20. Position of the stagnation zone and the resulting upwind vortex is governed by incident wind shear. For stronger shear wind the stagnation zone is higher up on the upwind face. Effect of turbulence on the stagnation zone is lesser than the shear. However, more turbulence reduces the size of the upwind vortex. The flow reattaches and generates region of wake where flow recirculation with high turbulence and low velocity is created. The flow recirculation continuously hits the sides and downwind surfaces with high turbulence creating suction on the faces.

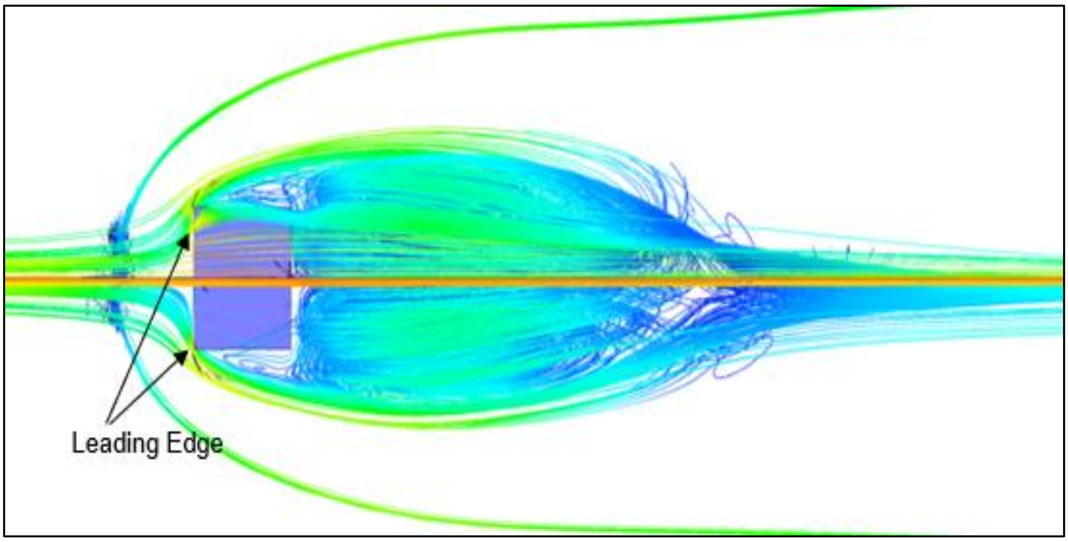

Figure 1. 18: Flow Separation and Recirculation

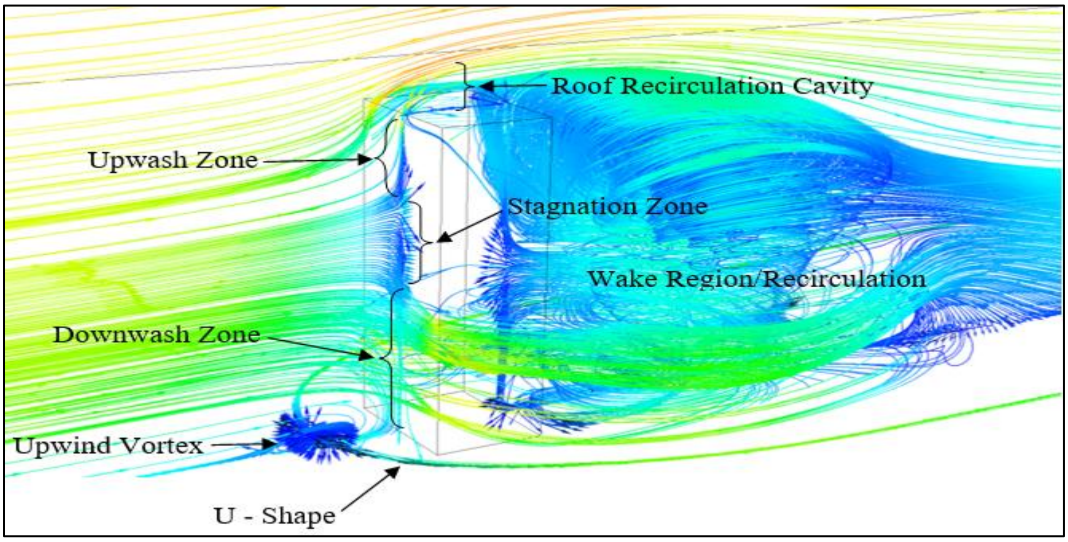

Figure 1. 19: Flow Pattern Around the Building

1.8 OBJECTIVE AND SCOPE OF THE PRESENT STUDY:

The main objective of the present work is to present a qualitative difference of wind flow pattern and estimation of flow of wind in terms of static pressure or coefficient of pressure values, base shear forces and base moments on different shapes of tall buildings, shown in Figure 1.21 to Figure 1.26, having same plan area of 300 sqm each and equal height of 50 m through application of numerical simulation using ANSYS (CFX) solver. ANSYS (CFX) is a finite element modelling CFD program of pressure-based solver technology suitable for low Mach No. (Ma) fluid flow.

The wind flow pattern around any bluff body is caused by a combination of upwind shear wind flow (boundary layer flow) and turbulence. Wind flow pattern and the static pressure depend on the shape and size of the bluff body for a similar wind flow characteristic. The quality assurance of the numerical application is closely related to the user's knowledge of wind behavior on bluff body and how carefully the natural wind condition is replicated during the simulation for prediction of flow around the body. In the present study, models have been subjected to an inflow of homogeneous steady state boundary layer flow with 5 % turbulence intensity to provide gustiness effect. In the study, partial differential equation of time averaged continuity, momentum and transport equations using the standard $k - \varepsilon$ model has been used. Since, oblique wind also causes a varied wind flow pattern around the body, as well as varying impact pressure on the surfaces, obliqueness of wind flow in clockwise direction is provided by rotating the model about its vertical axis in anticlockwise direction from 0° to 90° @ 15° for the symmetrical models having symmetricity about both axes in plan and from 0° to 180° @ 15° for the symmetrical models having symmetricity about only one axis in plan. However, due to paucity of space, discussion has been presented @ 30° wind incidence angles for both the cases.

The reliability and suitability of the numerical approach has been checked by comparing the coefficient of pressure generated for the two orthogonal direction (0° & 90°) on the faces of the rectangular model with those of different international wind codes and previous experimental results. As the result of numerical simulation depends upon the discretization of the domain and the model, the discretization of the domain, ground and the model faces were finalized with variable number of elements sizes for the domain, ground and the model surfaces. A finer meshing is required on the faces of the model and ground to map the high gradient region in the flow field close to them. For smooth transition of the mapped data from the domain to the model face, inflation was provided. Similar grid arrangements were made for all the models.

Even though, different approaches in the numerical simulation can be formulated for specific problems that may vary substantially in their approach, the approach presented herein is useful for preliminary stage of conceptualizing any project with confidence.

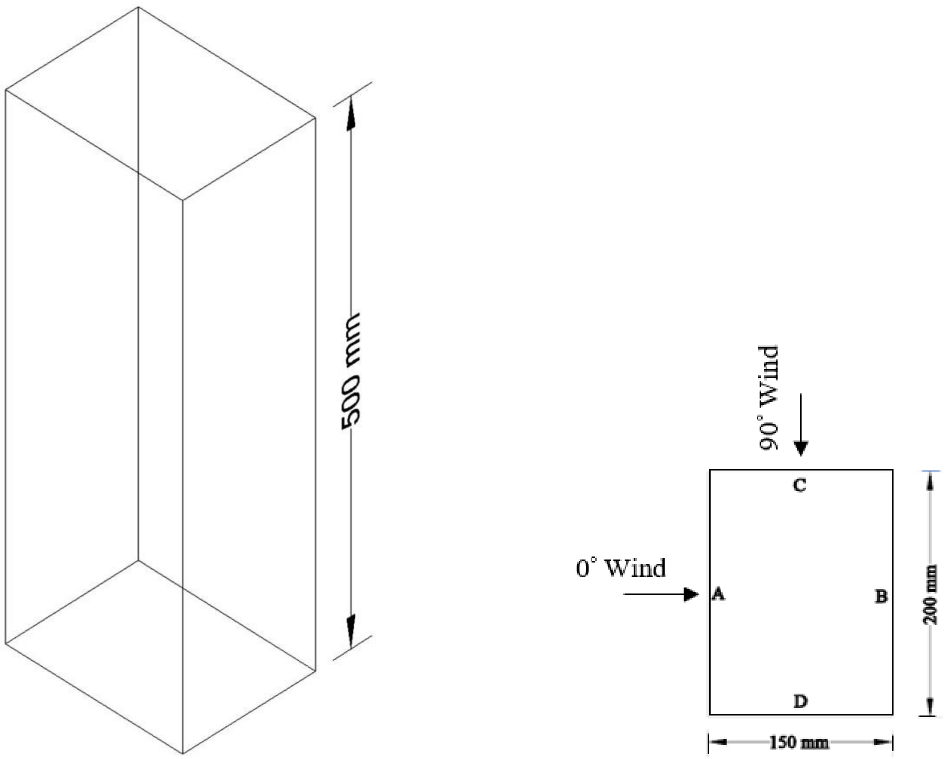

(a): Isometric View (b): Plan

Figure 1. 20: Rectangular Shape Model

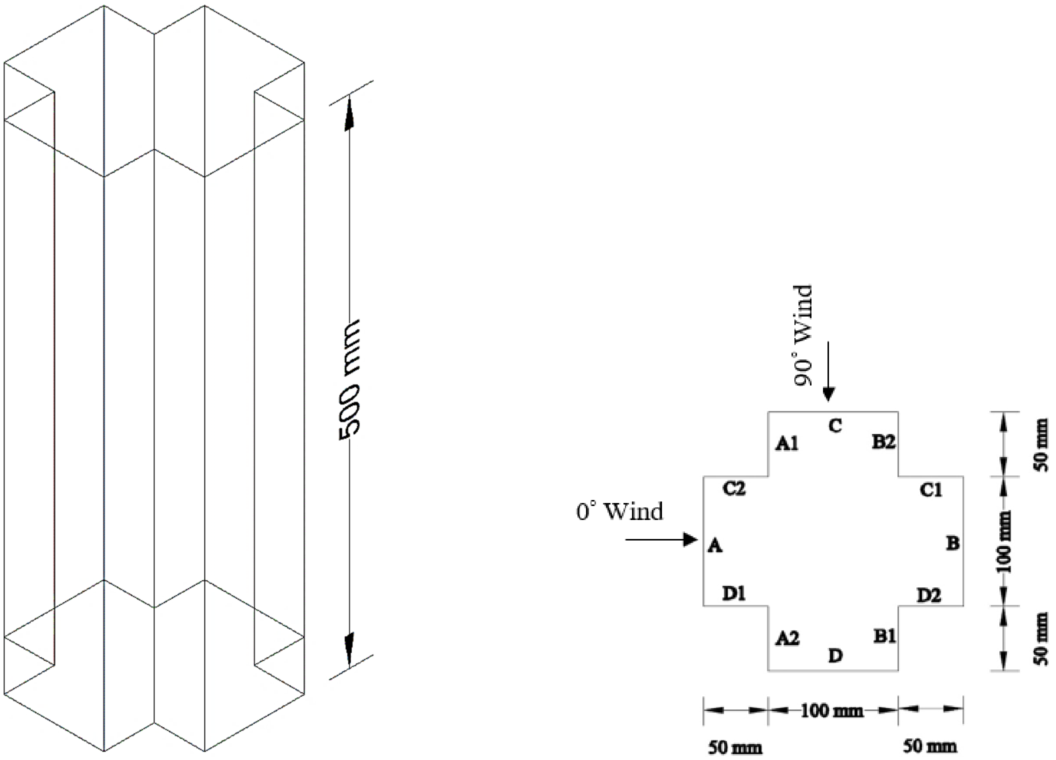

(a): Isometric View *(b): Plan*

Figure 1. 21: Plus Shape Model

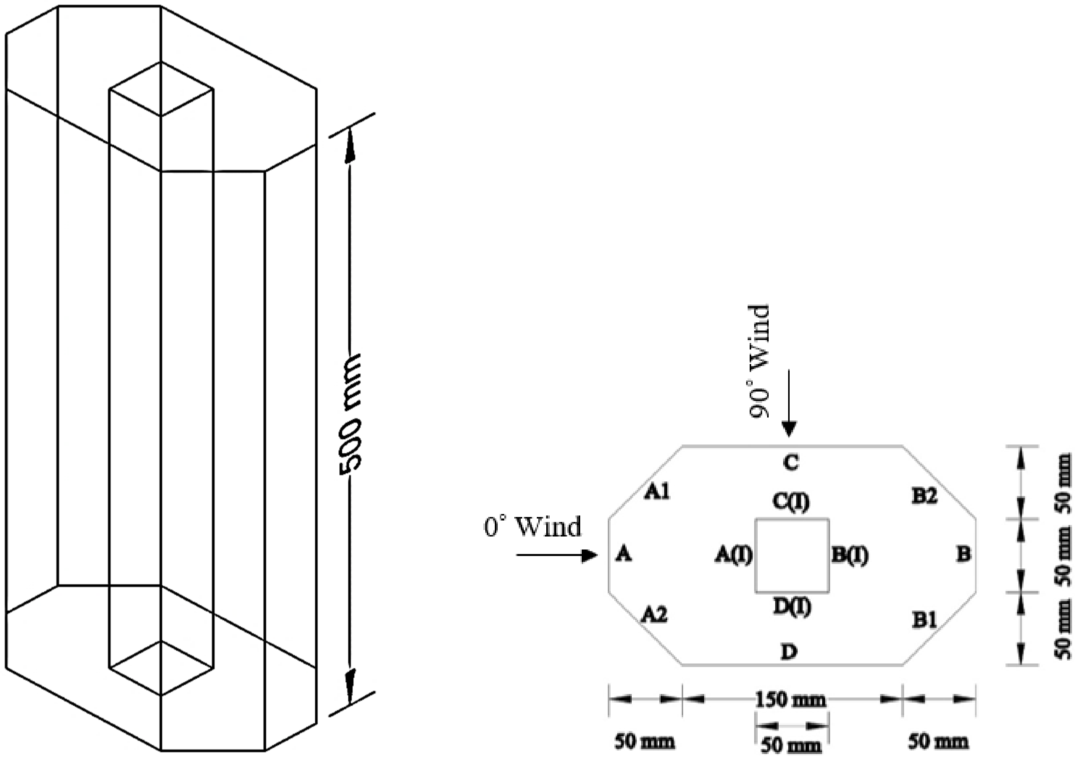

(a): Isometric View *(b): Plan*

Figure 1. 22: Octagonal-Oval Shape Model

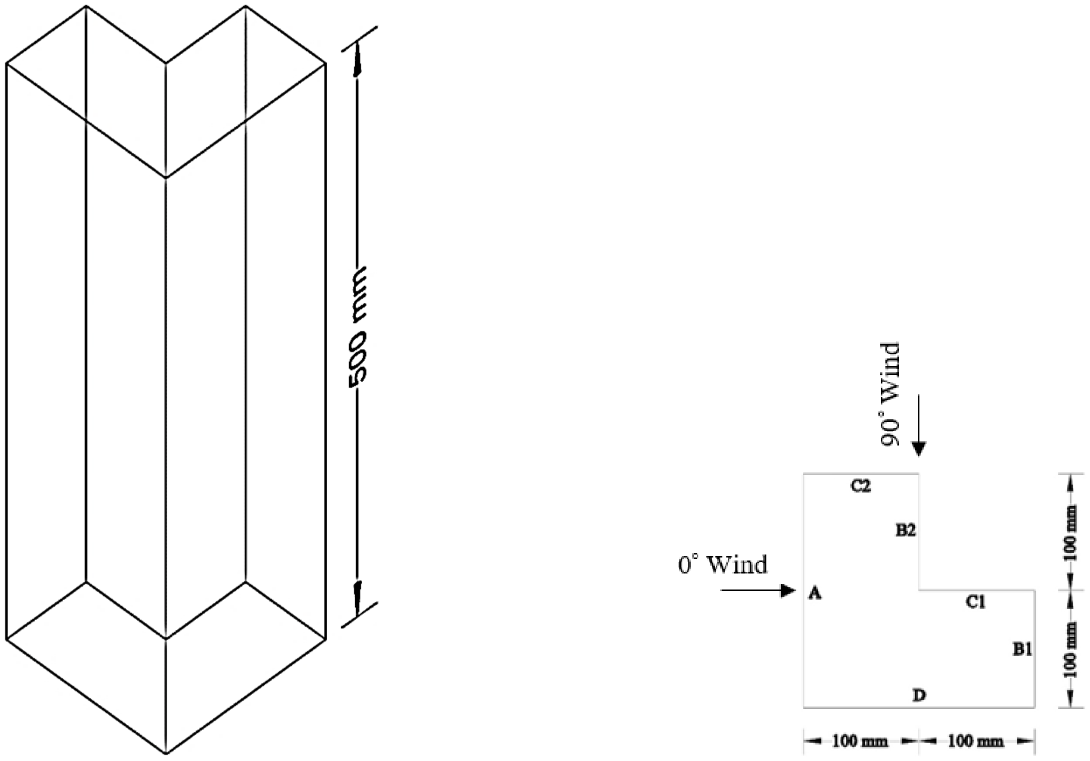

(a): Isometric View *(b): Plan*

Figure 1. 23: L- Shape Model

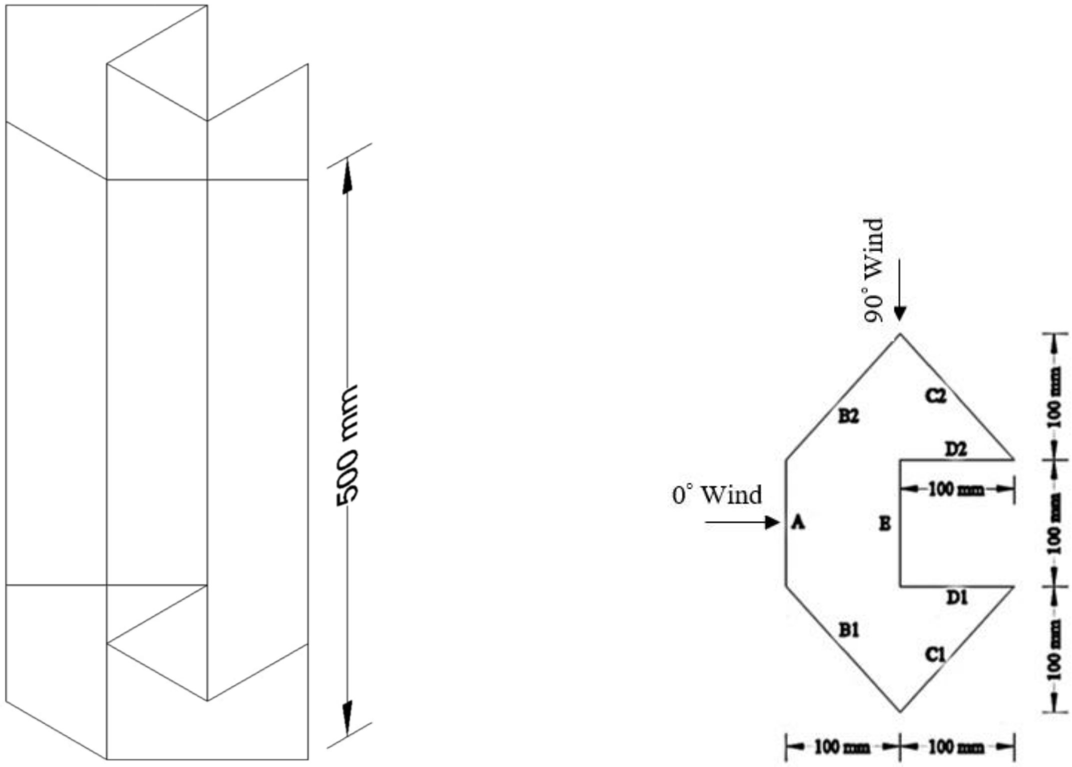

(a): Isometric View *(b): Plan*

Figure 1. 24: Diamond C- Shape Model

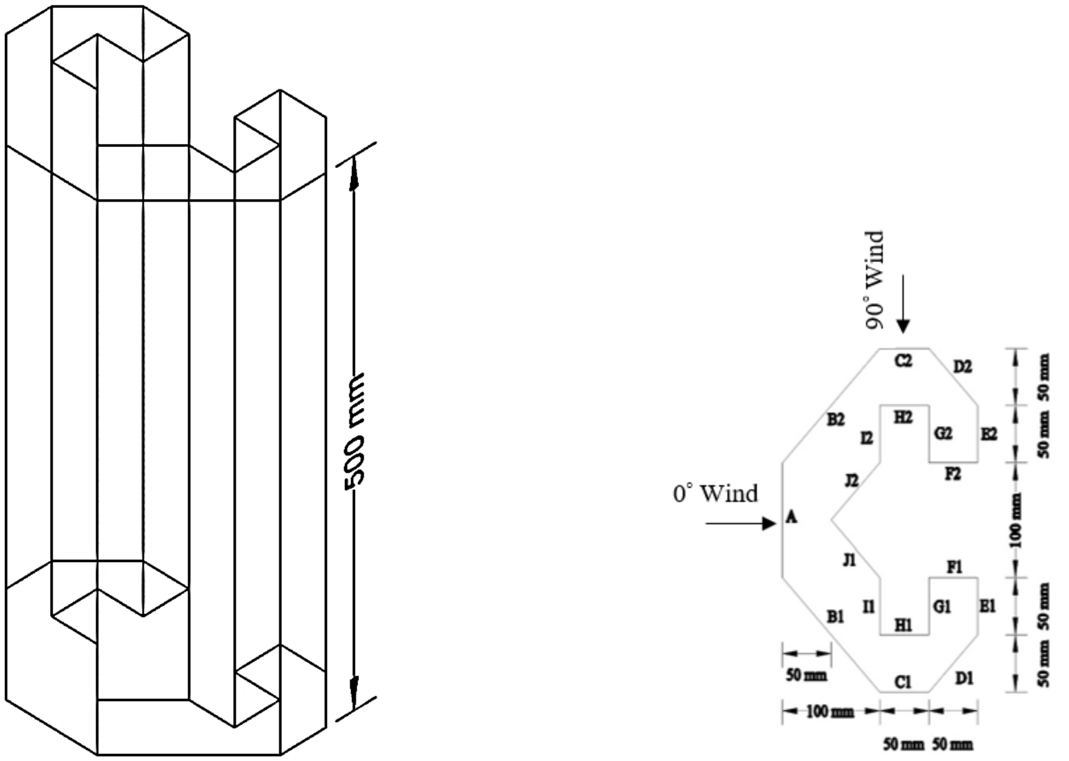

(a): Isometric View *(b): Plan*

Figure 1. 25: Wrench C-Shape Model

1.9 ORGANIZATION OF THE THESIS:

The thesis is presented in 7 chapters. In the introduction, which is the 1st chapter, a brief discussion is given about the type of winds encountered by tall buildings, classification of tall buildings around the globe and type of structures used to construct tall buildings, method of analytical calculation of wind loads for structural design of regular shaped clad buildings as per IS 875 (Part 3): 2015 and the design approach to safeguard cladding and its fixing units from failure during high wind, pattern of wind around any bluff body; and the objective and scope of the current study.

In chapter 2, a brief information about wind pressure distributions around building envelope has been discussed. Provisions of various international codes and standards for wind analysis on buildings have also been briefly discussed. Also, various research works related to flow modeling have been presented.

Details of the technique adopted for the geometric modelling and numerical simulation in ANSYS (CFX) solver has been presented in chapter 3. Validation and verification of results have also been discussed.

In chapter 4, coefficients of pressure on faces of the models having symmetry about both axes are discussed along with flow patterns around the model envelope for different wind incidence angles. The same for models having symmetry about one axis are discussed separately in chapter 5.

In chapter 6, base shear, base moment and twisting coefficients for different models with symmetry about both axes and symmetry about one axis are compared.

Conclusion of the whole study has been summarized in chapter 7. The list of references gone through during the present study is presented in the references. In the last papers published in various Scopus/SCI/ESCI journals and international conferences are presented.

CHAPTER 2 LITERATURE REVIEW

2.1 GENERAL:

In this chapter a brief information about wind pressure distribution on buildings in context of the research performed in the present study has been provided. A comparative difference in various codes/standard followed in various countries have been presented and discussed. Literature review on various research contributions in the field of wind engineering have also been presented. These are followed by detailed review of the work on buildings conducted through CFD analysis.

2.2 BRIEF INFORMATION:

Gustave Eiffel (1832 - 1923) during his aerodynamic experiments from Eiffel tower found that the air resistance of a body is closely related to the square of the air speed. He, later developed first wind tunnel and tested the air foil characteristics for early aeronautical designs. On the basis of his observations, concept of coefficient of pressure originated which is independent of size for similar shapes. The principle of geometric similarity and independence of Reynold's number for sharp edged bodies was established.

Baines (1963) [3] was the first to demonstrate how wind velocity distribution and fluid pressure affect tall buildings. He demonstrated the isobars of the mean wind pressure on the windward face to be positive and suction pressures on the side faces, lee face and roof top of a tall square structure.

Wind flow is a complex phenomenon. It exerts differential velocity and pressure around any bluff body obstructing its flow. Though, for ease in analysis a time averaged steady state of uniform flow condition is taken, wind does not flow with a uniform speed and in a constant direction. Wind speed consists of series of turbulences in the form of gusts which vary both in magnitude and direction very widely. Even the phenomenon of uniform and steady wind is not that much simple.

As such, the surface area of a building is subjected to randomly changing pressure due to anisotropic three-dimensional behaviour of wind velocity. At a given time, the pressure on the surface of a building is somewhere at peak and somewhere lull. Also, at a given point, the pressure can be high at one moment and seconds later be nothing. These variations of pressure on the surface of the building are addressed through coefficient of pressure, a dimensionless entity, which is a time and area averaging representation of pressure on the surface. This is used to know design pressures for varying area size on similar prototype building surfaces.

The load produced by the wind depends upon the form of the structure too. It becomes more relevant with the increase in height of the structure due to atmospheric boundary layer (ABL) effect and in high rise buildings due to cantilever effect with fixed end at the ground. When wind is at rest, the normal atmospheric pressure is acting all around any structure and the load on the structure is balanced in totality. As the wind starts its motion, at some point on the obstacle there is increase in pressure and at others decrease in pressure. The magnitude of these changes is usually less than 2 % of the normal pressure. These change in pressure distribution on the structure are converted into a single load/force as a resultant of them during the analysis of the structure. The maximum increase in pressure produced by the wind is $\frac{1}{2}\rho u^2$, where ρ is the density of air and u the wind speed encountered by the obstacle/structure. This is termed as velocity pressure. The change in pressure differences is mathematically expressed as coefficient of pressure (C_{Pe}) which is ratio of the pressure difference to the velocity pressure represented as:

$$C_{Pe} = \frac{\Delta P}{\frac{1}{2}\rho u^2} \qquad (Eq. 2.1)$$

Where, $\Delta P = P - P_o$, P being pressure at any point and P_o the reference pressure (atmospheric pressure in natural wind condition), ρ is density of air and u, the uniform velocity field.

In a boundary layer flow where gradient velocity field exists, it is not so simple to define the uniform velocity field. As such, u is chosen at a reference height or velocity at the level at which the pressure is measured. All C_{Pe} values in the present study have been worked out based on the velocity at the level of the top of the model where velocity is found to be maximum. In this way points corresponding to the maximum C_{Pe} can be identified where wind pressure is maximum. Although the maximum increase in pressure at any point is equal to the velocity pressure, the fluctuating wind produces pressure decrease of greater amount at any point on the surface and hence the average wind pressure resulting from the surface distribution over an area becomes greater than the velocity pressure.

The resulting coefficient is more or less independent of the wind speed and scale of model [4]. It is, however, influenced by form of the building, wind flow direction, terrain roughness, and proximity to other structures [5]. For structural design purpose we can find C_{Pe} values for regular plan shape buildings in different international codes/standards, but the data are available only for orthogonal directions of wind flow. The value of pressure coefficients given in the codes are adopted after a wide range of data fitting for different wind zones and seasonal variations of wind characteristics of the respective countries. For occupational safety of the buildings these pressure coefficient values are on conservative side and structural design based on these values provides uneconomical construction.

For various unconventional architectural shapes, now a days being used by architects, the values of C_{Pe} are either presumed from the codes which are relatively inaccurate, being approximated from the shapes given in codes, or from wind tunnel experiments, which are costly and time consuming. By the invent of complex computational facilities available now -a days, it is possible to know C_{Pe} values on buildings of different architectural shapes through computer simulation. Simulation also helps us to make decision earlier not only in the conceptual phase or in the schematic design phase but it enables us to predict physical behavior of our building and we can explore more design versions in a faster amount of time in parallel. The architects make different designs which are challenging for structural engineers. Many architects are interested for higher performance of buildings in terms of energy consumptions, less cost, keeping deadline, lower failure risk and engineers are interested in higher confidence and less failure risk. As such, early design decisions help us to do all of that with different stake holders and for different benefits. Flow simulation can help us for taking all these early decisions.

It has also been reported from various studies that magnitude of peak pressure and peak suction on faces of irregular shape buildings depends largely on the wind direction.

As such, experiments must be performed for every individual structure of irregular shape and for different angles of wind attack to appropriately investigate the critical value of the wind stresses to incorporate it in the structural design.

2.3 INFORMATION FROM VARIOUS INTERNATIONAL CODES

Various countries where tall buildings are in existence or being constructed have their own wind codes and standards for design of such buildings. Some of them are the American Society of Civil Engineers/Structural Engineering Institute (ASCE/SEI 7-10), the Australian and New-Zealand Standard (AS/NZS 1170.2:2011- Part 2), the Indian Standard [IS 875 (Part 3): 2015], Architectural Institute of Japan Recommendations (AIJ), the China National Standard (GB 50009-2001), the European Standard [EN1991-1-4:2005+A:2010 (E)], National Building Code of Canada (NBCC) and many more.

Wind codes of different countries vary and are not mutually compatible because each code is developed based on data of the natural wind phenomenon occurring in different regions of the country, their serviceability requirements and life span of the structure. The experimental data base generated in the country on different type of structures provides continual amendments in the codes.

The difference in wind force calculation from different codes is mainly due to different averaging times for basic wind velocity (V_b) and wind-induced response, reference height of building (h_{ref}), terrain exposure category (EC) etc. For the structural design relevant standards of wind loads are referred to predict the pressure on free standing regular shaped buildings such as square or rectangular cross sections for various range of side ratios and aspect ratios. However, all codes recommend use of wind tunnel tests/CFD simulations for the design of tall buildings with complex geometries and; for interference conditions to envisage wind loads. Some of the major differences in different codes and standards have been referenced in Table 2.1.

Table 2. 1: Comparison Between different Codes/Standards

Variable/Code	**ASCE**	**AS/NZS**	**IS**	**AIJ**	**CNS**	**EN**	**NBCC**
$\boldsymbol{V_b}$	3-sec gust speed	3-sec gust speed	3-sec gust speed	10-min mean speed	10-min mean speed	10-min mean speed	Hourly mean speed
Wind induced response	Hourly	10-min	10-min	10-min	10-min	10-min	Hourly
$\boldsymbol{h_{ref}}$	0.6 h	h	h	h	h	0.6 h	h
Where, h is the height of building							
Exposure category ($\boldsymbol{EC}$)	4 EC	4 EC	4 EC	5 EC	4 EC	5 EC	3 EC
Velocity Profile	Power Law	Logarithmic Law	Power Law	Power Law	Power Law	Logarithmic Law	Power Law

However, the general expression for static wind pressures (p_z) along wind direction on the building for all the codes/standards is same as described in section 1.4.1. Static wind load on the building is then determined by combining the wind pressures acting on the upwind and downwind surfaces of the building in wind direction. Moments are determined by multiplying the load at a given height by the corresponding height. Base shear forces and moments are then determined by the summation of the loads and moments at each floor level. The across wind response on the building and twisting moment differs significantly when calculated from different codes/standards.

The codes and standards usually predict wind forces that are higher than what is occurring in nature due to their generalized specifications. However, in wind tunnel experiments, testing is done on a specific structure for specific wind related phenomenon and hence, lower design loads are found than that calculated from wind load codes. Moreover, all codes/standards recommend that tall and irregular plan shaped buildings be designed using wind tunnel experiments.

2.4 RECENT RESEARCH WORKS

2.4.1 Wind Tunnel Studies

Davenport (1971) [6]: Aerodynamic and structural response on six building models were evaluated in atmospheric boundary layer by the researcher experimentally in a wind tunnel. It was reported that rectangular and triangular models (sharp edges models) observed highest peak deflection whereas, deflection for circular building model was the lowest.

Bailey et al. (1985) [7]: Dynamic response on a square tall building was studied due to neighboring similar tall building in wind tunnel under low turbulence and strong wind environments. It was reported that the dynamic load on the interfering building increased as much as 4.4 times of isolated condition; whereas that on the principal building downstream the interfering building increased up to 3.2 due to resonant buffeting. Along wind and across wind force spectra and a number of wake spectra have also been presented in the paper with their explanations. Authors have cautioned for careful consideration of interference excitation.

Kwok et al. (1987) [8]: Effect of aerodynamic devices were tested in a wind tunnel on tall buildings. It was reported that suitable small fins or vented fins to a square tower triggered an increase in the along-wind response while cross wind response was reduced for a limited range of reduction in velocities. For the use of slotted corners, it was reported to be useful in tall buildings as significant reductions in both the along-wind and cross-wind responses were observed.

Balendra et al. (1988) [9]: Investigated the along-wind response of a slender vertical structure in a turbulent boundary layer flow by using a time domain method. The methodology employs the classical flexural beam theory. The proposed model predicts the peak responses by using the predetermined drag coefficients of a given geometric shape. The predicted peak responses are found reasonably well with the published experimental results for a square building and a rectangular one.

Dionne and Davenport (1988) [10]: A relationship between wind induced static and fatigue failure of structures have been developed by the researchers using gust factor, mean strength and endurance limit of fatigue in a probabilistic manner.

Dutton and Isyumov (1990) [11]: Studied the aerodynamically modified slender tall building of square cross-section by introducing openings or gaps in the upper half of the building to reduce vortex shedding process. It was concluded that across-wind excitation can be reduced substantially by providing building gaps in the upper half of the building. With small gaps of 4%, the decrease in across-wind excitation was shown to be the maximum.

Hayashida and Iwasa (1990) [12]**:** The researchers have studied the effect of eight building plan shapes on aerodynamic forces and displacement response for super tall buildings (600 m) having equal plan area, equal height and equal density in a wind tunnel boundary layer flow for varying velocities. Out of the eight models, five were of their basic shapes and three models were with corner cut shapes of the basic. Out of the various plan shapes, it was observed that the displacement responses of square models (basic and corner cut) are more than the other models of Y shapes, triangular, circular and square corner rounded. The triangular models displayed the minimum response.

Hayashida et al. (1992) [13]**:** Aerodynamic characteristics of the super high rise (600 m) building shapes in plan greatly influence the vibration caused by the vortex in across wind direction of buildings. The authors have studied this effect in their research from the results obtained from wind forces using force balance, the response using a dynamic motion model and wind pressure on the faces of eight building shapes in plan – square, Y-shape, triangular, circular corner cut square, corner cut y-shape, corner cut triangular and rounded corner square have been presented.

Cermak and Cochran (1992) [14]**:** Mean wind speed with 10% turbulence intensity on a model scale of 1:100 was studied by reproducing 0.5 m deep atmospheric surface layer (ASL) in the boundary layer wind tunnel. ASL is the lowest 100 m thick atmospheric boundary layer (ABL). Flow properties were compared to field measurements taken on a 48.8-m high tower at the Texas Tech University (TTU). It was reported that integral length scales of the longitudinal turbulence component were in agreement with the field scales up to a height of about 20 m. However, above this height it did not match the field scales.

Beneke and Kwok (1993) [15]: Wind Torsional forces were investigated in a boundary layer wind tunnel on rectangular, triangular, diamond, and D-shaped building models of constant aspect ratio, density and damping with varying velocities, terrain roughness categories and wind incidence angles. Torsional response was found to vary substantially with change in cross sections. Triangular shaped model produced torsional response far in excess of any other model. Lesser torsional response was found on diamond shape and D-shaped models.

Zhang et. al. (1994)[16]**:** Torsional response of a tall square building due to interference of adjoining buildings of different shapes and sizes was studied by the researcher. Wind tunnel experiment on square tall building model using an aeroelastic test rig designed for pure torsional vibration was conducted. Four types of interfering models were used on upstream and downstream sides of the square building model under test at individual locations. It was found that the interference factor (IF) for torsional response was enhanced up to 2.2 when the vortex shedding from the interfering building caused a resonance with the natural frequency of the square building under investigation.

Yin Wang et al. (1996) [17]: Studied the scale effect in wind tunnel modelling and reported that the best similitude of the velocity profile in the wind tunnel test can be obtained if it is in the range of 200 – 400. They studied scale effect of pressure on the surface of a bluff body and reported that as long as the roughness height is correctly modelled, correct results of the pressure coefficients on the building surface can be obtained even if the scale ratio of the body size is not correctly selected. If the scale ratio of roughness height or boundary layer thickness is differently selected, a 10-15% larger difference in the pressure coefficient on the windward face of building model may be obtained. The negative pressure coefficients on the lee surface and side surfaces are slightly smaller.

Kawai (1998) [18]: Wind tunnel tests were conducted on corner modified square and rectangular models to investigate the effects of corner cut, recession and roundness on vortex-induced excitation and galloping oscillation. It was reported that small corner cuts and recession are beneficial in preventing the aeroelastic instabilities, but large corner cut and recession promote instability at low flow velocity.

Li et al. 2000 [19]**:** The researchers have presented the result of full-scale measurement on a super tall building (370 mtr.) in Hong Kong for wind speed, wind direction and wind induced acceleration responses including the data for two Typhoons namely Sally and Kent. The data were compared with that from wind tunnel results in boundary layer. It was concluded that the full-scale measurement acceleration for the two directions; along wind and across wind; were similar to those obtained in aero elastic models in wind tunnel tests.

Kim and You (2002) [20]: Study of dynamic responses of wind loads on tapered tall building were studied by the authors. Building models with tapering ratio of 5%, 10%, 15% and one basic building model of a square cross-section were tested in an open wind tunnel under two typical boundary layers representing suburban (power-law exponent of 0.15 with about 10% turbulence intensity at the top level of the model) and urban flow environment (power-law exponent a of 0.30 with about 15% turbulence intensity at the top level of the model). The effect of wind direction was also studied. It was observed that a tapering effect along height reduces wind-induced excitations. In suburban flow environment it is well-organized than that in urban flow environment. The effect was more significant in across wind direction than that in along wind direction.

Zhou et al. (2002) [21]: This paper presents a comprehensive assessment and comparison of the along wind loads on tall buildings recommended by major international codes and standards viz ASCE 7-98 (United States), AS1170.2-89 (Australia), NBC-1995 (Canada), RLB-AIJ-1993 (Japan), and Eurocode-1993 (Europe). Despite the fact that the ‘‘gust loading factor (GLF)” approach is common to all codes and standards, large scatter exists among along wind loads predicted by them. It is reported that the scatter in the predicted wind loads is primarily due to the variations in the definition of wind flow characteristics in the respective codes and standards.

Thepmongkorn et al. (2002) [22]: In the presence of a square building of comparable height upstream and downstream, the researchers studied interference effects on the

CAARC standard tall building model. The results indicated that when the interfering building was located diagonally upstream, the base moments were greatly enhanced.

Zhou et al. (2003) [23]: On the basis of data collected on High Frequency Force Balance (HFFB) in a wind tunnel on various isolated tall buildings of different side ratio, aspect ratio and turbulence characteristics, authors have presented non dimensional aerodynamic load database and analysis procedure for across wind and torsional response of tall buildings under the action of wind load.

Gu et.al. (2004) [24]: Tested 15 tall building models of rectangular and square and 14 corner modified cross sectional models with different side ratio and aspect ratio using HFFB technique in a wind tunnel and generated formulas for the power spectra of across wind dynamic force, base moment coefficient and shear force coefficient. Validation of the formula was also done by comparing the response of aeroelastic model of a square building with that of the computed results.

Ning Lin et al. (2005) [25]**:** The authors have studied the effect of local wind forces on nine isolated square & rectangular tall building models in a wind tunnel study in term of mean and RMS force coefficient, power spectral density, span wise cross correlation and span wise coherence. The results were compared with the information available in the literature and other database (UND). The effect of local wind forces on three parameters; elevation, aspect ratio and side ratio; were discussed. It was observed that between side ratios 0.63 to 3 influence of wind load was more.

Liang et al. (2005) [26]: This work presents simplified empirical formulae for estimating the across-wind dynamic responses of rectangular tall buildings. In a boundary layer wind tunnel research, simultaneous pressure measurements were made from a series of tall building models with varying side and aspect ratios. The applicability and correctness of the empirical formulae were investigated by comparing the across-wind responses from the formulas with results obtained from the wind tunnel tests. These formulas, it was suggested, might be utilized as an alternative for designing and analyzing wind impacts on rectangular tall structures.

Gupta et al. (2007): Wind tunnel study in boundary layer was studied by the authors for pressure distributions on four tall building models of different heights and unusual shapes in plan placed in close proximity with each other. For different incident angles between 0^0 to 360^0, pressure distributions for design wind speed were taken with Electronic Pressure Scanners (EPS) with 32 port each and a high speed 16-bit data acquisition system. Pressure measurements were taken along the heights of the models as well as across the cross sections for later use in design of the buildings.

Lim and Bienkiewicz (2007) [27]: HFFB approach was used to investigate the influence of structural coupling on the wind-induced response of twin-tall building models connected by a skybridge. The wind generated roof top acceleration was compared between the coupled and uncoupled twin building models. The results showed that structural coupling of twin buildings in close proximity can lessen the negative dynamic interference effects. The author suggested that structural connection be taken into account while designing twin tall structures for wind loads.

Zhao and Lam (2008) [28]**:** The researchers investigated interference effects on wind load fluctuations and dynamic building response on five square tall buildings arranged in an L- shape and T-shaped pattern in the wind tunnel. Separation of models were kept as half and a quarter width. They reported significant modifications of wind loads as compared with the isolated single building case. Sheltering effect was also observed on the inner buildings. The increase in wind loads was found on the most upwind corner building at oblique angle of wind attack. Negative drag force was also reported.

Fu et al. (2008) [29]: Presented field measurement results of boundary layer wind characteristics over typical open country and urban terrain for two super tall buildings. Full scale measurement results were compared with wind tunnel test data. It was observed that the results were within adequate limits (20%-25%) of acceptance.

Kim and Kanda (2010) [30]**:** The authors have studied the mechanism of aerodynamic force reduction for high rise building models tapered in plan with different tapering ratio and set-backed model in a wind tunnel test for varying boundary layers of urban and suburban flow conditions. It was concluded that the tapering or set-backed models reduces the mean drag force coefficient and fluctuating lift force coefficient in proportion of the tapering ratio. It was also concluded that the effectiveness in reducing the fluctuating lift force is more in set-backed model than that of in tapered models.

Ming and Yong (2011) [31]**:** A series of wind tunnel tests on typical tall building and structure models (121 general building models and dozens of real tall structure models) for different cross-section shapes, including square, rectangular, triangle, Y-type, polygon, L-type, corner-modified square cross-section shape, ladder shape, twin-tower shape, and with continuous contraction cross section were conducted by the researchers for cross wind loads. On the basis of their experiments across wind aerodynamic forces and across-wind aerodynamic damping database were created. A theoretical method of across-wind equivalent static wind loads was proposed which was adopted in the revised Chinese Code. It was revealed that when the short sides (l/b > 2, where, l is the larger dimension and b, the smaller dimension of building plan) of rectangular buildings are windward, the separated flow from the leading edges of the building reattaches at the side walls.

Lam et. al. (2011) [32]**:** The authors have studied the interference effects of row of square shape of tall buildings in two arrangements: parallel side–by–side pattern and diamond diagonal – by – diagonal pattern. In addition to the interference effects on the mean and fluctuating wind loads, wind induced dynamic responses for both the patterns were studied using the approach of Envelop Interference Factor (EIF) introduced by Xie and Gu (2007) [33]. For a row of parallel pattern, they have identified different ranges of EIF at five different wind incident angles caused by upwind interference and flow channeling. It has been suggested that the Peak Envelop Interference Factor (PEIF) can be used as a rough indicator for maximum interference for design purposes for rows of flow pattern. For the diamond pattern, the mean wind loads at most of the wind incident angles have been found to be magnified significantly.

Hui et al. (2012) [34]**:** Mutual interference effect on local peak pressure on two high rise buildings with different shapes has been investigated in this study by wind tunnel experiments. The results show that building shapes and wind directions have great influence on the values of local maximum and minimum local peak pressure due to interference effect. The minimum peak pressure was found to be 40 % higher than in the isolated condition.

Amin and Ahuja (2011a) [35]: Two L-shaped and two T-shaped models of same cross-sectional area and height but different limb lengths were studied for wind effect under boundary layer in a WT test under varying wind incidence angles. It is reported that both, the cross-sectional shapes and limb lengths affects the distribution of wind pressure on faces of the models. But, the magnitude of peak pressure and peak suction on the faces depends largely on the wind direction.

Amin and Ahuja (2011a) [36]: Two L-shaped and two T-shaped models of same cross-sectional area and height but different limb lengths were studied by the researchers for wind effect under boundary layer in wind tunnel test under varying wind incidence angles. It is reported that both, the cross-sectional shapes and limb lengths affect the distribution of wind pressure on faces of the models. But, the magnitude of peak pressure and peak suction of the faces depends largely on the wind direction.

Amin and Ahuja (2011) [37]: Mean interference of close proximity rectangular buildings placed in L and T plan shaped building were studied in wind tunnel for boundary layer wind flow over extended wind angles and comparison was made with the response of similar buildings in isolation. Interference effects was reported to be influenced by the position and arrangements of models and wind incidence angles.

Hui et al. (2013) [38] The authors have carried out experiments in wind tunnel for varied wind incident angles to find the interference effects of two high-rises rectangular buildings with parallel and perpendicular arrangements. The Width: Depth: Height ratio of the buildings was kept as 3:1:4. In the study, the interference effect for the largest positive and smallest negative peak pressure been discussed for both the parallel as well as perpendicular arrangements of interfering building and principal building. It has been found that the interference effect is largely dependent upon the configuration of the buildings and wind directions. For the largest peak pressure, the interfering building did not have a significant effect. But, for the smallest negative peak pressure, the interfering building did have a very strong effect. The edges and corners of the building were found to be sensitive to the negative pressures. So far as the wind direction is concerned, the interference effect was found to be stronger when the configuration of the interfering building was at upstream of the principal building. The author also conducted flow visualization experiments. It was found that the shear layer from the interfering building on upstream side caused high positive and negative pressures on the principal building on downstream side. But, in some configurations the downstream building also affected the upstream building.

Wong and lam (2013) [39]: investigated modification in the wind-induced loading and the dynamic response in tall buildings of H-shape of same square envelope and height to breadth ratio of 6. Building response was estimated by measuring fluctuating wind forces and moments on the building models by HFFB. Substantial reduction of across-wind excitations of the buildings for normal wind incidence was observed due to presence of recessed cavity.

Tanaka et al. (2013) [40]: Wind tunnel studies were used to illustrate aerodynamic properties of several irregular plan shaped tall buildings.

Raj and Ahuja (2013) [41]: Experimental study was carried out on rigid models of tall buildings of square and plus shaped cross sections having similar floor area but with varying recessed limbs of plus shape models in a boundary layer wind flow. It was reported that wind incidence angles as well as cross sectional shapes influence the structural parameters of base shear, base moments and torsional moments due to wind load.

Amin and Ahuja (2013) [42]: Experimental study in WT was conducted on a rectangular models of same plan area and height but different side ratios varying between 0.25 to 4 and pressure coefficient values on the faces were evaluated to understand the effect of side ratio at varied wind incidence angle from 0°to 90°@ 15°. It was reported that wind pressure distribution is greatly affected by side ratio on side walls and lee walls but, partially effected on upwind walls at 0° wind incidence angle. However, peak pressure and peak suction are affected by the change in wind angle and not on side ratio.

Amin and Ahuja (2013) [43]: The authors have studied the effect of side ratio on wind induced pressure distribution (mean, max. & Min.) on rectangular buildings having same plan area & height in a wind tunnel for varied wind incident angles from 0^0 to 90^0 with an interval of 15^0. It was observed that the magnitude of peak pressure and peak suction were unaffected by change of side ratio of same plan area at windward wall, but they do have considerable effect on leeward wall & sidewalls. However, wind incident angles affect the value of peak pressure & peak suction.

Li et al. 2013 [44]**:** Study of wind pressure distribution on isolated tall buildings and also surrounded by other buildings with a rigid model in wind tunnel test were done by the authors. It was yielded that the mean and fluctuating wind pressure coefficients on the windward side of the target building decreased at the bottom due to wake interference of the upstream building and that on side walls and leeward wall of target building are changed significantly due to the shielding effect and channeling effect of interfering buildings as compared to the isolated case.

Hui et al. (2013) [45]: Studied the interference effects on local peak pressures for different wind incidence angles and height ratios of interfering building. The results showed that the peak suction increased with higher height ratio. Oblique arrangement of the buildings generates severe peak negative pressure compared to series configuration.

Bandi et al. (2013) [46]: Effect of edge configurations on aerodynamic modifications on different configured models (tri corner cut, square corner cut, chamfered, clover, tapered, setback, setback & rotate, helical, tapered and helical etc.) among the cross-sectional shapes of triangular, square, pentagon, hexagon, octagon, dodecagon, circular of same height and volume were studied in a wind tunnel. It was reported that cross-sectional shapes and twist angles affect the peak pressures.

Yi and Li (2015) [47]**:** The authors have studied the fluctuating forces and pressure on a super tall building model in wind tunnel tests for isolated and surrounded conditions for different wind directions. The model tests were compared with full scale measurement during typhoons. It was reported that interference of upwind building significantly reduced the mean wind loads on target building downstream of wind. It was also reported that the interference effects of the surrounding buildings reduced the wind force coefficient on the target building below the height of 0.6 of target building. The natural frequency of the building was observed to be of lower from the wind tunnel test compared to field measurements. As such, the wind tunnel test can provide reasonable predictions of the structural resonant response.

Yu et al. (2015) [48]**:** The Envelope Interference Factor (EIF) of the base torsion response was studied by the researchers for different breadth ratio, height ratio, reduced velocity and turbulent intensity in high rise buildings in tandem. The mechanism and occurrence condition of wake-vortex exited resonance were also studied. The position of buildings for maximum and minimum EIF for torsional interference and its relative increase or decrease with height ratio and width ratio were found out. It was concluded that the interference effect should be focused when height ratio, $H_r \geq 1.0$. It was also observed that the wake- vortex induced resonance occurs at breadth ratio, $B_r = 0.4$ and that due to effect of vortex shedding from interfering building on the downstream principal building the turbulence intensity decreases thereby increasing the torsional amplification intensity.

Kwon et al. (2015) [49]: Based on ASCE 7 standard investigation of wind load factors such as wind speed, natural frequency & damping ratio of building were carried out by the researchers on flexible building in both along wind and across wind directions. They revealed that wind load factors defined in ASCE 7 based on rigid buildings are not adequate for flexible buildings on either wind directions. In across wind direction terrain type plays an important role on wind load factors.

Ahlawat and Ahuja (2015) [50]: On a T plan shaped tall building structural parameters (base shear, overturning moment and torsional moment) were evaluated in a boundary layer wind tunnel in isolated as well as interfering condition with similar model placed in tandem and side by side, both at varied spacings. Study was conducted at different wind incidence angles. It is reported that the position of the interfering building can change wind load on principal building considerably.

Goliya et al. (2016) [51]**:** The authors have critically reviewed the available literature of last two decades on interference effects on tall buildings. They have reported that in different situations, such as height of the interfering building, aspect ratio in rectangular buildings, terrain category, pattern and arrangements of interfering buildings and angle of wind incidence, interference response may increase or decrease significantly on the principal building.

Pundhir and Barde (2016) [52]**:** They have studied wind pressure effect on a model of 280 m tall building for different relative position of interfering building placed upstream of flow in series and at 45° angle from the centerline of the principal building. They have reported that when interfering building is very close to the principal building towards windward side, all surfaces of the principal building are under negative pressure. With the increase in the spacing, negative pressure on windward face changes to positive pressure and negative pressures on surfaces on downwind side of the building increases approaching to the value in isolated condition.

Chauhan and Ahuja (2017) [53]**:** Studied height effect of two rectangular interfering buildings on wind pressure distribution on the faces of a third rectangular building put in sequence through wind tunnel experiment. The interfering buildings heights were varied simultaneously and also height of only one interfering building was varied. In the first case, it is reported that, with increase in height of the interfering buildings the pressure distribution on the principal building tend to attain the same pressure as in the case of isolated building. Whereas, in the second case with the increase in height of the interfering building uniform pressure on the upwind side face is achieved. Suction on the lee face is enhanced and become more and more uniform. On the side faces large variation is observed.

Chauhan and Ahuja (2017) [54]**:** The effect of interference on the principal building was studied through wind tunnel test by the researchers under varying heights and orientations of the interfering buildings put closely on the upwind side. The heights of both the interfering buildings were varied whereas, orientation of only one of them was varied. Presence of interfering building was reported not to be always advantageous to the main building. Shielding effect and wind load on the principal building was seen to increase with the increase in the height of the interfering building. Negative drag force was observed in cases where large part of the principal building was shielded. Torsion in the principal building was amplified as high as ten times of that in the isolated case.

Nagar et al. (2020) [55]: Mean wind pressure distribution around square and H shape tall buildings were investigated in WT experiments for different wind directions. Interference effects with similar building model placed at various positions were also investigated. It is reported that higher wind load is subjected on H plan shape model than on square model. Also, that full blockage condition of interference produced more suction on the principal building.

Gu et al. (2020) [56]: Studied sixteen 2D prisms with varying chamfered corners and side ratios in a low-turbulence flow in wind tunnel. Effects of chamfered corners on the pressure coefficients and correlation coefficients on the side faces were studied by measuring wind pressure on the surfaces of models. Due to existence of chamfered corners, reattachment of separated flow did not occur to the side faces. The inclusion of chamfered corners reduces the mean and RMS values of drag and lift coefficients considerably.

Khanduri et al. (2000) [57]: The shielding effect of interfering building of varying heights on wind loads on the principal building was explored by the researchers. When two buildings were put in tandem, mean loads were found to be reduced while fluctuating loads were increased, according to the findings.

Lamberti et al. (2020) [58]: On a high-rise building, mean and RMS peak pressure coefficients were explored through high-resolution pressure measurements in the wind tunnel. Study was carried out in two types of wind tunnels: open circuit and closed circuit; and the results were compared. The local and face average pressure coefficients probability density functions were provided, and their significance in cladding design was explored.

Li et al. (2021) [59]: Presented the effects of area extreme pressure (AEP) reduction on large-scale cladding based on wind tunnel test data. Wind tunnel tests were conducted and based on the tests data, the effects of AEP reduction on the large-scale cladding were determined using area average and moving average methods. It was revealed that the AEP reduction at the edges and corners is more significant than the interior of the roof.

Pal et al. (2021) [60]: Investigated the impact of interference for a 100 percent blockage by shuffling square plan and triangular shape building models of similar plan area in front-to-front and back-to-back topology. The shape and position of interfering models was reported to have a considerable impact on the pressure and force created on the main building model.

Pal et al. (2021b) [61]: Reported on comparative research of wind-induced mutual interference on twin square and fish plan building models located at a distance of 10% of the height of the building with various combinations of front and rear orientation in a wind tunnel and presented induced pressure and base shear on the models.

Franek and Macák (2021) [62]**:** Studied the interference effect on external local peak pressure coefficients between two high-rise buildings, elliptical in cross section, in boundary layer wind tunnel test. Various arrangements of models, which were derived from the breadth ratio, were investigated. The peak value of the external wind pressure coefficient for a stand-alone model was measured and compared with the peak value in the case of interference. The measurements showed that the wind loads on buildings in a close vicinity are considerably different from those on a stand-alone building. The interference effects significantly affect negative pressure zones. The optimal and critical arrangements of buildings were evaluated.

Nagar et al. (2021) [63]: Studied the effects of interference between two plus-plan shaped high-rise structures in tandem and oblique positions creating no blockage, full blockage and half blockage conditions. It is reported that substantial increase or decrease in wind load on the buildings facades depends on relative position of the buildings. It was revealed that interreference effect on the main building resulted in reduced wind load on the faces at full blockage condition compared to half blockage or no blockage.

2.4.2 CFD Studies

Castro and Robins (1977) [64]: Studied flow around a surface mounted cube in uniform and atmospheric boundary layer flow. Mean surface pressure and velocity field around the model envelope were studied. In the turbulent boundary layer gradient flow velocity above 0.5 m/s at the model height, no Reynold number effect was seen for R_e above 4×10^3 based on cube height and velocity at that height. However, they suggested to take all pressure measurements at R_e greater than 10^5. It was also reported that addition of upstream turbulence and shear considerably reduces the size of the wake cavity zone.

Germi and Kalehsar (1992) [65]: Interference effect of two CAARC building models was studied for anisotropic wind flow condition using LES turbulence model in CFD. Mean and fluctuating coefficients of drag and lift forces and pressure coefficient were investigated. The aerodynamic response was compared with isolated condition of CAARC building. It was revealed that for most of the locations of interfering building the mean drag coefficient on the principal building was lowered due to shielding effect but fluctuating lift coefficient was widely dependent upon the location of interfering building.

Richards and Hoxey (1993) [66]: Have discussed suitable boundary conditions for computational wind engineering (CFD) using the $(k-\varepsilon)$ turbulence model for appropriate modelling of surface boundary layer. Comparing their findings with the full-scale measurement at Silsoe, Bedfordshire, England they suggested that along with suitable set of boundary conditions, a wind flow which produce homogeneous velocity and turbulence profiles should be modelled.

Zhang et al. (1993) [67]**:** Using $(k-\varepsilon)$ model on TEMPEST on a cubical building model, effect of shear and turbulence were studied by the researchers in four categories: shear + turbulence, shear + no turbulence, uniform flow + turbulence and uniform flow + no turbulence. Results were compared with experimental study of [64] and observed that the mean flow fields were predicted reasonably well by simulation. It was also reported that different meshing grid cell sizes produced identical mean velocity field around the building envelope.

Stathopoulos (1993) [68]: Examined the wind induced pressure for L shape of low-rise model through computational method for normal wind direction. The results between computational and experimental study were reported to be with good agreement between the two.

Bazeos and Beskos (1996) [69]: Have developed a mathematical model combining the ‘Boundary element method’ and ‘Discrete vortex method’ to determine wind pressure distribution around the cross section of an isolated or group of rigid buildings of arbitrary cross section to determine the torsional moment. The method is useful for design engineers. It gives an approximate but a rapid result with satisfactory accuracy, especially for isolated condition. In a group of buildings and when their shapes are complicated the selection of flow separation points are difficult – this is the only disadvantage in the method.

Cowan et al. (1997) [70]**:** This paper presents some aspects of computational numerical solutions around buildings. It has been shown that the results dependent on the mesh design, spatial discretization scheme and turbulence model. A solution obtained with the standard $(k - \varepsilon)$ turbulence model on a course grid can give results closer to experimental laboratory data than obtained with improved element size of the meshing grid.
Tominaga et al. (2006) [71]: The authors have presented a guideline for the use of CFD in environmental wind engineering around buildings after investigating influence of many computational conditions for different wind flow situations. The guideline for appropriate prediction and assessment of wind flow around the buildings has been developed using high Reynolds (R_e) number RANS turbulence model.

Reiter (2008) [72]: Studied wind pedestrian comfort level on a number of CFD simulations on FLUENT software. The relative error in speed between average speed simulated and average speed measured in the wind tunnel test was found to be within 20 % at all sections.

Cheng et al. (2009) [73]: Studied wind flow in the recessed cavity of a H shape tall building using CFD. The flow between the cavity and outside the cavity for different aspect ratio were studied. The flow within the cavity was found to be neither simply a cross flow nor a stagnation flow. It is reported that the flow pattern was complex within the cavity and dependent upon height and formation of two circulation vortices inside the cavity.

Montazeri et al. (2012) [74]: Wind comfort at the new façade concept balconies on high rise buildings were studied by the authors by performing steady Reynolds Averaged Navier Stokes (RANS) CFD simulation with realizable $(k - \varepsilon)$ turbulence model. The new façade concept consists of two layers of balcony façade. The first inner layer is the traditional façade and the second layer is staggered semi open permanent glass façade which shields the balconies from the wind. It was shown that the new façade concept is very effective for human wind comfort level at the balconies.

Pradeep et al. (2013) [75]: A model case study of Jamieson Place, Calgary Canada which is a 38-storey building was conducted for wind forces through ANSYS (CFX). The data was imported to structural model in SAP 2000 for structural analysis added with earthquake ground motion. It was suggested that high rise buildings should be designed for critical wind load and then checked for earthquake load.

Chakraborty and Dalui (2013) [76]: Mean wind pressure on a square plan shaped model was studied on CFD package of ANSYS (FLUENT) solver for 0˚, 30˚ and 45˚ wind incidence angles and comparison of coefficient of pressure for normal wind incidence angle was made with the provision of IS: 875 –1987 (Part 3).

Kheyari and Dalui (2014) [77]: Analytical study on ANSYS (CFX) was carried out at different wind angles on a rectangular model for interference effect due to another upstream rectangular model similar in plan area. Different aspect ratio of interfering and principal building models was gradually varied from 1:5 to 5:5. Validation of the work was carried out by comparing the pressure coefficient of the principal building in isolated condition with IS:875 (part-3)-1987. It was revealed that the wind load on main building depends upon the aspect ratio of both the principal and interfering models and wind directions as well.

Bhattacharyya et al. (2014) [78]: Pressure distribution on faces of symmetrical E plan shape tall building for varied wind angles from 0° to 180° @ 30° was investigated using ANSYS (CFX) software and in open circuit wind tunnel too. Mean pressure coefficient and pressure contour on faces of the model from both were found to be in good agreement with previous experimental results.

Verma et al. (2015) [79]**:** Studied wind effect on a regular octagonal shaped building model by numerical simulation through ANSYS (Fluent) and adopted second order steady state solution with pressure - velocity coupling approach. Validation of the atmospheric boundary layer was done by putting a mathematical equation at the inlet as user's defined function. The mathematical equation was developed through C programming from the wind tunnel experimental data conducted in the closed-circuit wind tunnel at the Department of Civil Engineering, Indian Institute of Technology Roorkee, Roorkee. Mean area average wind pressures on the faces of the building models have been presented for varying wind incident of 0º, 15º and 30º.

Paul and Dalui (2016) [80]**:** In this paper the authors have discussed their study of force coefficients and pressure coefficients for different surfaces of Z-plan shaped tall building using ANSYS (CFX) for wind incident angles 0^0 – 150^0 with an increment of 15^0. It has been reported that the force coefficient (C_f) along the windward direction is maximum for wind incident angle of 15^0 and in the across wind direction it is maximum for wind incident angle of 60^0. From the frictional flow separation and generation of vortices in the wake region due to combination of positive pressure on the windward faces and negative pressure in the leeward sides it has been shown that the structure is undergoing deflection.

Kar and Dalui (2016) [81]: Wind pressure variations on octagonal plan shape building model in isolated and interfering conditions from three square building models placed at different locations away between 0.4 to 2 of height of octagonal building using ANSYS (CFX) were studied. Effect of shielding and channeling on the octagonal building model due the interfering buildings models have also been presented in the form of Interference Factor (IF) and IF contours.

Dalui and Paul (2016) [82]: Wind induced response in along and across direction of wind were studied and compared between a regular Z plan shaped and another by varying the position of limbs of Z plan shaped model through ANSYS (CFX). Unsteady vortices in the wake region were observed. Force coefficients in along and across wind directions for the models have also been discussed for different wind angles.

Bairagi and Dalui (2017) [83]: A plus plan shape building model was studied for wind response and compared with angular cross plan shaped building by varying the internal angles between the limbs of plus shape building. Study by numerical analysis was carried out with help of ANSYS (CFX) for varied wind angles. Wind force in along direction of wind was observed to be less in cross shaped building compared to regular plus shape building.

Mukherjee and Bairagi (2017) [84]: Studied N plan shape building model for pressure and velocity distributions around the model using ANSYS (CFX) solver under boundary layer wind flow from 0° to 180° at 30° interval. Validation of the work was done by comparing pressure coefficient on the faces of a square plan shape model of equal area with various international codes.

Bairagi and Dalui (2018) [85]: Comparison of pressure on the faces and roofs of a square tall building and a square tall building with setback of 0.2L at 0.5H have been studied through ANSYS (CFX). It has been reported that the setback roof is subjected to 205.4% higher value of pressure than the top roof of setback model. Also, pressure on top roof of setback model has 13.64% higher value than square model for 0° wind incidence angle and 36.36 % less for 90° wind angle.

Mallick et al. (2018) [86]: Surface pressure on faces of a C-shaped building model with different aspect ratio was studied by the authors on ANSYS (Fluent) using $(k - \varepsilon)$ turbulent model for different wind incidence angles and the results were compared with experimental results. The study revealed that pressure on the model is significantly affected by its geometry, aspect ratios, and angle of incidence. They opined that the numerical technique predicted the pressure on the faces efficiently and accurately.

Sanyal and Dalui (2018) [87]: The variation in pressure on various faces of a rectangular tall building due to the presence of courtyard and opening was examined numerically through ANSYS (CFX). Unusual pressure distributions on faces were reported to be developed due to these courtyards and opening.

Alminhana et al. (2018) [88]: Numerical study was carried out on CAARC tall building models after corner modifications to study change in aerodynamic performance. Corner modifications were done as chamfered and recessed corners. Wind loads on the building models were studied using large eddy simulation (LES) turbulence method. The results were compared with previous experimental and numerical studies. Aerodynamic forces were found to be significantly reduced.

Chauhan and Ahuja (2020) [89]**:** Interference effect on a rectangular building due to another one placed to form a L-shape in plan were studied through modelling in STAAD Pro with varying height of the interfering building. It was reported that with the increase in height of the interfering building the along wind response in terms of displacement, twisting moment and bending moment are reduced whereas, these identities are increased in cross wind response.

Tomasello et al. (2019) [90]: Developed a CFD model to simulate natural ventilation in a semi open free stall barn for dairy cows (livestock building). Simulations were carried out in steady state condition. The validation of average value of data were done from on-site experimental data collected. They reported that CFD model can be relied upon.

Bairagi and Dalui (2020) [91]: Prediction of wind pressure coefficients on setback buildings for any wind incidence angles have been made using artificial neural network and fast Fourier transform from data of CFD simulations. For training of the network wind incidence angles were taken as input data and pressure coefficients on the faces for the respective wind incidence angles were taken as the output data. Error in predicted value of pressure coefficient for any random wind incidence angle from ANN was found to be 0.6 % to 2.5 %.

Sanyal and Dalui (2020a) [92]: In this study pressure distribution on chamfered and rounded corners of Y shape buildings have been presents by numerical study by ANSYS (CFX). The variation of the flow patterns, force and moment coefficient have also been evaluated. It was revealed that rounded corner shape is more efficient than the chamfered corner for wind load reduction.

Sanyal and Dalui (2020b) [93]: Shape modification such as helical, tapered, setback and recessed corner on a Y shape tall buildings have been studied numerically by ANSYS (CFX) for study of the effect on wind-induced force and distribution of pressure over the surfaces. It is reported that setback building model with rounded corner shape is most efficient but, with a disadvantage of huge suction on the corner regions.

Raj et al. (2020) [94]: Effectiveness of various bracing systems (V bracing, X bracing, single diagonal bracing and inverted V bracing) on the response of a plus shape tall building of RCC columns and beams was studied on STAAD Pro for 0°, 30° and 60° wind incidence angles. Structural parameters (base shear, base moment and twisting moment) and deflection have been presented for the prototype building without bracing and for all the bracing systems for all wind directions studied.

Raj et al. (2020) [95]: On a H shape tall building model wind effect under isolated and interference conditions by similar plan shape model at different locations through numerical simulation using ANSYS (CFX) were studied. Pressure coefficients for isolated condition, interreference conditions have been presented along with interreference factors.

Bairagi and Dalui (2021) [96]: Fluctuations in wind flow at pedestrian level for various single and double side setbacks in tall buildings at different heights have been studied by the researchers using numerical simulation. It was reported that double-side double setback buildings are efficient in reducing the velocity in upstream as well as downstream sides of the building. It was also reported that frequency of fluctuating velocity in along and across wind directions can also be controlled by setback buildings.

Mandal (2021) [97]: CFD Study of aerodynamic modifications (chamfered and rounded corner) in a U plan shape building model was done for force and pressure coefficients at varied wind directions. Validation was done by comparing the results from a research article on a U shape building model. Reduction in force coefficient was reported at the cost of increase in pressure on the modified faces. Wind load was significantly reduced on rounded corner configuration than the chamfered corner.

Sanyal and Dalui (2021) [98]: Mean pressure, force and moment coefficients of Y plan shaped tall buildings for different internal angles of limbs have been compared using ANSYS (CFX) solver using $k-\varepsilon$ and SST turbulence models. Wind tunnel results of CAARC building was used to validate the CFD models. The deviation among the pressure coefficient values for $k-\varepsilon$ and SST turbulence model and wind tunnel experiment were found to be negligible. The $k-\varepsilon$ model results were reported to be with good agreement with the experimental results.

Sanyal and Dalui (2021b) [99]: Wind pressure on a Y shape tall building for different side ratio keeping constant plan area was numerically studied by ANSYS (CFX) and expressions of force, moment and torsional coefficients were proposed.

2.4.3 Wind Tunnel & CFD Studies

Kato et al. (1997) [100]**:** The authors have provided a concept of "chained analysis" on cross ventilation of large-scale market building. In this method, using wind tunnel testing, total pressure difference between windward and leeward openings and overall cross-ventilation airflow rate are measured. Based on these values and the boundary condition of the measured values of pressure distribution, analysis of indoor flow, which cannot be carried out by wind tunnel test, is then carried out using CFD. The simulated overall airflow rate of cross ventilation is then compared with that obtained from the wind tunnel test and the reliability of the CFD is validated. Based on this "chained analysis of wind tunnel test and CFD" cross ventilation of a large indoor space is proposed.

Gomes et al. 2005 [101]**:** The researchers carried out closed circuit wind tunnel test for mean pressure distributions of L – shaped and U – shaped models in plan with different wind incident angles. The same test was carried out with a cube – shaped model for experimental validation. The pressure distribution data for L – shaped and U-shaped models found were different, especially for wind incident angles other than normal, than those expected for rectangular blocks from code. A computational Fluid Dynamics (CFD) code was used to explain the flow patterns and pressure distributions around these irregular shaped models.

Mendis et al. (2007) [102]: Studied the interreference effect as well as along wind & across wind effects for tall buildings using wind tunnel tests and CFD. It was observed that the experimental and the analytical results were within the acceptable limit between 20% - 25%.

Lam et al. (2008) [103]: Interference effects were studied in a wind tunnel on square tall buildings in close proximity in tandem for various separation distances between buildings and wind angles. Wind drag force and moments on the inner building models were found to be reduced due to sheltering effect for most of the wind directions as compared to isolated condition. Even negative drag force was exhibited. Through numerical simulation it was found out that at 30° wind angle, wind flow occurred through the narrow building gaps at high speeds.

Mukherjee et al. (2014) [104]: In this study numerical and experimental analysis on Y shape building models has been done using ANSYS (CFX) and WT for pressure distribution on faces for varied wind angles from 0° to 60°. Due to interreference effect among the limbs abnormal pressure distributions on the faces have been reported.

Bhattacharyya and Dalui (2015) [105]: Force and pressure coefficients of an unsymmetrical E plan shaped tall building have been studied for two orthogonal wind directions (along and across wind direction) through experimental and numerical methods in WT and ANSYS (CFX) respectively. In across wind direction dynamic effect on the model is reported to occur in the lee side. Comparison of results between experimental and numerical study showed good agreement between the two.

Alminhana et al. (2018) [106]: Aerodynamic changes on CAARC tall building models by chamfering and recessing the corners were studied numerically as well as experimentally in a wind tunnel. Numerical study was carried out using finite element method with LES turbulence model. Numerical predictions were compared with the results of the wind tunnel test. Results in terms of aerodynamic forces were found to be similar in both – numerical as well as experimental studies indicating the authenticity of use of CFD investigations for aerodynamic investigation on tall buildings.

Bhattacharyya and Dalui (2018) [107]: A comprehensive study of pressure distribution was carried out through experimental as well as numerical methods on E plan shaped building model. Large variation of pressure is reported on some faces at 120° skewed wind angle of attack resulting in negligible mean C_{Pe} on those faces. The accuracy of numerical method has also been established by comparing the results of numerical method and experimental method.

Biswarupand Kumar (2020) [108]: Experimental and numerical study on E plan shape building model for different wind incidence angles have been presented by the authors in terms of mean pressure coefficients. For various element meshing sizes, values of coefficient of pressure on faces were reported to have an error between 17% - 24 % with respect to wind tunnel values.

2.5 LIMITATIONS

Preceding Para shows that research in the field of wind environmental effect on tall buildings have been conducted widely on wind tunnel and/or CFD models on different shapes and sizes of tall buildings. In majority of the cases, wind pressure and force on tall buildings have been studied on either regular shape of the buildings for oblique wind angles which are not incorporated in wind codes/standards; or on irregular and complex shapes of tall buildings, data for which are not available in codes/standards for structural design. For complex and irregular shape of tall buildings structural designers generally make approximations from codes/standards or depend on documented research articles. Also, little importance has been found in the research studies about pressure on roof surfaces for design of roof structures and for design of cladding/glazing units which generally collapse on account of excessive local suction pressure.

In the present study it is envisaged to conduct numerical study to access wind pressure and force on models, pressure/suction on roofs and claddings on a rectangular and five irregular shapes of tall buildings of same height and plan area as that of the rectangular shape.

CHAPTER 3 SIMULATION PROGRAMME

3.1 GENERAL

A body can be considered as an aerodynamically “bluff” when flow streamlines do not follow the surface of the body, but separate from its leading edges, reattaches forming a wide trailing wake behind the body. Most of the manmade structures including tall buildings are aerodynamically bluff bodies. Therefore, it is important to understand the flow pattern and the resulting pressure distribution around the buildings.

When wind flow is obstructed by a bluff body/building the flow gets separated into two distinct regions. In the vicinity of those regions high velocity flow exists. On the windward side of the body, flow stagnation takes place which increases the positive pressure on the surface and drag force in the direction of wind. Leeward side of the building is generally in the wake where low negative pressure with high turbulence exists. This causes drag forces on the surface in the flow direction. Separated flows get re-attached at rear stagnation point in the leeward direction of the building. The zone between rear stagnation points and the building is significantly turbulent.

Wind pressure exerted on any structure is an important factor in the design of structure. It becomes more relevant with the increase in height of the structure due to the effect of atmospheric boundary layer. The available data in various codes of practices provide guidelines for regular shapes of structures only. These data are based on various experiments, field investigations, or wind tunnel studies. Moreover, the amount, distribution and duration of the wind stress is not precisely defined in the codes. Another important factor is complexity of the wind phenomenon as the stress due to wind depends upon form of structure, size of structure, speed and direction of wind, characteristics of terrain and location of surrounding structures. Many types of experiments need to be performed to know exact stress produced on the structure.

Wind does not blow with uniform speed and in a constant direction. Wind speed consists of series of gusts which varies both in magnitude and direction very widely.

Even the phenomenon of uniform and steady wind is not that much simple. Considering the gusts of wind to be a local phenomenon, in fact it is not global, and happening everywhere in the same way, the mean speed over a large area at an instant time may be considered to be the mean speed over a long time at one place.

As such, there is no definite wind pressure corresponding to a given wind speed applicable to all type of structures. Many researchers have worked on the effect of various form variations of the structure and many more are needed to model the structure more closely the actual structure and the wind environment. Recent development in CFD has made the investigation of wind pressure on structure easy. The pressure coefficients on building façade are considered to be the basic parameter in analysing the wind effect. It has also been analysed that critical coefficient of pressure along and across wind directions may not be perpendicular to the wind incident angle. As, such, detailed study on various wind incident angles is required for getting the exact scenario. The wind pressure and forces on the building are estimated in terms of coefficient of pressure (C_{Pe}) and force coefficient (C_f). Whereas, the coefficient of pressure/force coefficients are needed for structural design and difference in pressure coefficients at various location of the building surface for deciding natural ventilation, flow pattern/velocity field around the building provides us the overall all wind environment around the building to exactly know the pollution dispersion.

For the purpose of prediction of airflow around building boundary layer wind tunnels are useful tools. Performing wind tunnel tests requires considerable resources not within easy reach to all practicing engineers and it is a time consuming and expensive effort too. Therefore, researchers looked into other options to substitute wind tunnel experiments and computational fluid dynamics (CFD) was introduced as a promising alternative option to wind tunnel. It is a branch of fluid mechanics that uses numerical methods and algorithms to solve and analyse problems by discretising a fluid into a continuous arrangement of smaller volumes bounded by a set of known conditions and the application of a suitable form of the Navier-Stokes equations of continuity and momentum for the fluid flow. With the advancement of computer capabilities, it is possible to simulate complex numerical simulations with adequate accuracy and shorter period of time compared to wind tunnel experiments. In the past few decades, research on the application of CFD has been conducted extensively in areas such as pressure on the building surfaces, pedestrian wind comfort and safety, exterior building surface heat transfer, pollutant dispersion around buildings, and natural ventilation of buildings. CFD has also been used effectively in modelling aerodynamics effect on automotive. Therefore, it has shown a considerable accuracy in simulating atmospheric boundary layer effect. This highlights the possibility of using a similar approach to simulate the wind behaviour around the buildings [109].

Ongoing research yields software that improves the accuracy and speed of complex simulation for wind environment. ANSYS (CFX) have been successfully used to calculate flow around buildings. One of the advantages of using ANSYS (CFX) is its ability to provide wind induced area average pressure coefficient (C_{Pe}), base shear $\left(F_x \;\&\; F_y\right)$, base moment $\left(M_x \;\&\; M_y\right)$ and torsion moment (M_Z) of the building directly, which is a key governing design criterion in most of the tall buildings. The quality of CFX-post processor allows us clear visualisation of flow results, which is not possible in the wind tunnel experiments. CFX results can be integrated with modern computer aided design tools for quick structural design too.

3.2 WIND FLOW CHARACTERISTICS

Structural wind engineering aims to quantify the forces a structure will experience due to flow of wind throughout its expected life. In evaluating basic lateral force resisting system of a building, wind load plays an important role for tall buildings. Traditional approach to wind loading for design of rigid tall buildings is to analyse the static pressure on the building envelope. The static pressure is applied to the various structural elements such as the structural frame and the curtain walls which support cladding units and glazing surfaces of the building provided for thermal insulation and protection from weather. At corners building failure occurs due to high suction. In the case of a static analysis of wind maximum force the building will be subjected to is calculated.

It is important to know atmospheric wind flow characteristics on or around buildings. The structure of the atmospheric boundary layer is comprised of two distinct regions – inner and outer. In the inner layer, which is the layer of air within the roughness zone comprising the land or sea surface, the flow is mainly dependent on the surface roughness characteristics which exists up to 10 m from the surface of the earth. Whereas, in the outer region, flow is mainly influenced by the Earth's rotation (Coriolis effect) from where the velocity of wind becomes constant (free stream velocity/gradient velocity). This height (gradient height) from the surface of the earth ranges between 300 m to 400 m within which the velocity increases asymptotically depending upon the roughness created by vegetation and structures at the ground. This is referred as atmospheric boundary layer (ABL). The boundary layer thickness is defined as the height from the surface of earth at which the wind velocity is 99 % of the gradient velocity/freestream velocity.

It is not so easy to mimic exactly the flow characterises in the ABL. Actual representations of the atmospheric boundary layer is still under debate. However, various empirical formulae, described below, were developed for experimental analysis of effect of wind ABL flow on structures.

(1) Parabolic Law:

$$u = u_{Ref}\sqrt{\frac{Z+22}{Z_{Ref}+22}} \qquad (Eq.\ 3.1)$$

Where, u_{Ref}= Reference Wind Speed in m/s

Z_{Ref} = Reference height 10 m.

u = Time averaged longitudinal velocity at heigh Z above ground

(2) Power Law:

$$u = u_{Ref}\left(\frac{Z}{Z_{Ref}}\right)^{\alpha} \qquad (Eq.\ 3.2)$$

Where, α is a function of terrain roughness.

While power Law is an improvement in the Parabolic Law, it is not analytically correct for the bottom 10 m of ABL. Still, it is widely used for its simplicity.

(3) Logarithmic Law:

$$u = \frac{1}{k} u_0 L_n \left(\frac{Z - Z_d}{Z_0} \right) \qquad (Eq. 3.3)$$

Where, k = 0.4 (Von Karman Constant)

u_0 = Friction Velocity; $u_0 = \sqrt{\frac{\tau_w}{\rho}}$; τ_w = Wall Shear Stress = $\mu \left(\frac{du}{dy} \right)_{y=0}$

and ρ = Density of Air.

Z_0 = Aerodynamic roughness length which is a surface roughness parameter.

Z_d = Zero plane displacement i.e., the height of zero wind speed achieved above the ground

Logarithmic Law is applicable to lower 10 m height from the ground. However, it becomes less accurate at altitudes of more than 100 -200 m where power law represents the velocity profile better.

3.3 NUMERICAL SIMULATION WITH $k - \varepsilon$ TURBULENCE MODEL IN ANSYS (CFX)

Three-dimensional unsteady flow of any fluid is defined by the Navier-Stokes Equations of Continuity and Momentum. The velocity and pressure in the fluid flow environment is governed by them.

In computational fluid dynamics (CFD), wind simulation is created in virtual wind tunnel called domain within which model is kept alike as in the wind tunnel experiment. CFD models attempt to resolve the flow of the fluid around any bluff body by simulating the flow at finite grid locations. Based on the continuity and momentum equations various mathematical models, researchers have developed, to know the flow characteristics and the effect of turbulence in a fluid flow. Different models have been developed to match the near real scenario occurring in the nature. However, no model has been developed so far to know the exact turbulence flow characteristics. The technique involves the discretisation of a fluid into a continuous array of smaller volumes bounded by a set of known conditions on which a form of the Navier-Stokes equations of fluid flow, suitable to address the specific problem, is applied.

One model is the k-epsilon ($k - \varepsilon$) model. It is the most commonly used and validated turbulence model for planar shear layer and recirculating flow model in CFD simulation for environmental wind flow. It simulates the mean fluid flow using the time-averaged Navier Stokes (N-S) equations. It is known as the Reynolds Averaged Navier Stokes (RANS) equations. It gives time-averaged results while wind tunnel study gives fluctuating values. Time-averaging removes the turbulent terms but introduces an extra set of terms to the N-S equations. This means that the RANS equations cannot be solved directly and some extra equations are needed to describe the extra terms. The exact $k - \varepsilon$ model equation contains many variables and unknowns which are unmeasurable. In the standard $k - \varepsilon$ model, applied in the present study using ANSYS (CFX) software, description of turbulence is defined by two transport equations in partial differential form. The first transport equation is in terms of the variable "Turbulence Kinetic Energy (k)" and the second equation is in terms of the variable "Dissipation of Turbulence Kinetic Energy (ε)". It is the simplest model for which only initial and/or boundary conditions needs to be supplied.

Turbulence Kinetic Energy (TKE) is produced by shear, friction or buoyancy or by small eddies developed by fluid flow. It is the mean kinetic energy per unit mass associated with eddies in turbulent flow having dimension of [L^2T^{-2}]. Physically, the TKE is characterized by root mean square (RMS) velocity fluctuations. TKE is transferred into turbulence energy which is dissipated, (turbulent eddy dissipation (ε), by viscous forces at microscale (Kolmogorov scale) producing heat. ε has the dimension of [L^2T^{-3}] i.e., turbulent kinetic energy per unit time. In ANSYS (CFX) the Navier-Stokes of continuity and momentum for fluid flow and the differential transport equations of turbulent kinetic energy and turbulent eddy dissipation have been taken as in equation (Eq. 3.4) to (Eq. 3.11) [110]. The solution technique in ANSYS (CFX) is that it solves momentum equations explicitly and pressure equation implicitly. Turbulent kinetic energy and dissipation of kinetic energy and other scaler transport equations are solved implicitly.

Continuity Equation

$$\frac{\partial \rho}{\partial t} + \frac{\partial}{\partial x_j}\left(\rho U_j\right) = 0 \qquad (Eq. 3.4)$$

Momentum Equation

$$\frac{\partial \rho U_i}{\partial t} + \frac{\partial}{\partial x_j}\left(\rho U_i U_j\right) = -\frac{\partial p'}{\partial x_i} + \frac{\partial}{\partial x_j}\left[\mu_{eff}\left(\frac{\partial U_i}{\partial x_j} + \frac{\partial U_j}{\partial x_i}\right)\right] + S_M \qquad (Eq. 3.5)$$

Where S_M is sum of body forces, μ_{eff} is effective viscosity accounting for turbulence and p' is the modified pressure defined as below. Rest symbols are carrying usual meanings.

$$p' = p + \frac{2}{3}pk + \frac{2}{3}\mu_{eff}\frac{\partial U_k}{\partial x_k} \qquad (Eq. 3.6)$$

$$\mu_{eff} = \mu + \mu_t \qquad (Eq. 3.7)$$

Where μ_t is the turbulent viscosity which is linked to the turbulence kinetic energy and dissipation by the flowing equation:

$$\mu_t = C_\mu \rho \frac{k^2}{\varepsilon} \qquad (Eq. 3.8)$$

Where $C_\mu = 0.09$, a constant called k- ε turbulence model constant.

On the basis of differential transport equations of continuity and momentum above, turbulence kinetic energy and rate of turbulent eddy dissipation are expressed respectively as:

Turbulent Kinetic Energy Equation

$$\frac{\partial(\rho k)}{\partial t} + \frac{\partial}{\partial x_j}\left(\rho U_j k\right) = \frac{\partial}{\partial x_j}\left[\left(\mu + \frac{\mu_t}{\sigma_k}\right)\frac{\partial k}{\partial x_j}\right] + P_k - \rho\varepsilon + P_{kb} \qquad (Eq. 3.9)$$

Turbulent Eddy Dissipation Equation

$$\frac{\partial(\rho \varepsilon)}{\partial t} + \frac{\partial}{\partial x_j}\left(\rho U_j \varepsilon\right) = \frac{\partial}{\partial x_j}\left[\left(\mu + \frac{\mu_t}{\sigma_\varepsilon}\right)\frac{\partial \varepsilon}{\partial x_j}\right] + \frac{\varepsilon}{k}\left(C_{\varepsilon 1}P_k - C_{\varepsilon 2}\rho\varepsilon + C_{\varepsilon 1}P_{\varepsilon b}\right) \quad (Eq. 3.10)$$

Where, $C_{\varepsilon 1}$, $C_{\varepsilon 2}$, σ_k and σ_ε are $\mathrm{k} - \varepsilon$ turbulent model constants, the values of whom have been arrived after numerous iterations of data fitting for a wide range of turbulence flows as:

$C_{\varepsilon 1}$ = 1.44, $C_{\varepsilon 2}$ = 1.92, σ_k = 1.0 and, σ_ε = 1.3

P_k is turbulence production due to viscous forces and P_{kb} & $P_{\varepsilon b}$ represents the buoyancy production term. For incompressible flow,

$$P_k = \mu_t \left(\frac{\partial U_i}{\partial x_j} + \frac{\partial U_j}{\partial x_i} \right) \frac{\partial U_i}{\partial x_j} \qquad (Eq. 3.11)$$

3.4 AIMS AND OBJECTIVE

As discussed in the previous para $(k - \varepsilon)$ turbulence model in the ANSYS (CFX) solver will provide us time averaged results of coefficient of pressure (C_{Pe}), base shear $(F_x$ & $F_y)$, base moment $(M_x$ & $M_y)$ and torsion moment (M_Z) which are the main governing design factors for static analysis of tall buildings. To achieve this, the following aims were set:

1. To compare simulation pressure coefficient results for the rectangular model with the different international codes and previous experimental results, assessing the velocity and pressure results in terms of their accuracy in prediction of structural loads.
2. Based on the result of these studies, to run simulations for other plan shaped models symmetrical about both axes and symmetrical about one axis having same plan area and height.
3. To understand the flow pattern and to predict area average surface pressure coefficients and local peak suction pressures on faces and structural parameters for structural design.

3.5 SIMULATION METHODOLOGY FLOW CHART

Figure 3.1 shows the flow chart of systematic procedure of numerical study carried out with model of rectangular building having plan area (300 sqm) and height (50 m) as that of the five models of building under study. It is done to validate the results by comparing the values with different code of practices and previous experimental results. The same wind flow characteristics and boundary conditions was applied for study of other plan shape models.

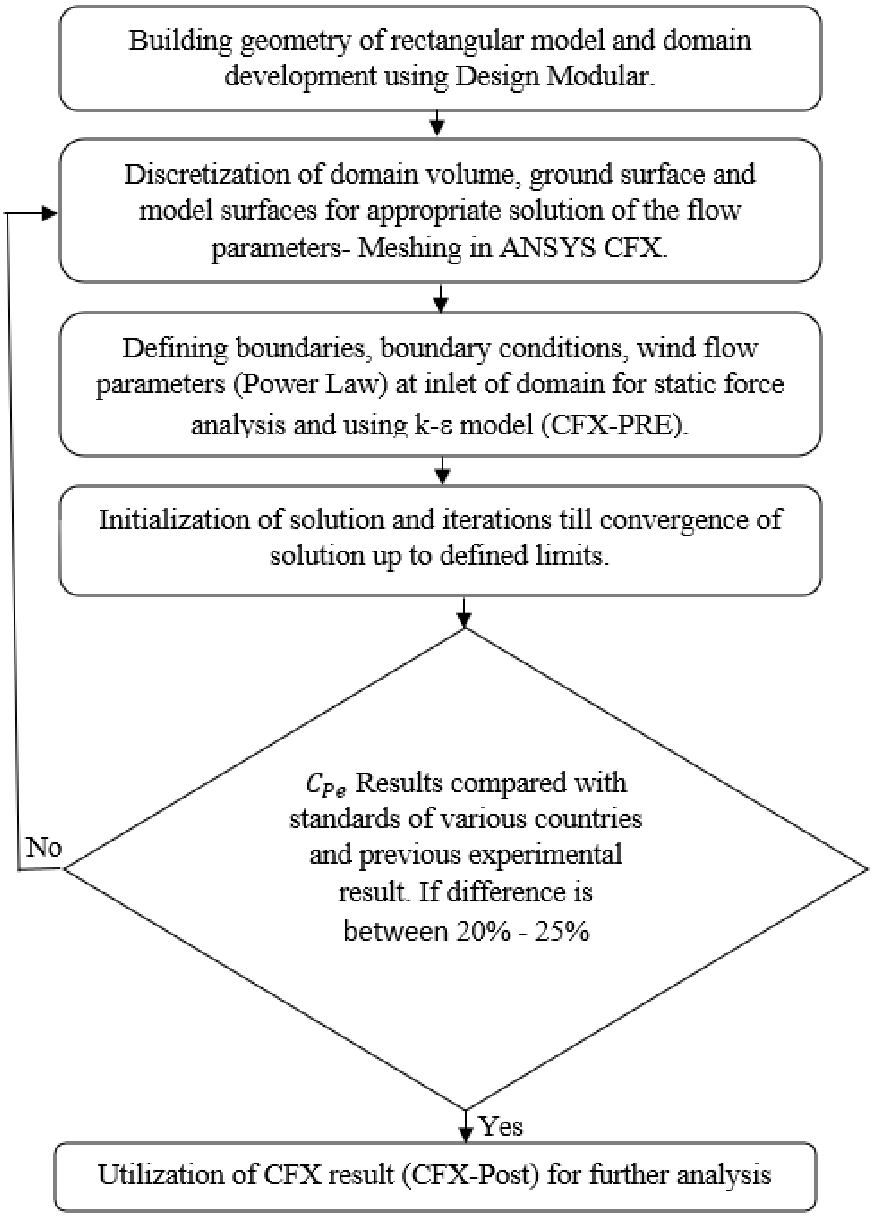

Figure 3. 1: Flow Chart of ANSYS CFX Simulation of Model

3.6 MODEL AND COMPUTATIONAL DOMAIN

In the present study the building model is placed within the domain, which is analogous to a wind tunnel and built as a parallelopiped in ANSYS workbench. Domain size is selected such that its boundaries are not affected by the model placed in it or in other words the computational domain is kept large enough to avoid reflection of fluid streams and to evade abnormal fluid pressure field around the model and also to keep the blockage ratio less than 3%. At the same time velocity fluctuations, uplift force and backwash, vortex generation in the wake region etc. should be effectively created during the simulation. The domain size should also not be large otherwise it will require a larger number of computational cells for analysis which needs more time and higher computational facility for the solution to converge. Recommendations of Revuz et al. 2012 [111] in the matter have been adopted in the present study. The size of the computational domain in the flow direction and the side domain walls are kept equal to 5H each from the respective faces of the model, H being the height of the model. The distance behind the model is kept as 15H so that proper wake and vortex is generated behind the model. The height of the domain above the domain floor is kept as 6H. In the present study the domain of size L =10.3 m, B = 5.3 m and H = 3.0 m with the model (1:100 scale) kept within from the respective domain boundaries are taken as shown in Figure 3.2.

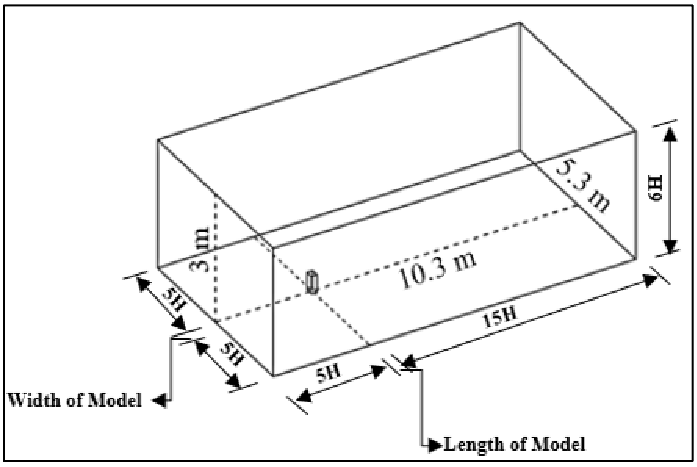

(a) Isometric view

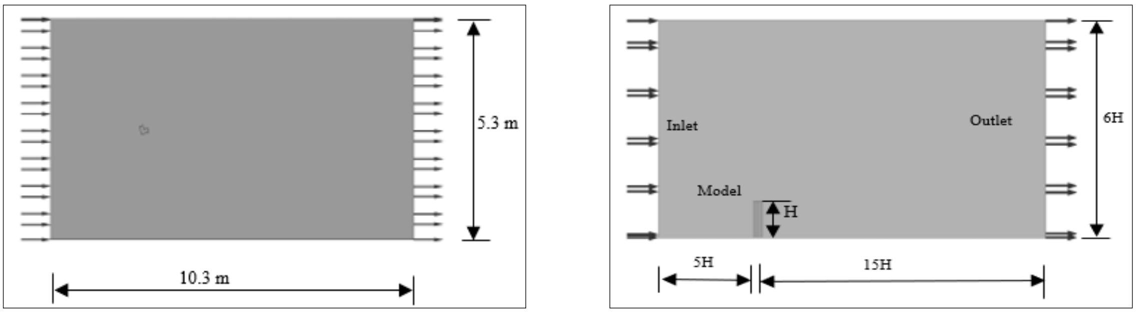

(b) Plan *(c) Elevation*

Figure 3. 2: Schematic Diagram of Computational Domain

3.7 COMPUTATIONAL GRID AND GRID SENSITIVITY

Most of the numerical simulations for solving engineering problems are partial differential equations. To solve these equations, we need to convert them into an algebraic form i.e., we need to discretize the domain to solve these equations. In order to discretize we need finite number of points/nodes in our computational domain. For this meshing is done. Also, higher order terms in the differential equations are neglected and approximation is done for unmeasurable quantities. The result of the simulation depends significantly on the discretized grid topology of the computational domain and the model. Two types of grid topologies are generally used to capture the geometrical details of domains: structured grids (hexahedral shape) and unstructured grids (tetrahedral shape). Though, hexahedral grids provide more accurate results than tetrahedral grids at similar densities, tetrahedral grid which can be generated automatically are preferred for building simulations. In the present study tetrahedral elements in the domain volume and prism at the wall faces were generated.

Now comes the grid resolution. The mesh element size in the domain volume and surface of the model affects the convergence of solution considerably. The grid resolution was set to precisely capture crucial physical factors of the flow such as pressure on surface of model, separation of flow, formation of wake and vortices, reattachment of flow and so on. Because the primary goal was to measure pressure on the surface of the model, it was discretized into finer elements than the computational domain. Meshing technique for better solution depends upon the approach to discretize the domain and model surface into smaller elements. In the present study, different regions of the domain were discretized with different element sizes and it was ensured that the solution reaches a steady state. Coarser mesh in tetrahedral cells of the domain was generated at first instance and then refinement was done. Numerical errors or uncertainty in ANSYS (CFX) was, thus, reduced to negligible amount. The ratio of element size in the base was varied between 0.50 to 0.40 times the element size of domain and; model face sizing was varied between 0.25 to 0.2 times the element size of domain. However, on smaller mesh elements solution took more time (Franke 2004) [112]. It was also reported by Cowan et al. (1997) [70] that with standard $k-\varepsilon$ model coarser grid can give results closer to the experimental laboratory data than obtained with improved finer elements of meshing grid. The mesh elements on the model surface were inflated to achieve smooth transition from the domain elements so that the velocity gradients can be mapped precisely near no-slip walls of the model surfaces and to map pressure on surfaces normal to wall surfaces.

One of the largest sources of error is CFD simulations is the discretization error arising due to bad mesh quality. It also plays a significant role in convergence of the solution and accurate results. Spectrum of important mesh metrics (skewness and orthogonal quality) of the meshing elements for quality meshing grid has been provided by ANSYS Inc. [113]. For good quality meshing grid, the value range of skewness of elements should be low and value range of orthogonal quality of elements should be high. It was insured during the present work that both the mesh metrics remain in the quality range of good to excellent.

After various trials with the meshing techniques, final result was adopted with 0.44 times element size of domain on base and 0.22 times on model faces having 90 mm element size in the domain volume. At this resolution the solution reached a steady state and the residual RMS error for mass and momentum convergence was achieved between 10^{-4} to 10^{-5} for momentum in the three directions and up to 10^{-6} for mass respectively. The corresponding domain imbalances in the values were 0.001 % for momentum in the three directions and 0 % for mass. Meshing on the models are shown in Figure 3.3. The total number of nodes obtained in the domain were in the order of 465000 out of which about 96.4 % nodes were mapped during the analytical solution. The total number of discretized elements were found to be 2550000.

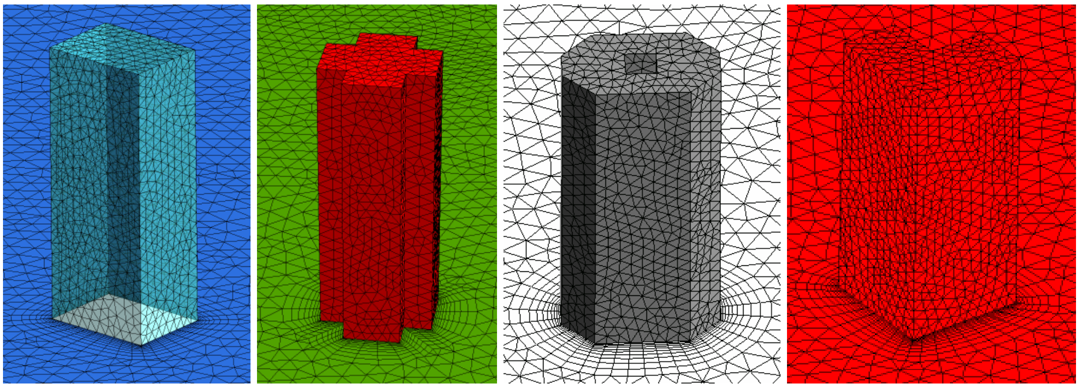

Figure 3. 3: Meshing on Models (Contd.)

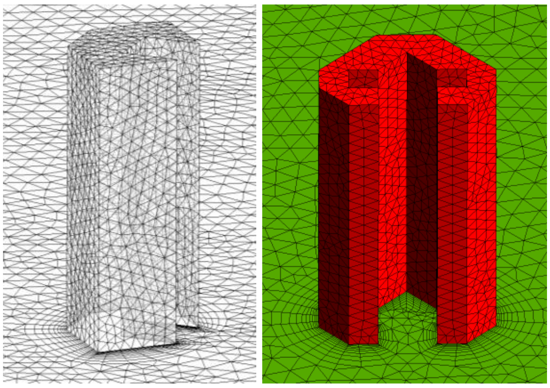

Figure 3. 3: Meshing on Models

3.8 BOUNDARY CONDITIONS

When fluid flows past a solid body, the fluid particles adhere to the boundary and condition of no slip occurs. In other words, velocity of fluid remains as that of the boundary. If the boundary is stationary, velocity of fluid at the boundary is zero. Farther away from the boundary velocity is higher. As a result of this variation velocity gradient exists. Velocity of fluid increases from zero at the contact surface of the solid boundary to the free stream velocity in the direction normal to the boundary i.e., boundary layer is created. Fluid thus exerts shear on the wall of the solid boundary. Above the region from where velocity equals free stream velocity, velocity gradient and shear stress become zero. As such, the position of boundary walls of the computational domain within which model is kept influences the result. This effect of the external surrounding on the flow and dispersion within the computational domain are defined through boundary conditions. This is also the case for the boundary conditions at solid surfaces (model surfaces). Proper choice of the boundary conditions is very important as they determine the quality of results, and flow variables at the boundaries and the surfaces. The domain sides & top wall and the roof top wall of the model were defined as free slip walls ($\tau_{wall} = 0; u_{wall} = 0$) where τ_{wall} is the wall shear stress and u_{wall} is velocity normal to the wall. This means, component of fluid velocity parallel to wall has a predetermined value, which is computable. But, component of velocity normal to wall as well as fluid shear on wall, are both zero. The model faces and the domain ground were specified as no slip walls ($u_{wall} = 0$), which means component of fluid velocity at the boundary of wall is zero and the wall is not moving i.e., wall velocity is also zero. To obtain different wind angle of attack, models were rotated about its mass center of gravity in anticlockwise direction thus, making change in the wind angle of attack in clockwise direction without rotating the flow field, keeping the model boundary conditions and flow parameters unchanged. By this way wind axes and body axes were kept the same, the drag force equals the shear force in wind direction and the lift force equals the shear force across wind direction.

3.9 WIND FLOW PARAMETER:

At the inlet a mean velocity profile corresponding to the upwind terrain is provided. Castro and Robins (1977) [64] during their study of flow around a surface-mounted cube in uniform and turbulent streams reported that no Reynolds number effects were discernible for free stream gradient velocities above about 0.5 m/s (corresponding to a Reynolds number based on cube height and the velocity at that height in the undisturbed flow of about 4×10^3). According to Cermak and Cochran (1992) [14] in computational models of wind engineering problem within the atmospheric surface layer, which is the lowest 100 m of ABL, turbulent intensity varies by only 5 to 10%. They provided power law exponent of 0.14 for the mean wind profile up to a height of 50 m. Keeping in view the above facts, since this study is for 50 m height of buildings in terrain category-II as per IS 875 (Part 3): 2015, a homogeneous and steady state ABL wind flow velocity of 0.5 m/s at a height of 0.1 m (corresponding to basic wind speed of 50 m/s with a length scale of 1:100 as that of the model) was provided at the inlet. Terrain roughness coefficient, $\alpha = 0.143$, was taken as 1/7th rule of power law at the inlet. The velocity profile at inlet achieved is shown in Figure 3.4. With this velocity profile, velocity at the model height achieved was 0.63 m/s. Free wind velocity and turbulence intensity profile along the height of building model were plotted and compared with experimental data from Nagar et al. (2020) [55] for the same terrain category and are shown in Figure 3.5 and 3.6 respectively. Boundary conditions and flow parameters are shown in Table 3.1.

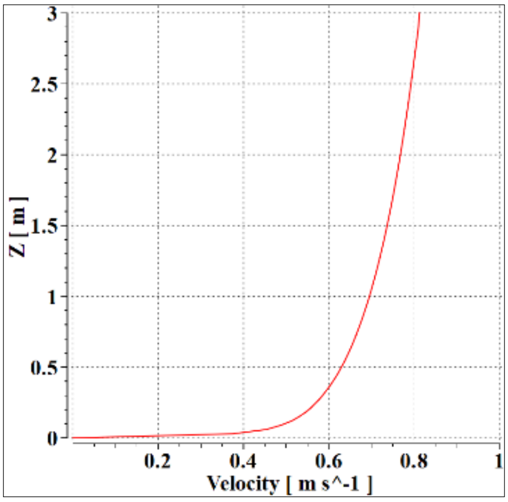

Figure 3. 4: Velocity Profile at Inlet of Domain

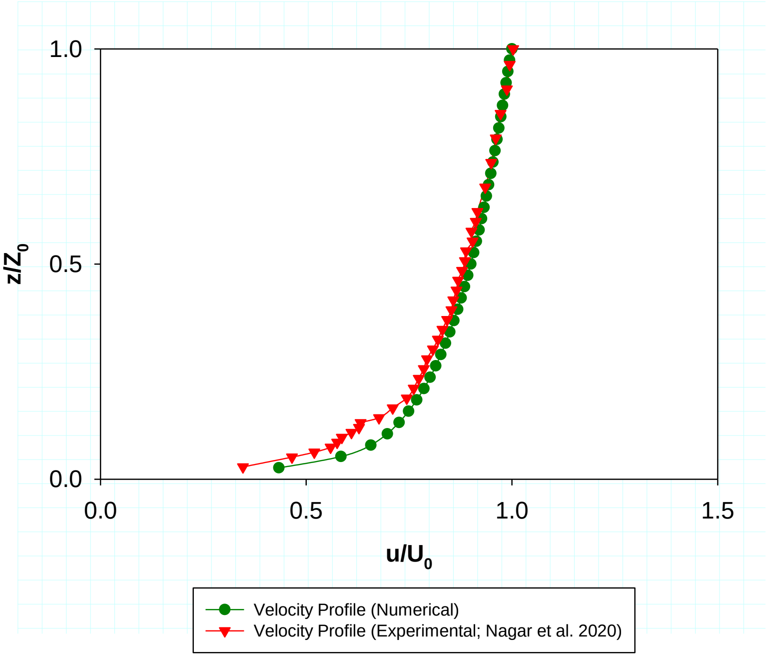

Figure 3. 5: Comparison of Mean Wind Velocity Profile from Experimental Data

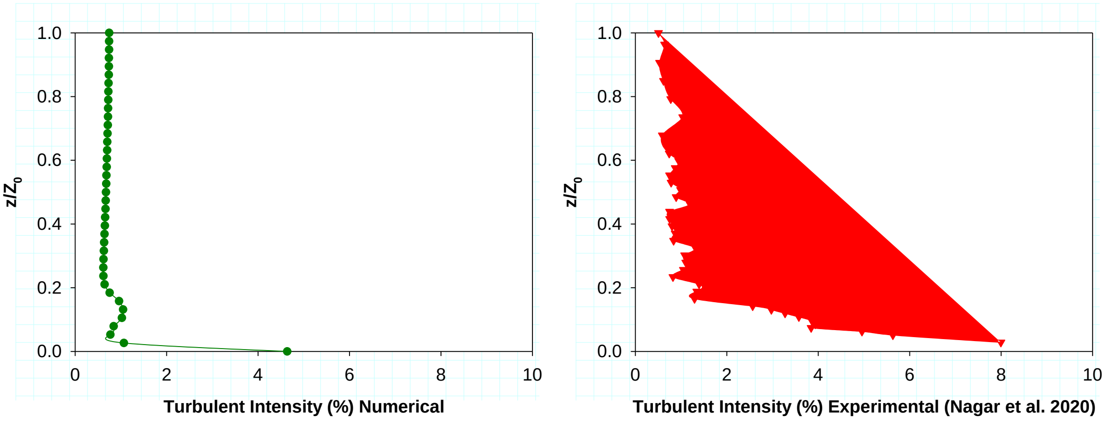

Figure 3. 6: Comparison of Mean Wind Turbulent Intensity Profile from Experimental data

Table 3. 1: Boundary Conditions and Flow parameters

Description	**Parameter**
Solver	CFX
Flow analysis type	Steady state flow
Flow Regime	Subsonic Air at 25^0 C with reference pressure of 1 atm
Turbulence Model	k- ε model
Inlet Condition	Velocity of flow = normal speed by Power Law with 5% turbulence intensity
Power Law (As given in $Eq. 3.2$)	$u = u_{Ref}\left(\frac{Z}{Z_{Ref}}\right)^{\alpha}$
Outlet Condition	Average Static Pressure with Relative Pressure = 0 Pa
Domain Side walls, top wall and Model Roof Top	Free Slip Walls i.e., $u_{wall} = 0$, and $\tau_{wall} = 0$
Ground and Model walls	No Slip wall i.e., $u_{wall} = 0$
Model wall roughness	Smooth wall
Reynolds Number	2.23E+05 to 2.47E+05

3.10 CONVERGENCE OF SOLUTION

To ensure a valid solution of simulation of the RANS equations it is ensured that they reach a steady state. Following three considerations were confirmed for appropriate convergence of the solution.

1. Monitor points of mass and momentum and the RMS of dissipation of kinetic energy (ε) and turbulent kinetic energy (k) reaches a steady state condition. One of the monitor values for octagonal-oval shaped model are reproduced below in Figure 3.7.
2. Residual RMS error values in the solver control of CFX-Pre was fixed as 10^{-5} and achieved between 10^{-4} to 10^{-5} for the momentum in three directions and up to 10^{-6} for mass.
3. The domain imbalances were found to be less than 0.001% for the momentum in three directions and zero for total mass.

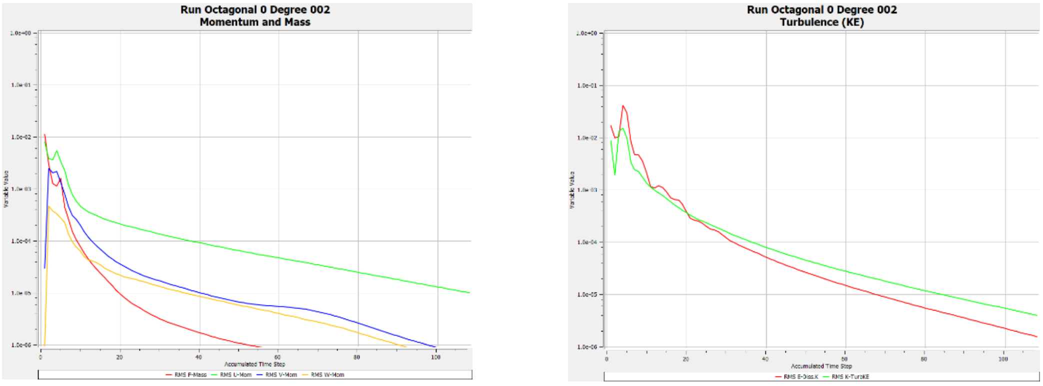

(a) Mass and Momentum *(b) E-Diss K and Turb KE*

Figure 3. 7: RMS Residual Values

3.11 VALIDATION AND VERIFICATION

Validation and verification of the results from CFD modelling has been an issue with the researchers. The validation and verification of the results by many researchers have been made with the wind tunnel measurements and/or with full scale measurements. Less work has been seen on the verification of the CFD results with the provision given in the codes/standards. In the present study, validation and verification of the results from ANSYS (CFX) has been done by analysing a rectangular plan shaped building model of same height and plan area as that of the other models and in the same wind environment, boundary conditions and solver settings, which were employed for simulation of other models. The C_{Pe} results on faces of rectangular model for the two orthogonal directions of wind were compared with those in relevant codes of different countries and for 90° wind angle from experimental data from Amin and Ahuja 2013 [43]. The comparisons for the two orthogonal directions are presented in Figure 3.8 and Figure 3.9 respectively. It can be seen that the C_{Pe} values from different codes vary within themselves, particularly on the leeward side and the side faces. However, present simulation predictions are closely similar to the provisions given in IS 875 (Part 3): 2015. The variation on the windward face is 12.5 % in case of 0° wind incidence angle and 15 % for 90° wind incidence angle. Whereas, the variation in predicted value of leeward C_{Pe} for 0° and 90° wind incidence angles are 12 % and 8 % respectively. This variation can be attributed to the method of pressure measurements in ANSYS (CFX). The values of C_{Pe} in the current study has been taken as area average value of C_{Pe} using the function calculator in CFD post. This is the area weighed average value taking into account the mesh element sizes. Without the area weighing function, the C_{Pe} value would have been biased due to different mesh densities in different regions on the faces. Also, the averaging is for the entire region of the face including the edges where high turbulence exists and pressure is highly negative. In codes, the coefficient values are adopted after data fitting for a wide range of wind tunnel tests corresponding to wind characteristics prevailing in different zones of the respective countries. In wind tunnel tests, pressure measurement is taken in a symmetrical grid pattern concentric from the centreline of the face in both directions. The pressure measurements at the edges, where high turbulence exists, are not possible due to thickness of the sheet from which the model is assembled and pressure records at the edges are either interpolated or extrapolated.

At the same time, C_{Pe} values provided in the codes are given for orthogonal directions and different range of side ratios and aspect ratios of building. Also, modification in C_{Pe} values for calculation of wind pressure and forces on building have been given in para 7.2.1 and 7.2.2 of IS: 875 (Part 3): 2015 as wind directionality factor (K_d) and area averaging factor (K_a) respectively. For clad rectangular building of plan area $20\ x\ 15\ m$ and height $50\ m$, C_{Pe} values given in the code may be reduced by factors $K_d = 0.9$ and $K_a = 0.8$ for comparison with the predicted values from present simulation. Altogether, a factor of 0.72 may be multiplied with the C_{Pe} values given in the IS code for comparison with the predicted C_{Pe} values.

Keeping in view of the above discussion it can be said that simulated prediction of C_{Pe} values are within the acceptable range for static wind load predictions. Moreover, the numerical simulation has captured the main flow characteristics such as regions of flow acceleration, separation, reattachment, and observation of rooftop and ground level vortices which supports the reasonability of the approach for further study on other models under similar wind characteristics, boundary conditions and solver settings.

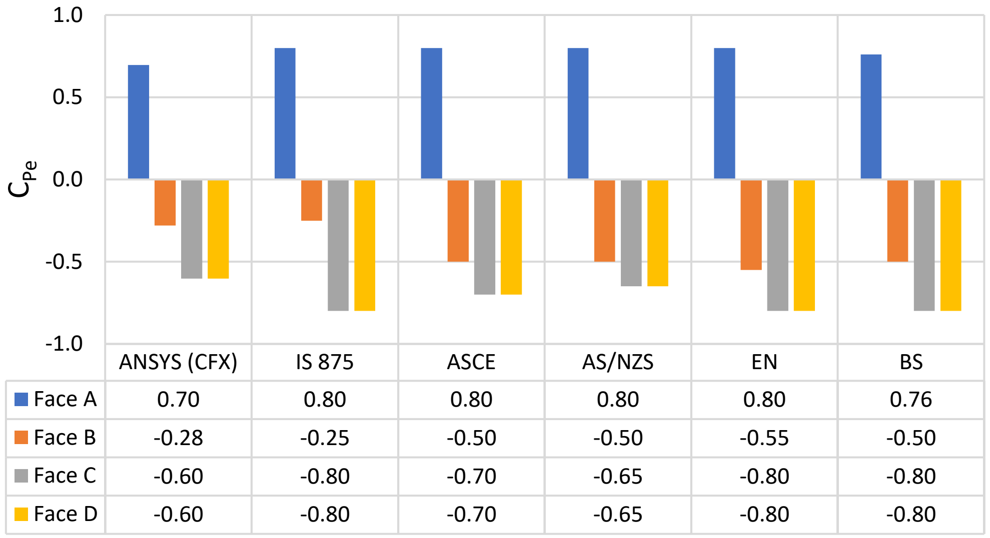

	ANSYS (CFX)	IS 875	ASCE	AS/NZS	EN	BS
🟦 Face A	0.70	0.80	0.80	0.80	0.80	0.76
🟧 Face B	-0.28	-0.25	-0.50	-0.50	-0.55	-0.50
⬜ Face C	-0.60	-0.80	-0.70	-0.65	-0.80	-0.80
🟨 Face D	-0.60	-0.80	-0.70	-0.65	-0.80	-0.80

Figure 3. 8: Comparison of Area Average C_{Pe} on Faces of Rectangular Model 0° Wind Angle

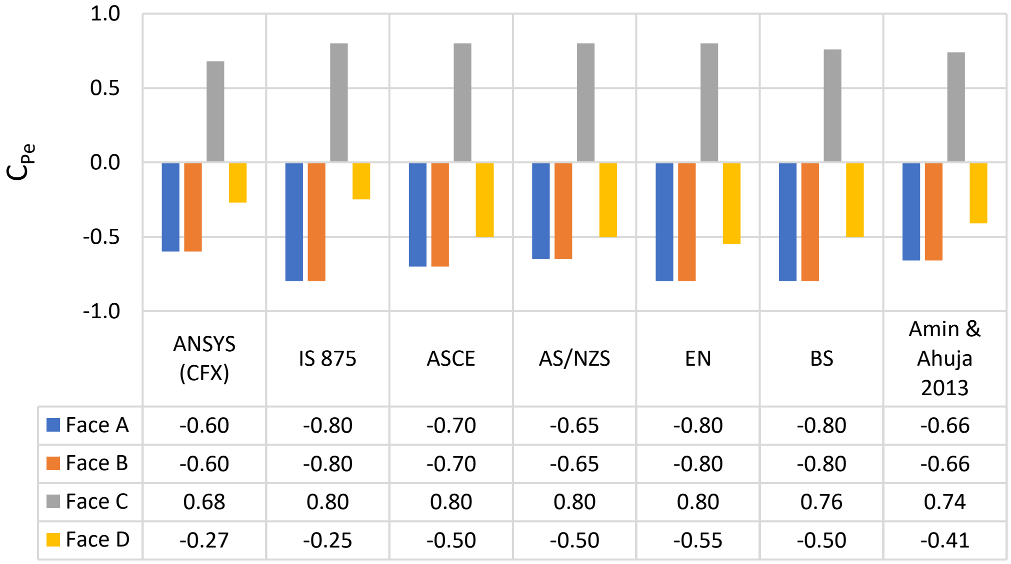

	ANSYS (CFX)	IS 875	ASCE	AS/NZS	EN	BS	Amin & Ahuja 2013
🟦 Face A	-0.60	-0.80	-0.70	-0.65	-0.80	-0.80	-0.66
🟧 Face B	-0.60	-0.80	-0.70	-0.65	-0.80	-0.80	-0.66
⬜ Face C	0.68	0.80	0.80	0.80	0.80	0.76	0.74
🟨 Face D	-0.27	-0.25	-0.50	-0.50	-0.55	-0.50	-0.41

Figure 3. 9: Comparison of Area Average C_{Pe} on Faces of Rectangular Model 90° Wind Angle

CHAPTER 4 RESULTS AND DISCUSSIONS - I

4.1 GENERAL

In this chapter pressure distribution coloured contour plots on the faces of the models and the wind flow characteristics in terms of surface streamlines, velocity contour plots and vector plots have been discussed for models having symmetry about both axes. Velocity streamline along wind direction on central vertical plane for different wind angles have also been discussed. Symmetry of the models have been reckoned with respect to the plan area centroid which happen to be the global origin of construction of model geometry in these cases. For the models (Rectangular, Plus and Octagonal-Oval models) wind angles of attack from 0° to 90° @ 15° has been studied during the simulation. The steps of wind angle @ 15° from 0° to 90° are sufficient to understand the influence of flow for 360° wind angle of attacks. However, due to lack of space discussion has been made for 30° interval of change of wind angle. Distribution of C_{Pe} Along Building Perimeter and on central vertical line on faces have also been discussed.

Contour plots help in identifying pressure variation on the faces with high or low value of pressure on the surfaces. The region between isolines of contours are shown with a fixed colour which can be corelated by the colour legend provided alongside.

Surface streamline images show region of recirculation and are helpful in identifying direction of fluid particle within the domain and around the model envelope.

Velocity contour plots are velocity field of mean velocity magnitude and the contour lines are constant magnitude of mean velocity.

Velocity vector plots show the direction of flow and circulation region. Concentration of vector arrows in a certain region shows high fluid velocity region. Direction of arrows in the vector plot gives direction and the size/colour indicates magnitude.

Velocity streamline along wind direction on central vertical plane shows intensity and region of upwind vortex at ground level and; position of upwash, downwash and stagnation zones on the windward face. Recirculation and creation of shear layer at roof top, vorticity circulation and reattachment of flow behind the model can also be visualized through streamlines.

4.2 RECTANGULAR MODEL

Rectangular shape model is termed as the basic model for which C_{Pe} data for orthogonal angles are available in wind code of different countries. Comparison of area average C_{Pe} for the two orthogonal wind incidence angles (0° and 90 are presented in the previous chapter (Figure 3.8 and 3.9) for validation and verification of the numerical approach. Discussion of the simulation is presented below.

4.2.1 C_{Pe} Contour 0° Wind Angle

Figure 4.1 shows the pressure distribution on the faces of rectangular plan model. Pressure on windward face A which is perpendicular to the wind direction is, as expected, parabolic at the centre of the face and symmetrical from the edges. Pressure is increasing in the vertical direction due to increase in velocity along height owing to atmospheric boundary layer flow as per power law given during the simulation. The flow is separating from the leading edges and the roof with high speed of flow and hence suction is created there. The maximum C_{Pe} on the face is 0.82 and the minimum is -1.01 with an area average value of C_{Pe} = 0.70.

Face B is on the leeward direction and under wake region. It is seen that the minimum suction is created at the middle of the face. Above and below suction value is marginally more than that at the centre and propagates from the centre in all directions. The isobars of the pressure contours are almost circular. At the edges high suction is noticed. The area average C_{Pe} is -0.28.

Side faces C and D, being opposite faces, are subjected to negative pressure of similar magnitude. The pattern of suction isobars is vertical in nature. Suction is seen to be higher at the near end edges of the faces with high gradient relative to the far end edges. The area average C_{Pe} on the faces are almost equal (Table 4.1).

On the roof top high negative pressure zone is developed immediately after the separation of flow from the roof top windward edge due to formation of turbulent eddies.

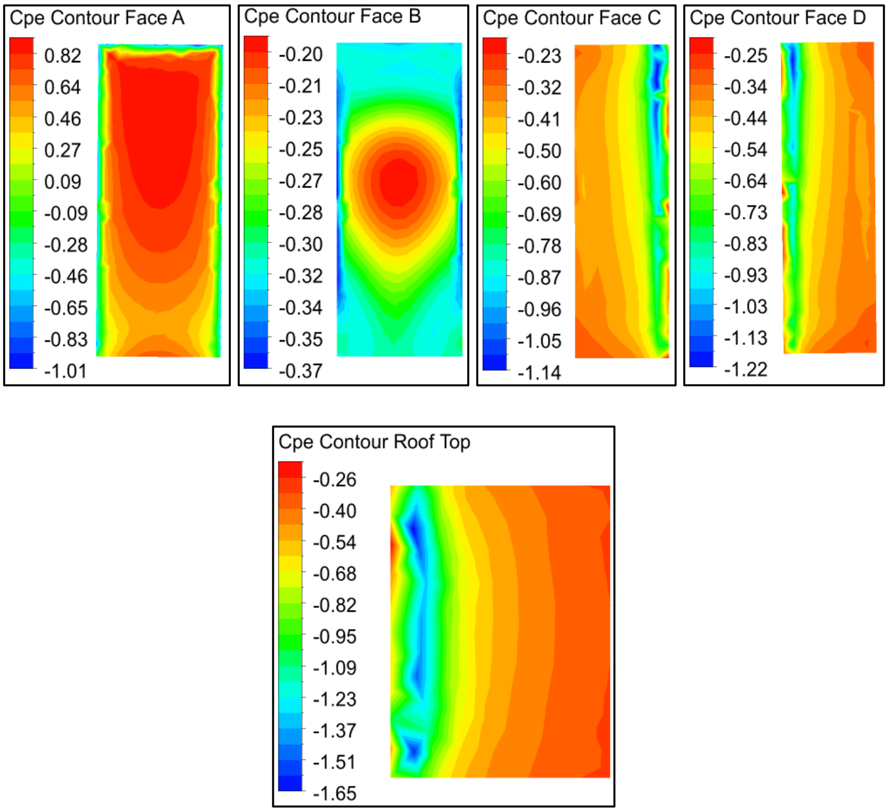

Figure 4. 1: C_{Pe} Contour on Faces & Roof Rect Model 0° Wind Angle

Table 4. 1: Area Average C_{Pe} on Faces

AoA	C_{Pe} Face A	C_{Pe} Face B	C_{Pe} Face C	C_{Pe} Face D	C_{Pe} Roof Top
0°	0.70	-0.28	-0.60	-0.60	-0.75
30°	0.59	-0.41	-0.08	-0.49	-0.78
60°	0.04	-0.43	0.59	-0.48	-0.76
90°	-0.60	-0.60	0.68	-0.27	-0.64

4.2.2 C_{Pe} Contour 30° Wind Angle

At 30° wind incidence angle the flow is still striking on face A. Face A is inclined in this case and hence the stagnation zone is shifted towards face C. As such, the positive pressure contour is half parabolic and shifted towards the near end edge of the face meeting with face C. Towards the far end edge of the face pressure is negative.

Flow seems to be surfing past face C and finally separation is taking place from the meeting edge of face B and C. On face C pressure is positive at the near end edge with high density of isobars and negative at the far end edge. On the centre of face C low intensity pressure exists. The area average C_{Pe} on face C is almost zero (-0.08).

On another side flow separation is taking place from the far end edge of face A. Thus, high gradient of pressure is developed on face A. The area average C_{Pe} on face A is still positive (0.59).

On faces B and D suction is minimum at the bottom and increasing gradually towards top. The isobars are horizontal in nature on most part of the face. However, high suction is observed at the meeting edge of face B and D above 1/ 3rd height (approx.) where the isobars are vertical. High turbulence due to formation of vortices is expected in this region. Similar is the situation on face D.

On the roof top suction exists throughout progressively reducing from the windward side to leeward side. The area average C_{Pe} on roof is -0.78 which is highest for all wind directions. High concentration of suction pressure in the blue coloured region is observed towards the windward face. This zone is vital for design of roof sheds/structures like hoardings, solar panel etc.

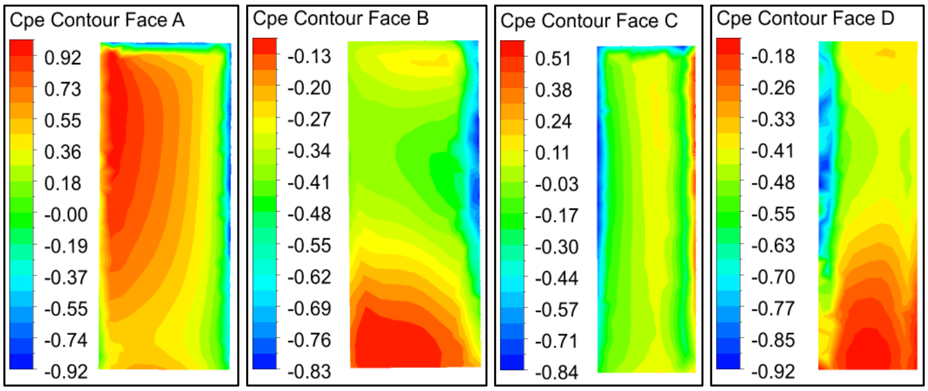

Figure 4. 2: C_{Pe} Contour on Faces & Roof Rect Model 30° Wind Angle (Contd.)

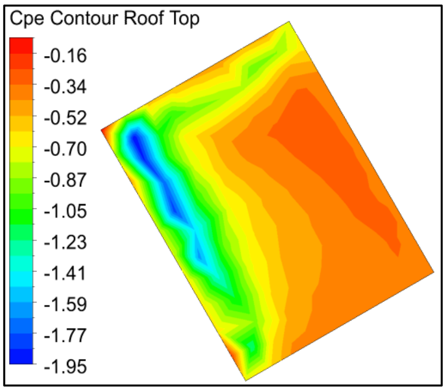

Figure 4. 2: C_{Pe} Contour on Faces & Roof Rect Model 30° Wind Angle

4.2.3 C_{Pe} Contour 60° Wind Angle

Flow at this angle of wind attack is impinging on face C. The stagnation line is adjacent to the meeting edge of faces A and C. As such, the pressure contours are half parabolic, not symmetrical from the edges like that in 0° wind angle. It is spreading from the meeting edge of face A and C towards the meeting edge of face B and C. High gradient of negative pressure exists at the meeting edge of face B and C due to separation of flow from this edge. On another side flow separation is taking place from the far end edge of face A giving rise to suction pressure at this edge. The minimum and maximum C_{Pe} values on face C are -0.95 and 0.92 respectively with area average value of C_{Pe} = 0.59 equal to that on face A for 30° wind angle.

Face A is side face but inclined in respect of flow direction. A small vertical strip of positive pressure is observed with high gradient of pressure at the near end edge of the face. In the middle of the face low intensity positive pressure exists which changes to negative pressure towards the far end. It is observed that the suction pressure is more rapid on the upper height of this edge of the face. The area average C_{Pe} on face A is almost zero (0.04).

Face B is in the wake region. Suction is increasing from bottom to top due to back wash created by the vortex. The isobars are horizontal except near the meeting edge of face B and C where it is vertical due to effect of side wash. High turbulence can be expected at this location. Similar is the case on face D on which the pressure contours are vertical at the meeting edge of face A and D due to side wash. The isobars on face D on the remaining part are horizontal due to back wash.

On roof surface, except at the corner of face A and C, suction pressure exists. Bubble of high suction pressure can be seen near the top of face C on roof top suggesting creation of local eddies at the place.

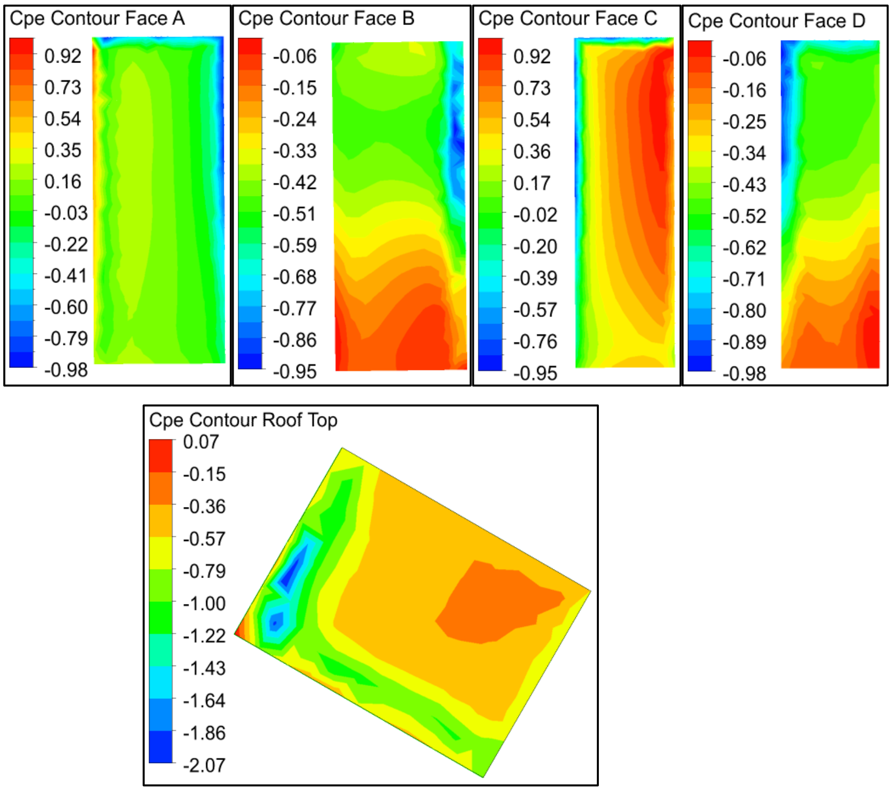

Figure 4. 3: C_{Pe} Contour on Faces & Roof Rect Model 60° Wind Angle

4.2.4 C_{Pe} Contour 90° Wind Angle

At 90° wind incidence angle flow is impinging on face C orthogonally. The pressure contours on face C are parabolic, symmetrical from the edges and in increasing magnitude with height due to atmospheric boundary layer flow effect (Figure 4.4). Flow separation is taking place from the leading edges of the windward face C.

Face D is in the wake region. On this face suction is increasing from bottom to top due to back wash. Faces A and B are side faces. Pressure on the faces is negative and pattern of the pressure contours are vertical due to side wash. Suction is more on the faces near the leading edges from where separation of flow is taking place with high magnitude of velocity and reducing towards the lee side edges. Formation of local eddies on upper heights of both the faces A and B can be seen towards the windward side.

On roof top pressure is mostly negative. High suction towards the windward side, reduces first with high gradient and then smoothly towards the leeward side is observed. Region of high eddy zones can also be seen in blue colours. The area average C_{Pe} on the roof is -0.64, minimum for all wind angles.

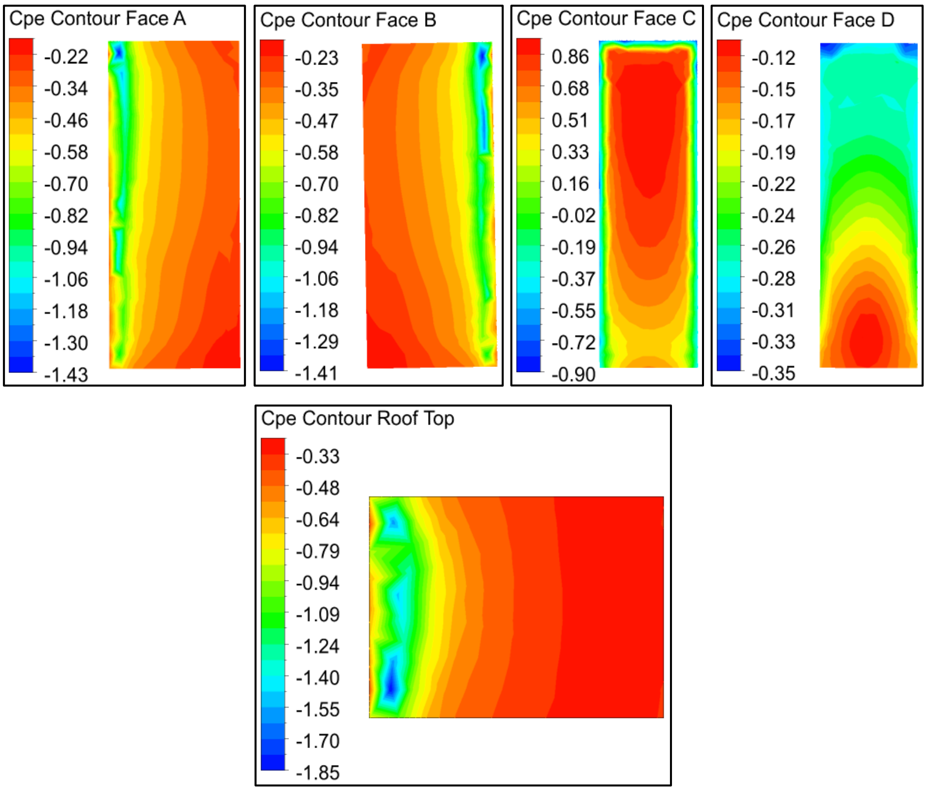

Figure 4. 4: C_{Pe} Contour on Faces & Roof Rect Model 90° Wind Angle

4.2.5 Wind Flow Pattern

Figure 4.5, 4.8, 4.11 & 4.14 show the streamline of flow for different heights of the model viz Z = 0.165 m, Z = 0.250 m and Z = 0.335 m for different wind incidence angles from 0° to 90° @ 30° and Figure 4.6, 4.9, 4.12 & 4.15 show the velocity contours at same heights for different wind incidence angles. Velocity vector diagrams at different heights for varied wind angles are shown in Figure 4.7, 4.10, 4.13 & 4.16.

The pictures are helpful in understanding the effect of wind flow in pressure distribution on the faces of the model. Pattern of pressure distribution on faces are closely related to the velocity of flow at different points and the streamlines of flow depicts the direct impact of flow around the model envelope. Flow patterns are different in intensity and strength at different levels of height and also for different wind angles. It can be observed that the distance between the streamlines is not constant. Where spacing between the streamlines moves apart, flow is expected to slows down. Before striking the model, the streamlines are moving apart which indicates reduction in velocity of the flow. Where the streamlines come closure, it indicates speeding up of fluid greater than the free stream speed. At the separation corners, flow speed is greater than the free stream velocity. Largest velocity change occurs from where detachment of flow from the model is taking place. Downstream of the model where reattachment of flow occurs, the flow stream recovers the free stream value. Beyond a distance far away from the model in the upper and lower part of the diagram, flow is deflected but the distance between the streamlines changes little and the corresponding flow change in stream is relatively small.

Since coefficient of pressure is a mathematical representation of impact or velocity pressure of wind striking on the surfaces, it largely depends upon the variation of flow field around the model. Hence, it is expected to impart different pressure distributions on similar faces of the model. The size of the wake formed behind the model can be related directly with the drag force on the model. When wake is smaller it helps in reduction of drag.

At 0° wind angle the flow is striking on face A and separation of flow is occurring from the leading edges. As such, positive pressure distribution occurs on the wind ward face A. Reattachment of flow occurs behind the model after wake in which two distinct symmetrical vortices are formed. Variation in the intensities of the two vortices are due to three-dimensional character of wind striking a bluff body. The variation in size and intensities of the streamlines along height provides information about the suction pressure distribution on leeward face. Figure 4.5 shows that the streamlines for different heights differ marginally in size and strength and it confirms minimum variation of suction pressure distribution on the leeward face due to backwash along height, as discussed earlier. Towards the side faces of the model streamlines and velocity contours are similar and hence side wash on the faces is creating similar pattern of pressure isobars.

At 30° wind incidence angle it can be seen that the flow is still interrupted by face A but obliquely and not perpendicularly. Accordingly, the streamlines are dissimilar towards the side faces and behind the model. It is observed that the vortices as well as velocity contours of flow are reducing in size along the vertical height of the model. Though two distinct vortices are formed, one behind face B and another behind face D, the pattern of vortices are a combination of backwash and sidewash both. The faces are showing pattern of isobars accordingly on the faces.

At 60° wind angle the streamlines and velocity contours are similar as that for 30° wind angle. The only difference is that face A has been replaced by face C and faces B and C have been replaced by faces D and B respectively in position.

At 90° wind angle of attack two distinct vortices behind the model are formed and secondary small vortex each is formed towards the side faces. The size of the streamlines and velocity contours are bigger than that at 0° wind angle. However, in this case, unlike in 0° wind incidence angle, the size and intensities of the streamlines as well as that of velocity contours are reducing along height of the model. This prompts that suction on the leeward face is increasing along height as the backwash is from bottom to top.

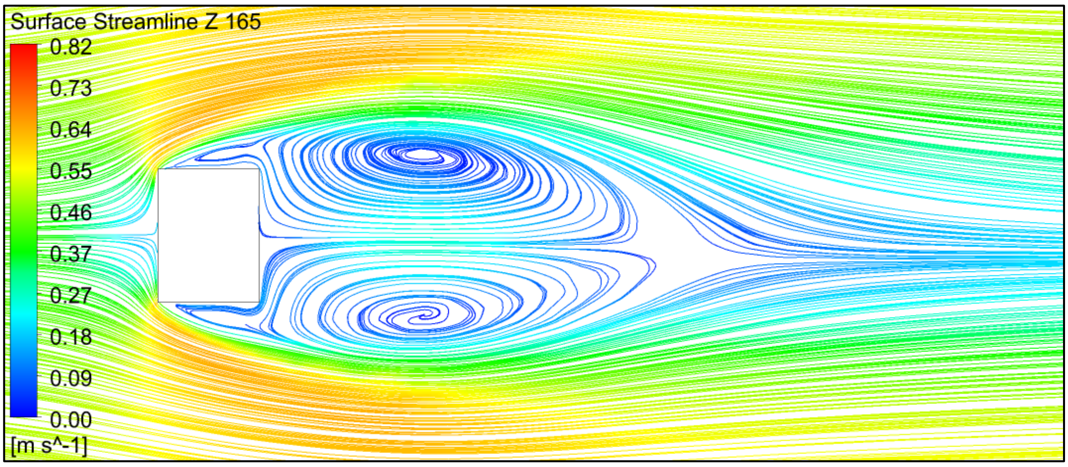

(a) Surface Streamline at Height Z = 165 mm

Figure 4. 5: Surface Streamline Rect Model 0° Wind Angle (Contd.)

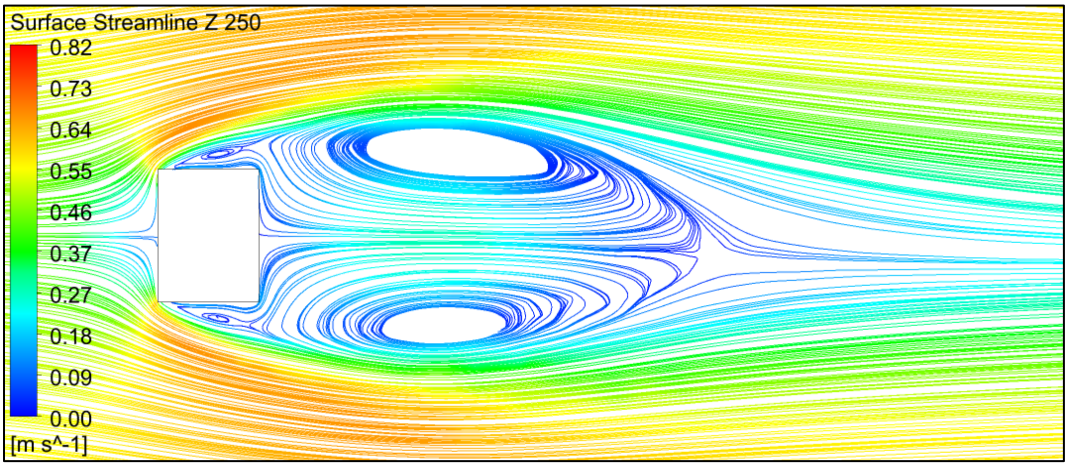

(b) Surface Streamline at Height Z = 250 mm

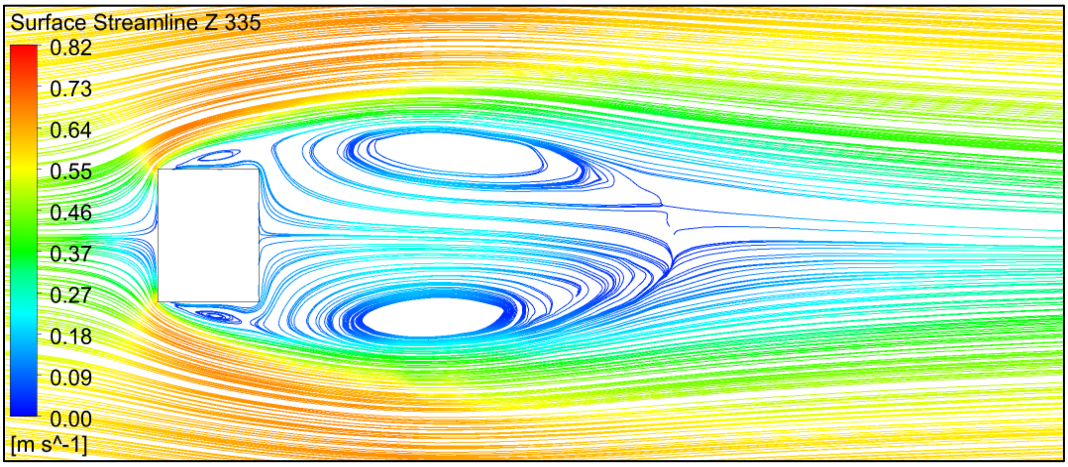

(c) Surface Streamline at Height Z = 335 mm

Figure 4. 5: Surface Streamline Rect Model 0° Wind Angle

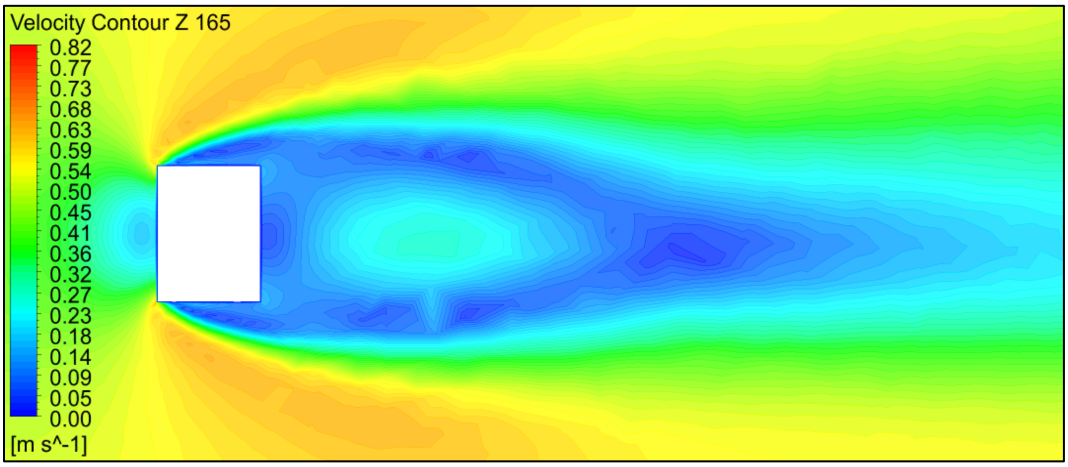

(a) Velocity Contour at Height Z = 165 mm

Figure 4. 6: Velocity Contour Rect Model 0° Wind Angle (Contd.)

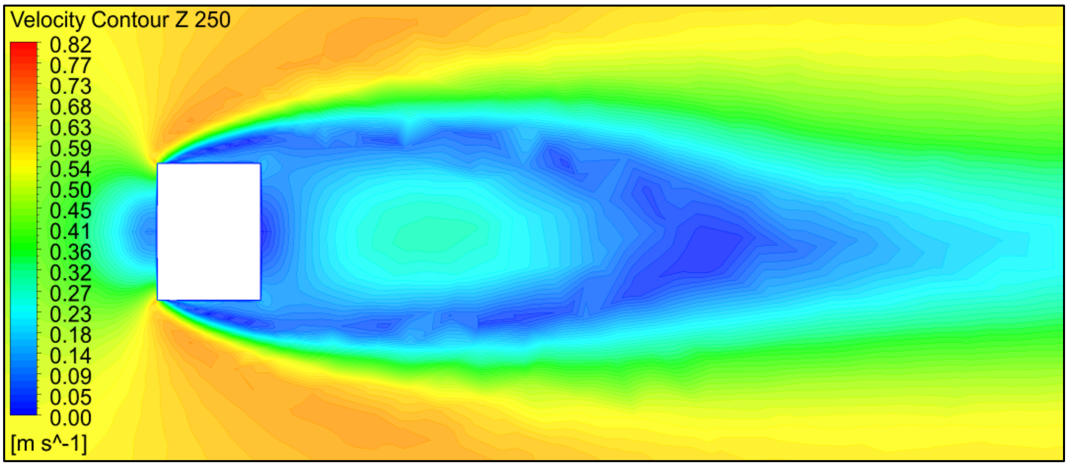

(b) Velocity Contour at Height Z = 250 mm

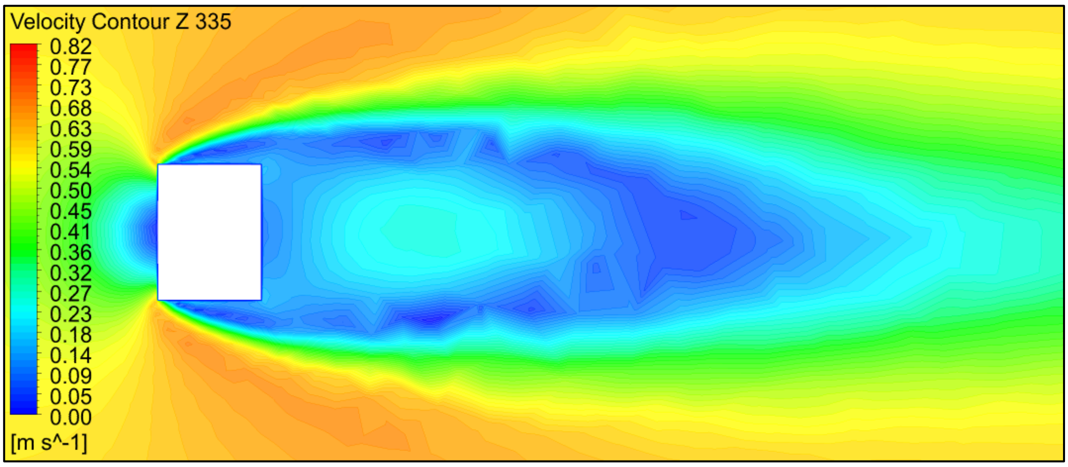

(c) Velocity Contour at Height Z = 335 mm

Figure 4. 6:Velocity Contour Rect Model 0° Wind Angle

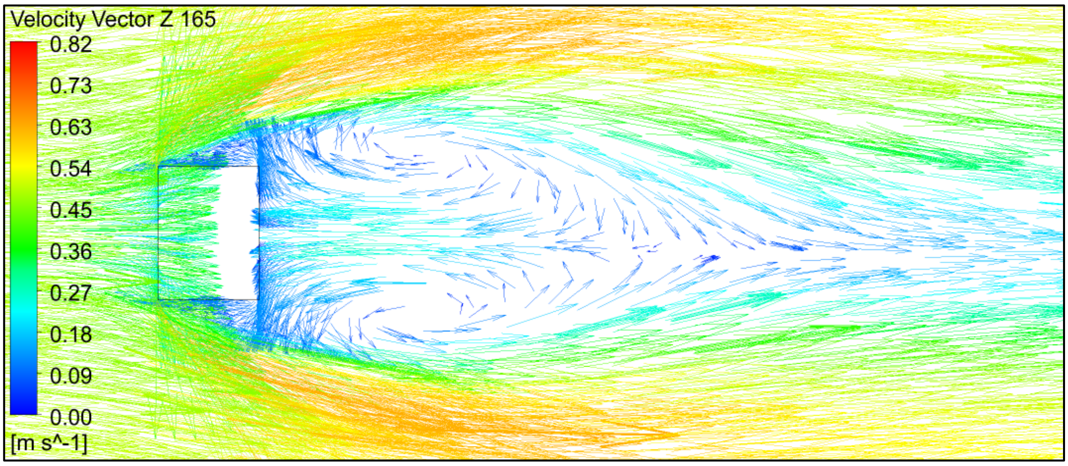

(a) Velocity Vector at Height Z = 165 mm

Figure 4. 7: Velocity Vector Rect Model 0° Wind Angle (Contd.)

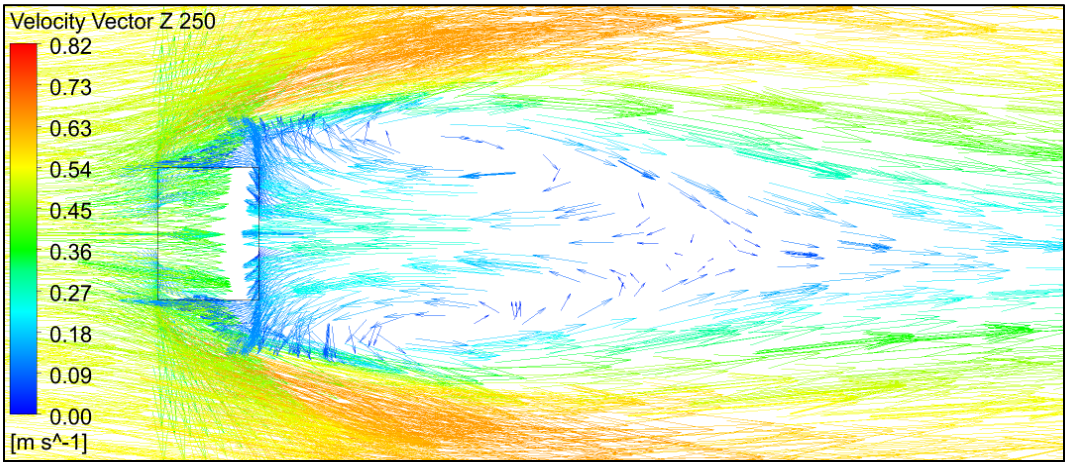

(b) Velocity Vector at Height Z = 250 mm

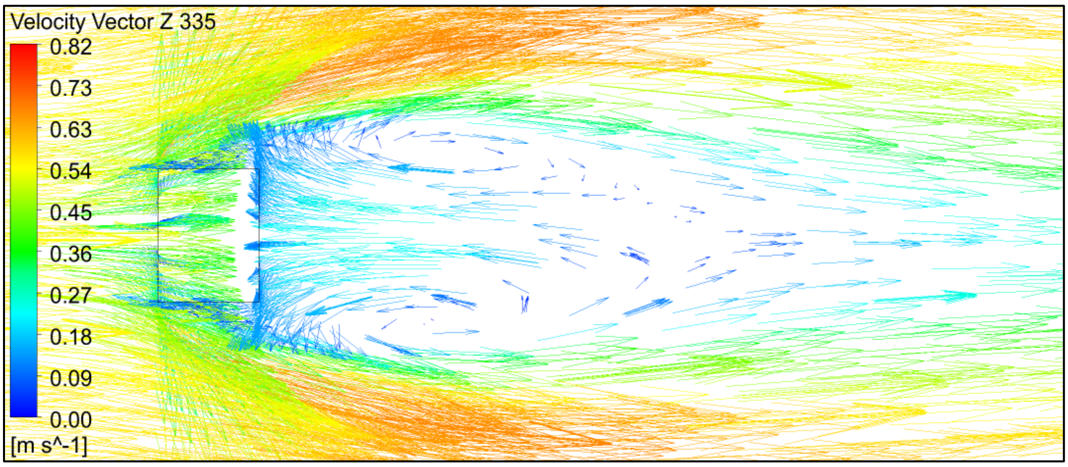

(c) Velocity Vector at Height Z = 335 mm

Figure 4. 7: Velocity Vector Rect Model 0° Wind Angle

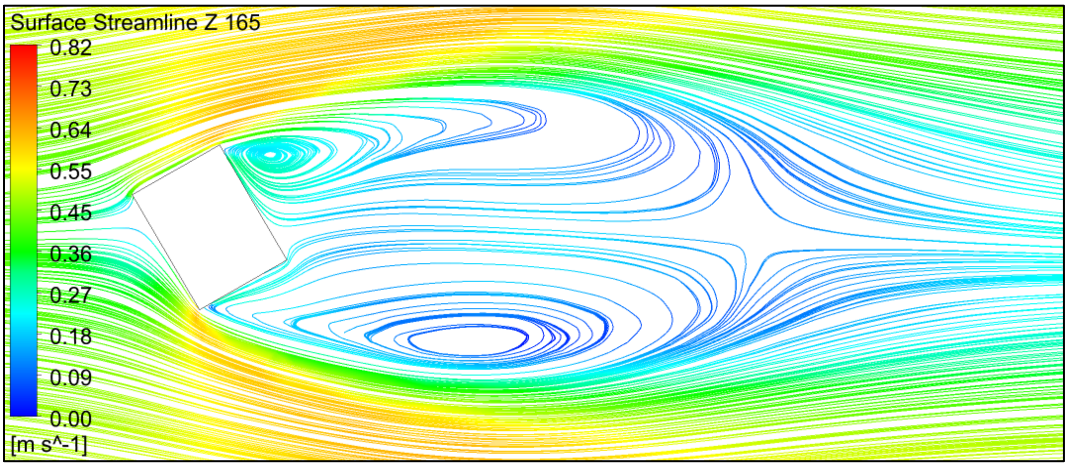

(a) Surface Streamline at Height Z = 165 mm

Figure 4. 8: Surface Streamline Rect Model 30° Wind Angle (Contd.)

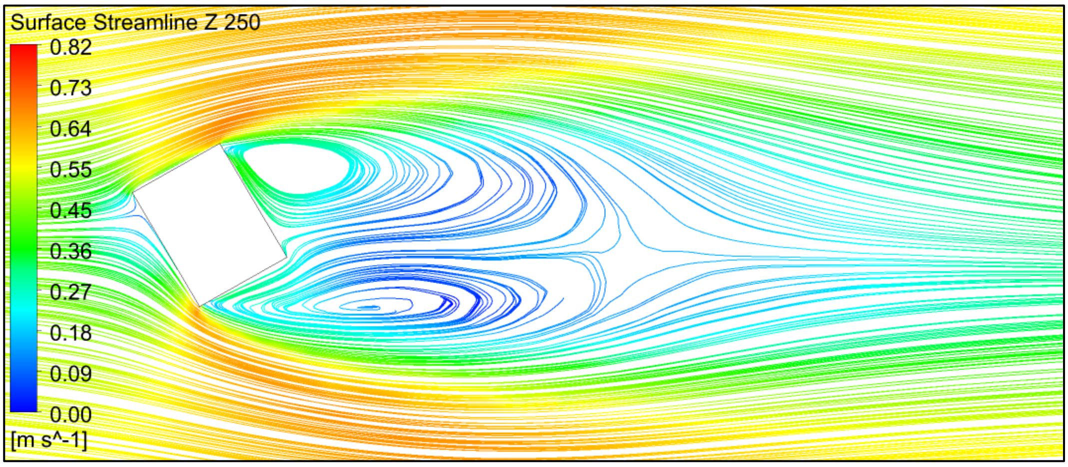

(b) Surface Streamline at Height Z = 250 mm

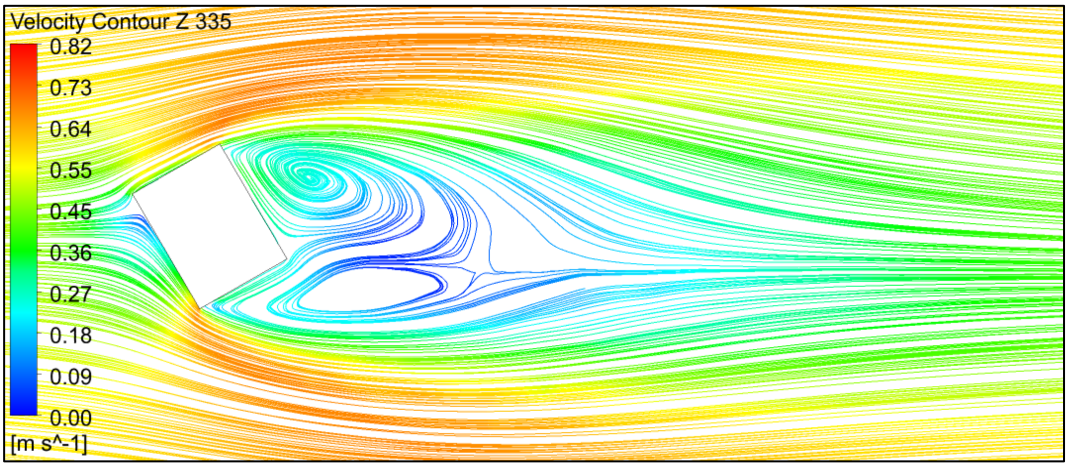

(c) Surface Streamline at Height Z = 335 mm

Figure 4. 8: Surface Streamline Rect Model 30° Wind Angle

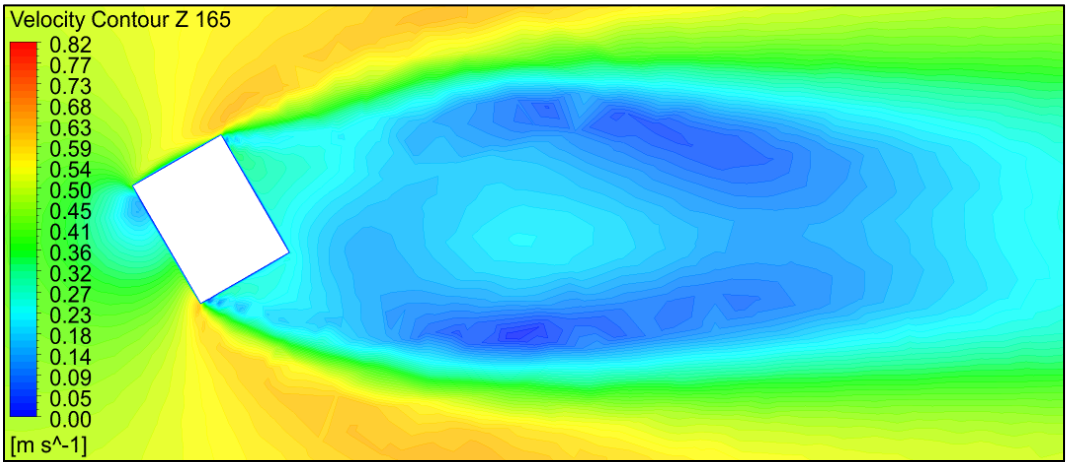

(a) Velocity Contour at Height Z = 165 mm

Figure 4. 9: Velocity Contour Rect Model 30° Wind Angle (Contd.)

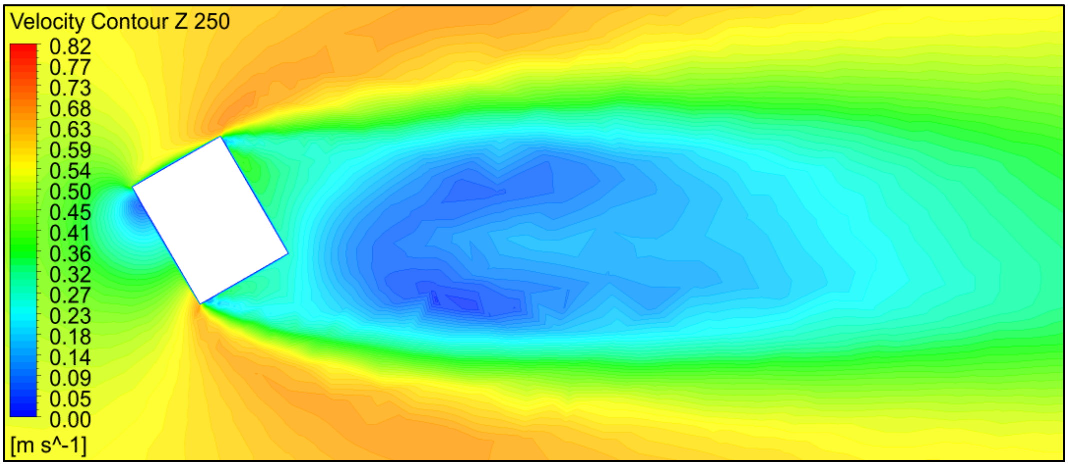

(b) Velocity Contour at Height Z = 250 mm

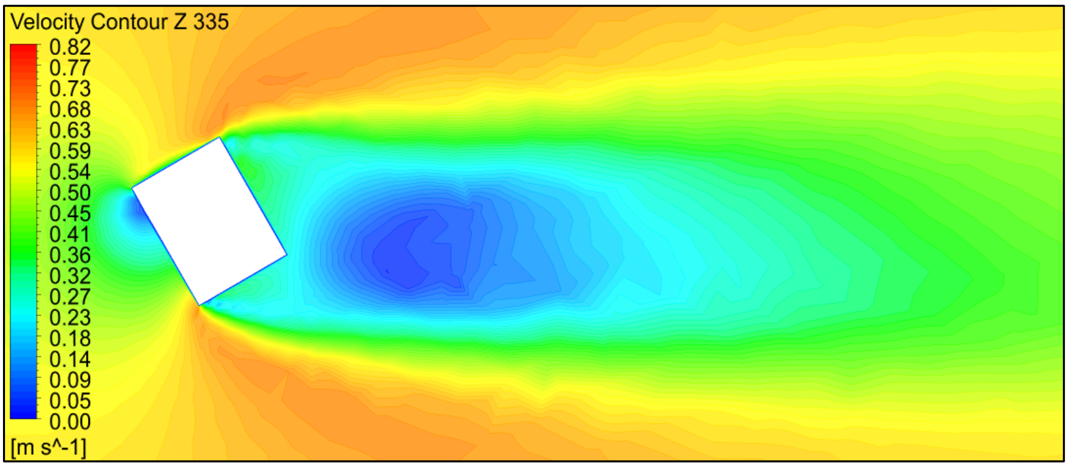

(c) Velocity Contour at Height Z = 335 mm

Figure 4. 9: Velocity Contour Rect Model 30° Wind Angle

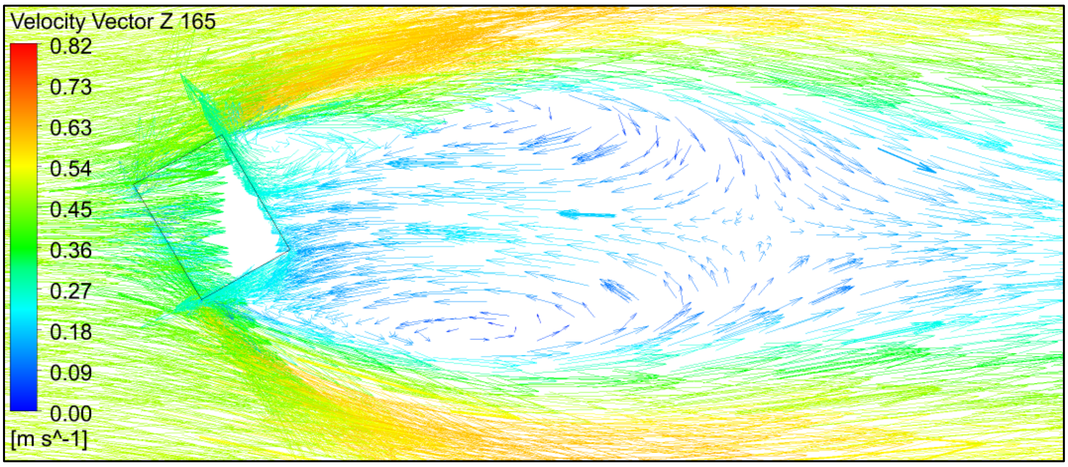

(a) Velocity Vector at Height Z = 165 mm

Figure 4. 10: Velocity Vector Rect Model 30° Wind Angle (Contd.)

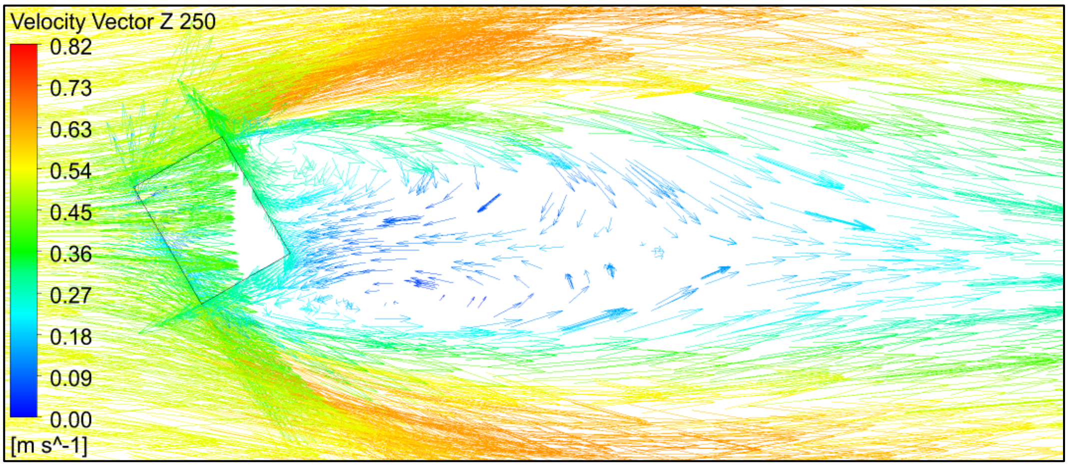

(b) Velocity Vector at Height Z = 250 mm

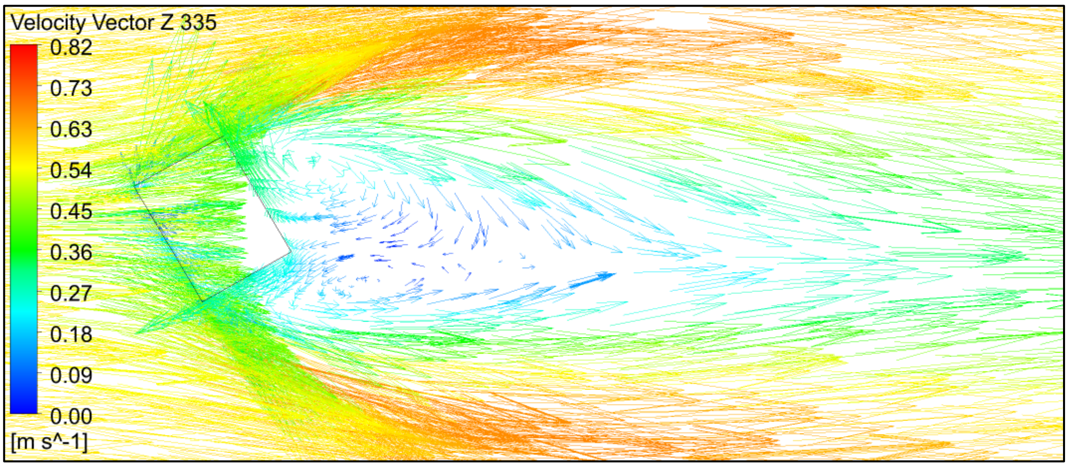

(c) Velocity Vector at Height Z = 335 mm

Figure 4. 10: Velocity Vector Rect Model 30° Wind Angle

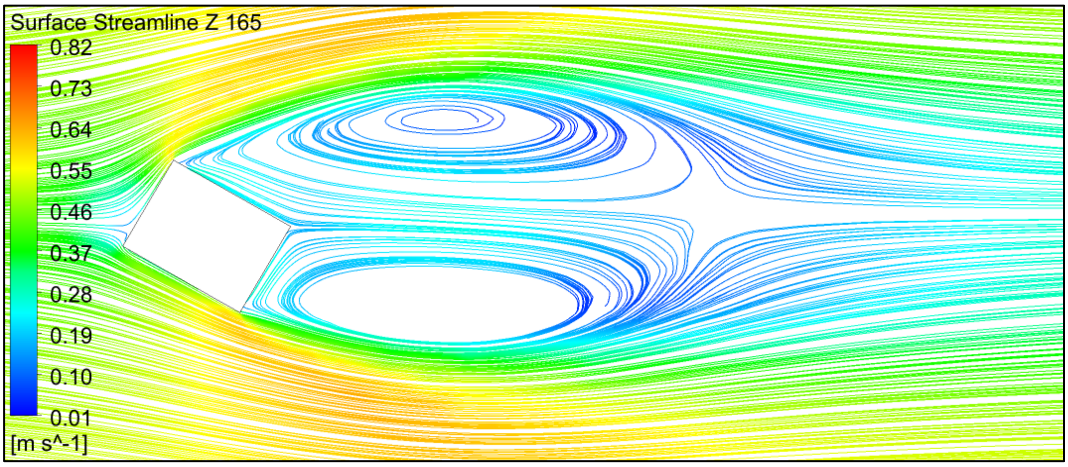

(a) Surface Streamline at Height Z = 165 mm

Figure 4. 11: Surface Streamline Rect Model 60° Wind Angle (Contd.)

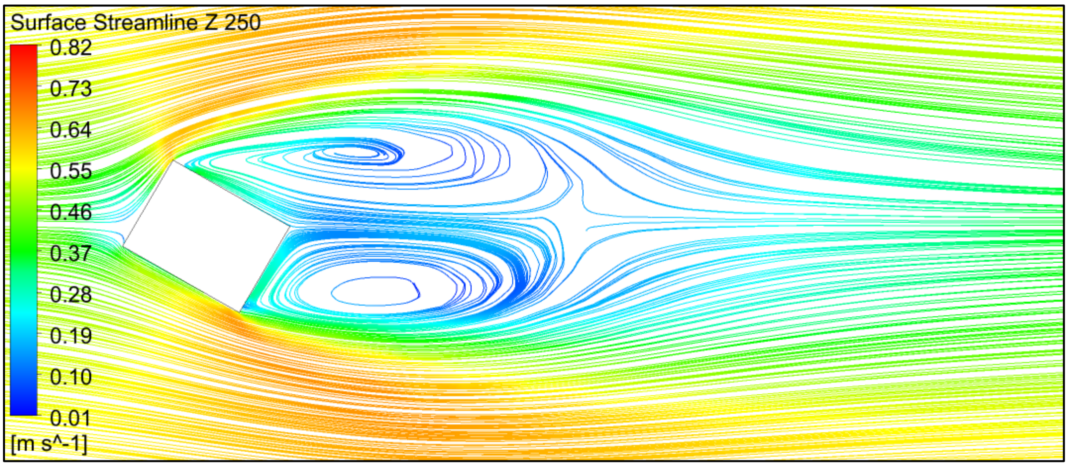

(b) Surface Streamline at Height Z = 250 mm

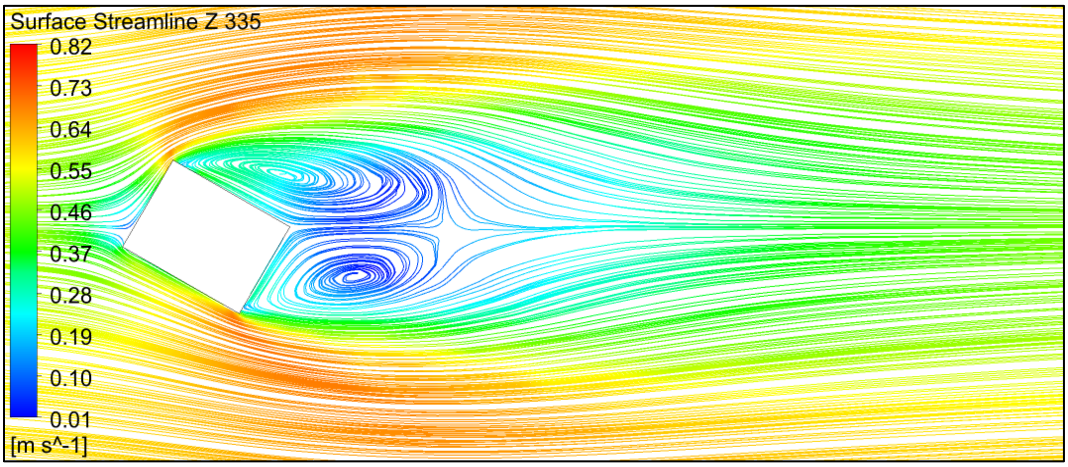

(c) Surface Streamline at Height Z = 335 mm

Figure 4. 11: Surface Streamline Rect Model 60° Wind Angle

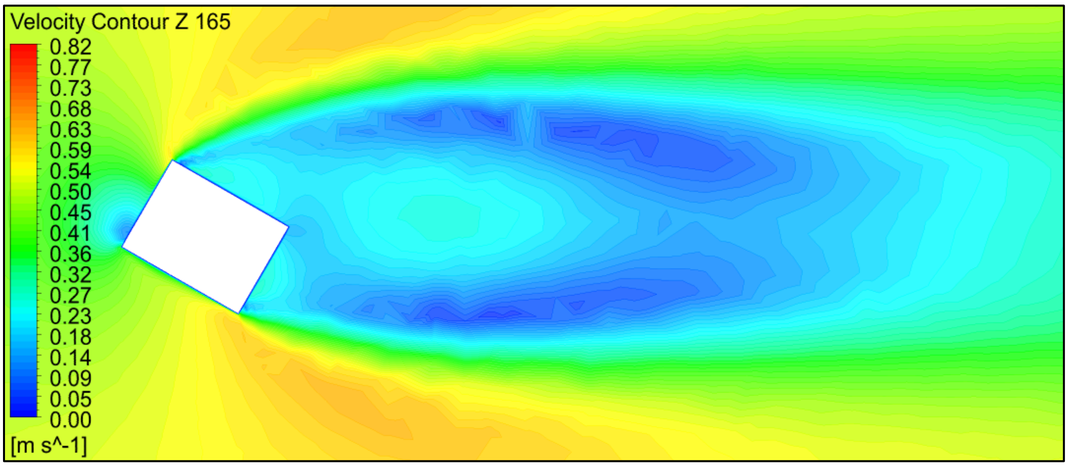

(a) Velocity Contour at Height Z = 165 mm

Figure 4. 12: Velocity Contour Rect Model 60° Wind Angle (Contd.)

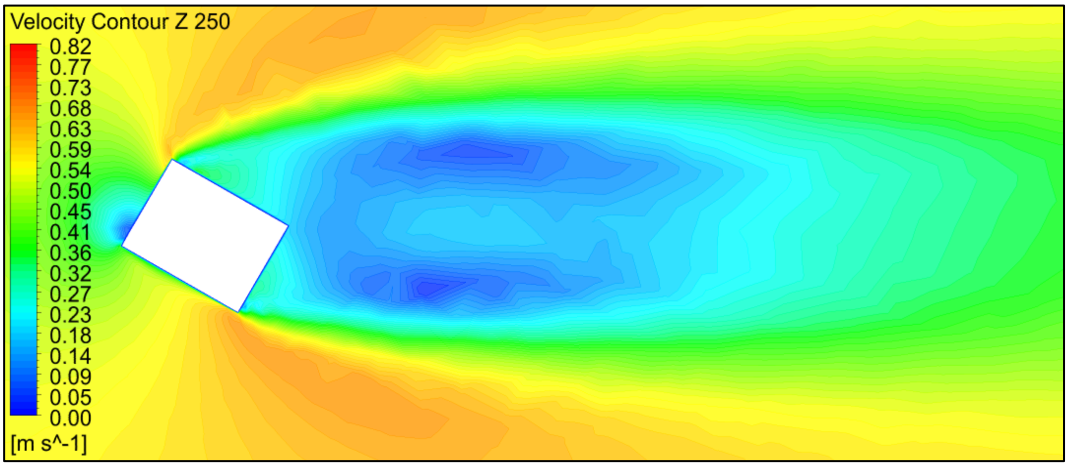

(b) Velocity Contour at Height Z = 250 mm

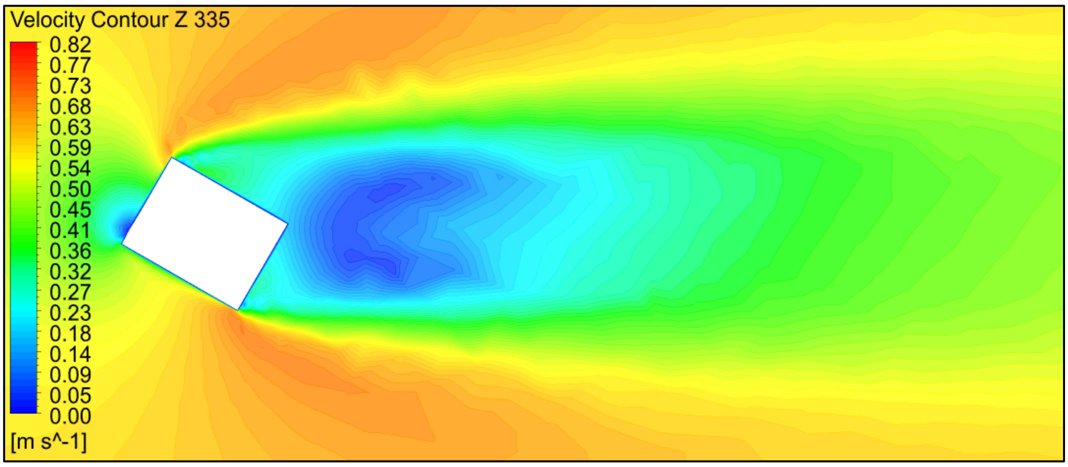

(c) Velocity Contour at Height Z = 335 mm

Figure 4. 12: Velocity Contour Rect Model 60° Wind Angle

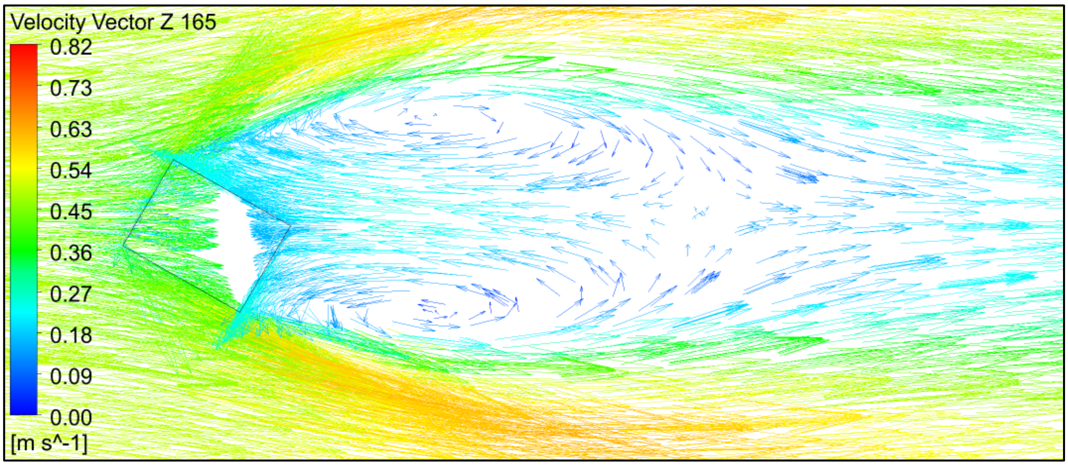

(a) Velocity Vector at Height Z = 165 mm

Figure 4. 13: Velocity Vector Rect Model 60° Wind Angle (Contd.)

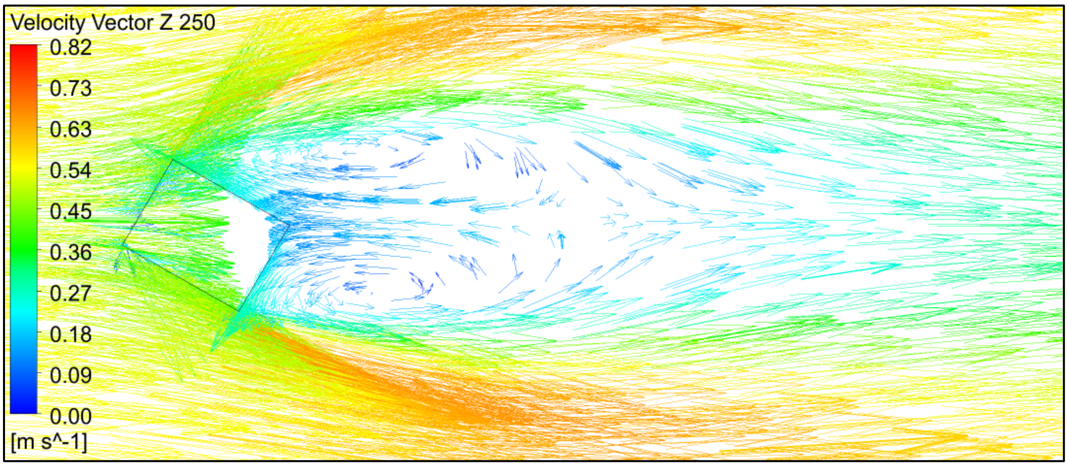

(b) Velocity Vector at Height Z = 250 mm

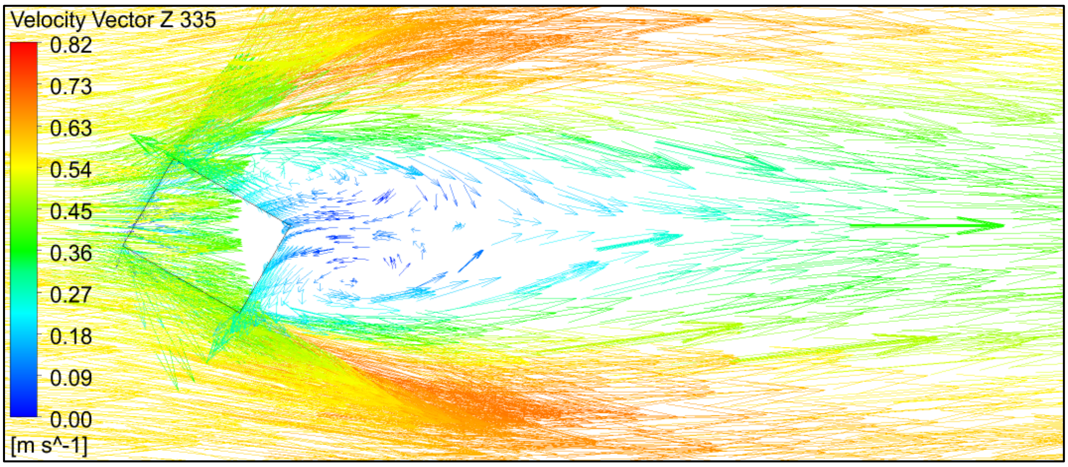

(c) Velocity Vector at Height Z = 335 mm

Figure 4. 13: Velocity Vector Rect Model 60° Wind Angle

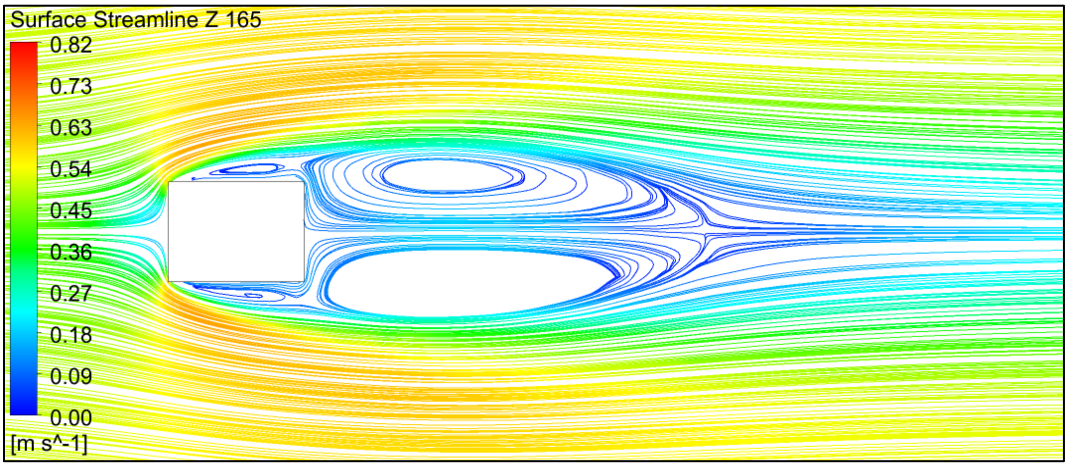

(a) Surface Streamline at Height Z = 165 mm

Figure 4. 14: Surface Streamline Rect Model 90° Wind Angle (Contd.)

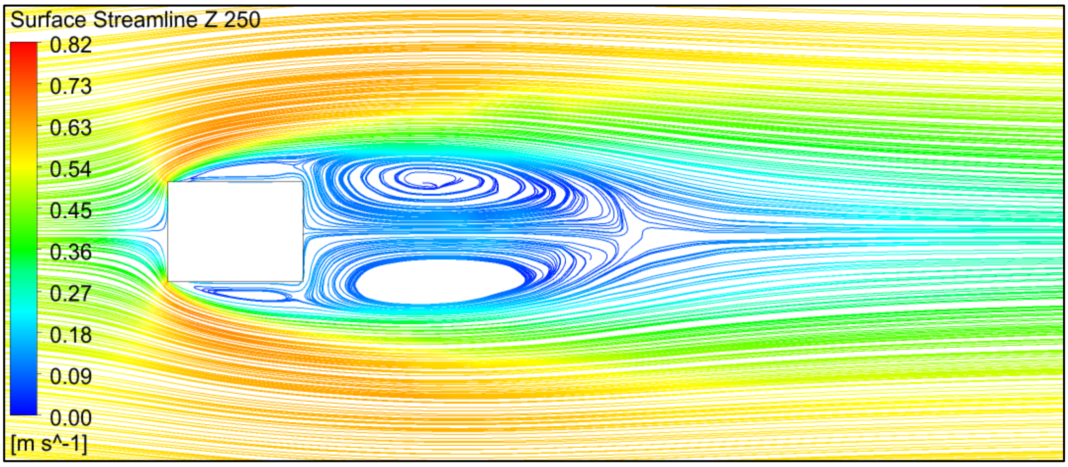

(b) Surface Streamline at Height Z = 250 mm

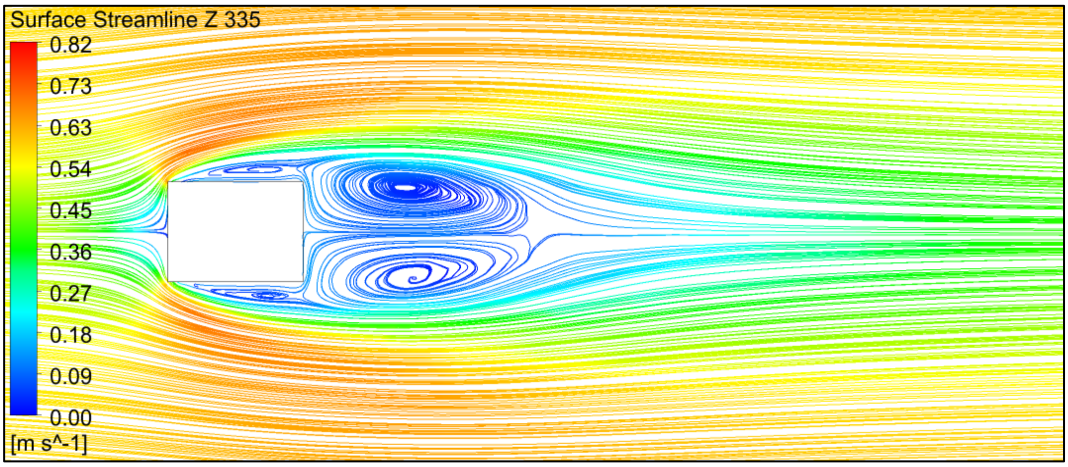

(c) Surface Streamline at Height Z = 335 mm

Figure 4. 14: Surface Streamline Rect Model 90° Wind Angle

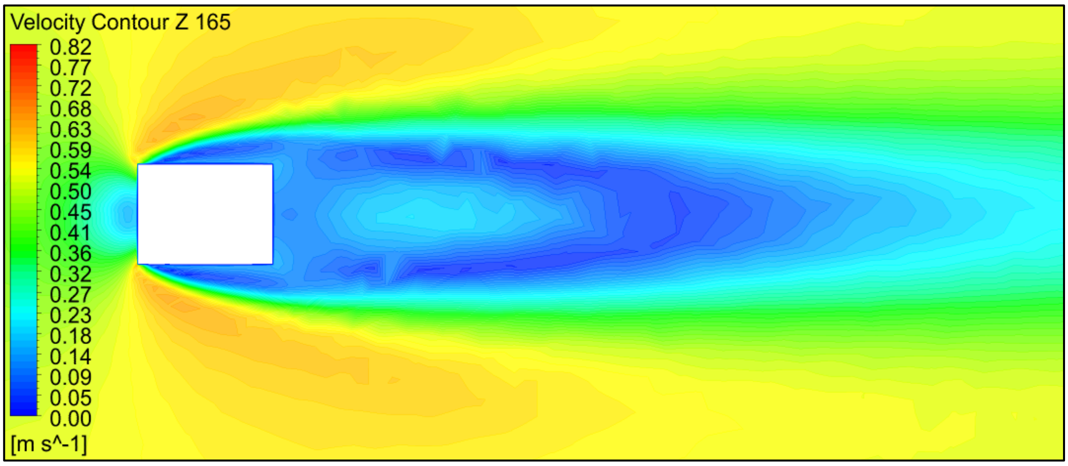

(a) Velocity Contour at Height Z = 165 mm

Figure 4. 15: Velocity Contour Rect Model 90° Wind Angle (Contd.)

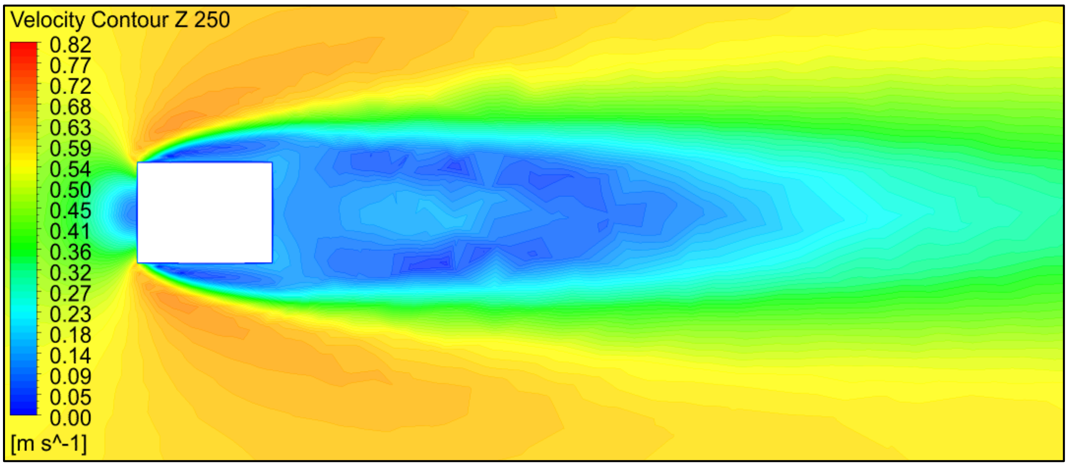

(b) Velocity Contour at Height Z = 250 mm

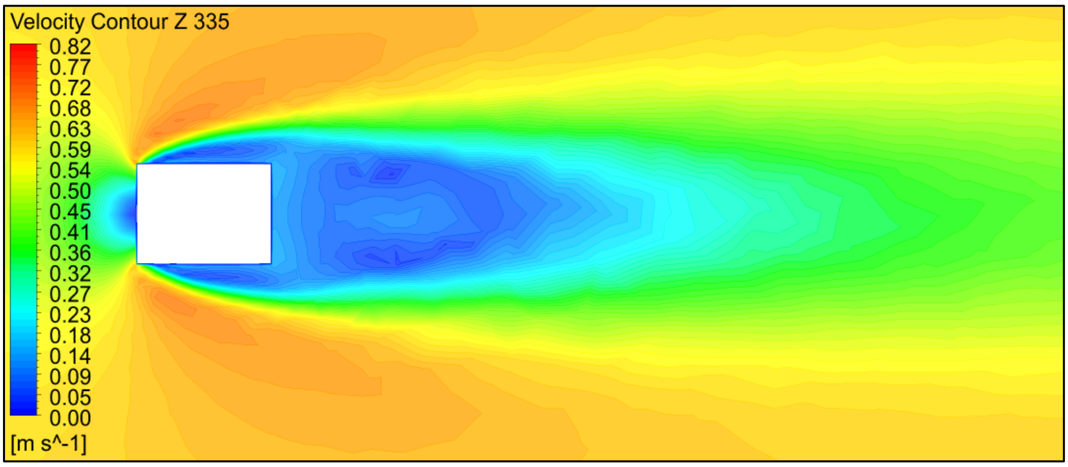

(c) Velocity Contour at Height Z = 335 mm

Figure 4. 15: Velocity Contour Rect Model 90° Wind Angle

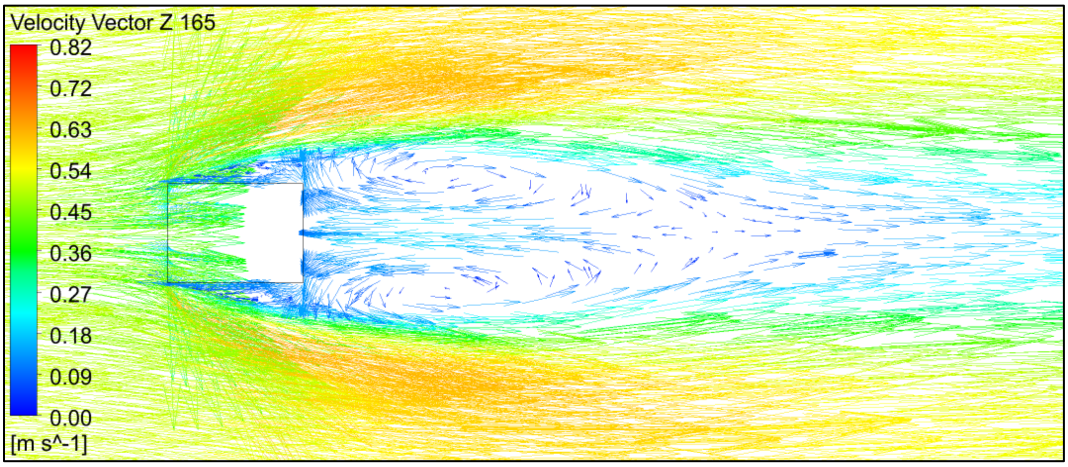

(a) Velocity Vector at Height Z = 165 mm

Figure 4. 16: Velocity Vector Rect Model 90° Wind Angle (Contd.)

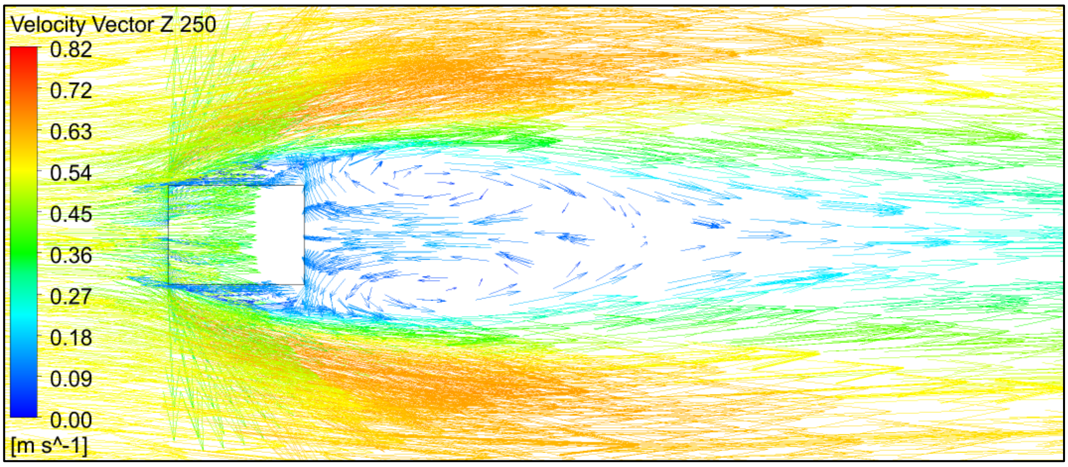

(b) Velocity Vector at Height Z = 250 mm

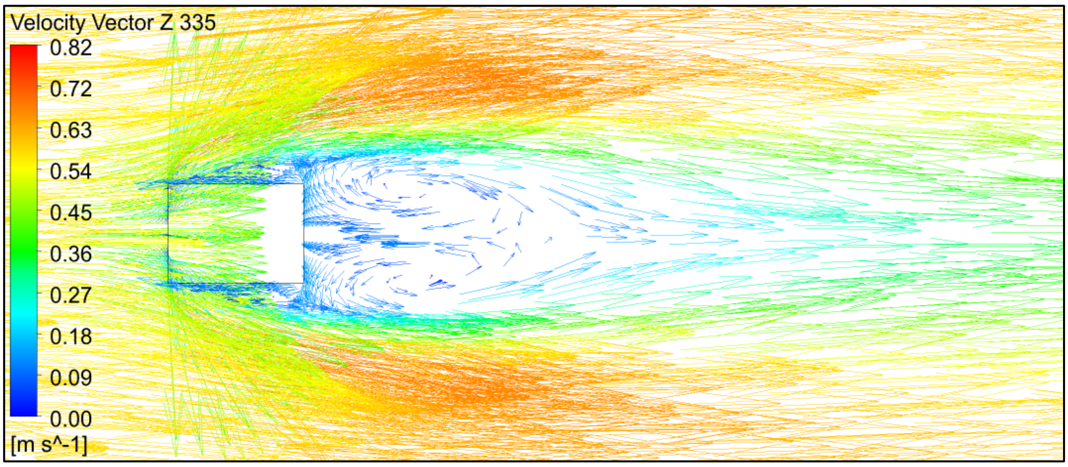

(c) Velocity Vector at Height Z = 335 mm

Figure 4. 16: Velocity Vector Rect Model 90° Wind Angle

4.2.6 Velocity Streamline Along Wind Direction on Central Vertical Plane

Figure 4.17, 4.18, 4.19 & 4.20 show flow streamline along wind direction on cross section through central vertical plane for different wind incidence angles from 0° to 90° @ 30° respectively. The upwind vortex at ground level, the upwash, downwash and stagnation zones on the windward face can be visualized. Flow reversal and creation of eddies at roof top and reattachment of flow behind the model can also be seen.

The intensity of upwind ground vortex is more prominent at 0° and 90° wind angles comparative to other wind angles. At 0° wind angle the location of upwind vortex is at more distance away from the windward face comparative to that at 90°, as width of the windward face normal to the wind at 0° wind angle is more than that at 90° wind angle.

The vorticity of clockwise circulation of wind in the wake are also apparent in the pictures. It is observed that the recirculation zone at roof top is created at 0° and 90° wind angles only. At 0° wind angle two vorticity points are seen, one near the ground and another near the roof with a distance apart between the them along wind direction.

Clearly the backwash from the former is hitting near the centre of the leeward face from where downwash along the height is created, whereas upwash on the leeward face is created due to another one. Accordingly, the suction pressure is minimum at the centre of the leeward face B increasing towards both, the top and bottom of the face. For other wind angles only one vorticity point near the top is seen.

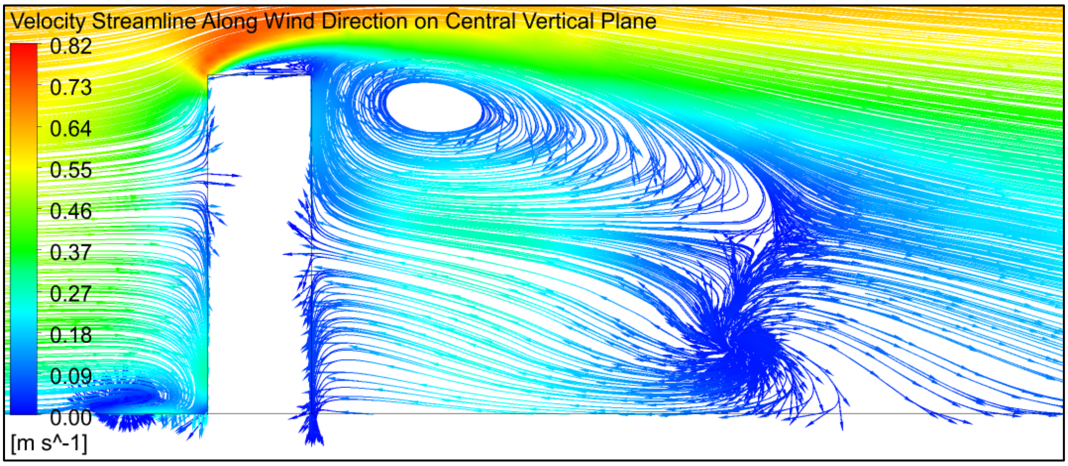

Figure 4. 17: Velocity Streamline Along Wind Direction on Central Vertical Plane Rect Model 0° Wind Angle

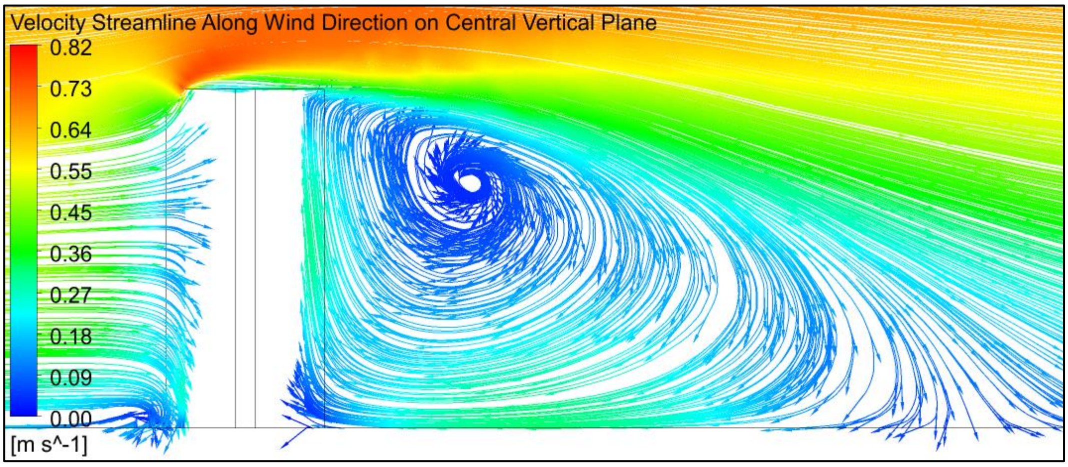

Figure 4. 18: Velocity Streamline Along Wind Direction on Central Vertical Plane Rect Model 30° Wind Angle

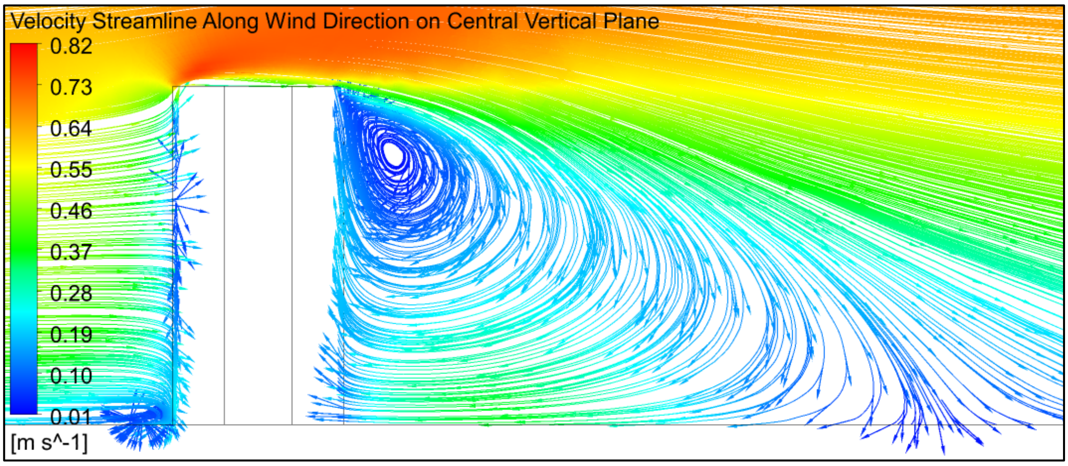

Figure 4. 19: Velocity Streamline Along Wind Direction on Central Vertical Plane Rect Model 60° Wind Angle

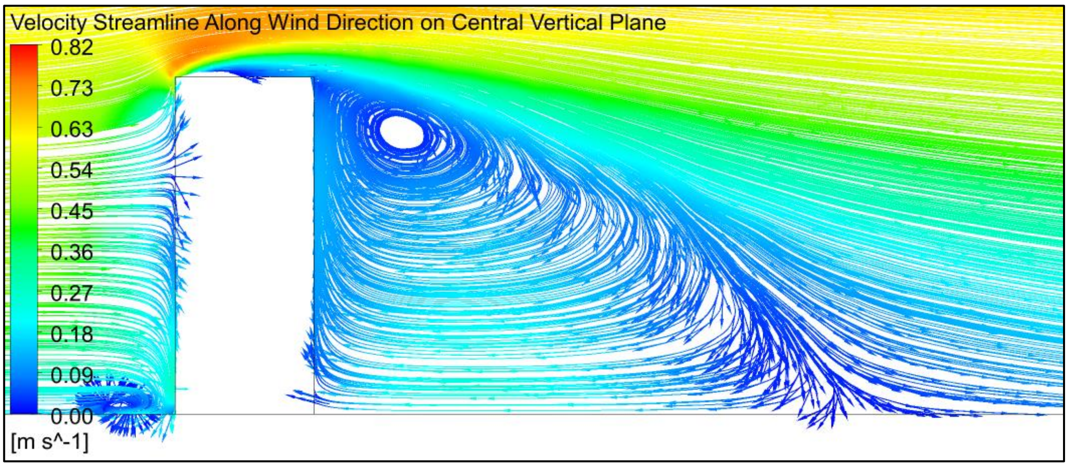

Figure 4. 20: Velocity Streamline Along Wind Direction on Central Vertical Plane Rect Model 90° Wind Angle

4.2.7 C_{Pe} Along Building Perimeter

Graphical plot representing the variation of C_{Pe} on the building façade at three different heights Z = 0.165 m (about 1/3rd height of the model), Z = 0.25 m (1/2 height of the model) and Z = 0.335 m (about 2/3rd height of the model) for different wind angles of attack from 0° to 90° @ 30° have been shown in Figure 4.21, 4.22, 4.23 & 4.24 respectively.

For all wind angles the maximum positive C_{Pe} values on the exposed faces are almost touching 1 (one). Along the C_{Pe} line on the faces, small variation in the value indicates formation of eddies and local turbulences at the point, whereas, huge variation in the value indicates formation of pressure region on the face at that point. At the meeting edges of the faces sudden increase in suction values of C_{Pe} indicates formation of large eddies and flow reversal. Generally, these eddies are formed at the meeting edges or on the faces near the meeting edges especially at sharp corners, as in the present case, where high suction is created. Such portions on the building façade are sensitive to failure in claddings due to wind. Care must be taken by the designers to take suction values at these corners thoroughly to avoid such situations.

The detailed suction C_{Pe} values for different wind angles on the corners are shown in Table 4.2 for the type and size of rectangular buildings discussed here. For symmetrical faces these values should have been similar, but due to anisotropic three-dimensional behaviour of wind there are minor differences in these values. For cladding design maximum value may be adopted to be on safer side. When cladding design is performed from the block contour diagrams prepared according to this data, it will be economical and cheaper at the same time cladding units will remain protected against failure due to wind.

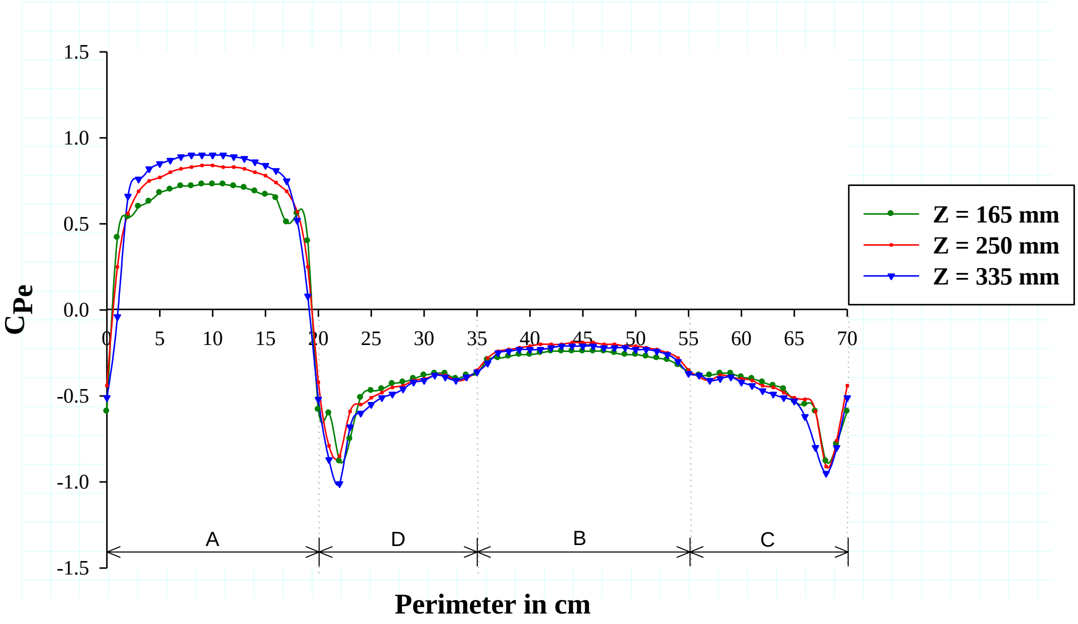

Figure 4. 21: C_{Pe} Along Perimeter Rect Model 0° Wind Angle

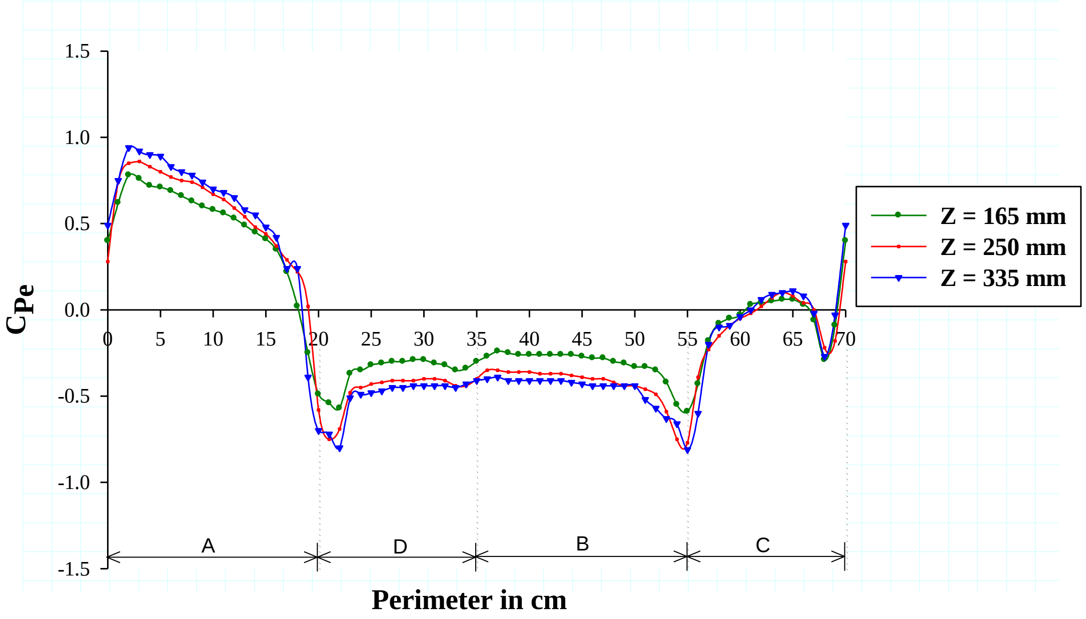

Figure 4. 22: C_{Pe} Along Perimeter Rect Model 30° Wind Angle

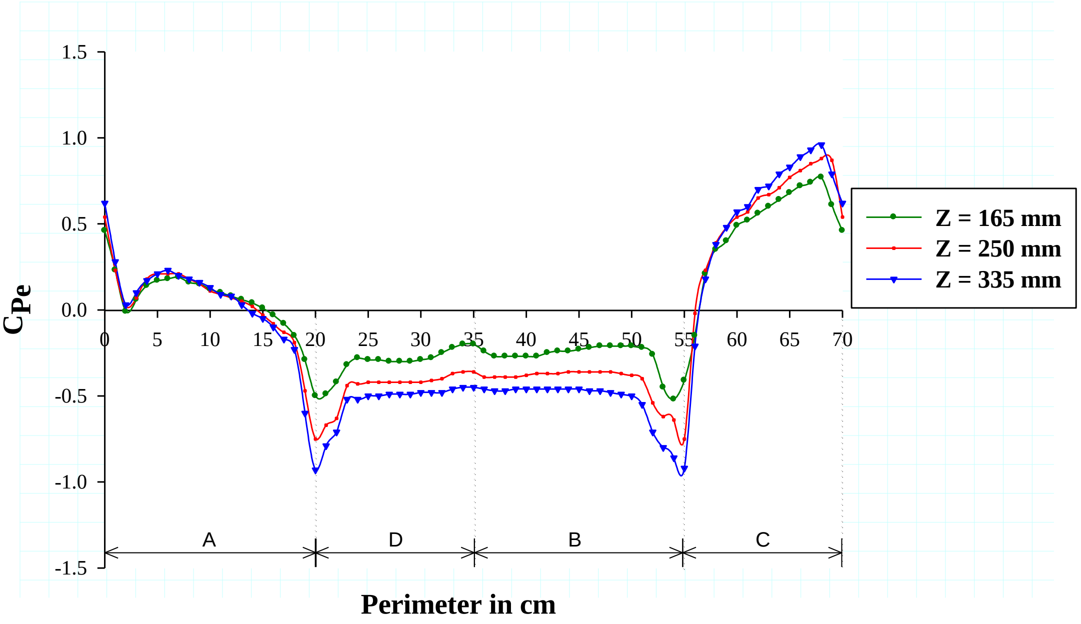

Figure 4. 23: C_{Pe} Along Perimeter Rect Model 60° Wind Angle

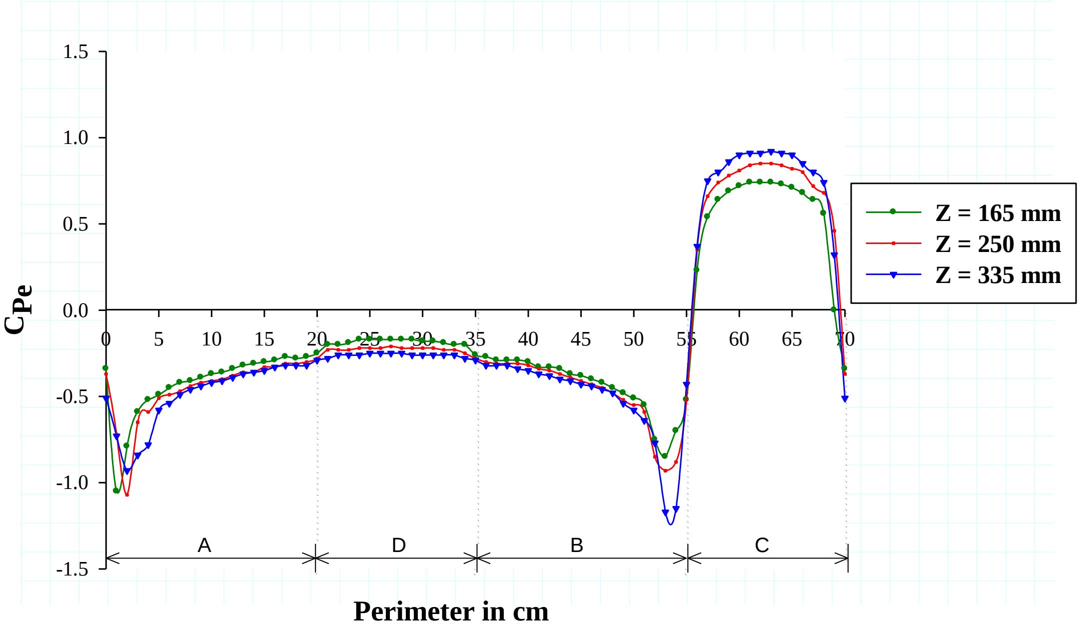

Figure 4. 24: C_{Pe} Along Perimeter Rect Model 90° Wind Angle

Table 4. 2: Maximum Suction in Terms of C_{Pe} For Cladding Design

AoA	0°		30°		60°		90°	
Z/Location	Corner		Corner		Corner		Corner	
	AD	AC	AD	BC	AD	BC	AC	BC
0.165 m	-0.88	-0.88	-0.58	-0.59	-0.49	-0.52	-0.95	-0.95
0.250 m	-0.91	-0.91	-0.75	-0.77	-0.75	-0.75	-1.00	-1.00
0.335 m	-1.01	-1.01	-0.80	-0.89	-0.93	-0.92	-1.04	-1.04

4.2.8 C_{Pe} Along Central Vertical Line on Faces

Figure 4.25, 4.26, 4.27 & 4.28 show plots of C_{Pe} values along central vertical line on the faces. The plots provide us realistic and fine picture of pattern of pressure coefficients along the height of the faces. Change in flow pattern along the height on the faces can be understood from them.

Pressure on faces on which wind is impinging upon directly show positive value of C_{Pe} and the maximum value along the height comes nearly 1.0 (equivalent to the velocity pressure or the impact pressure). The side faces experiencing the separation of flow and leeward face under wake region show negative pressure of coefficient (suction). For other than orthogonal impact of wind, the maximum C_{Pe} value along the line is less than 1.0. Also, symmetrical faces along the wind direction show overlapping C_{Pe} value along the central vertical line.

At 0° wind incidence angle in the instant case C_{Pe} is positive on the windward face A and the maximum value of C_{Pe} along the line is nearly equal to 1.0 at 0.475 m height of the model. On the leeward face the minimum suction C_{Pe} is -0.19 at 0.25 m height of the model. On side faces C and D almost equal suction throughout the height are seen, overlapping on each other. This shows that the faces are similar and opposite with respect to wind direction.

At 30° wind angle of attack faces A and C are showing positive values of C_{Pe}. On face A the maximum value along the line is around 0.8 at 0.475 m height of the model. On face C it is nearly 0.1 at the same height. Almost vertical profile on face C is observed with value less than 0.1. On face B and D suction exist along the central vertical line.

Variation of C_{Pe} along the lines are almost parallel with maximum suction C_{Pe} values between -0.43 to -0.45 at 0.3 m height of the model.

At 60° wind angle positive pressure exists on faces A and C. In this case the flow impinges obliquely on face C and flow separation is taking place from the far end of face A, hence face A is also under positive pressure as flow is surfing past this face. However, lesser magnitude C_{Pe} of almost constant values along the line on face A is observed than that on face C. On faces B and D C_{Pe} values are negative along the line and the pattern are similar to that on faces B and D for 30° wind angle of attack. The only difference is that at the roof level the C_{Pe} values sharply change to more suction.

For 90° wind angle the patterns of C_{Pe} variation along the central vertical lines on the faces are similar to that of 0° wind angle. Only the face name is changed according to the orientation of the model with respect to the wind direction – namely A to C, B to D, D to A and C to B.

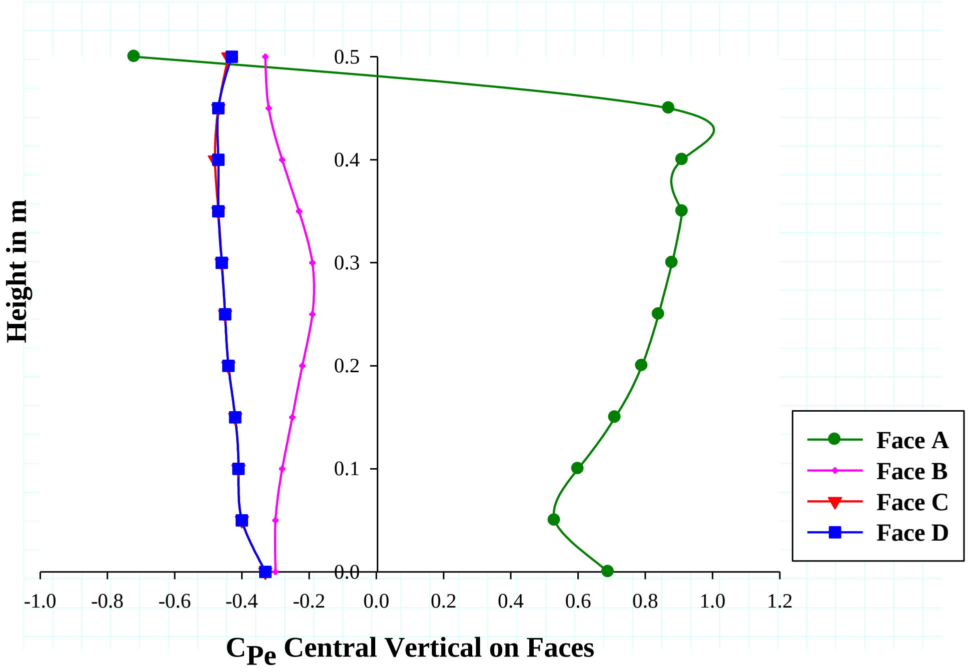

Figure 4. 25: C_{Pe} Along Central Vertical Line on Faces Rect Model 0° Wind Angle

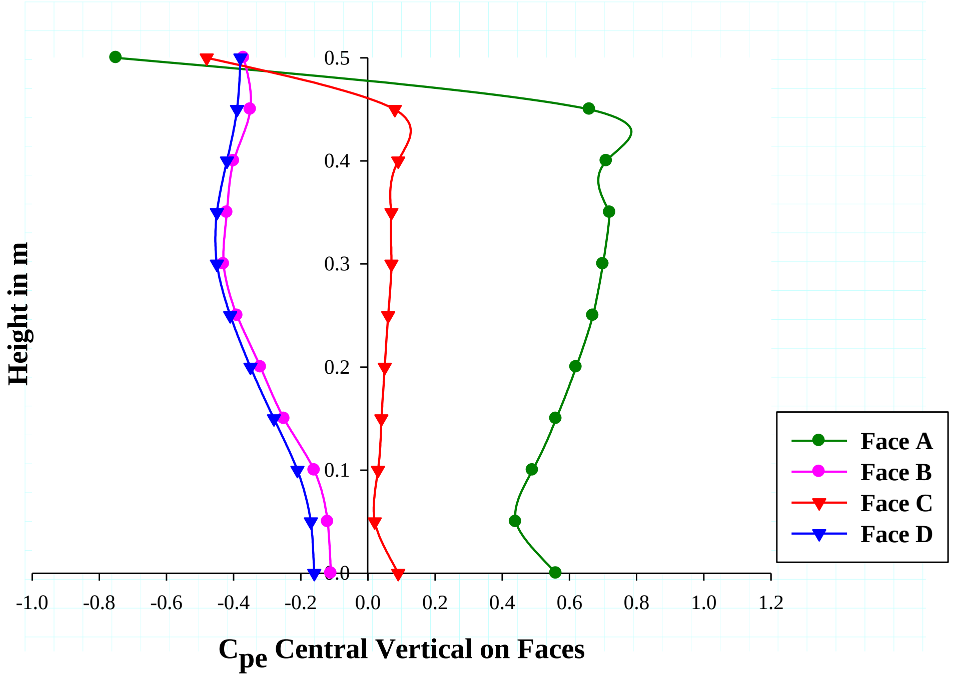

Figure 4. 26: C_{Pe} Along Central Vertical Line on Faces Rect Model 30° Wind Angle

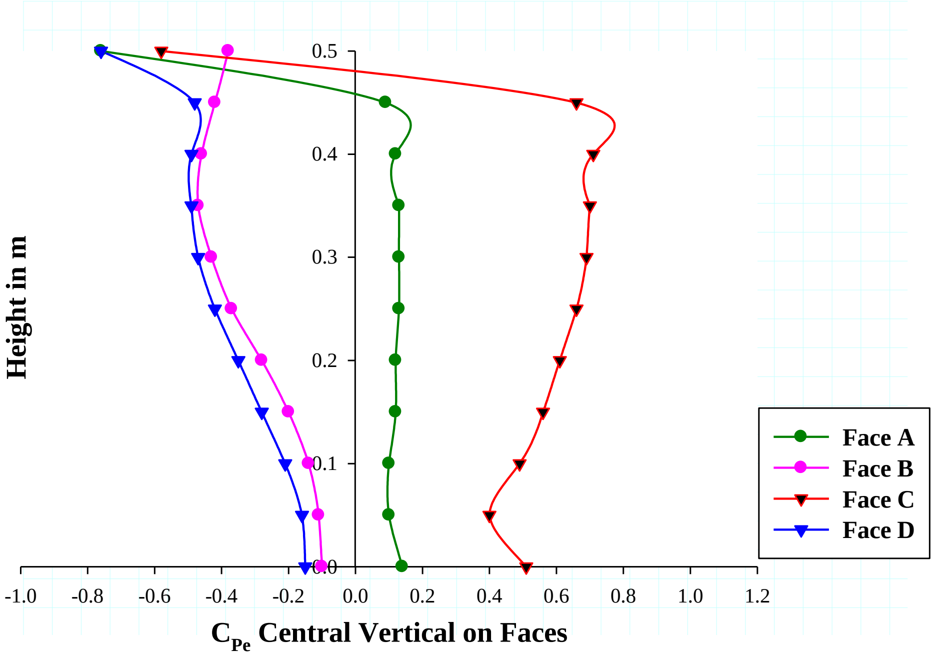

Figure 4. 27: C_{Pe} Along Central Vertical Line on Faces Rect Model 60° Wind Angle

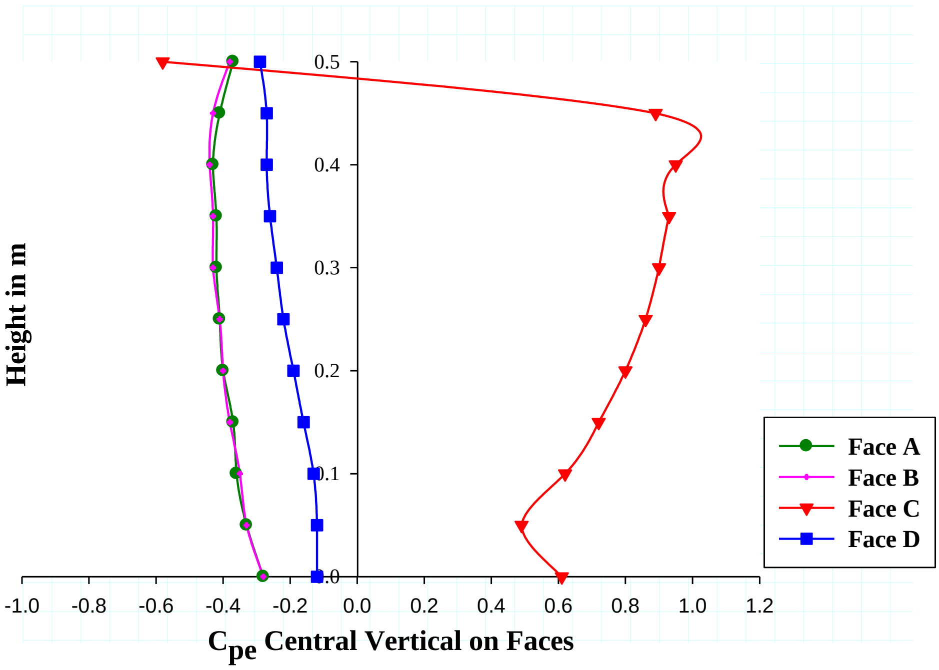

Figure 4. 28: C_{Pe} Along Central Vertical Line on Faces Rect Model 90° Wind Angle

4.3 PLUS SHAPE MODEL

Plus shape model is also symmetrical about both axes in plan hence, study from 0° to 90° of wind angle of attack is sufficient to understand the impact of wind from all angles of wind direction of flow.

4.3.1 C_{Pe} Contour 0° Wind Angle

Since the model is symmetrical about both the axes in plan, symmetrical faces are having identical response of wind effect. For 0° wind angle of attack faces A, D1, A2, D, B1, D2 and B are sufficient to study the pressure distribution on the model as symmetrical faces exhibit mirror images of contour isobars. Figure 4.29 shows the pressure distribution on the faces of plus plan shaped model. Flow is separating before impinging on face A.

Face A is having symmetrical pressure distribution about the central vertical line. Maximum pressure is around the middle and is increasing with height as velocity of wind is increasing along the height owing to the atmospheric boundary layer flow. The pressure is predominantly positive on the face which decreases symmetrically towards the edges.

Unlike the case of a rectangular model where side faces are subjected to negative pressure, face D1 is subjected to positive pressure. The pressure is not uniform across the width of the face but increasing from the meeting edge with face A towards the re-entrant corner i.e., corner of face D1 and A2. Negative concentration of pressure is seen at the top.

Face A2 is mainly subjected to positive pressure with concentration of negative pressures near the top corners – one at free end and another at the re-entrant corner. Pressure is concentrated at the middle of the face with high value near top.

Pressure distribution on face D is suction in nature with maximum suction at the near end edge. The isobars are vertical due to side wash.

On the downwind side face B1 is under negative pressure of almost uniform nature. Concentration of maximum suction is observed on both edges of face B1 at almost the middle height. This indicates maximum turbulence at the locations. At two locations – one at the bottom towards the free edge and another near top at the re-entrant corner minimum suction concentration is observed on face B1.

On face D2 minimum suction is concentrated at the re-entrant corner and maximum at the free end edge near the bottom elevation.

Face B is also subjected to negative pressure, as anticipated, being on the wake region. Suction pressure distribution is horizontal and symmetrical about the vertical centre line; almost uniform but increasing from bottom to top. Minimum suction is concentrated at the lower half of the bottom edges.

Negative pressure exists throughout the roof top with a symmetrical pattern about the centre line along the wind direction**.** Concentration of negative pressure are developed immediately after the separation of flow from the roof top. Table 4.3 shows the face average C_{Pe} on the faces.

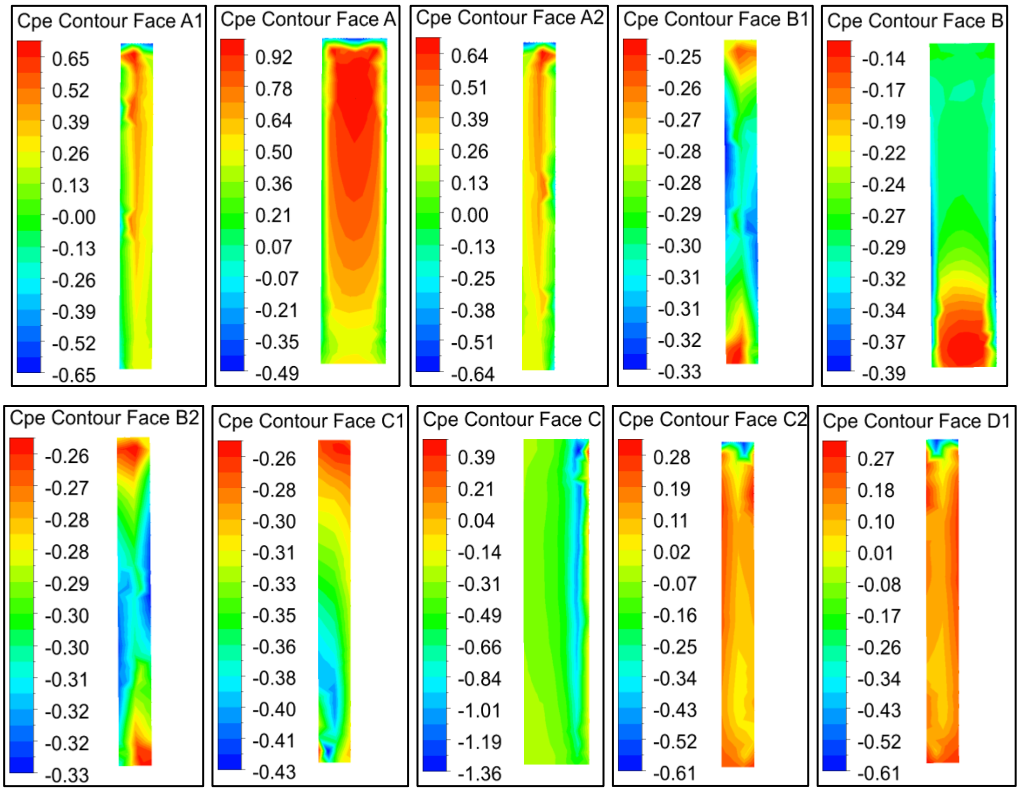

Figure 4. 29: C_{Pe} Contour on Faces & Roof Plus Model 0° Wind Angle (Contd.)

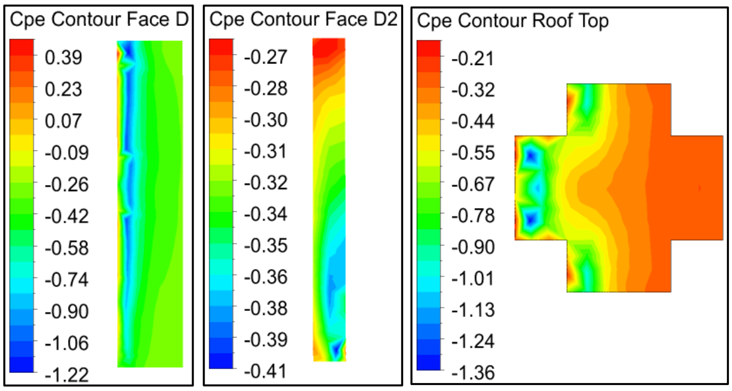

Figure 4. 29: C_{Pe} Contour on Faces & Roof Plus Model 0° Wind Angle

Table 4. 3: Area Average C_{Pe} on Faces

C_{Pe}	Angle of Attack of Wind			
	0°	30°	60°	90°
Face A1	0.23	0.66	0.71	0.11
Face A	0.65	0.35	-0.30	-0.48
Face A2	0.23	-0.35	-0.35	-0.34
Face B1	-0.30	-0.24	-0.24	-0.34
Face B	-0.26	-0.26	-0.29	-0.48
Face B2	-0.30	-0.49	-0.68	0.11
Face C1	-0.34	-0.35	-0.34	0.23
Face C	-0.48	-0.29	0.35	0.65
Face C2	0.11	0.72	0.65	0.23
Face D1	0.11	-0.69	-0.50	-0.30
Face D	-0.48	-0.30	-0.25	-0.26
Face D2	-0.34	-0.24	-0.23	-0.30
Roof Top	-0.50	-0.56	-0.56	-0.50

4.3.2 C_{Pe} Contour 30° Wind Angle

At 30° wind incidence angle the flow separation is taking place before the meeting edge of face A and C2. Face A is predominantly subjected to positive pressure but the concentration is shifted towards the confluence edge of face A and C2. The isobars are parabolic but unsymmetrical. Towards the far end edge of the face A pressure is negative due to flow separation from that edge.

Face A1 and C2 are also experiencing positive pressure but, the isobars are horizontal in nature increasing from bottom to top in values. It is due to creation of stagnation zone at the re-entrant corner where the flow tends to contour the sides rather than flowing into the cavity.

On face D1 there exists suction pressure of high gradient, predominately on height, at the near end edge due to separation of flow from that edge. A concentration of low suction can be seen at the bottom re-entrant corner.

Suction is also created on most part of face A2. At the re-entrant corner suction is more than that at the free end. A localized positive pressure zone is seen at the top free end corner of face A2.

On face D suction isobars can be seen to be vertical except at a small portion at the bottom where it is pyramidal at the centre. On most part of the face suction is uniform but near the meeting edge with face A2 the gradient is high.

On face D2 almost uniform pressure exists. However, at the bottom, low suction due to backwash is seen. On face B1 and B similar situation exist as that on face D2.

On face B2 contour patterns are vertical in nature. A high concentration of suction is noticed towards the re-entrant corner on upper height. Low concentration of suction exists at the bottom.

On face C high gradient of positive pressure exists at the near end edge immediately followed by concentration of negative pressure due to flow separation from this edge. At the other end again high concentration of negative pressure is seen. In between the two high value suction zones on the face almost uniform suction exists. The isobars are vertical in nature.

On roof a thin concentration of positive pressure is seen at the corner of face A and C2. High concentrations of suction pressure are also observed above the re-entrant faces A1 and C2 which are facing the wind. This concentration zone is vital for design of roof sheds/structures like hoardings, solar panel etc. The average area C_{Pe} values on the faces are shown in table 4.3.

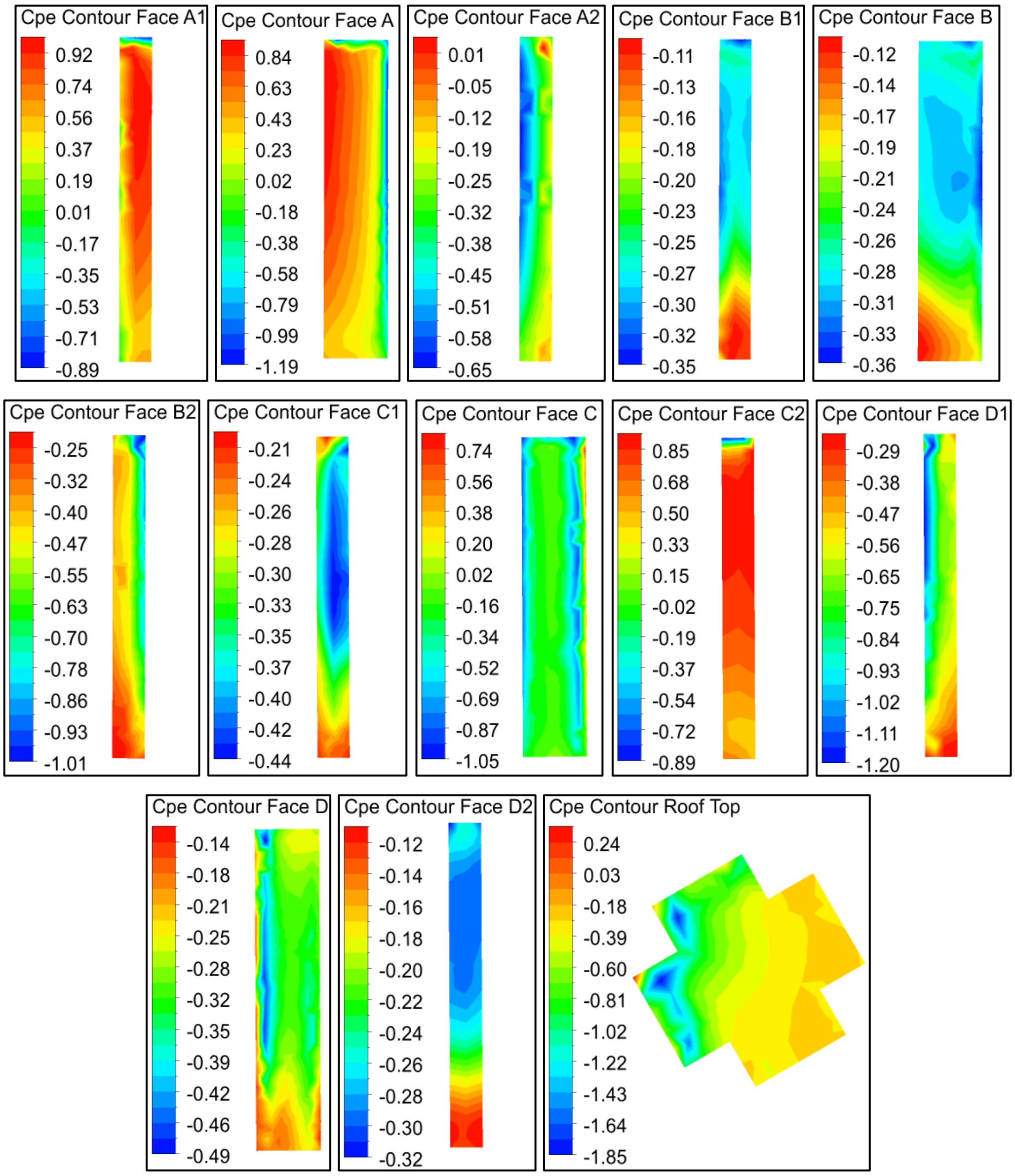

Figure 4. 30 C_{Pe} Contour on Faces & Roof Plus Model 30° Wind Angle

4.3.3 C_{Pe} Contour 60° Wind Angle

Flow at this angle of wind attack is impinging on face C as well as re-entrant corner faces A1 and C. Since the model is symmetrical about both the axes in plan, pressure contours on the faces for 60° wind angle of attack are mirror images of the pressure contours on similar faces with respect to the wind direction for 30° wind angle of attack. The face couples are A1 - C2, A – C, A2 – C1, B1 – D2, B – D, B2 – D1, C1 – A2, C – A, C2 – A1, D1 – B2, D – B and D2 – B1. Some minor differences on the faces on which suction pressure is occurring are due to local anisotropic generation of eddies and turbulences. However, the main characteristic of flow has been seized by the simulation and area average C_{Pe} on faces are analogous for the two wind angles.

On roof surface, except at the corner of face A1 and C where positive pressure concentration is seen, suction pressure exists throughout. Bubble of high suction pressure can be seen near the top re-entrant corner of face A1- C and A - C2 on roof top suggesting creation of local eddies at the place.

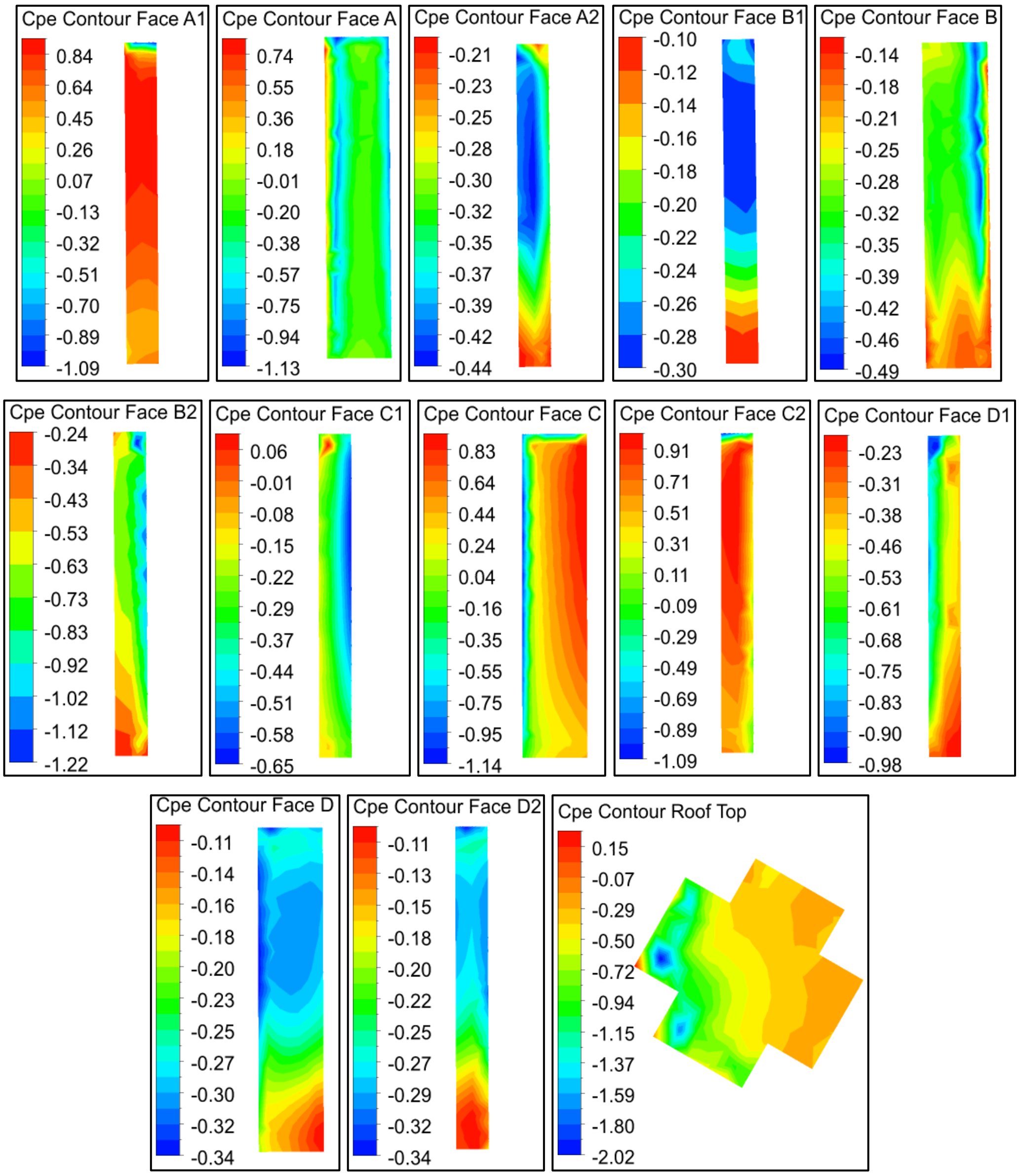

Figure 4. 31: C_{Pe} Contour on Faces & Roof Plus Model 60° Wind Angle

4.3.4 C_{Pe} Contour 90° Wind Angle

At 90° wind incidence angle flow is impinging on face C orthogonally like it is impinging on face A in 0° angle of wind incidence. The pattern of pressure contours on faces for 90 ° wind angle is similar to that in 0° wind angles on corresponding faces with respect to the direction of wind angles viz windward face C to A, leeward face D to B and so on. However, minor differences in pattern of pressure contours have been observed on the corresponding faces due to the reason explained in para 4.3.3 above.

On roof top pressure is mostly negative. Concentration of high negative pressure at two locations are seen near the wind ward face C. The area average C_{Pe} on the roof is -0.50. Pressure isobars on surfaces are shown in Figure 4.32

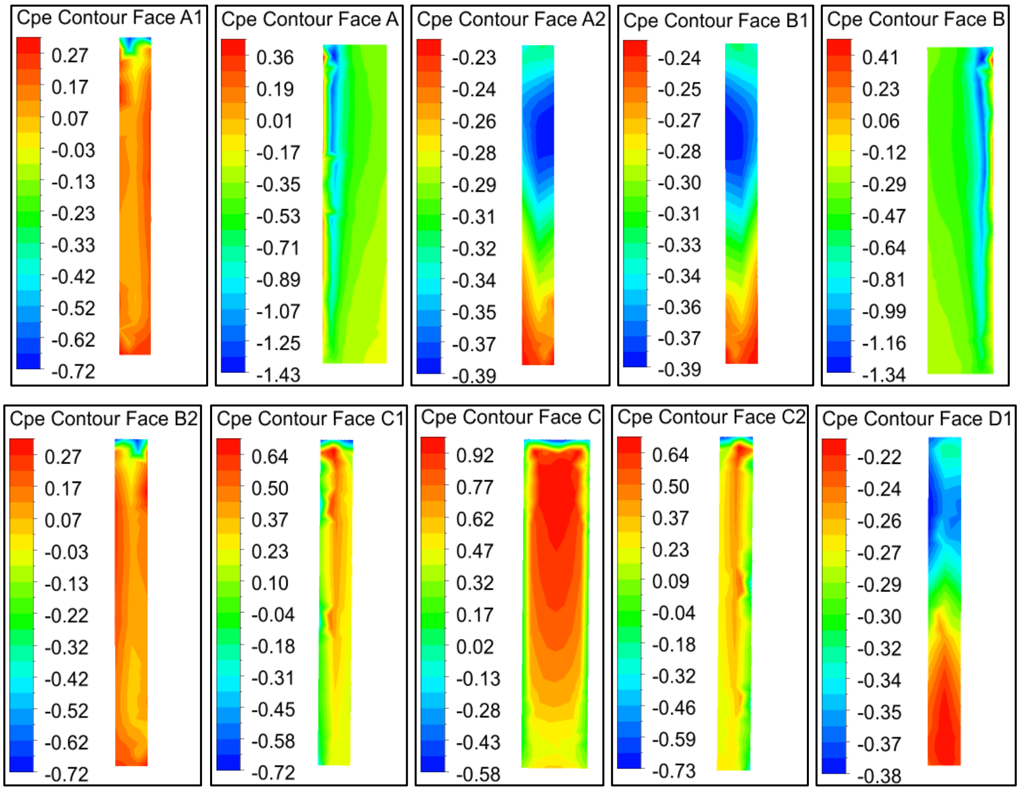

Figure 4. 32: C_{Pe} Contour on Faces & Roof Plus Model 90° Wind Angle (Contd.)

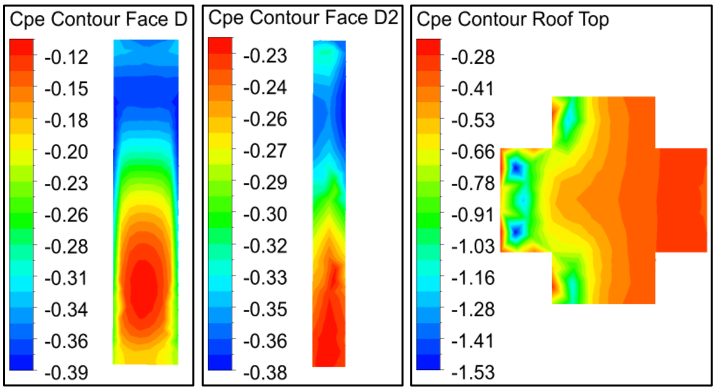

Figure 4. 32: C_{Pe} Contour on Faces & Roof Plus Model 90° Wind Angle

4.3.5 Wind Flow Pattern

Figure 4.33, 4.36, 4.39 & 4.42 show the streamline of flow at different heights of the model viz Z = 0.165 m, Z = 0.250 m and Z = 0.335 m for different wind incidence angles from 0° to 90° @ 30° and Figure 4.34, 4.37, 4.40 & 4.43 show the velocity contours at the same heights for different wind incidence angles. Velocity vector diagrams at different heights for varied wind angles are shown in Figure 4.35, 4.38, 4.41 & 4.44.

The importance of these picture in understanding the effect of wind flow in pressure distribution around model envelope and their characteristics has already been discussed in para 4.1 and 4.2.5.

At 0° wind angle the flow is directly impinging on face A. Separation of flow is taking place before it impacts on face A. Wind is also hitting windward faces A1 and A2 and finally separating from the outer edges of these faces with high velocity. Accordingly, positive pressure distribution occurs on face A, A1 and A2. After hitting face A1 and A2 wind is reflecting on the side faces C2 and D2 respectively. Hence these side faces are also experiencing positive pressure. Two similar large wakes spreading on the side faces are formed behind the model before wind reattaches on the leeward side. The intensity (spacing between the streamlines) at Z = 0.335 m is more than that on other heights. It shows higher velocity in flow direction at this height. Suction pressure on leeward faces is largely dependent on the variation in size and intensities of the streamlines along height. On studying velocity vector diagrams on three level of heights, it is observed that the concentration of vector arrows in the wake region is increasing along height. This indicates speed of flow is increasing along height. Due to similarity of streamlines in the wake, suction on the re-entrant faces is mirror images of corresponding faces in the direction of wind. Similar is the case with side faces C and D.

At 30° wind angle flow is striking on face A and C2, both obliquely. Flow is traversing the cavity of re-entrant corner A1C2 and separating from the free edge of face A1 on one side. On another side flow is separating from the far end edge of face A. One secondary small vortex each is also seen to be formed within the re-entrant corners A2D1 and B2C1.The small vortices are less prominent at Z = 0.250 m height of the model. Behind the model still two distinct large vortices are formed as found at 0° wind incident angle. There is minute difference in their symmetries of the vortices probably due to obliqueness of wind attack and small change in blockage area of the model at 30° wind angle compared to that at 0° wind angle. The suction pressure pattern on the faces under wake, as discussed above, are in tune with the pattern of streamlines.

At 60° wind incidence angle, as discussed in para 4.3.3 that the faces are producing mirror effect on the faces as compared to corresponding faces at 30° wind angle, the flow patterns for 60° wind angle are also in the same path.

Likewise, at 90° wind angle the flow patterns are similar to that at 0° wind angle.

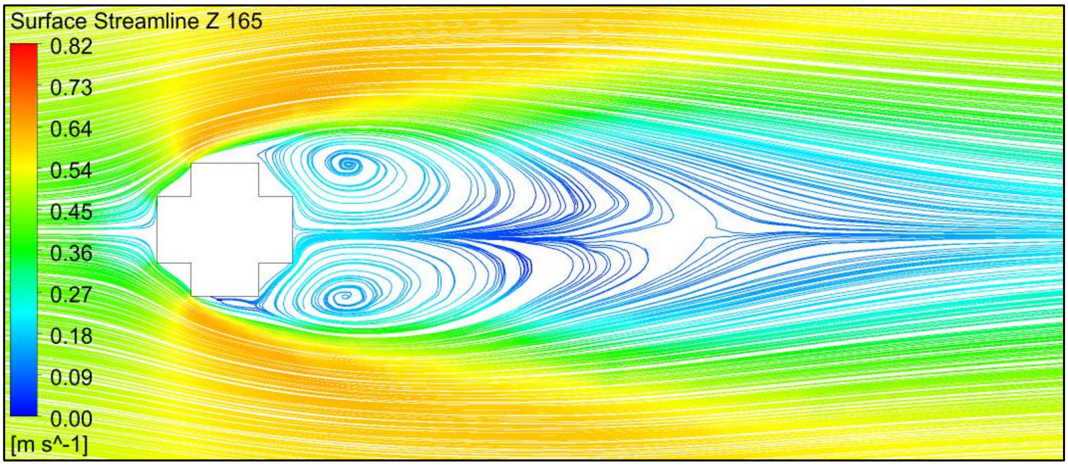

(a): Surface Streamline at Height Z = 165 mm

Figure 4. 33: Surface Streamline Plus Model 0° Wind Angle (Contd.)

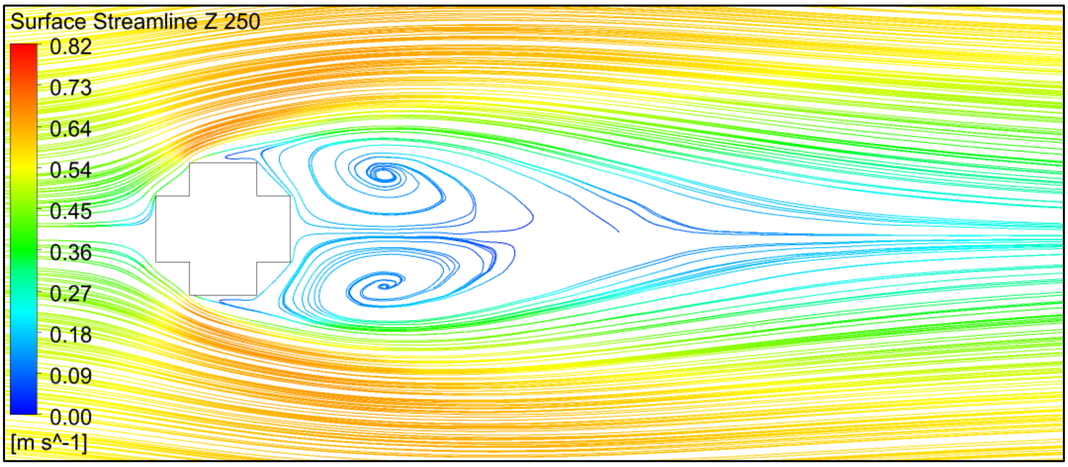

(b): Surface Streamline at Height Z = 250 mm

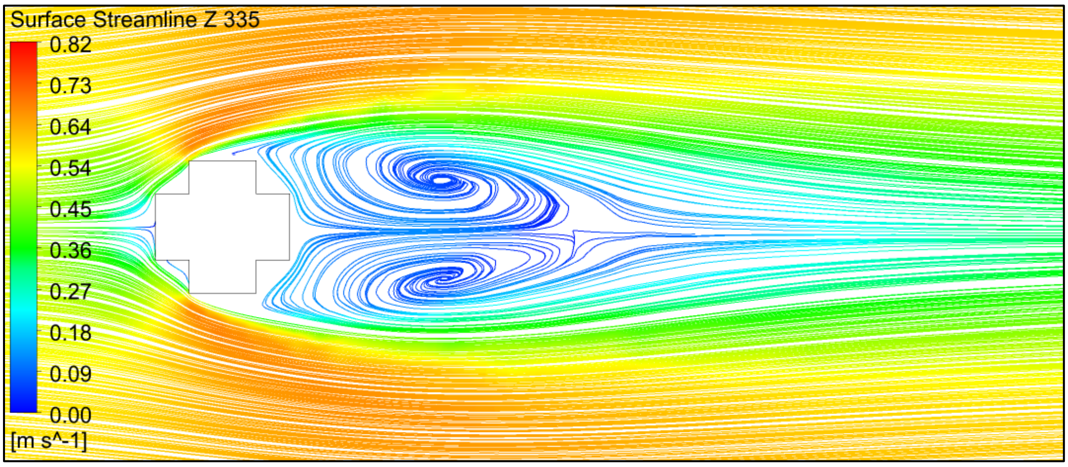

(c): Surface Streamline at Height Z = 335 mm

Figure 4. 33: Surface Streamline Plus Model 0° Wind Angle

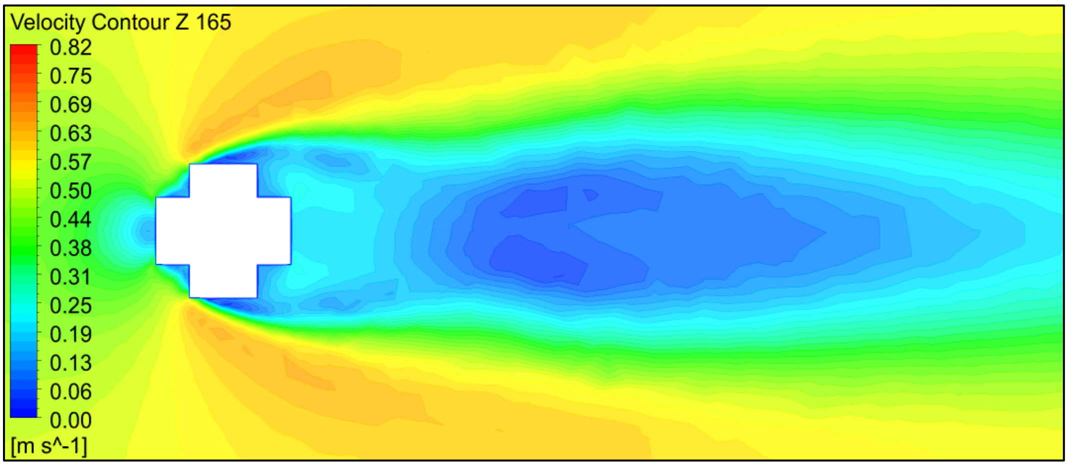

(a): Velocity Contour at Height Z = 165 mm

Figure 4. 34: Velocity Contour Plus Model 0° Wind Angle (Contd.)

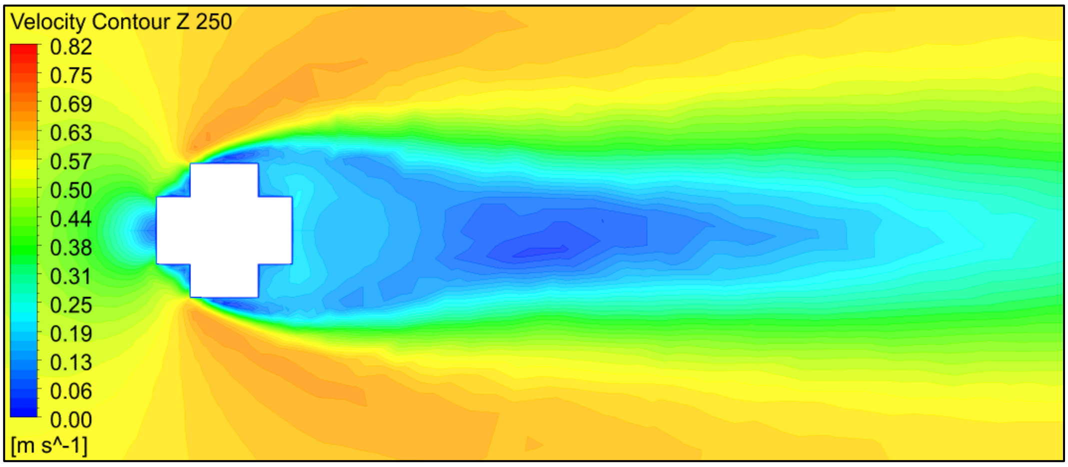

(b): Velocity Contour at Height Z = 250 mm

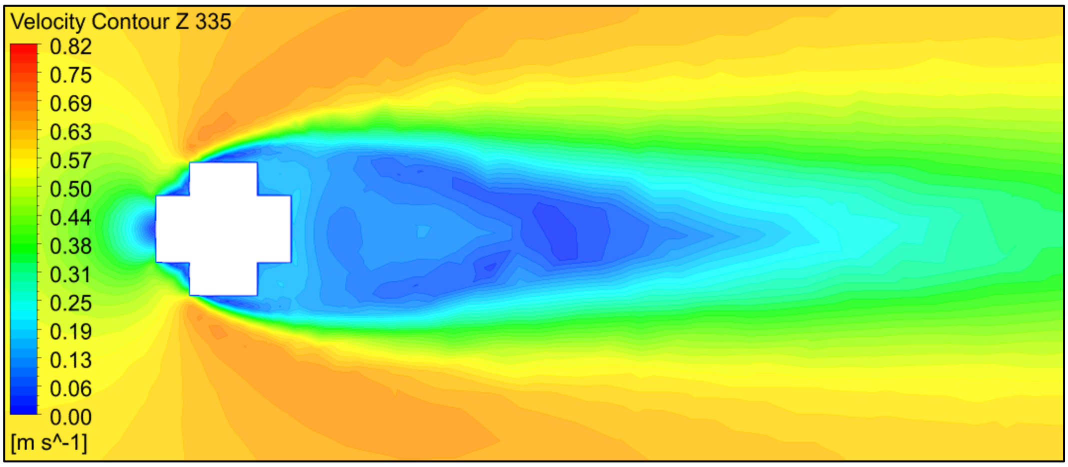

(c): Velocity Contour at Height Z = 335 mm

Figure 4. 34: Velocity Contour Plus Model 0° Wind Angle

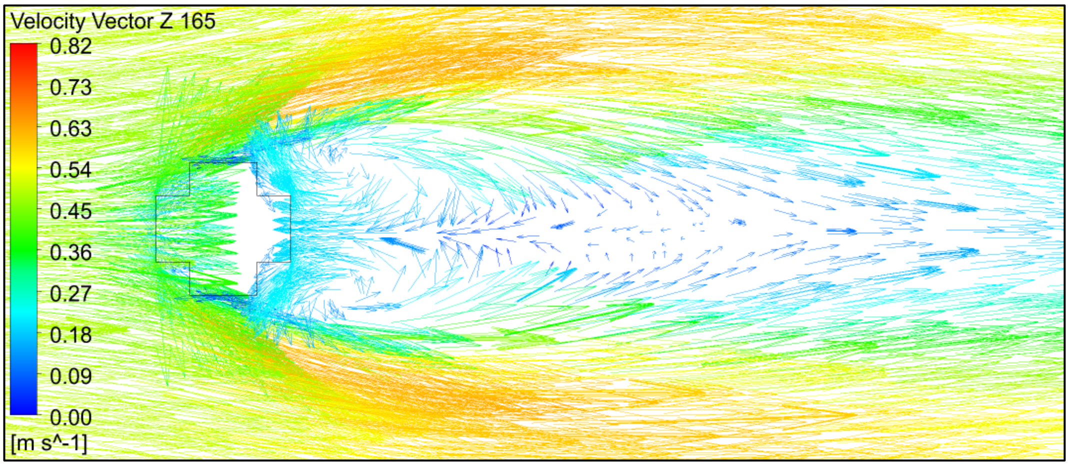

(a): Velocity Vector at Height Z = 165 mm

Figure 4. 35: Velocity Vector Plus Model 30° Wind Angle (Contd.)

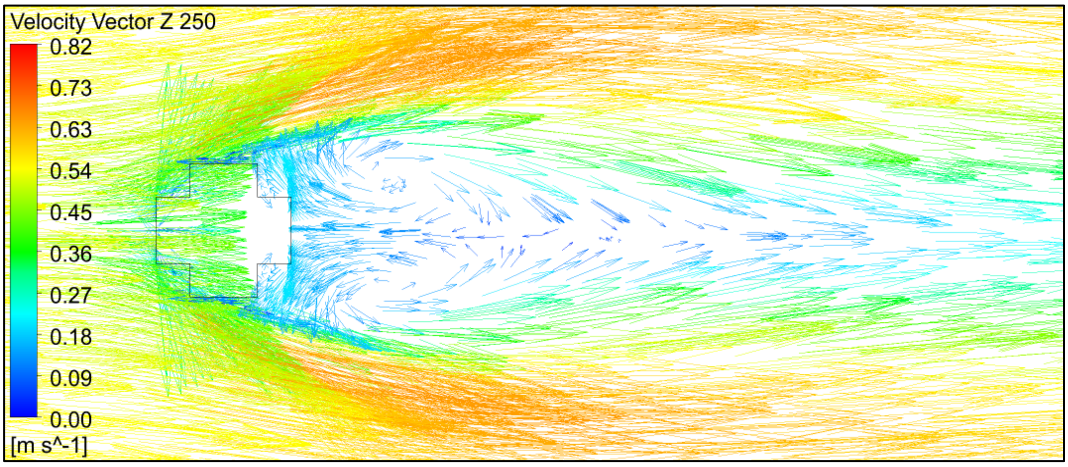

(b): Velocity Vector at Height Z = 250 mm

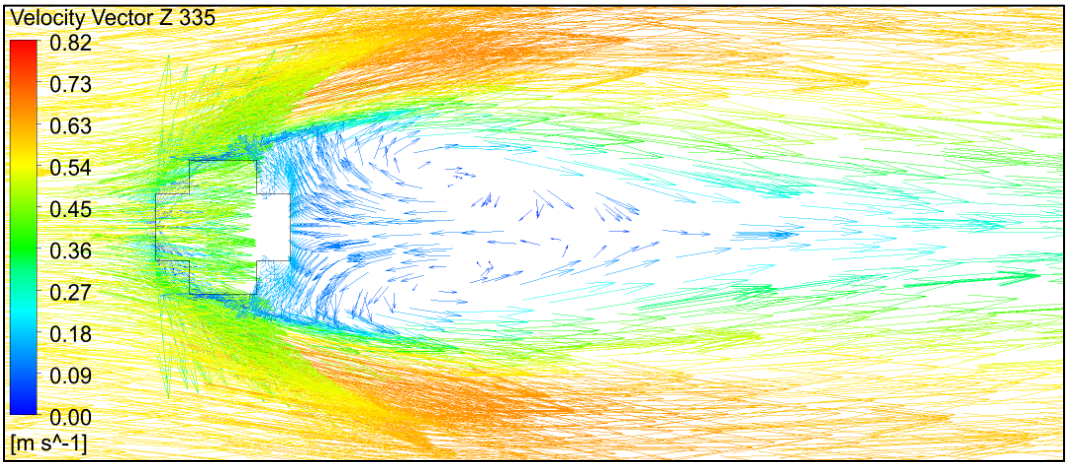

(c): Velocity Vector at Height Z = 335 mm

Figure 4. 35: Velocity Vector Plus Model 30° Wind Angle

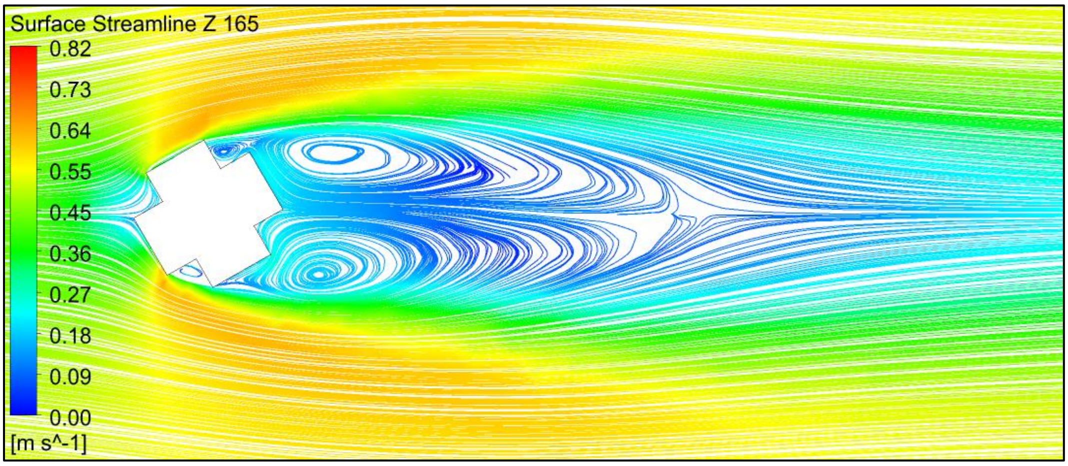

(a): Surface Streamline at Height Z = 165 mm

Figure 4. 36: Surface Streamline Plus Model 30° Wind Angle (Contd.)

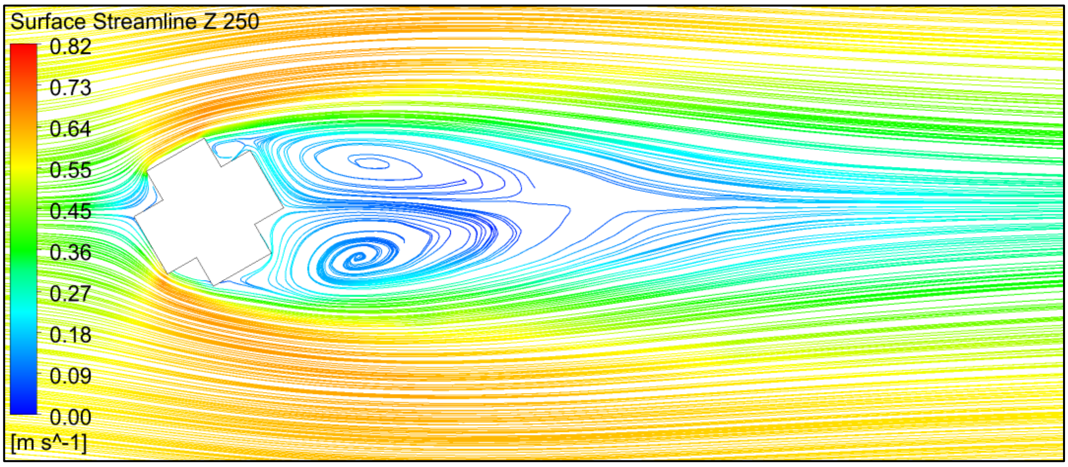

(b): *Surface Streamline at Height Z = 250 mm*

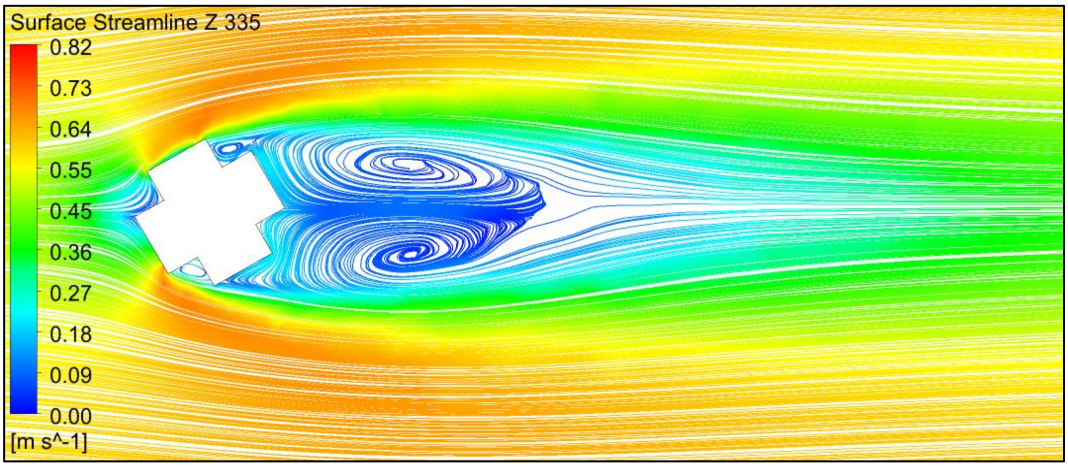

(c): *Surface Streamline at Height Z = 335 mm*

Figure 4. 36: Surface Streamline Plus Model 30° Wind Angle

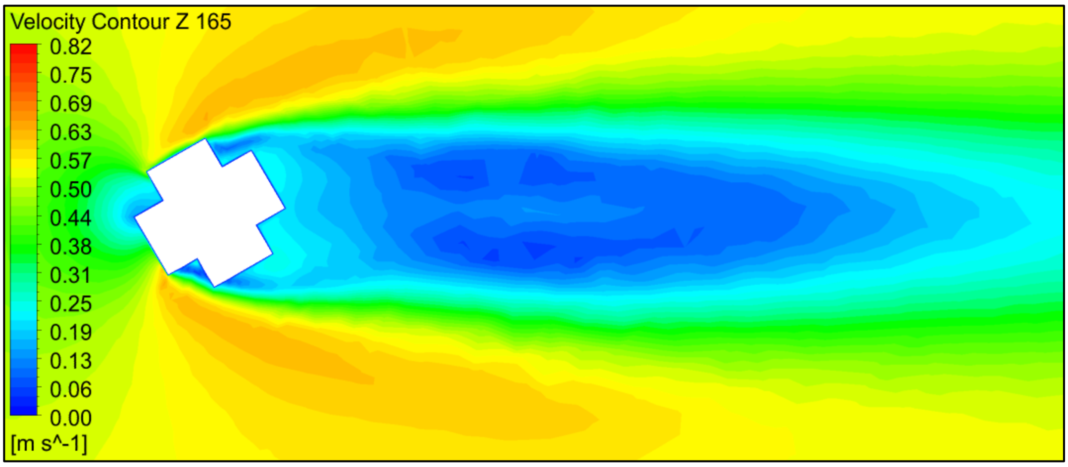

(a): *Velocity Contour at Height Z = 165 mm*

Figure 4. 37: Velocity Contour Plus Model 30° Wind Angle (Contd.)

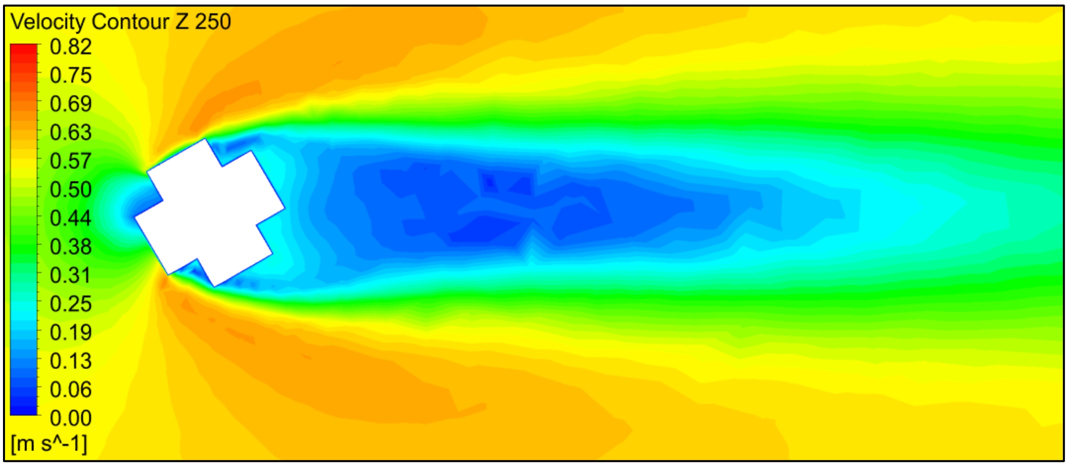

(b) Velocity Contour at Height Z = 250 mm

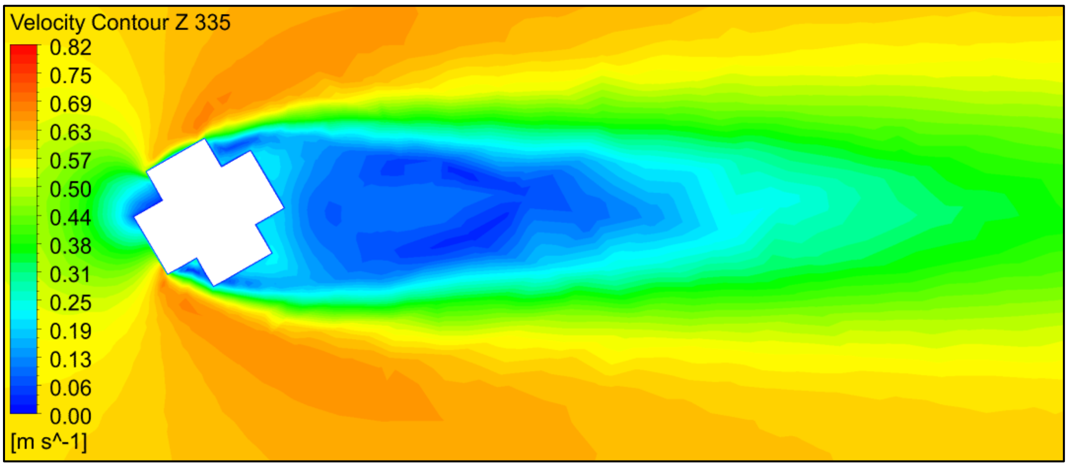

(c) Velocity Contour at Height Z = 335 mm

Figure 4. 37: Velocity Contour Plus Model 30° Wind Angle

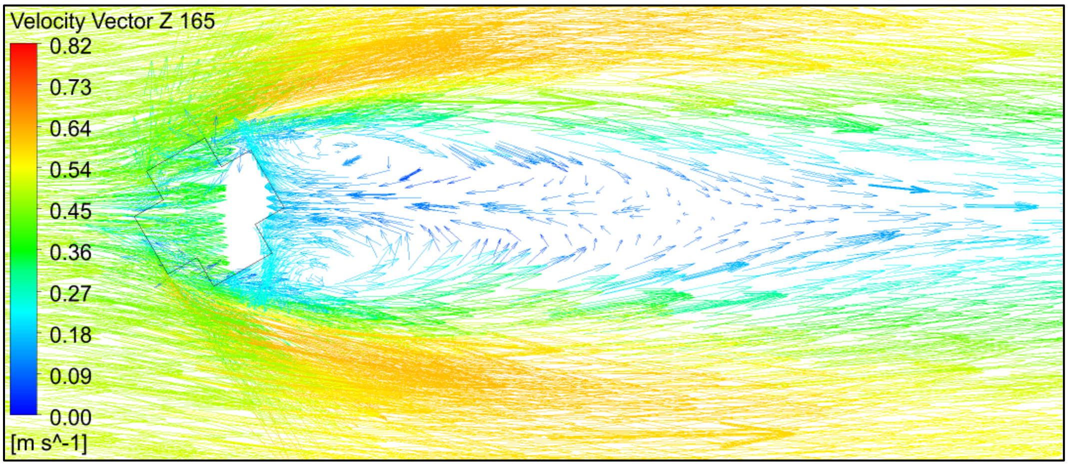

(a): Velocity Vector at Height Z = 165 mm

Figure 4. 38: Velocity Vector Plus Model 30° Wind Angle (Contd.)

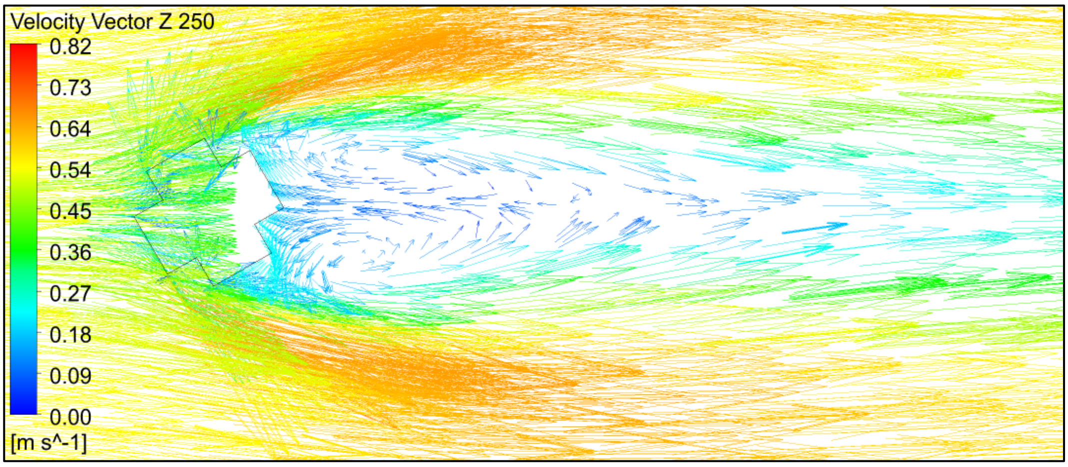

(b): Velocity Vector at Height Z = 250 mm

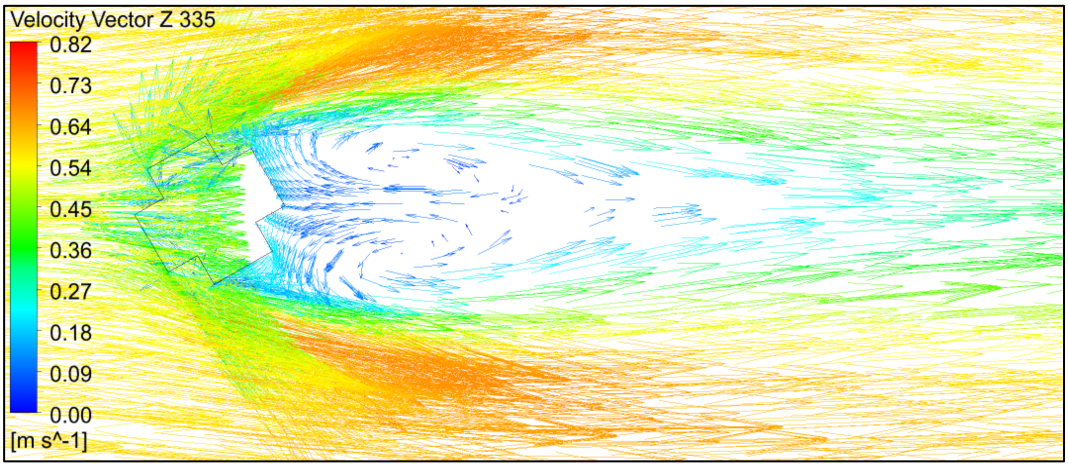

(c): Velocity Vector at Height Z = 335 mm

Figure 4. 38: Velocity Vector Plus Model 30° Wind Angle

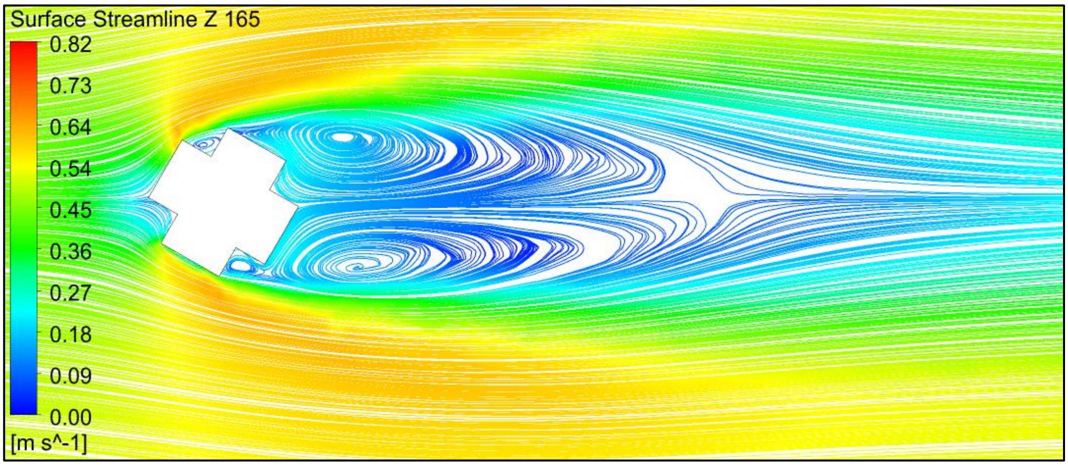

(a): Surface Streamline at Height Z = 165 mm

Figure 4. 39: Surface Streamline Plus Model 60° Wind Angle (Contd.)

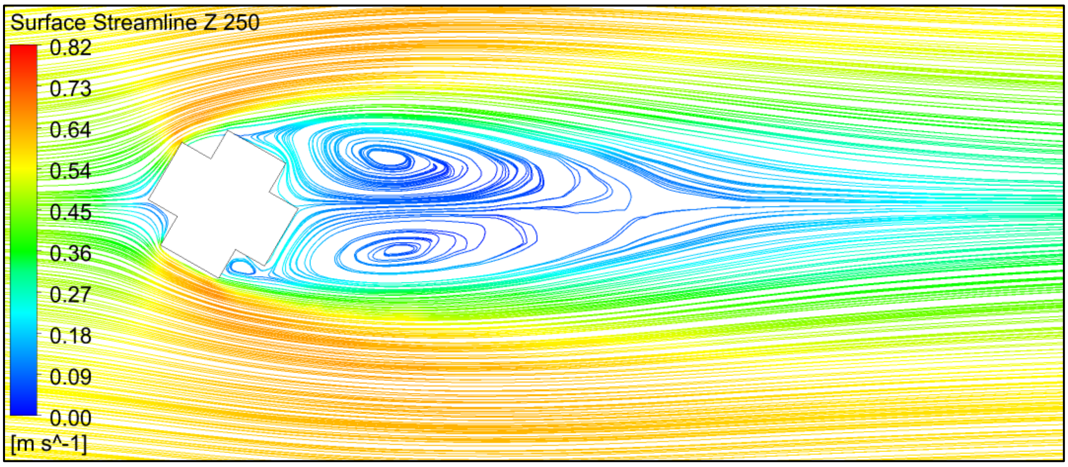

(b): Surface Streamline at Height Z = 250 mm

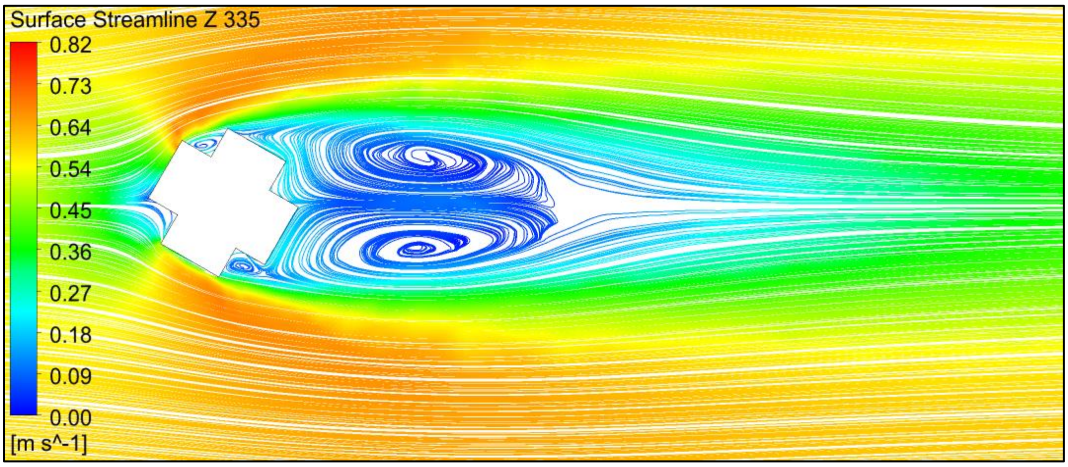

(c): Surface Streamline at Height Z =335 mm

Figure 4. 39: Surface Streamline Plus Model 60° Wind Angle

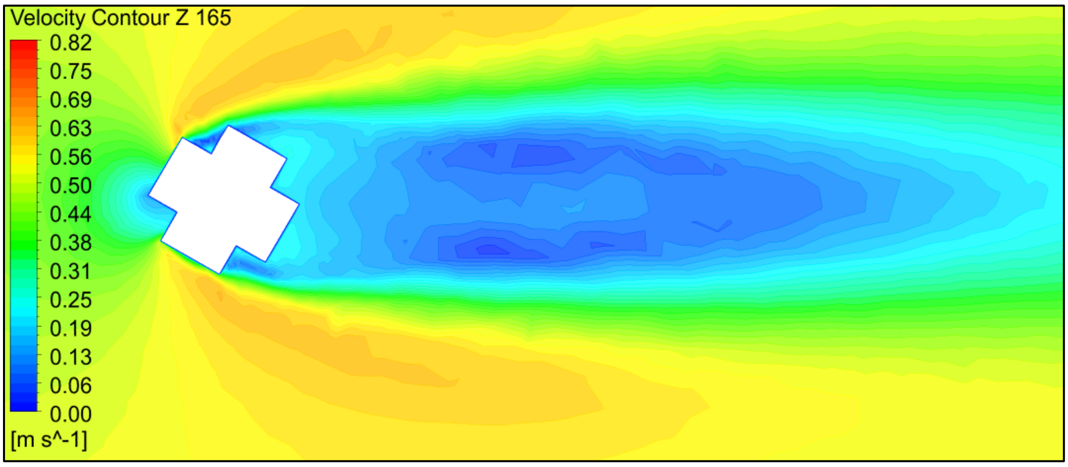

(a): Velocity Contour at Height Z = 165 mm

Figure 4. 40: Velocity Contour Plus Model 60° Wind Angle (Contd.)

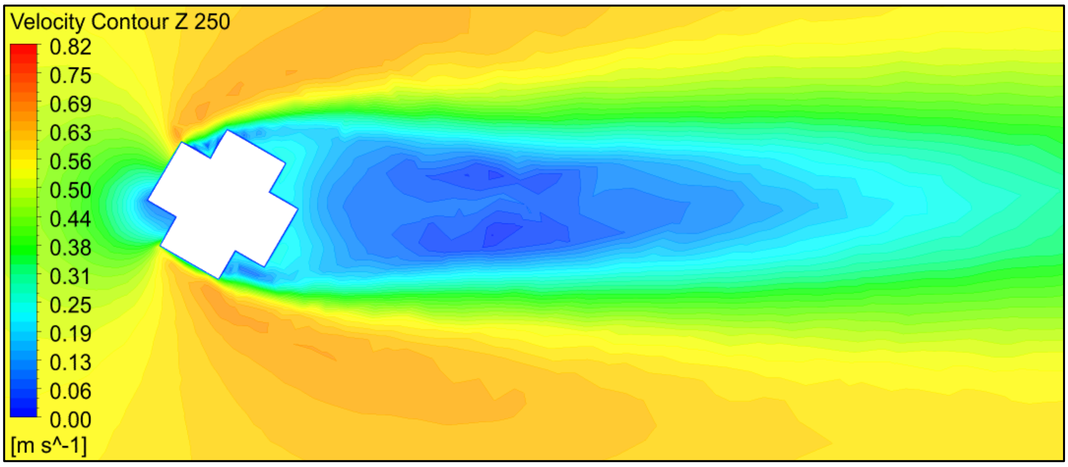

(b): Velocity Contour at Height Z = 250 mm

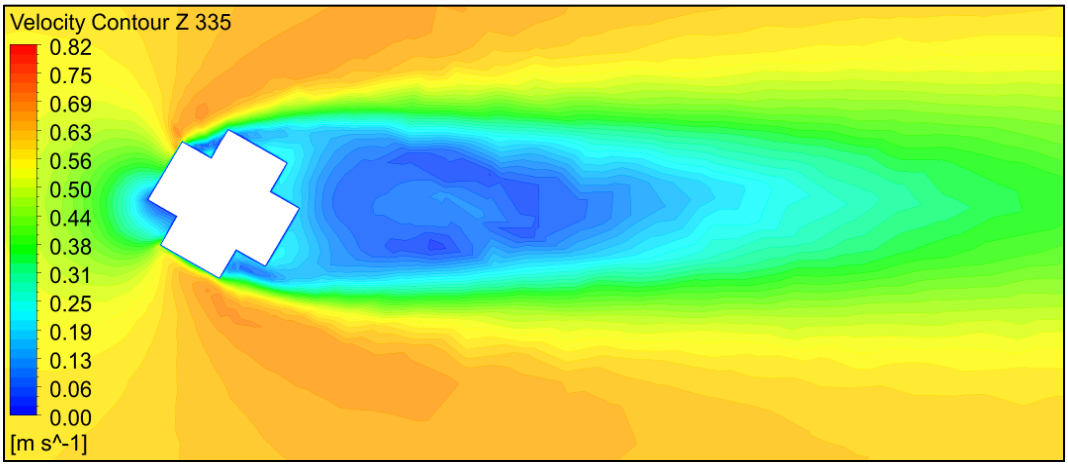

(c): Velocity Contour at Height Z = 335 mm

Figure 4. 40: Velocity Contour Plus Model 60° Wind Angle

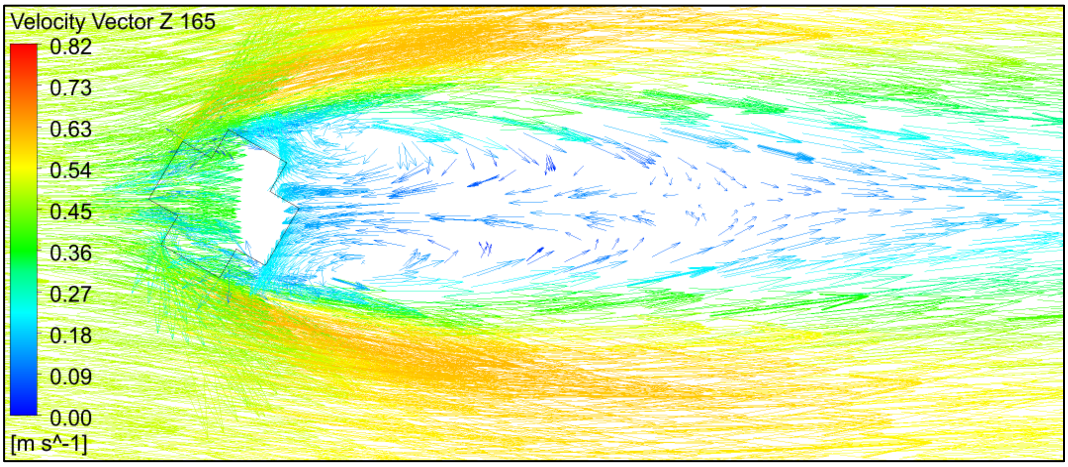

(a): Velocity Vector at Height Z = 165 mm

Figure 4. 41: Velocity Vector Plus Model 60° Wind Angle (Contd.)

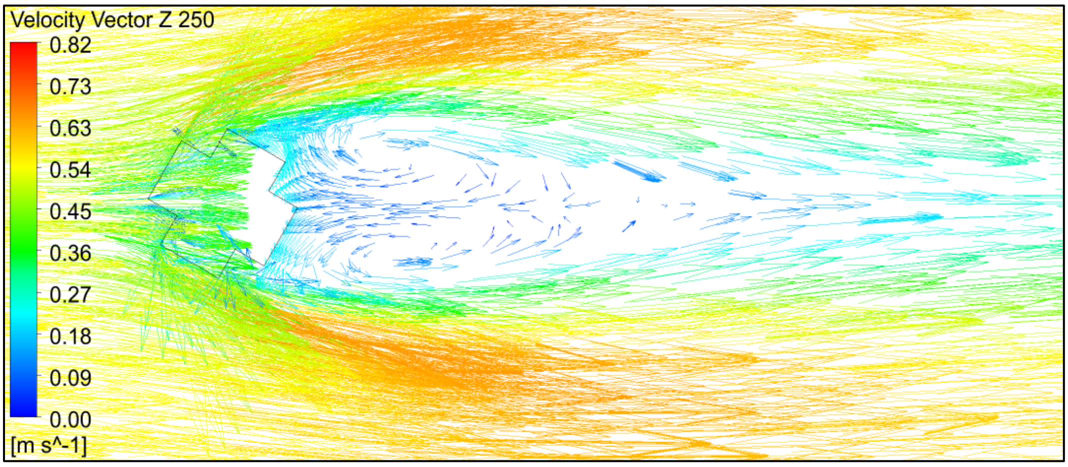

(b): Velocity Vector at Height Z = 250 mm

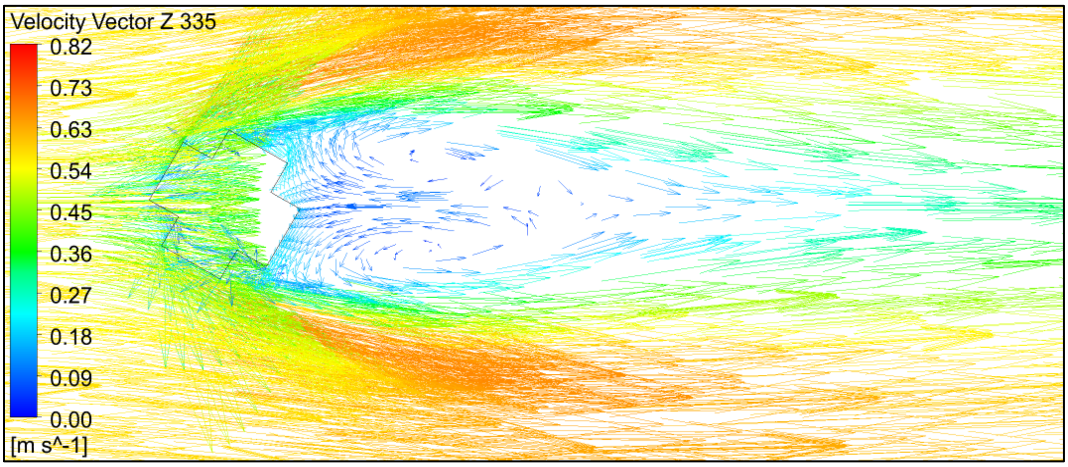

(c): Velocity Vector at Height Z = 335 mm

Figure 4. 41: Velocity Vector Plus Model 60° Wind Angle

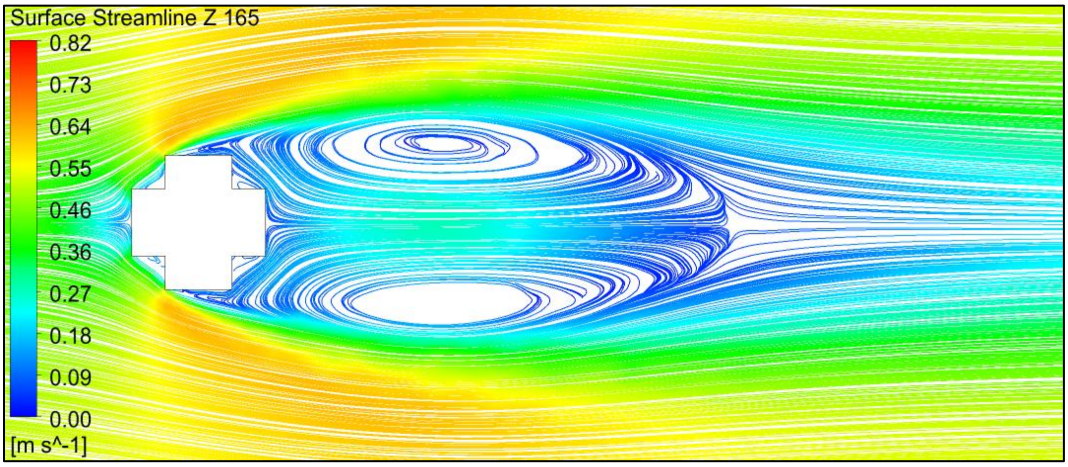

(a): Surface Streamline at Height Z = 165 mm

Figure 4. 42: Surface Streamline Plus Model 90° Wind Angle (Contd.)

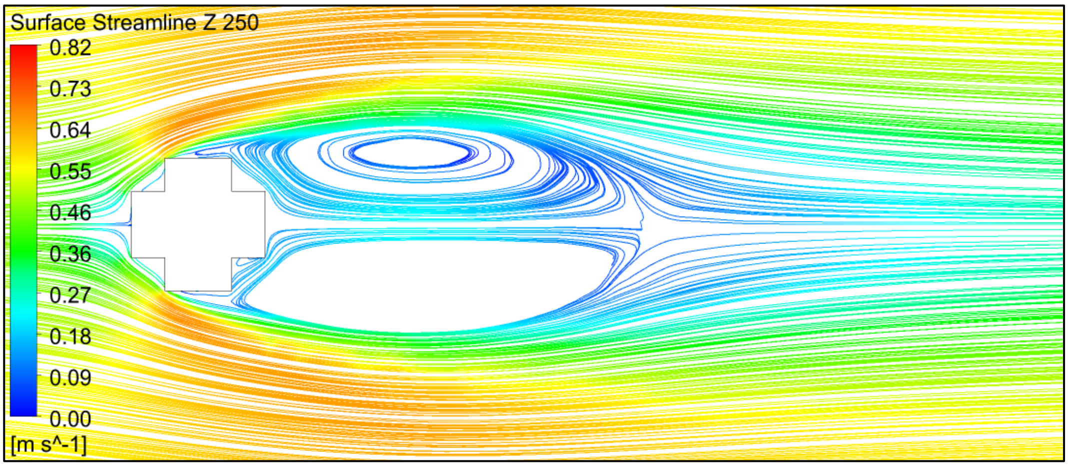

(b) Surface Streamline at Height Z = 250 mm

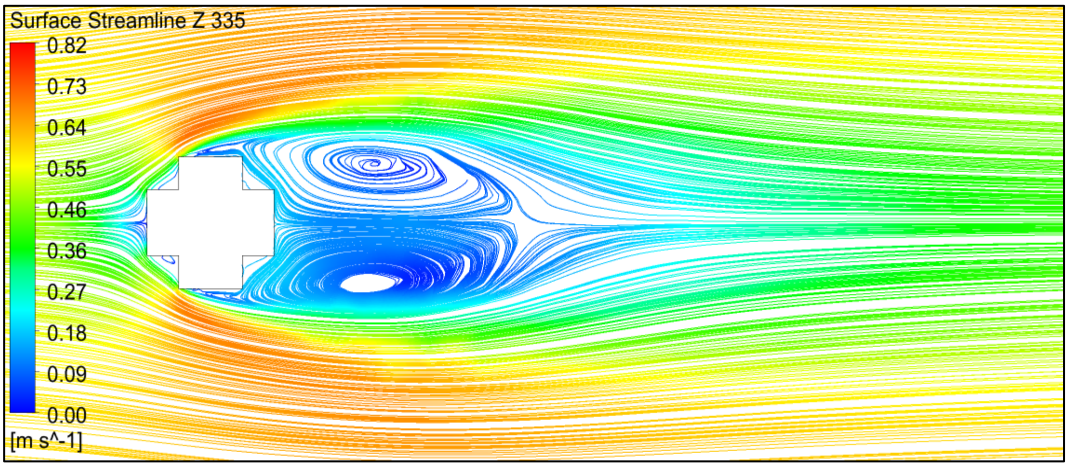

(c) Surface Streamline at Height Z = 335 mm

Figure 4. 42: Surface Streamline Plus Model 90° Wind Angle

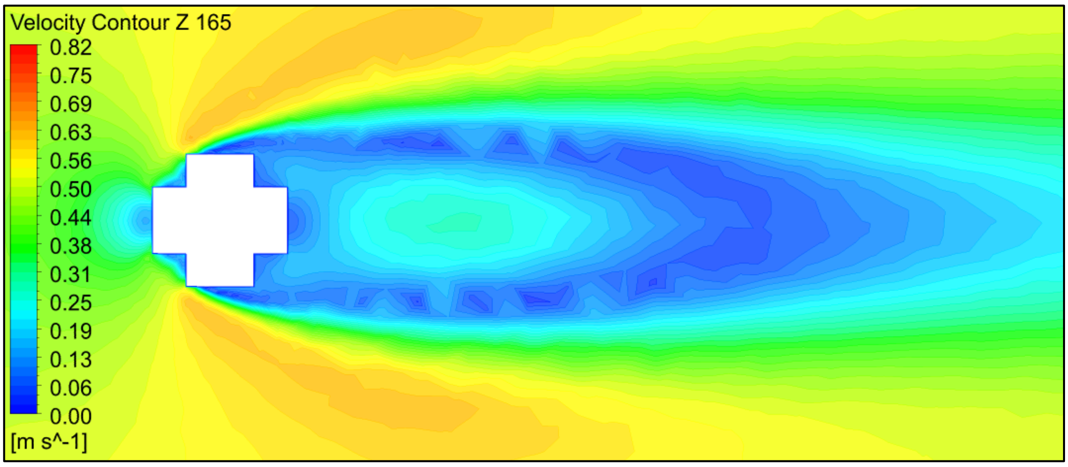

(a): Velocity Contour at Height Z = 165 mm

Figure 4. 43: Velocity Contour Plus Model 90° Wind Angle (Contd.)

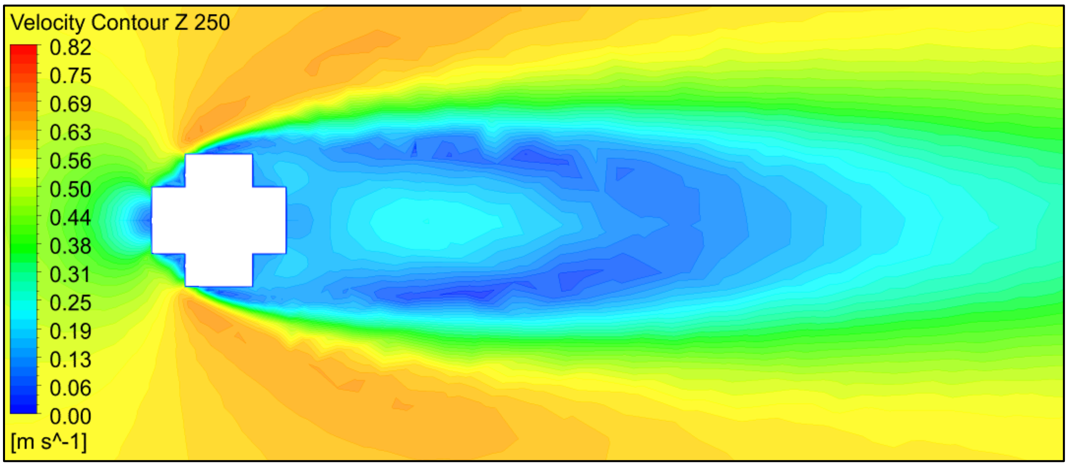

(b): Velocity Contour at Height Z = 250 mm

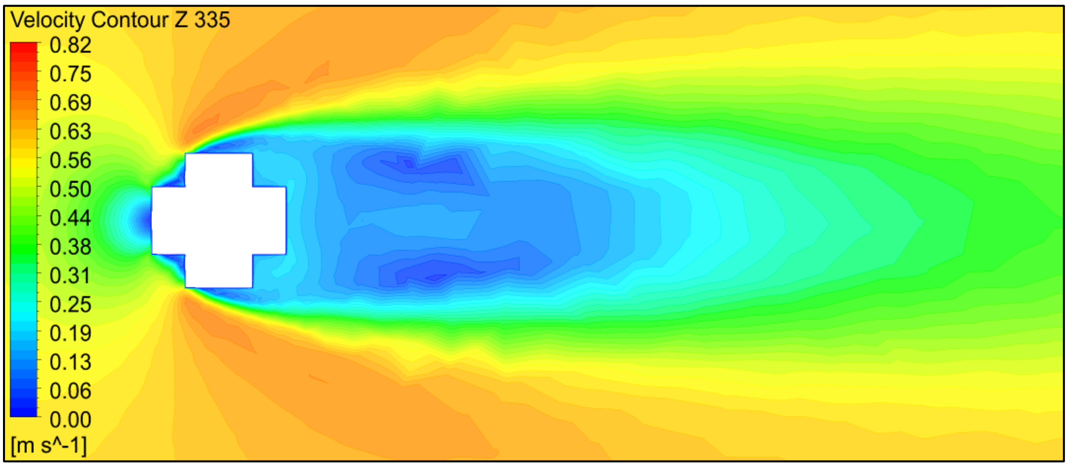

(c): Velocity Contour at Height Z = 335 mm

Figure 4. 43: Velocity Contour Plus Model 90° Wind Angle

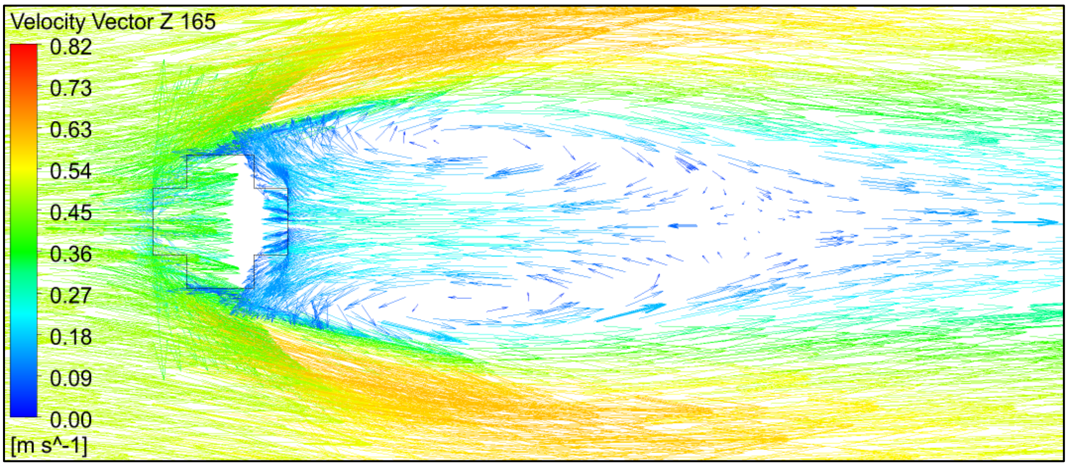

(a): Velocity Vector at Height Z = 165 mm

Figure 4.44: Velocity Vector Plus Model 90° Wind Angle (Contd.)

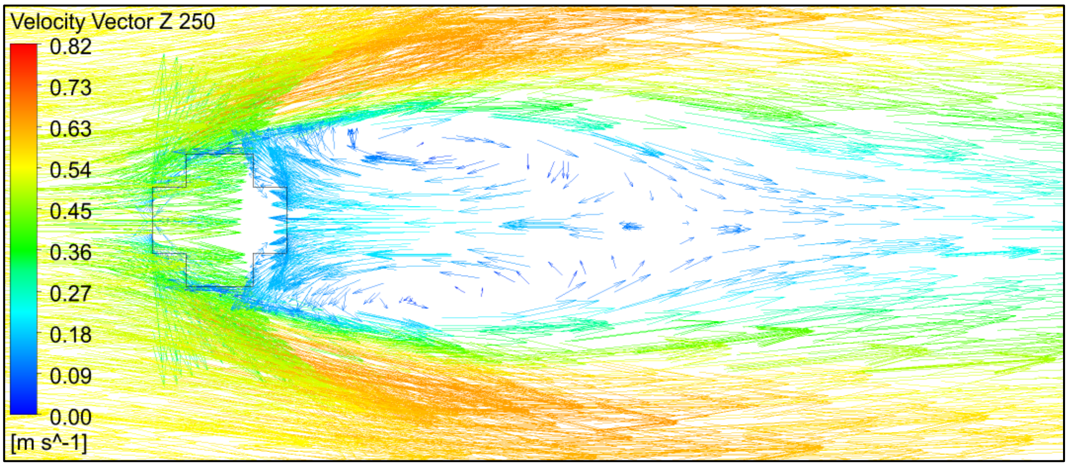

(b): Velocity Vector at Height Z = 250 mm

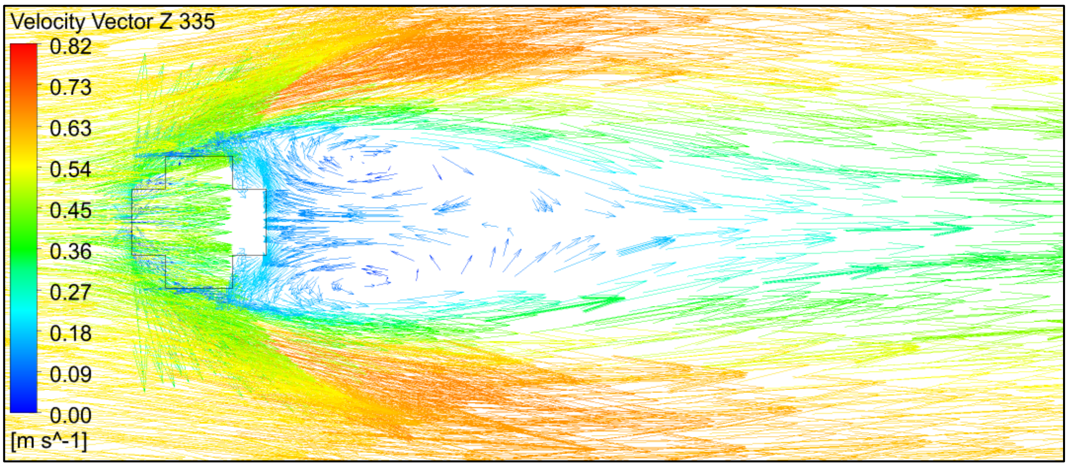

(c): Velocity Vector at Height Z = 335 mm

Figure 4. 44: Velocity Vector Plus Model 90° Wind Angle

4.3.6 Velocity Streamline Along Wind Direction on Central Vertical Plane

Figure 4.45, 4.46, 4.47 & 4.48 show the velocity streamline on cross section through central vertical plane along the wind direction. The upwind vortex at ground level, the upwash, downwash and stagnation zones on the windward face can be visualized. Recirculation and creation of shear layer at roof top and reattachment of flow behind the model can also be seen. Thin shear layer at roof top for all wind angles are seen. Wake length for all wind angles is almost identical.

The vorticity of clockwise circulation of wind in the wake are also apparent in the pictures. For all the wind angles the vorticity points are at the upper height of the model.

Flow from ground level upwind vortex which is carried around the model is responsible for deposition of dust and debris close to the ground level, thus contaminating the air environment are also identical in strength and intensity for all wind angles.

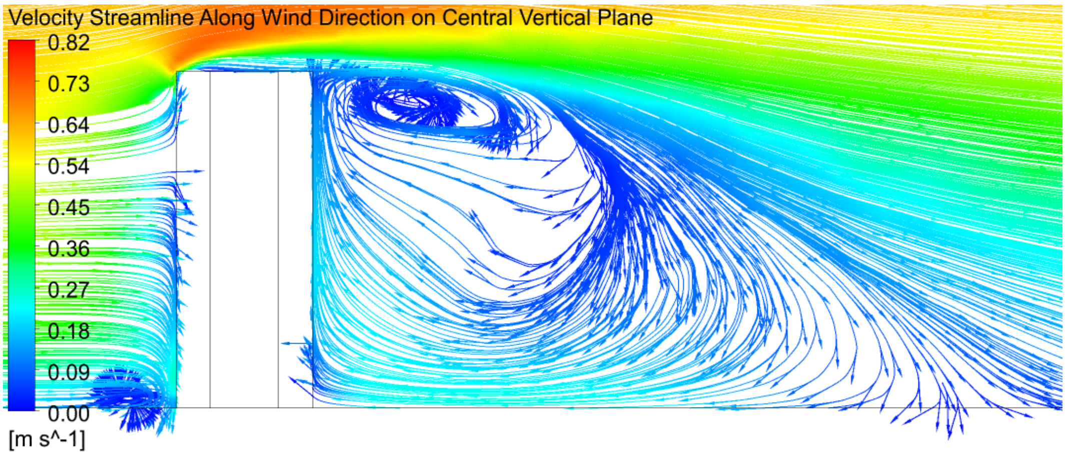

Figure 4. 45: Velocity Streamline Along the Wind Direction on Central Vertical Plane Plus Model 0° Wind Angle

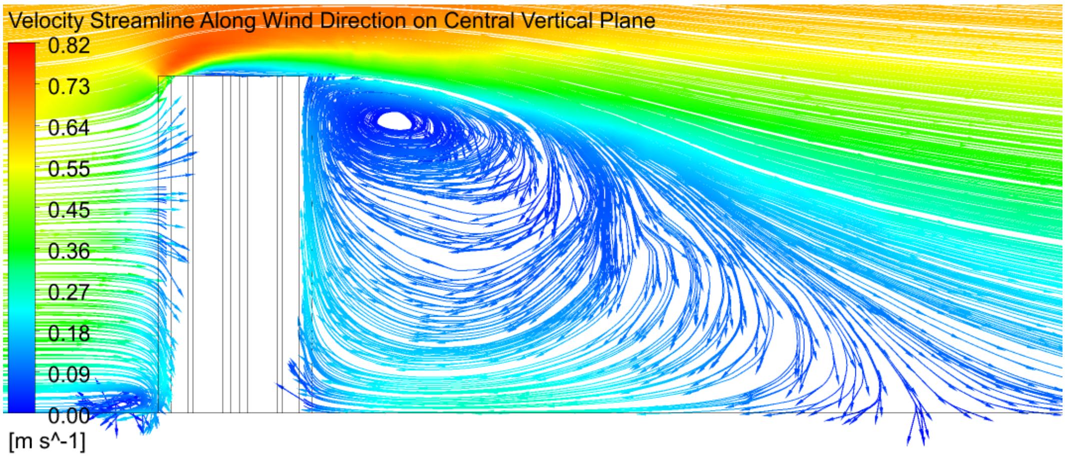

Figure 4. 46: Velocity Streamline Along the Wind Direction on Central Vertical Plane Plus Model 30° Wind Angle

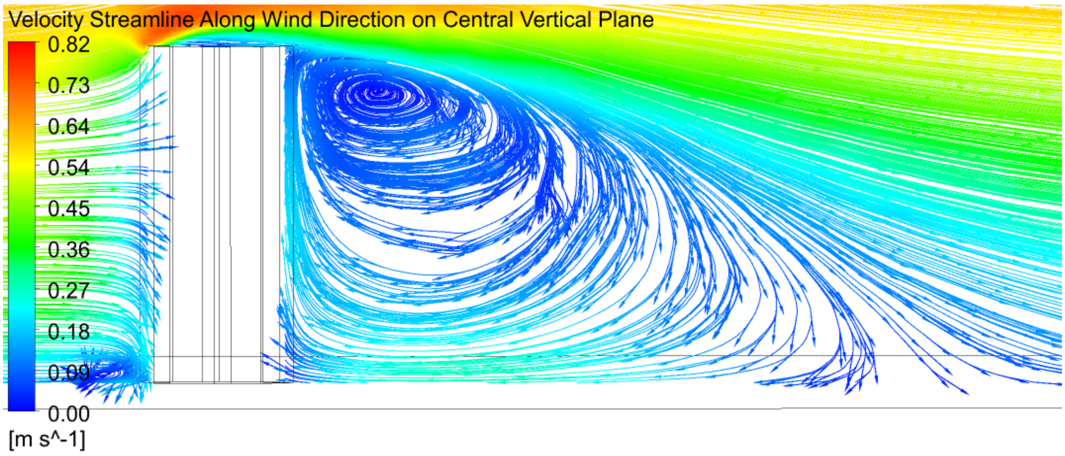

Figure 4. 47: Velocity Streamline Along the Wind Direction on Central Vertical Plane Plus Model 60° Wind Angle

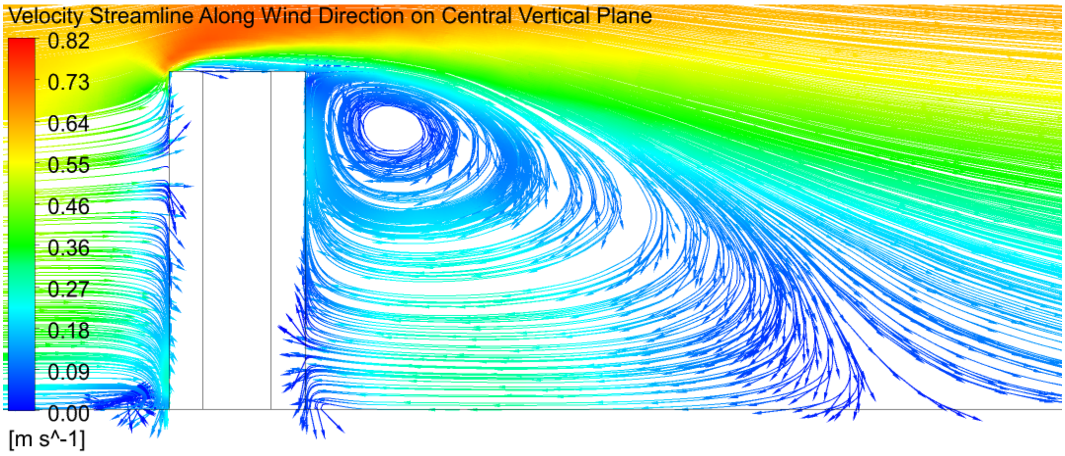

Figure 4. 48: Velocity Streamline Along the Wind Direction on Central Vertical Plane Plus Model 90° Wind Angle

4.3.7 C_{Pe} Along Building Perimeter

Graphical plot representing the variation of C_{Pe} on the building façade at three different heights Z = 0.165 m (about 1/3rd height of the model), Z = 0.25 m (1/2 height of the model) and Z = 0.335 m (about 2/3rd height of the model) for different wind angles of attack from 0° to 90° @ 30° have been shown in Figure 4.49, 4.50, 4.51 & 4.52 respectively.

The relevance to study C_{Pe} distribution along the building façade has already been discussed in para 4.2.7. For all wind angles the maximum positive C_{Pe} values are almost touching 1.0. The C_{Pe} values are higher along the height where positive pressure occurs, whereas, it is lower in most of the case where suction occurs. Minute differences in the C_{Pe} values are due to inability of the simulation to capture micro level eddies and turbulence where separation of flow occurs. The detailed suction C_{Pe} values for different wind angles on the corners are shown in Table 4.4 for the type and size of plus plan shape building model. When block contour diagrams for cladding design is prepared according to this data, it will be economical and cheaper at the same time cladding units will remain protected against failure due to wind suction.

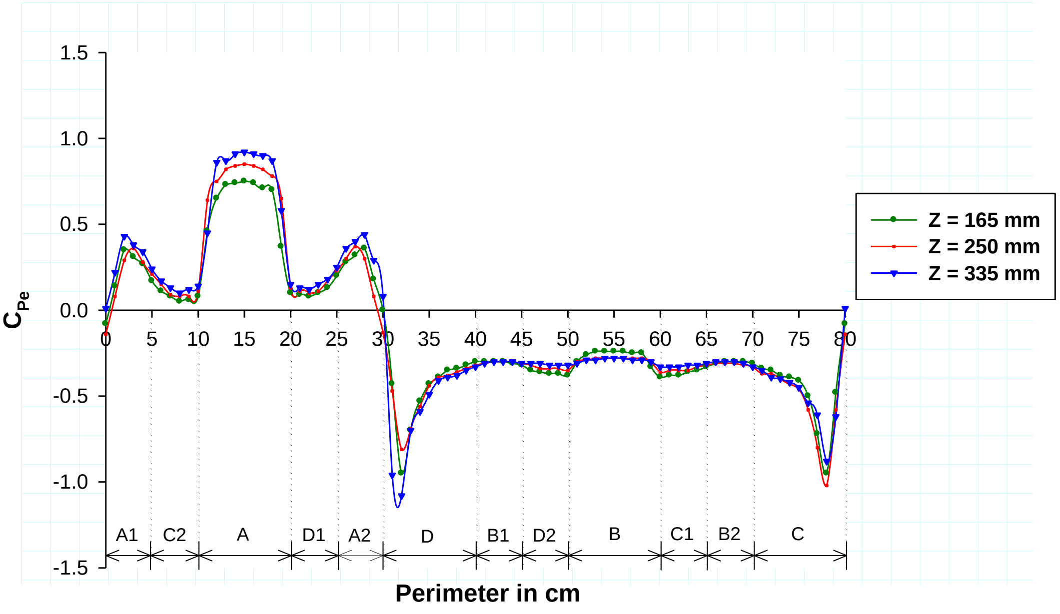

Figure 4. 49: C_{Pe} Along Perimeter Plus Model 0° Wind Angle

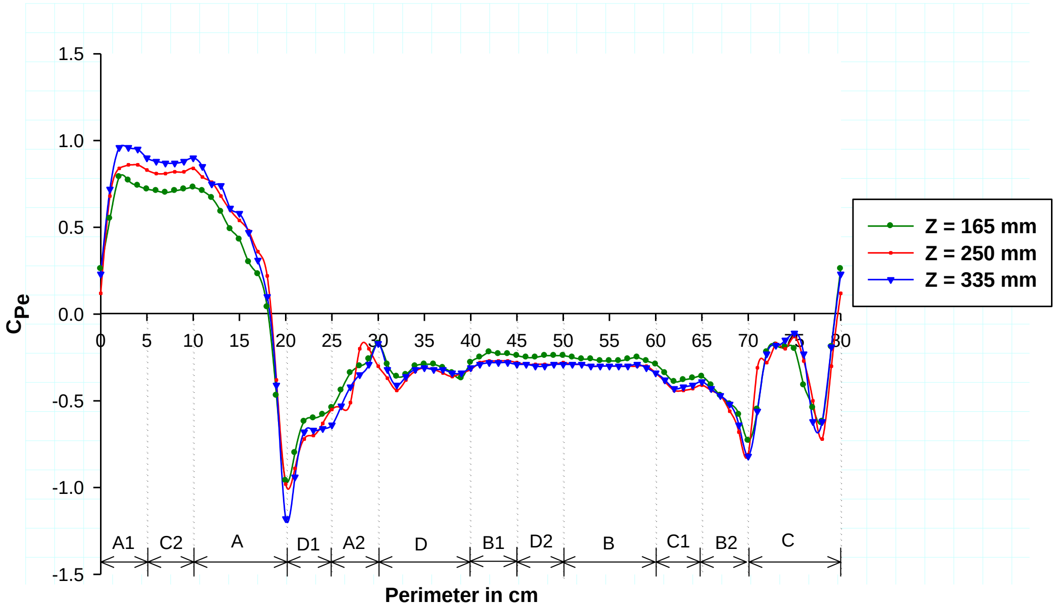

Figure 4. 50: C_{Pe} Along Perimeter Plus Model 30° Wind Angle

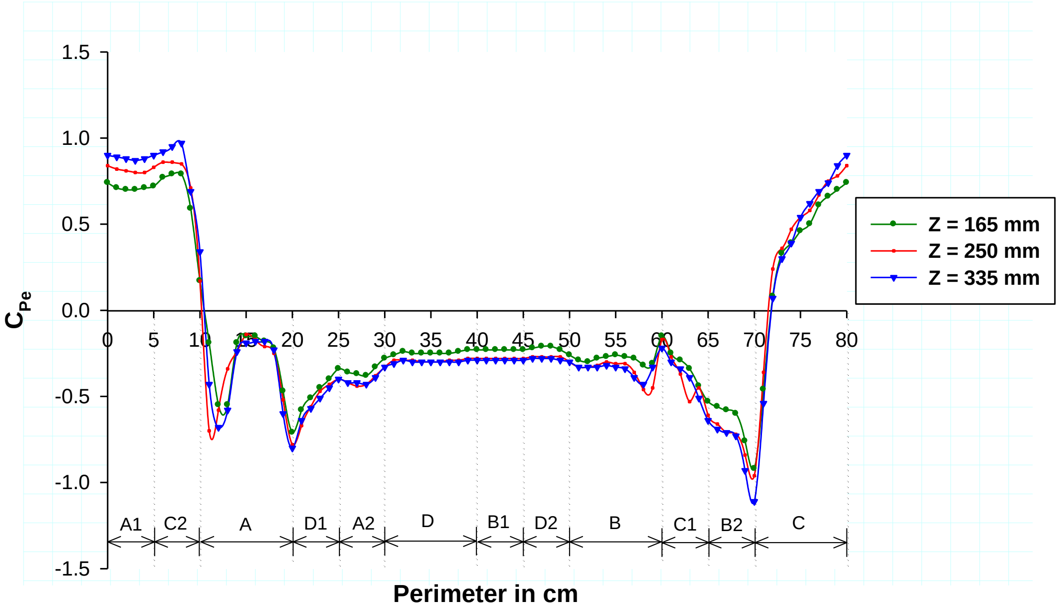

Figure 4. 51: C_{Pe} Along Perimeter Plus Model 60° Wind Angle

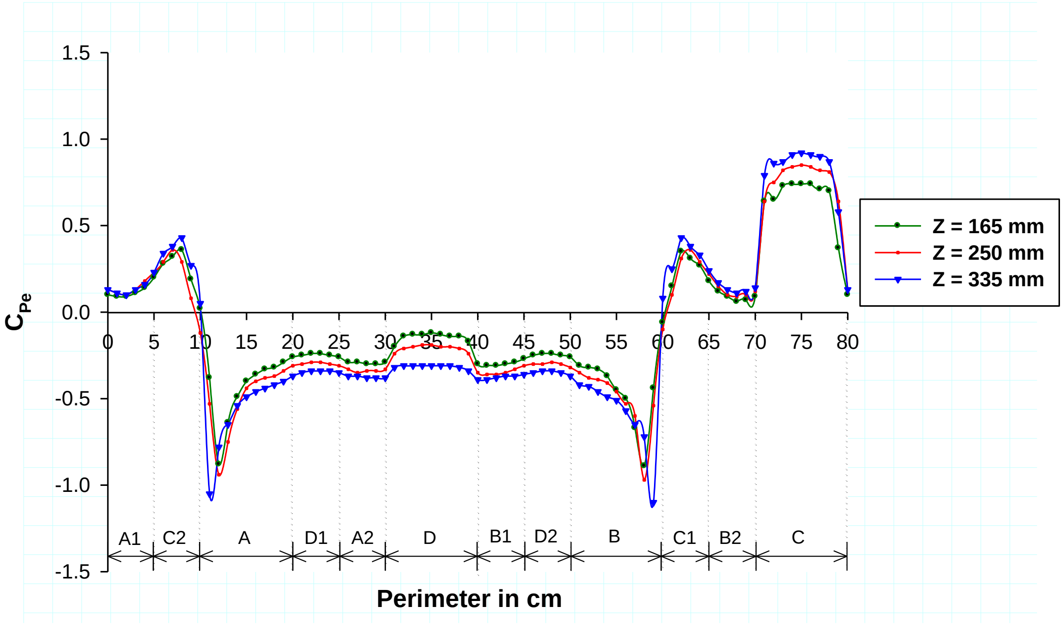

Figure 4. 52: C_{Pe} Along Perimeter Plus Model 90° Wind Angle

Table 4. 4: Maximum Suction in Terms of C_{Pe} For Cladding Design

AoA	0°		30°	60°	90°	
Z/Location	Corner		Corner	Corner	Corner	
	A2D	A1C	AD1	B2C	AC2	BC1
0.165 m	-0.92	-0.92	-0.94	-0.94	-0.92	-0.92
0.250 m	-0.95	-0.95	-0.97	-0.97	-0.95	-0.95
0.335 m	-1.07	-1.07	-1.14	-1.14	-1.07	-1.07

4.3.8 C_{Pe} Along Central Vertical Line on Faces

Figure 4.53, 4.54, 4.55 & 4.56 show plots of C_{Pe} values along central vertical line on the faces for wind angles from 0° to 90° @ 30° respectively. The relevance of such plot has already been discussed in para 4.2.8.

At 0° wind incidence angle in the instant case C_{Pe} is positive on the windward face A and the maximum value of C_{Pe} along the line is nearly equal to 1.0 in between 0.4 m to 0.5 m height of the model. On the re-entrant windward faces A1 and A2 positive pressure exist but the maximum value of C_{Pe} is less than 1.0. Being symmetrical faces, the line is overlapping with each other. The side re-entrant faces do also have positive pressure overlapping with each other. The value at the ground level on faces C2 and D1 are almost same as that of the faces A1 and A2 but at higher level the values are relatively small. On leeward face B suction is seen to be increased above half the height of the model and then becomes constant. Symmetrical faces B1 & B2 and C1 & D2 do have similar overlapping suction throughout height. Side faces C & D also have overlapping suction, almost equal, throughout height.

At 30° wind angle Face A1 is having maximum C_{Pe} of almost 1.0 at 0.4 m height of the model. Face A and C2 do have positive pressure throughout height varying according to the flow characteristics. Local fluctuations on face A1 are observed which indicates micro level turbulence at the place. Rest faces are under suction. Local fluctuations along height on face B2, C and D1 are observed.

At 60° wind angle positive pressure exists on face A1, C and C2, rest faces are under suction. Except on face B2 suction is almost similar on the faces.

At 90° wind angle almost similar vertical centreline C_{Pe} values are observed on the faces corresponding to similar faces at 0° wind angle.

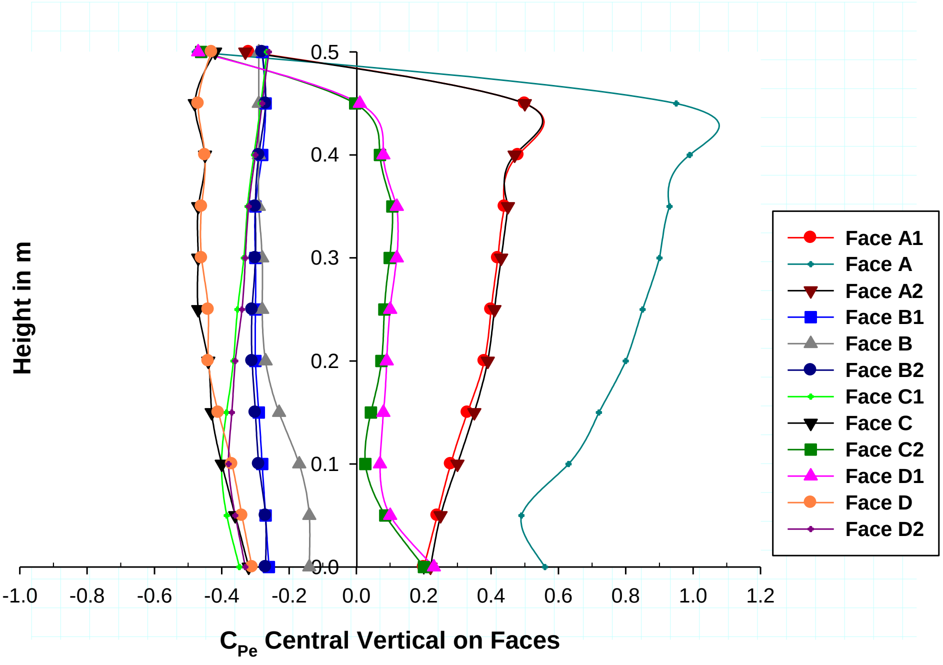

Figure 4. 53: C_{Pe} Along Central Vertical Line on Faces Plus Model 0° Wind Angle

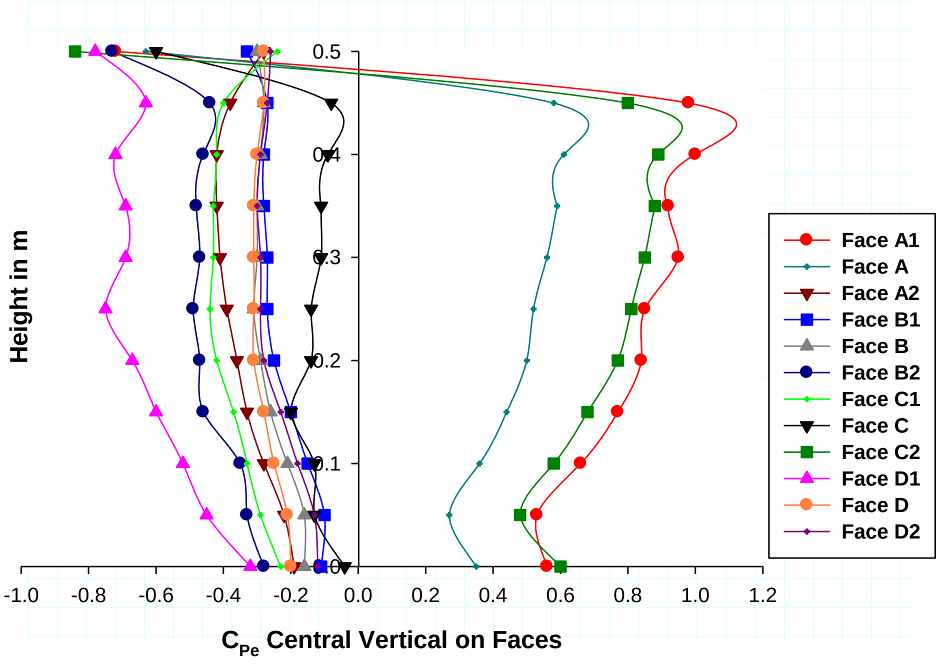

Figure 4. 54: C_{Pe} Along Central Vertical Line on Faces Plus Model 30° Wind Angle

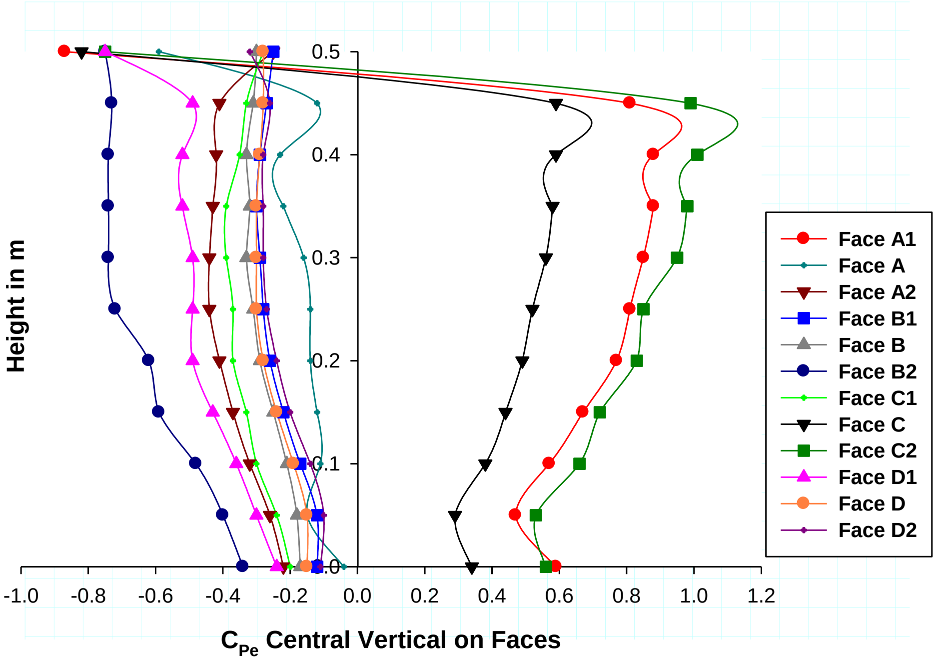

Figure 4. 55: C_{Pe} Along Central Vertical Line on Faces Plus Model 60° Wind Angle

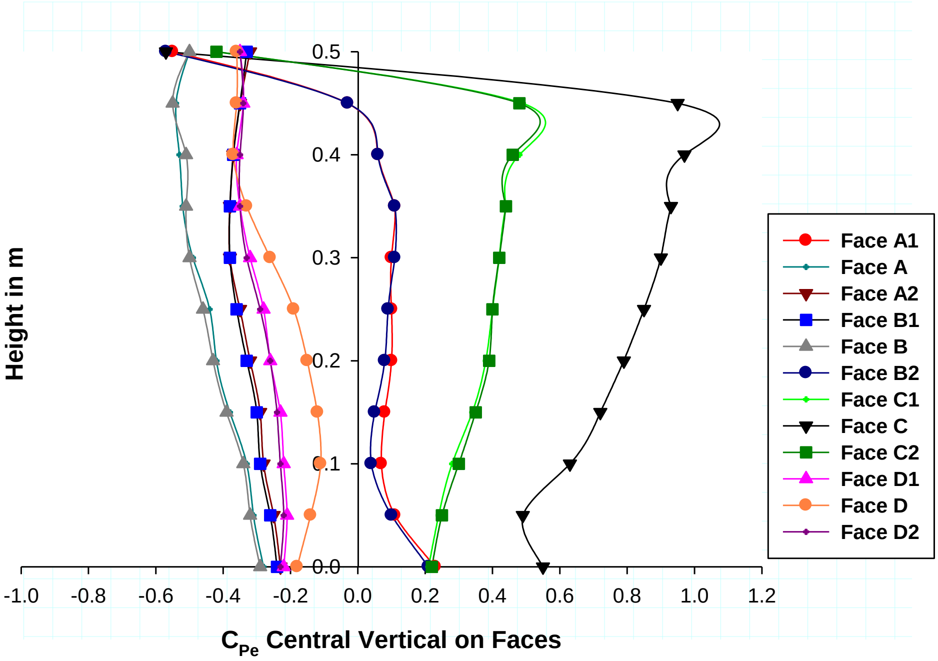

Figure 4. 56: C_{Pe} Along Central Vertical Line on Faces Plus Model 90° Wind Angle

4.4 OCTAGONAL - OVAL SHAPE

The pressure and wind flow patterns on the faces of octagonal-oval shape model with a central cavity are discussed here for extended angle of wind attack from 0° to 90° @ 30°. Wind flow impinging on the wind ward face A at right angle is taken as 0° wind incidence angle. The flow direction of wind has been varied in clockwise direction.

4.4.1 C_{Pe} Contour 0° Wind Angle

At 0° wind incidence angle separation of wind is taking place before it impinges on windward face A perpendicularly. Face A is experiencing maximum positive pressure which is increasing from bottom to top of the face due to increase in velocity with height. Unlike the previous models of rectangular or plus shapes in which case the pressure contour on windward face is parabolic, the pattern of pressure contour in the instant case is sharp parabolic, almost triangular, with maximum positive pressure along the centreline. The pressure decreases towards the edges. Suction is seen at the roof top near the centre of the width, and not throughout the width, from where wind is expected to flow past the model with high velocity.

Inclined faces A1 and A2 are experiencing positive pressure at their near ends and negative pressure at their far ends from where flow separation is taking place with high velocity (Figure 4.65). High negative pressure is created around the far ends of face A1 and A2 due to flow reversal on surface in the region. The isobars are vertical in nature with high gradient. Since very large variation of pressure from positive to negative is noticed on faces A1 and A2, these faces are critical from design point of view as thrust and suction both are occurring on these faces simultaneously.

Suction pressure exists on the leeward face B. Concentration of backwash at bottom with horizontal isobars and in the centre of the face in elliptical formation in vertical direction i.e., with vertical isobars is seen. In most part of the face suction is almost similar.

On the inclined leeward faces B1 and B2 suction of higher values than on face B are observed. The contour isobars are almost vertical and gradient of pressure is negative from the lee side to upwind side. At the bottom of the faces inclined isobars due to influence of backwash are observed on the faces. High suction points at the top outer corners are seen suggesting high turbulence and formation of local eddies.

On side faces C and D similar pattern of pressure contours exists due to symmetry of the model for 0° wind angle of attack. It can be seen that the high suction exists on the side faces with vertical isobars than that on the inclined leeward faces. Negative gradient of pressure exists on both the side face from lee side to upwind side. At the bottom the suction contours are horizontal on the lee side owing to the turbulence effect created by the wake behind the model. Some differences in the pattern of pressure contours on these symmetrical faces suggests the three-dimensional dynamic nature of wind.

On all the inner faces suction exists throughout the faces. However, on face A (Inner) maximum suction exists compared to other inner faces. It is pertinent to know that orientation of face A (Inner) is in the lee side with respect to wind direction. Face B (Inner) is fronting the wind direction, whereas, face C (Inner) and face D (Inner) are the side faces. Near the top variation of pressure on the inner faces are noticeable.

On the roof top overall pressure is suction, symmetrical along the centreline in wind direction. The area average C_{Pe} on the roof is lowest for all wind directions at this angle of wind attack and is -0.46. High suction exists towards the windward side with concentration of local eddies and turbulence near top of windward face A. This portion is sensitive for the design of roof structures.

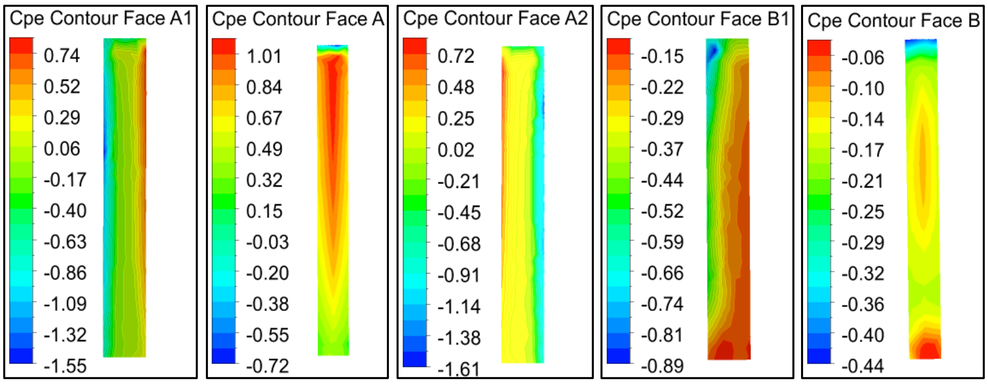

Figure 4.57: C_{Pe} Contour on Outer Faces & Roof Top Octa Model 0° Wind Angle (Contd.)

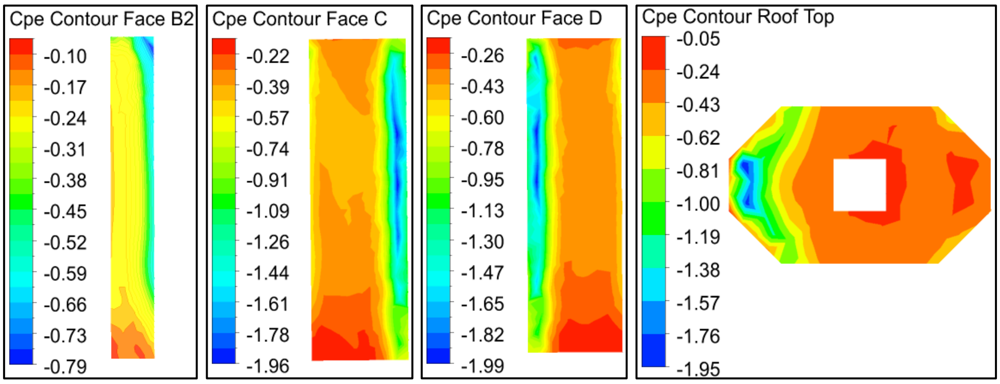

Figure 4. 57: C_{Pe} Contour on Outer Faces & Roof Top Octa Model 0° Wind Angle

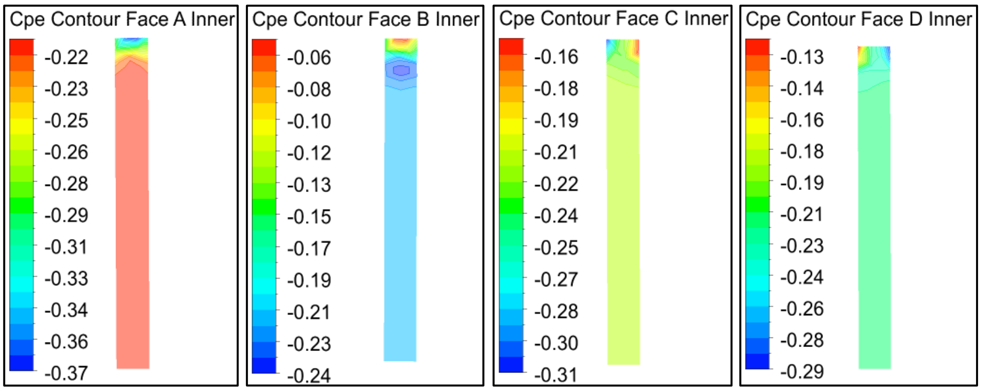

Figure 4. 58: C_{Pe} Contour on Inner Faces Octa Model 0° Wind Angle

Table 4. 5: Area Average C_{Pe} on Faces & Roof Octa Model

Face	Wind Incidence Angle			
	0°	30°	60°	90°
A1	-0.11	0.64	0.42	-0.52
A	0.72	0.15	-1.11	-1.53
A2	-0.11	-0.80	-0.85	-0.44
A (Inner)	-0.22	-0.35	-0.62	-0.63
B1	-0.29	-0.22	-0.26	-0.44
B	-0.16	-0.28	-0.61	-1.53
B2	-0.29	-0.90	-1.03	-0.52
B (Inner)	-0.21	-0.35	-0.62	-0.63
C	-0.59	-0.28	0.35	0.61
C (Inner)	-0.21	-0.35	-0.62	-0.63
D	-0.59	-0.34	-0.24	-0.21
D (Inner)	-0.21	-0.35	-0.62	-0.64
Roof Top	-0.45	-0.58	-0.75	-0.73

4.4.2 C_{Pe} Contour 30° Wind Angle

In this case of wind angle of attack wind is impinging on inclined face A1 obliquely. The pressure is half parabolic with a triangular shape at bottom and concentrated towards the near end of the face. It is increasing along height, as expected. Towards the far end the isobars are vertical. Pressure is almost positive throughout the face.

On face A at the meeting edge of face A1 and A, pressure is positive and the contour patterns are vertical. At the far end of the face suction exists due to frictional force of wind on the surface and formation of eddies. On inclined face A2 negative pressure exists throughout the face. High concentration of negative pressure with a vertical and elliptical formation is seen near the middle width of the face suggesting formation of high eddies at the place. At the bottom a region of low suction is seen.

Face B, B1 and D are under wake region (Figure 4.68). On face B, which is facing the wake, the isobars are inclined. At the top corner towards the confluence of face B and B2, concentration of high suction is seen. Suction airstream is hitting the bottom and creating an upwash on face B1. Another concentration of suction airstream is seen at the centre of the face which is due to effect of vorticity (Figure 4.78). Pattern of pressure contours on face B1 is horizontal in nature with little variation in value suggesting vertical formation of eddies on the face. Face D is partially in the wake region. It is experiencing backwash towards the lee side and side wash towards the windward side. As such, the isobars are horizontal towards the lee side and vertical towards the windward side. High suction at top towards the near end is seen on the face.

Inclined face B2 is facing maximum variation of suction with vertical isobars on its face. The area average C_{Pe} on the face is -0.90. On face B2 towards the meeting edge of face B2 and B the suction pressure contours are inclined at the bottom corner. On another edge of face B2 isobars of high turbulence is observed.

Pressure on face C is found to be positive at the near end edge and negative at the far end edge. The gradient of suction pressure on the face is hight, though the area average C_{Pe} on the face is -0.28. In the major part of the face in middle portion pressure is almost null. As both positive and negative pressure exist on the face, care must be taken while designing the claddings.

The suction pressure on the inner faces is almost similar. Horizontal contours at the upper height with minimal difference are seen on the faces. The area average C_{Pe} on the faces are almost same (between -0.34 & -0.35).

On the roof top, the area average coefficient of pressure is -0.58. Negative pressure exists on the roof throughout with a high concentration towards windward side near the corner of meeting edges A and A1.

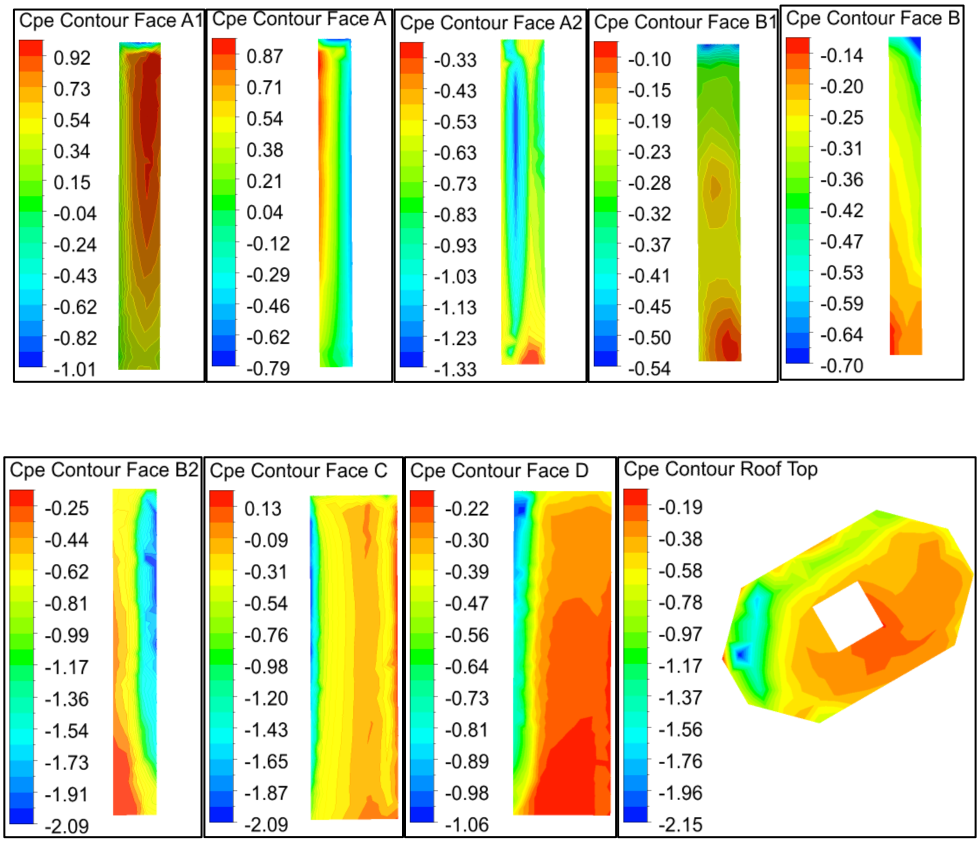

Figure 4. 59: C_{Pe} Contour on Outer Faces & Roof Top Octa Model 30° Wind Angle

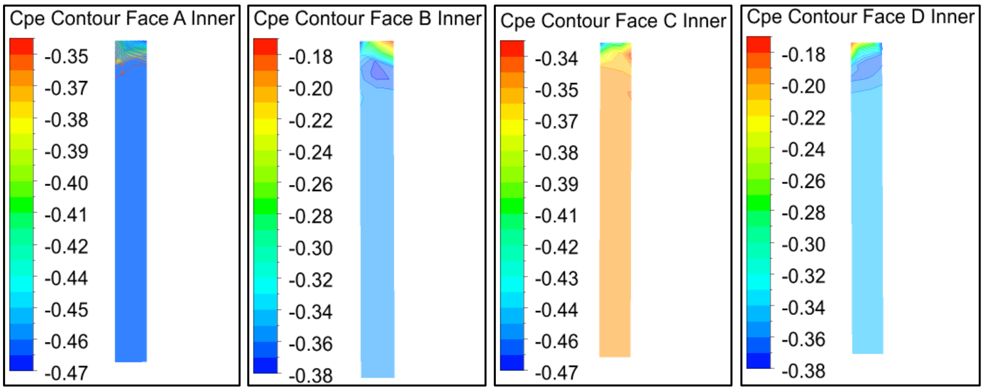

Figure 4. 60: C_{Pe} Contour on Inner Faces Octa Model 30° Wind Angle

4.4.3 C_{Pe} Contour 60° Wind Angle

At 60° wind angle of attack flow is impinging at the confluence of face A1 and C. Hence, both the faces are experiencing positive pressure on the face, concentration of which is towards the confluence with half parabolic formation of pressure contours. Pressure on face A1 is positive throughout except at the roof top whereas, suction exists at the far end on face C from where flow separation is taking place. The area average C_{Pe} on face A1 and C are respectively 0.42 and 0.35.

On another side flow separation is taking place from the confluence of face A and A2 (Figure 4.71). Pressure isobars on face A are vertical and suction is increasing from the near end edge to far end edge. Uniform gradient of pressure exists towards the near end of face A till middle decreasing suddenly with high negative value towards the far end edge. Effect of backwash is also seen. Area average suction C_{Pe} on the face is -1.11. On face A2 similar pressure effect as that on face A is observed, but in reverse order. The area average C_{Pe} on face A2 is -0.85.

Face D is under wake and having horizontal suction pressure contour pattern on its face. Suction is increasing from bottom to top. Face average coefficient of pressure on face D is -0.24. Concentration of high suction is seen at the top corner towards the meeting edge of face A2.

Face B1 is also under wake. The pressure contour at the bottom is initially in the diamond form towards face B converting to vertical formation after certain height. A upside down L shape formation of suction at the top corner towards face B is seen. The area C_{Pe} on the face is -0.26.

Face B is showing contour patterns of vertical in nature like we find on side faces. However, at the bottom towards face B1 effect of backwash is also seen. Suction towards the confluence of face B2 is high. Face average coefficient of pressure on face B is 0.61.

On face B2 high area average suction pressure coefficient (-1.03) exists. The pressure isobars are vertical with decreasing pressure gradient from the lee side towards windward side where flow separation is taking place. At the bottom towards face B effect of backwash is apparent.

On inner faces almost equal face average C_{Pe} = -0.62 is found on all faces which is almost throughout the face except little variation near top.

On the roof top maximum face average coefficient of pressure, for all wind angles of attack, is found which is equal to -0.75. Pressure contours are perpendicular to the wind direction with high suction towards the windward side. High concentration of suction zone towards the windward side above the corner of face A1 and C is appearing on the diagram.

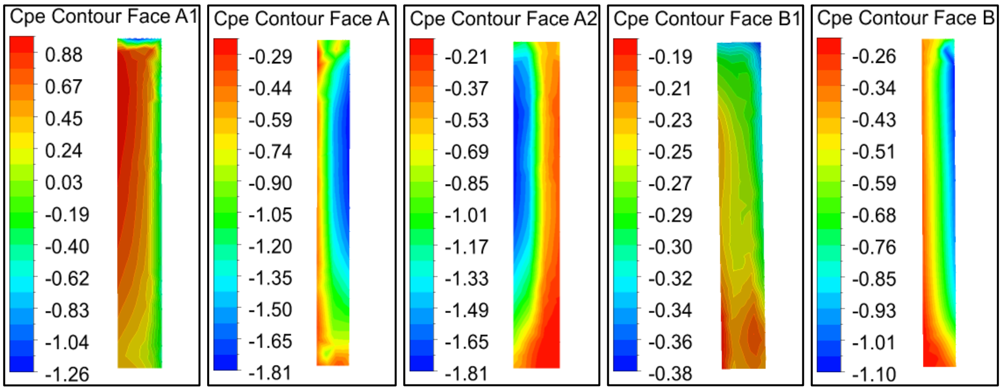

Figure 4. 61: CPe Contour on Outer Faces & Roof Top Octa Model 60° Wind Angle (Contd.)

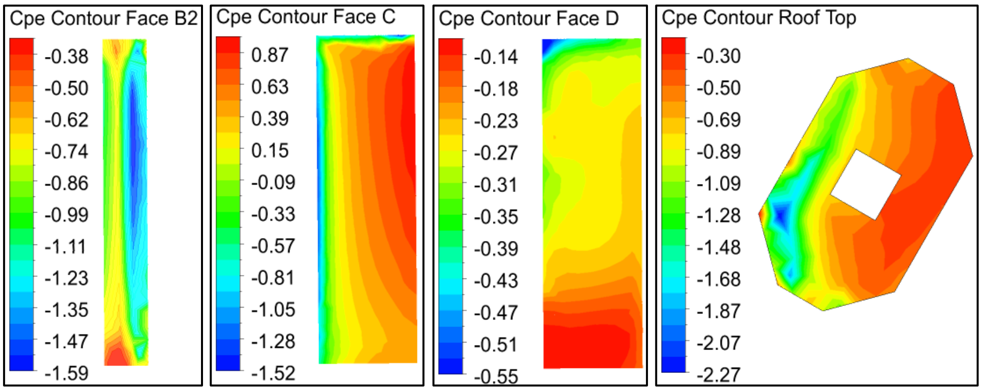

Figure 4. 61: C_{Pe} Contour on Outer Faces & Roof Top Octa Model 60° Wind Angle

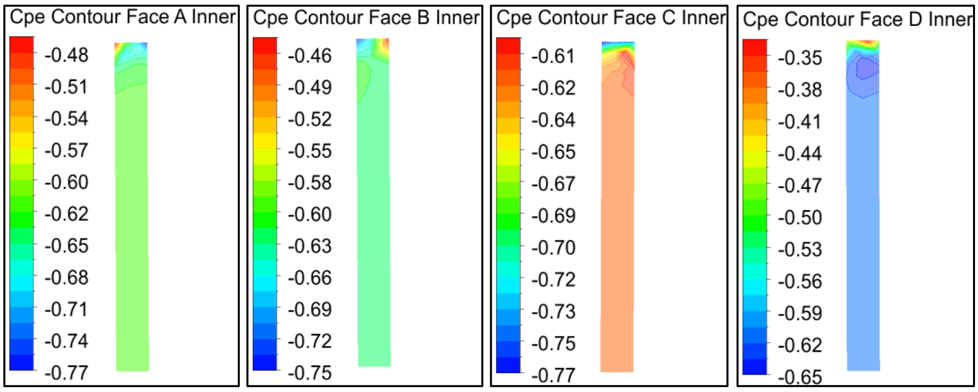

Figure 4. 62: C_{Pe} Contour on Inner Faces Octa Model 60° Wind Angle

4.4.4 C_{Pe} Contour 90° Wind Angle

Wind at 90° angle of attack is striking on face C shearing off the surfaces of inclined faces A1 and B2. Wind separation is taking place from the far ends of face A1 and B2. Face A and B are the side faces and face D is leeward face. Inclined faces A2 and B1 are partially in the wake (Figure 4.74). Accordingly, as expected, face C is experiencing parabolic pressure contour increasing with height, centred at the middle vertical line and symmetrical from the edges. It is not sharp parabolic and triangular as seen at 0° wind angle.

Inclined faces A1 and B2 are experiencing high gradient of pressure suggesting eddies and local turbulences created due to shear force by the wind on the surfaces. The pressure contours on the faces are vertical and ranging from positive at the near end edge to negative at the far end edge from where flow separation is taking place. The area average C_{Pe} on face A1 and B2 are -0.53 and 0.50 respectively. Minor difference, which should otherwise be equal for symmetrical faces, is due to three-dimensional behaviour of wind and also the incapability of numerical simulation to capture velocity of flow in the suction zone appropriately.

Pressure contours on face A and B are vertical in nature as would be expected on side faces, increasing in value from the near end from where flow separation is taking place towards the far end. Moreover, high region of suction is observed on these faces in the middle heights from mid of the faces extending towards the far end edges.

Face A2 and B1 are partially in the backwash and partially on the sidewash region. Pressure contours are vertical with high gradient due to shear force created by wind. Negative gradient of suction pressure exists on the faces from the windward side towards the lee side. Face D is completely on the wake region and pressure is almost similar on the entire face. The area C_{Pe} on the face is -0.21.

On the inner faces negative pressure on all faces are similar in nature. On roof suction pressure is perpendicular to wind direction like that of on other wind angle of attack. Pressure is throughout negative with higher suction on half area towards the windward side. Concentration of higher suction is observed towards the windward face above face C.

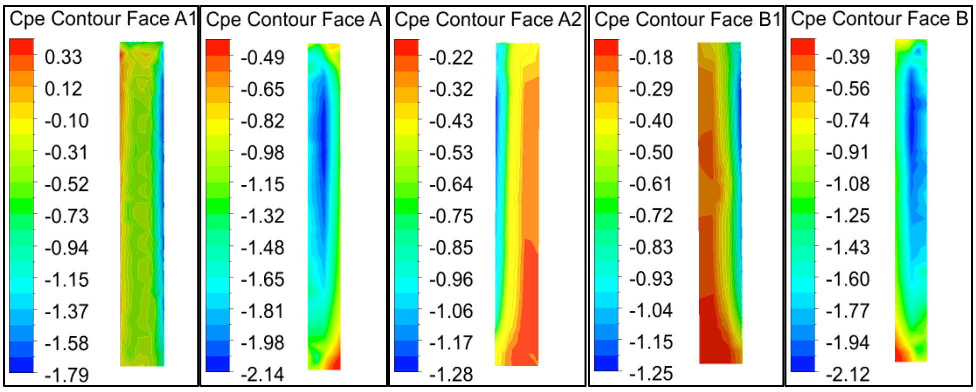

Figure 4. 63: C_{Pe} Contour on Outer Faces & Roof Top Octa Model 90° Wind Angle (Contd.)

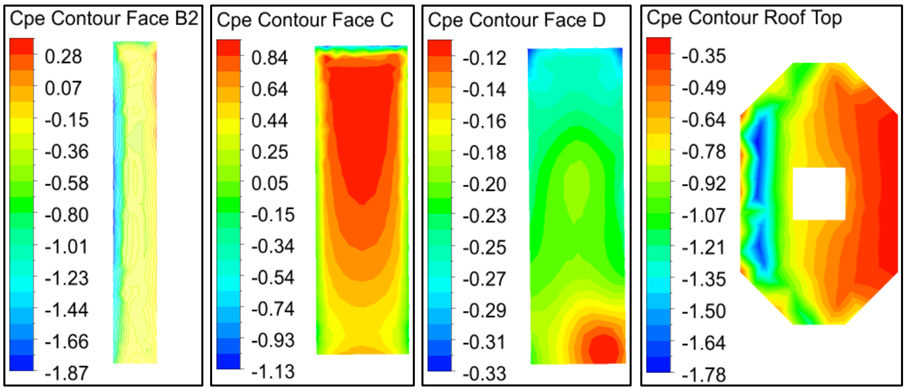

Figure 4. 63: C_{Pe} Contour on Outer Faces & Roof Top Octa Model 90° Wind Angle

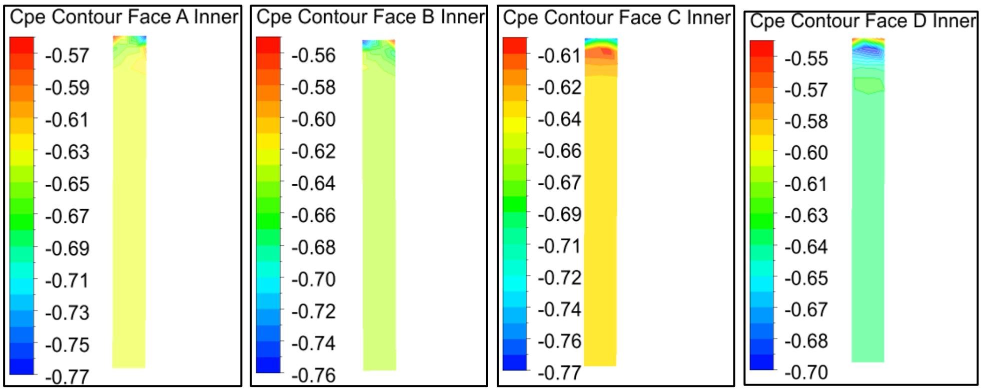

Figure 4. 64: C_{Pe} Contour on Inner Faces Octa Model 90° Wind Angle

4.4.5 Wind Flow Pattern

Figure 4.68, 4.71, 4.74 & 4.77 show the streamline of flow at different heights of the model viz Z = 0.165 m, Z = 0.250 m and Z = 0.335 m for different wind incidence angles from 0° to 90° @ 30° and Figure 4.69, 4.72, 4.75 & 4.78 show the velocity contours at the same heights for different wind incidence angles. Velocity vector diagrams at different heights for varied wind angles are shown in Figure 4.70, 4.73, 4.76 & 4.79.

Flow patterns are different in intensity and strength for different wind angles and for different levels of height. Hence, it is expected to impart different pressure distributions on faces of the model as discussed earlier on other model shapes. Besides the vortices formed behind the model vortices are also seen in the central cavity opening for all wind angles.

At 0° wind angle the intensity and strength of the symmetrical vortices in the wake are less compared to other model shapes discussed earlier. The size of the wake is smaller due to streamlined flow effect on the inclined faces where less frictional force is required for the flow reversal. Flow is separating from the far end edges of the inclined faces and reattachment of flow on the side faces C and D occurs before creation of wake, being a long after body. Inside the central cavity the vortices are formed in a very complex manner.

At 30° & 60° wind incidence angle two dissimilar vortices are created behind the model. The intensity of wake is less in strength at the mid-level i.e., at Z = 250 mm in comparison to that at Z = 165 mm and the streamlines are more apart. However, at still higher level distinct and higher intensity vortices are formed and streamlines come closer. It indicates slow stream velocity in the flow direction at mid height.

Again at 90° wind angle the intensity and strength of symmetrical vortices are increasing along height. Distinct creation of wake behind the model is seen. Reattachment of flow on the side faces after separation from the leading edges of inclined faces A1 and B2 can be ruled out.

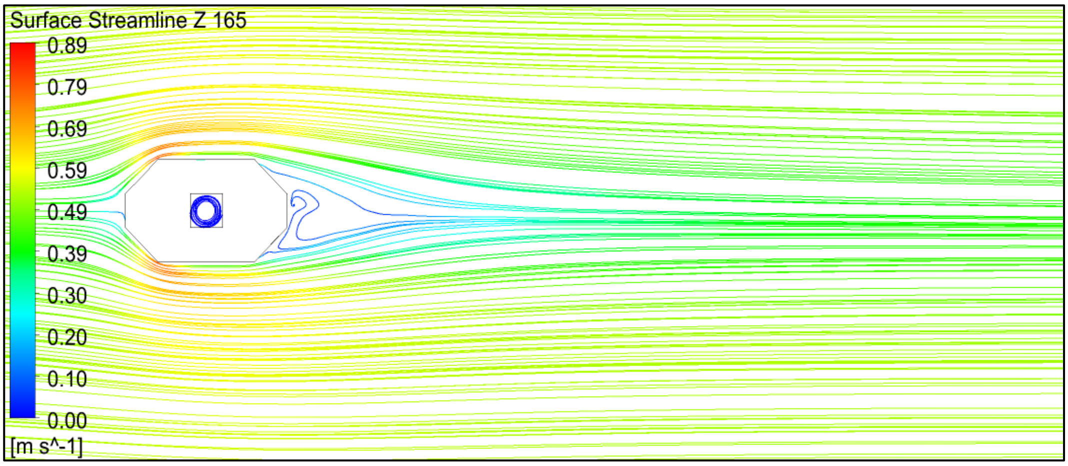

(a) Surface Streamline at Height Z = 165 mm

Figure 4. 65: Surface Streamline Octa Model 0° Wind Angle (Contd.)

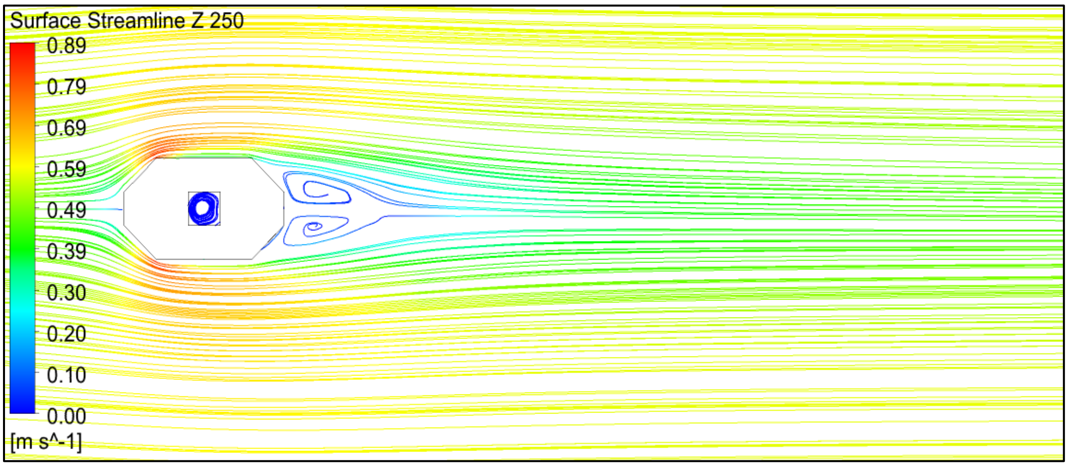

(b) Surface Streamline at Height Z = 250 mm

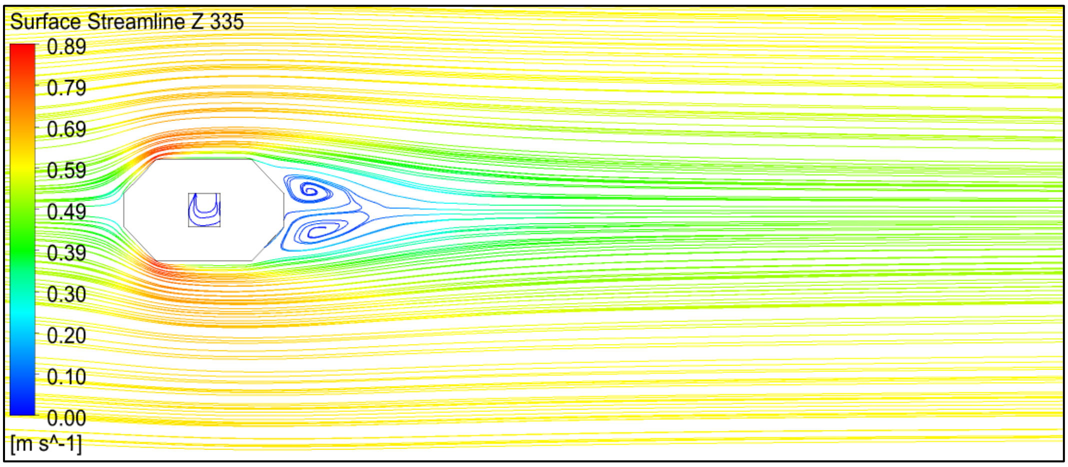

(c) Surface Streamline at Height Z = 335 mm

Figure 4. 65: Surface Streamline Octa Model 0° Wind Angle

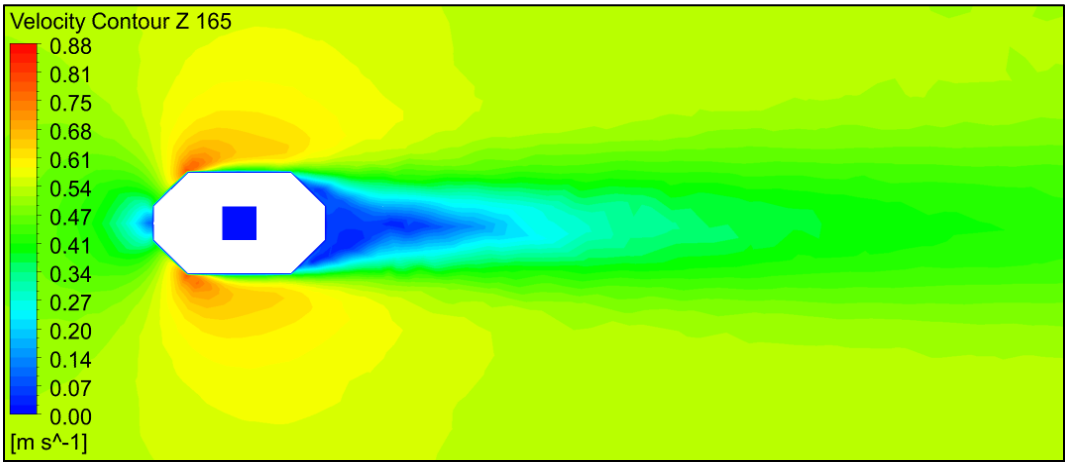

(a) Velocity Contour at Height Z = 165 mm

Figure 4. 66: Velocity Contour Octa Model 0° Wind Angle (Contd.)

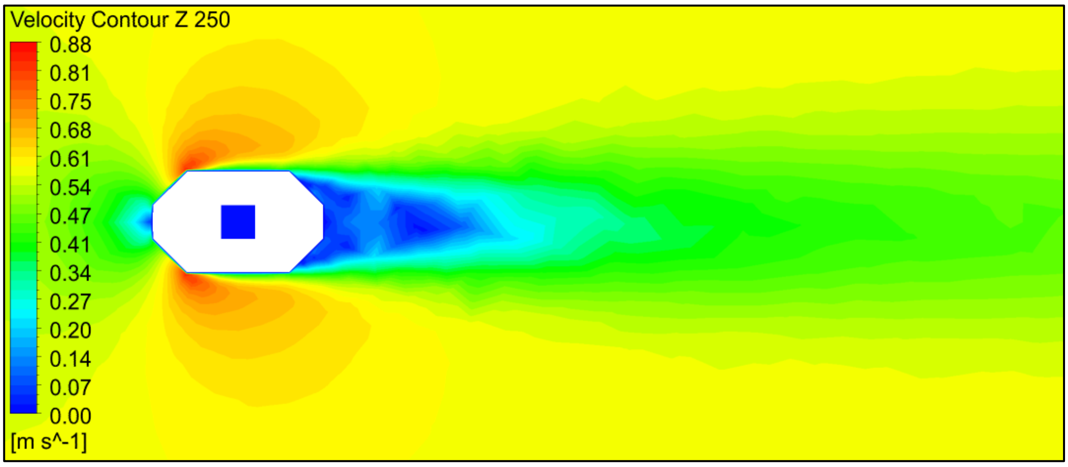

(b) Velocity Contour at Height Z = 250 mm

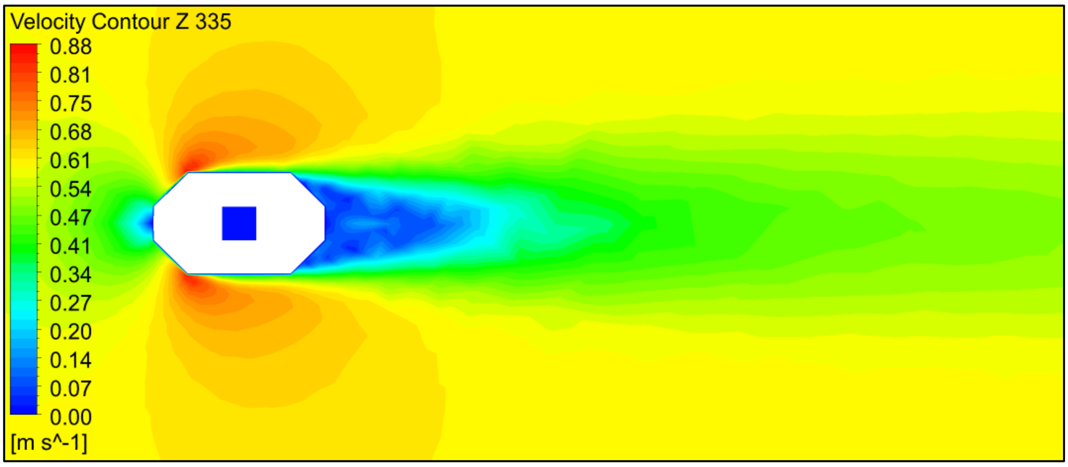

(c) Velocity Contour at Height Z = 335 mm

Figure 4. 66: Velocity Contour Octa Model 0° Wind Angle

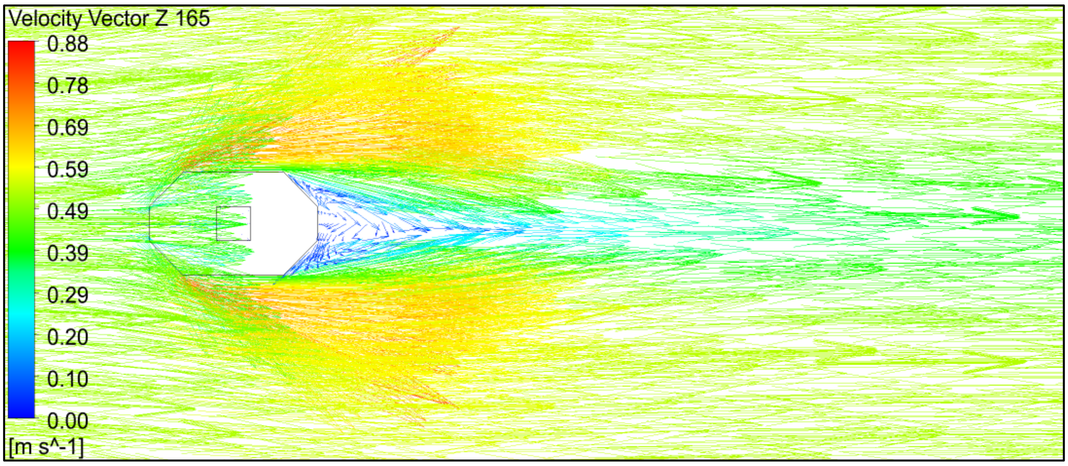

(a) Velocity Vector at Height Z = 165 mm

Figure 4. 67: Velocity Vector Octa Model 0° Wind Angle (Contd.)

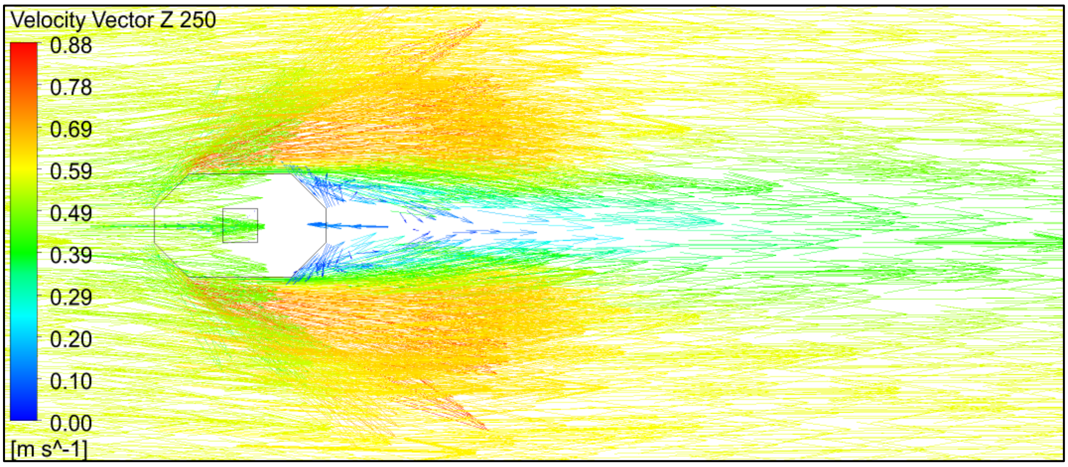

(b) Velocity Vector at Height Z = 250 mm

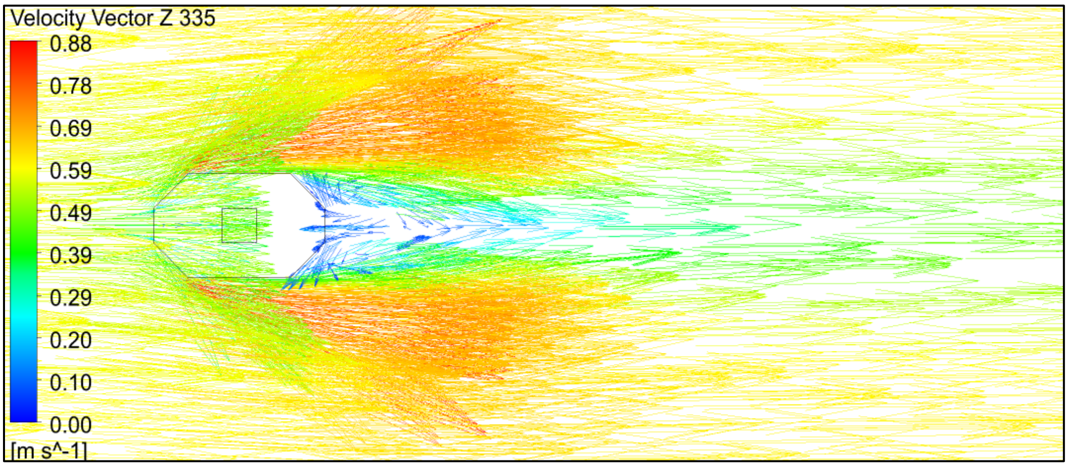

(c) Velocity Vector at Height Z = 335 mm

Figure 4. 67: Velocity Vector Octa Model 0° Wind Angle

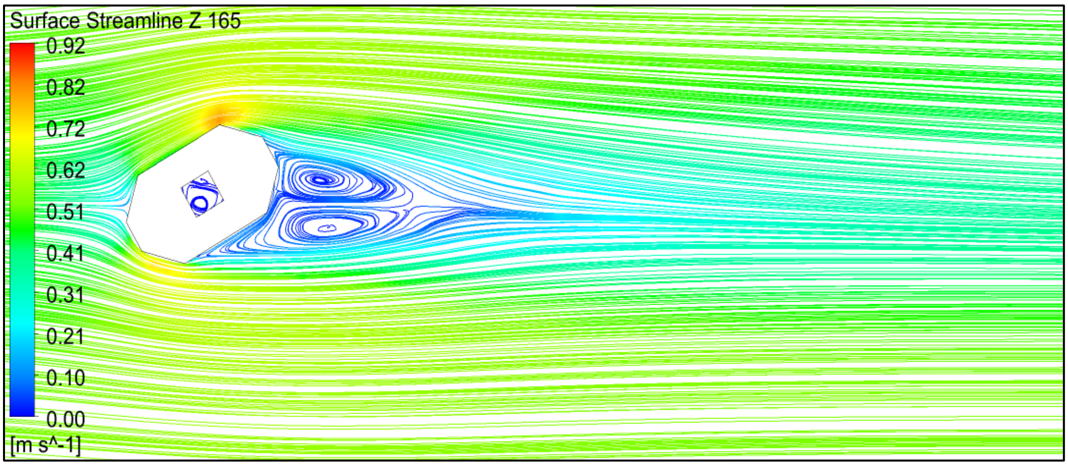

(a) Surface Streamline at Height Z = 165 mm

Figure 4. 68: Surface Streamline Octa Model 30° Wind Angle (Contd.)

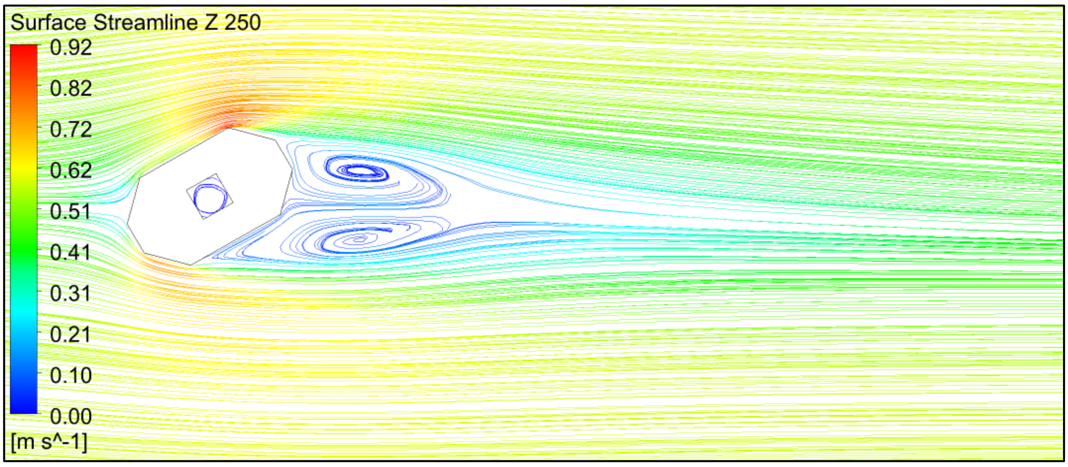

(b) Surface Streamline at Height Z = 250 mm

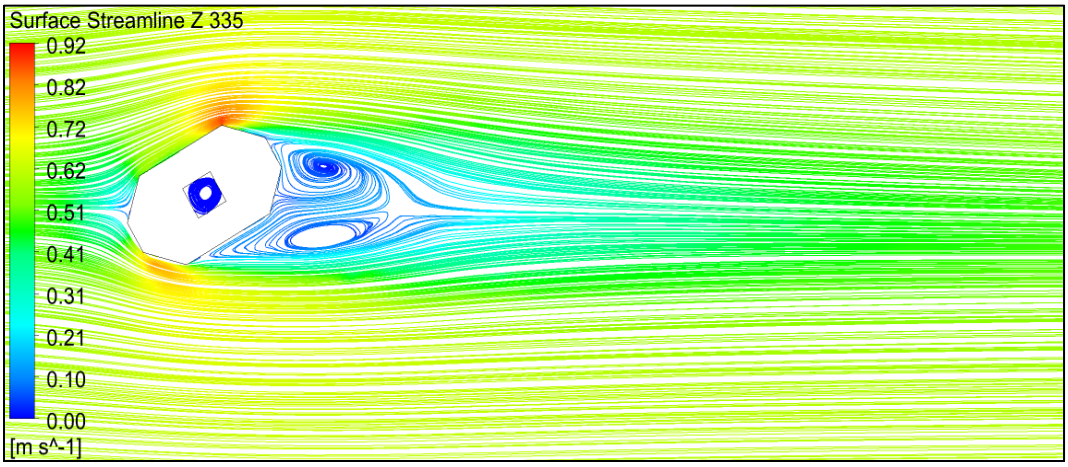

(c) Surface Streamline at Height Z = 335 mm

Figure 4. 68: Surface Streamline Octa Model 30° Wind Angle

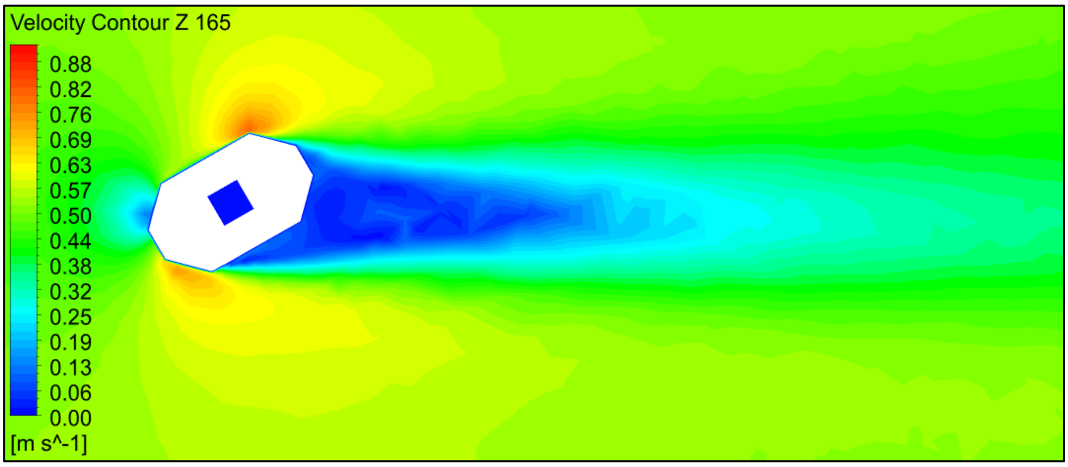

(a) Velocity Contour at Height Z = 165 mm

Figure 4. 69: Velocity Contour Octa Model 30° Wind Angle (Contd.)

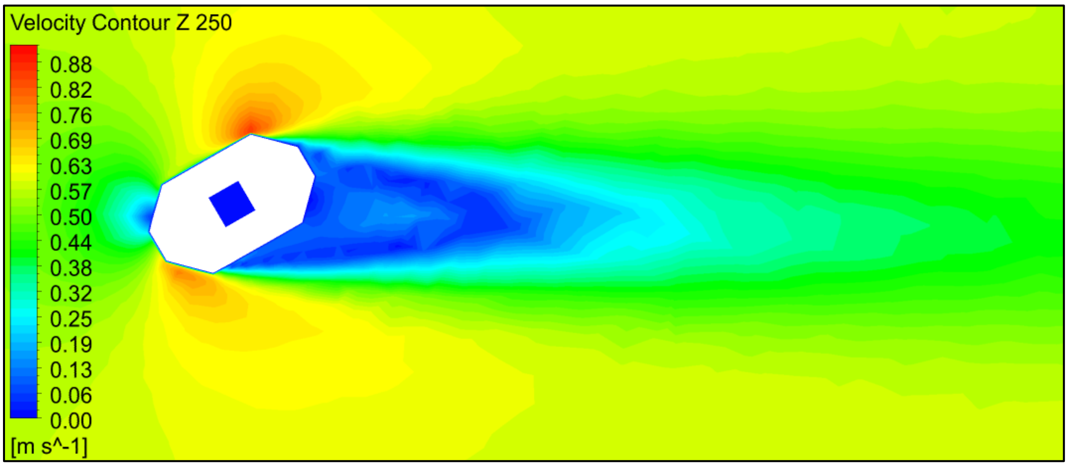

(b) Velocity Contour at Height Z = 250 mm

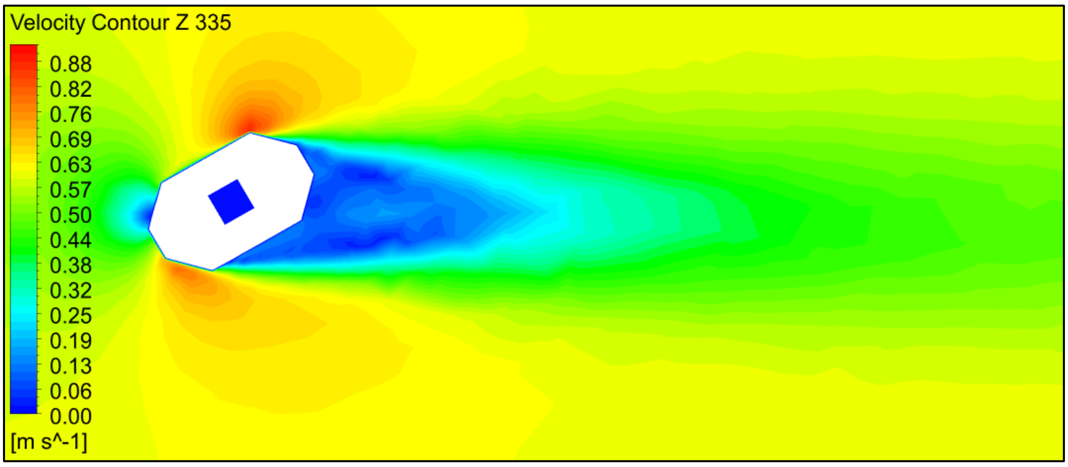

(c) Velocity Contour at Height Z = 335 mm

Figure 4. 69: Velocity Contour Octa Model 30° Wind Angle

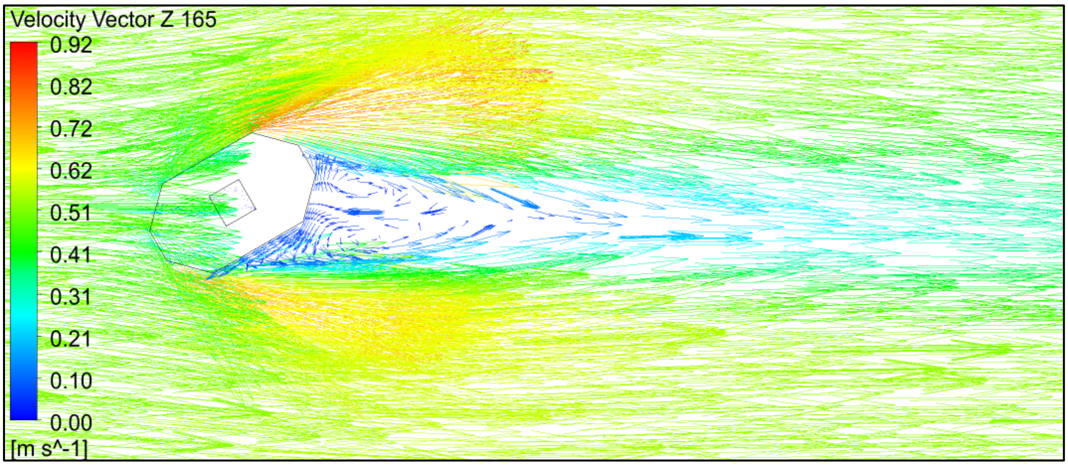

(a) Velocity Vector at Height Z = 165 mm

Figure 4. 70: Velocity Vector Octa Model 30° Wind Angle (Contd.)

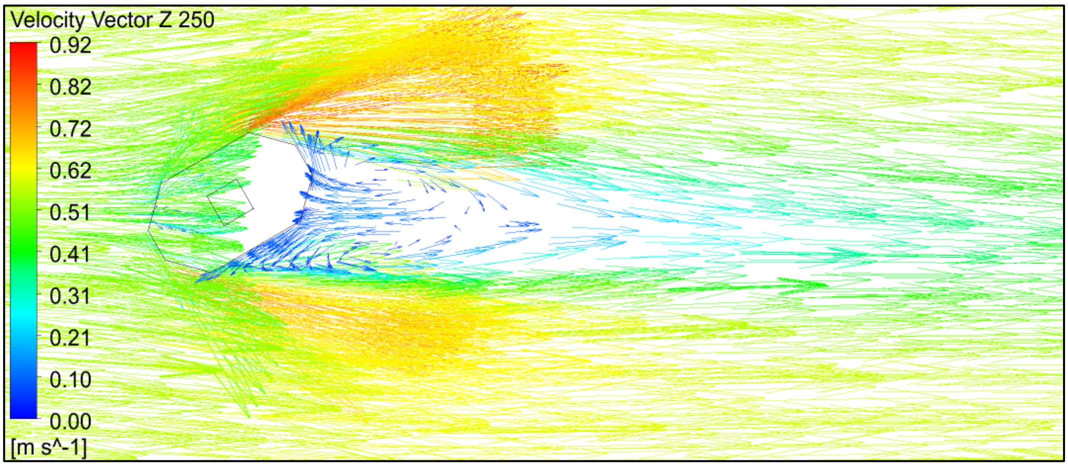

(b) Velocity Vector at Height Z = 250 mm

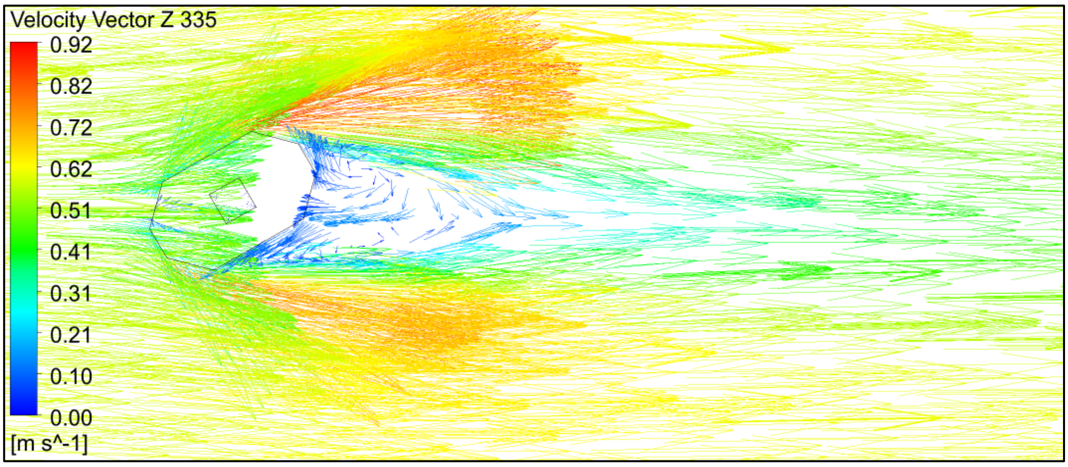

(c) Velocity Vector at Height Z = 335 mm

Figure 4. 70: Velocity Vector Octa Model 30° Wind Angle

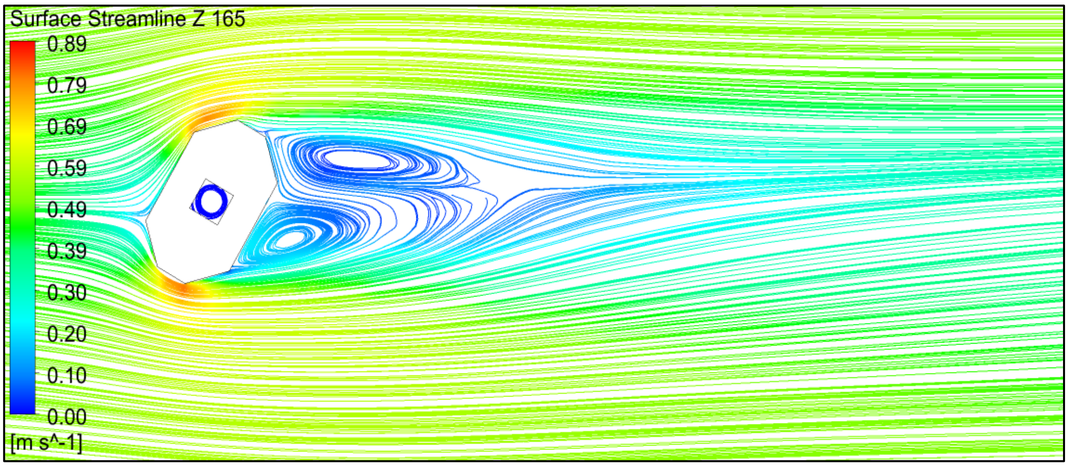

(a) Surface Streamline at Height Z = 165 mm

Figure 4. 71: Surface Streamline Octa Model 60° Wind Angle (Contd.)

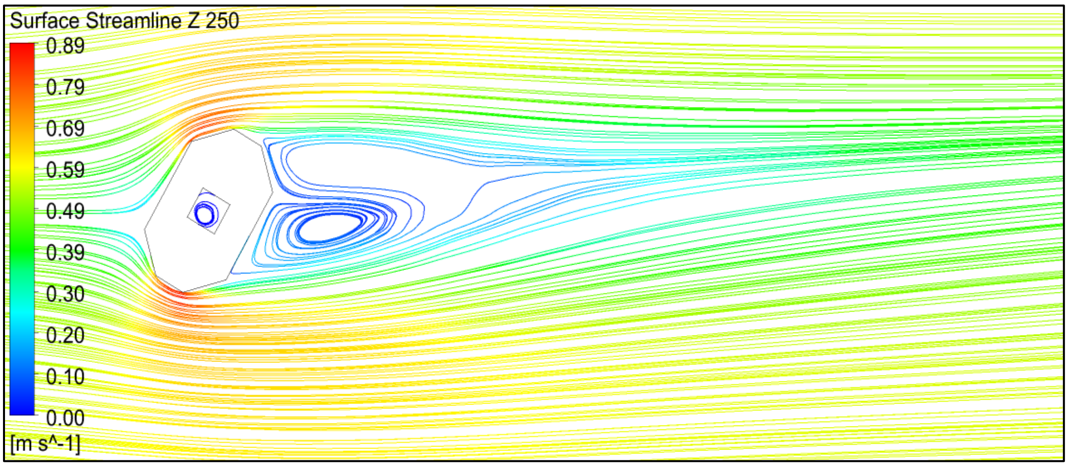

(b) Surface Streamline at Height Z = 250 mm

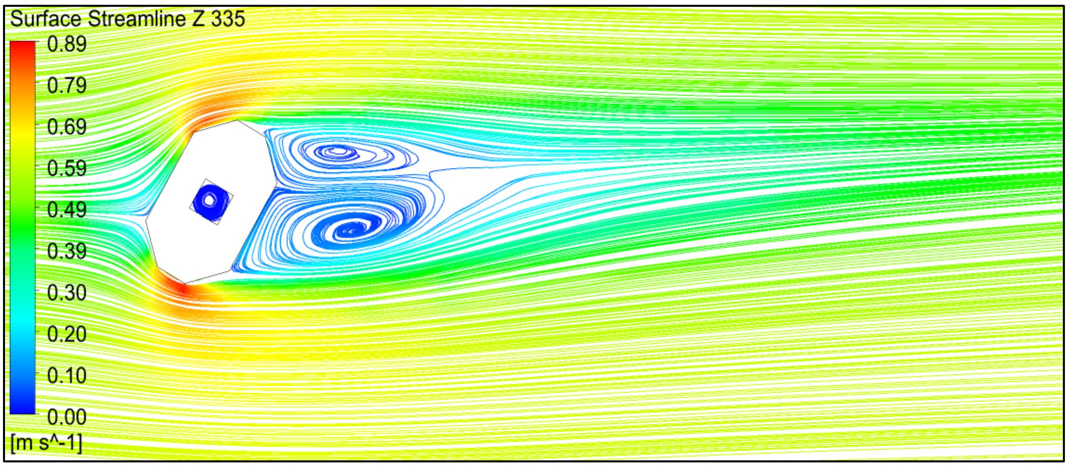

(c) Surface Streamline at Height Z = 335 mm

Figure 4. 71: Surface Streamline Octa Model 60° Wind Angle

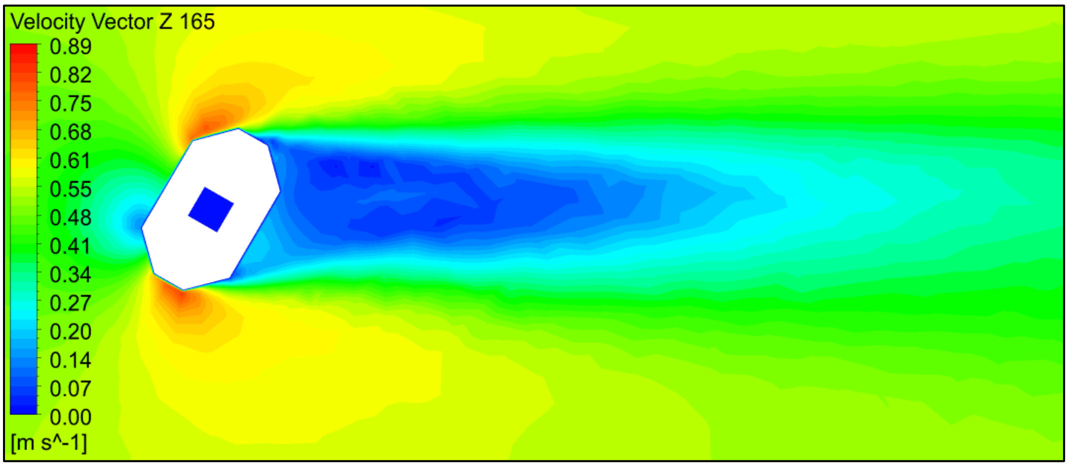

(a) Velocity Contour at Height Z = 165 mm

Figure 4. 72: Velocity Contour Octa Model 60° Wind Angle (Contd.)

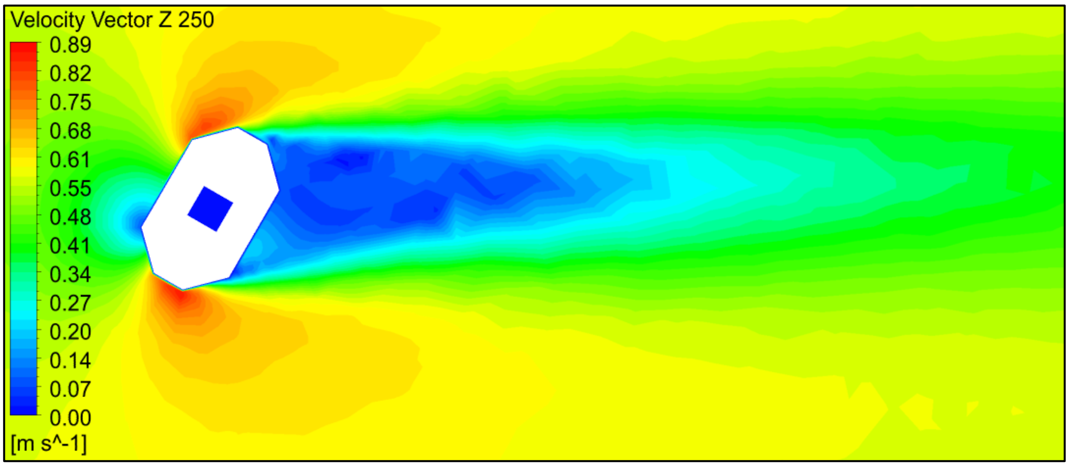

(b) Velocity Contour at Height Z = 250 mm

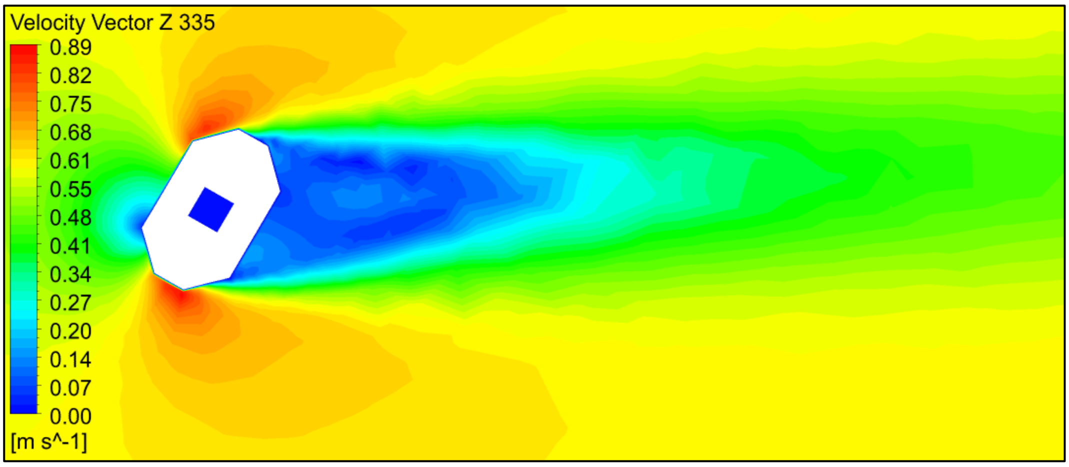

(c) Velocity Contour at Height Z = 335 mm

Figure 4. 72: Velocity Contour Octa Model 60° Wind Angle

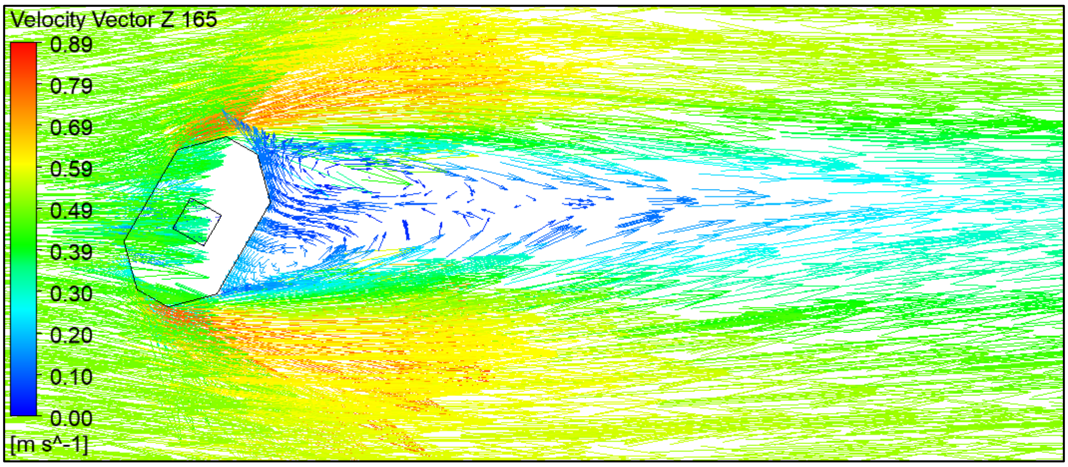

(a) Velocity Vector at Height Z = 165 mm

Figure 4. 73: Velocity Vector Octa Model 60° Wind Angle (Contd.)

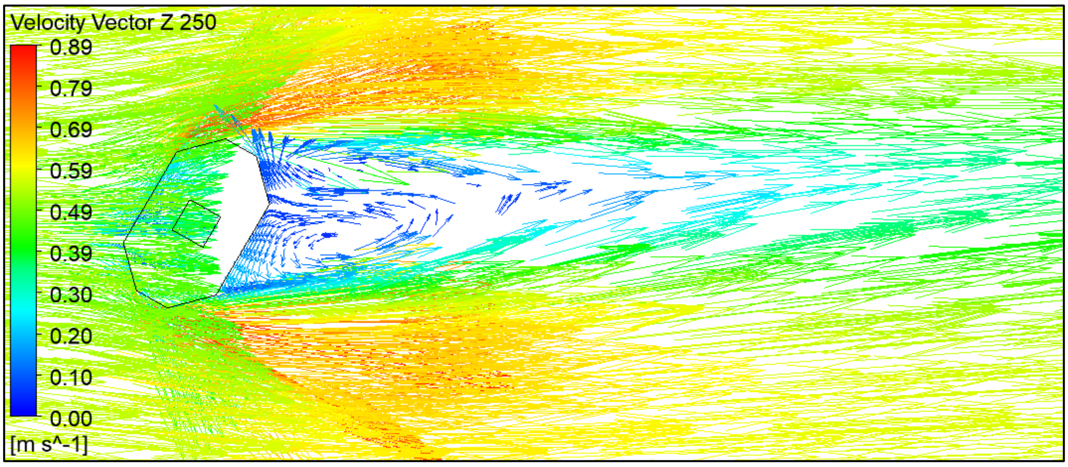

(b) Velocity Vector at Height Z = 250 mm

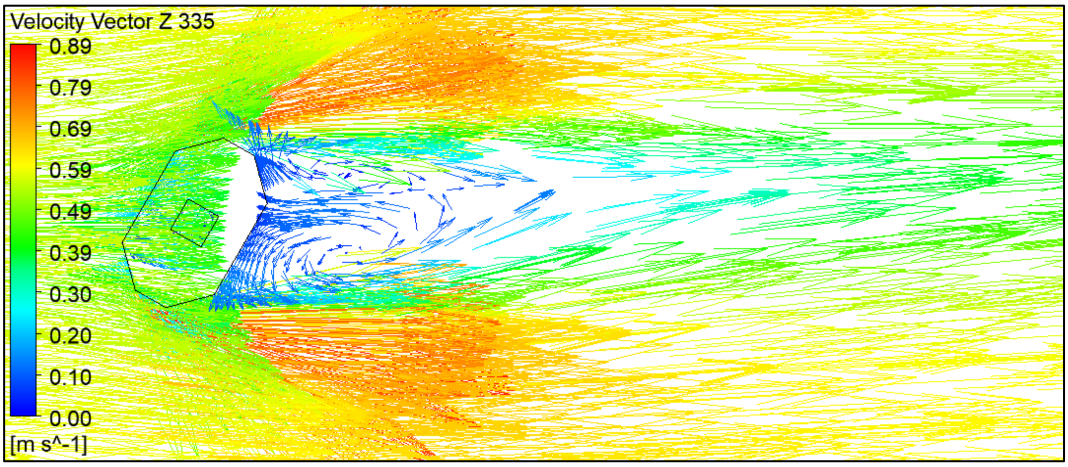

(c) Velocity Vector at Height Z = 335 mm

Figure 4. 73: Velocity Vector Octa Model 60° Wind Angle

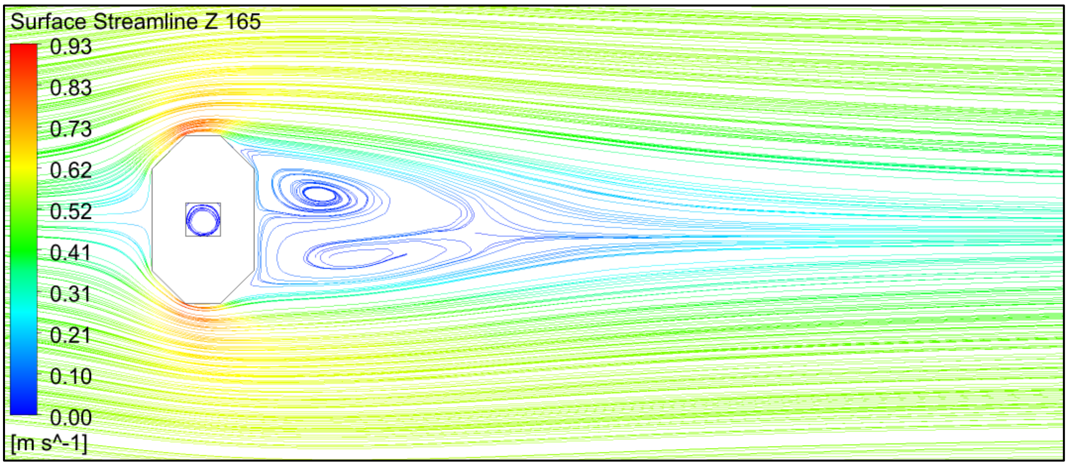

(a) Surface Streamline at Height Z = 165 mm

Figure 4. 74: Surface Streamline Octa Model 90° Wind Angle (Contd.)

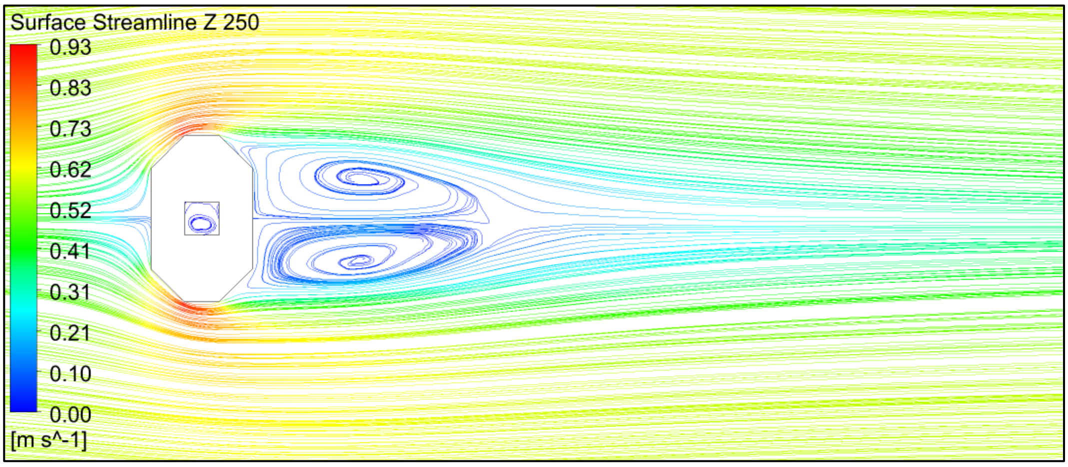

(b) Surface Streamline at Height Z = 250 mm

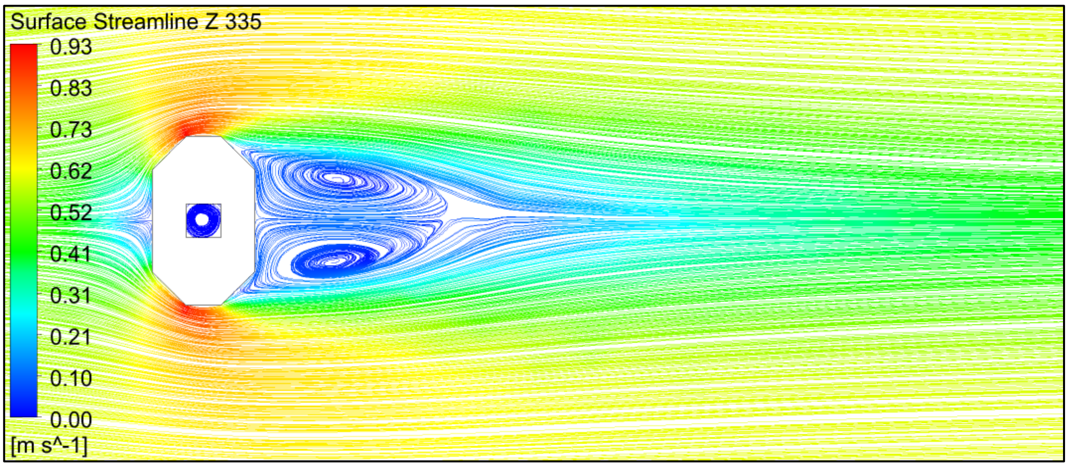

(c) Surface Streamline at Height Z = 335 mm

Figure 4. 74: Surface Streamline Octa Model 90° Wind Angle

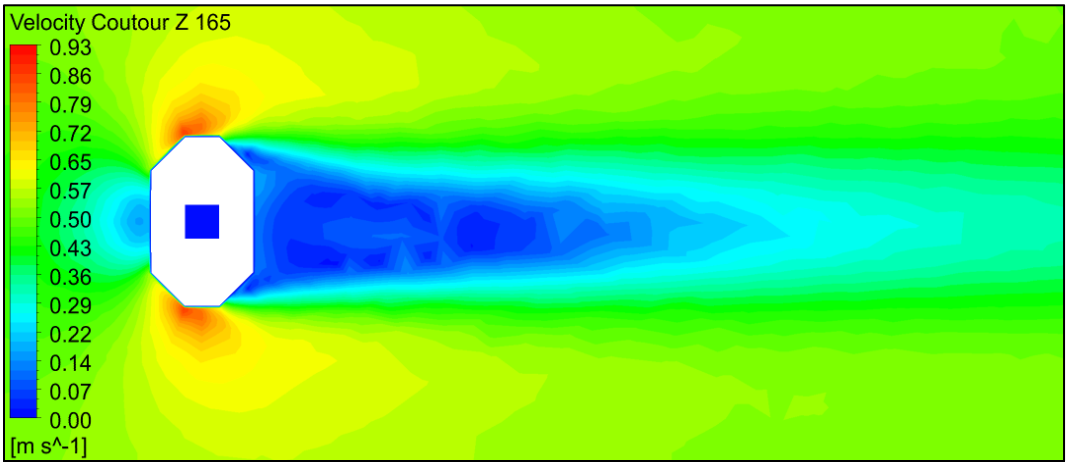

(a) Velocity Contour at Height Z = 165 mm

Figure 4. 75: Velocity Contour Octa Model 90° Wind Angle (Contd.)

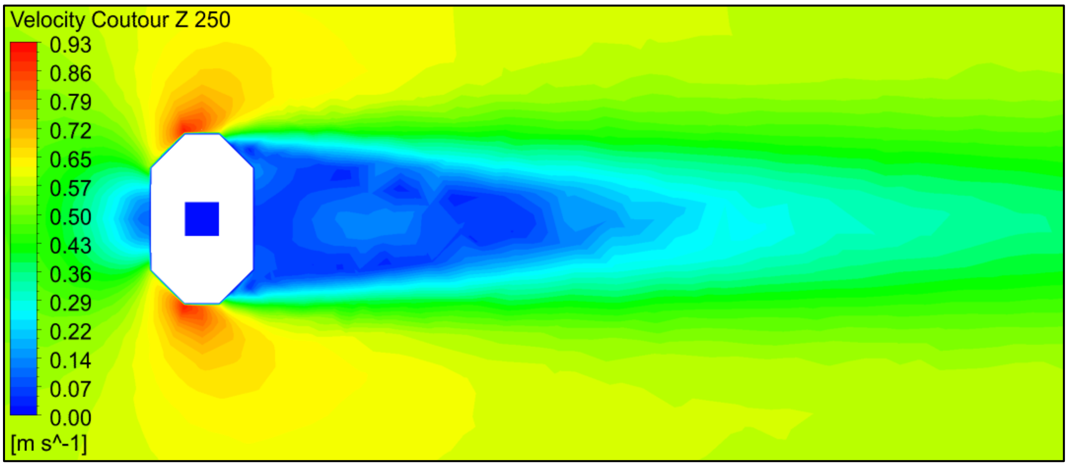

(b) Velocity Contour at Height Z = 250 mm

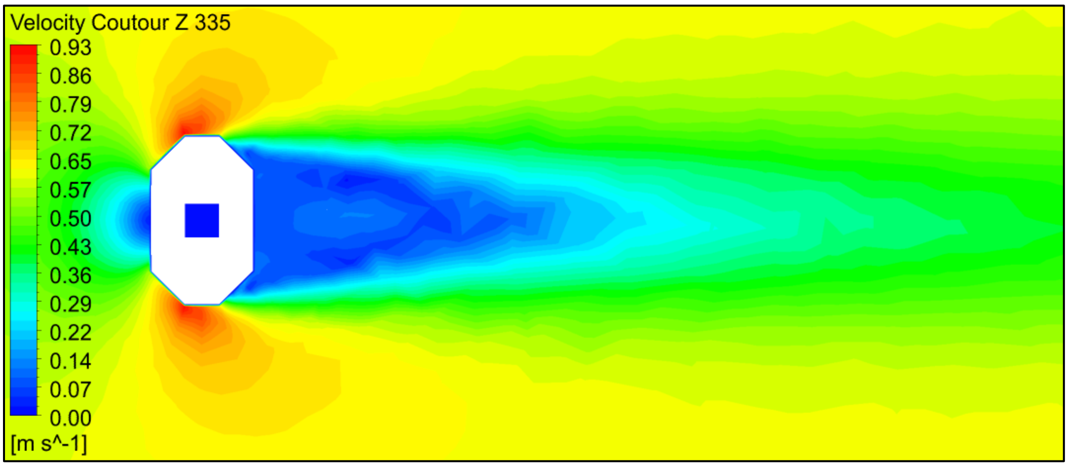

(c) Velocity Contour at Height Z = 335 mm

Figure 4. 75: Velocity Contour Octa Model 90° Wind Angle

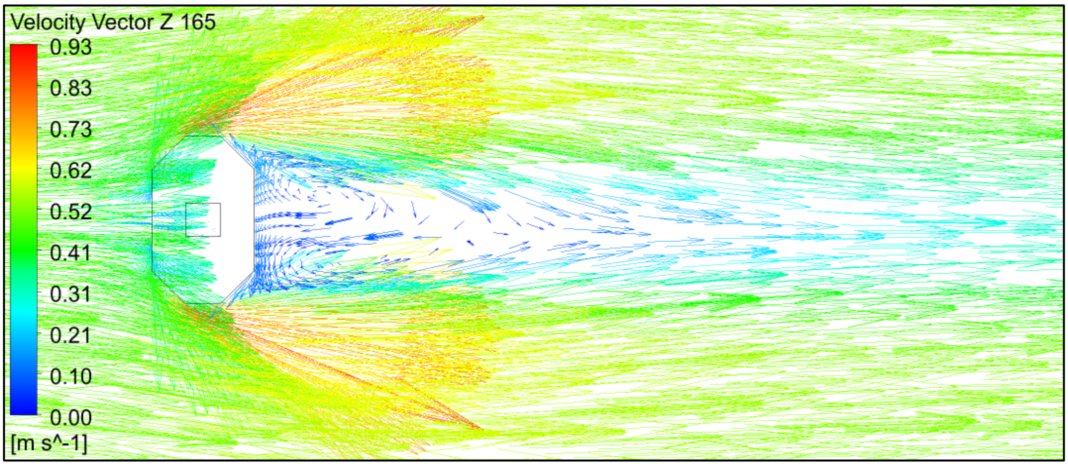

(a) Velocity Vector at Height Z = 165 mm

Figure 4. 76: Velocity Vector Octa Model 90° Wind Angle (Contd.)

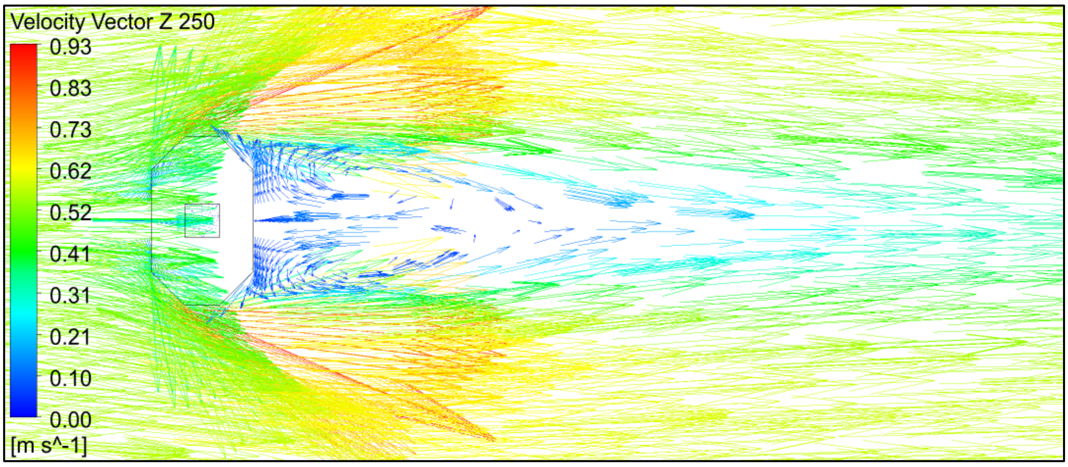

(b) Velocity Vector at Height Z = 250 mm

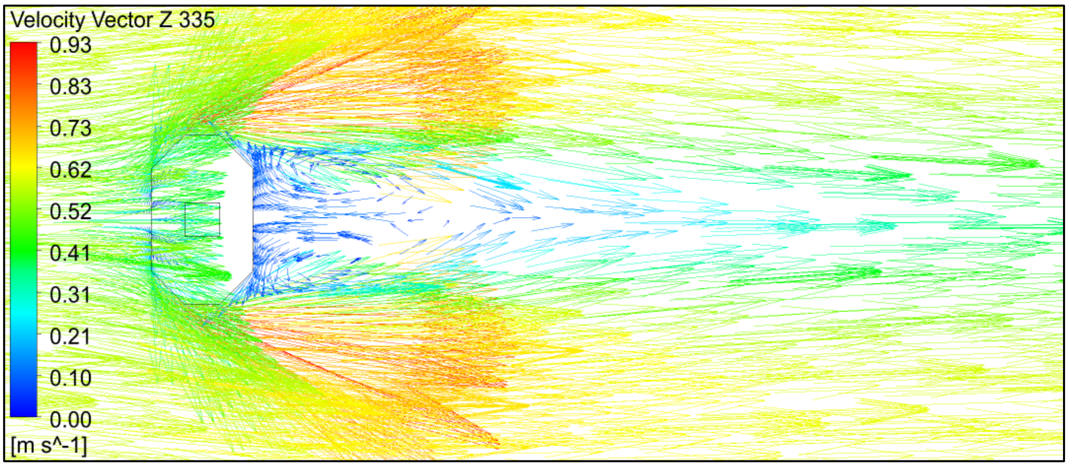

(c) Velocity Vector at Height Z = 335 mm

Figure 4. 76: Velocity Vector Octa Model 90° Wind Angle

4.4.6 Velocity Streamline Along Wind Direction on Central Vertical Plane

Figure 4.77, 4.78, 4.79 & 4.80 show the flow streamline on cross section through central vertical plane along the wind direction. The upwind vortex at ground level, the upwash, downwash and stagnation zones on the windward face can be visualized. Recirculation and creation of shear layer at roof top and reattachment of flow behind the model can also be seen.

Two distinct velocity curls are developed behind the model for all wind angles. For 0° & 90° wind angle – one around 1/3rd height and another near the top. At 30° & 60° wind angle velocity curls are near top and ½ height from ground. Effect of backwash due to these velocity curls can be seen along the height of the model. The strength and intensity of velocity curls are increasing with the change in wind angles. The impact of upwind vortex at 60° and 90° wind angle of attack is seen more than at 0° and 30° wind angle.

Inside the cavity, as pointed out earlier that the flow is very complex and that there exist two counteracting vortices, it is not a simple flow or a stagnation flow. The flow in the cavity at different heights are horizontal, downward or upward – in all directions. In all cases, at the roof top the flow is outward from the central opening. This can be attributed to influence of shear layer created by separation of wind at the roof top above central opening. The velocity direction from the vortices is spreading in all directions. So, the central opening can be used as wind induced natural ventilation in taking up smoke and gases from these types of cavities.

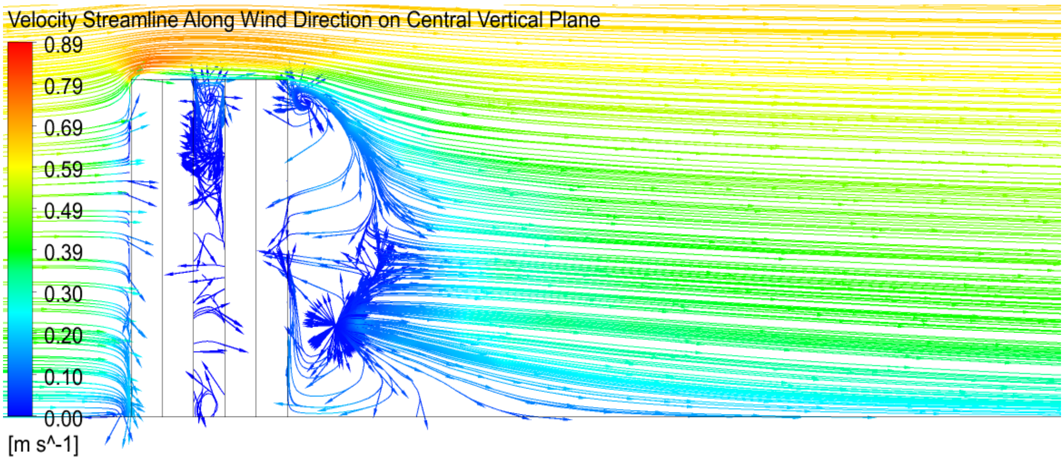

Figure 4. 77: Velocity Streamline Along the Wind Direction on Central Vertical Plane Octa Model 0° Wind Angle

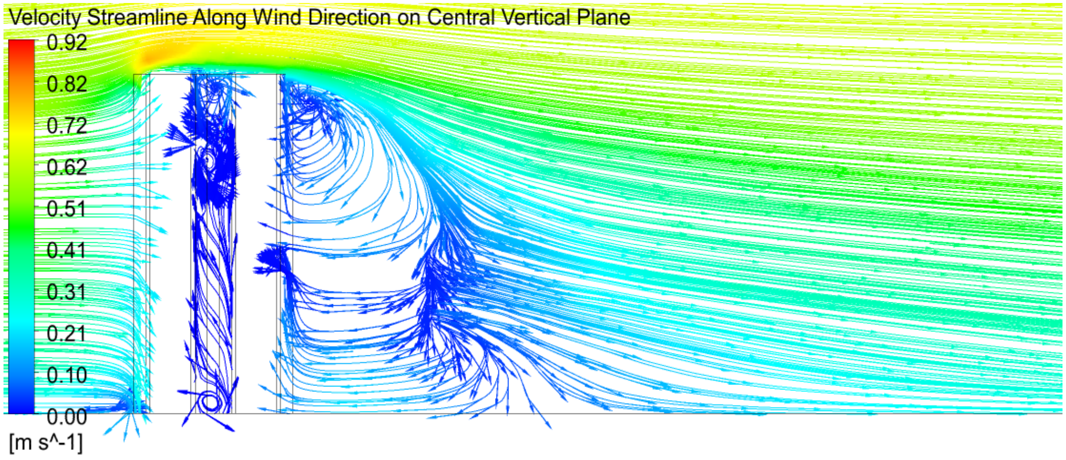

Figure 4. 78: Velocity Streamline Along the Wind Direction on Central Vertical Plane Octa Model 30° Wind Angle

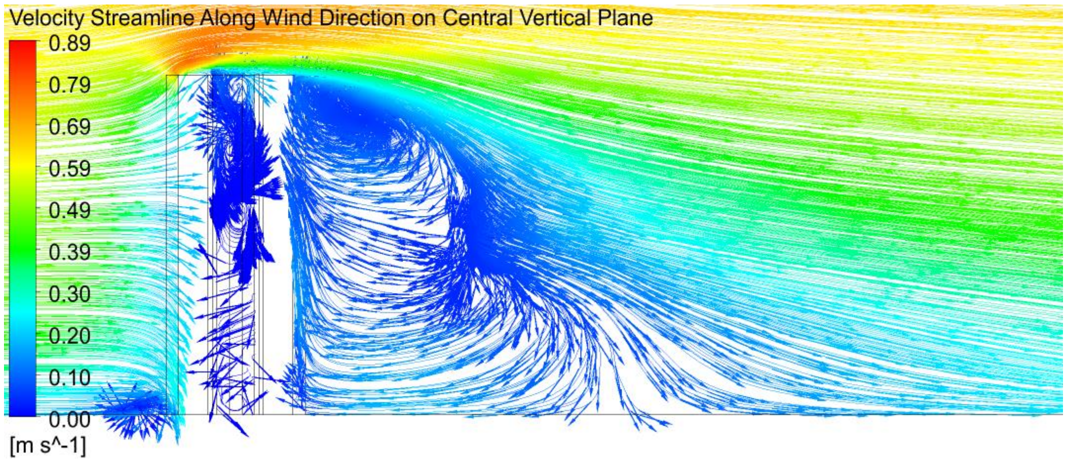

Figure 4. 79: Velocity Streamline Along the Wind Direction on Central Vertical Plane Octa Model 60° Wind Angle

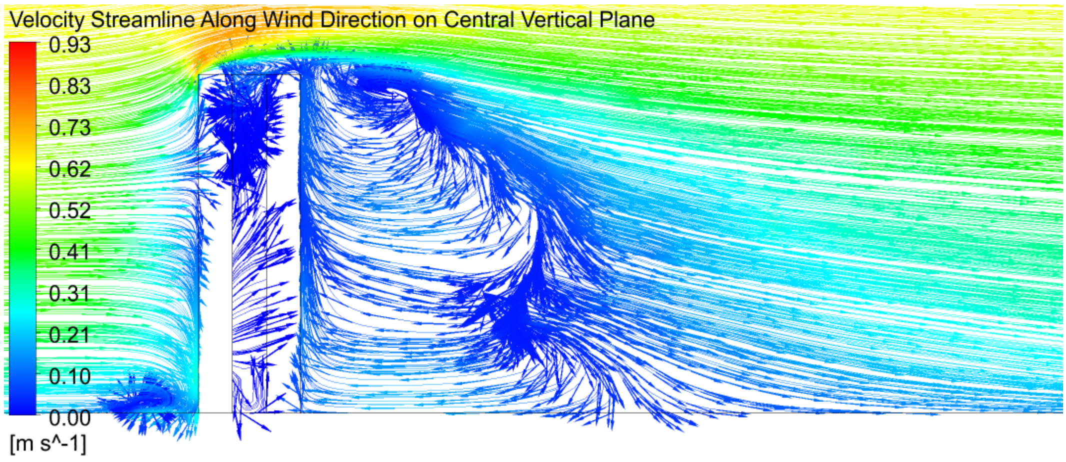

Figure 4. 80: Velocity Streamline Along the Wind Direction on Central Vertical Plane Octa Model 90° Wind Angle

4.4.7 C_{Pe} Along Building Perimeter

Graphical plot representing the variation of C_{Pe} on the building façade at three different heights Z = 0.165 m (about 1/3rd height of the model), Z = 0.25 m (1/2 height of the model) and Z = 0.335 m (about 2/3rd height of the model) for different wind angles of attack from 0° to 90° @ 30° have been shown in Figure 4.81, 4.82, 4.83 & 4.84 respectively. For all the wind angles the maximum positive coefficient of pressure is almost reaching the value of 1. As explained earlier in para 4.2.7, trivial variations in C_{Pe} on the faces shows swirl of wind whereas, immense rise in the values suggests formation of pressure region on the face. Sudden decrease in C_{Pe} values between the confluence of faces or near it on faces shows formation of eddies and high suction at the place. Where maximum suction exist is vital for design of cladding units.

The detailed suction C_{Pe} values for different angle of wind incidence on the corners or near corner on faces are shown in Table 4.6. It is quite evident that maximum suction (-2.18) occurs on the face A and B for 90° wind angle of attack and also at the confluence of faces B2C (-2.12) for 30° wind angle of attack which shall govern the design of cladding units for this shape and size of the octagonal-oval plan shaped building. However, if the cladding design is done considering the coefficient on face-to-face basis and after preparation of contour block diagrams on the basis of suction coefficients as detailed in the Table 4.6, it will be economically cheaper at the same time the building will be safer against failure of cladding design.

Table 4. 6: Maximum Suction in Terms of C_{Pe} For Cladding Design

AoA	0°		30°		60°		90°	
Z/Location	Face		Face	Corner	Corner	Face	Face	Face
	D	C	A2	B2C	AA2	B2	A	B
0.165 m	-1.35	-1.35	-1.16	-1.73	-1.55	-1.43	-1.87	-1.87
0.250 m	-1.68	-1.68	-1.25	-1.96	-1.74	-1.47	-1.99	-1.99
0.335 m	-1.83	-1.83	-1.34	-2.12	-1.83	-1.62	-2.18	-2.18

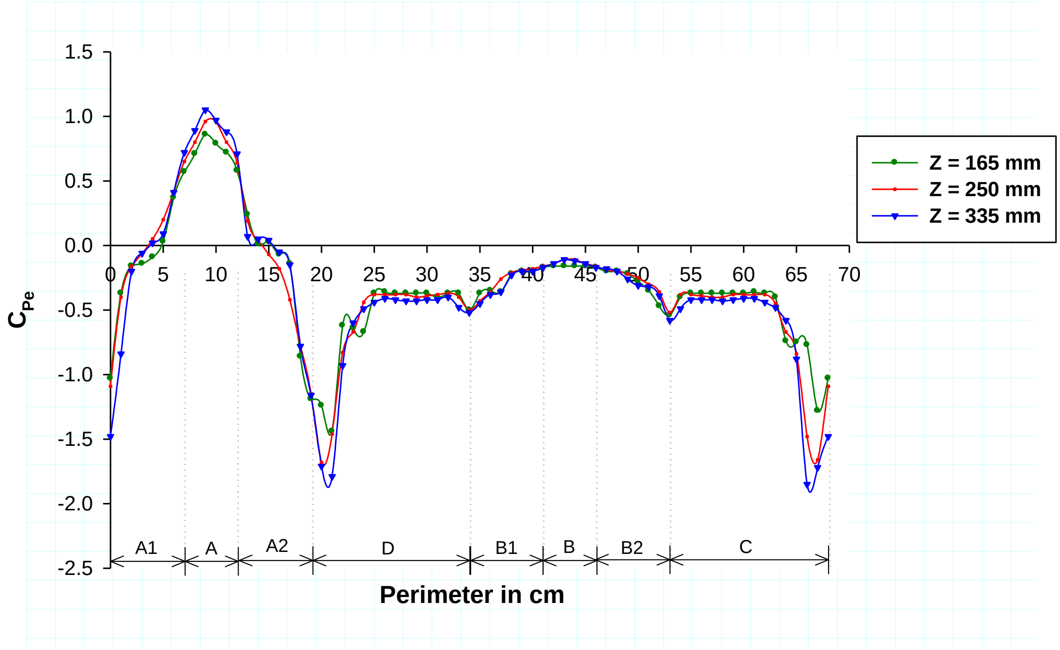

Figure 4. 81: C_{Pe} Along Perimeter Octa Model 0° Wind Angle

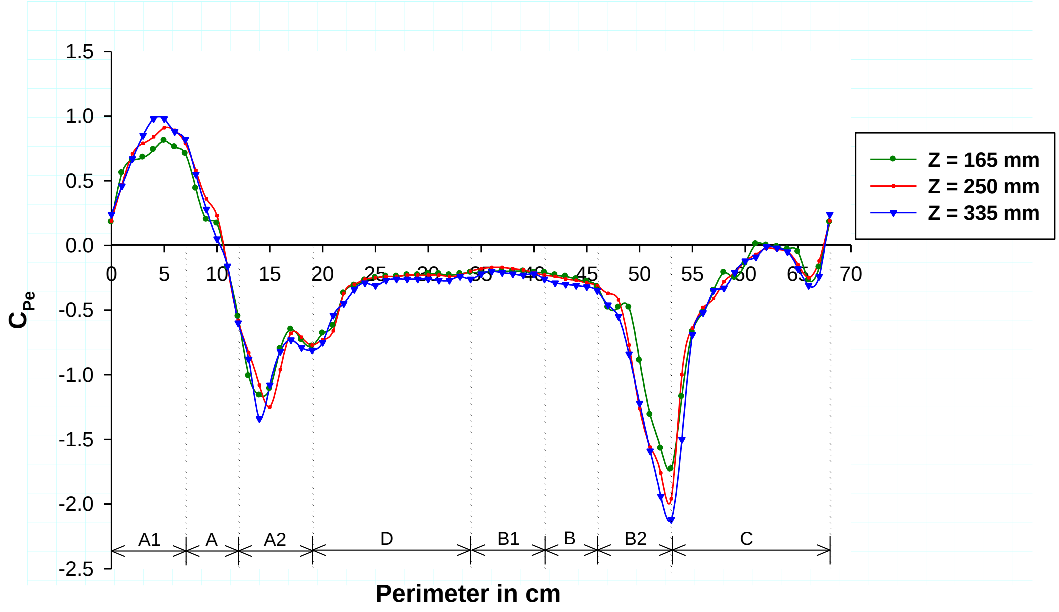

Figure 4. 82: C_{Pe} Along Perimeter Octa Model 30° Wind Angle

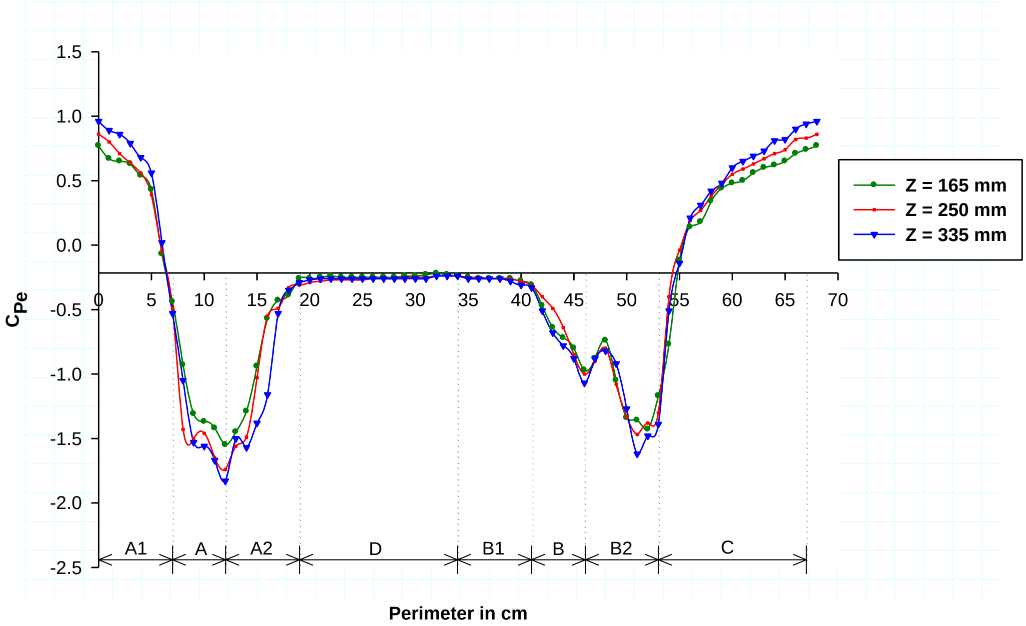

Figure 4. 83: C_{Pe} Along Perimeter Octa Model 60° Wind Angle

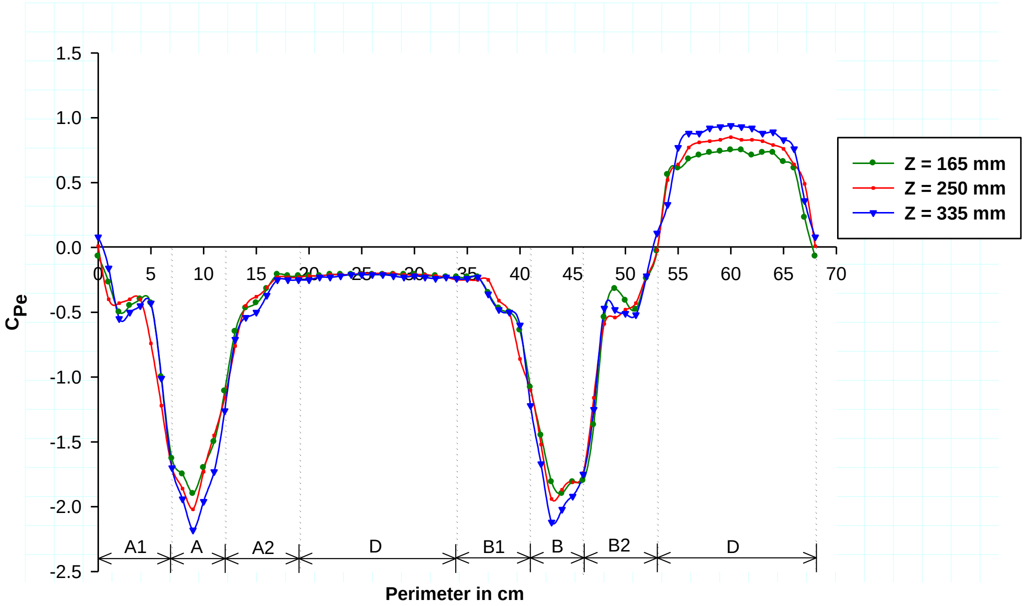

Figure 4. 84: C_{Pe} Along Perimeter Octa Model 90° Wind Angle

4.4.8 C_{Pe} Along Central Vertical Line on Faces

Variation of pressure coefficient along the central vertical line on the outer faces are shown in Figure 4.85, 4.87, 4.89 & 4.91 and those on inner faces are shown in Figure 4.86, 4.88, 4.90 & 4.92. As stated on para 4.2.8 the variation of pressure coefficient along the centre line on faces gives the idealized pattern of pressure coefficients throughout the height on faces. It also depicts fine picture of the change in flow pattern along the height of the faces. It is observed that in most cases where positive pressure exists on the face due to direct impingement of wind, the maximum value of C_{Pe} along the central vertical line is nearly equal to 1.0. Also, symmetrically opposite faces show mirror image of the C_{Pe} values along the line.

At 0° wind incidence angle face A is facing the wind orthogonally and the maximum positive C_{Pe} is slightly greater than 1.0. It occurs at 0.475 m height of the model. From there the value sharply becomes negative due to escaping of wind from the roof top. Rest all faces are showing negative values of C_{Pe} of almost equal magnitude. On the inner faces the centreline C_{Pe} values are following the same path until the height of 0.35 m from where they deviate drastically. On face A (Inner), which is on the lee side of wind suction C_{Pe} value further increases whereas on face B (Inner) which is fronting the wind suction C_{Pe} value reduces after the height of 0.45 m. On the side faces C (Inner) and D (Inner) the deviation is not much.

At 30° wind angle positive C_{Pe} value on face A and A1 is observed. On rest other faces they are negative. Except on face A2 and B2 suction on faces are showing almost similar value. On face A2 suction in the middle height is almost constant. On face B2 high fluctuations in the C_{Pe} values along the central vertical line observed. It indicates high turbulence on the face. On the inner faces pressure on the central vertical line are similar up to 0.40 m height. However, suction value increases on face A (Inner) and C (Inner) and reduces on face B (Inner) and D (Inner) from the height of 0.45 m.

At 60° wind angle pressure along the central vertical line on face A1 and C are showing positive values whereas, on rest all faces suction is observed along the line. On inner faces suction value along the line on faces are almost same throughout. But it is increased on face C (Inner) and decreased on face D (Inner) after 0.45 m height.

At 90° wind angle coefficient of pressure along central vertical line is positive. Along the line suction pressure is observed all other faces. Among them high suction is seen on face A and B. High fluctuation in the coefficient values along the central vertical height on inclined faces A1 and B2 are observed. C_{Pe} central vertical line on inner faces is almost same throughout. But it is increased on face C (Inner) and decreased on face D (Inner) after 0.45 m height.

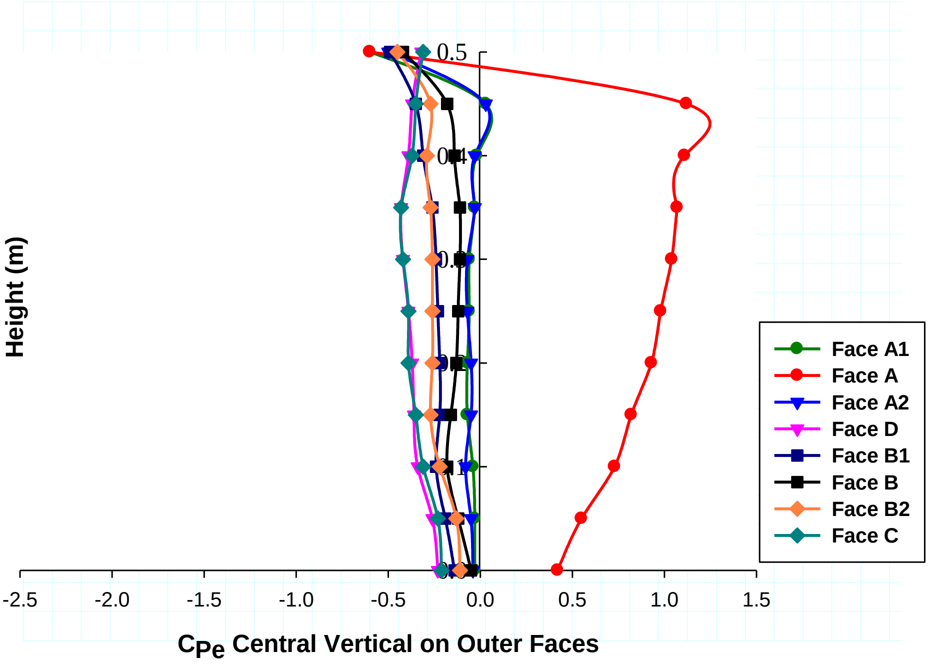

Figure 4. 85: C_{Pe} Along Central Vertical Line on Outer Faces Octa Model 0° Wind Angle

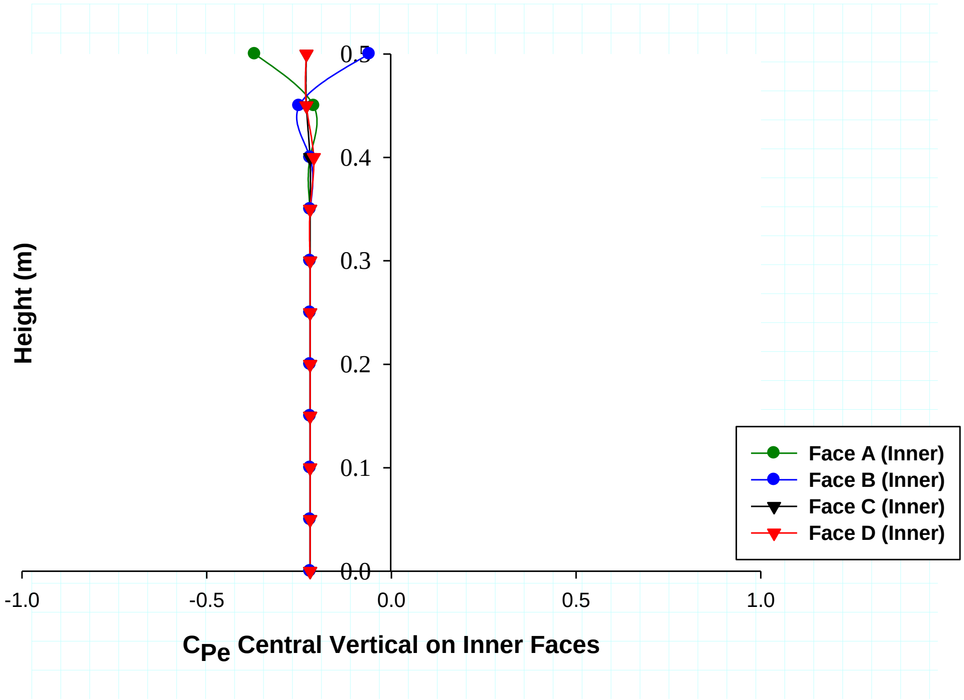

Figure 4. 86: C_{Pe} Along Central Vertical Line on Inner Faces Octa Model 0° Wind Angle

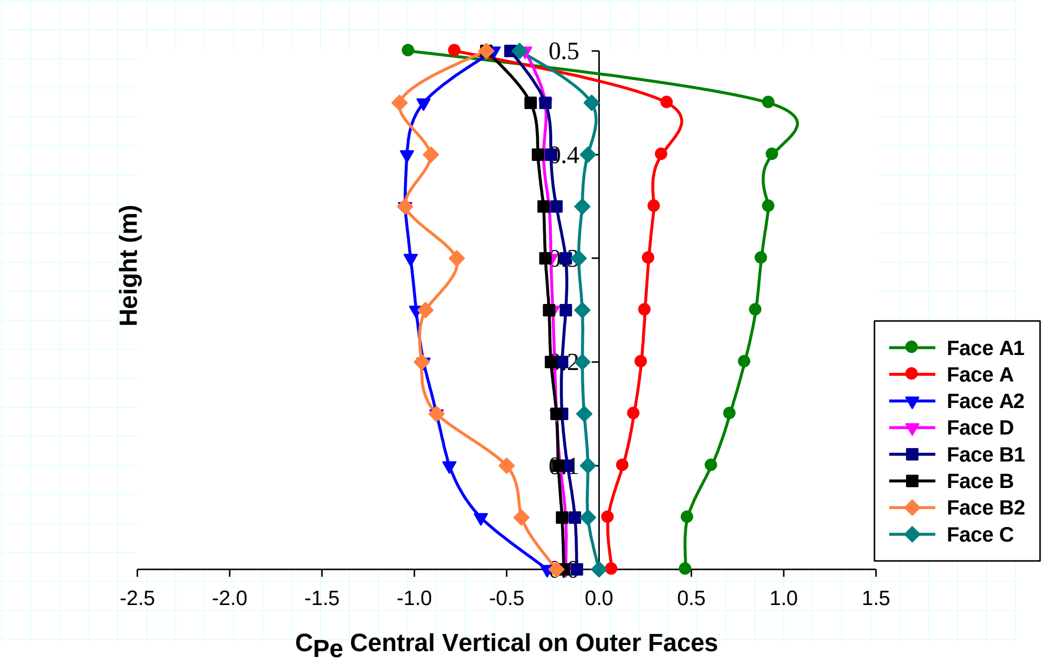

Figure 4. 87: C_{Pe} Along Central Vertical Line on Outer Faces Octa Model 30° Wind Angle

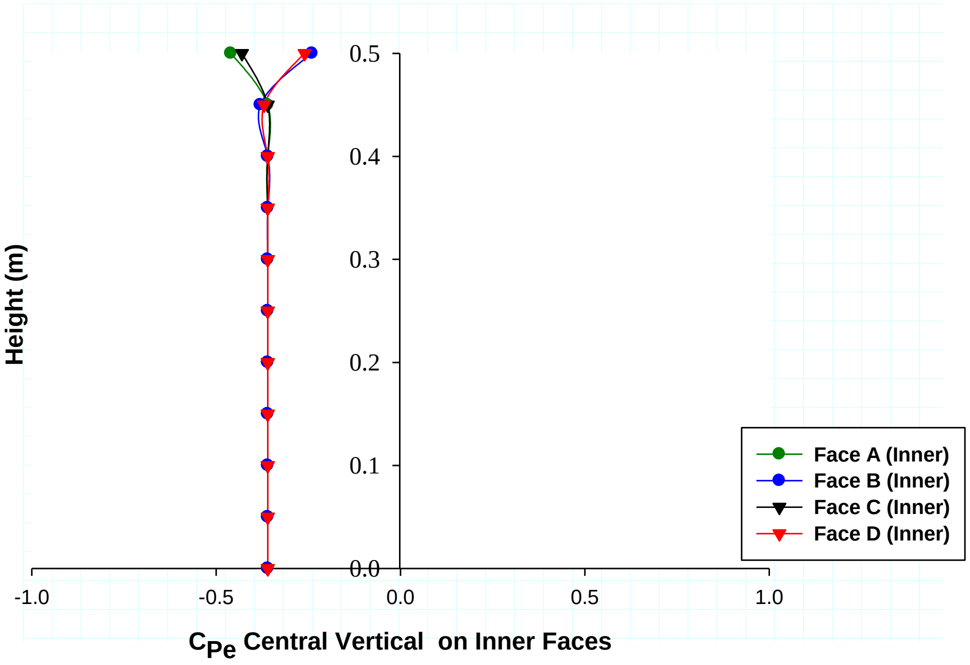

Figure 4. 88: C_{Pe} Along Central Vertical Line on Inner Faces Octa Model 30° Wind Angle

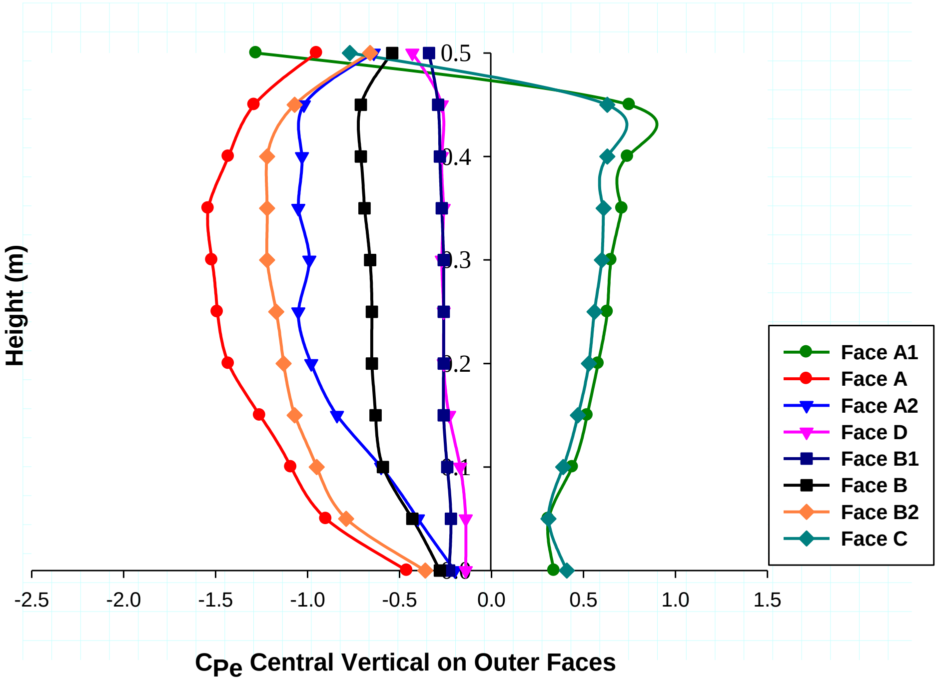

Figure 4. 89: C_{Pe} Along Central Vertical Line on Outer Faces Octa Model 60° Wind Angle

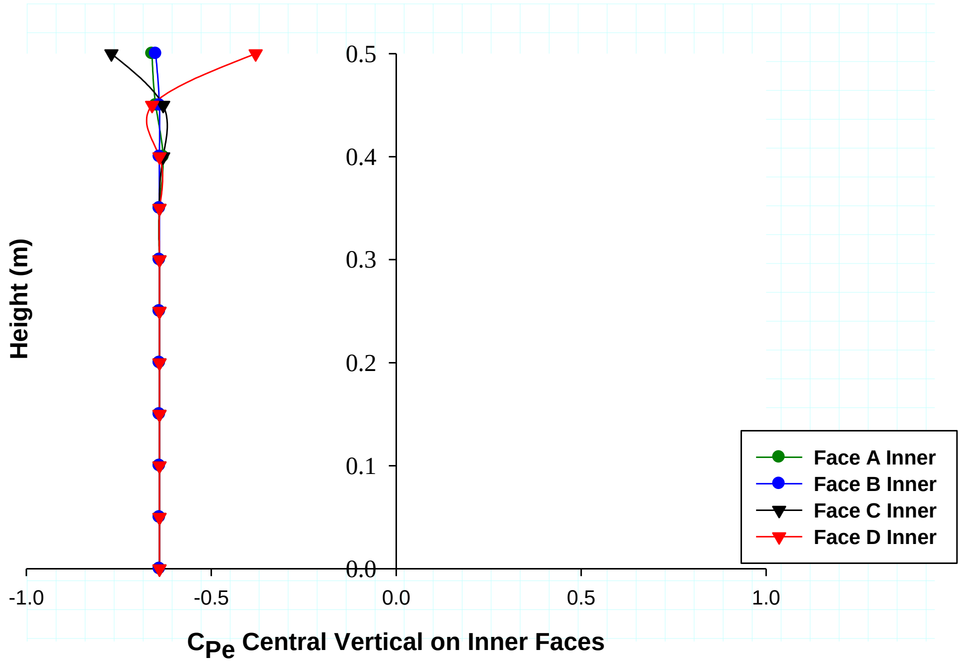

Figure 4. 90: C_{Pe} Along Central Vertical Line on Inner Faces Octa Model 60° Wind Angle

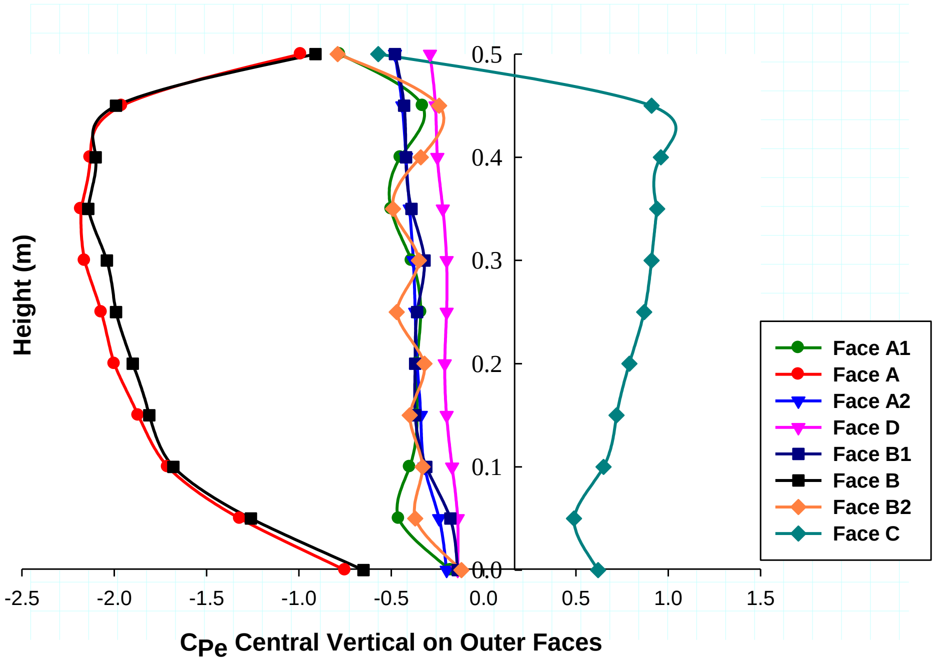

Figure 4. 91: C_{Pe} Along Central Vertical Line on Outer Faces Octa Model 90° Wind Angle

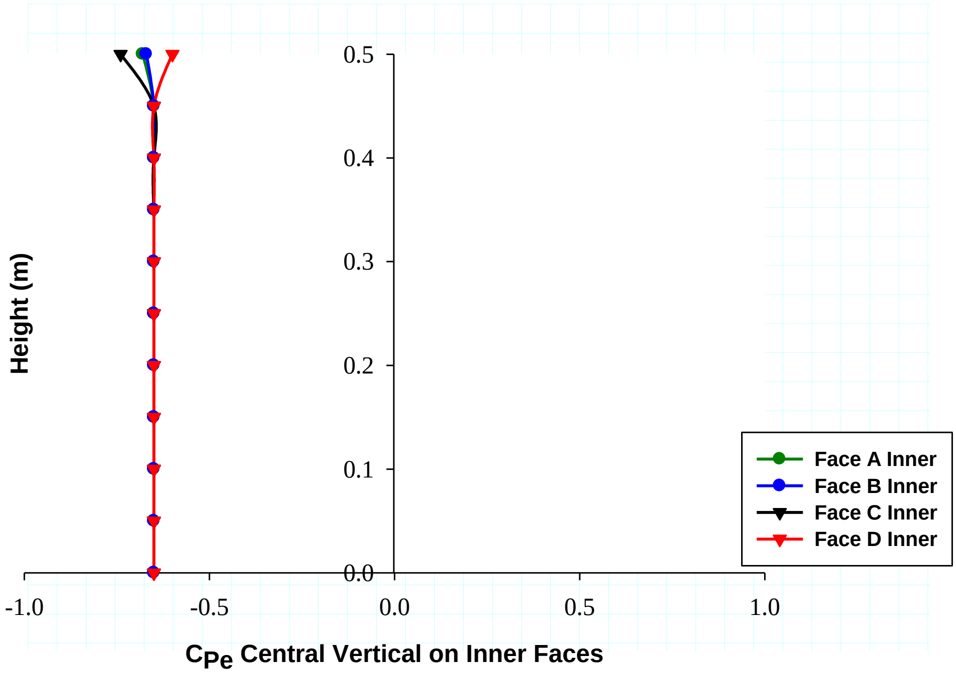

Figure 4. 92: C_{Pe} Along Central Vertical Line on Inner Faces Octa Model 90° Wind Angle

CHAPTER: 5 RESULTS AND DISCUSSIONS - II

5.1 GENERAL

In this chapter pressure distributions on the faces of the models and the wind flow characteristics are discussed for models symmetrical about one axis. Symmetry of the models have been reckoned with respect to the centroid of crops section in plan which are different from the global origin of construction of model geometry in these cases. For the models (L - shape, Diamond C- shape and Wrench C - shape models) wind angles of attack from 0° to 180° @ 15° has been studied during the simulation varied in the clockwise direction. The steps of wind angles from 0° to 180° @ 15° are sufficient to understand the influence of flow for 360° wind angle of attacks. However, due to lack of space discussion has been made at 30° interval of change of wind angle.

5.2 L - SHAPE MODEL

L plan shaped model is symmetrical about one axis in plan. Illustration of flow pattern around the model for better understanding in terms of flow separation, reattachment of flow, creation of wakes and vortices etc. have been discussed. The surface pressure generated around the model has been studied and discussed in terms of coefficient of pressure on the faces with emphasis on the re-entrant corner faces as unusual/critical coefficient of pressure on these faces have been observed. The pressure on these re-entrant wing faces have been found critical between 75° & 180° wind incident angles.

5.2.1 C_{Pe} Contour 0° Wind Angle

At 0° wind angle wind flows around the model very similar to that of the rectangular model in the windward region. But the flow pattern is totally different in the leeward region. Unsymmetrical vortices (Figure 5.8) are formed behind the model with a secondary vortex in the L cavity behind face B2 and C1, unlike in the rectangular model in which two similar vortices are formed behind the model.

The upwind face A is subjected to similar pressure pattern as found in the rectangular model on the windward face. The remaining faces are under flow separation or wake.

On the lee side on face B1 the backwash is concentrated in the middle and towards re-entrant corner. Suction is increasing towards upper and lower side both. However, on the upper side suction is more comparative to lower side. On the confluence of face B1 and side face D again suction is more comparative to overall face B1.

On face B2 the backwash is more towards its free end and decreasing towards both the edges. It is observed that, the maximum and minimum C_{Pe} on both the faces B2 and C1 are similar due to interference effect between the two. The pressure contours are inclined from the re-entrant corner and becoming vertical towards the other ends.

On side face C2 the pattern of pressure contour is almost vertical with more suction towards the near end. Concentration of eddies at the near end edge are also observed indicating high turbulence.

On face D, pressure pattern is vertical. Suction is increasing from the leeward side to windward side. Concentration of high eddies are also observed towards the near end edge.

On roof top the area average coefficient of pressure is negative with nearly orthogonal contour lines with respect to wind direction. High concentration of suction towards the windward side is observed indicating high turbulence and formation small vortices at the place.

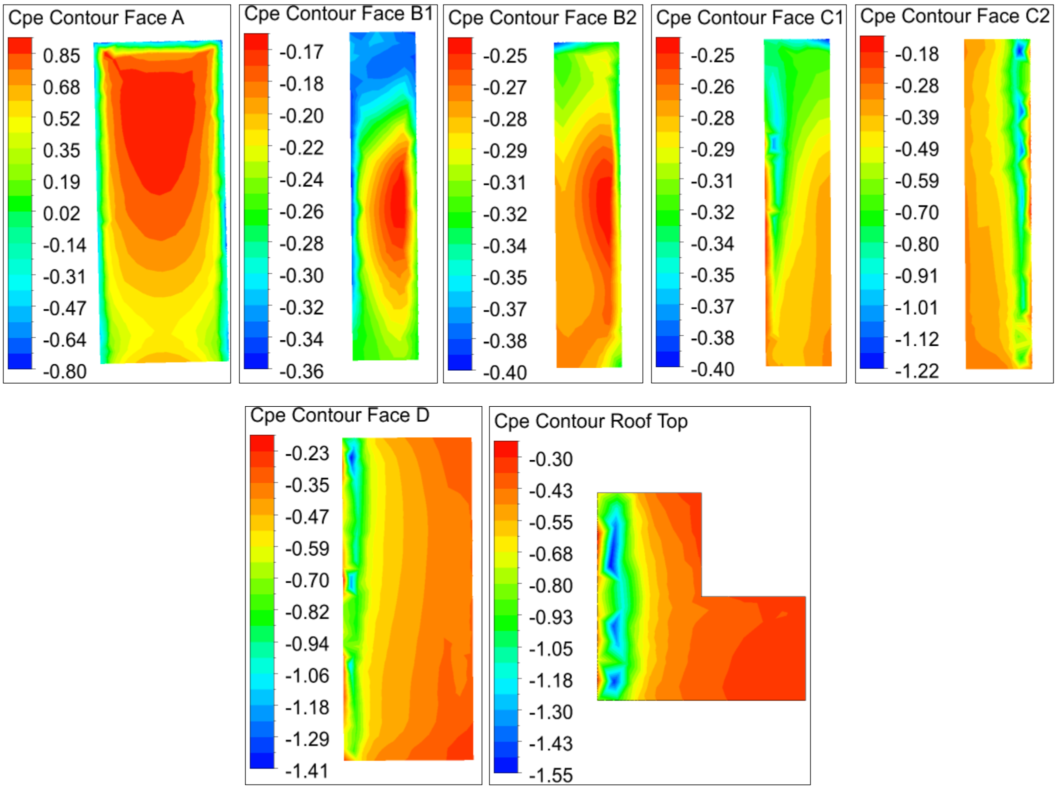

Figure 5. 1: C_{Pe} Contour on Faces & Roof L-Shape Model 0° Wind Angle

Table 5. 1: Area Average C_{Pe} on Faces L-Shape Model

AoA	0°	30°	60°	90°	120°	150°	180°
Face A	0.58	0.49	0.12	-0.42	-0.33	-0.31	-0.27
Face B1	-0.25	-0.29	-0.36	-0.46	-0.37	0.36	0.58
Face B2	-0.28	-0.40	-0.48	0.37	0.70	0.65	0.46
Face C1	-0.30	-0.33	-0.28	0.45	0.65	0.70	0.39
Face C2	-0.49	-0.22	0.45	0.60	0.37	-0.36	-0.45
Face D	-0.48	-0.37	-0.31	-0.27	-0.32	-0.34	-0.49
Roof Top	-0.57	-0.67	-0.54	-0.48	-0.73	-0.72	-0.45

5.2.2 C_{Pe} Contour 30° Wind Angle

In this case wind is still impinging on inclined face A, not orthogonally but obliquely towards the confluence of face A and C2. Separation is taking place from face C2 and far end of face A. As such, face A is experiencing positive pressure, half parabolic in nature concentrated towards the confluence of face A and C2. Negative pressure exists towards the other edge of face A from where separation is taking place.

Face D is under wake and is experiencing negative pressure throughout. At the bottom suction created due to backwash is increasing along height in most part of the face. Towards the near end of face D from where wind is separating, pressure contours are vertical in nature with high suction above the upper part of the face due to sidewash mixed with the effect of backwash from the wake. Towards the bottom portion of face D, which is fully submerged into wake, isobars of triangular nature with a circular isobar at the bottom are observed. The roundness is flattening and becoming almost horizontal after mid height of the face as expected to be on the face under backwash.

Faces B1, B2 and C1 are also under wake. Backwash is hitting face B1 obliquely (Figure 5.11). Overall pressure on face B1 is suction varying from bottom to top. At Top it is higher. High concentration of negative pressure is seen at the top corner towards the confluence of face B1C1. Flow is highly complex in nature within the re-entrant corner.

On face B2 flow is surfing along the face horizontally through face C1 and the re-entrant corner. The pattern of pressure isobars is changing from oblique to vertical from the re-entrant corner to the open end. Concentration of high suction is observed on the top outer corner of the face.

On face C1 almost similar pressure distribution exists on most part of the face. On most part of face C2 effect of sidewash exists. Towards the upwind side positive pressure of vertical isobars exists which is decreasing with high gradient to negative pressure towards the downwind side.

On rooftop overall entire area is under suction with a concentration of strip of negative pressure above face A. This strip is crucial for placement of roof structures.

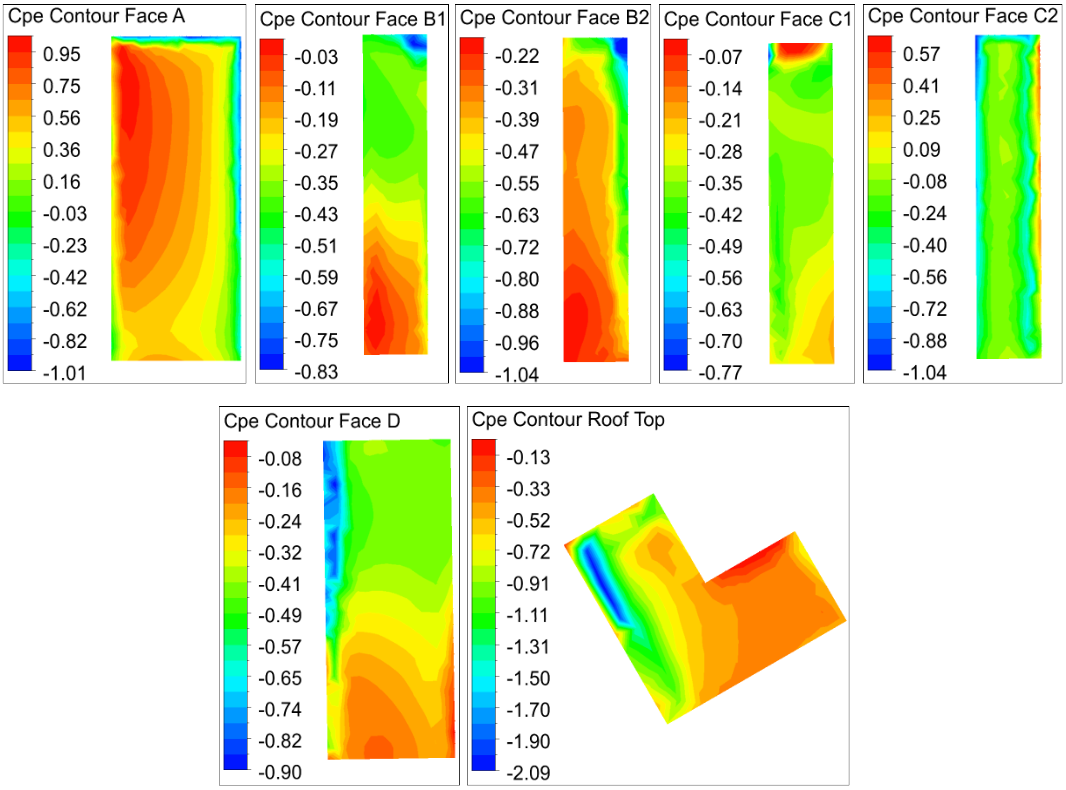

Figure 5. 2: C_{Pe} Contour on Faces & Roof L-Shape Model 30° Wind Angle

5.2.3 C_{Pe} Contour 60° Wind Angle

For this wind angle of attack wind is striking on face C2 obliquely and surfing on face A. Both the faces are having positive pressure. Area average C_{Pe} on the face A and C2 are 0.12 and 0.45 respectively. On face A high gradient of coefficient of pressure between 0.78 to -0.93 exists with vertical isobars. Positive pressure is towards the near end edge and suction is towards the far end edge.

On Face C2 positive pressure in formation of half parabolic isobars unsymmetric from the edges, concentrated towards the meeting edge with face A exists. From another edge of face C2 wind is separating with high velocity (Figure 5.14) and hence, suction is seen there.

On face C1 suction of high potential is seen at the re-entrant corner due to formation of shear layer as wind tends to sweep face B2 from the re-entrant corner towards its outer edge. As such, face B2 is also having negative pressure on its face with vertical isobars. Suction gradient on face B2 is increasing from the re-entrant corner towards the outer edge. Area average C_{Pe} on face B2 and C1 is -0.48 and -0.28 respectively.

Face B1 and D are under wake. Effect of sidewash is prominent on the upper portion of the faces. Suction is increasing from bottom to top unlike the case in the rectangular model in which the face under wake is having almost similar negative pressure. On face D at the meeting edge with face A high suction vertical isobars is observed in upper half of the face supposed to be due to separation of wind.

On roof top the pressure is negative throughout with a small negligible value of positive coefficient of pressure at the corner of confluence of face AC2. Eddies with negative coefficient of pressure = -1.94 is formed above face C2.

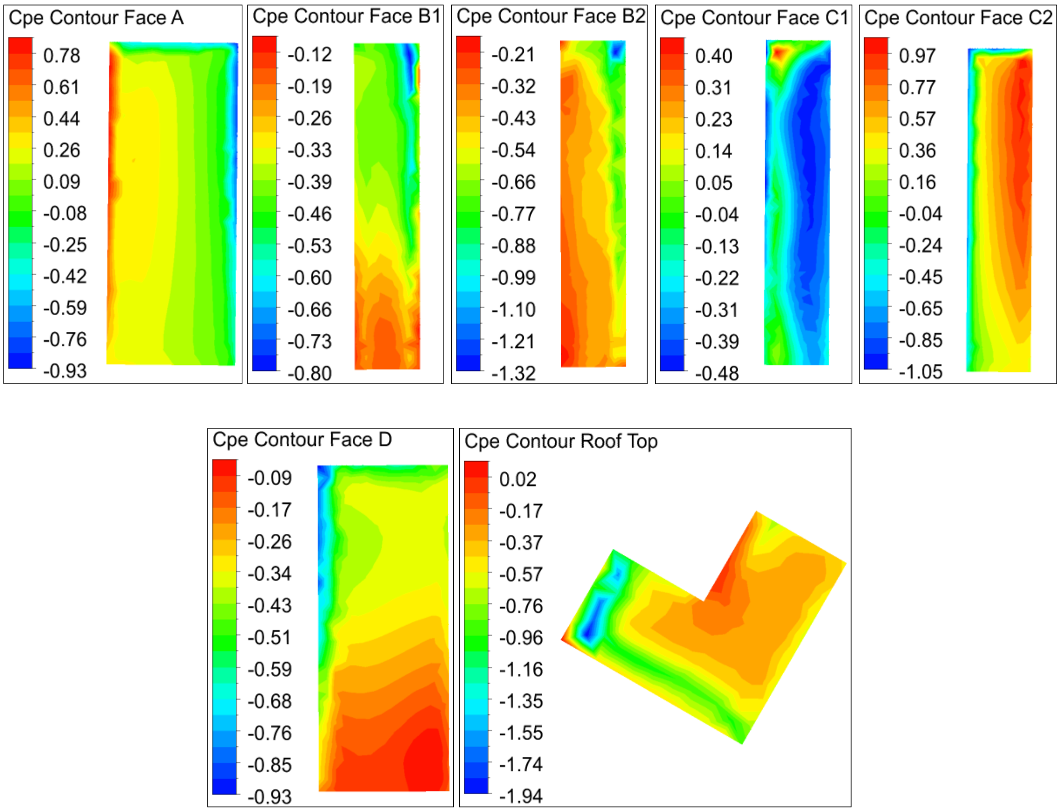

Figure 5. 3: C_{Pe} Contour on Faces & Roof L-Shape Model 60° Wind Angle

5.2.4 C_{Pe} Contour 90° Wind Angle

At 90° wind angle separation of flow is taking place before face C2. Wind is striking on Face C2 and a portion of face C1 on its outer side i.e., towards the confluence of face B1C1. Area average positive coefficient of pressure 0.45 and 0.60 exist on faces C1 and C2 respectively. Isobars on face C2 it is almost parabolic but not symmetrical from the edges. The concentration of pressure is shifted towards the re-entrant corner. At another edge flow separation is taking place giving negative pressure at the edge.

On face C1 positive pressure distribution is elliptical with its major axis along vertical direction concentrated towards the meeting edge B1C1. Separation of wind is also taking place from this edge and hence suction exists.

Face B2 is also subjected to positive pressure, despite being side face, due to stagnation of flow on face C1 and reflection of flow from there to face B2.

Side faces A and B1 are experiencing suction due to sidewash. The pattern of contours on the faces are vertical with greater suction at the near end edge of the faces. Gradually suction is reducing with a semi triangular formation at the bottom due to effect of back wash from the wake.

Face D is the lee side and completely submerged into wake. Pressure isobars are horizontal and face area average of C_{Pe} on the face is -0.27.

On roof top overall area average C_{Pe} is -0.48. The isobars are almost in the form of mirror image of L shape. High concentration of suction exists above the windward face C1 & C2.

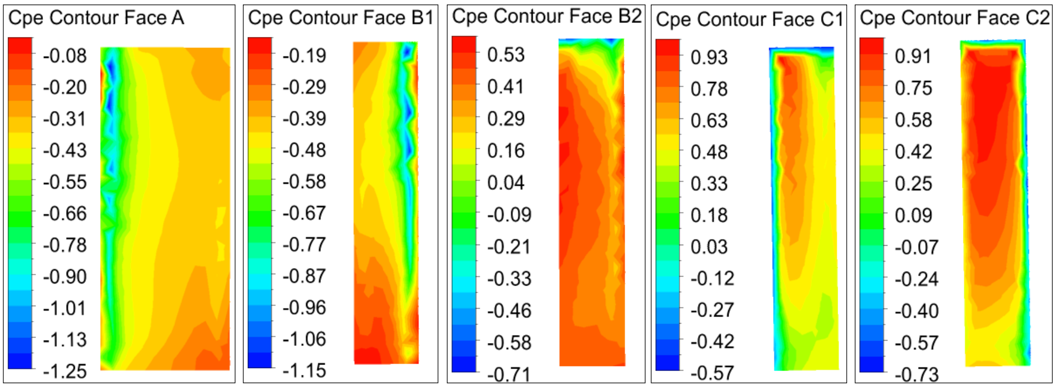
Cpe Contour Face A

Cpe Contour Face B1

Cpe Contour Face B2

Cpe Contour Face C1

Cpe Contour Face C2

Figure 5. 4: C_{Pe} Contour on Faces & Roof L-Shape Model 90° Wind Angle (Contd.)

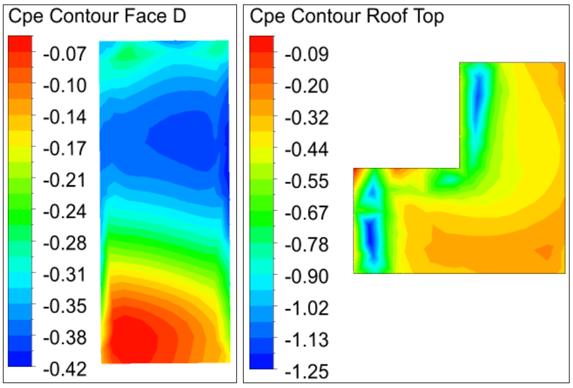

Figure 5. 4: C_{Pe} Contour on Faces & Roof L-Shape Model 90° Wind Angle

5.2.5 C_{Pe} Contour 120° Wind Angle

At this wind angle of attack flow is striking into the re-entrant corner (Figure 5.20). Flow is contouring from the re-entrant wing face B2 to wing face C1. Stagnation of air is causing positive pressure of almost similar values on face B2 and C1. Also, the pattern of pressure contours is similar on the faces.

The pressure pattern on face C2 is half parabolic concentrated towards the re-entrant corner. Negative pressure at the far end of face C2 exists from where flow separation is taking place.

Face A and D, both are under wake and experiencing almost similar suction on the faces. The area average C_{Pe} on the faces are -0.33 & -0.32 respectively. Moreover, towards the near end of face A high suction exists on the upper half of the model which does not exists on face D. Only a spot of high concentration of suction at the top corner towards the near end of face D is seen.

Face B1, being the side face, is experiencing negative pressure of vertical isobars. Concentration of high turbulent eddies exists near the edge from where wind separation is taking place.

On roof top pressure is overall negative with area average of suction coefficient (C_{Pe} = -0.73) which is highest for all wind angles. Formation of high negative suction in the localized spot above the confluence of face B1C1 and that of fae B2C2 is observed.

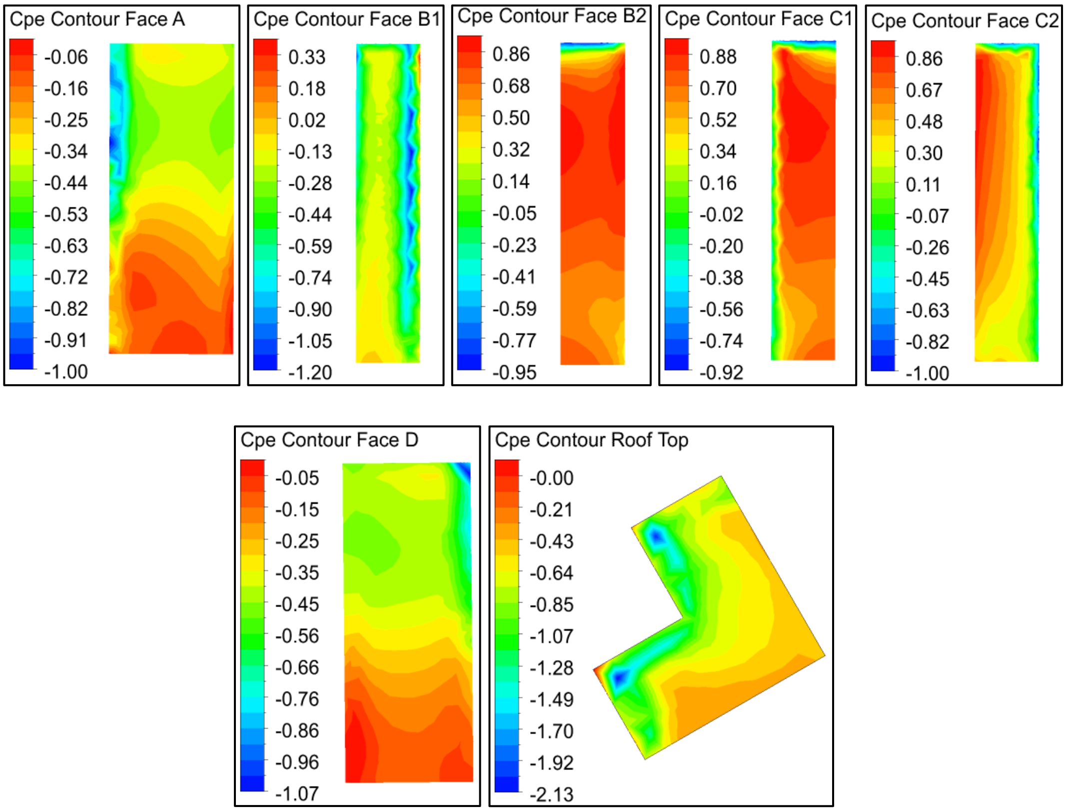

Figure 5. 5: C_{Pe} Contour on Faces & Roof L-Shape Model 120° Wind Angle

5.2.6 C_{Pe} Contour 150° Wind Angle

At wind incident angle of 150° face B1, B2 and C1 are subjected to positive pressure. The area average C_{Pe} on the faces are 0.36, 0.65 and 0.70 respectively. As we see (Figure 5.23), flow is separating before the meeting edge of face B1 and C1 and impinging on the faces. On face B1 the pressure pattern is half parabolic and shifted towards the re-entrant corner. Flow separation is taking place from the far end of face B1, as such suction exists at the edge.

Positive pressure exists on face B2 which is higher than that on face B1. Flow after striking face C1 is contouring along the face horizontally towards face B2. In most part of face B2 positive pressure of almost similar nature exists except near the outer edge from where flow is separating with high velocity causing suction pressure.

Face C1 is also subjected to positive pressure due to direct impact of flow on it. The pressure isobars are almost horizontal. In fact, the flow impinging almost parallel on face C1 is becoming stagnant further in the direction of flow is flowing around the re-entrant corner towards face B2 (Figure 5.23).

Face A and D are under the influence of backwash and hence experiencing suction. Localized suction pressure isobars, vertical in nature, are observed at some part on face A. Similarly on face D at upper height high suction towards the windward side is seen.

On face C2, though area average C_{Pe} is -0.36, high gradient of suction pressure exists. Towards the windward side of face C2 sawtooth formation of high suction along the height is seen suggesting formation of eddies there.

On roof top the pattern of contour formation is upside down L-shape. A spot of high concentration area average of coefficient of pressure (C_{Pe} = -2.11) is observed above the confluence of face B1 and C1.

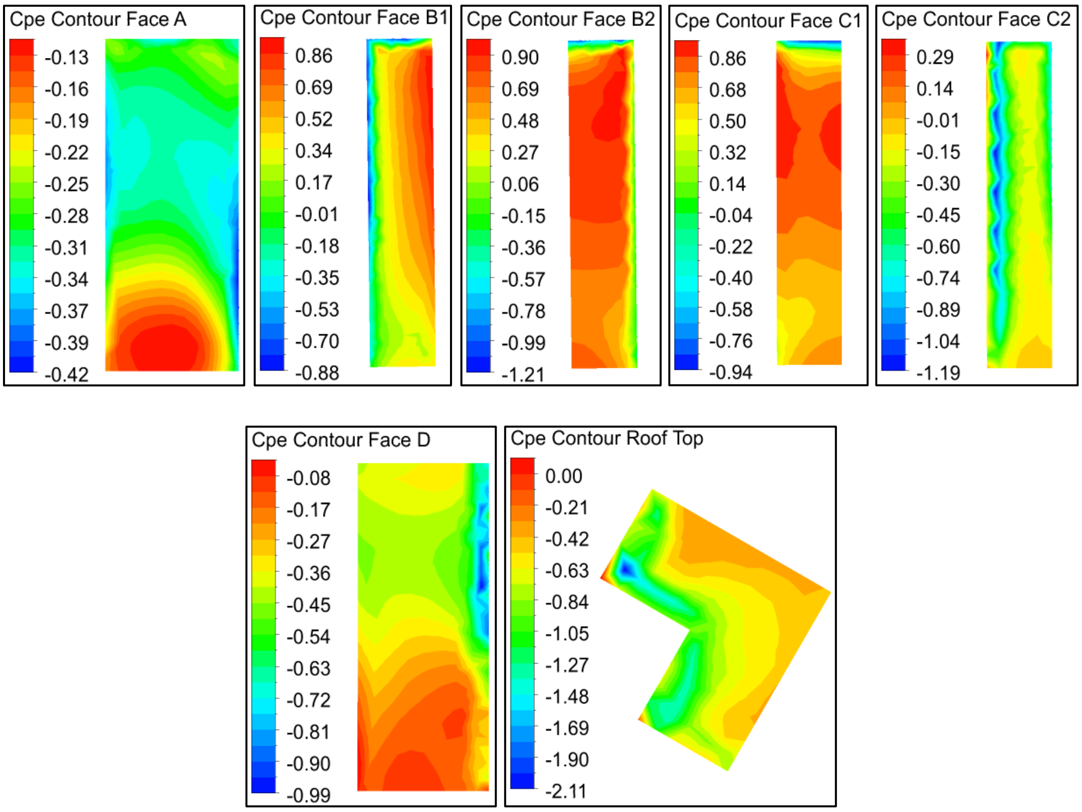

Figure 5. 6: C_{Pe} Contour on Faces & Roof L-Shape Model 150° Wind Angle

5.2.7 C_{Pe} Contour 180° Wind Angle

Figure 5.7 shows the pressure contours of L shaped model at 180° wind angle of attack. It is observed that face B1 is subjected to positive pressure with an area average C_{Pe} = 0.58. But, the distribution of pressure coefficient is not symmetrical about the vertical centre line as in the case of rectangular model. Towards the meeting edge of face B1 and D suction exists from where wind separation is taking place (Figure 5.26). The pressure contours, almost parabolic, is shifted towards the re-entrant corner.

Inner wing faces B2 and C1 of the re-entrant corner are also subjected to positive pressure with area average C_{Pe} = 0.46 and 0.39 respectively. On face B2 concentration of positive pressure is towards the free edge from where wind separation is taking place producing negative pressure at the edge. Face C1, yet being a side face, is subjected to positive pressure due to stagnation of flow within the re-entrant corner and reflection of flow from face B2. Suction pressure at the roof is seen on face C1.

Side faces C2 and D are subjected to negative pressure due to sidewash. The area average C_{Pe} on the faces are -0.45 and -0.49 respectively. Suction on the faces is decreasing from the upwind side to lee side. Towards the windward side the pattern of contour on fae C2 and D are vertical. However, towards the lee side they are a bit inclined at the top and bottom portion of the faces.

At the roof top pattern of suction pressure is in an upside-down L shape with overall negative area average of C_{Pe} = -0.45, least for all wind angles. High concentration of suction is seen above the windward face due to creation of roof recirculation cavity at that place.

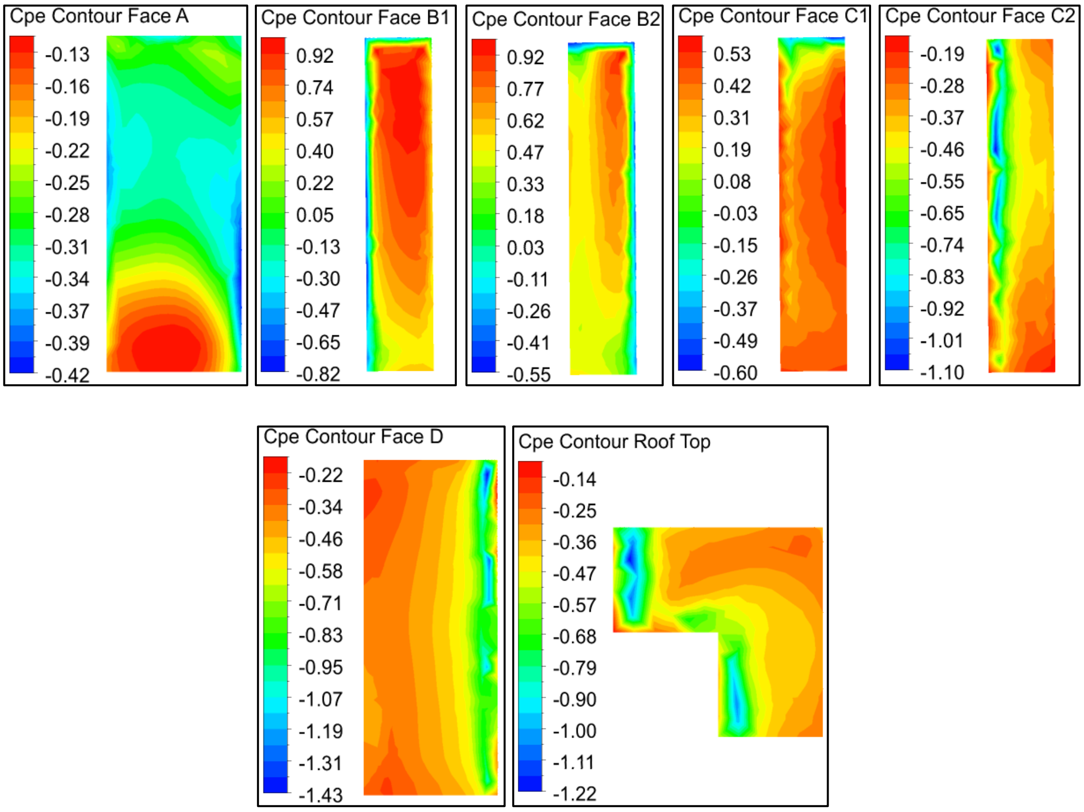

Figure 5. 7: C_{Pe} Contour on Faces & Roof L-Shape Model 180° Wind Angle

5.2.8 Wind Flow Pattern

Streamlines of wind flow patterns for all the discussed wind angles from 0° to 180° @ 30° have been shown in Figure 5.8, 5.11, 5.14 & 5.17, 5.20, 5.23 & 5.26 at different heights of the model viz Z = 0.165 m, Z = 0.250 m and Z = 0.335 m and Figure 5.9, 5.12, 5.15, 5.18, 5.21, 5.24 & 5.27 show the velocity contours at the same heights for different wind incidence angles. Velocity vector diagrams at different heights for varied wind angles are shown in Figure 5.10, 5.13, 5.16, 5.19, 5.22, 5.25 & 5.28.

The importance of these picture in understanding the effect of wind flow in pressure distribution around model envelope and their characteristics has already been discussed in para 4.1 and 4.2.5.

Flow separation and vortices can be seen from the flow patterns. Small vortex is created within the re-entrant corner for different wind angles other than where wind is directly hitting the corner. Flow patterns are different in intensity and strength for different wind angles and for different levels of height. It is observed that the size of wake formed behind the model is decreasing as we move along height for all wind angles. It can be observed also that the distance between the streamlines is not constant. Where spacing between the streamlines moves apart, flow is expected to slows down. Before striking the model, the streamlines are moving apart which indicates reduction in velocity of the flow. At 60° wind angle of attack this separation before the wind strikes the model is very little.

It can be visualized that the size of the vortices formed behind the model is relatively large compared to other models discussed earlier. It is due to the shape of the model and the projected width of obstruction perpendicular to wind flow.

At 0° wind incidence angle two vortices behind the model, slightly dissimilar, are developed. A secondary small vortex within the re-entrant corner is also seen. Towards the windward side the flow separation is taking place before the flow strikes the model at Z = 165 mm height and the spacing between the streamlines are wider compared to those at upper heights i.e., Z = 250 mm and Z = 335 mm. Spacing between the streamlines are getting closer along the height as the wind speed is increasing along height. The magnitude of velocity shown by the length of arrow in the velocity diagram also validates this finding.

At 30° and 60° wind angle vortex within the re-entrant corner becomes larger and clearer compared to that at 0° wind angle. Vortices in the wake region are almost similar in intensity but size is reducing along height. At 90° two dissimilar vortices reducing in size appear behind the model along with one secondary small vortex within the re-entrant corner.

At 120° and 150° wind angle no re-entrant corner secondary vortex is created. However, behind the model two vortices of almost equal size reducing along height are seen. At 180° wind incidence angle the small vortex within the re-entrant corner is again found to be developed with two dissimilar vortices in the wake. The flow movement in magnitude and direction can be clearly visualized in velocity vector diagram.

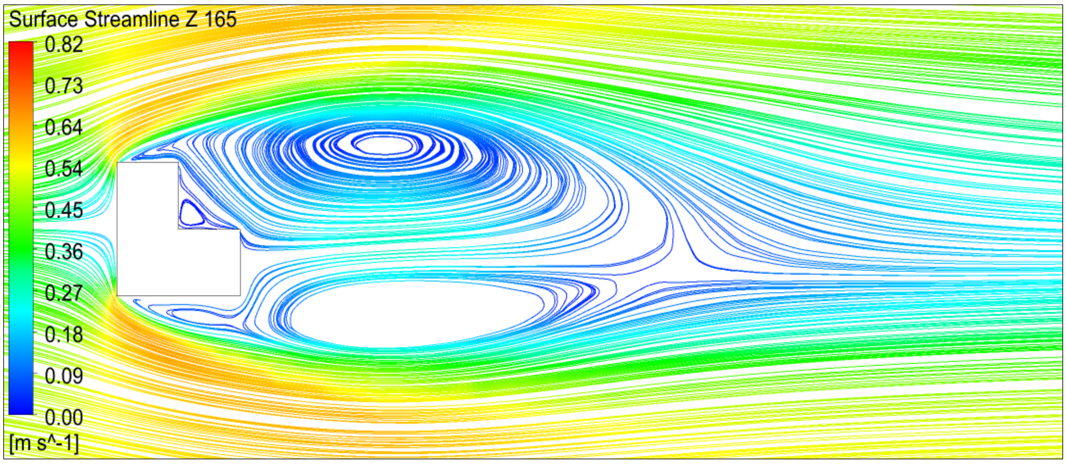

(a) Surface Streamline at Height Z = 165 mm

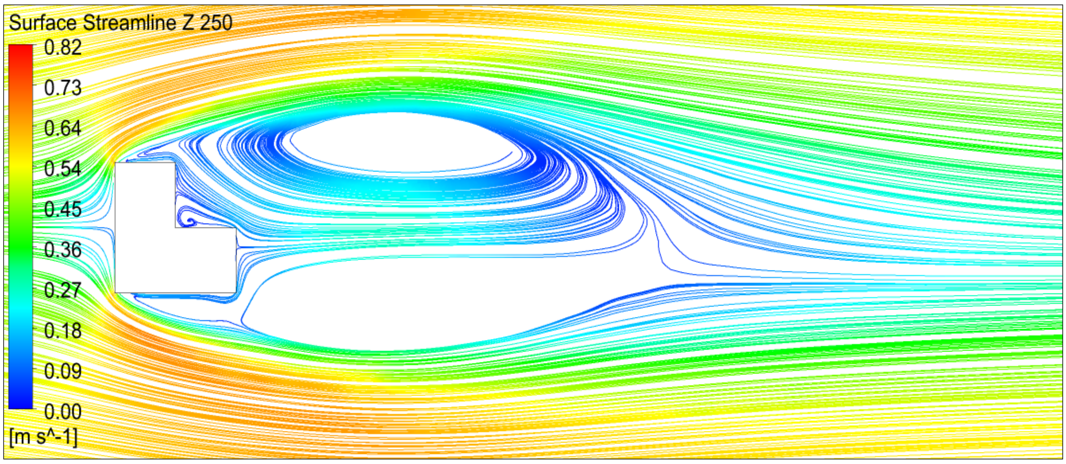

(b) Surface Streamline at Height Z = 250 mm

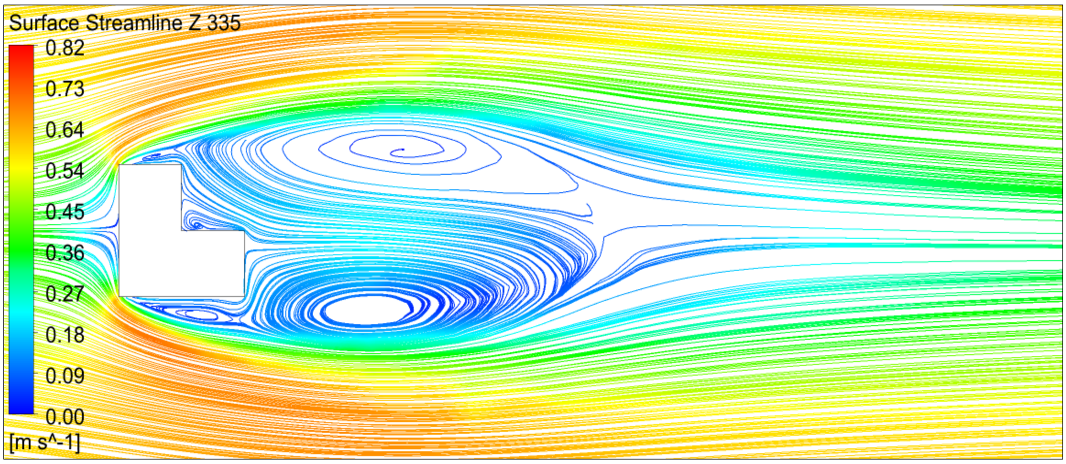

(c) Surface Streamline at Height Z = 335 mm

Figure 5. 8: Surface Streamline L-Shape Model 0° Wind Angle

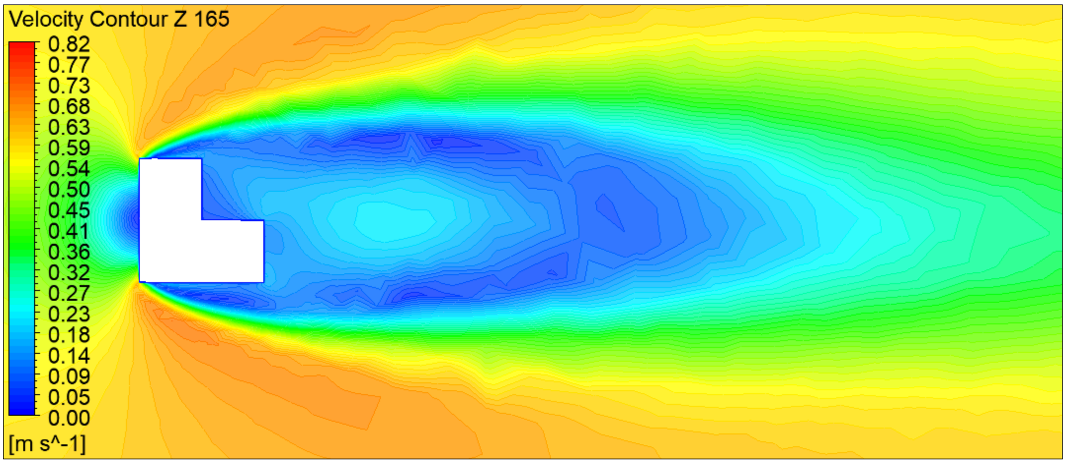

(a) Velocity Contour at Height Z = 165 mm

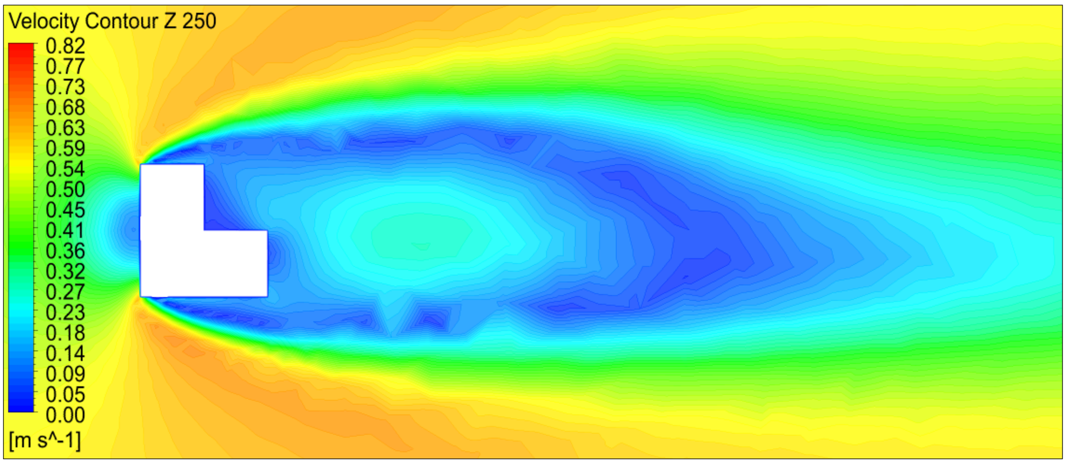

(b) Velocity Contour at Height Z = 250 mm

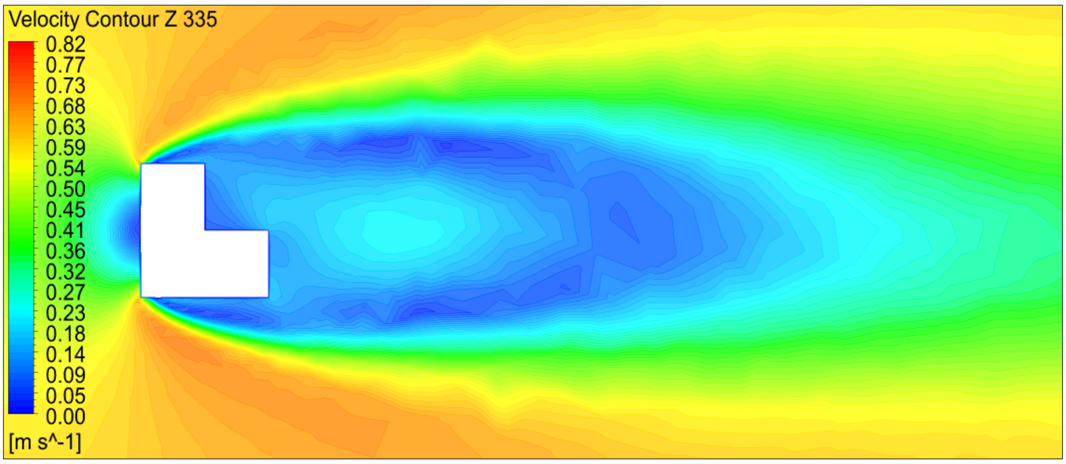

(c) Velocity Contour at Height Z = 335 mm

Figure 5. 9: Velocity Contour L-Shape Model 0° Wind Angle

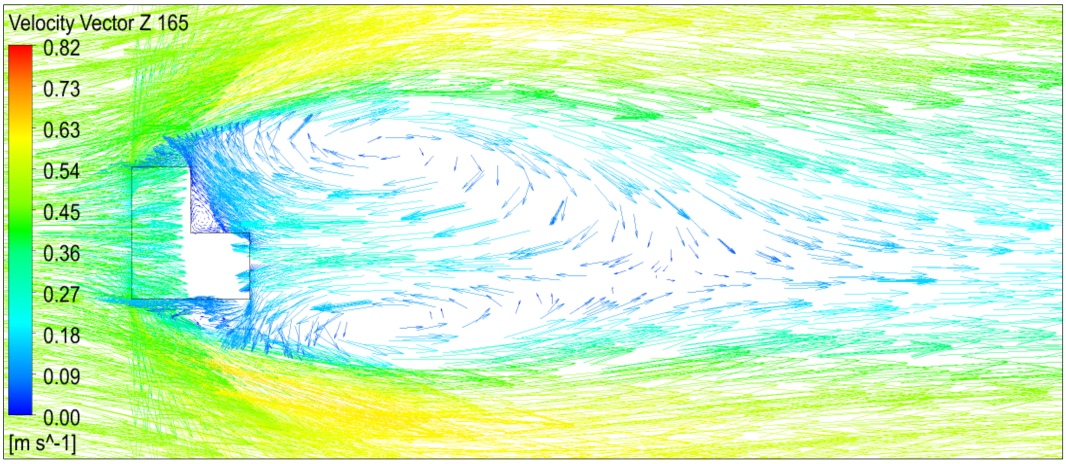

(a) Velocity Vector at Height Z = 165 mm

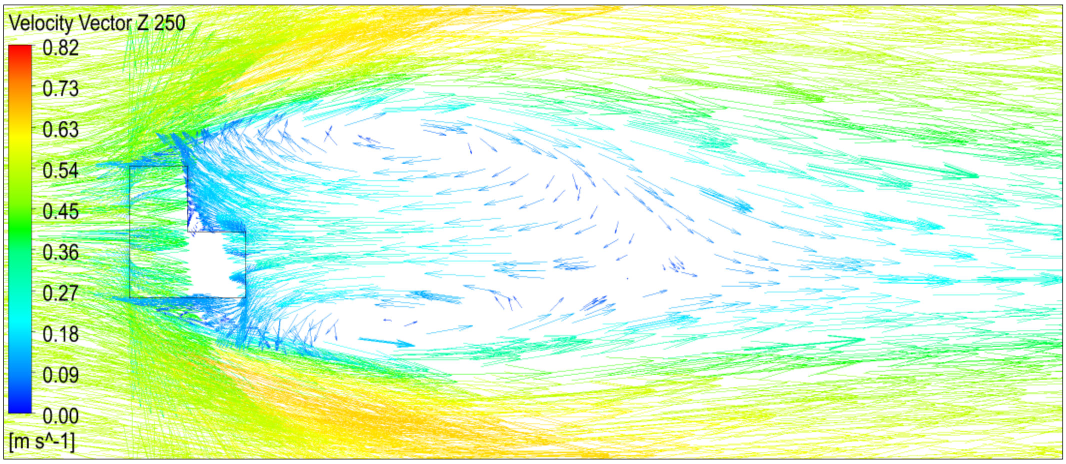

(b) Velocity Vector at Height Z = 250 mm

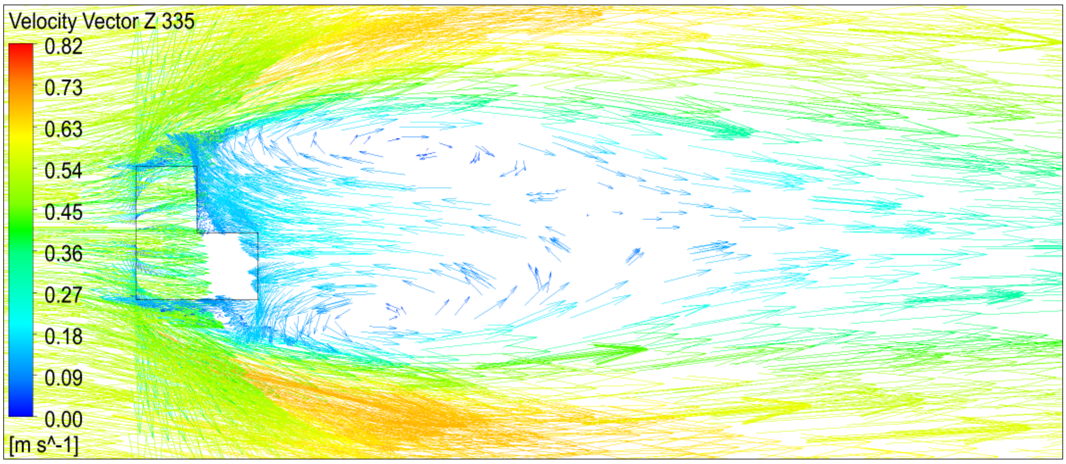

(c) Velocity Vector at Height Z = 335 mm

Figure 5. 10: Velocity Vector L-Shape Model 0° Wind Angle

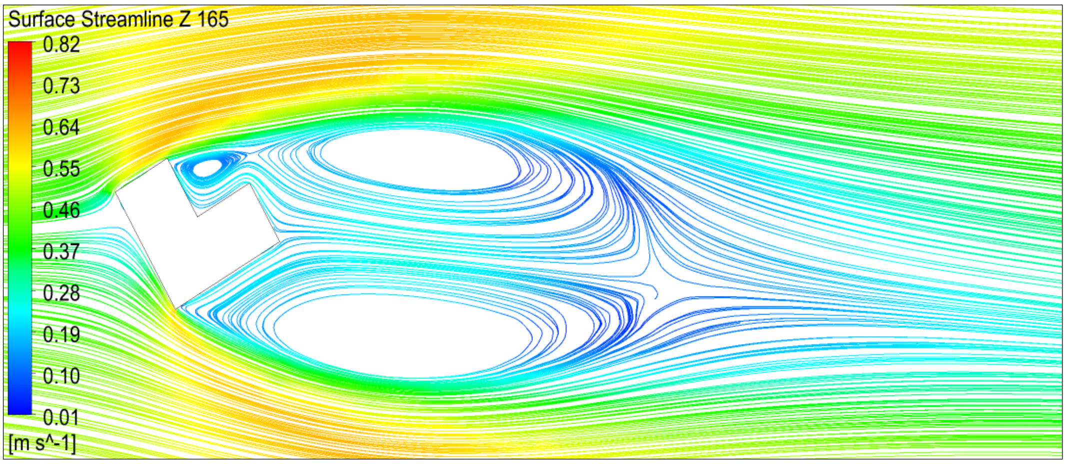

(a) Surface Streamline at Height Z = 165 mm

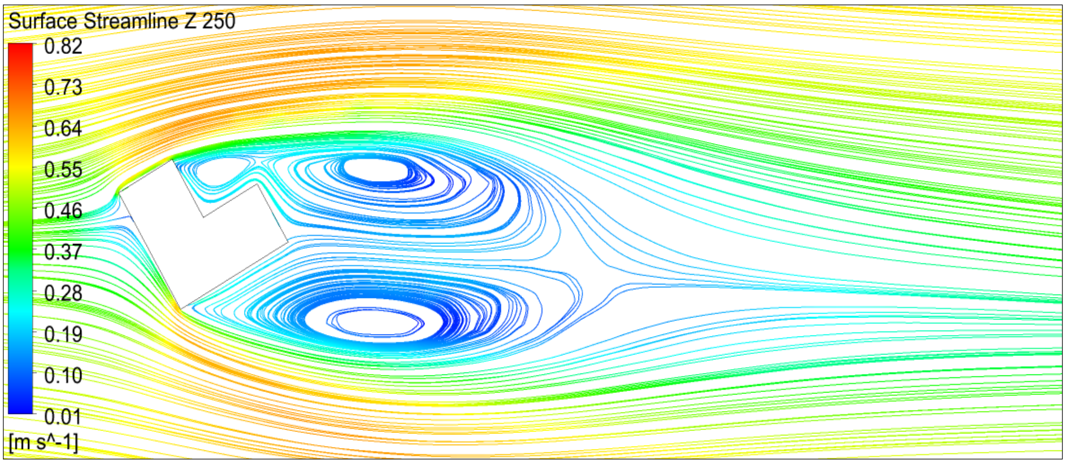

(b) Surface Streamline at Height Z = 250 mm

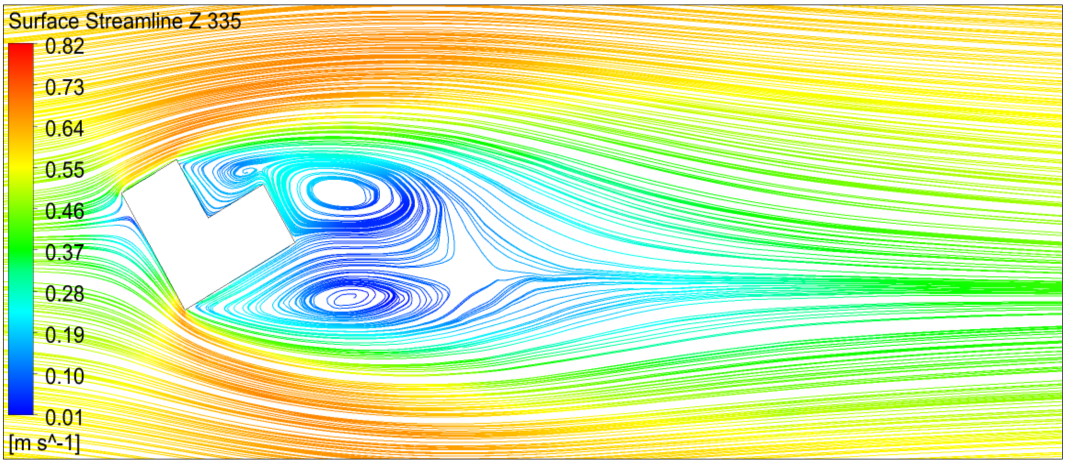

(c) Surface Streamline at Height Z = 335 mm

Figure 5. 11: Surface Streamline L-Shape Model 30° Wind Angle

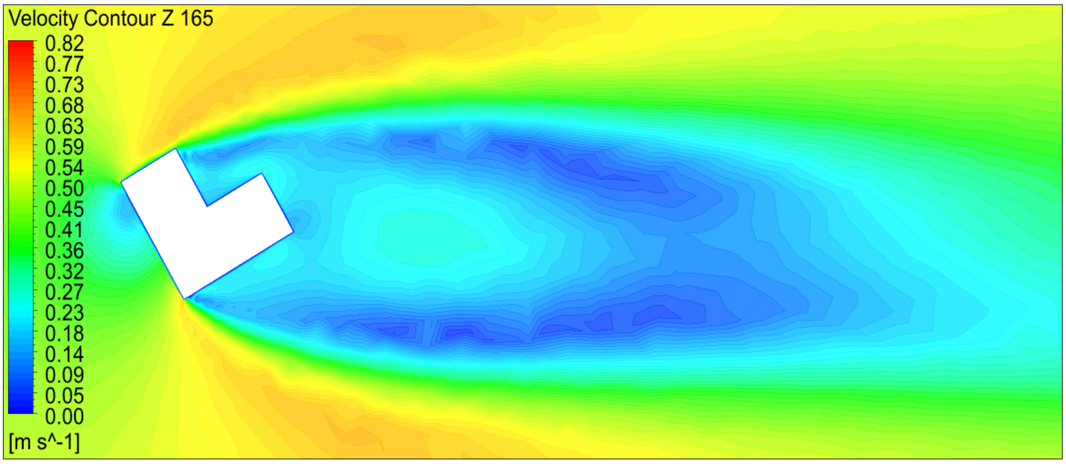

(a) Velocity Contour at Height Z = 165 mm

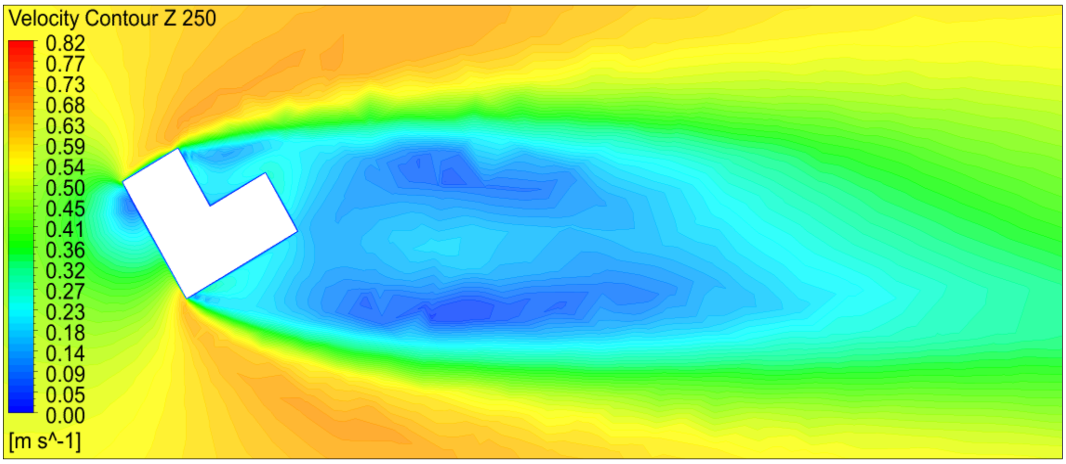

(b) Velocity Contour at Height Z = 250 mm

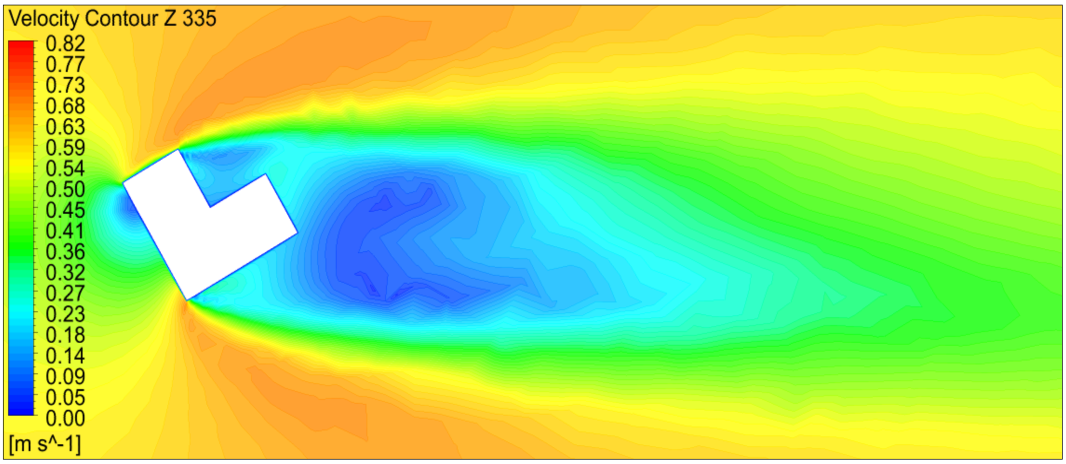

(c) Velocity Contour at Height Z = 335 mm

Figure 5. 12: Velocity Contour L-Shape Model 30° Wind Angle

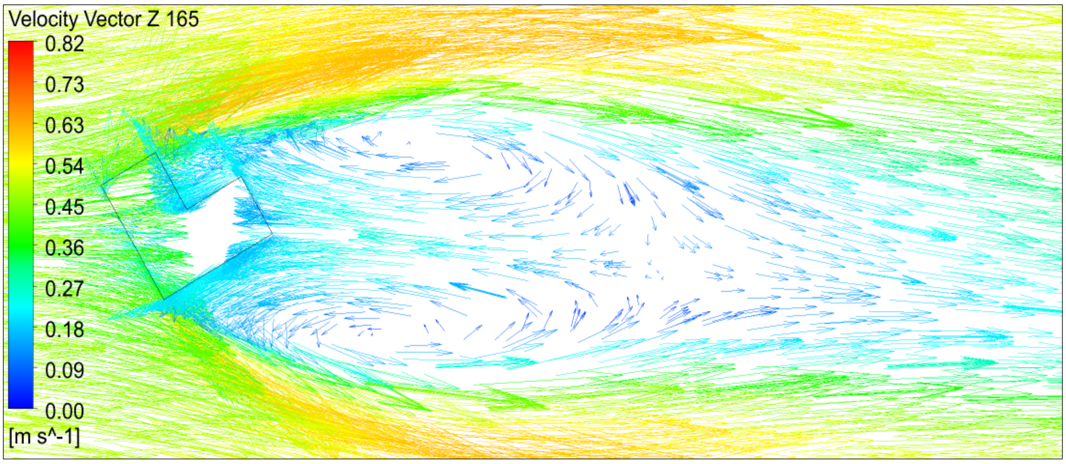

(a) Velocity Vector at Height Z = 165 mm

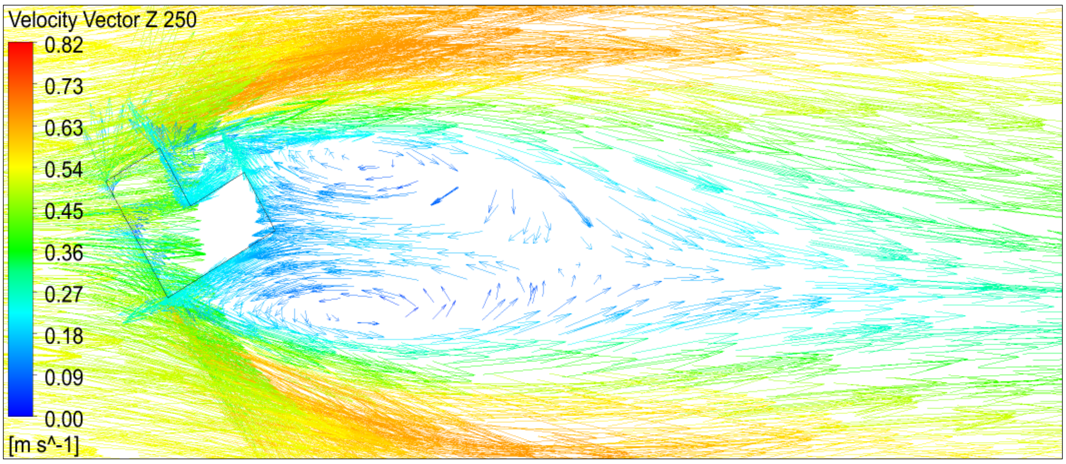

(b) Velocity Vector at Height Z = 250 mm

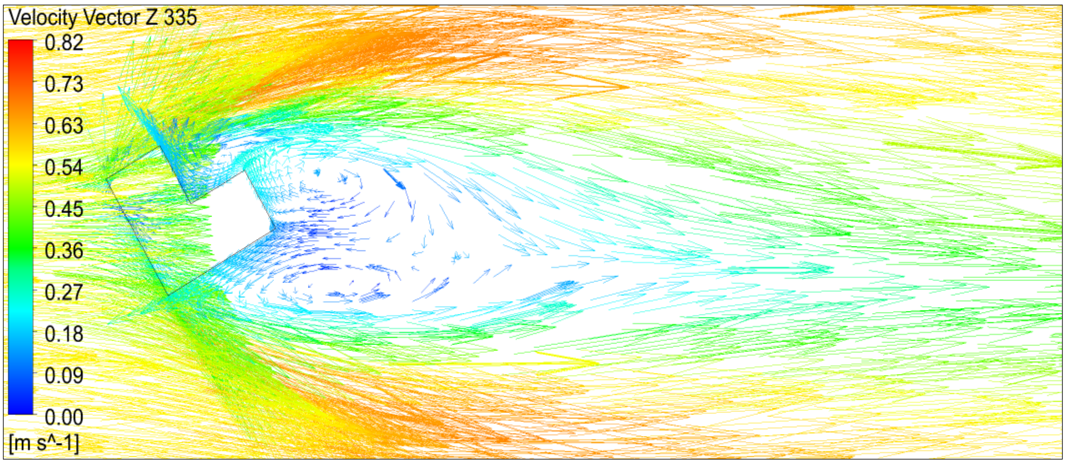

(c) Velocity Vector at Height Z = 335 mm

Figure 5. 13: Velocity Vector L-Shape Model 30° Wind Angle

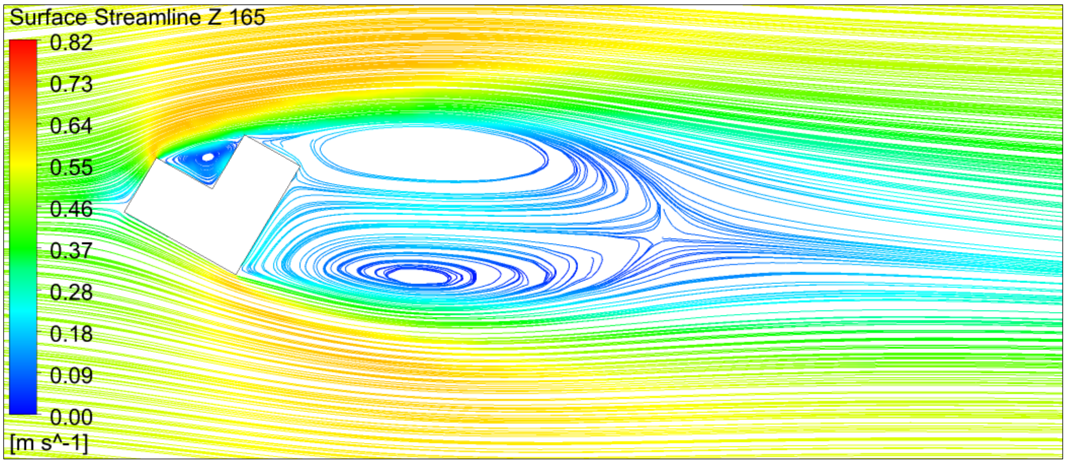

(a) Surface Streamline at Height Z = 165 mm

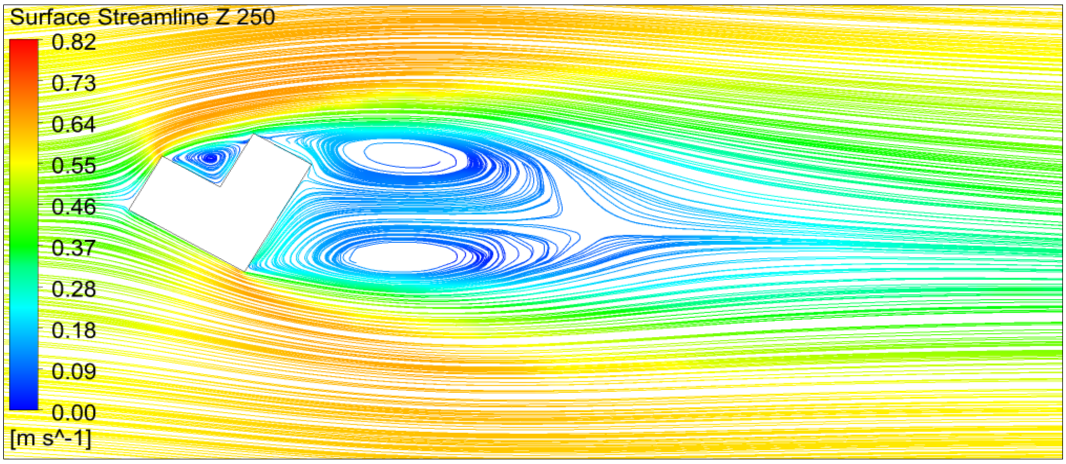

(b) Surface Streamline at Height Z = 250 mm

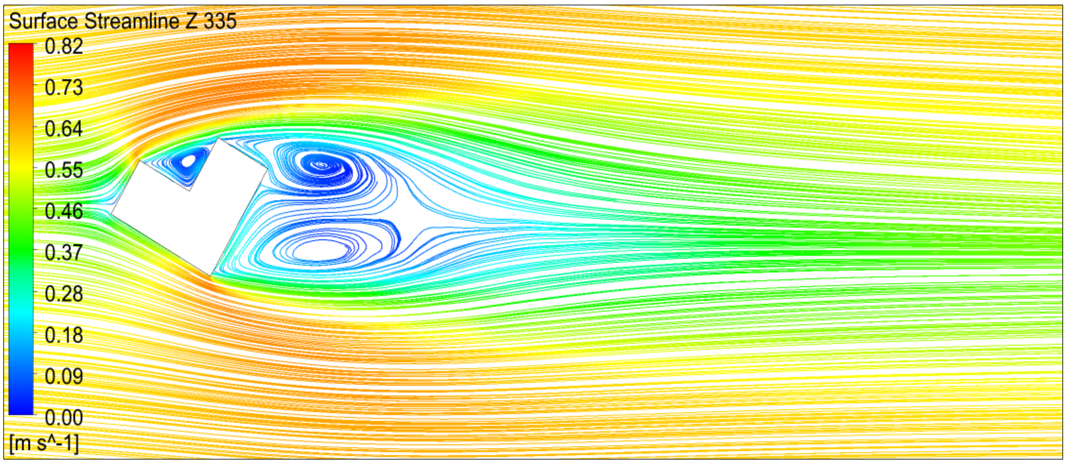

(c) Surface Streamline at Height Z = 335 mm

Figure 5. 14: Surface Streamline L-Shape Model 60° Wind Angle

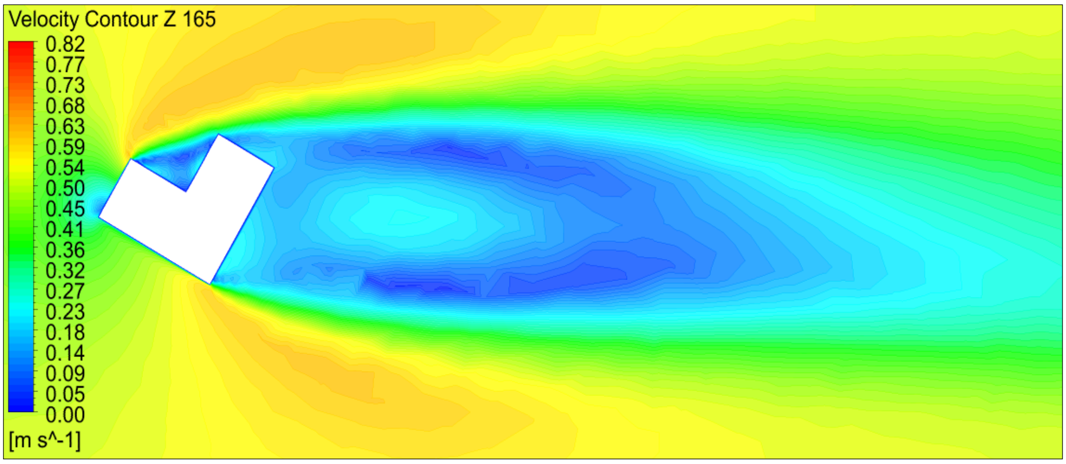

(a) Velocity Contour at Height Z = 165 mm

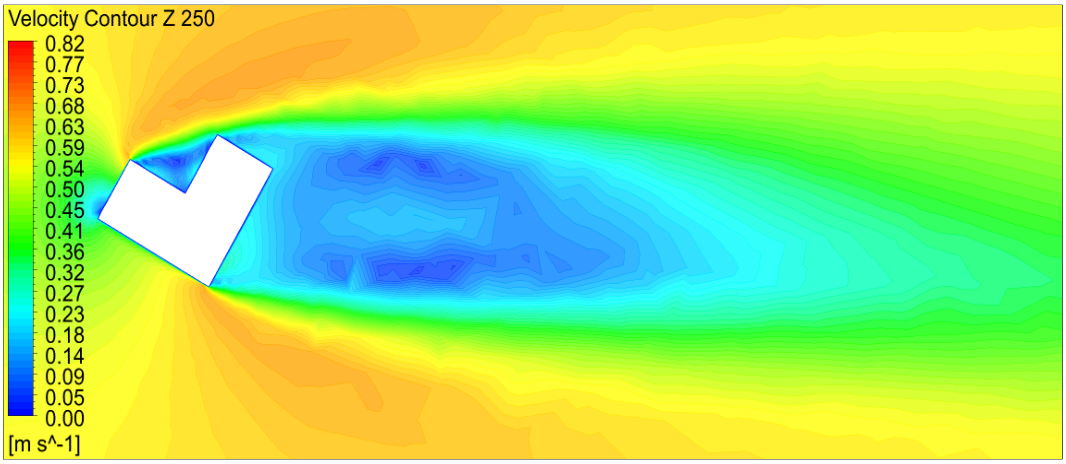

(b) Velocity Contour at Height Z = 250 mm

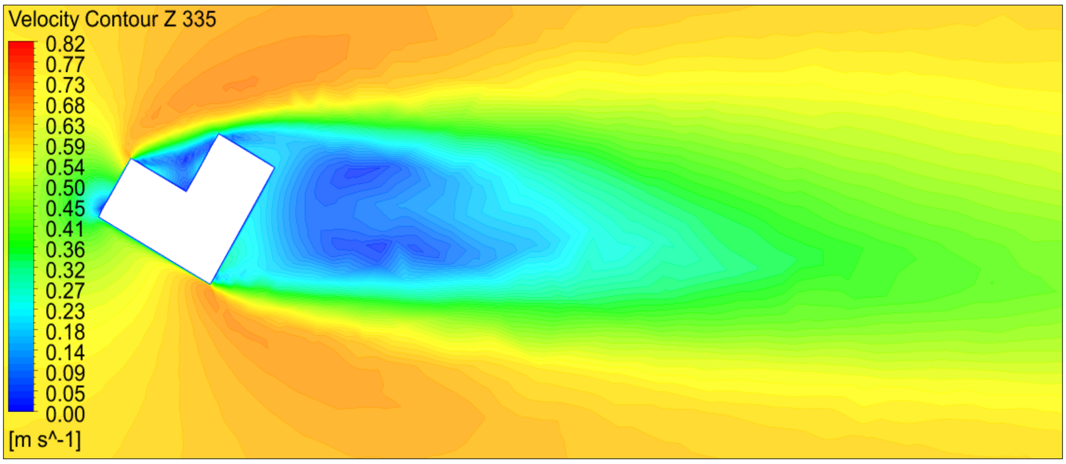

(c) Velocity Contour at Height Z = 335 mm

Figure 5. 15: Velocity Contour L-Shape Model 60° Wind Angle

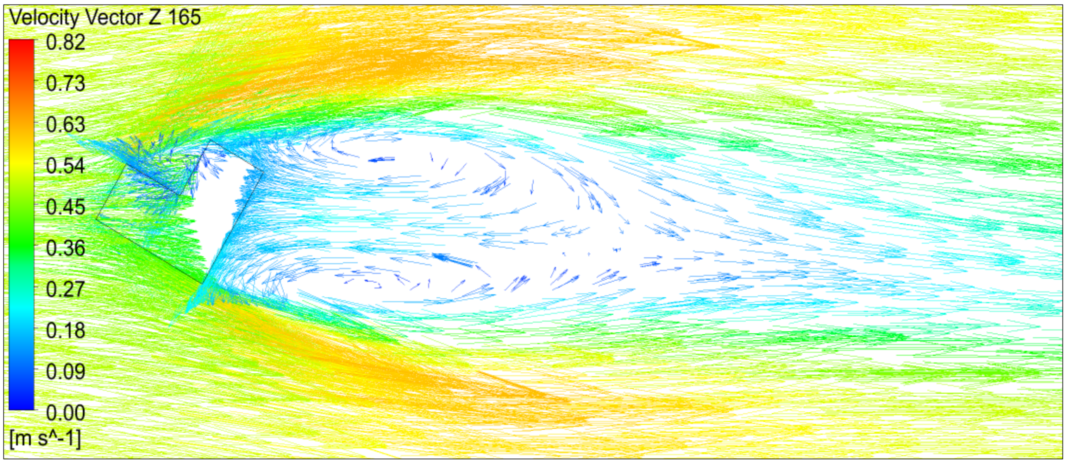

(a) Velocity Vector at Height Z = 165 mm

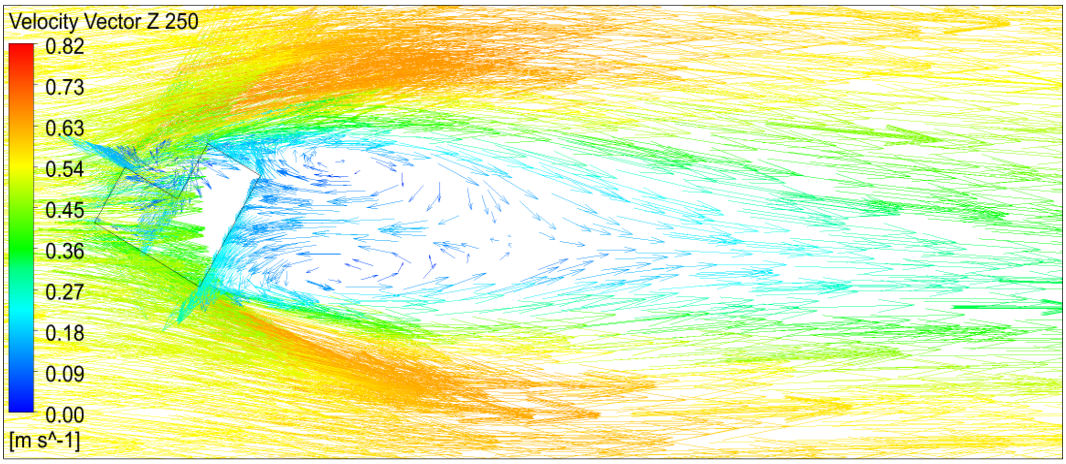

(b) Velocity Vector at Height Z = 250 mm

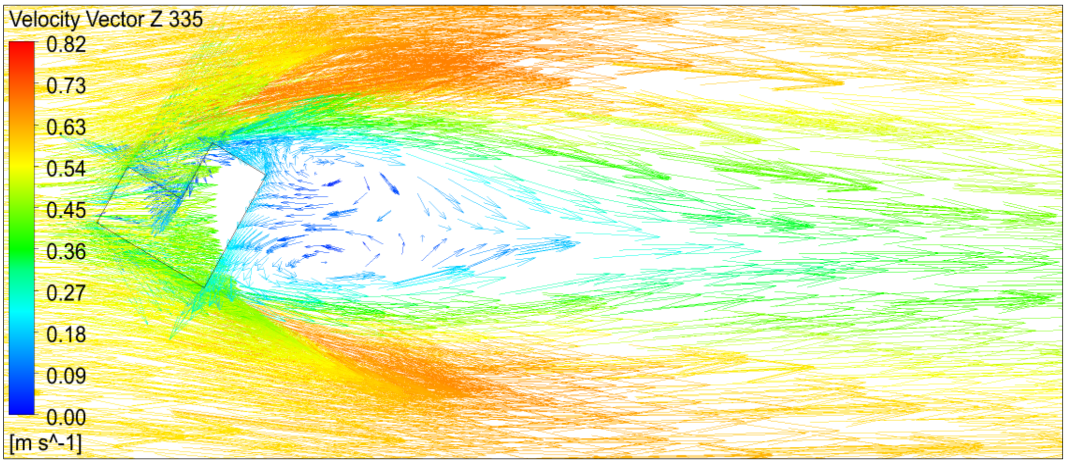

(c) Velocity Vector at Height Z = 335 mm

Figure 5. 16: Velocity Vector L-Shape Model 60° Wind Angle

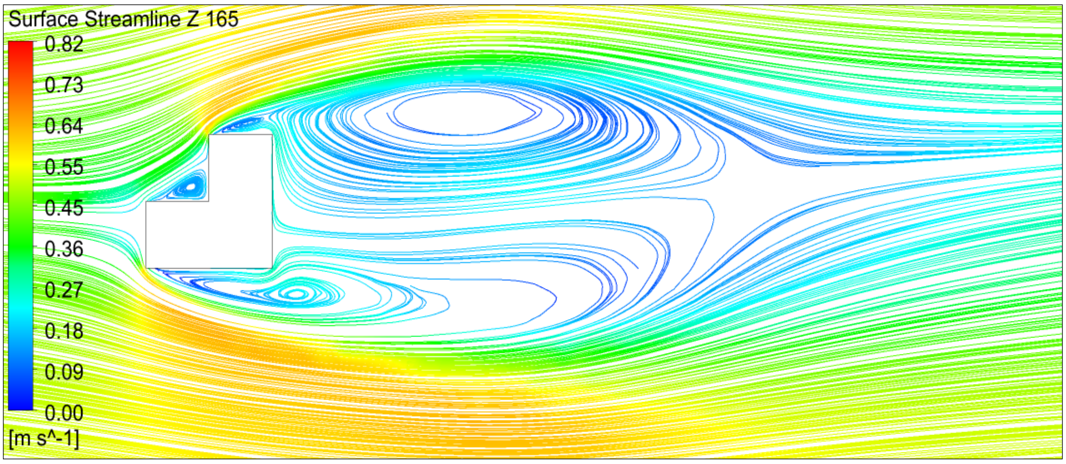

(a) Surface streamline at Height Z = 165 mm

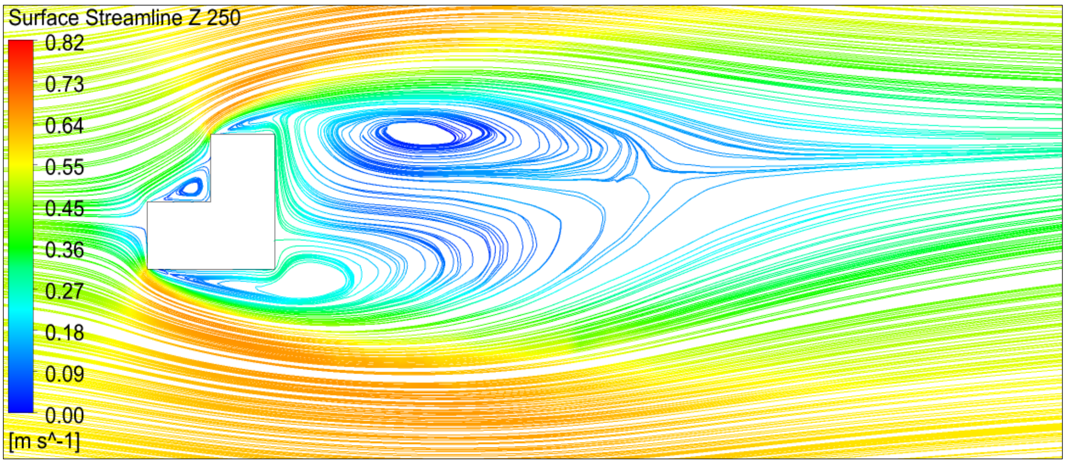

(b) Surface streamline at Height Z = 250 mm

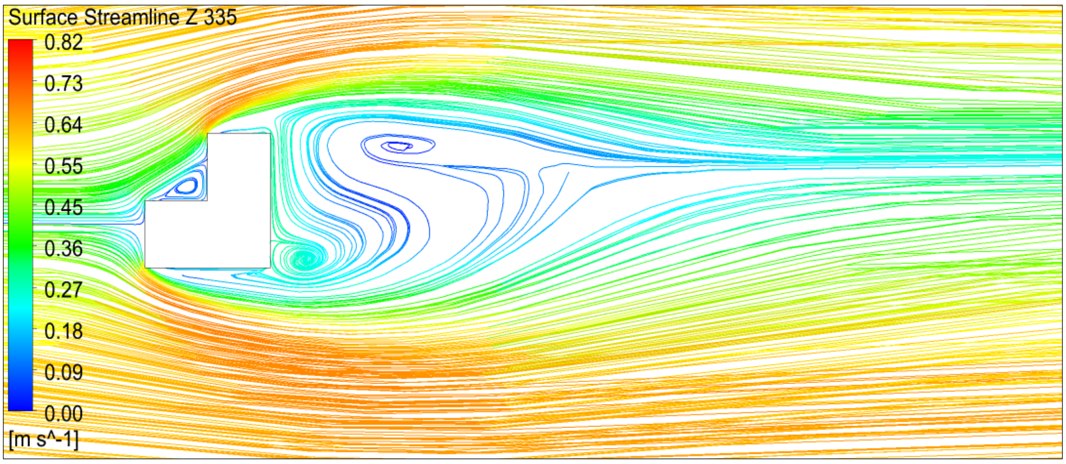

(c) Surface streamline at Height Z = 335 mm

Figure 5. 17: Surface Streamline L-Shape Model 90° Wind Angle

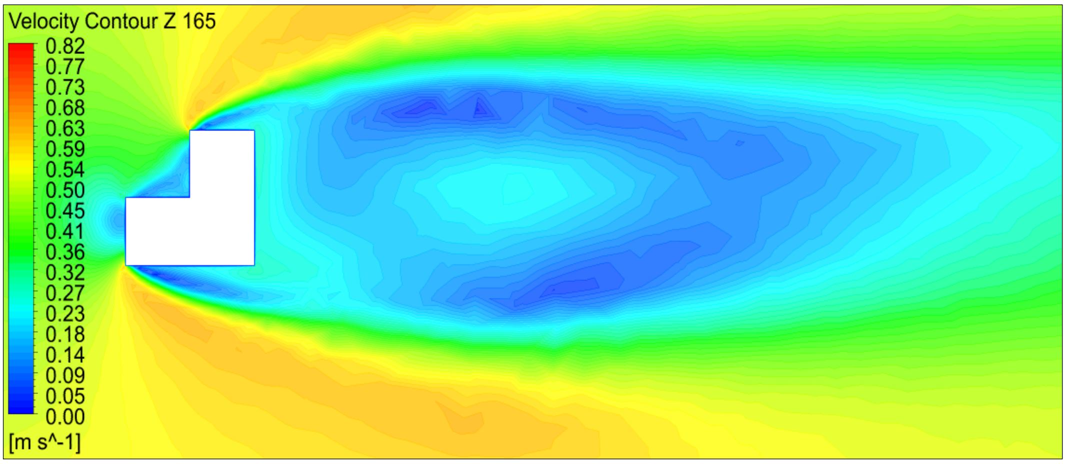

(a) Velocity Contour at Height Z = 165 mm

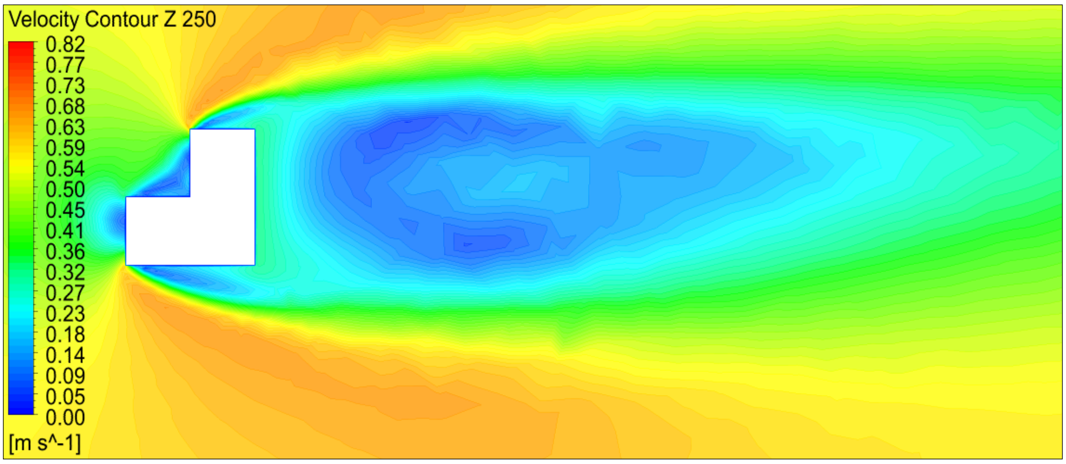

(c) Velocity Contour at Height Z = 250 mm

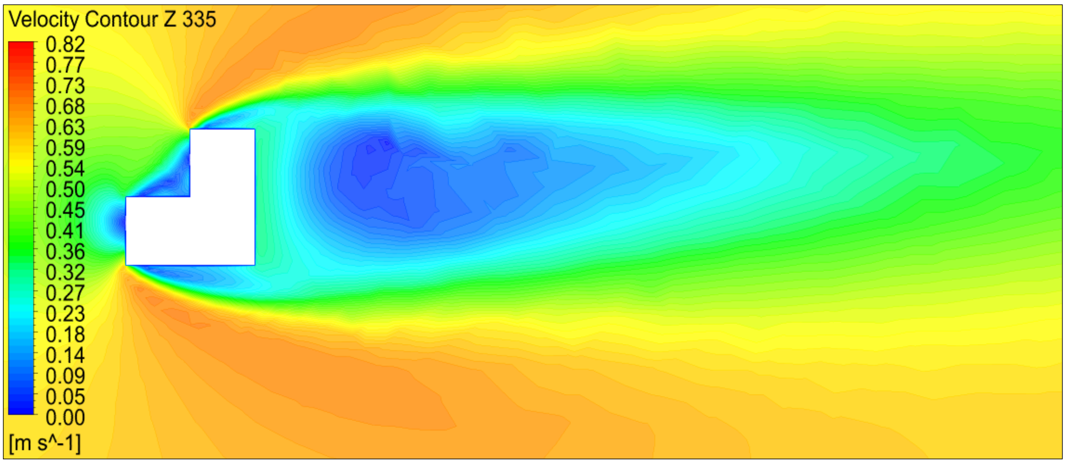

(c) Velocity Contour at Height Z = 335 mm

Figure 5. 18: Velocity Contour L-Shape Model 90° Wind Angle

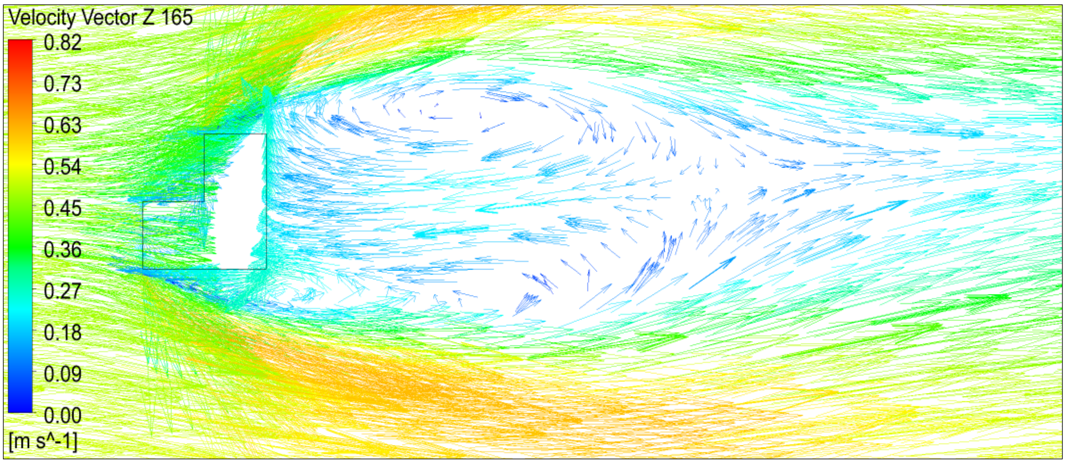

(a) Velocity Vector at Height Z = 165 mm

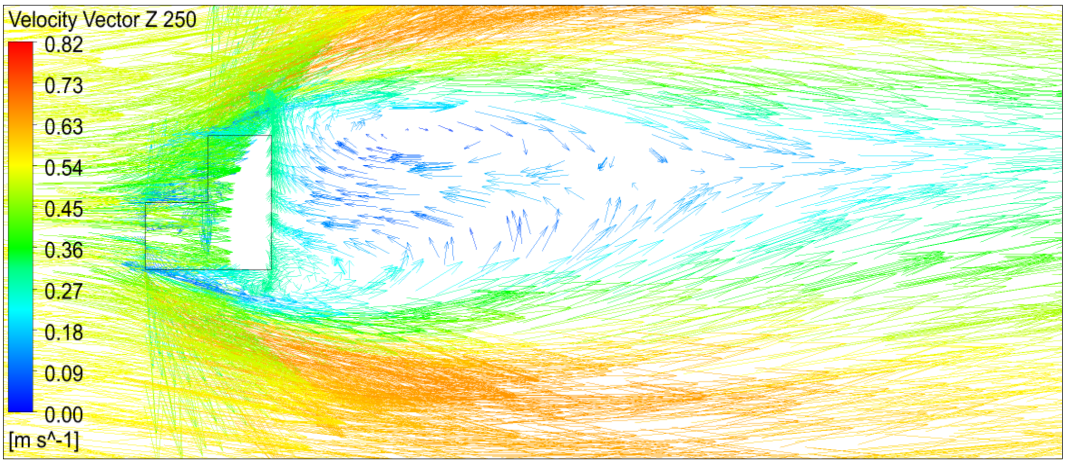

(b) Velocity Vector at Height Z = 250 mm

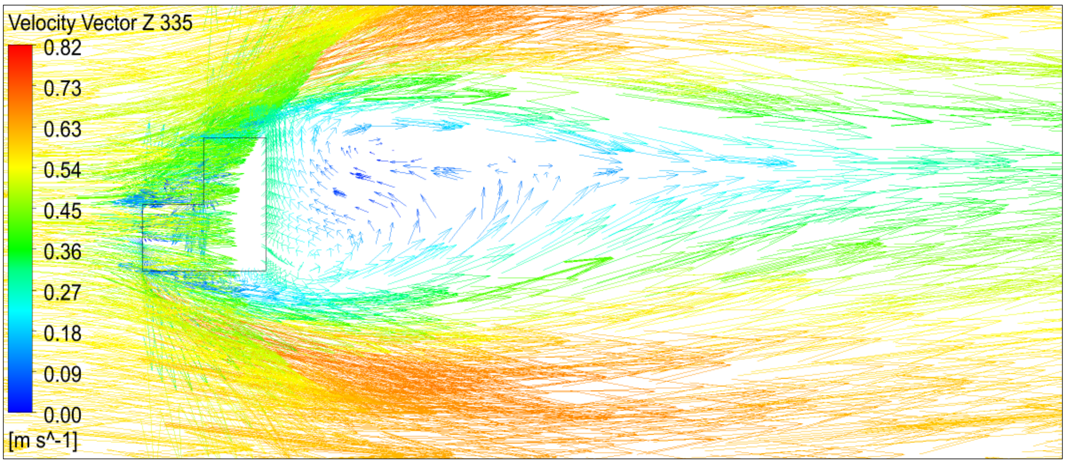

(c) Velocity Vector at Height Z = 335 mm

Figure 5. 19: Velocity Vector L-Shape Model 90° Wind Angle

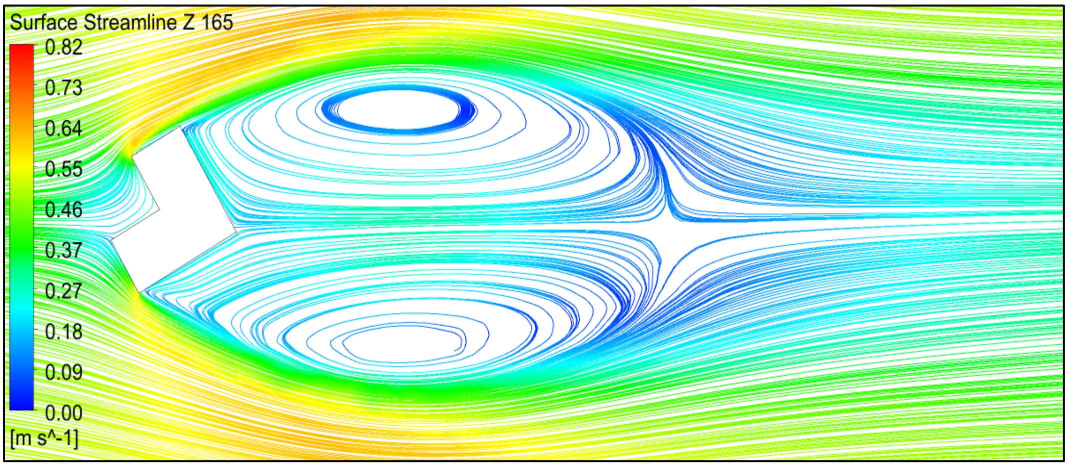

(a) Surface Streamline at Height Z = 165 mm

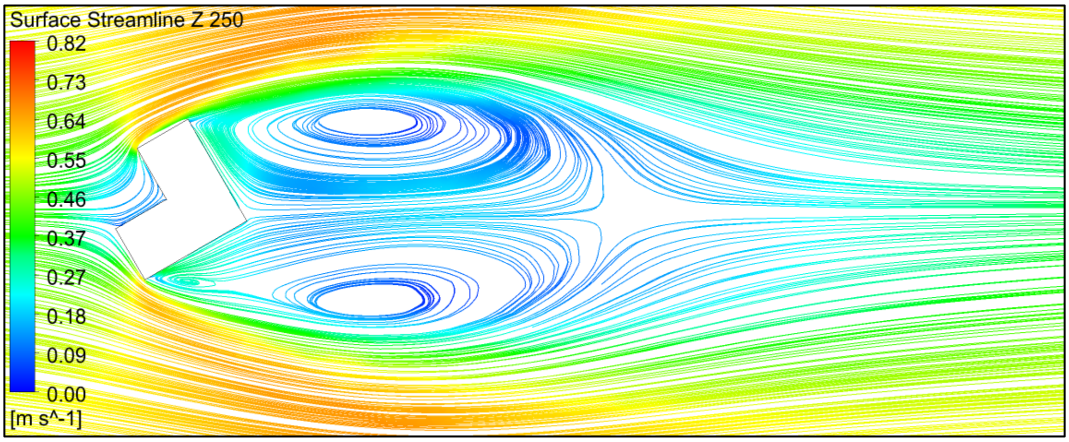

(b) Surface Streamline at Height Z = 250 mm

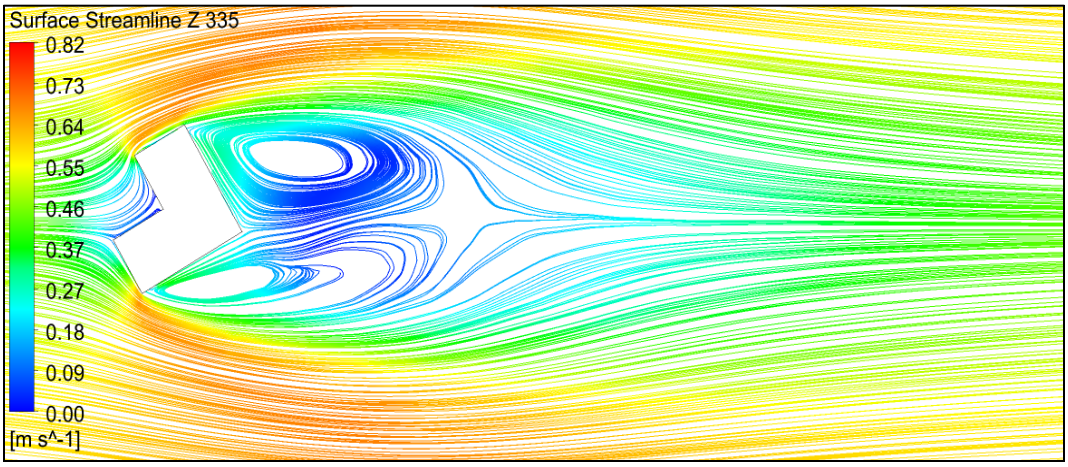

(c) Surface Streamline at Height Z = 335 mm

Figure 5. 20: Surface Streamline L-Shape Model 120° Wind Angle

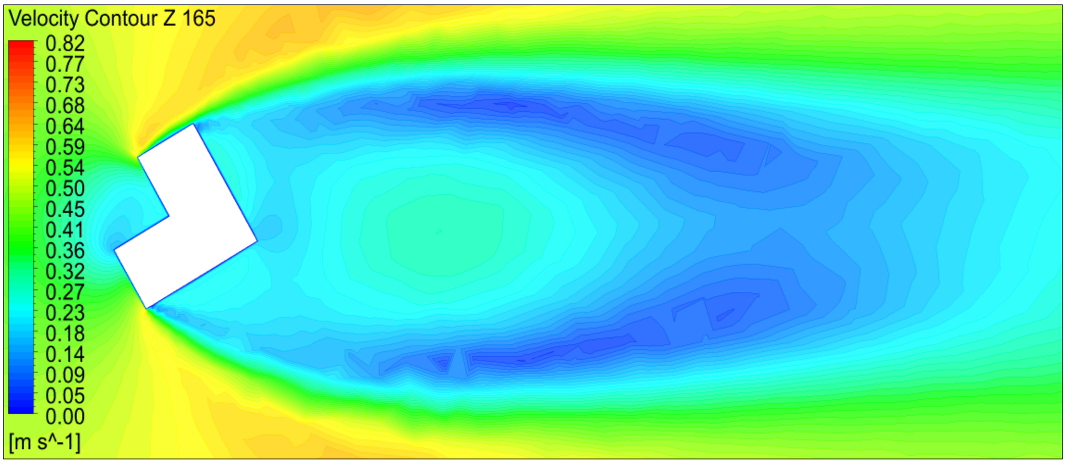

(a) Velocity Contour at Height Z = 165 mm

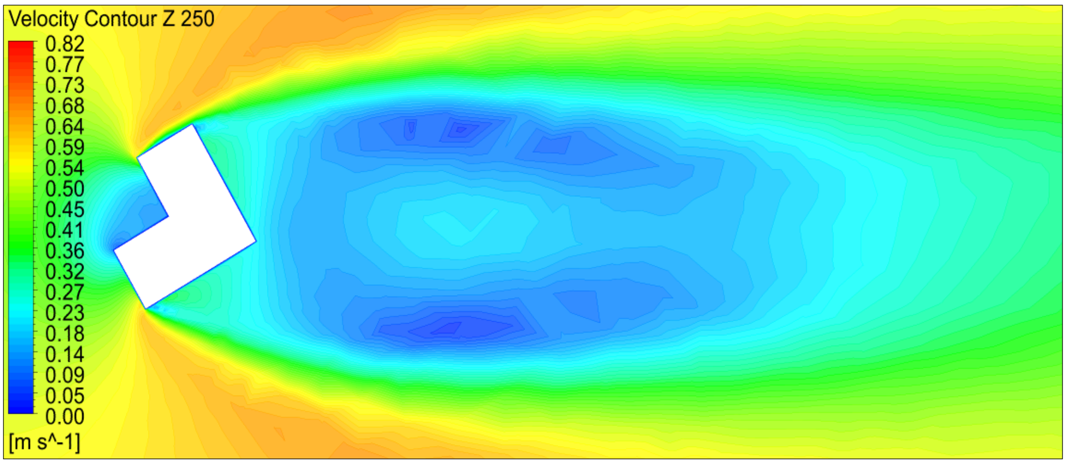

(b) Velocity Contour at Height Z = 250 mm

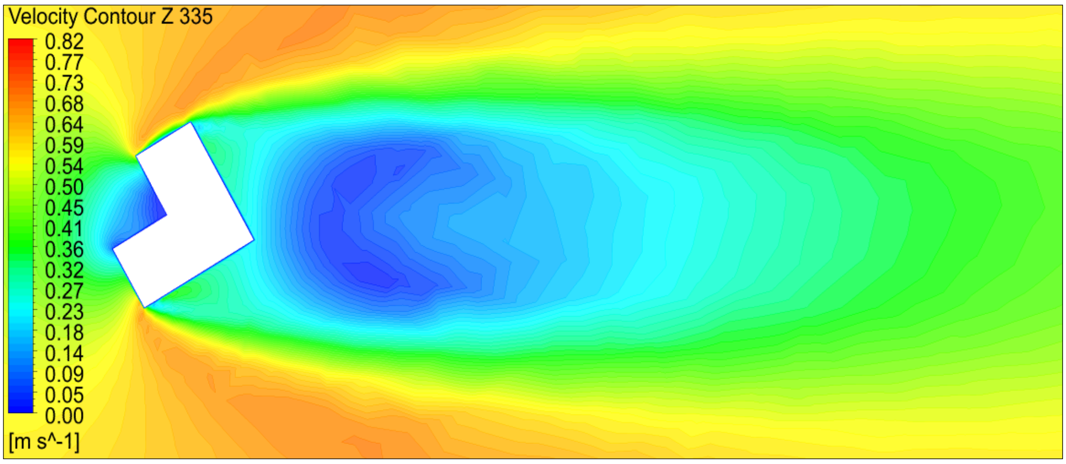

(c) Velocity Contour at Height Z = 335 mm

Figure 5. 21: Velocity Contour L-Shape Model 120° Wind Angle

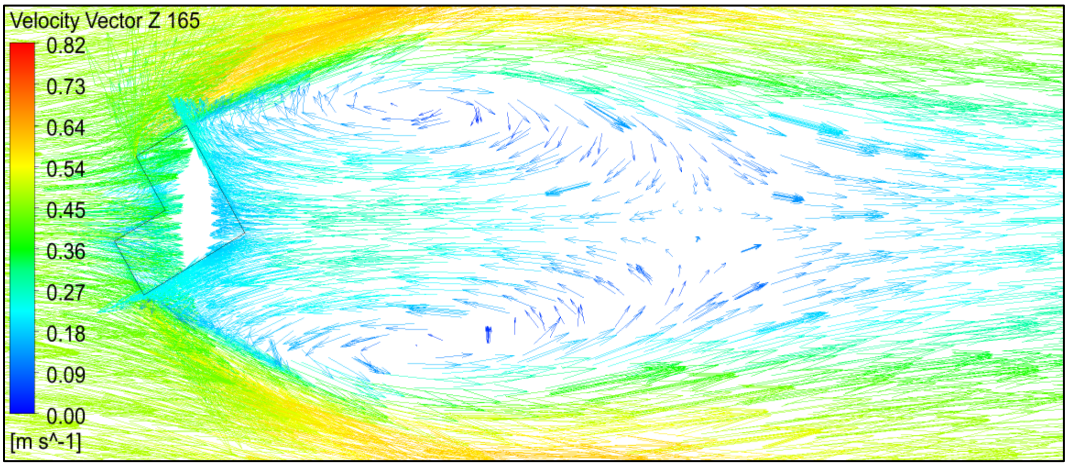

(a) Velocity Vector at Height Z = 165 mm

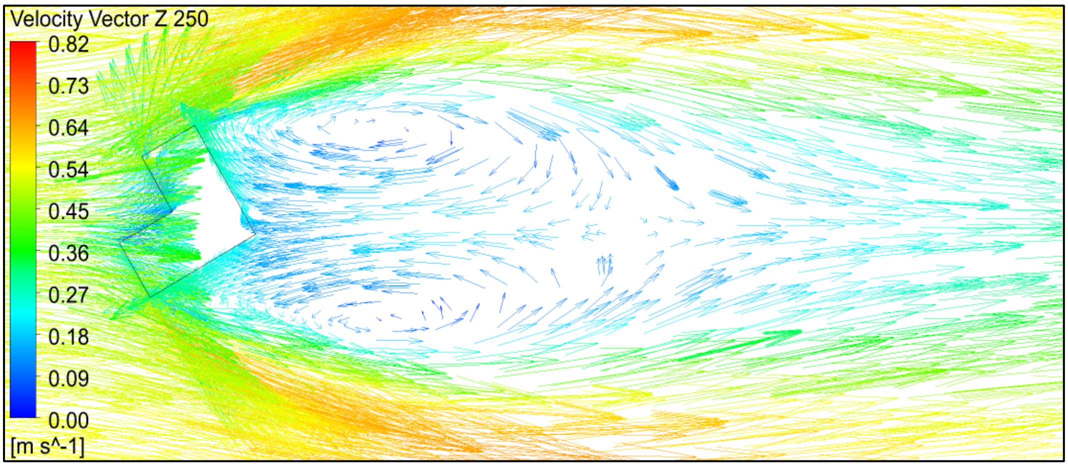

(b) Velocity Vector at Height Z = 250 mm

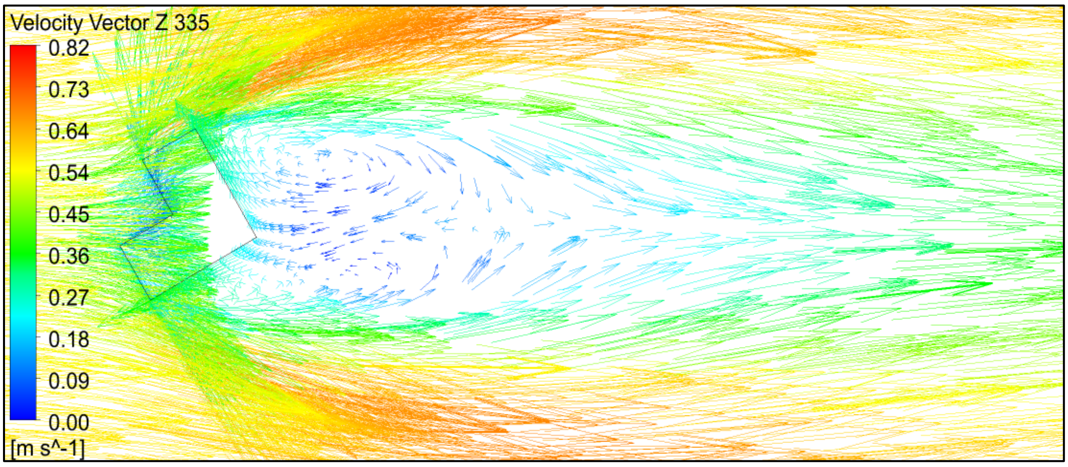

(c) Velocity Vector at Height Z = 335 mm

Figure 5. 22: Velocity Vector L-Shape Model 120° Wind Angle

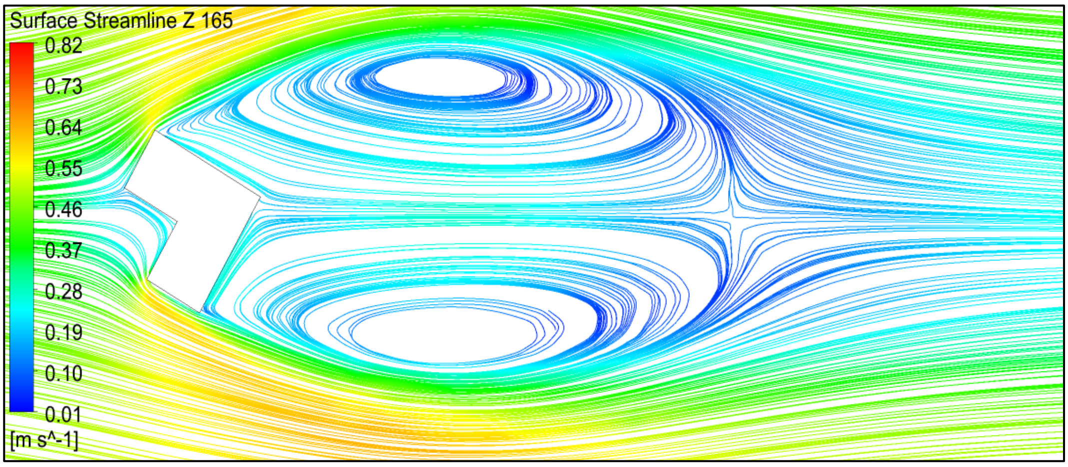

(a) Surface Streamline at Height Z = 165 mm

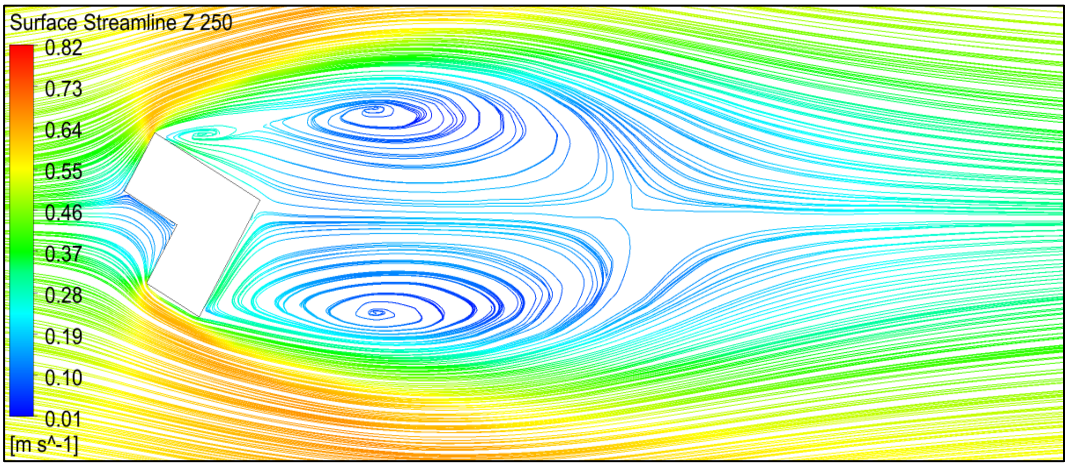

(b) Surface Streamline at Height Z = 250 mm

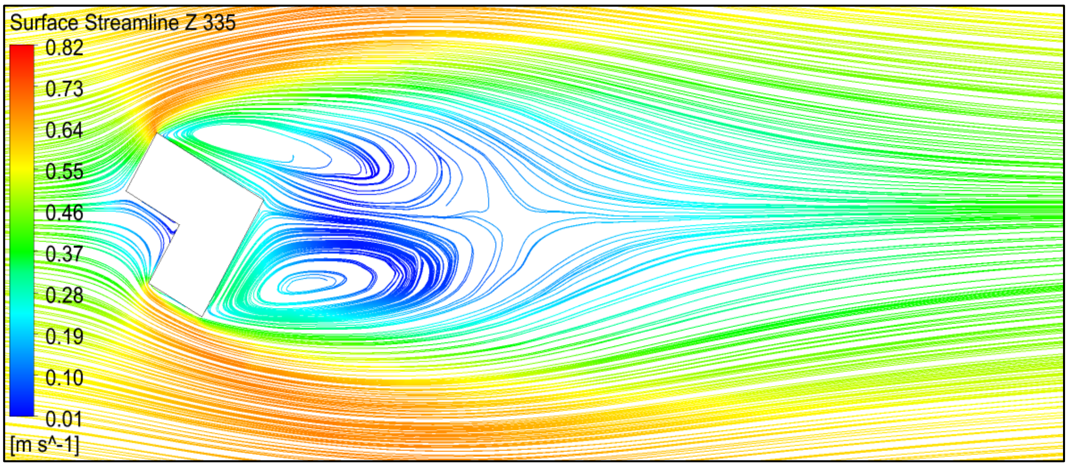

(c) Surface Streamline at Height Z = 335 mm

Figure 5. 23: Surface Streamline L-Shape Model 150° Wind Angle

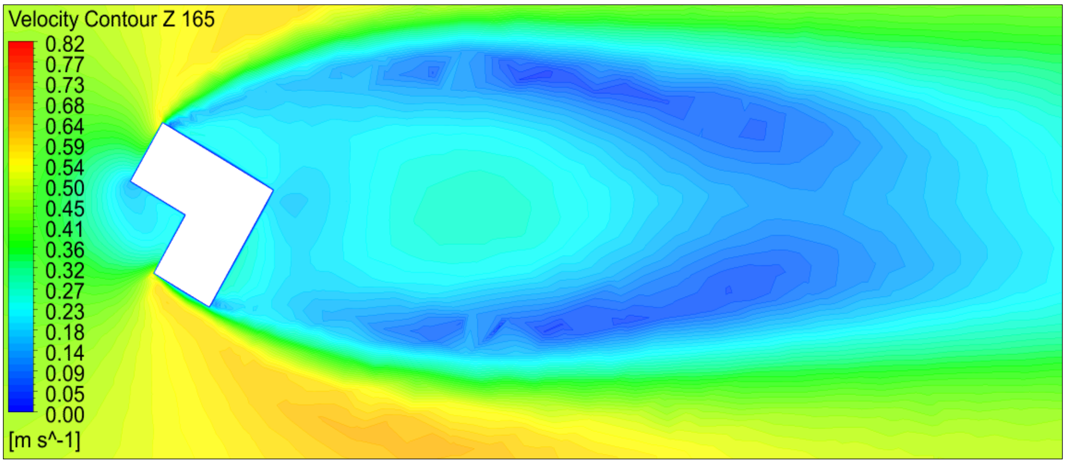

(a) Velocity Contour at Height Z = 165 mm

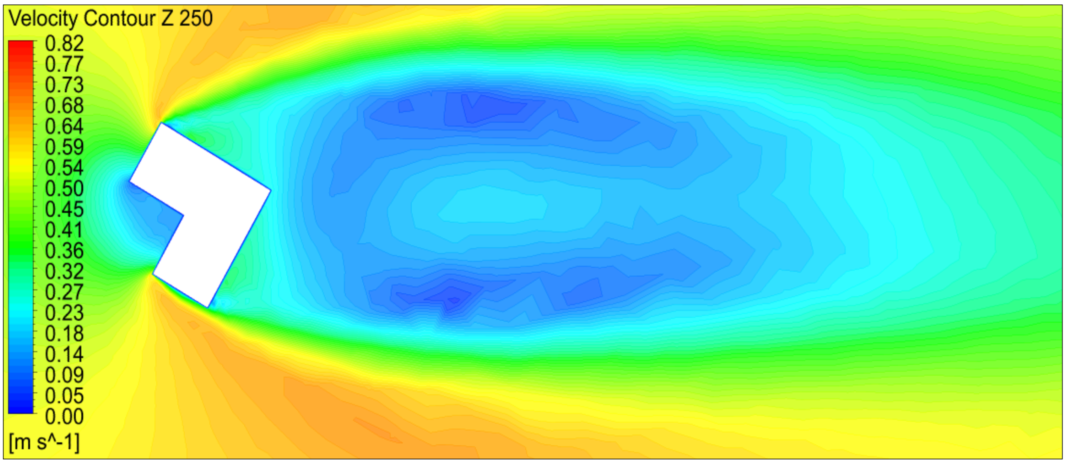

(b) Velocity Contour at Height Z = 250 mm

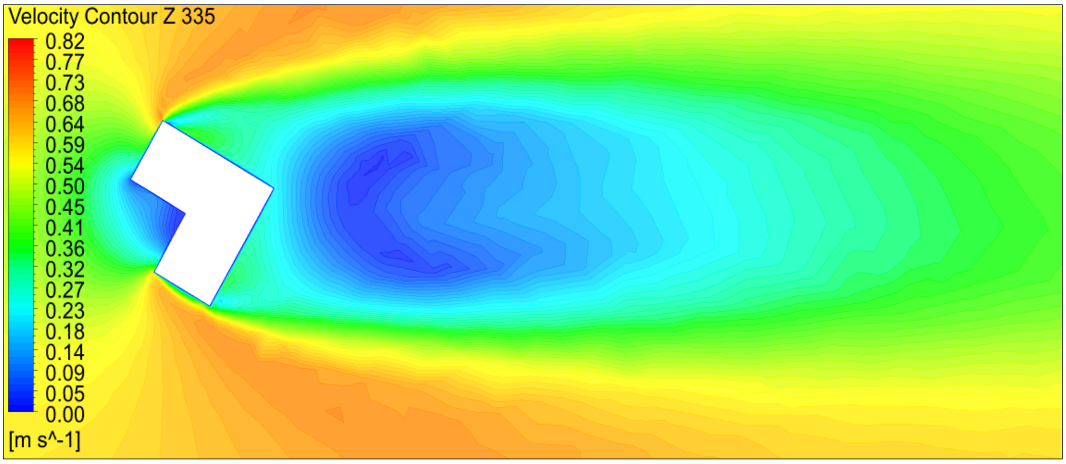

(c) Velocity Contour at Height Z = 335 mm

Figure 5. 24: Velocity Contour L-Shape Model 150° Wind Angle

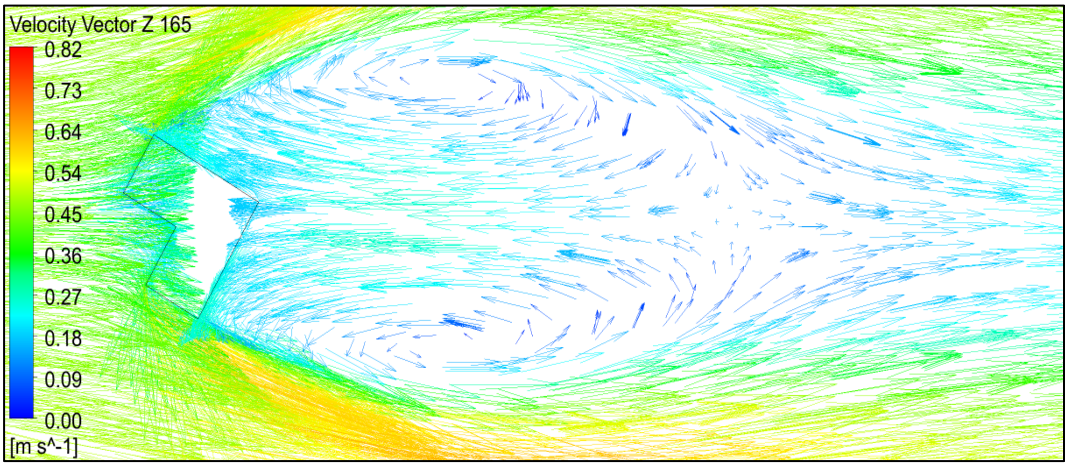

(a) Velocity Vector at Height Z = 165 mm

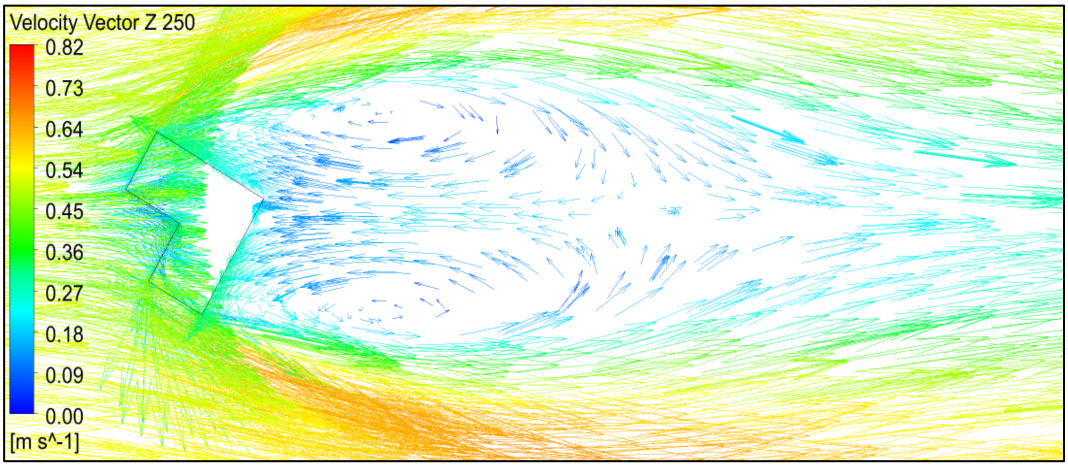

(b) Velocity Vector at Height Z = 250 mm

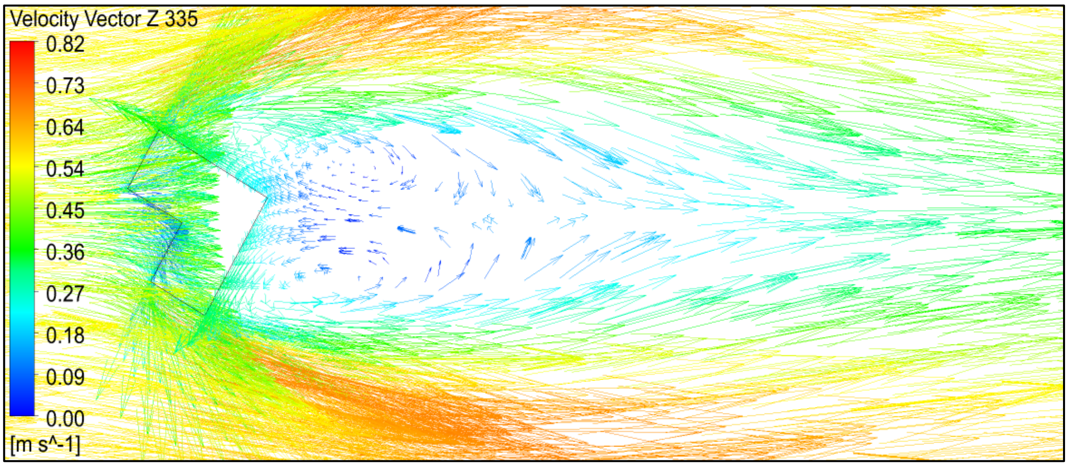

(c) Velocity Vector at Height Z = 335 mm

Figure 5. 25: Velocity Vector L-Shape Model 150° Wind Angle

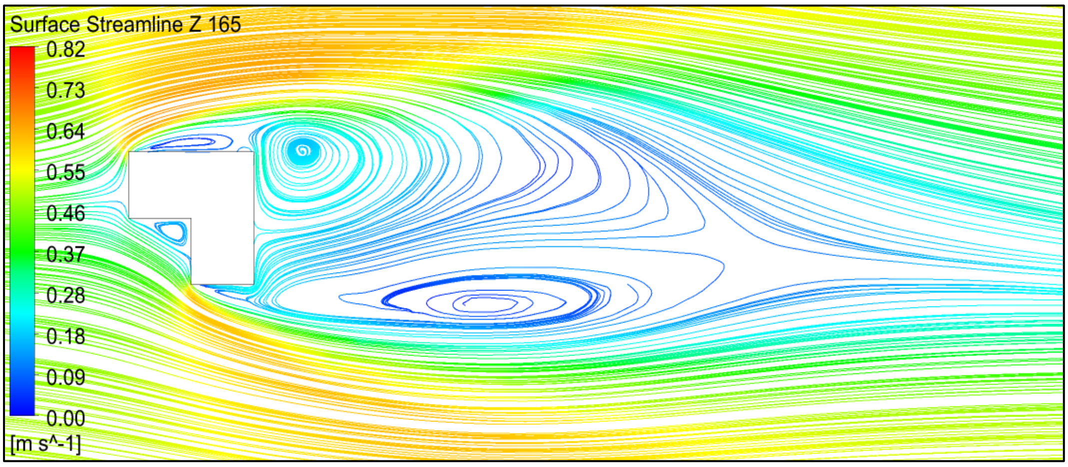

(a) Surface Streamline at Height Z = 165 mm

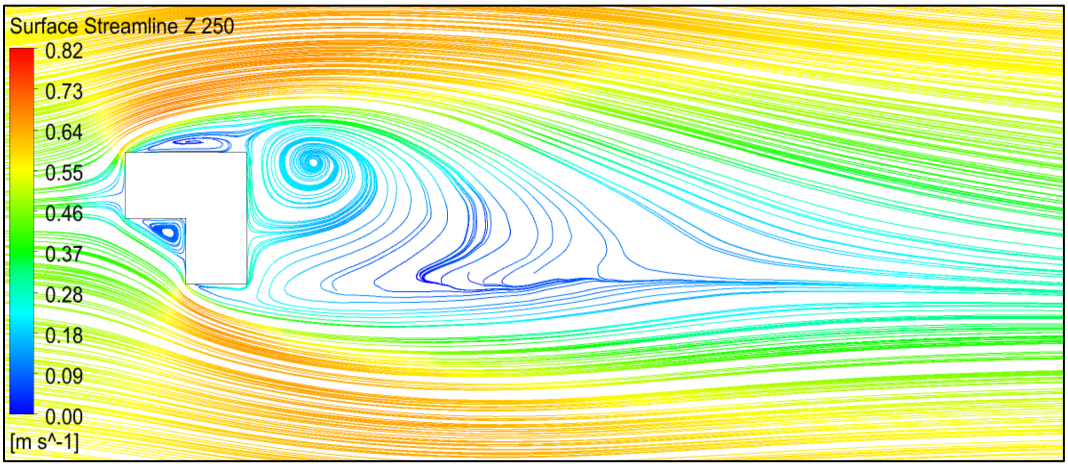

(b) Surface Streamline at Height Z = 250 mm

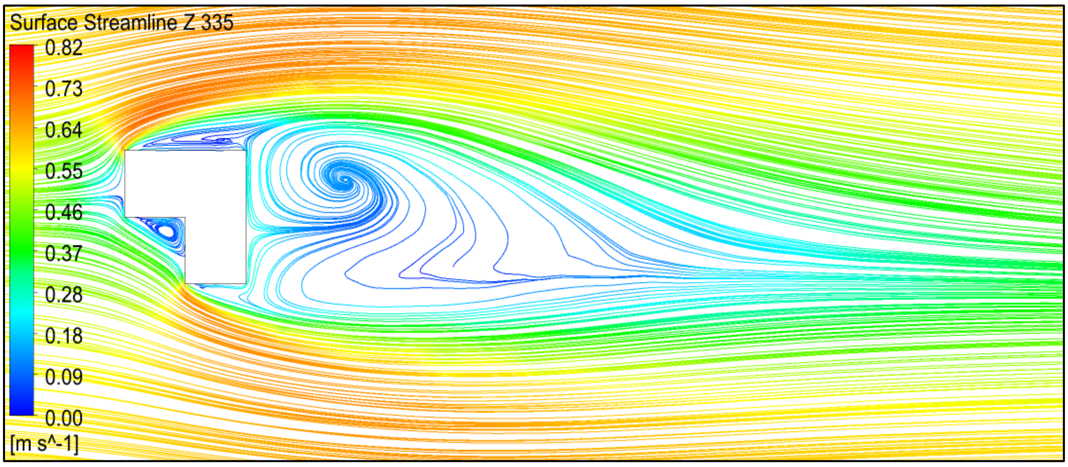

(c) Surface Streamline at Height Z = 335 mm

Figure 5. 26: Surface Streamline L-Shape Model 180° Wind Angle

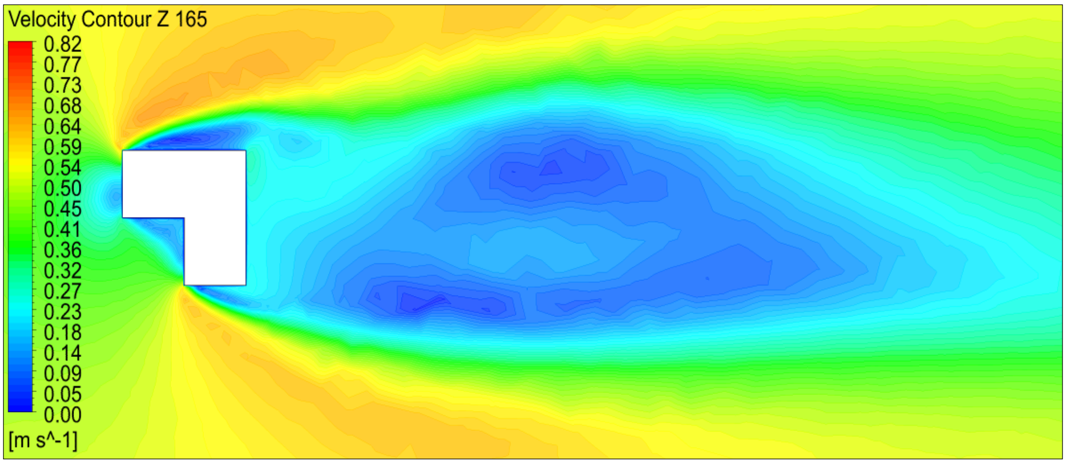

(a) Velocity Contour at Height Z = 165 mm

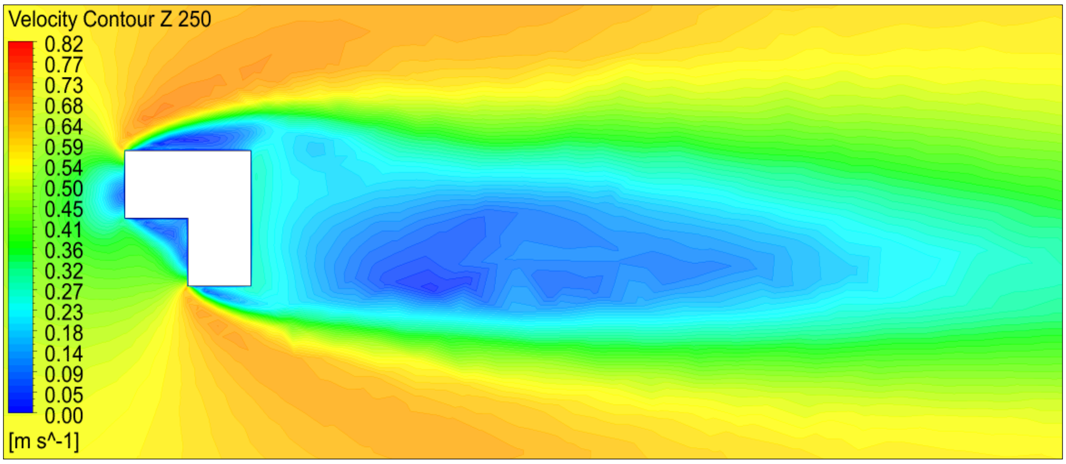

(b) Velocity Contour at Height Z = 250 mm

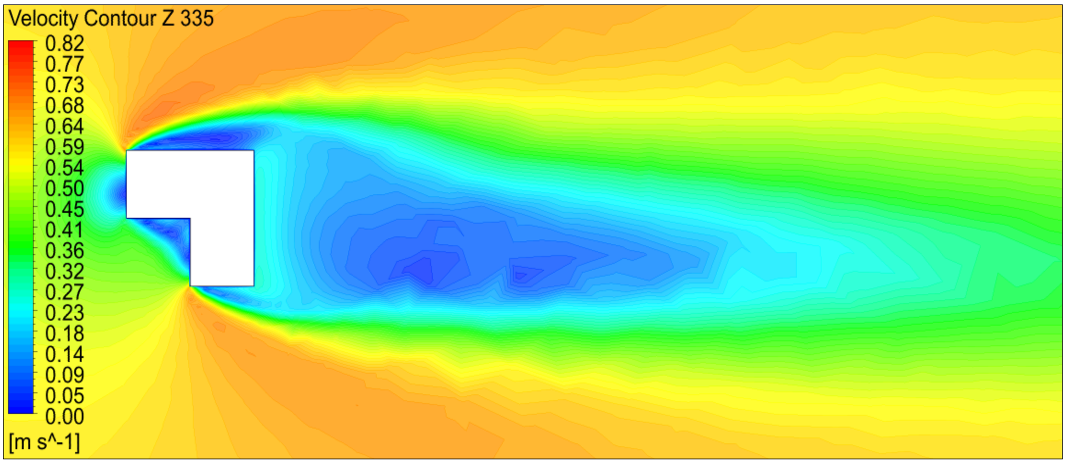

(c) Velocity Contour at Height Z = 335 mm

Figure 5. 27: Velocity Contour L-Shape Model 180° Wind Angle

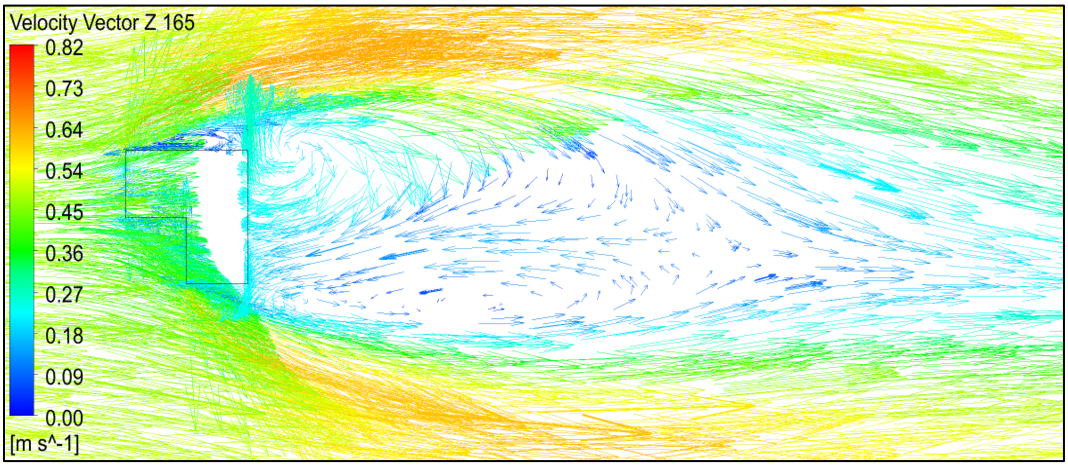

(a) Velocity Vector at Height Z = 165 mm

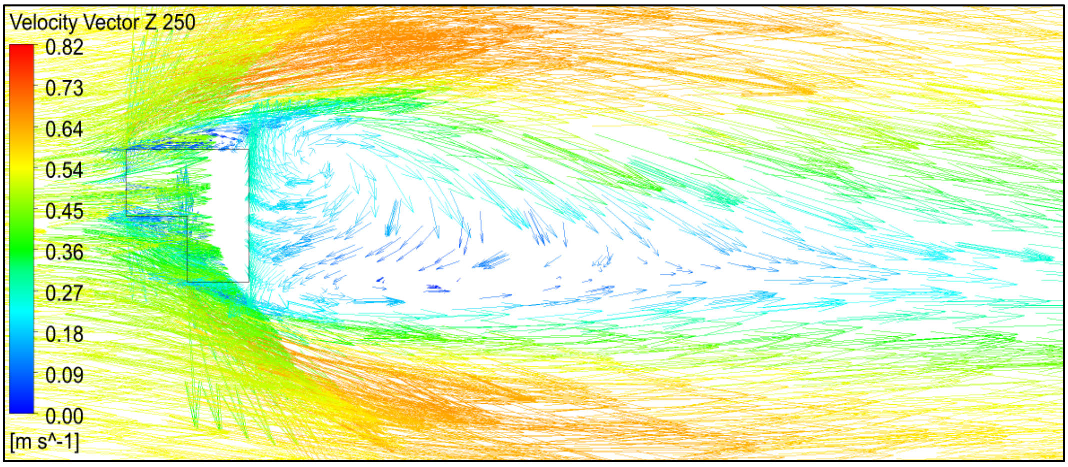

(b) Velocity Vector at Height Z = 250 mm

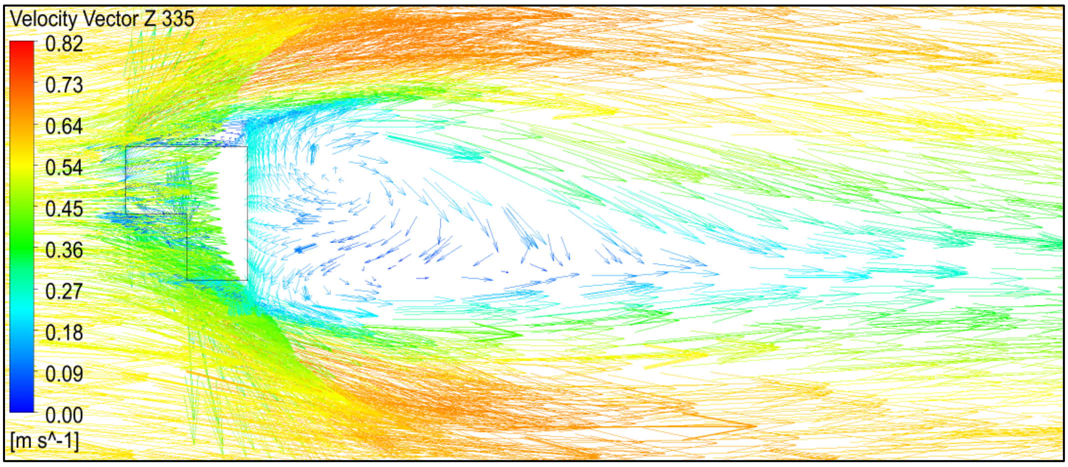

(c) Velocity Vector at Height Z = 335 mm

Figure 5. 28: Velocity Vector L-Shape Model 180° Wind Angle

5.2.9 Velocity Streamline Along Wind Direction on Central Vertical Plane

Figure 5.29, 5.30, 5.31, 5.32, 5.33, 5.34 & 5.34 show the streamline with flow direction on cross section through central vertical plane along the wind direction. The upwind vortex at ground level, the upwash, downwash and stagnation zones on the windward face can be visualized. Recirculation and creation of shear layer at roof top and reattachment of flow behind the model can also be seen. It is observed that for all the wind angles the ground level upwind vortex is created, but the intensity and strength at 60° wind angle is weakest. Vorticity behind the model is seen at all wind angles but with different height, inclination and intensities. At 0° wind angle the backwash is seen to be flowing into the cavity up to 1/3rd height of the model from where it is flowing into height. Roof level recirculation is not prominent at 30° and 60° wind angle of attack.

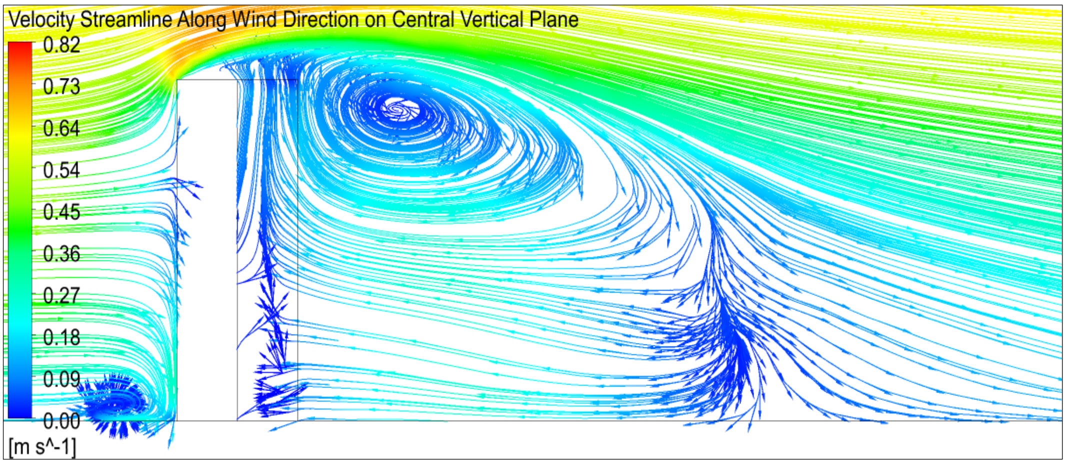

Figure 5. 29: Velocity Streamline Along the Wind Direction on Central Vertical Plane L-Shape Model 0° Wind Angle

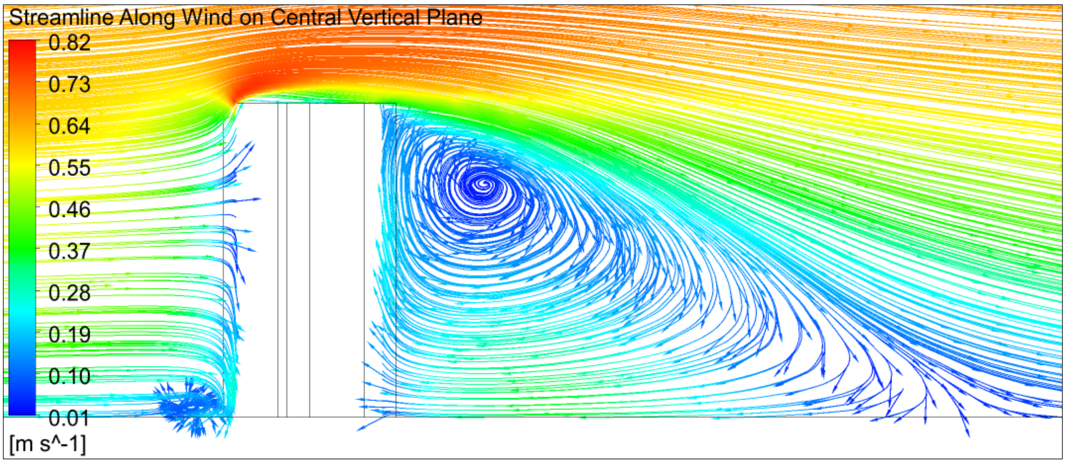

Figure 5. 30:Velocity Streamline Along Wind Direction on Central Vertical Plane L-Shape Model 30° Wind Angle

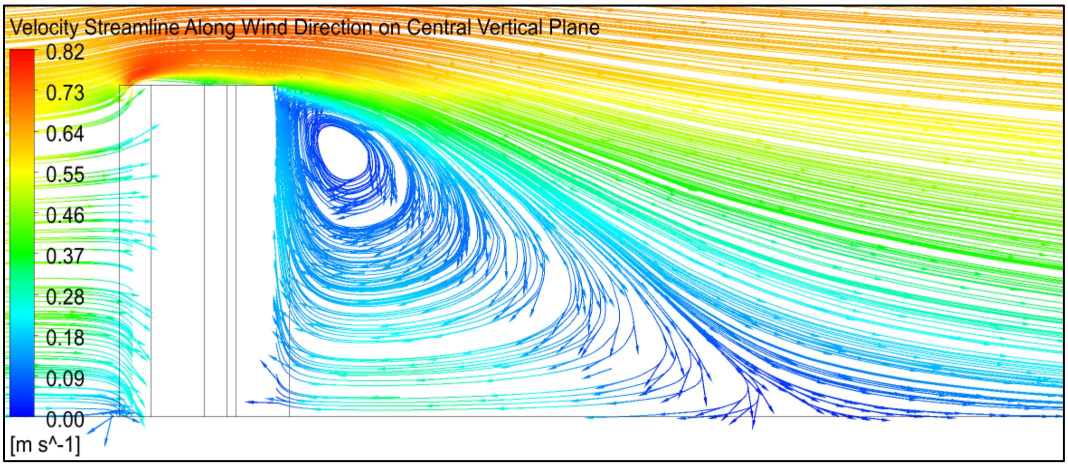

Figure 5. 31: Velocity Streamline Along the Wind Direction on Central Vertical Plane L-Shape Model 60° Wind Angle

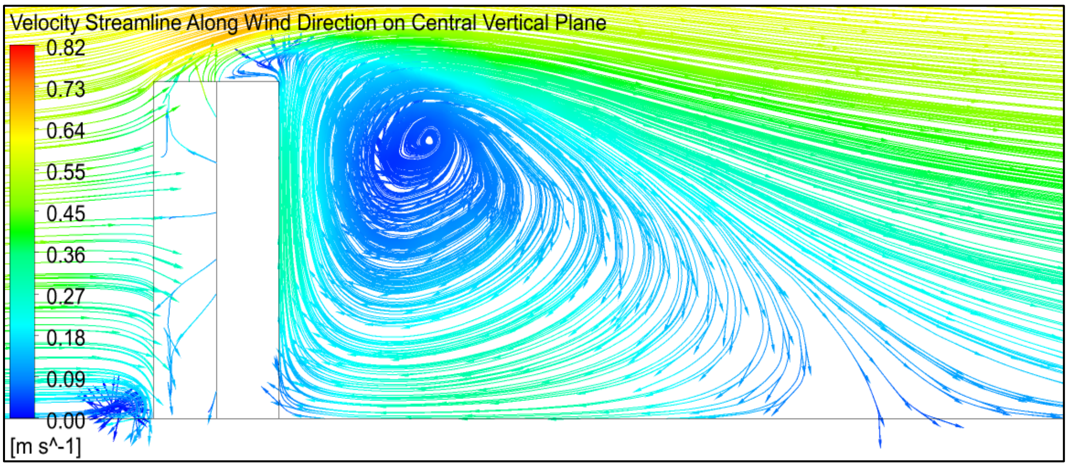

Figure 5. 32: Velocity Streamline Along the Wind Direction on Central Vertical Plane L-Shape Model 90° Wind Angle

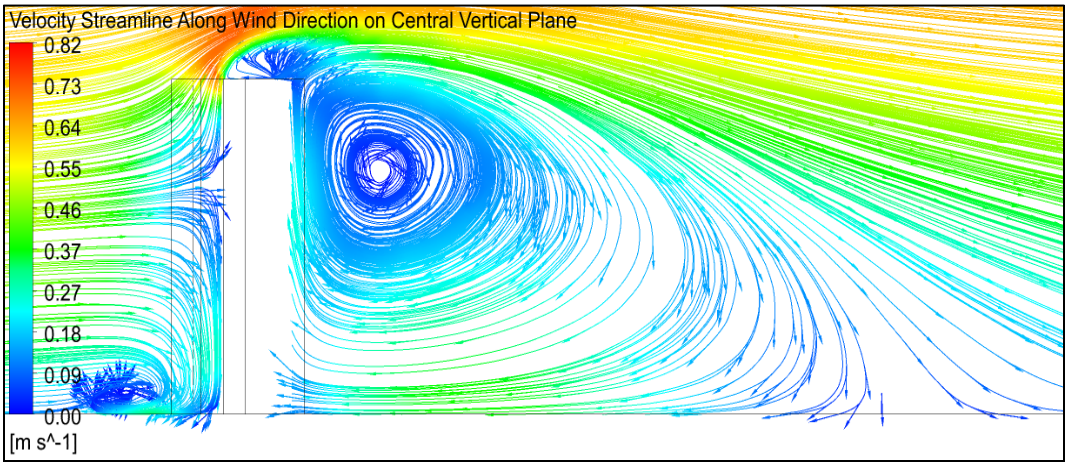

Figure 5. 33: Velocity Streamline Along the Wind Direction on Central Vertical Plane L-Shape Model 120° Wind Angle

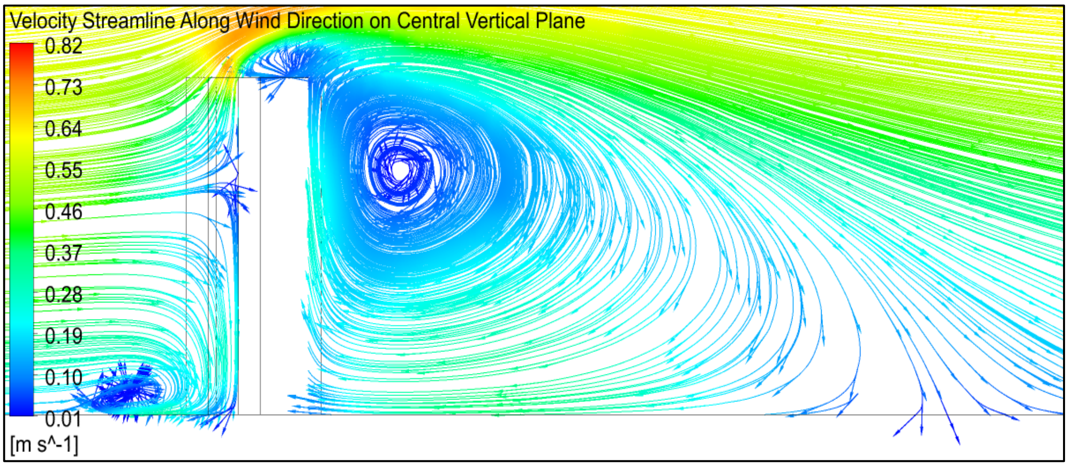

Figure 5. 34: Velocity Streamline Along the Wind Direction on Central Vertical Plane L-Shape Model 150° Wind Angle

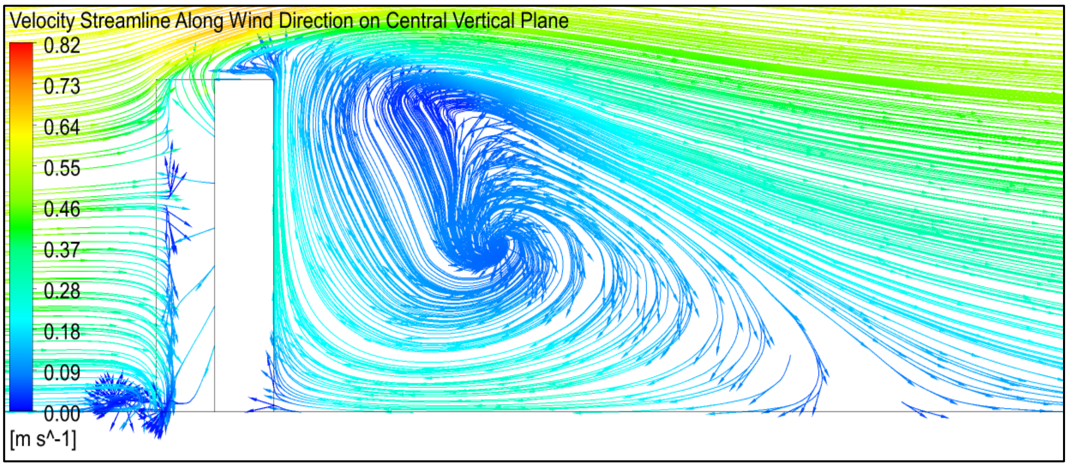

Figure 5. 35: Velocity Streamline Along the Wind Direction on Central Vertical Plane L-Shape Model 180° Wind Angle

5.2.10 C_{Pe} Along Building Perimeter

Graphical plot representing the variation of C_{Pe} on the building façade at three different heights Z = 0.165 m (about 1/3rd height of the model), Z = 0.25 m (1/2 height of the model) and Z = 0.335 m (about 2/3rd height of the model) for different wind angles of attack from 0° to 180° @ 30° have been shown in Figure 5.36, 5.37, 5.38, 5.39, 5.40, 5.41 & 5.42 respectively. This graphical representation provides us clear picture of pressure (positive or negative) on the faces and also, fluctuations/gradient of pressure across the edges of the individual faces. Maximum coefficient of pressure on the face exposed to direct wind reaches a value of 1 on the graph. C_{Pe} variation of small value represents formation of eddies on the place, whereas, large variation shows formation of pressure or suction region. For L – shaped model it is observed that pressure on the faces at different heights differ largely compared to other models.

For 0° wind angle, from the graph, it can be concluded that face A is exposed to direct wind. Rest all faces are under suction. High gradient of suction on face C2 and D exists. For 30° wind incidence angle face A is still facing the impact of direct wind. However, at the meeting edge with face D suction of high value exists. Rate of change in pressure across the face is rapid. At Z = 165 mm height fluctuation of pressure indicates formation of local eddies due to turbulence at the place. On face C2 suction at the middle of the face is least, decreasing with high gradient towards face B2. Towards face A suction is decreasing and then becoming positive with high gradient at the edge. This portion is vulnerable for cladding units. At 60° wind angle face A and C2 both are partially exposed to direct wind. Gradient of pressure is highest on face C2. Local turbulence at Z = 165 mm height is also noticed to occur on face C2. Suction pressure on face C1 across the width is fluctuating widely.

At 90° wind angle face B2, C1 and C2 are possessing positive pressure. High gradient of pressure on face C1 and C2 exists towards face B1 and A respectively. As such the meeting edge of AC2 and B1C1 are sensitive for cladding units. For 120° wind angle positive pressure still exists on face B, C1 and C2. At 150° wind incidence angle, face B1, B2 and C1 are under positive pressure. On face C2 low suction exists at the centre which is increasing towards both edges. At 180° angle of attack positive pressure still exists on face B1, B2 and C1. On face C2 and D high gradient of pressure exists.

Where maximum suction exist is vital for design of cladding units. The detailed suction C_{Pe} values for different angle of wind incidence on the corners or faces are shown in Table 5.2. It is quite evident that maximum suction ($C_{Pe} =$ -1.22) occurs on face D for 180° wind angle of attack which shall govern the design of cladding units for this shape and size of the L- plan shaped building. However, if the cladding design is done considering the coefficients on face-to-face basis and preparation of block contour diagrams, it will be economically cheaper at the same time the building will be safe against failure of cladding design.

Table 5. 2: Maximum Suction in Terms of C_{Pe} for Cladding Design

AoA	Location	Height (Z)		
		0.165 m	0.250 m	0.335 m
0°	Face C2	-0.78	-0.91	-1.08
	Face D	-0.88	-0.85	-1.02
30°	Corner B2C2	-0.60	-0.70	-0.64
	Face D	-0.53	-0.73	-0.68
60°	Face B2	-0.71	-0.76	-0.82
	Corner AD	-0.43	-0.71	-0.75
90°	Face A	-0.80	-0.90	-0.93
	Face B1	-0.82	-0.83	-1.01
120°	Corner AC2	-0.31	-0.73	-0.99
	Face B1	-0.74	-1.02	-0.81
150°	Face D	-0.48	-0.87	-0.78
	Face C2	-0.73	-0.79	-0.70
180°	Face C2	-0.63	-0.95	-1.01
	Face D	-0.91	-0.86	-1.22

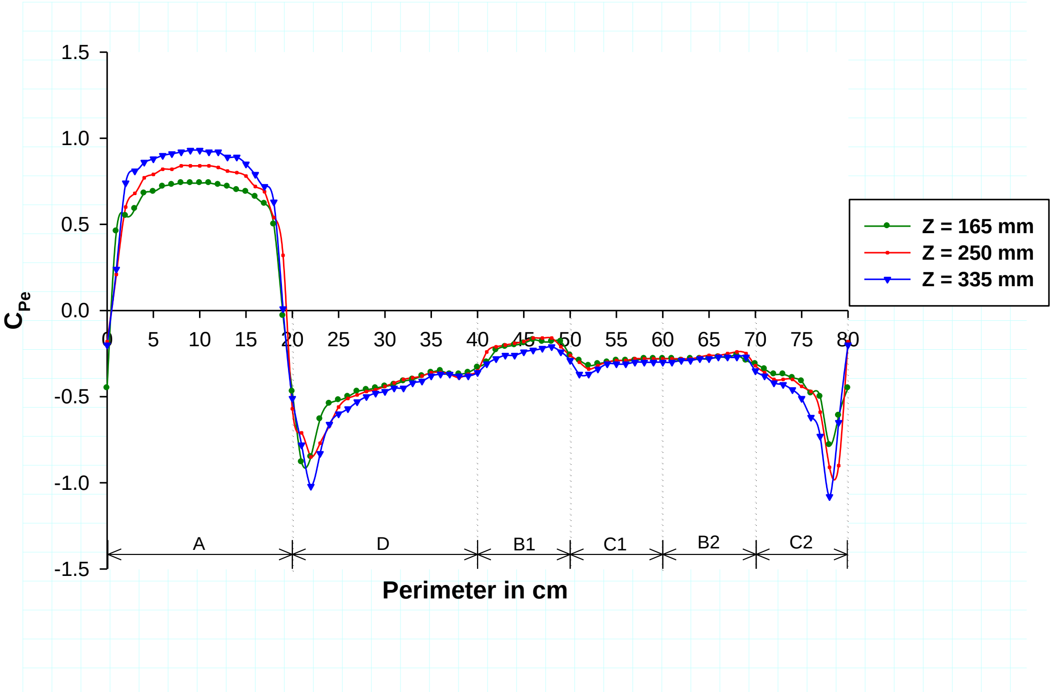

Figure 5. 36: C_{Pe} Along Perimeter L-Shape Model 0° Wind Angle

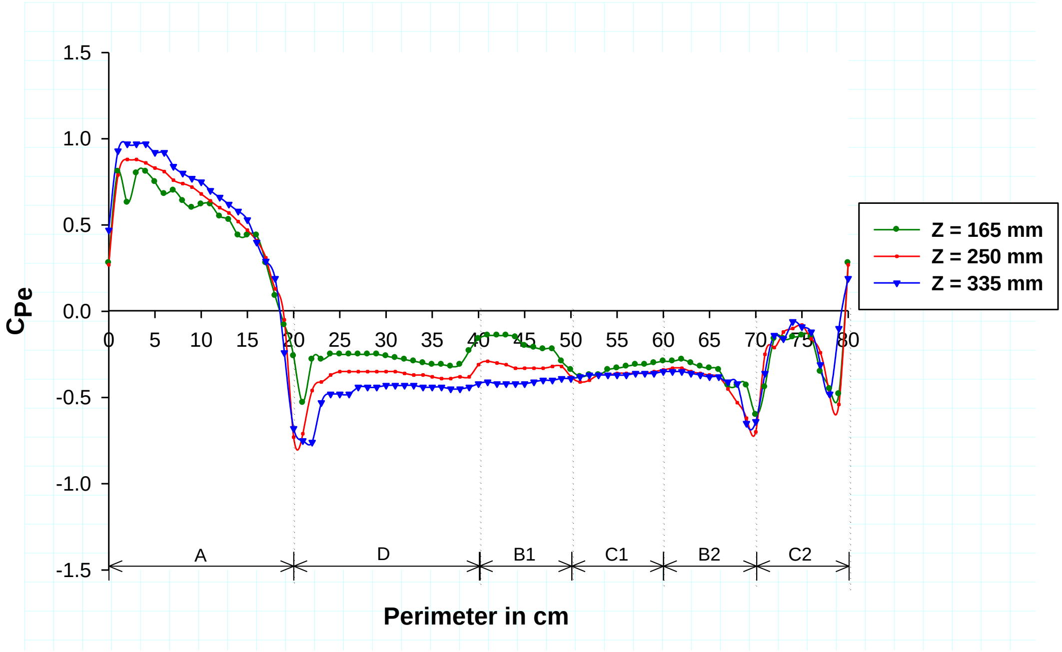

Figure 5. 37: C_{Pe} Along Perimeter L-Shape Model 30° Wind Angle

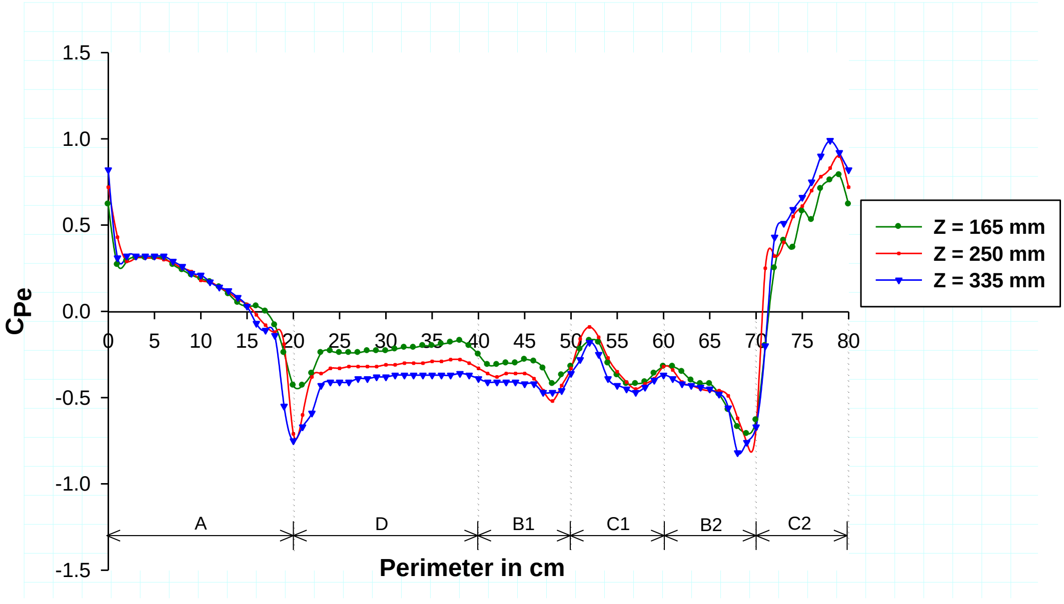

Figure 5. 38: C_{Pe} Along Perimeter L-Shape Model 60° Wind Angle

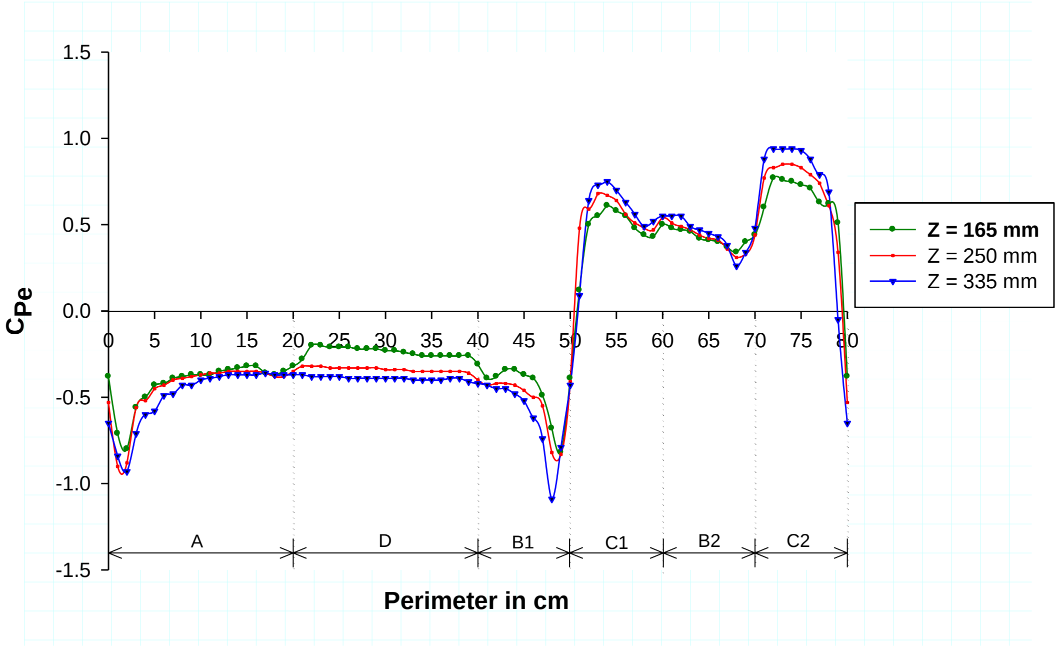

Figure 5. 39: C_{Pe} Along Perimeter L-Shape Model 90° Wind Angle

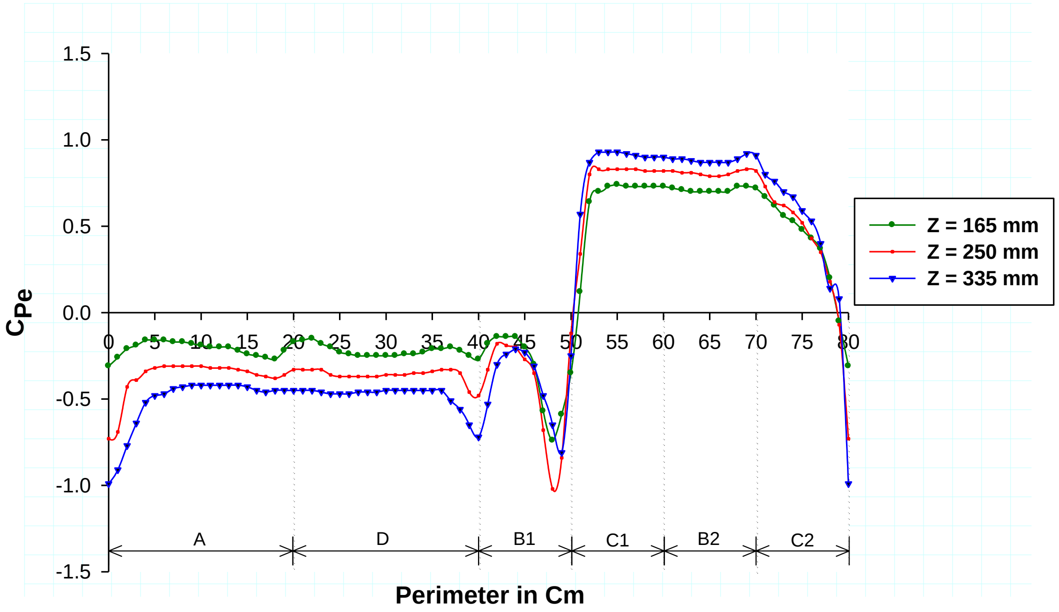

Figure 5. 40: C_{Pe} Along Perimeter L-Shape Model 120° Wind Angle

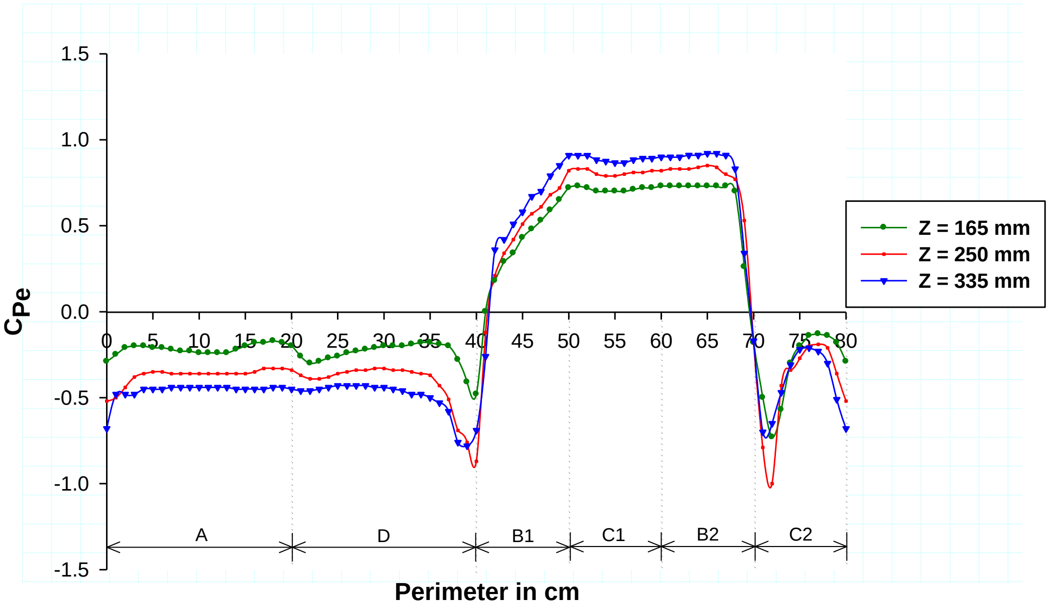

Figure 5. 41: C_{Pe} Along Perimeter L-Shape Model 150° Wind Angle

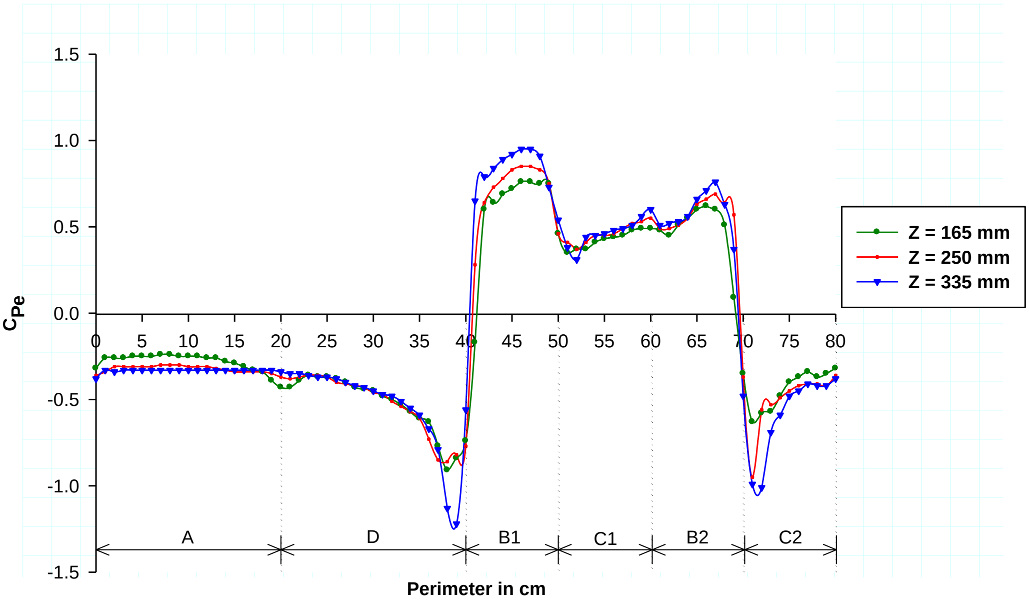

Figure 5. 42: C_{Pe} Along Perimeter L-Shape Model 180° Wind Angle

5.2.11 C_{Pe} Along Central Vertical Line on Faces

Variation of pressure coefficient along the central vertical line on faces are shown in Figure 5.43, 5.44, 5.45, 5.46, 5.47, 5.48 & 5.49 respectively for various wind incidence angles @ 30°. Coefficient of pressure along the central vertical line on faces provides us a complete representation of realistic pressure pattern along heigh. Maximum C_{Pe} value on the face on which positive pressure exists due to direct exposure of wind reaches a value very near to 1.0.

At 0° wind incidence angle face A is perpendicular to direction of wind and exposed to it. We find maximum C_{Pe} value nearly equal to 1.0 on the face at a height of 0.425 m. Rest faces are under suction.

At 30° wind angle face A still possesses positive pressure but the maximum C_{Pe} is less than 1.0 as wind is impinging obliquely on the face. Suction pressure coefficient on faces except on face C2 is almost equal at height of 0.35 m. On face C2 fluctuation in C_{Pe} value along height is observed due to formation of local eddies and high turbulence.

At 60° wind angle both face A and C2 are exposed to wind, but their orientation is not orthogonal. As such positive pressure on the faces exists but the maximum value of coefficient of pressure is less than 1.0. At height of 0.35 m suction pressure coefficient is equalling on all faces bearing suction pressure.

At 90° wind angle face C2 is under direct exposure of wind. Face B2 and C1 do also have positive pressure. However, on face C1, being on the windward side orthogonally, the maximum C_{Pe} value is lower than 1.0 as it is being shadowed by face B2.

At 120° wind angle positive pressure exists on face B2, C1 and C2. On face A and D, C_{Pe} on central vertical lines are almost similar, indicating that the wake flow pattern is similar on the faces. On face B1 suction is almost similar along height. However, local fluctuations at the lower height are observed.

150° face B1, B2 and C1 are possessing positive pressure. On face B2 and C1, which are re-entrant wing faces, almost similar pressure along the height is observed.

At 180° wind angle positive pressure still exists on face B1, B2 and C1. However, since face B1 is directly exposed to wind maximum C_{Pe} value on the face reaches nearly equal to 1.0. Face B2, though on windward side, is being shadowed by face C1 hence the maximum C_{Pe} value on the face is less than 1.0. It is also observed that for all angles of wind incidence suction C_{Pe} on the faces which are under wake region are increasing up to mid height of the model from where it becomes constant.

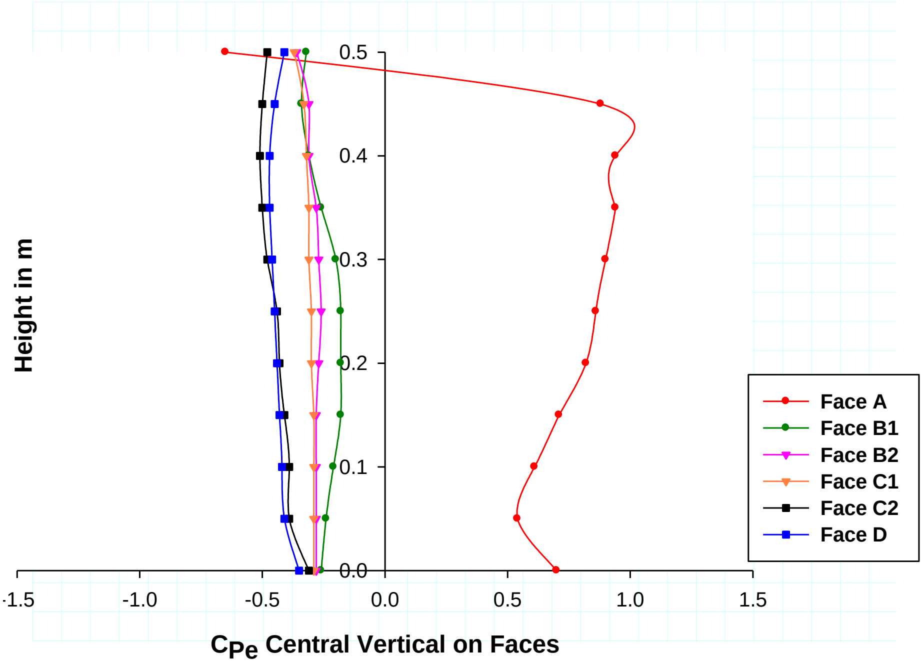

Figure 5. 43: C_{Pe} Along Central Vertical Line on Faces L-Shape Model 0° Wind Angle

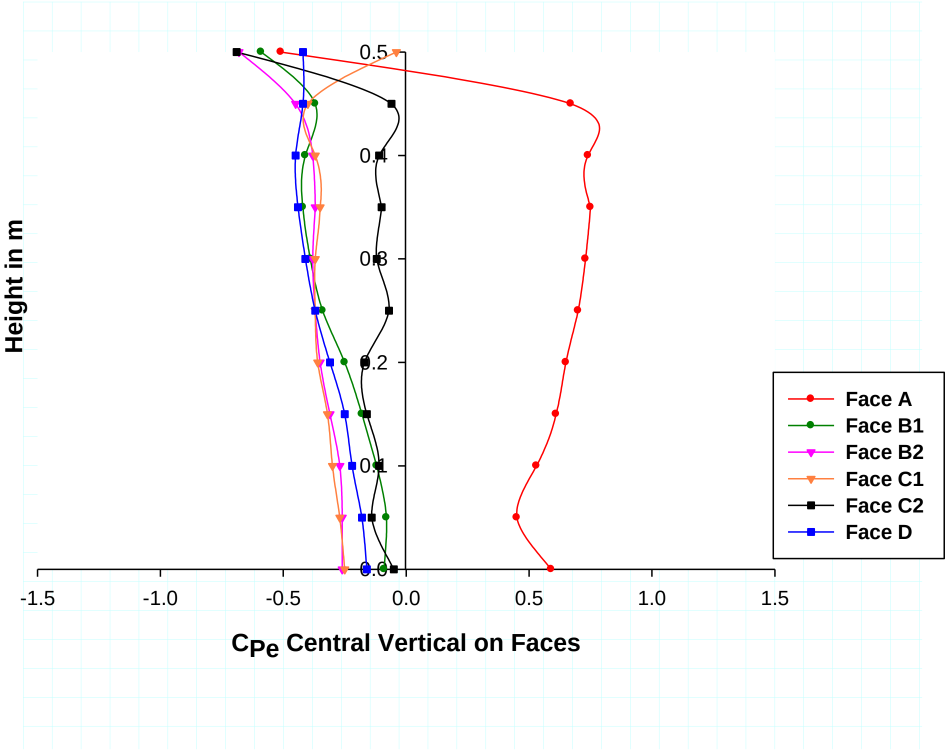

Figure 5. 44: C_{Pe} Along Central Vertical Line on Faces L-Shape Model 30° Wind Angle

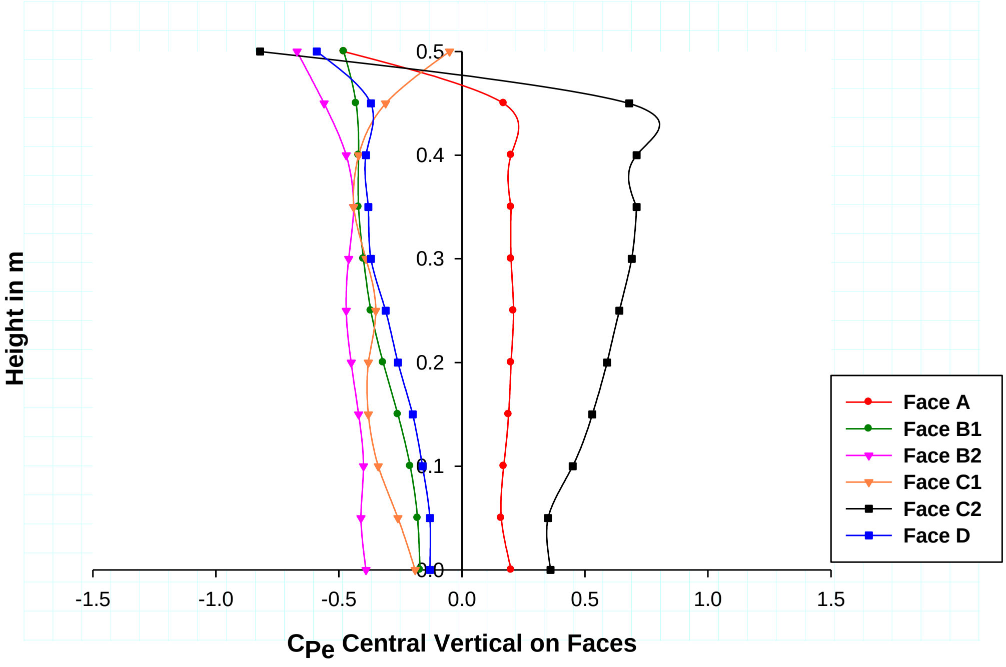

Figure 5. 45: C_{Pe} Along Central Vertical Line on Faces L-Shape Model 60° Wind Angle

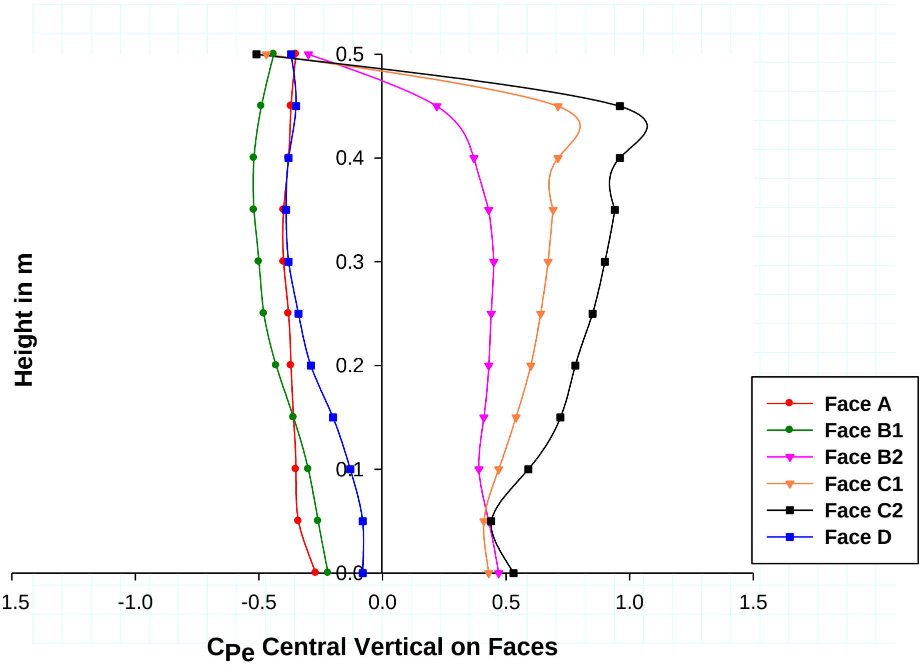

Figure 5. 46: C_{Pe} Along Central Vertical Line on Faces L-Shape Model 90° Wind Angle

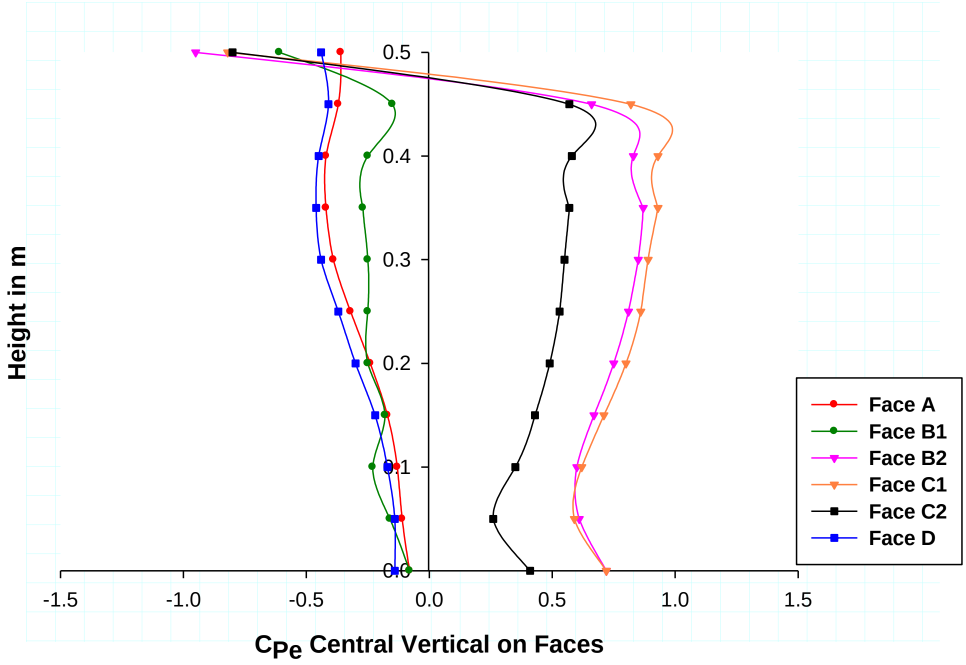

Figure 5. 47: C_{Pe} Along Central Vertical Line on Faces L-Shape Model 120° Wind Angle

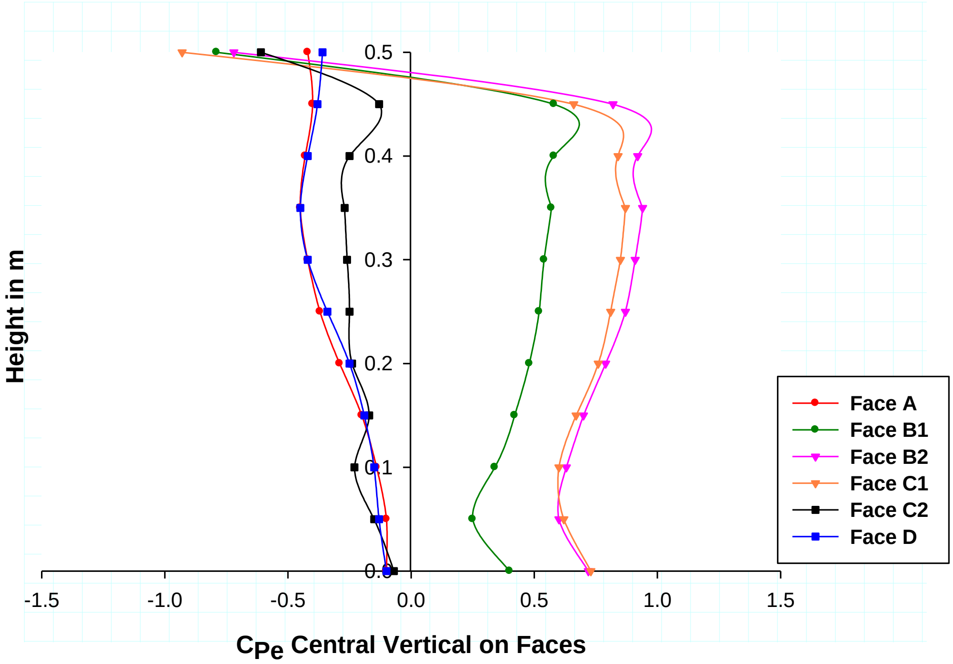

Figure 5. 48: C_{Pe} Along Central Vertical Line on Faces L-Shape Model 150° Wind Angle

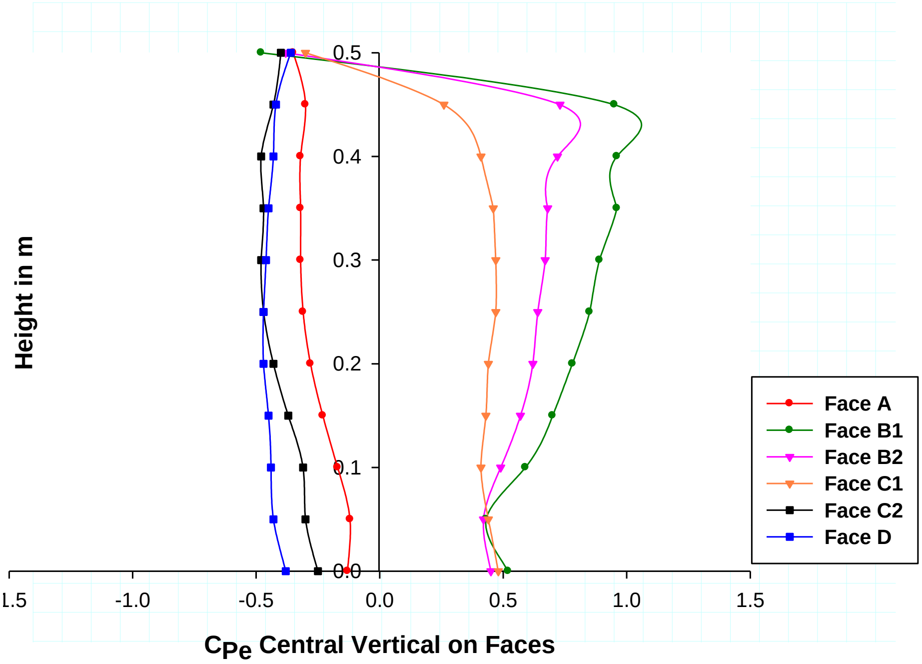

Figure 5. 49: C_{Pe} Along Central Vertical Line on Faces L-Shape Model 180° Wind Angle

5.3 DIAMOND C-SHAPE MODEL

Diamond C shaped model is also symmetrical about one axis in plan. The surface pressure generated around the model has been studied in terms of coefficient of pressure on the faces and flow pattern around the model. Study of wind effect for wind angles from 0° to 180° @ 15° has been conducted. However, due to paucity of space discussion @ 30° in clockwise direction is presented.

5.3.1 C_{Pe} Contour 0° Wind Angle

The distribution of mean coefficient of pressure (C_{Pe}) on the faces of Diamond-shaped model for 0° wind angle of attack is shown in Figure 5.50. Face A is normal to the wind and we find an increase of pressure near the centre of the face. The maximum value of C_{Pe} is 0.85 over a large part of the upper height of the face, falling off rapidly near the edges symmetrically from the vertical centre line of the face. The pressure distribution is parabolic and increases along the height due to increase in wind velocity along the height. The minimum C_{Pe} is -0.83 at the roof edge of the face from where the flow is separating at high speed. The face average value of C_{Pe} is 0.68 (Table 5.3).

The flow separation is taking place from the far end of inclined faces B1 and B2 at high speed. It can be seen in the flow diagram in Figure 5.57. On face B1 and B2 there is steep gradient of pressure from the near end edges to the far end edges. Positive pressure is occurring at the near end of the faces and negative pressure at the far end due to flow separation from the far end edges.

The inclined faces C1 and C2 are under the wake region. It is seen that symmetrical pressure zones are formed on these faces due to vortex generation (Figure 5.57). The pressure is highly negative near the middle height of common edges of inclined faces B1C1 and B2C2 respectively. This due to creation eddies as flow separates from theses edges causing flow reversal.

The recessed faces D1, D2 and E are under wake region. High negative value at the mid height of the model is seen on the recessed faces due to vortex generation created at that height (Figure 5.77).

At the roof Top the difference between the maximum and minimum value of C_{Pe} is -0.27 and -1.47 respectively, the average observed is - 0.53. High suction on the roof top towards the windward face A suggests creation of recirculation cavity on the roof. This phenomenon is important for the design of roof structures.

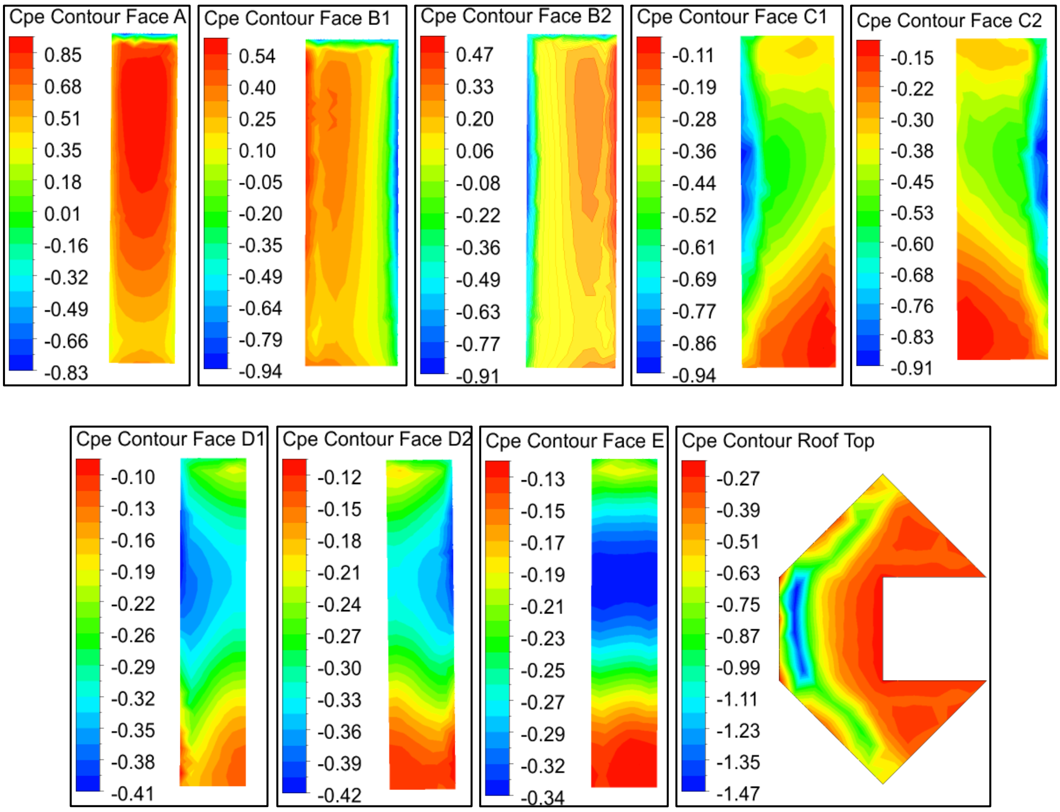

Figure 5. 50: C_{Pe} Contour on Faces & Roof Diamond Shape Model 0° Wind Angle

Table 5. 3: Area Average C_{Pe} on Faces Diamond Shape Model

Face	Wind Incidence Angle						
	0°	30°	60°	90°	120°	150°	180°
A	0.68	0.22	-0.55	-0.83	-0.32	-0.29	-0.27
B1	0.14	-0.48	-0.54	-0.29	-0.23	-0.30	-0.32
B2	0.14	0.55	0.55	0.08	-0.50	-0.42	-0.32
C1	-0.40	-0.35	-0.23	-0.25	-0.37	-0.47	0.21
C2	-0.40	-0.45	-0.41	0.32	0.58	0.57	0.21
D1	-0.27	-0.26	-0.33	-0.42	-0.19	0.48	0.73
D2	-0.27	-0.25	-0.34	-0.54	-0.35	0.32	0.73
E	-0.24	-0.25	-0.32	-0.46	-0.26	0.39	0.76
Roof Top	-0.53	-0.61	-0.57	-0.58	-0.46	-0.58	-0.52

5.3.2 C_{Pe} Contour 30° Wind Angle

At this angle of wind attack orientation of wind is skewed on face A. The maximum value of $C_{Pe(Max)}$ is 0.78, occurring at the leading edge first struck by the wind. Steep gradient of pressure is observed on this face. Towards the far end the decrease in pressure gradient is first slow and becomes more rapid giving minimum value of $C_{Pe(Min)}$ = -1.24. The face average value of C_{Pe} is 0.22.

Separation of flow is occurring a bit upstream from the meeting edge of face AB1. Face B1 is subjected to suction pressure throughout due to side wash. The distribution of pressure variation is vertical on this face. The face average value of C_{Pe} is -0.48.

Portion of face B2 is facing the wind directly and hence subjected to average C_{Pe} of 0.55. The maximum value of coefficient of pressure is at the leading edge near the top. The distribution of pressure variation is half parabolic on the face which reduces at the far end edge.

Face C1 and C2 are under wake. Effect of back wash as well as side wash can be seen on the pressure contour of face C1. The coefficient of pressure on face C1 near the left upper half of the figure is low (-0.77) and the maximum is -0.15 at the lower right half of the diagram. But, pressure distribution on face C2 is almost vertical with high gradient.

The recessed faces D1, D2 and E are also under wake. Due to reflection of flow within the recessed portion, area average C_{Pe} on the faces are almost same (-0.26, -0.25 and -0.25 respectively).

Now coming to the roof top, the small portion in blue colour near the leading edge suggest a recirculation cavity with high suction (C_{Pe} = -1.86). The pressure distribution is horizontal and is maximum on the leeward side.

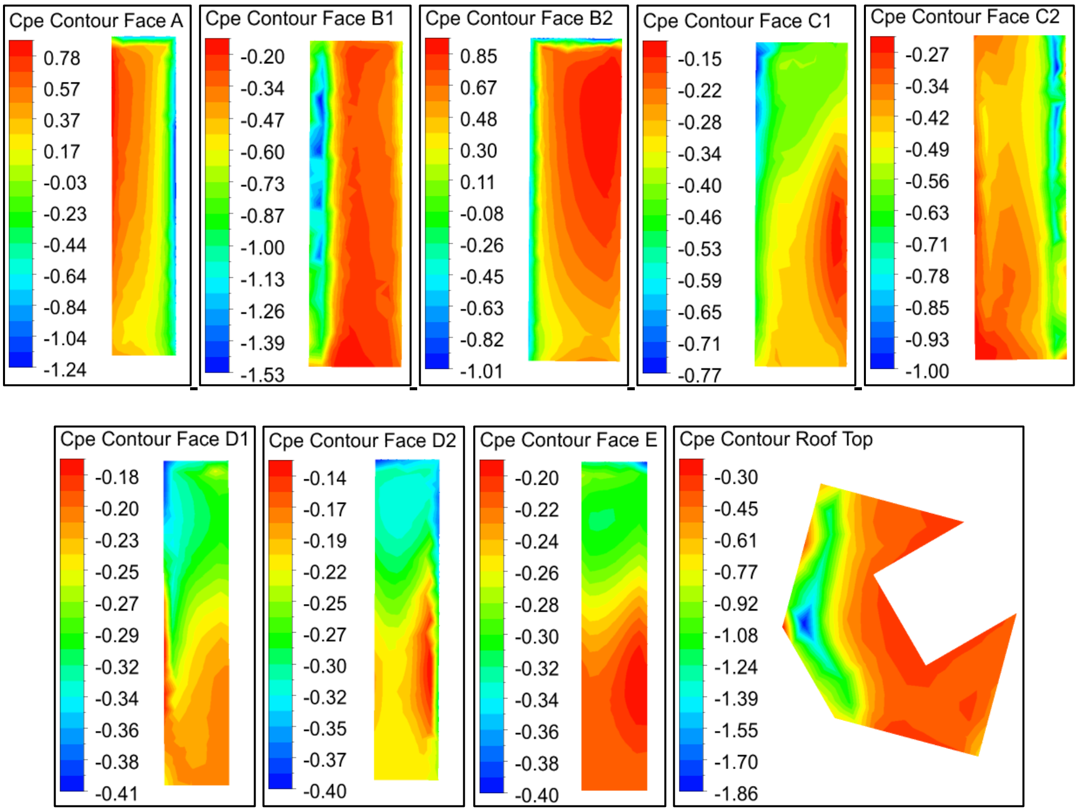

Figure 5. 51: C_{Pe} Contour on Faces & Roof Diamond Shape Model 30° Wind Angle

5.3.3 C_{Pe} Contour 60° Wind Angle

Due to skewed angle of incident of wind, face A is subjected to highly fluctuating suction pressure across the width. Wind is separating from the near end edge as well as far end edge of face A (Figure 5.63). Bubbles of concentration of pressure is observed at the near end edge and in the middle of the face. This is due to creation of small eddies and shear layer at the points. The pressure gradient is seen negative from the middle towards both edges. Towards the far end edge gradient is highly negative. The face average C_{Pe} on face A is -0.55.

Major portion of the face B1 is under wake. Wind separation is taking place from the near end edge of the face. High suction is observed (C_{Pe} = -1.95) at edge on upper heights. The contour isobars are almost vertical leaning towards the far end bottom. Pressure in major portion of the face is almost identical and reducing towards the near end with high gradient.

Face B2 is facing the wind not exactly orthogonally but a bit inclined. Wind is striking the face eccentrically (Figure 5.63) and hence the pressure isobars are not exactly symmetrical about the central vertical axes. The face area average value of C_{Pe} is 0.55.

Face C1 is under wake and suction is increasing from bottom to top due to backwash. High suction is observed at the top corners.

Face C2 is the side face. Wind is separating from the near edge of the face and effect of side wash can be seen. The contour isobars are vertical in nature. In most part of the face pressure is not varying much, but towards the rear edge pressure gradient is high. The face area average C_{Pe} on face C2 is -0.41.

The re-entrant faces D1, D2 and E are under wake region. The face average C_{Pe} on these faces are almost same. Vales are -0.33, -0.34 and -0.32 respectively. A small vortex is created within the recessed cavity (Figure 5.63) and hence some interfering effects might not be ruled out.

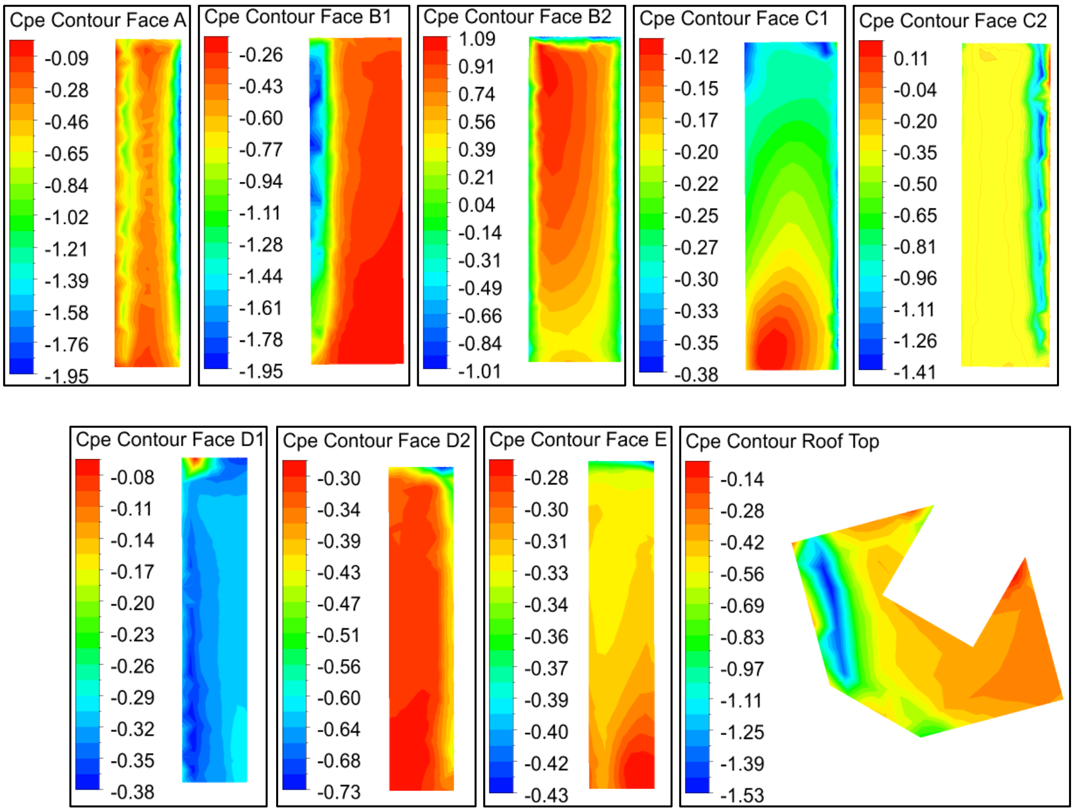

Figure 5. 52: C_{Pe} Contour on Faces& Roof Diamond Shape Model 60° Wind Angle

5.3.4 C_{Pe} Contour 90° Wind Angle

Wind is striking at the common edge of face B2 and C2. The separation of wind is taking place from the far ends of the faces. Pressure on face B2 and C2 are almost identical. Half parabolic pressure distribution is seen on both the faces. The pressure is more at the near ends and reducing towards the far end of the faces.

Face A is side face for this angle of wind attack. Since flow is separating from the meeting edge of oblique face B2 and face A, large suction is seen at the near end edge of face A suggesting formation of shear layer and micro level eddies at the place. The contour isobars are vertical and pressure gradient at the near end edge of face A is higher. At the centre it becomes almost identical with little variation towards the far end edge. Among all the faces and for all wind angles of attack face A is subjected to maximum area average suction coefficient value (C_{Pe} = -0.83).

Face B1 and C1 are both under wake. The pattern of contour isobars is almost identical and face area average coefficient of pressure are varying slightly, being -0.29 on face B1 and -0.25 on face C1.

Secondary small vortex is seen within the re-entrant cavity of faces D1, D2 and E (Figure 5.66). Due direct incidence of wind at top corner of face D1 and E, positive pressures at the corner are developed. On rest parts of face D1 and E and also on face D2 suction is created due to effect of secondary vortex created within the re-entrant cavity. On most part of face D2 identical pressure is developed. However, pressure at the top right outer corner of the face suction pressure having intense value (C_{Pe} = -1.50) is seen. During the cladding design this aspect must be born in mind by the designers. The face average coefficient of pressure on faces D1, D2 and E are -0.42, -0.54 and -0.46 respectively.

On the roof top recirculation cavity is seen parallel to windward faces B2 and C2 with high intensity of suction (C_{Pe}= -2.05). Positive pressure is observed at the roof edge of face D1. The average C_{Pe} on the roof is -0.58.

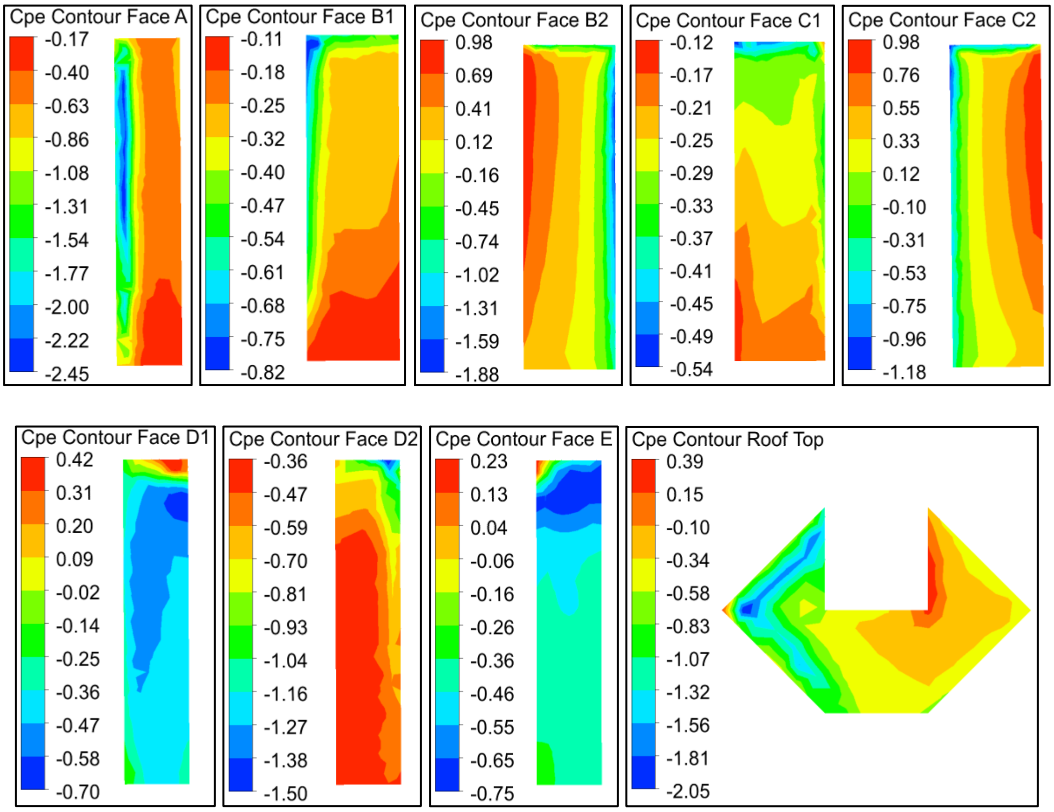

Figure 5. 53: C_{Pe} Contour on Faces & Roof Diamond Shape Model 90° Wind Angle

5.3.5 C_{Pe} Contour 120° Wind Angle

Wind is striking on inclined face C2 (nor orthogonal to wind direction) eccentrically (Figure 5.69). Positive pressure is seen on fae C2. The shape of pressure distribution is half parabolic, shifted towards the position of stagnation point. The area average C_{Pe} on the face is 0.58. Flow is separating from the leading edges with unequal intensity. The intensity of velocity at the point of separation nearest to the stagnation point is more than the other edge.

Face A, B1, and C1 are under wake region. As such, these faces are under suction pressure. The pattern of pressure distribution on face A is more or less vertical isobars except at the bottom where it is diagonal near bottom. On face B2, the isobars are horizontal and effect of upwash is seen on the face as suction is increasing along the height. On face C1 the pattern is vertical with high negative gradient away from the wake. A portion at the top corner of the far end edge from wake positive pressure is seen.

Flow is striking at top corner of the upwind edge of face D1 where positive pressure is observed. On rest of the face isobars are vertical of almost uniform nature. The aera average C_{Pe} on face D1 is -0.19. A secondary vortex is created within the recessed cavity of face D1, D2 and E. Pattern of pressure on face D2 and E are vertical. On face D2 gradient of isobars are from the recessed corner towards the outer side of the face. Suction at roof level on face E is high suggesting that wind is escaping from there forming a recirculation cavity at the roof level (Figure 5.81).

Face B2 is side face for this angle of attack. The pressure contours are vertical in nature. Towards the near end suction is more due to creation of local eddies. It is progressively recovering towards the middle and again reducing towards the far end. The face area average C_{Pe} on this face is -0.50.

On the roof top high suction is seen above the stagnation point on face C2. Major portion of roof is under constant suction pressure with face average coefficient being -0.46. For all wind angles area average suction on roof is lowest for this angle of wind attack.

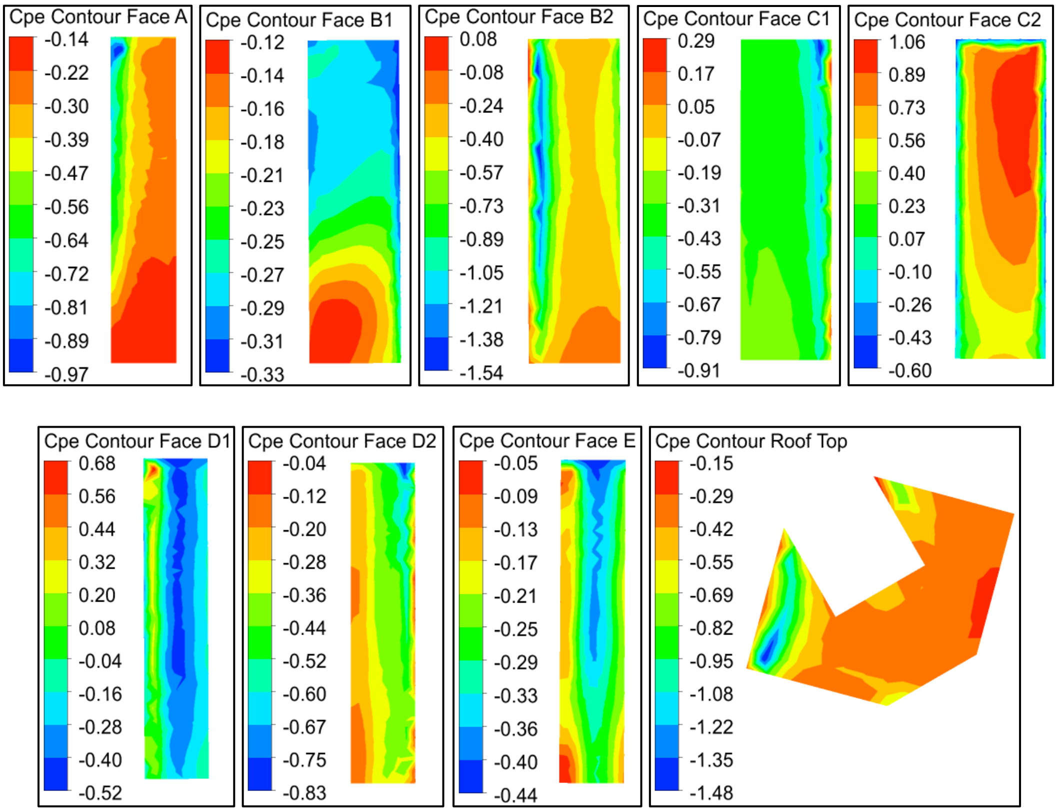

Figure 5. 54: C_{Pe} Contour on Faces & Roof Diamond Shape Model 120° Wind Angle

5.3.6 C_{Pe} Contour 150° Wind Angle

The stagnation point on this angle of attack is still on face C2, but its position is shifted towards the other side of the face in comparison to 120° wind angle of attack. Accordingly, as expected, positive pressure is developed on face C2 but the concentration of isobars is shifted towards face D2. The area average ($C_{Pe} = 0.57$) on this face is still almost the same as that of in case of 120° wind angle. The separation of flow is taking place from the far end edge of face C2 and near end edge of confluence of face C1D1 (Figure 5.72).

The flow is also striking on face D1 at the open-end edge. As a result, circulation of wind within the recessed cavity of faces D1, D2 and E is seen creating an interference effect on faces E and D2. The pressure is positive on all the three recessed cavity faces D1, D2 and E with area average C_{Pe} being 0.48, 0.32 and 0.39 respectively. The pattern of pressure contours on these faces are more or less vertical. On perusal of C_{Pe} contours (Figure 5.55) it is seen that suction on these faces is created at the roof top.

Face B2 and C1 are the side faces. The pattern of pressure isobars is vertical on these faces. Moreover, high negative pressure is seen on face C1 near the edge from where flow separation is taking place. The maximum value of suction on face C1 is -1.33.

Face A and B1 are under wake region. The contour pattern on face A is slant. On face B1 it is almost horizontal. The area average C_{Pe} are almost equal, being -0.29 on face A and -0.3 on face B1.

On the roof a high suction point is seen at the top of face D1 on the outer side unlike in other cases of wind angles where it is above the face on which the wind is striking first.

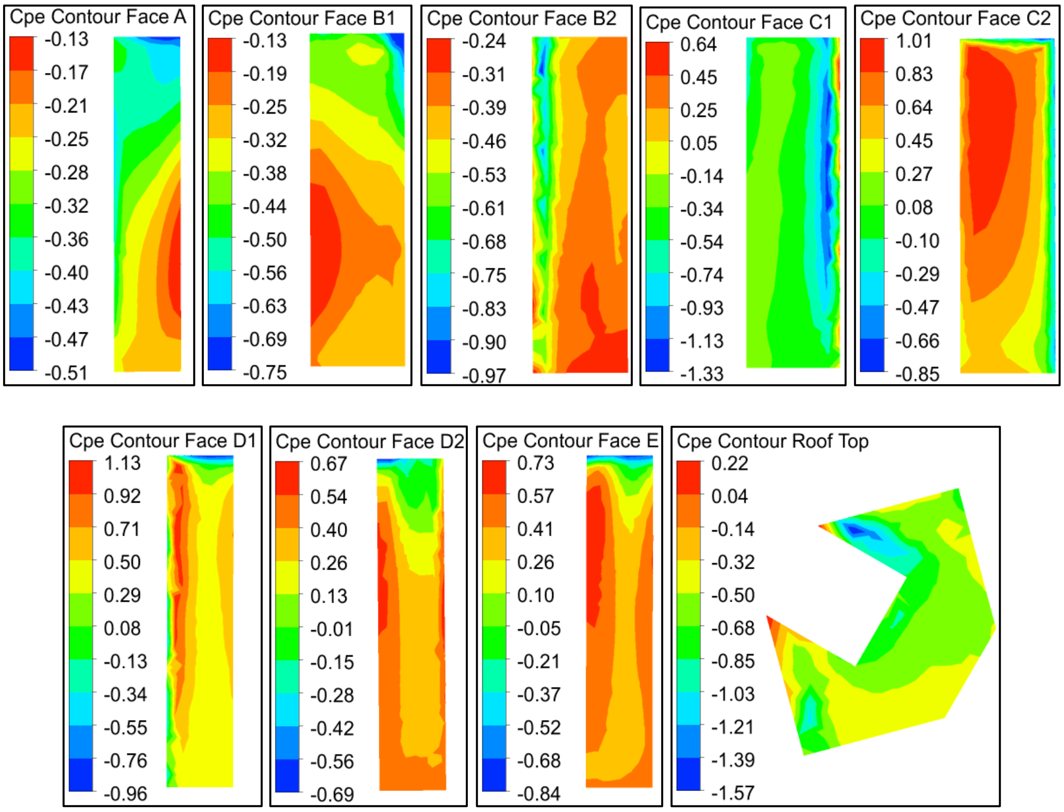

Figure 5. 55: C_{Pe} Contour on Faces & Roof Diamond Shape Model 150° Wind Angle

5.3.7 C_{Pe} Contour 180° Wind Angle

For 180° angle of attack, the flow is striking on face E and stuck up within the recessed cavity. Interference effect is seen on faces D1 and D2 as the flow is reflecting from face E to D1 and D2. Being the side faces the pressure on face D1 and D2 are not negative but positive in nature due to interference effect. The contour isobars on all the three recessed faces D1, D2 and E are horizontal. For all wind angle of attack and for all faces maximum C_{Pe} = 0.76 on face E is observed. Face D1 and D2 are having area average C_{Pe} = 0.73 each.

Flow is slipping past the surface of faces C1 and C2 before separating from the far ends of the faces. As such, positive pressure is also developed on these faces. The area average of C_{Pe} on the face C1 and C2 both is 0.21 each. The pattern of pressure contours on these faces are half parabolic and positive at the near end of the faces. This half parabolic positive contour lines are changing progressively to vertical suction isobars towards far end edges.

Faces A, B1 and B2 are under wake. Relatively larger wake formation is seen on the leeward side (Figure 5.75). The area average C_{Pe} values on faces B1 and B2, is -0.32 each. On face A the area average C_{Pe} is -0.27. Contour lines are almost horizontal on all the tree faces.

On the roof large portion along the recessed faces high suction is seen especially above face E on which the flow is impinging. This is the vital portion for design of roof structures. On most part of the roof suction does exist except at the small portion of the corners towards the upwind direction where positive pressure exists.

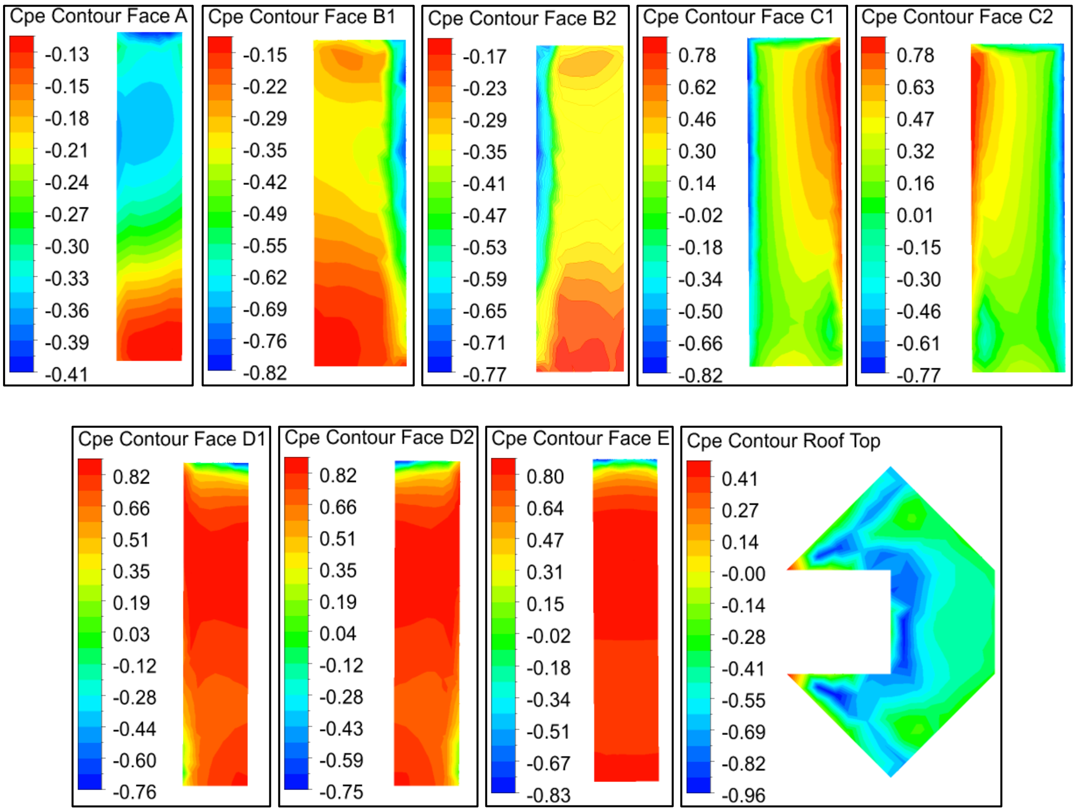

Figure 5. 56: C_{Pe} Contour on Faces & Roof Diamond Shape Model 180° Wind Angle

5.3.8 Wind Flow Pattern

Streamlines of wind flow patterns for all the discussed wind angles from 0° to 180° @ 30° have been shown in Figure 5.57, 5.60, 5.63, 5.66, 5.69, 5.72 & 5.75 at different heights of the model viz Z = 0.165 m, Z = 0.250 m and Z = 0.335 m and Figure 5.58, 5.61, 5.64, 5.67, 5.70, 7.73 & 5.76 show the velocity contours at the same heights for different wind incidence angles. Velocity vector diagrams at different heights for varied wind angles are shown in Figure 5.59, 5.62, 5.65, 5.68, 5.71, 5.74 & 5.77

The importance of these picture in understanding the effect of wind flow in pressure distribution around model envelope and their characteristics has already been discussed in para 4.1 and 4.2.5.

It can be observed that separation of wind flow and formation of vortices in the wake region are different in intensity and size for different wind angle of attack. Pattern of pressure distribution on different faces are corelated with the flow pattern and the velocity contours. Positive pressure on faces occurred due to direct wind force. Negative pressure occurred on faces due to suction force acting on the surfaces. Similarities in pressure coefficient on faces occurred due to equal and opposite faces and the wind flow equally affecting the faces when the flow patterns are symmetrical. In case of unsymmetrical flow pattern, the pressure on faces is dissimilar.

At 0° wind incident angle two distinct symmetrical vortices with a larger gap in between the two are formed. One secondary small vortex each is also formed on the leeward face C1 and C2. The size of the vortices is gradually reducing form bottom to top. Wake width is more compared to earlier models. As such, higher drag force is expected on the model.

At 30° wind incidence angle two distinctly large, almost symmetrical, vortices are seen behind the model. No vortex is seen behind face C1 or C2. But, a secondary vortex is observed within the recessed cavity. Width of the wake is smaller compared to 0° wind angle of attack.

At 60° wind incidence angle two dissimilar vortices are formed with one secondary small vortex within the recessed cavity at the corner of faces D1 and E. Width of the wake is still smaller than that at 30° wind angle.

At 90° wind angle, nearly similar vortices are formed with a small secondary vortex within the recessed cavity near face D1. Due to presence of recessed cavity, concentration of velocity arrows on the surface of face C1 indicates that flow is speeding up on this face compared to the adjacent similarly oriented face B1.

At 120° wind angle of attack beside the two large dissimilar vortices one secondary vortex within the recessed cavity engulfing the entire cavity are formed.

At 150° wind angle the size of the vortices behind the model are larger than that in case of 120° wind angle and secondary vortex is seen within the entire recessed cavity.

At 180° wind incident angle even more larger vortices similar in nature are developed behind the model and no vortex is seen within the recessed cavity as wind is directly striking into it on face E. Wake width seems to be more than that at 0° wind angle.

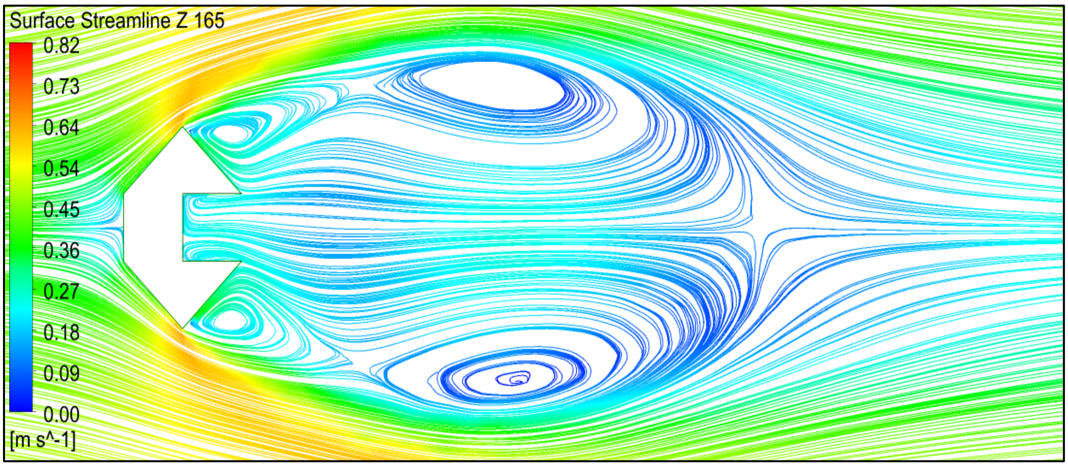

(a) Surface Streamline at Height Z = 165 mm

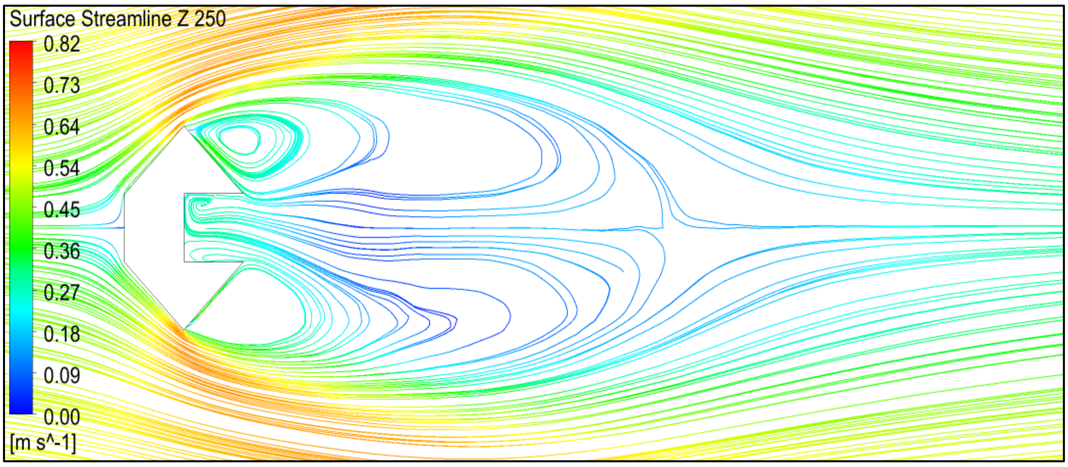

(b) Surface Streamline at Height Z = 250 mm

Figure 5. 57: Surface Streamline Diamond Shape Model 0° Wind Angle (Contd.)

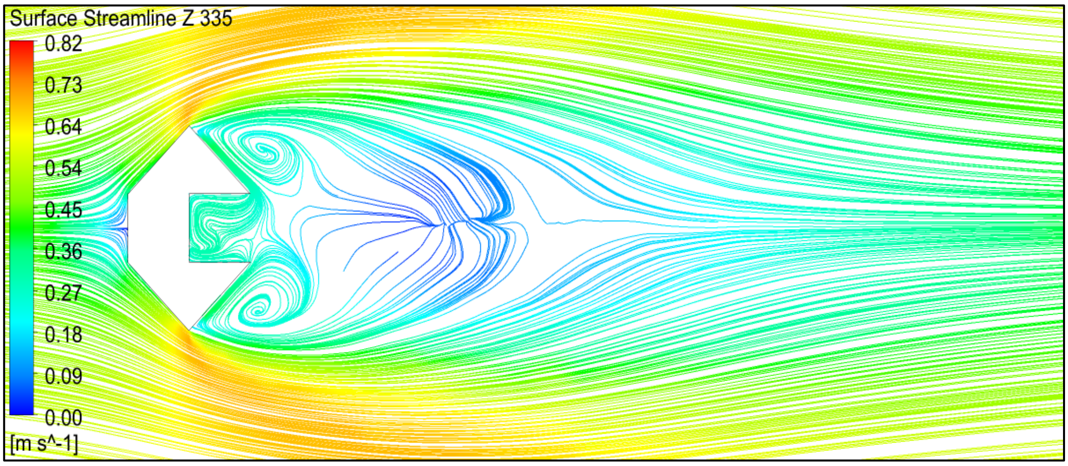

(c) Surface Streamline at Height Z = 335 mm

Figure 5. 58: Surface Streamline Diamond Shape Model 0° Wind Angle

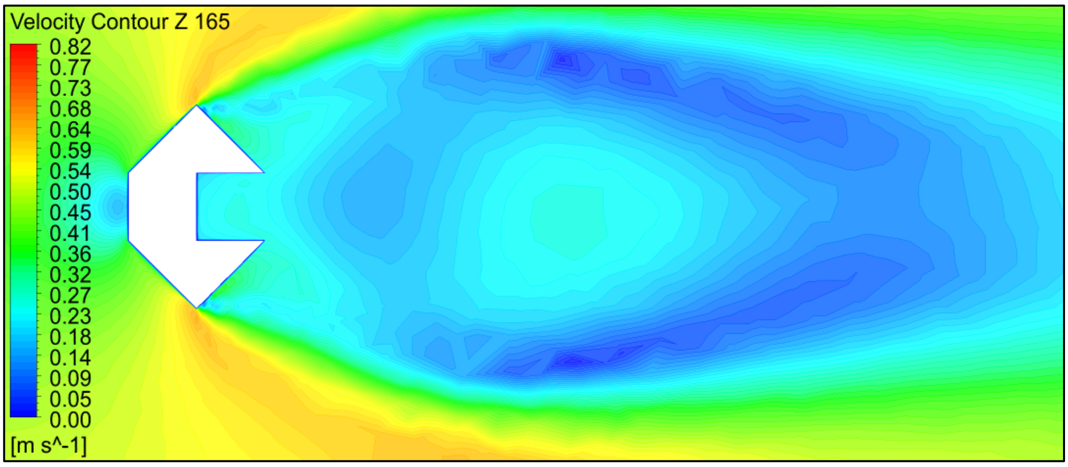

(a) Velocity Contour at Height Z = 165 mm

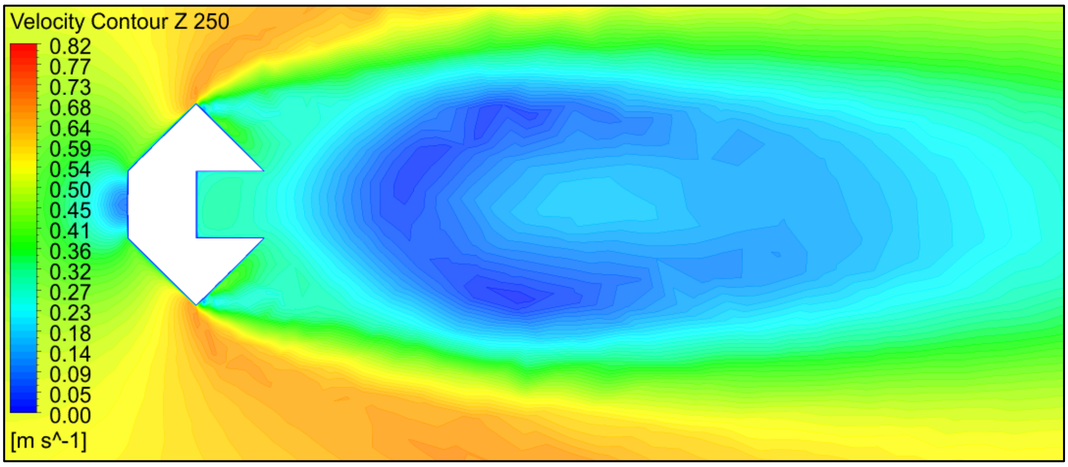

(b) Velocity Contour at Height Z = 250 mm

Figure 5.58: Velocity Contour Diamond Shape Model 0° Wind Angle (Contd.)

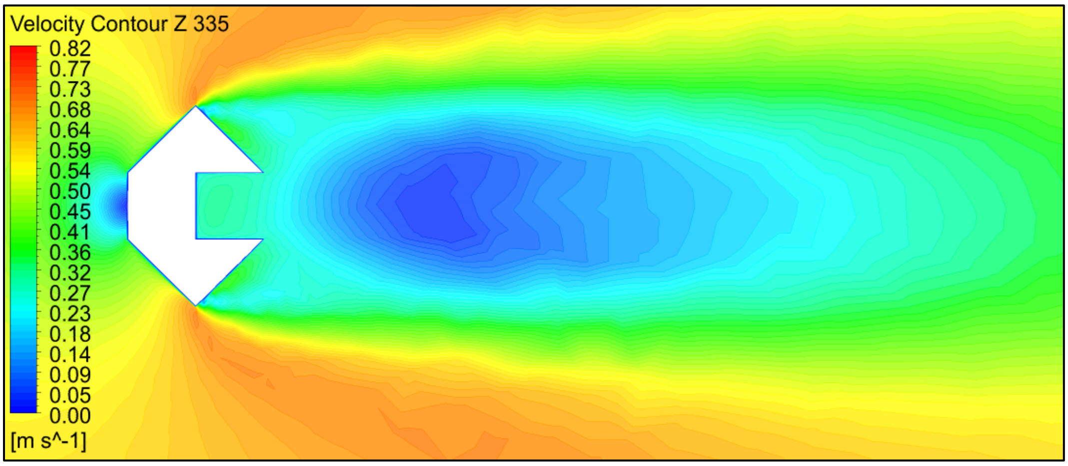

(c) Velocity Contour at Height Z = 335 mm

Figure 5. 59: Velocity Contour Diamond Shape Model 0° Wind Angle

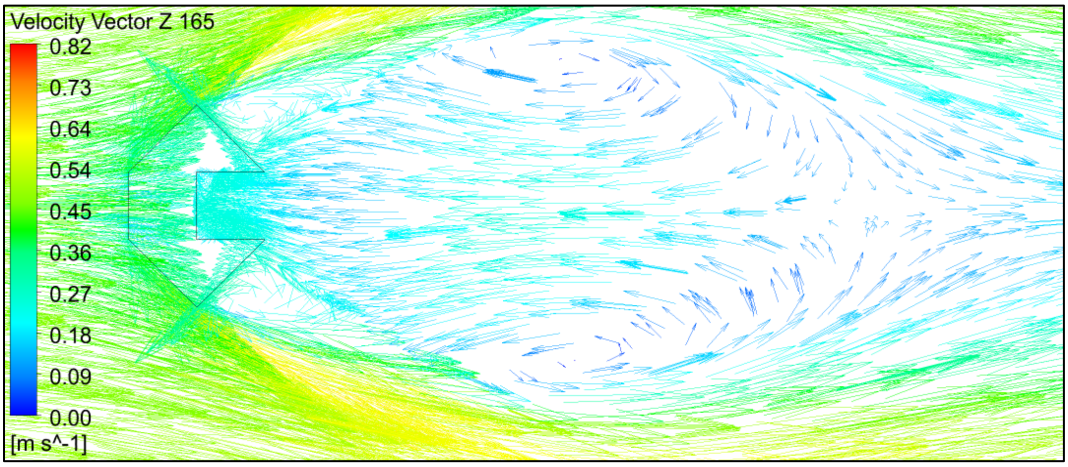

(a) Velocity Vector at Height Z = 165 mm

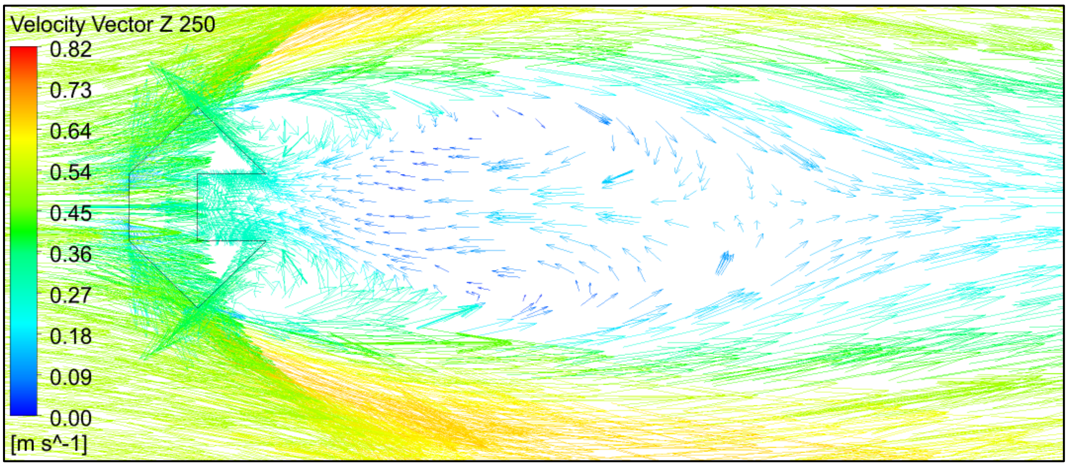

(b) Velocity Vector at Height Z = 250 mm

Figure 5. 59: Velocity Vector Diamond Shape Model 0° Wind Angle (Contd.)

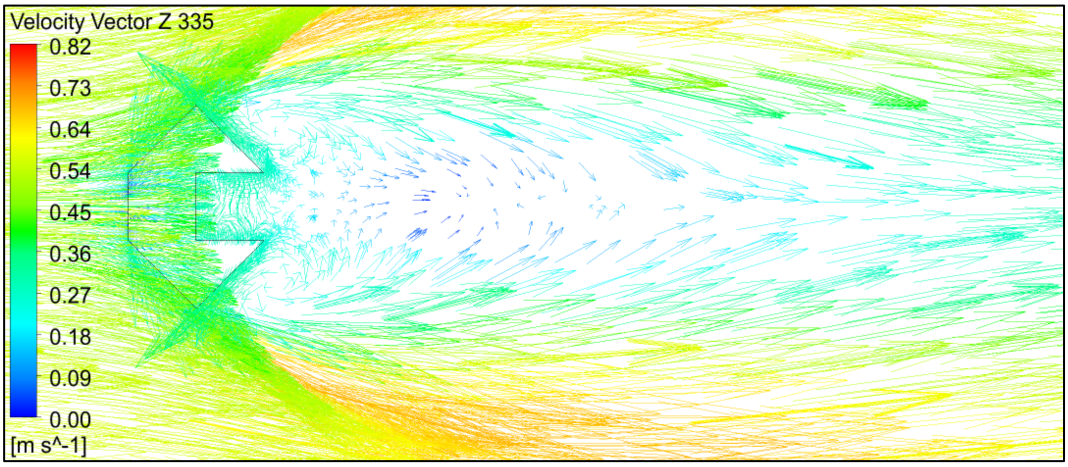

(c) Velocity Vector at Height Z = 335 mm

Figure 5. 60: Velocity Vector Diamond Shape Model 0° Wind Angle

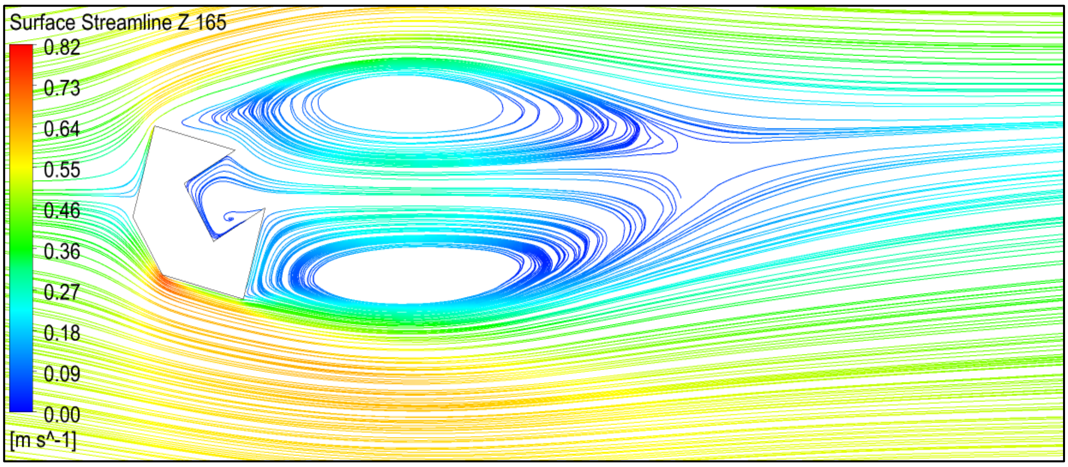

(a) Surface Streamline at Height Z = 165 mm

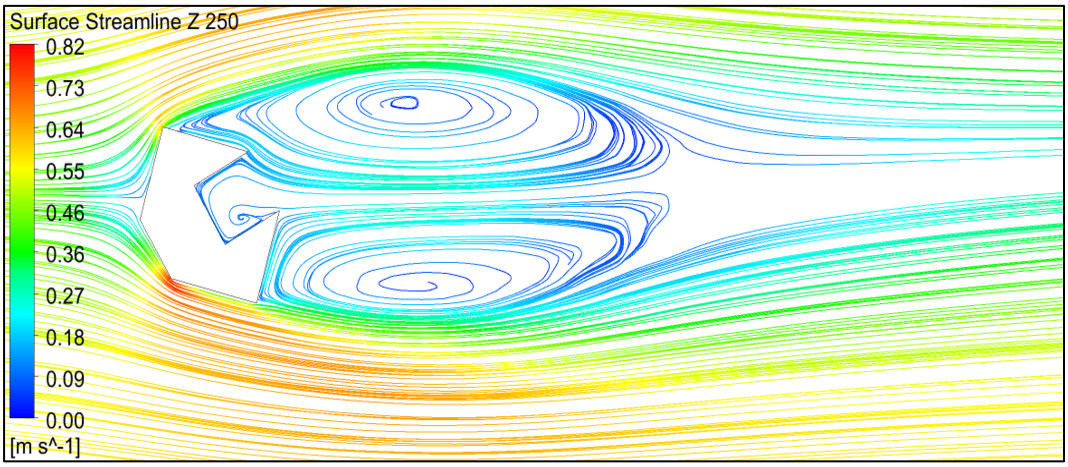

(b) Surface Streamline at Height Z = 250 mm

Figure 5.60: Surface Streamline Diamond Shape Model 30° Wind Angle (Contd.)

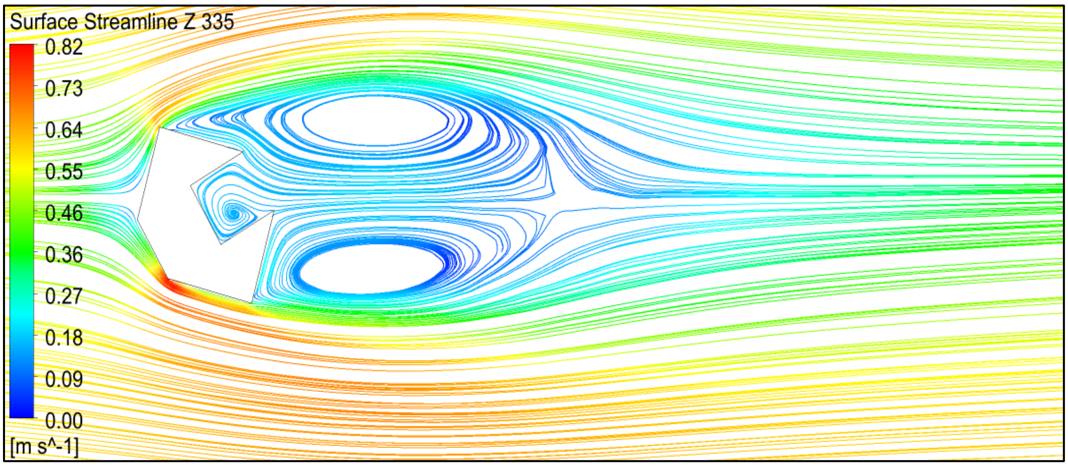

(c) Surface Streamline at Height Z = 335 mm

Figure 5. 61: Surface Streamline Diamond Shape Model 30° Wind Angle

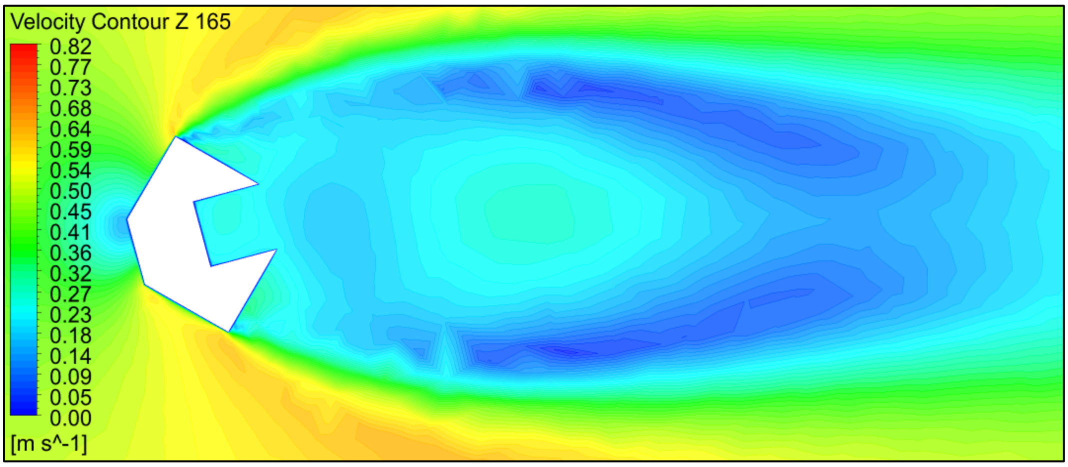

(a) Velocity Contour at Height Z = 165 mm

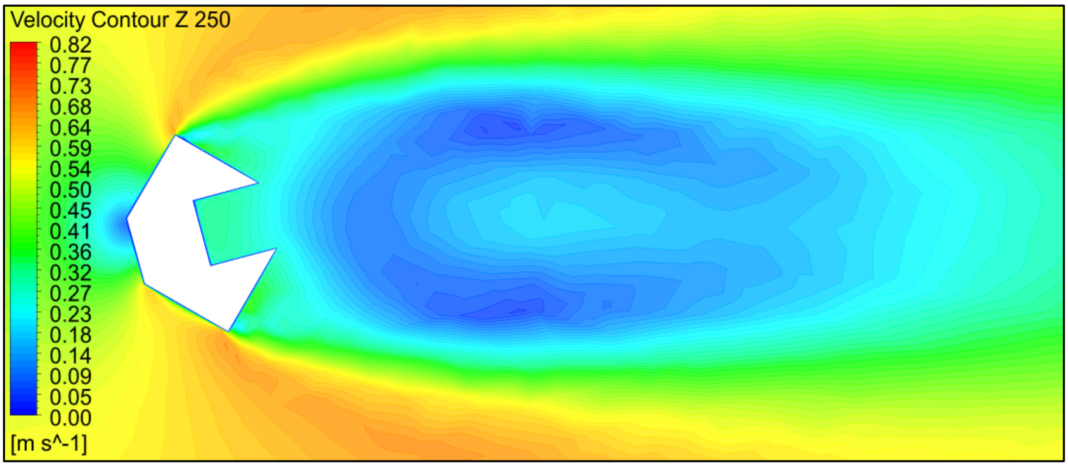

(b) Velocity Contour at Height Z = 250 mm

Figure 5.61: Velocity Contour Diamond Shape Model 30° Wind Angle (Contd.)

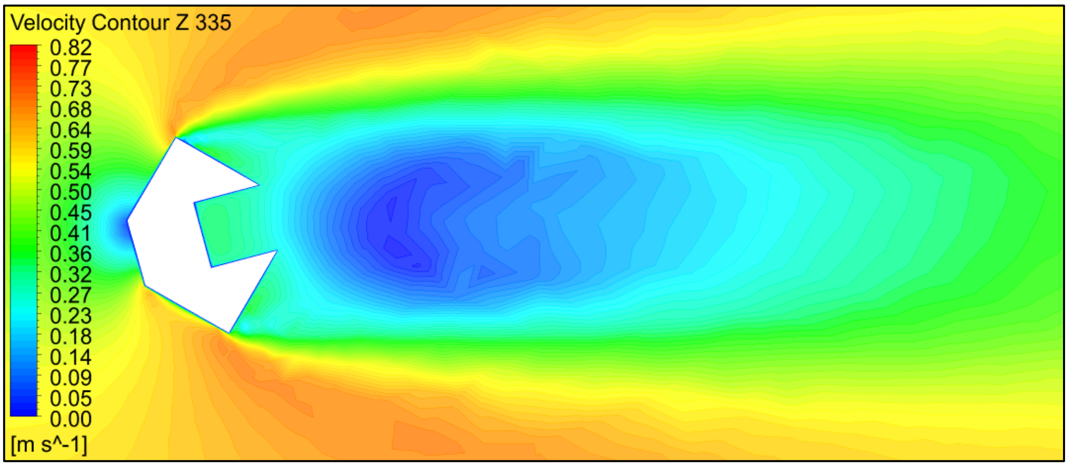

(c) Velocity Contour at Height Z = 335 mm

Figure 5. 62: Velocity Contour Diamond Shape Model 30° Wind Angle

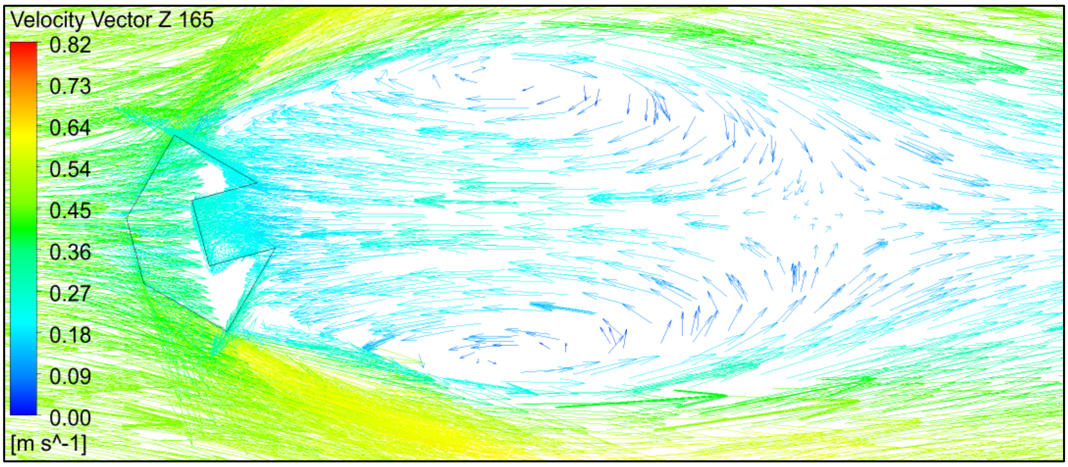

(a) Velocity Vector at Height Z = 165 mm

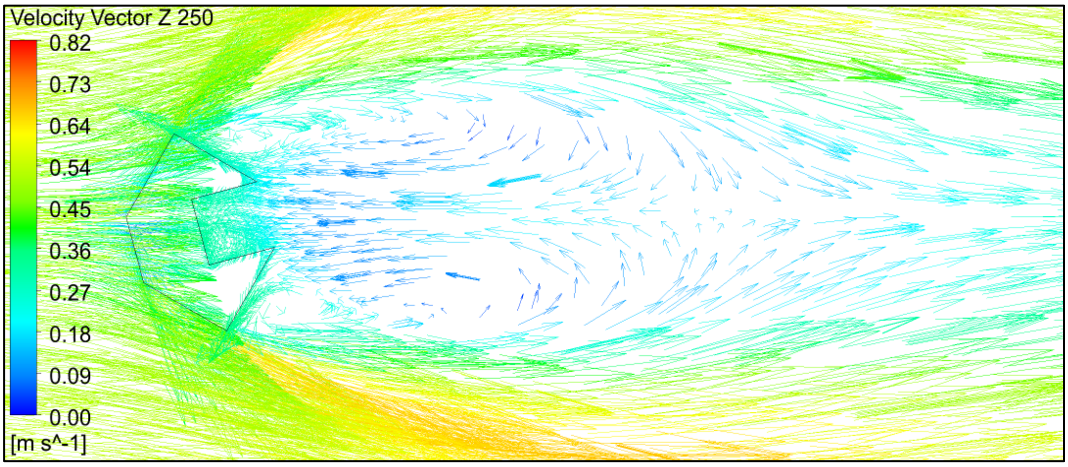

(b) Velocity Vector at Height Z = 250 mm

Figure 5. 62: Velocity Vector Diamond Shape Model 30° Wind Angle (Contd.)

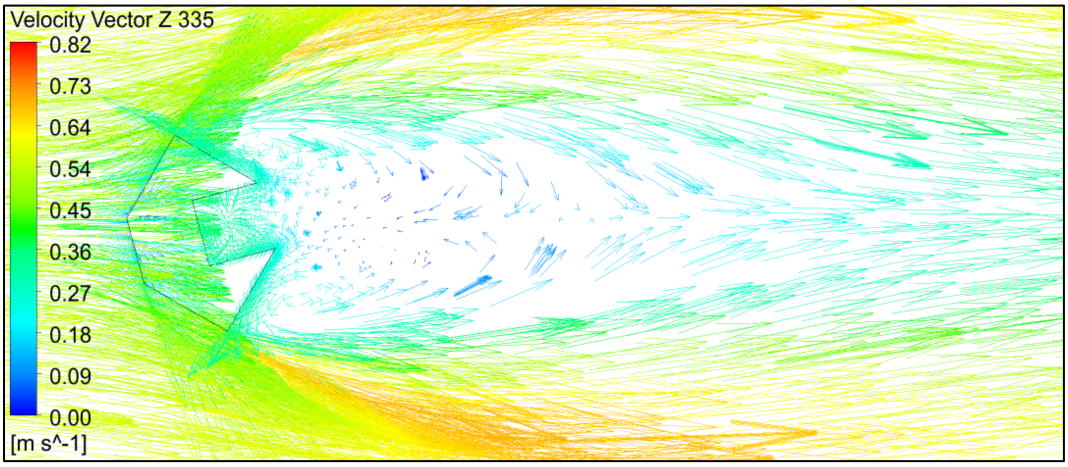

(c) Velocity Vector at Height Z = 335 mm

Figure 5. 63: Velocity Vector Diamond Shape Model 30° Wind Angle

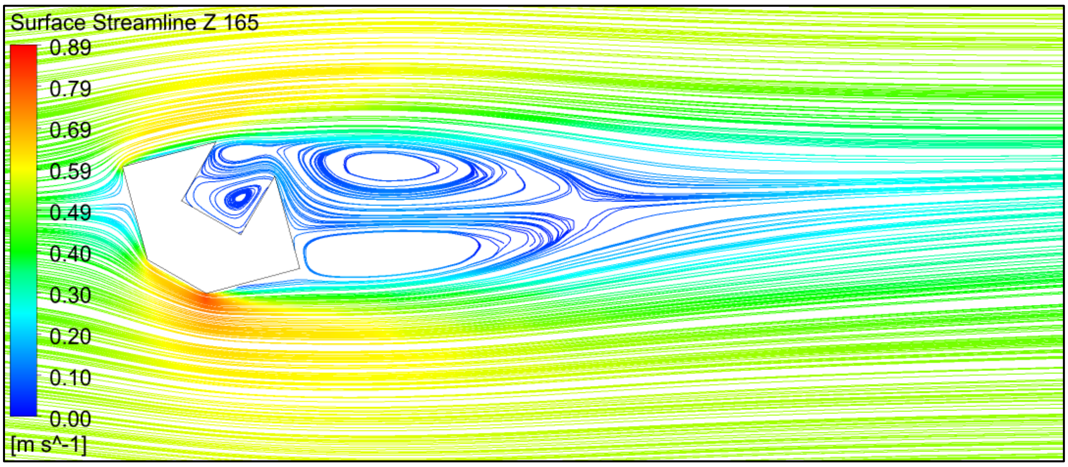

(a) Surface Streamline at Height Z = 165 mm

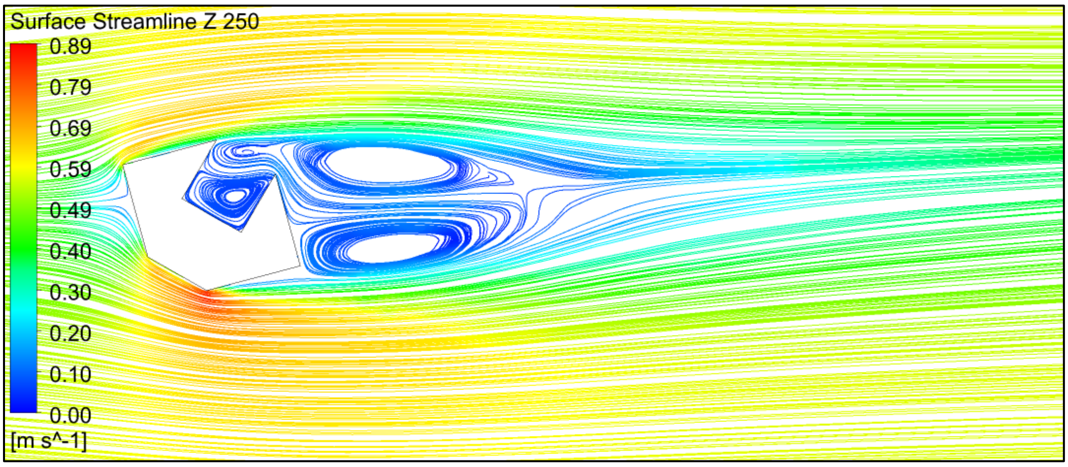

(b) Surface Streamline at Height Z = 250 mm

Figure 5.63: Surface Streamline Diamond Shape Model 60° Wind Angle (Contd.)

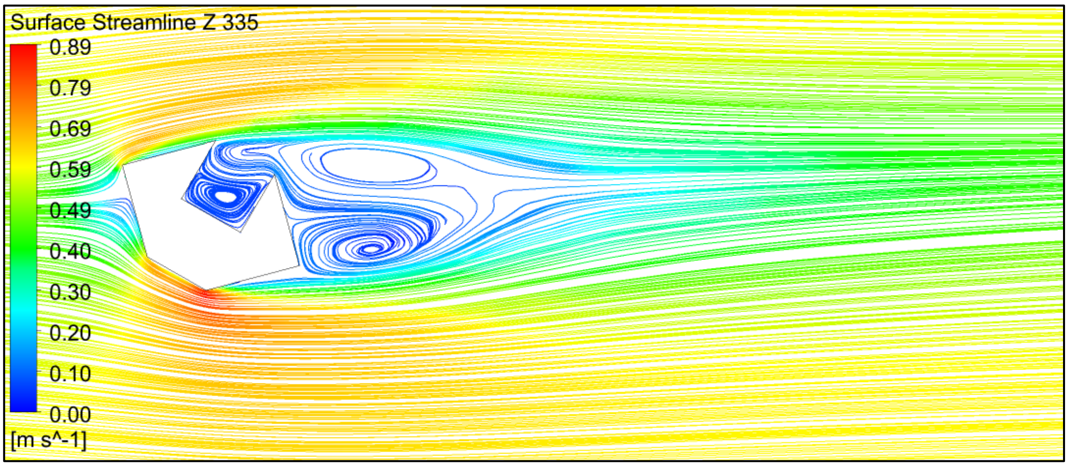

(c) Surface Streamline at Height Z = 335 mm

Figure 5. 64: Surface Streamline Diamond Shape Model 60° Wind Angle

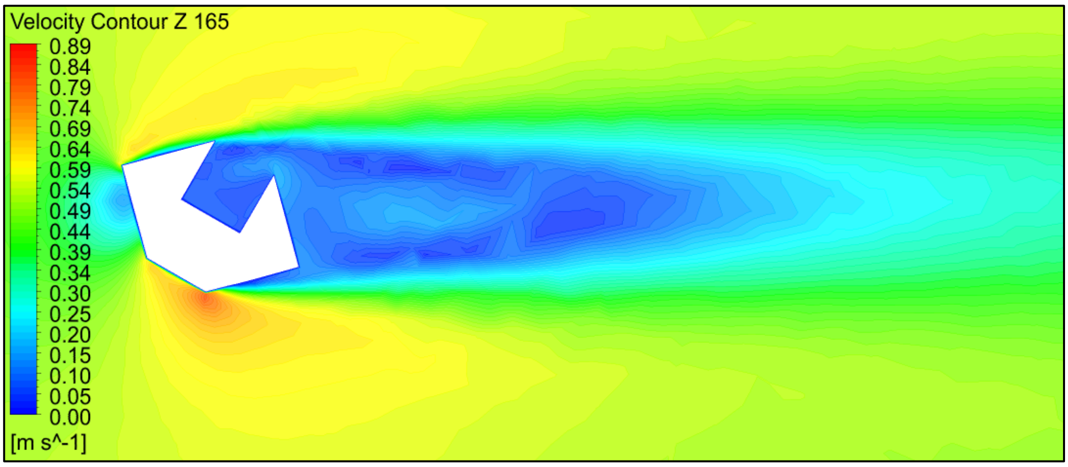

(a) Velocity Contour at Height Z = 165 mm

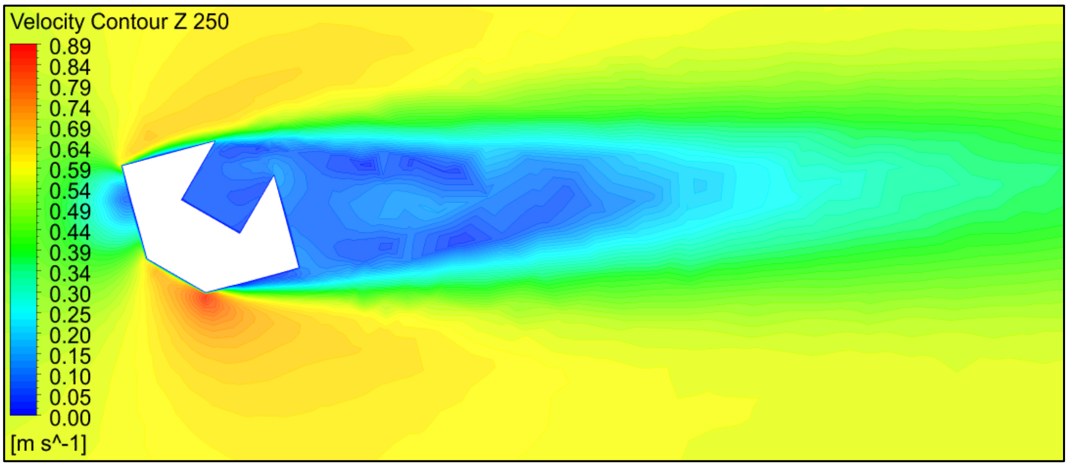

(b) Velocity Contour at Height Z = 250 mm

Figure 5.64: Velocity Contour Diamond Shape Model 60° Wind Angle (Contd.)

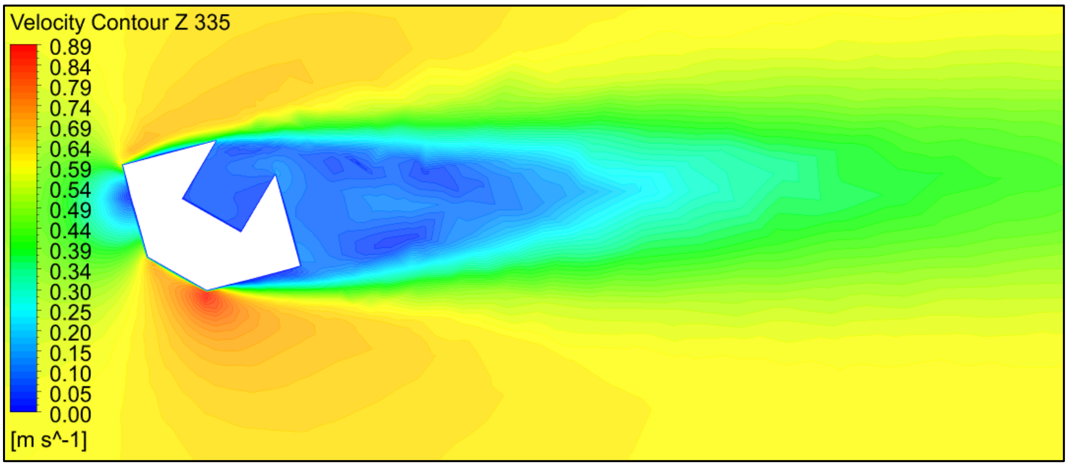

(c) Velocity Contour at Height Z = 335 mm

Figure 5. 65: Velocity Contour Diamond Shape Model 60° Wind Angle

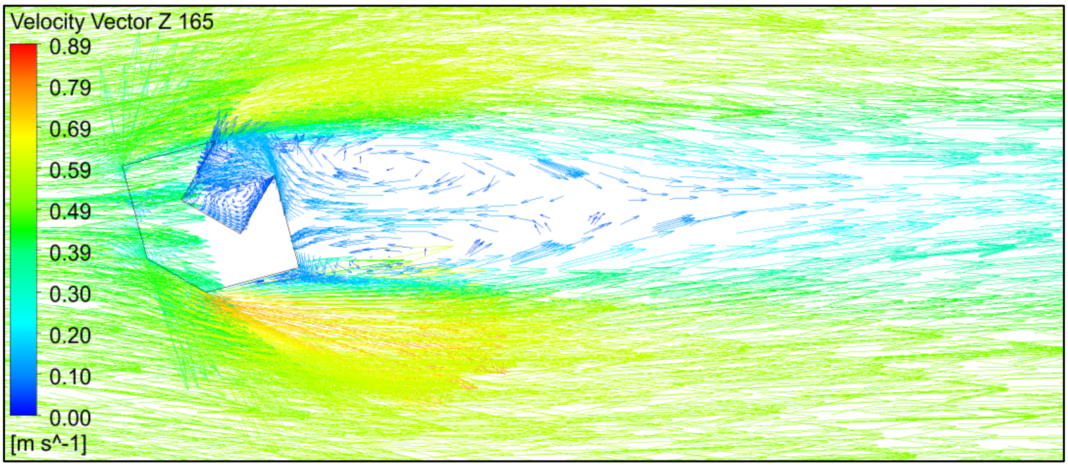

(a) Velocity Vector at Height Z = 165 mm

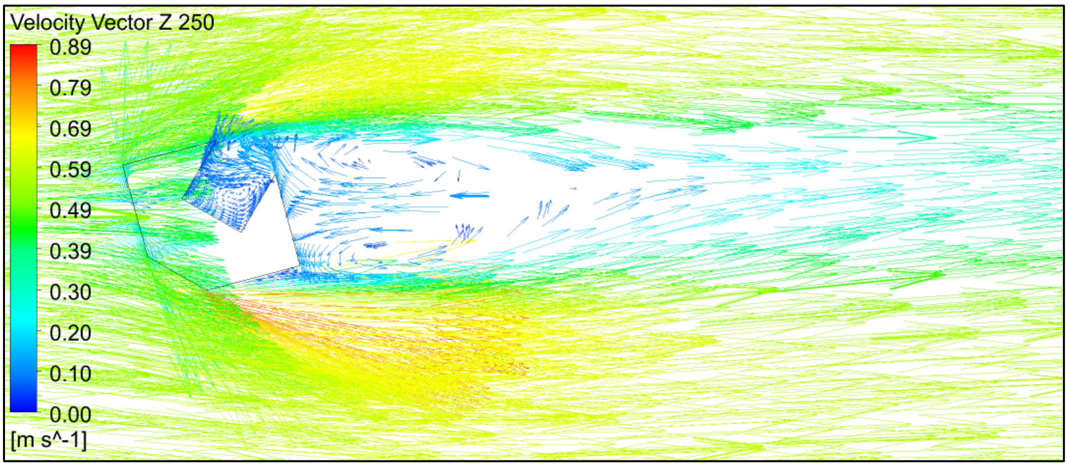

(b) Velocity Vector at Height Z = 250 mm

Figure 5.65: Velocity Vector Diamond Shape Model 60° Wind Angle (Contd.)

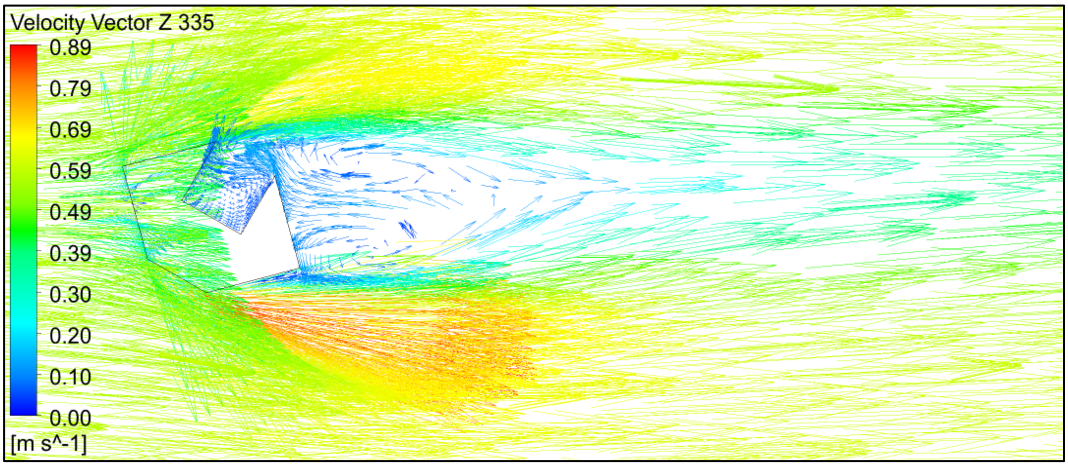

(c) Velocity Vector at Height Z = 335 mm

Figure 5. 66: Velocity Vector Diamond Shape Model 60° Wind Angle

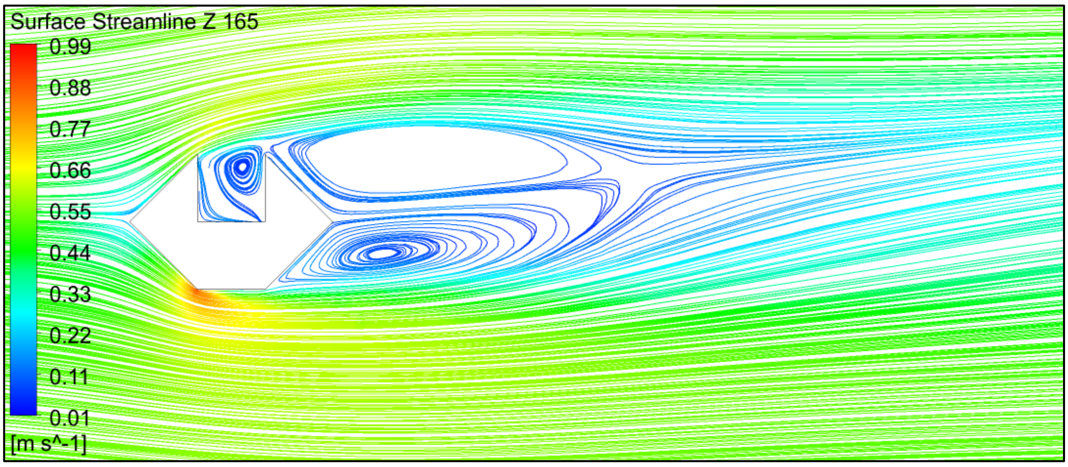

(a) Surface Streamline at Height Z = 165 mm

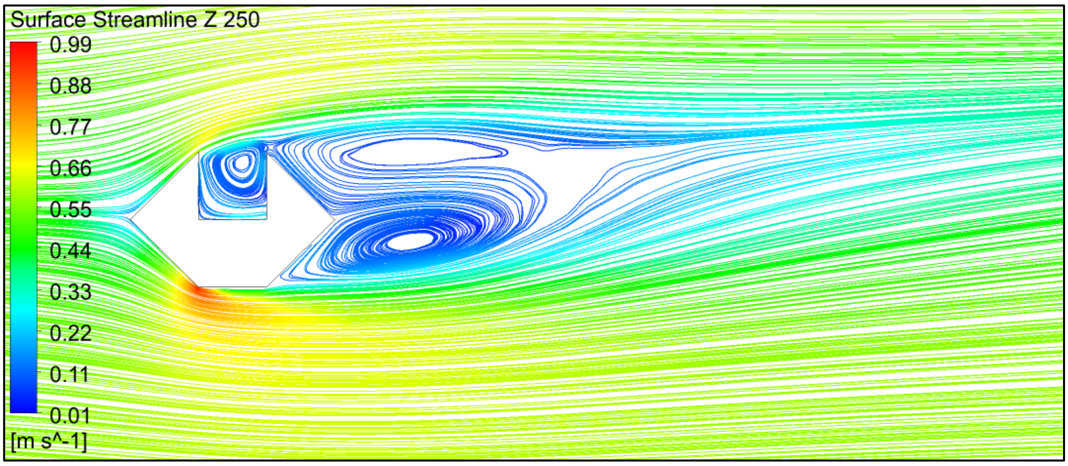

(b) Surface Streamline at Height Z = 250 mm

Figure 5.66: Surface Streamline Diamond Shape Model 90° Wind Angle (Contd.)

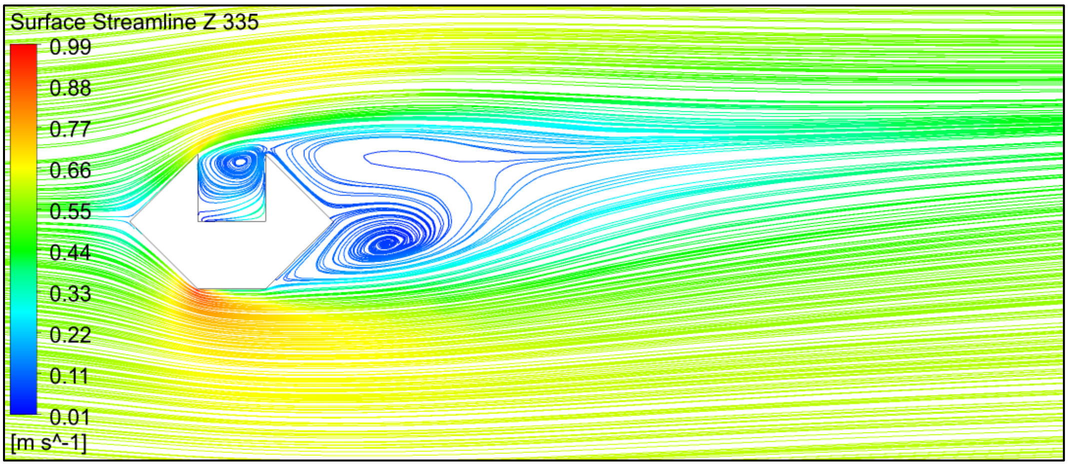

(c) Surface Streamline at Height Z = 335 mm

Figure 5. 67: Surface Streamline Diamond Shape Model 90° Wind Angle

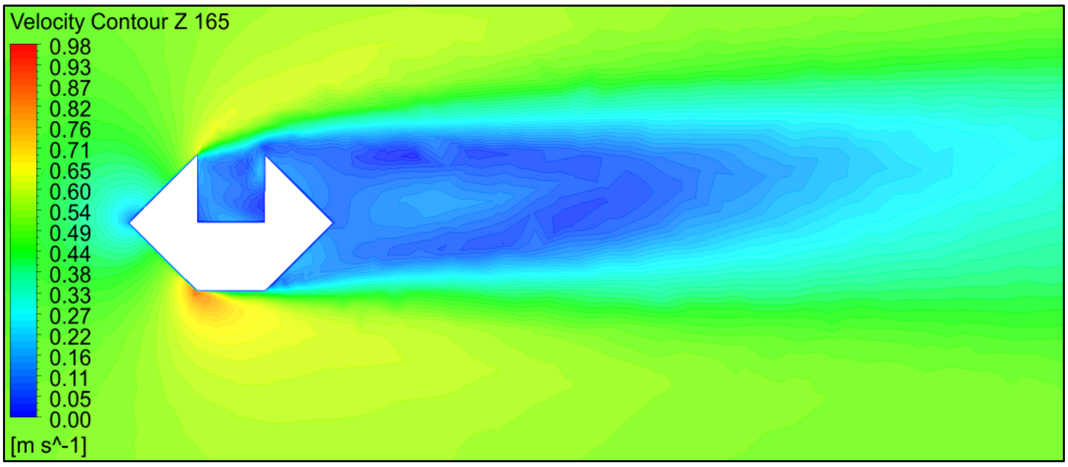

(a) Velocity Contour at Height Z = 165 mm

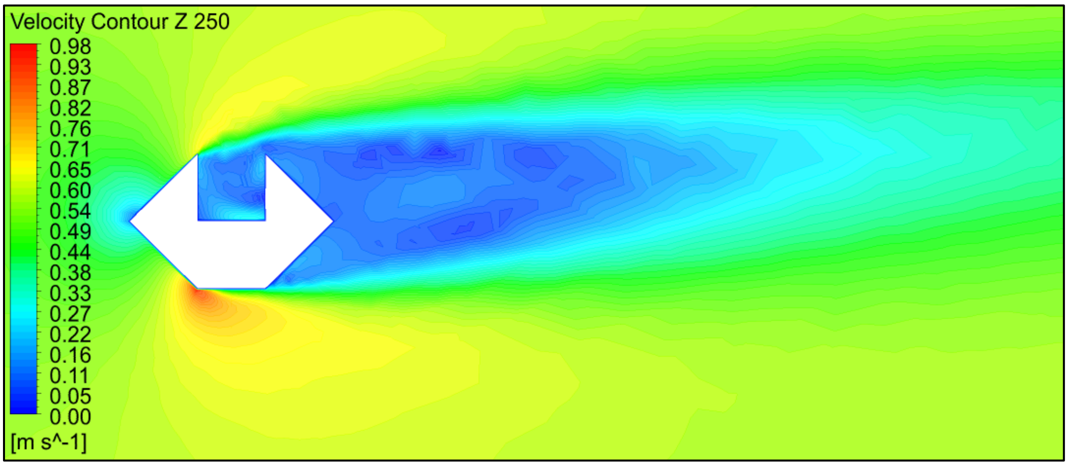

(b) Velocity Contour at Height Z = 250 mm

Figure 5. 67: Velocity Contour Diamond Shape Model 90° Wind Angle (Contd.)

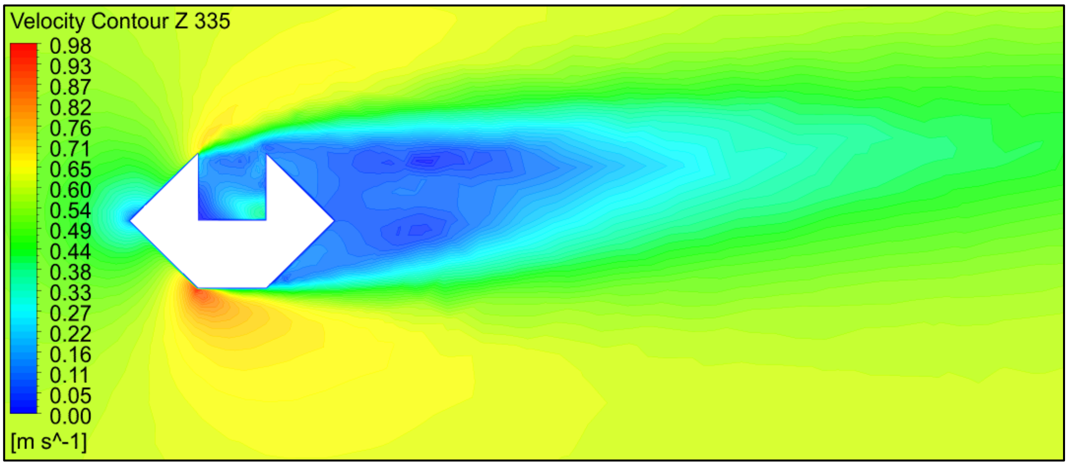

(c) Velocity Contour at Height Z = 335 mm

Figure 5. 68: Velocity Contour Diamond Shape Model 90° Wind Angle

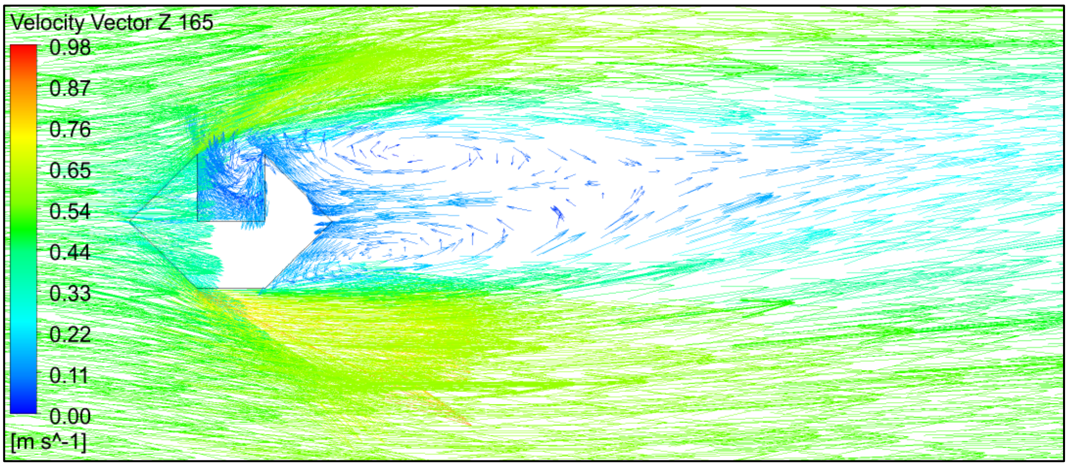

(a) Velocity Vector at Height Z = 165 mm

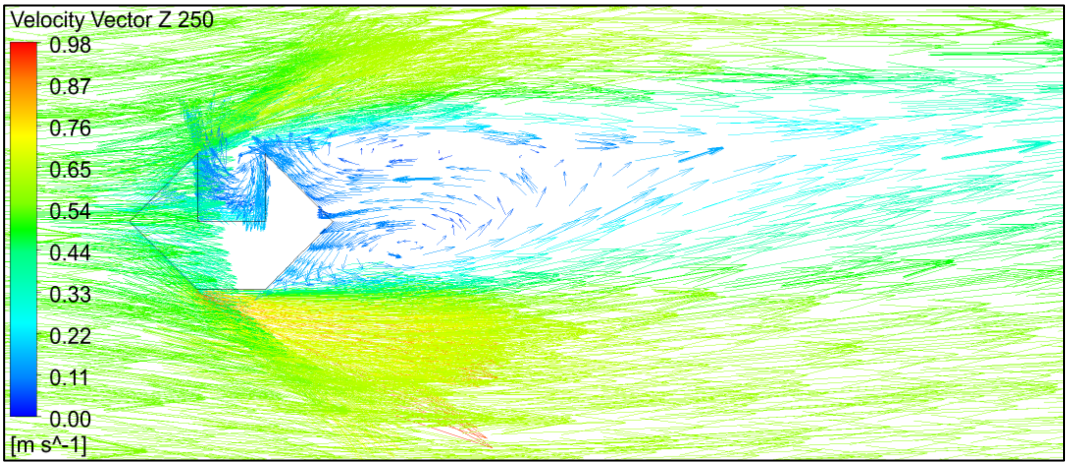

(b) Velocity Vector at Height Z = 165 mm

Figure 5. 68: Velocity Vector Diamond Shape Model 90° Wind Angle (Contd.)

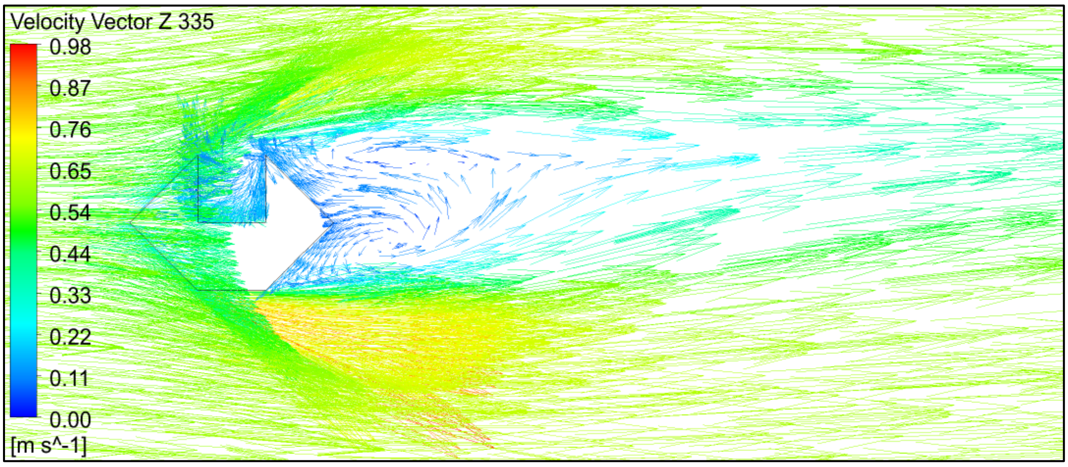

(c) Velocity Vector at Height Z = 335 mm

Figure 5. 69: Velocity Vector Diamond Shape Model 90° Wind Angle

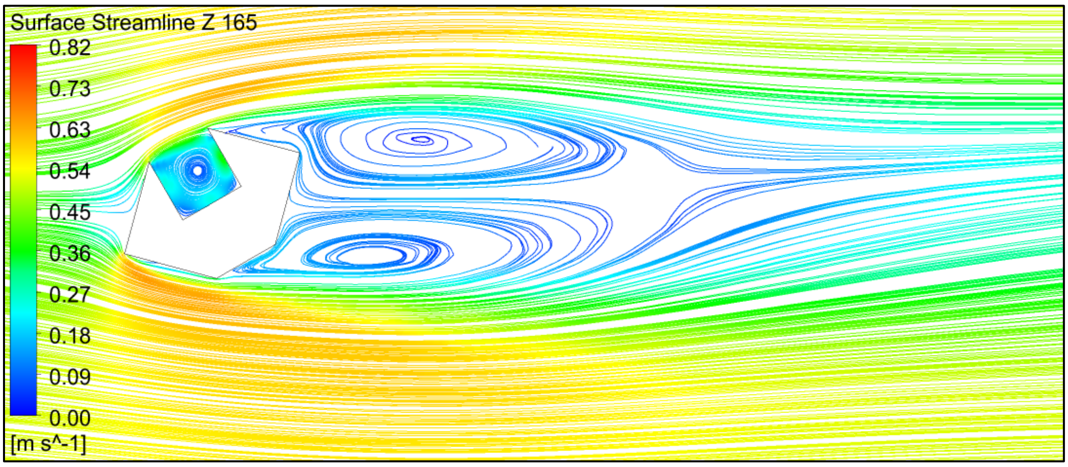

(a) Surface Streamline at Height Z = 165 mm

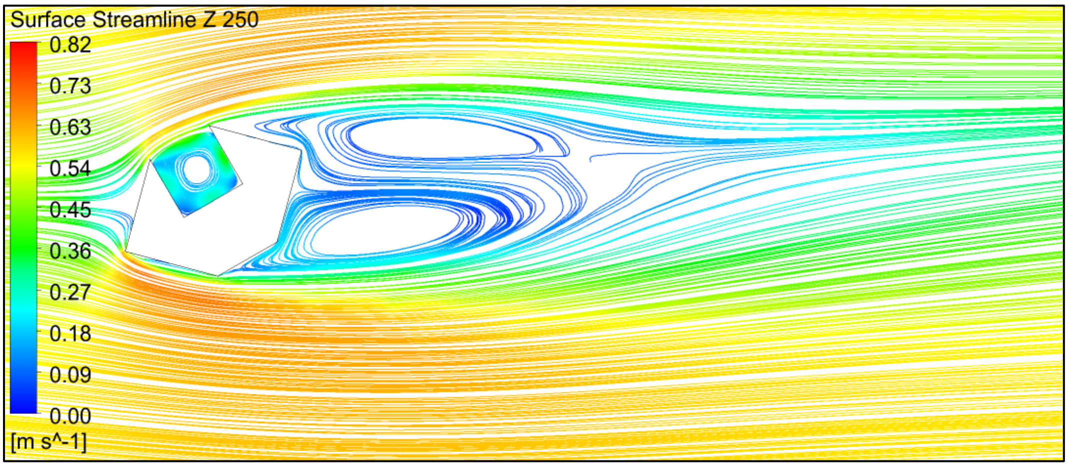

(b) Surface Streamline at Height Z = 250 mm

Figure 5. 69: Surface Streamline Diamond Shape Model 120° Wind Angle (Contd.)

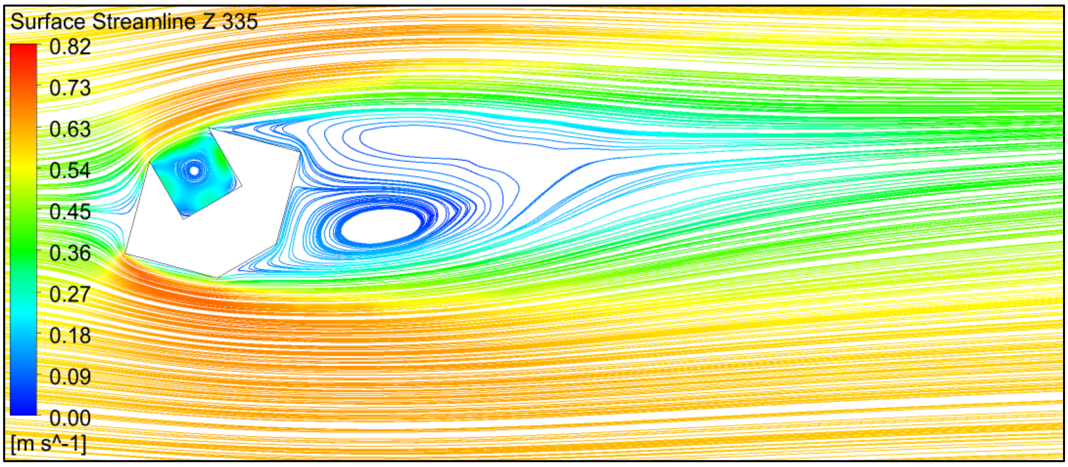

(c) Surface Streamline at Height Z = 335 mm

Figure 5. 70: Surface Streamline Diamond Shape Model 120° Wind Angle

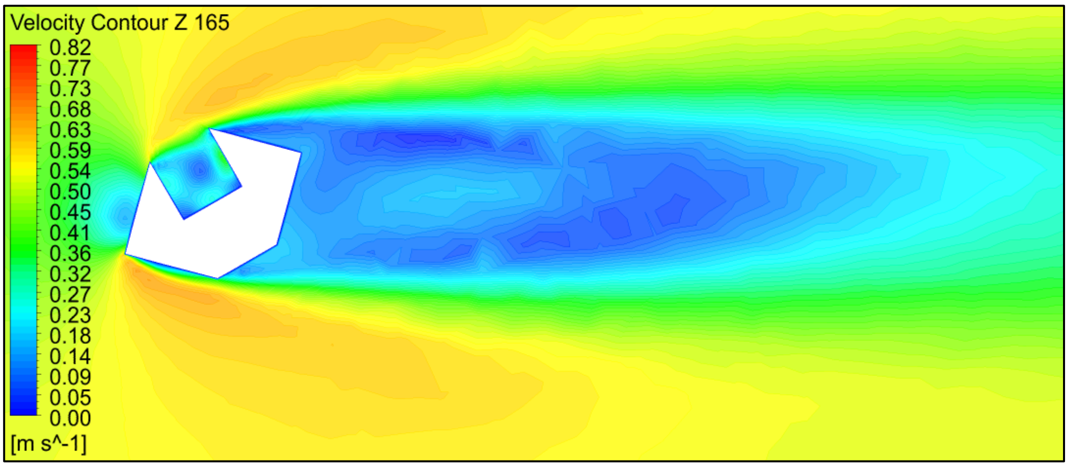

(a) Velocity Contour at Height Z = 165 mm

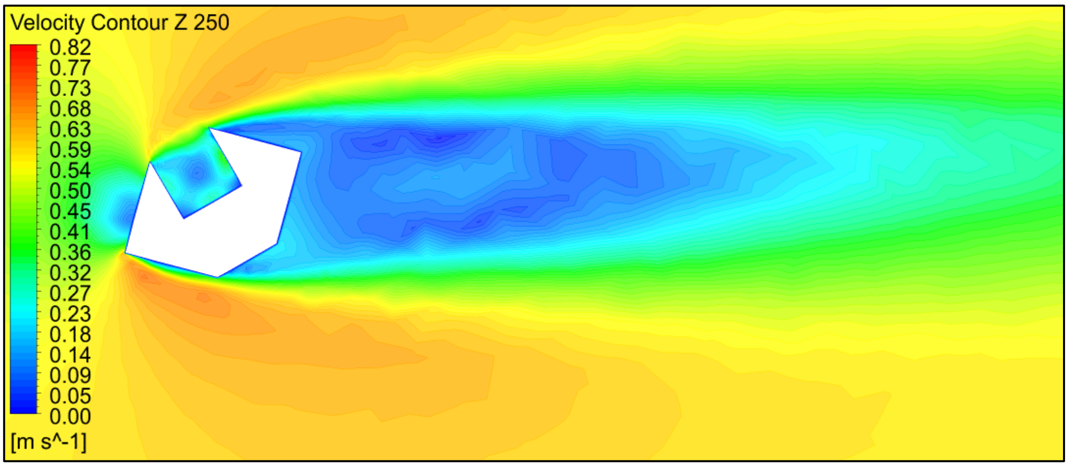

(b) Velocity Contour at Height Z = 250 mm

Figure 5. 70: Velocity Contour Diamond Shape Model 120° Wind Angle (Contd.)

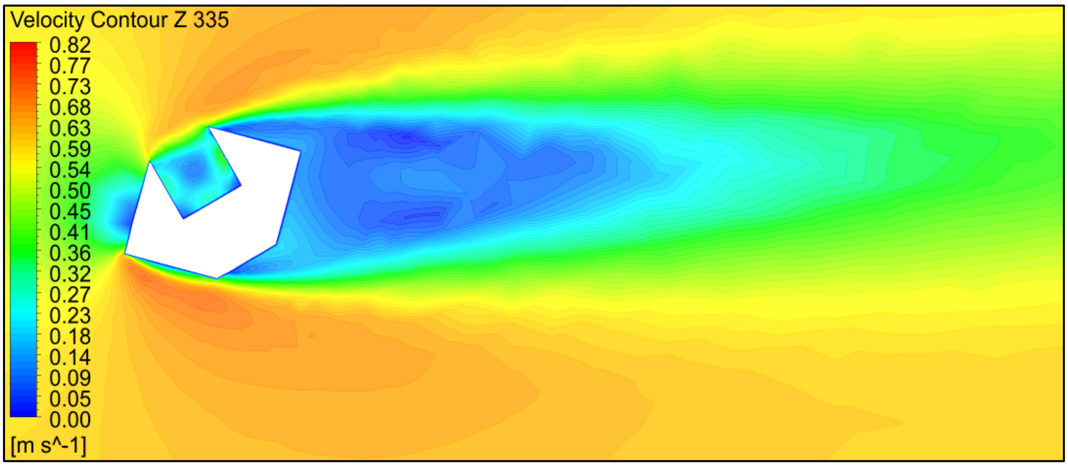

(c) Velocity Contour at Height Z = 335 mm

Figure 5. 71: Velocity Contour Diamond Shape Model 120° Wind Angle

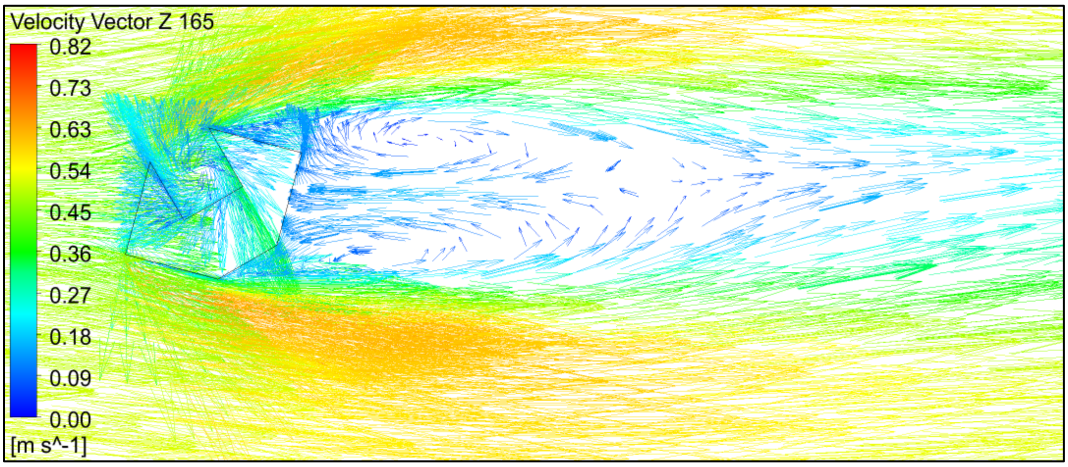

(a) Velocity Vector at Height Z = 165 mm

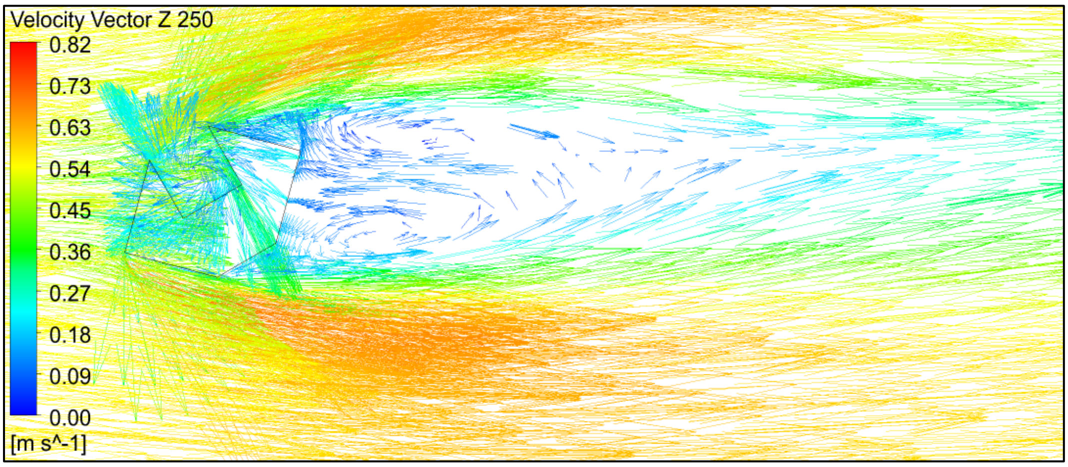

(b) Velocity Vector at Height Z = 250 mm

Figure 5.71: Velocity Vector Diamond Shape Model 120° Wind Angle (Contd.)

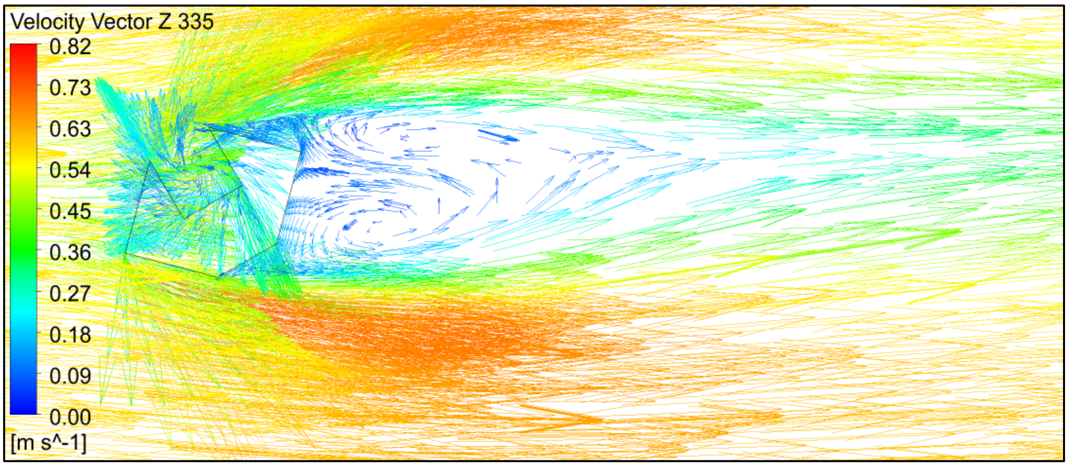

(c) Velocity Vector at Height Z = 335 mm

Figure 5. 72: Velocity Vector Diamond Shape Model 120° Wind Angle

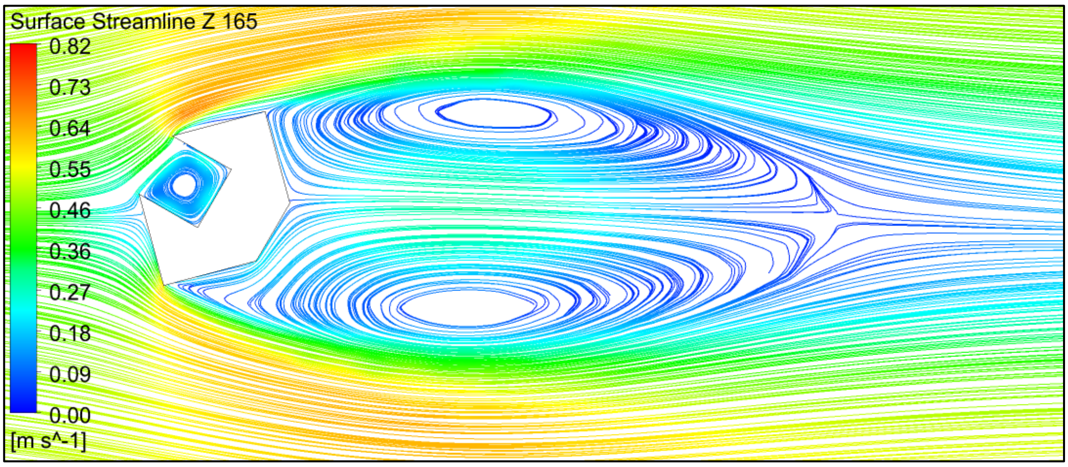

(a) Surface Streamline at Height Z = 165 mm

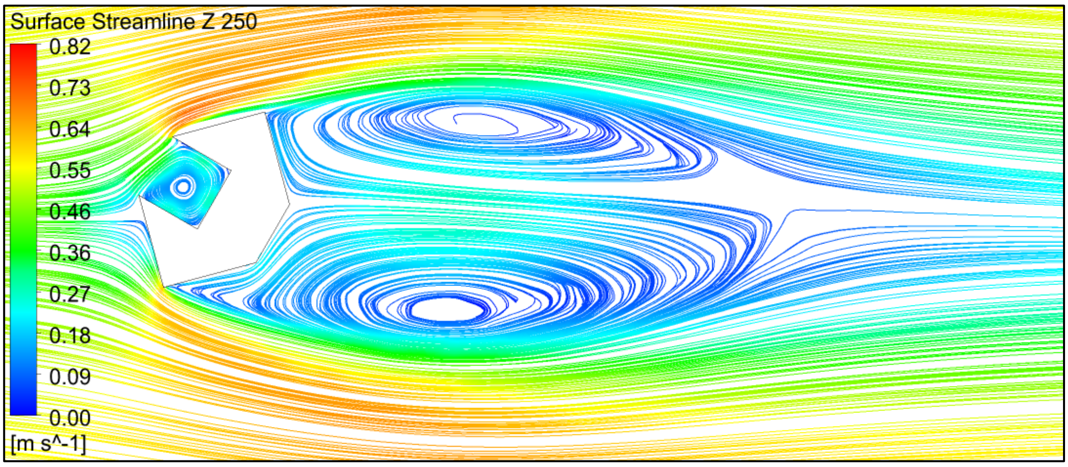

(b) Surface Streamline at Height Z = 250 mm

Figure 5. 72: Surface Streamline Diamond Shape Model 150° Wind Angle (Contd.)

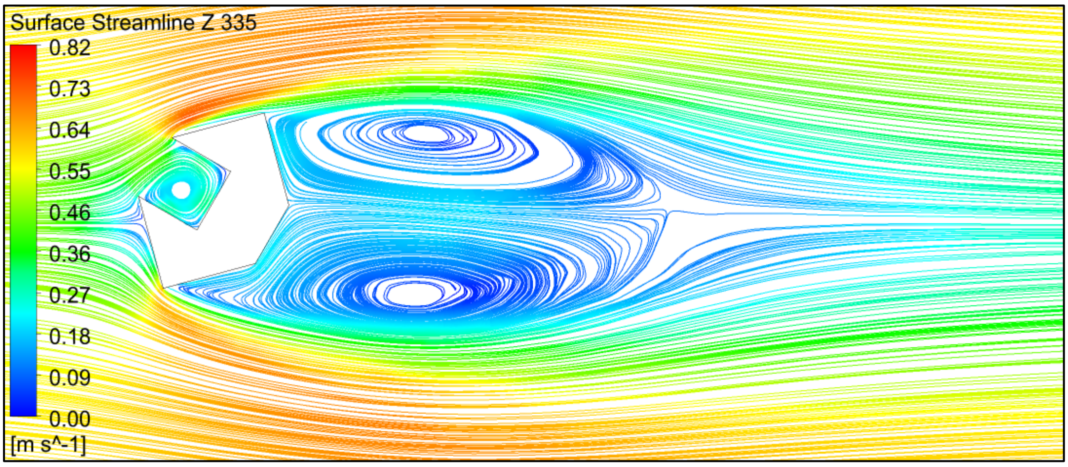

(c) Surface Streamline at Height Z = 335 mm

Figure 5. 73: Surface Streamline Diamond Shape Model 150° Wind Angle

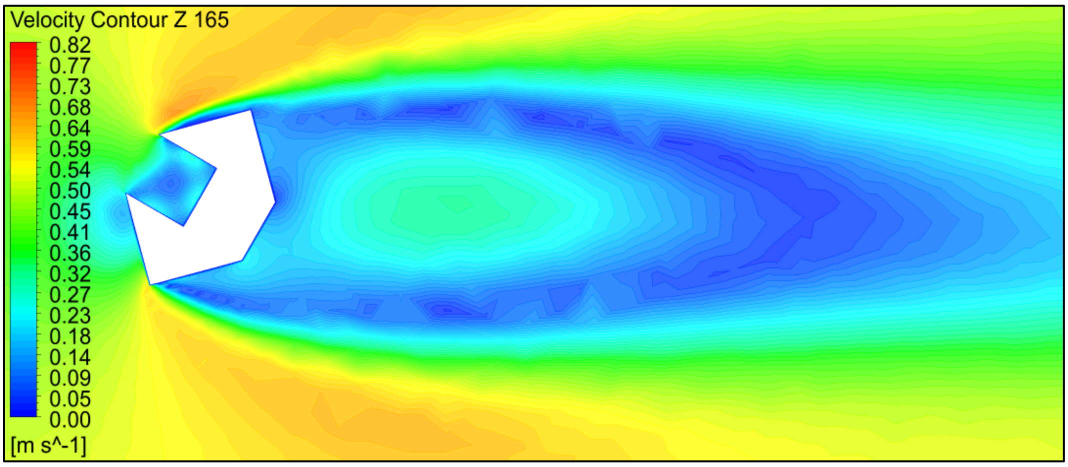

(a) Velocity Contour at Height Z = 165 mm

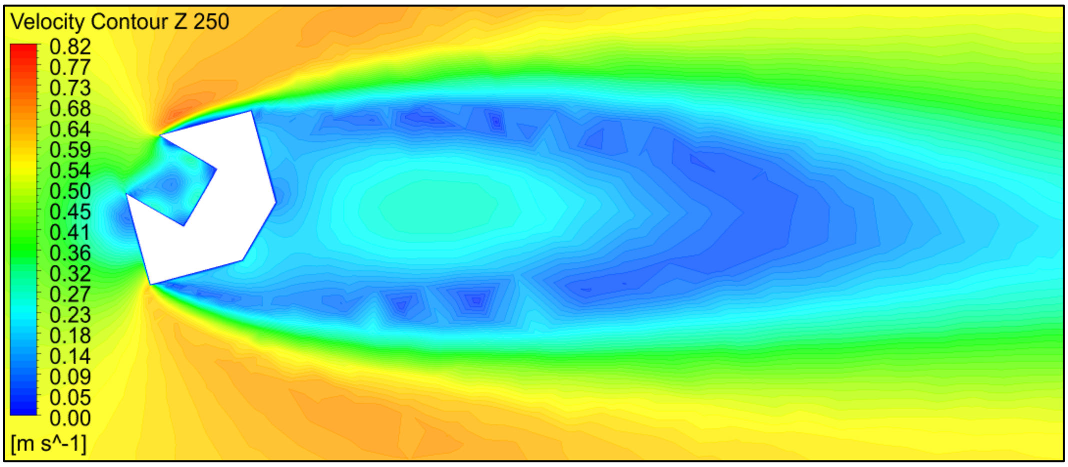

(b) Velocity Contour at Height Z = 250 mm

Figure 5. 73: Velocity Contour Diamond Shape Model 150° Wind Angle (Contd.)

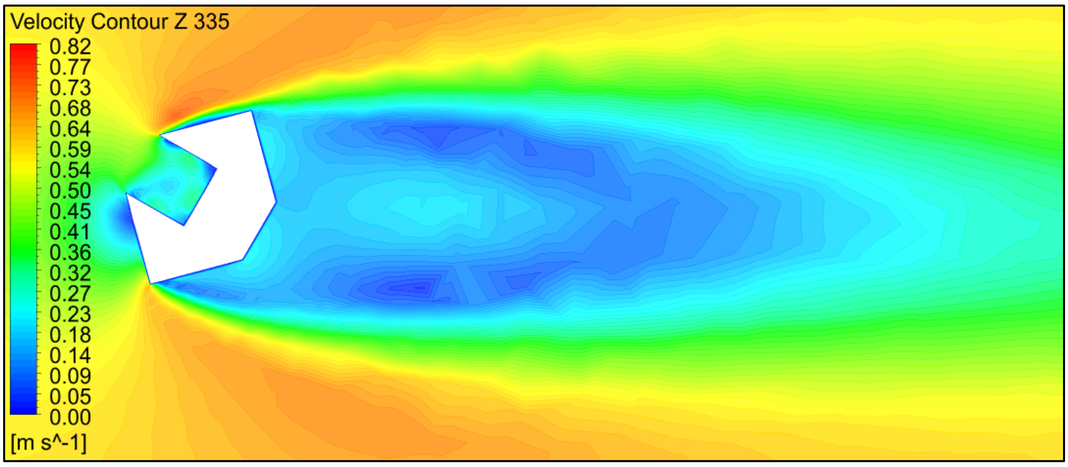

(c) Velocity Contour at Height Z = 335 mm

Figure 5. 74: Velocity Contour Diamond Shape Model 150° Wind Angle

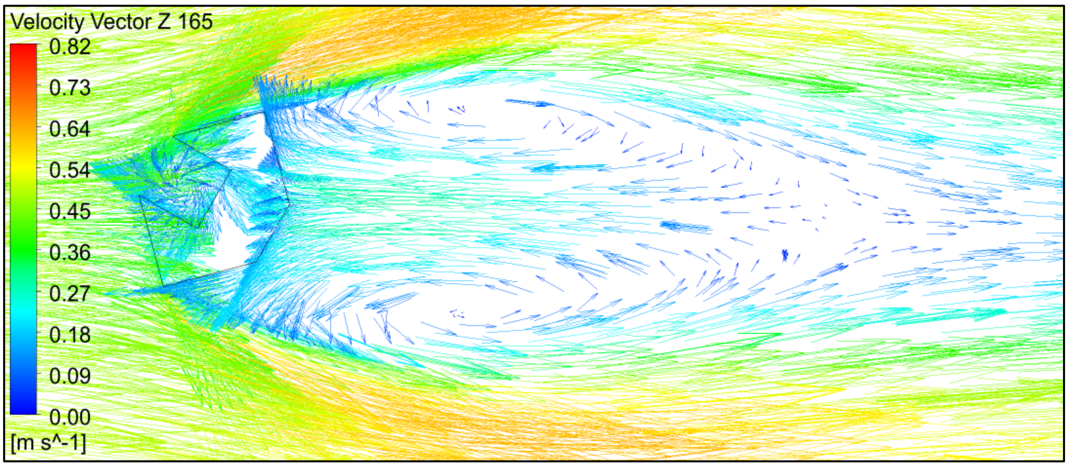

(a) Velocity Vector at Height Z = 165 mm

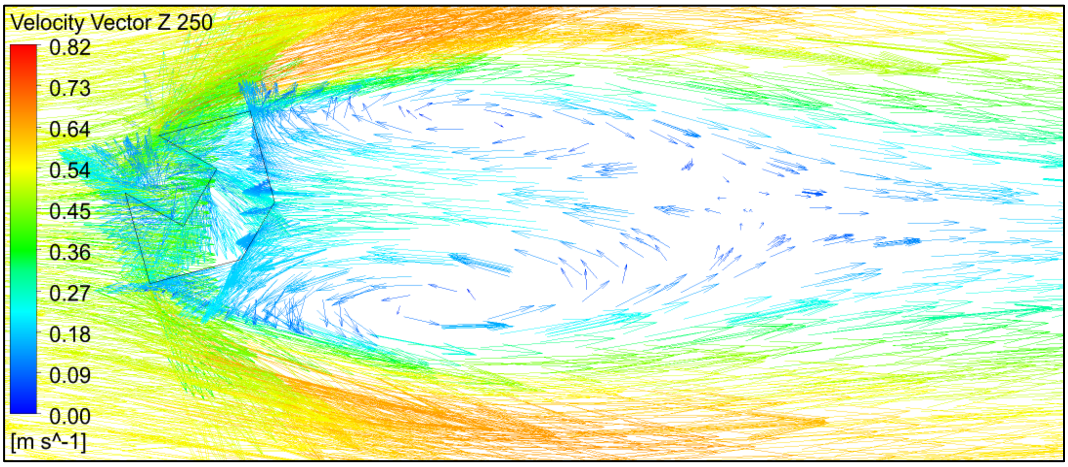

(b) Velocity Vector at Height Z = 165 mm

Figure 5.74: Velocity Vector Diamond Shape Model 150° Wind Angle (Contd.)

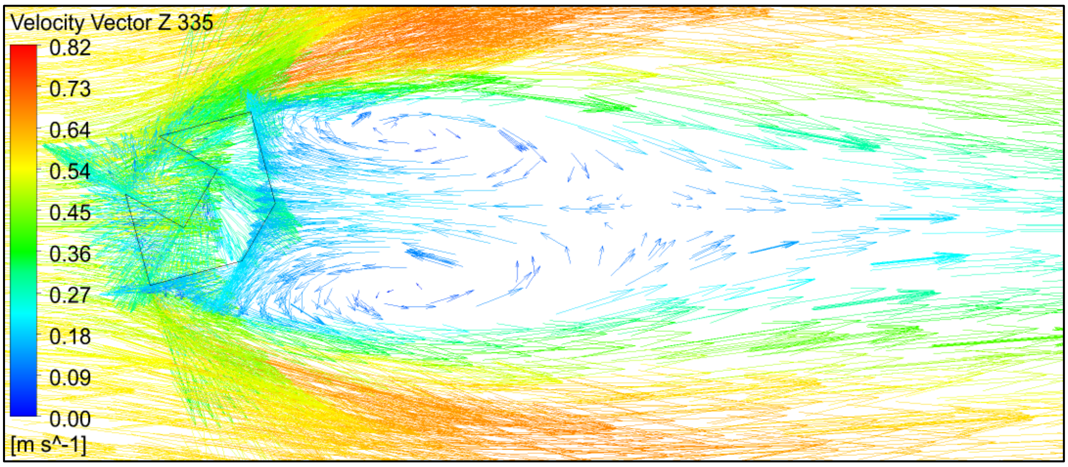

(c) Velocity Vector at Height Z = 335 mm

Figure 5. 75: Velocity Vector Diamond Shape Model 150° Wind Angle

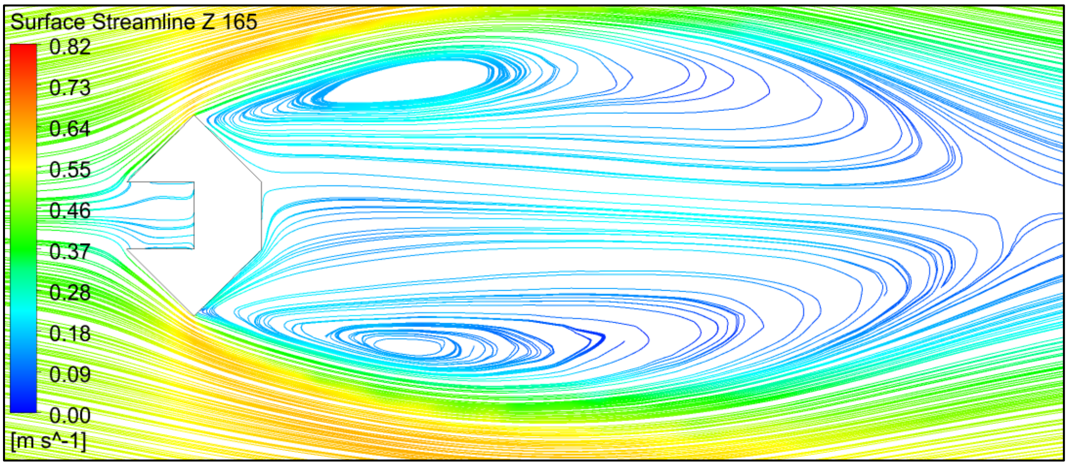

(a) Surface Streamline at Height Z = 165 mm

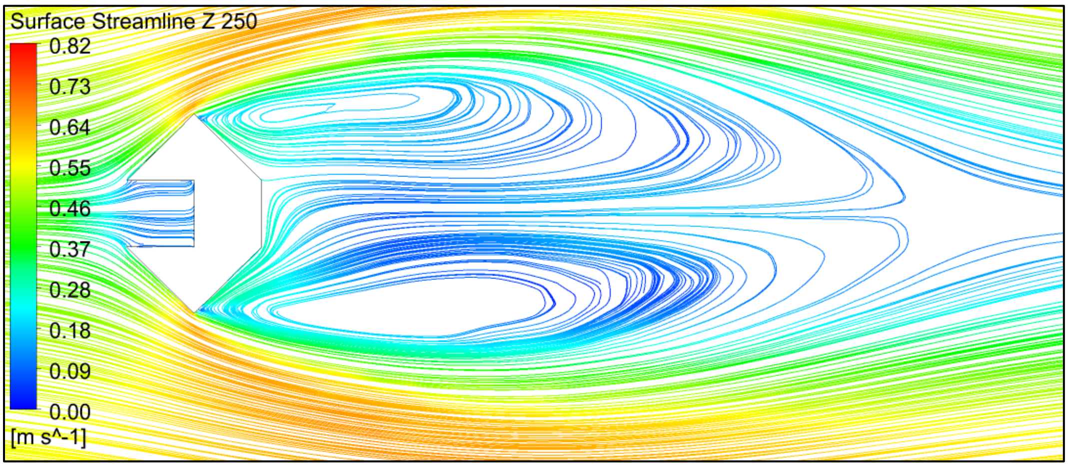

(b) Surface Streamline at Height Z = 250 mm

Figure 5. 75: Surface Streamline Diamond Shape Model 180° Wind Angle (Contd.)

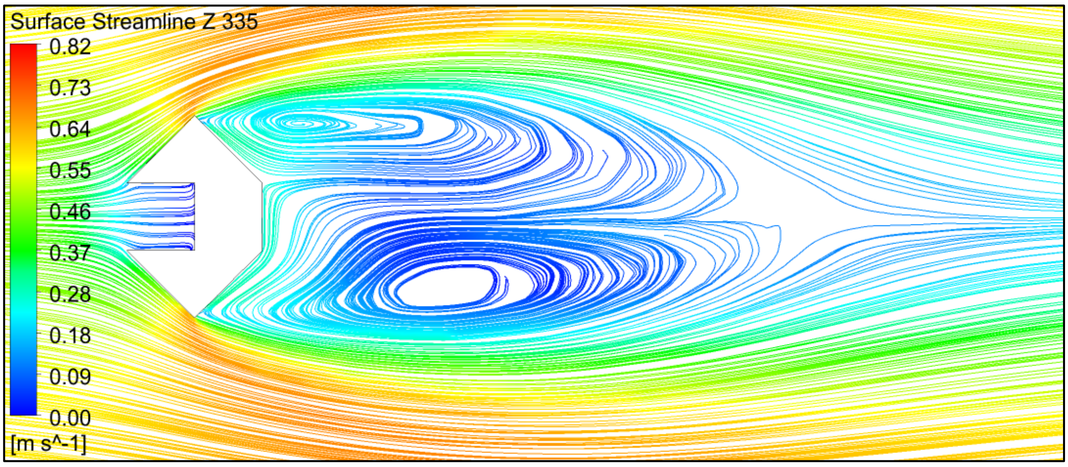

(c) Surface Streamline at Height Z = 335 mm

Figure 5. 76: Surface Streamline Diamond Shape Model 180° Wind Angle

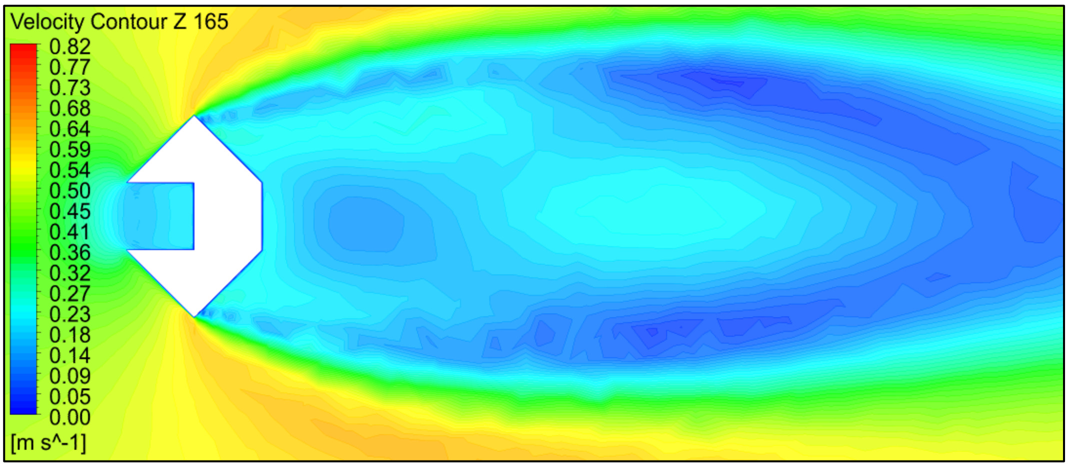

(a) Velocity Contour at Height Z = 165 mm

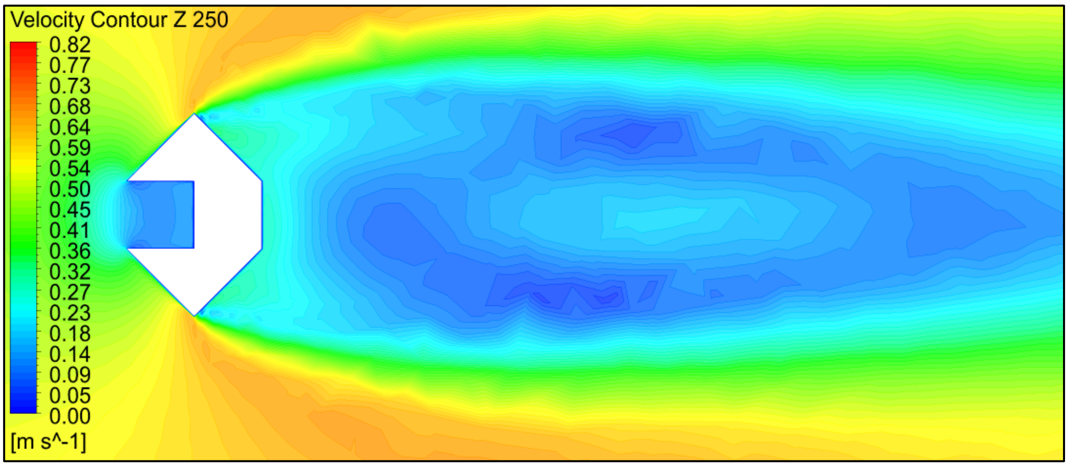

(b) Velocity Contour at Height Z = 250 mm

Figure 5. 76: Velocity Contour Diamond Shape Model 180° Wind Angle (Contd.)

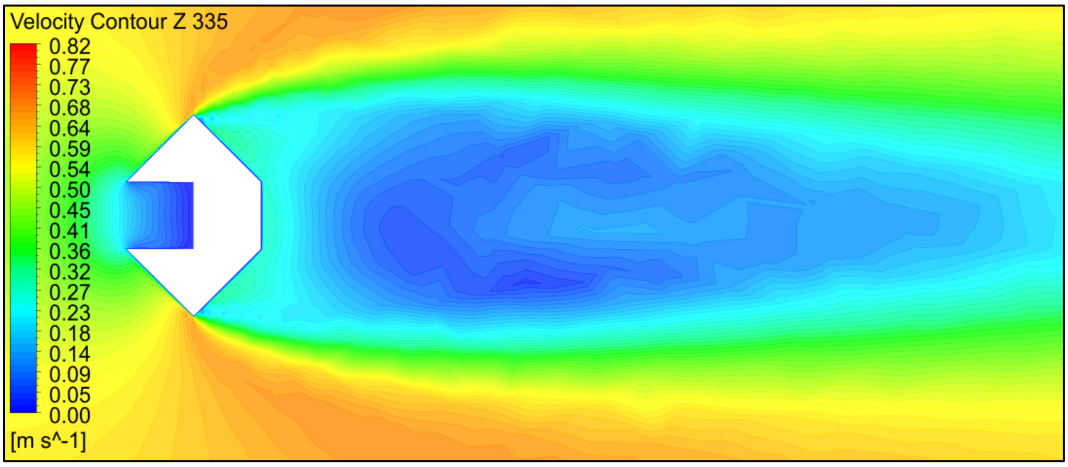

(c) Velocity Contour at Height Z = 335 mm

Figure 5. 77: Velocity Contour Diamond Shape Model 180° Wind Angle

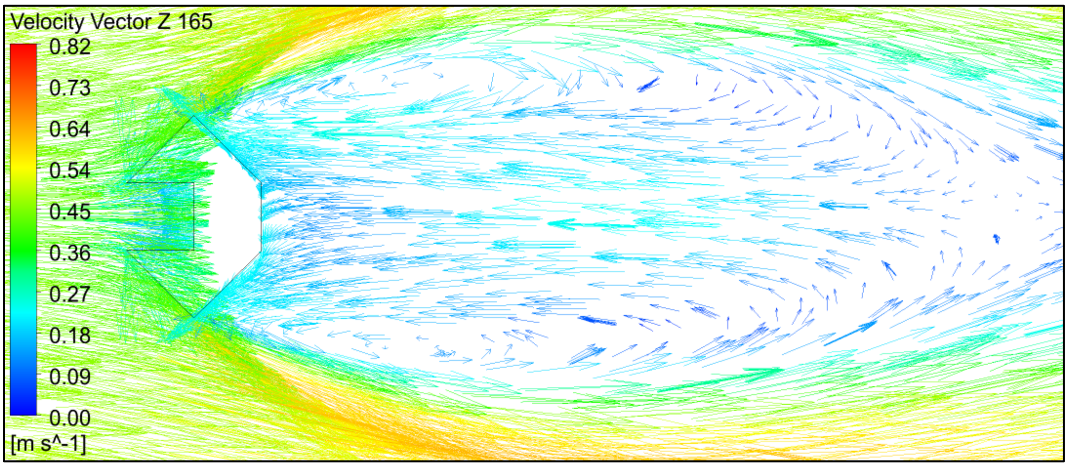

(a) Velocity Vector at Height Z = 165 mm

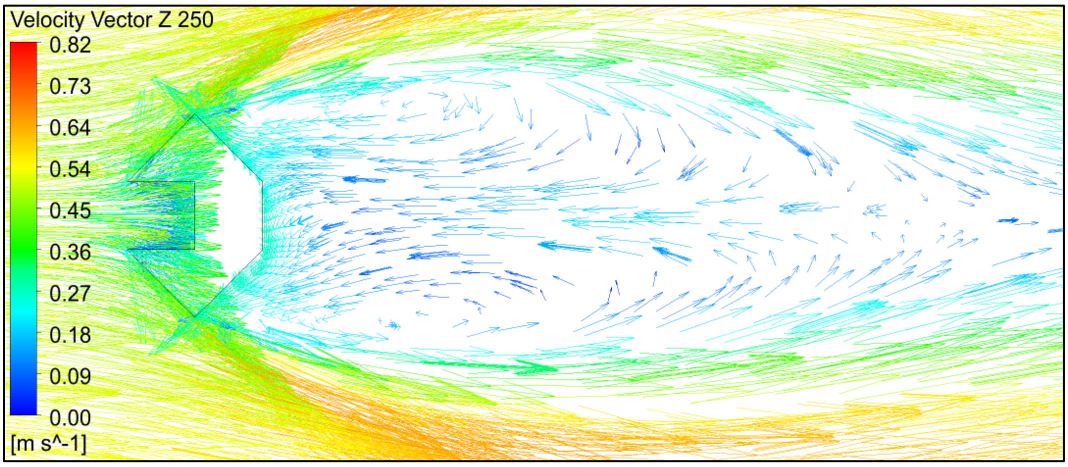

(b) Velocity Vector at Height Z = 250 mm

Figure 5. 77: Velocity Vector Diamond Shape Model 180° Wind Angle (Contd.)

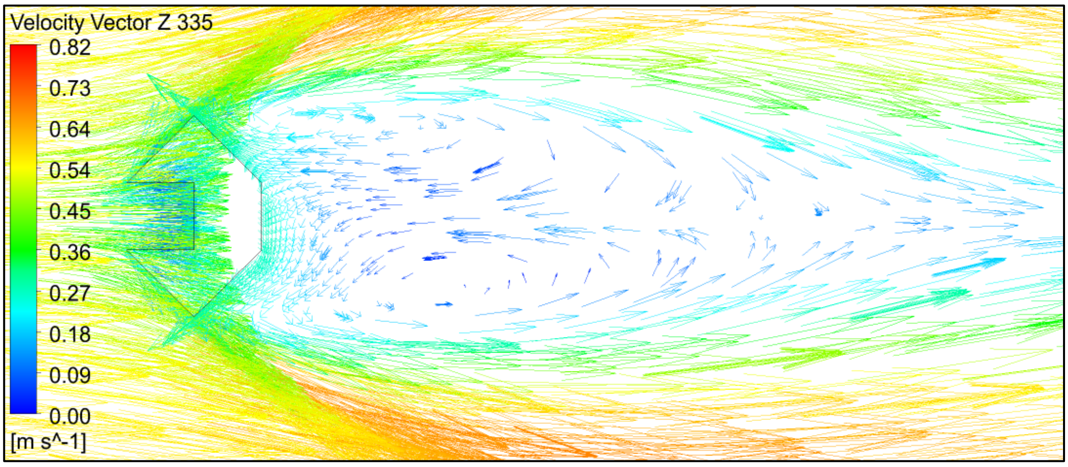

(c) Velocity Vector at Height Z = 335 mm

Figure 5. 78: Velocity Vector Diamond Shape Model 180° Wind Angle

5.3.9 Velocity Streamline Along Wind Direction on Central Vertical Plane

The streamlines showing the flow directions on cross section through central vertical plane of the model along the wind direction for different wind incidence angles are shown in Figure 5.78, 5.79, 5.80, 5.81, 5.82, 5.83 & 5.84. The recirculation of flow behind the model and formation of vorticity, the upwind vortex at ground level, upwash, downwash and stagnation zones on the windward faces and recirculation cavity formed at the roof level can be seen. It can be visualized that the effects are different for different angles of wind attack.

At 0° angle of wind attack the vorticity created behind the model is at middle height of the model. Whereas, in most of the wind attack angles it is created near the top. At 90° wind angle the vorticity is very close to the model. The spacing between the streamlines are very small at 0° and 180° wind angles. It can be concluded that flow recirculation speed in the region at 0° and 180° angle of wind attack is more compared to other wind angles. At 90° wind angle the spacing between the streamlines are wider when compared with those at other wind angles and hence we can say that recirculation speed is least at this angle of wind attack.

The intensity and strength of upwind vortex is reducing from 0° to 90° wind angle. At 90° wind angle it is the least and then increasing till 180° wind angle. At 180° wind angle the intensity and strength is the highest.

Wind from within the recessed cavity makes an exit from the roof level. Together with the wind flow in direction of wind, roof recirculation cavity of different intensity is formed at various wind angles. However, at 90° wind angle the phenomenon is not prominent.

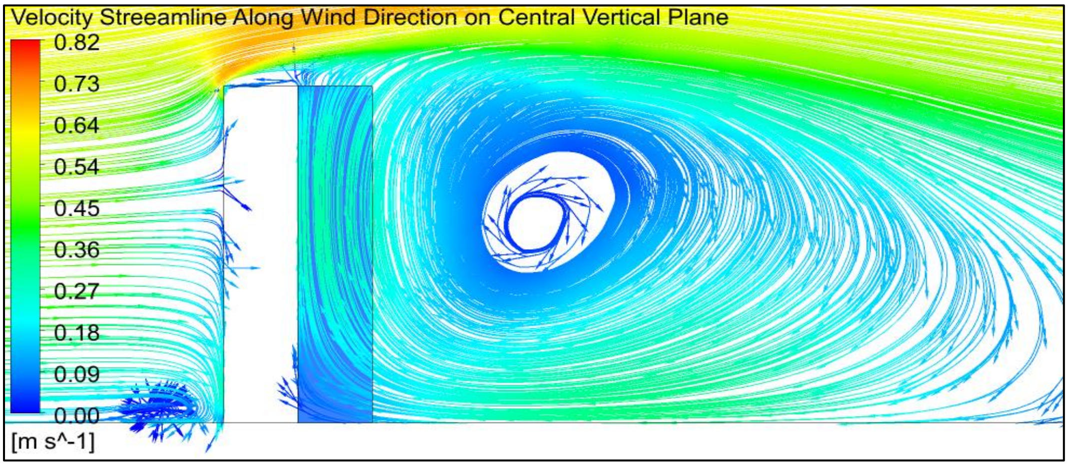

Figure 5. 79: Velocity Streamline Along the Wind Direction on Central Vertical Plane Diamond Shape Model 0° Wind Angle

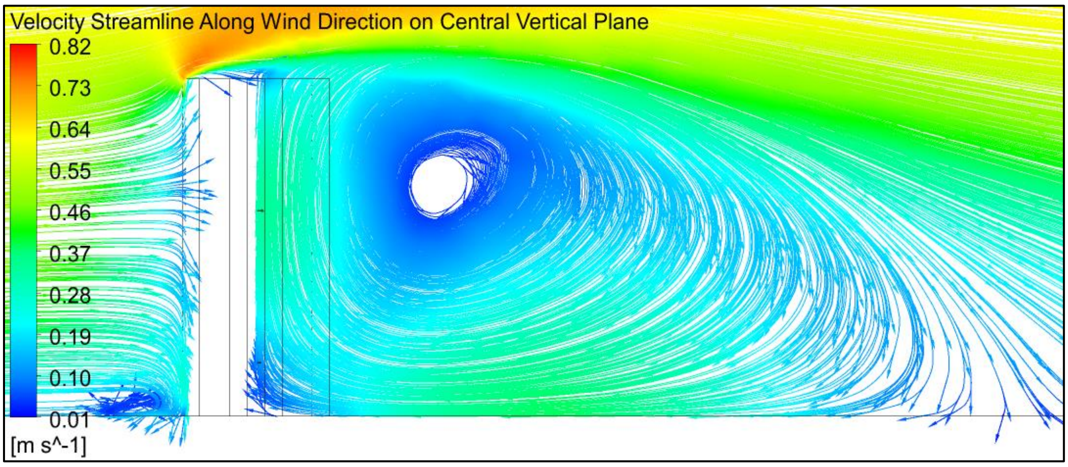

Figure 5. 80: Velocity Streamline Along the Wind Direction on Central Vertical Plane Diamond Shape Model 30° Wind Angle

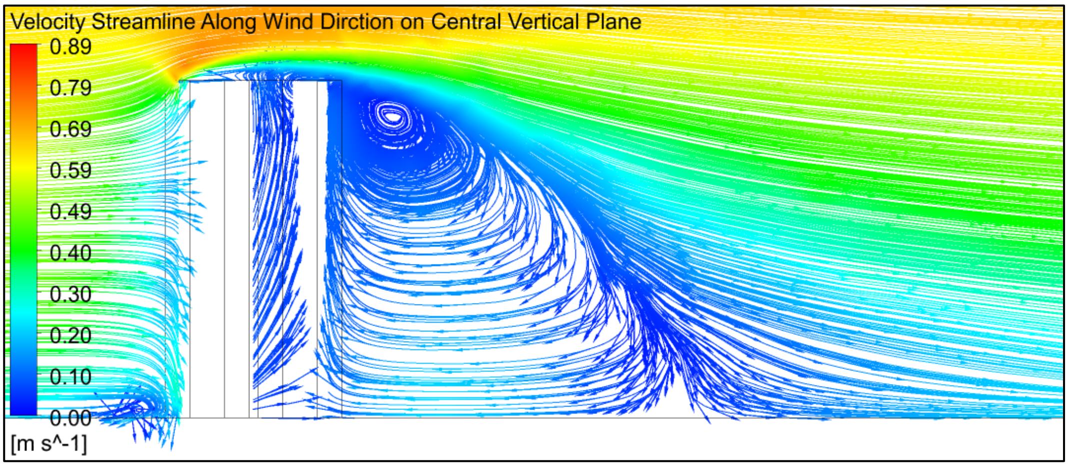

Figure 5. 81: Velocity Streamline Along the Wind Direction on Central Vertical Plane Diamond Shape Model 60° Wind Angle

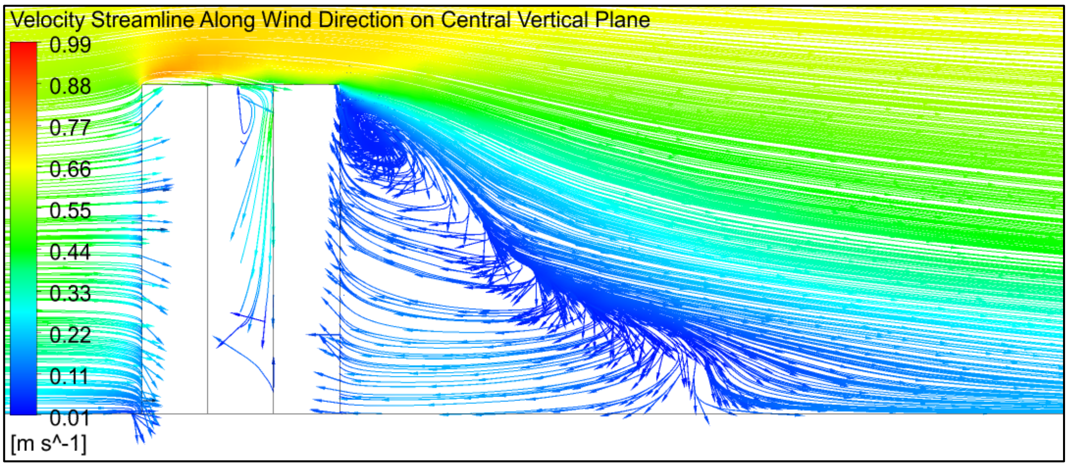

Figure 5. 82: Velocity Streamline Along the Wind Direction on Central Vertical Plane Diamond Shape Model 90° Wind Angle

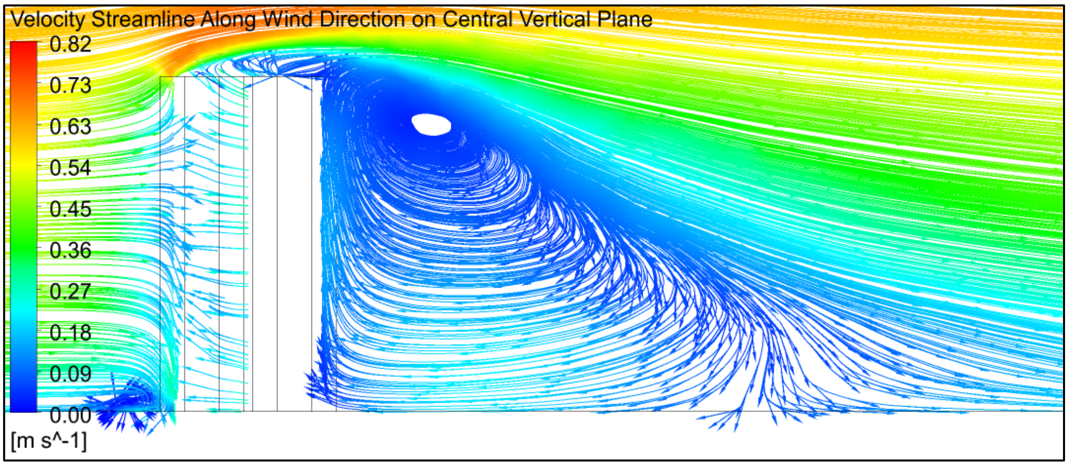

Figure 5. 83: Velocity Streamline Along the Wind Direction on Central Vertical Plane Diamond Shape Model 120° Wind Angle

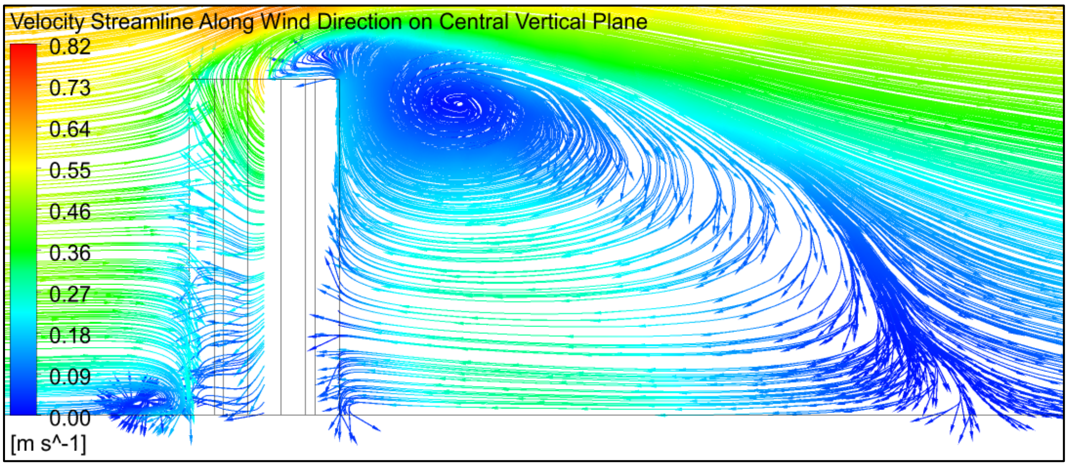

Figure 5. 84: Velocity Streamline Along the Wind Direction on Central Vertical Plane Diamond Shape Model 150° Wind Angle

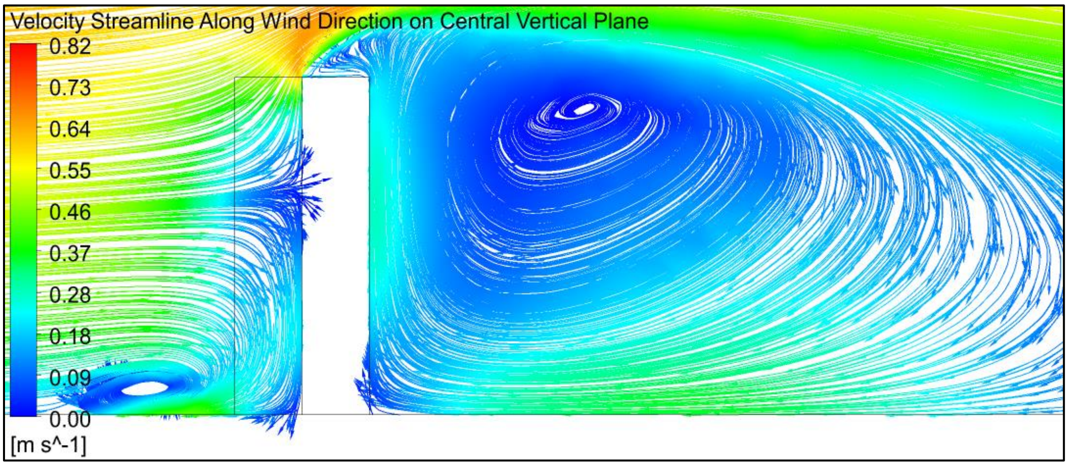

Figure 5. 85: Velocity Streamline Along the Wind Direction on Central Vertical Plane Diamond Shape Model 180° Wind Angle

5.3.10 C_{Pe} Along Building Perimeter

Graphical plot representing the variation of C_{Pe} on the building façade at three different heights Z = 0.165 m (about 1/3rd height of the model), Z = 0.25 m (1/2 height of the model) and Z = 0.335 m (about 2/3rd height of the model) for different wind angles of attack from 0° to 180° @ 30° are shown in Figure 5.85, 5.86, 5.87, 5.88, 5.89, 5.90 & 5.91 respectively. For all the wind angles the maximum positive coefficient of pressure almost reaching the value of 1. Trivial variations in C_{Pe} on the faces shows swirl of wind whereas, immense rise in the values suggests formation of pressure region on the face. Sudden decrease in C_{Pe} values between the confluence of faces shows formation of eddies and flow reversal at the place creating suction. The corners at the confluence of faces where maximum suction exist are vital for design of cladding units. The detailed suction C_{Pe} values for different angle of wind incidence on the corners are shown in Table 5.4. It is quite evident that maximum suction (-2.44) occurs on the faces near the confluence of face AB2 for 90° wind angle of attack (AoA) at mid height of the model. This shall govern the design of cladding units for this shape and size of the diamond C-shaped building. Wide variation on the suction coefficients on the faces are observed. So, if the cladding design is done considering the coefficient on face-to-face basis after incorporating block contour diagrams on the faces, it will be economically cheaper at the same time the building will be protected from failure of cladding design.

Table 5. 4: Maximum Suction in Terms of C_{Pe} For Cladding Design

AoA	0°		30°	60°	90°	120°	150°	180°	
Z/Location	Corner		Corner	Corner	Corner	Corner	Corner	Corner	
	B1C1	B2C2	AB1	AB1	AB2	B2C2	C1D1	B1C1	B2C2
0.165 m	-0.68	-0.68	-0.97	-1.47	-1.60	-1.25	-1.12	-0.60	-0.60
0.250 m	-0.88	-0.88	-1.15	-1.70	-2.44	-1.26	-1.31	-0.71	-0.71
0.335 m	-0.90	-0.90	-1.23	-1.88	-2.30	-1.45	-1.26	-0.77	-0.77

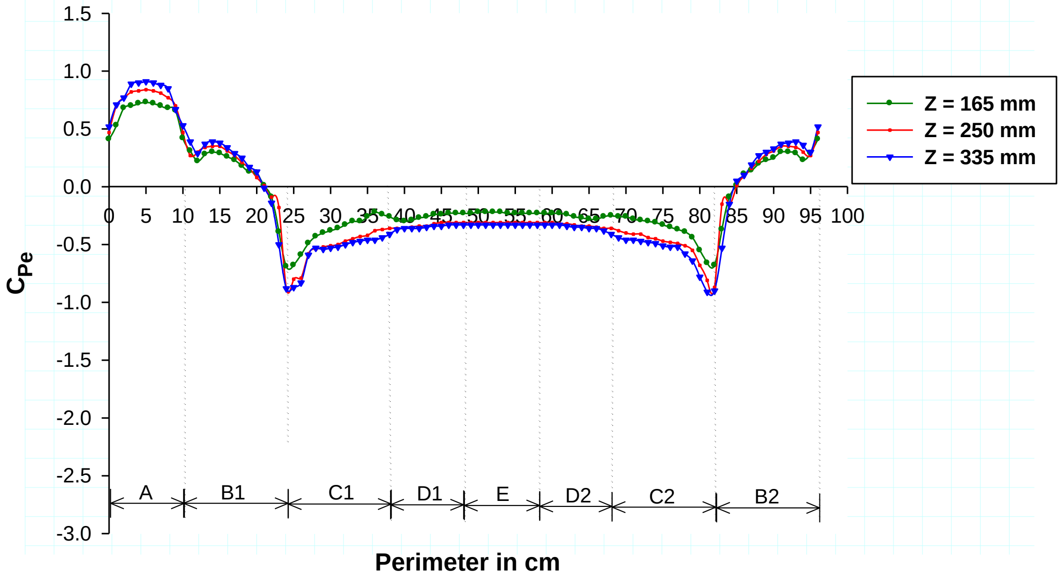

Figure 5. 86: C_{Pe} Along Perimeter Diamond Shape Model 0° Wind Angle

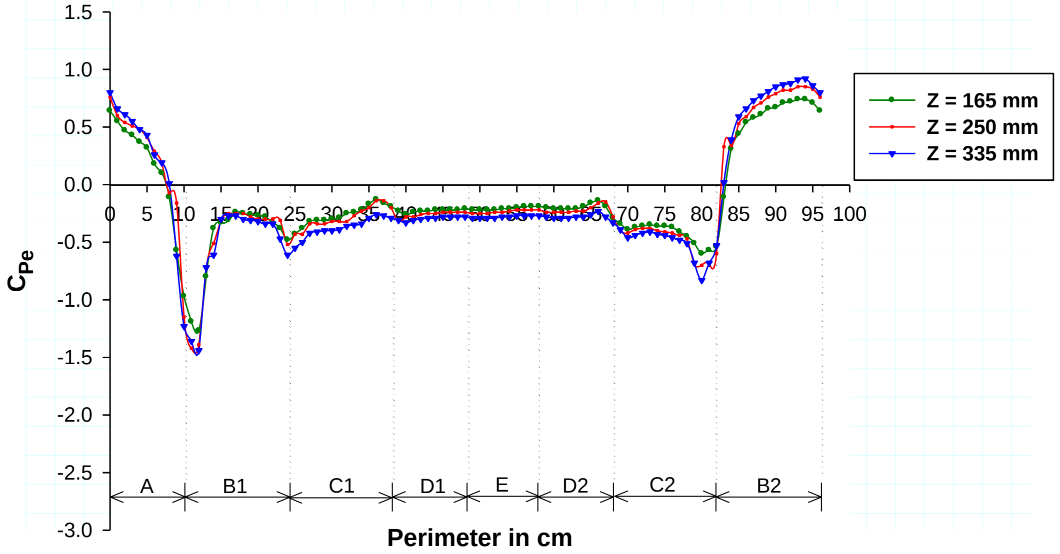

Figure 5. 87: C_{Pe} Along Perimeter Diamond Shape Model 30° Wind Angle

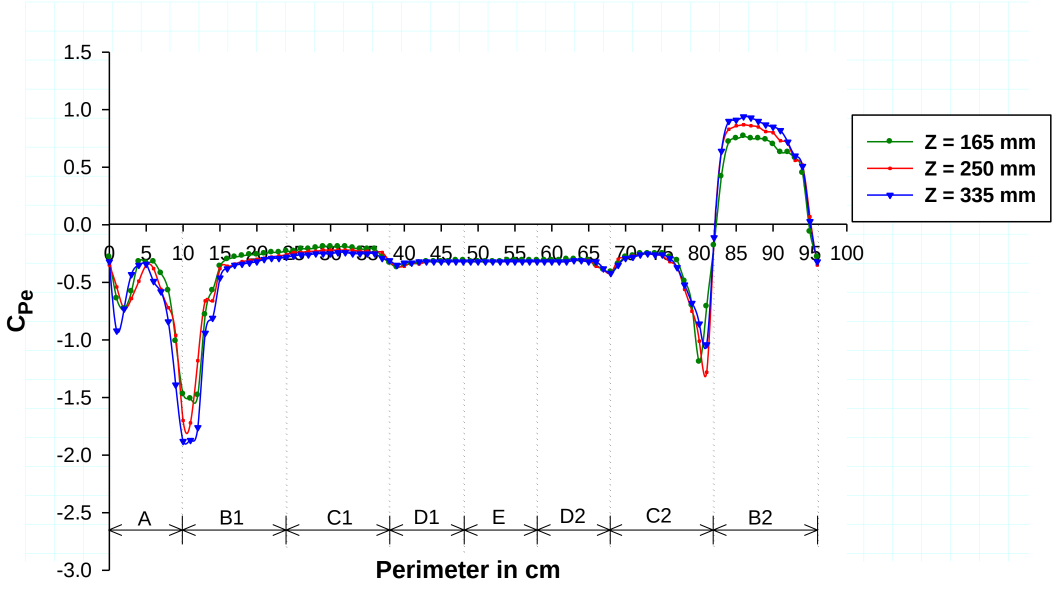

Figure 5. 88: C_{Pe} Along Perimeter Diamond Shape Model 60° Wind Angle

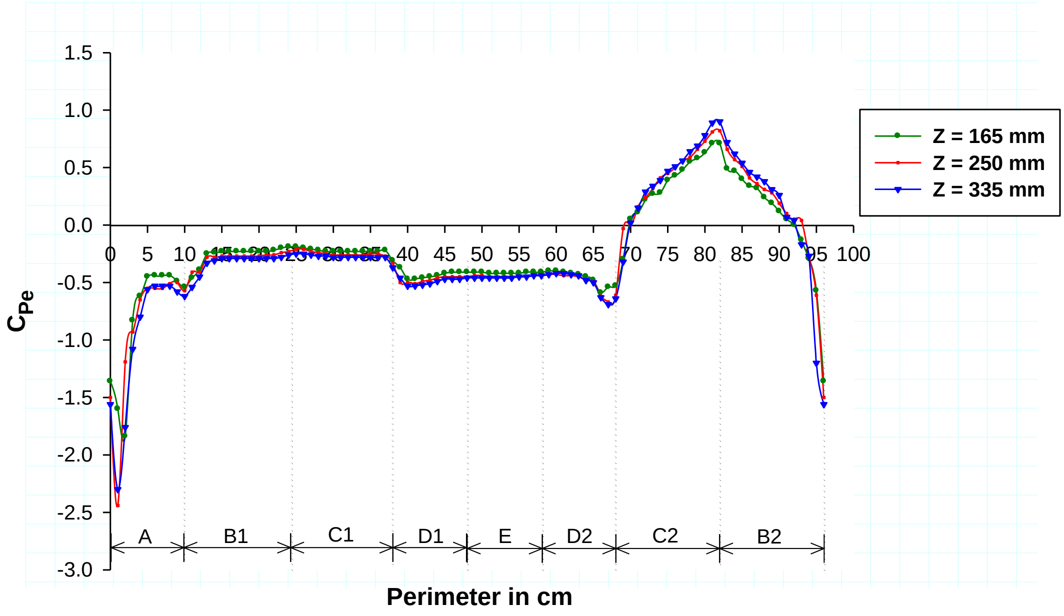

Figure 5. 89: C_{Pe} Along Perimeter Diamond Shape Model 90° Wind Angle

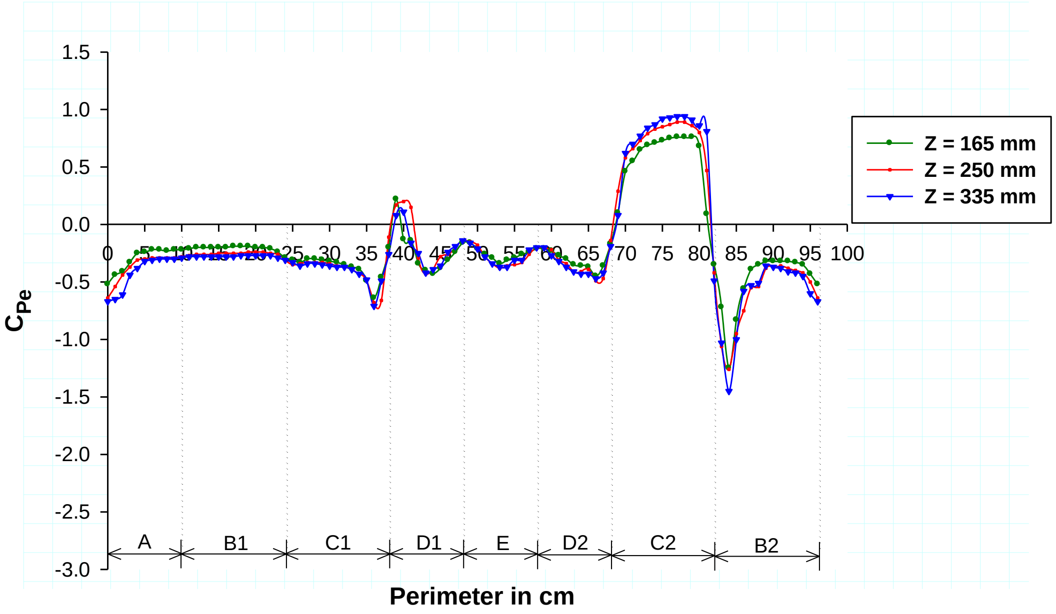

Figure 5. 90: C_{Pe} Along Perimeter Diamond Shape Model 120° Wind Angle

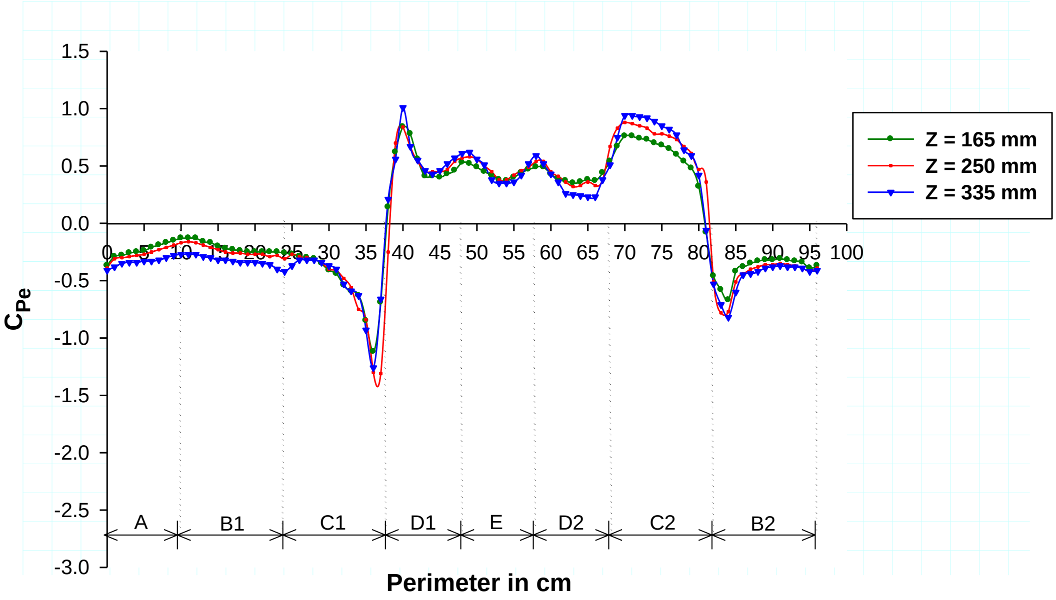

Figure 5. 91: C_{Pe} Along Perimeter Diamond Shape Model 150° Wind Angle

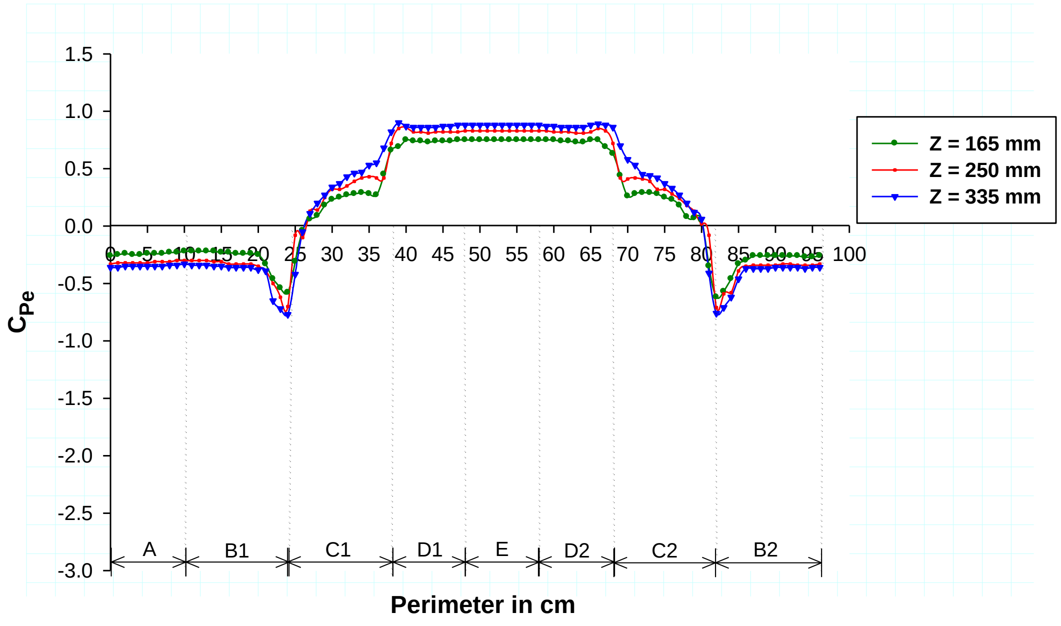

Figure 5. 92: C_{Pe} Along Perimeter Diamond Shape Model 180° Wind Angle

5.3.11 C_{Pe} Along Central Vertical Line on Faces

Variation of pressure coefficient along the central vertical line on faces are shown in Figure 5.92, 5.93, 5.94, 5.95, 5.96, 5.97 & 5.98. This gives the idealized pattern of pressure coefficients throughout the height on faces. In general, the faces bearing the impact of the wind directly show positive pressure and faces under wake or facing separation of flow from the edges show suction. The vertical centre line plots give a fine picture of the change in flow pattern along the height of the faces. It is observed that in most cases where wind is impinging on the face orthogonally the maximum value of C_{Pe} along the central vertical line is nearly equal to 1.0. For oblique impact of wind on the face maximum C_{Pe} values along the line are lower on the face than 1.0. Also, symmetrically opposite faces show mirror image of the C_{Pe} values along the line.

At 0° wind incidence angle face A is facing the wind orthogonally and hence the maximum positive C_{Pe} is nearly 1.0. It occurs at 0.475 m height of the model. From there the value sharply becomes negative due to escaping of wind from the roof top. Faces B1 and B2 are facing the wind obliquely and hence are having lesser maximum values of C_{Pe} along the line than that on face A. Being symmetrically opposite the plots for face B1 and B2 are overlapping on each other. Since the flow is separating from the confluence of faces B1C1 at one side and B2C2 on another side, the plots of central vertical C_{Pe} values on faces C1 and C2 are showing suction and almost overlapping with each other. The maximum C_{Pe} is -0.5 at the height of 0.25 m of the model. Faces D1, D2 and E being on wake region are showing maximum suction C_{Pe} values between -0.33 to -0.35 at a height of 0.3 m.

At 30° wind incidence angle the line for faces A and B1 are showing positive values whereas all other faces are having nearly equal suction values throughout the height with little fluctuation between C_{Pe} -0.2 to -0.45.

At 60° wind incidence angle positive pressure exists on face B2 whereas all other faces are experiencing suction along their respective central vertical line. High fluctuation along the height on face A is observed. It is due to creation of eddies and turbulence in flow on the face.

At 90° wind incidence angle wind is impinging at the meeting edge of faces B2 and C2 and separating from the respective far edges of the faces. As such, positive pressure exists on the near side of the faces and negative pressure on the far side of the faces i.e., high gradient of pressure exists on these faces. The central vertical lines on the faces are, as expected, subjected to lower than 1.0 maximum value of C_{Pe}. Other faces are facing suction at this wind incident angle. However, it is observed that the values of C_{Pe} on face D1 is recovering from suction to positive pressure (C_{Pe} = 0.26) at roof height and on face D2 suction is increased to C_{Pe} = -1.08 from an average value of -0.45. On face A maximum suction (C_{Pe} = -0.56) is observed at 0.3 m height of the model.

At 120° wind angle face C2 is experiencing positive pressure. Rest other faces are experiencing suction with marginal fluctuations along the height.

At 150° wind angle wind impact is direct on face C2 and hence the maximum C_{Pe} value on the central vertical line on face C2 is nearly 1.0. The re-entrant faces D1, D2 and E are also experiencing positive pressure along the line. As anticipated, they are changing sigh at roof level but; on face D2 this change is gradual. Rest other faces do have suction along the central vertical line with marginal fluctuations.

At 180° wind angle the situation of 0° wind angle is reversed. Faces A, B1 and B2 are facing suction along the central vertical line and other faces are experiencing positive pressure. The plot of C_{Pe} on face D1 and D2 are showing positive pressure along the central vertical line and overlapping on each other, being symmetrical faces. Face E is experiencing maximum C_{Pe} value of almost 1 as wind is directly hitting the face. Positive pressure does exist on the plot of faces C1 and C2 also. But, due to obliqueness of faces, the maximum values of C_{Pe} on the faces are lower than 1.0.

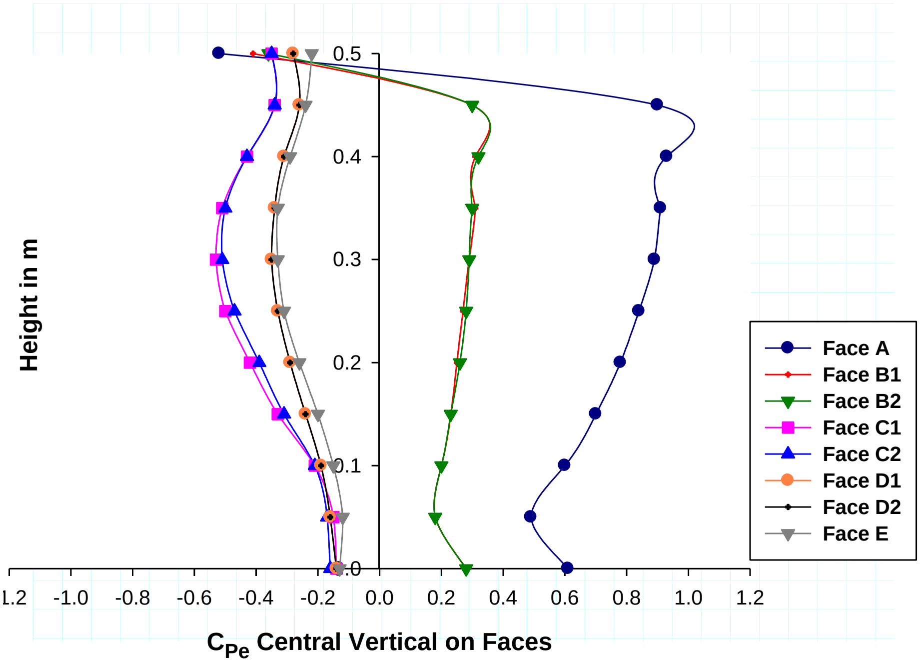

Figure 5. 93: C_{Pe} Along Central Vertical Line on Faces Diamond Shape Model 0° Wind Angle

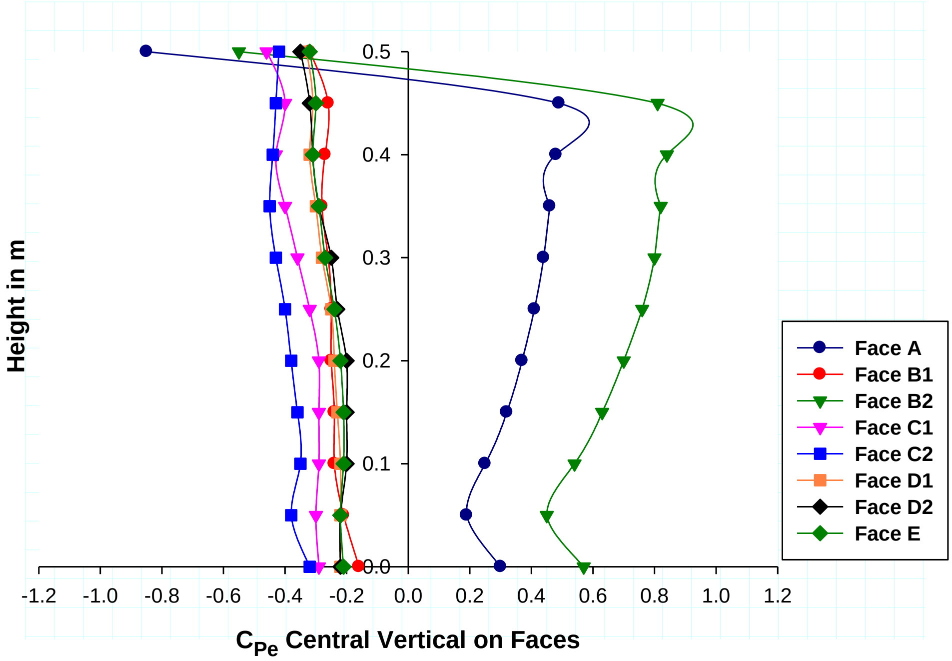

Figure 5. 94: C_{Pe} Along Central Vertical Line on Faces Diamond Shape Model 30° Wind Angle

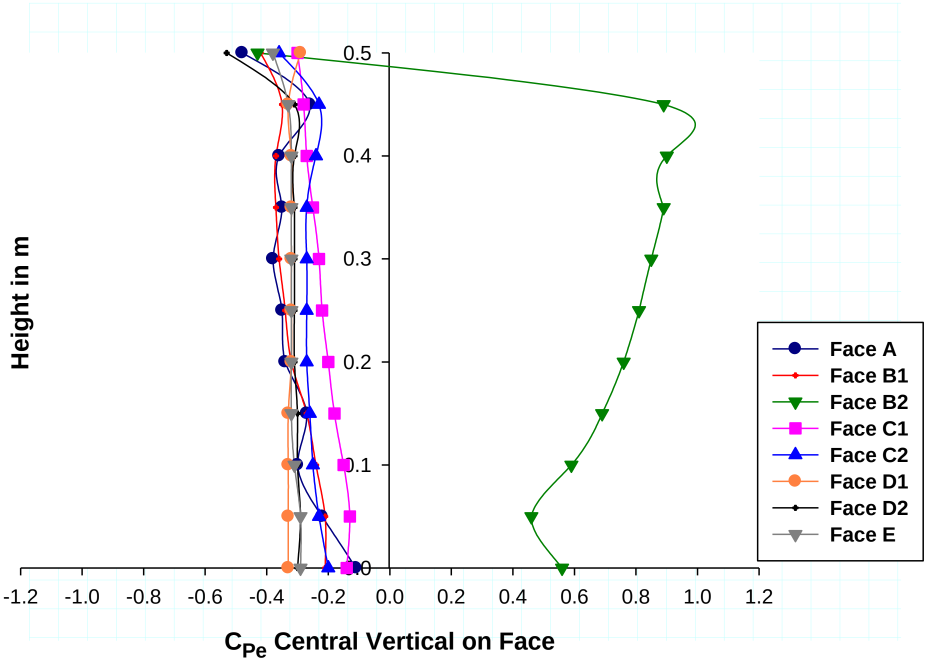

Figure 5. 95: C_{Pe} Along Central Vertical Line on Faces Diamond Shape Model 60° Wind Angle

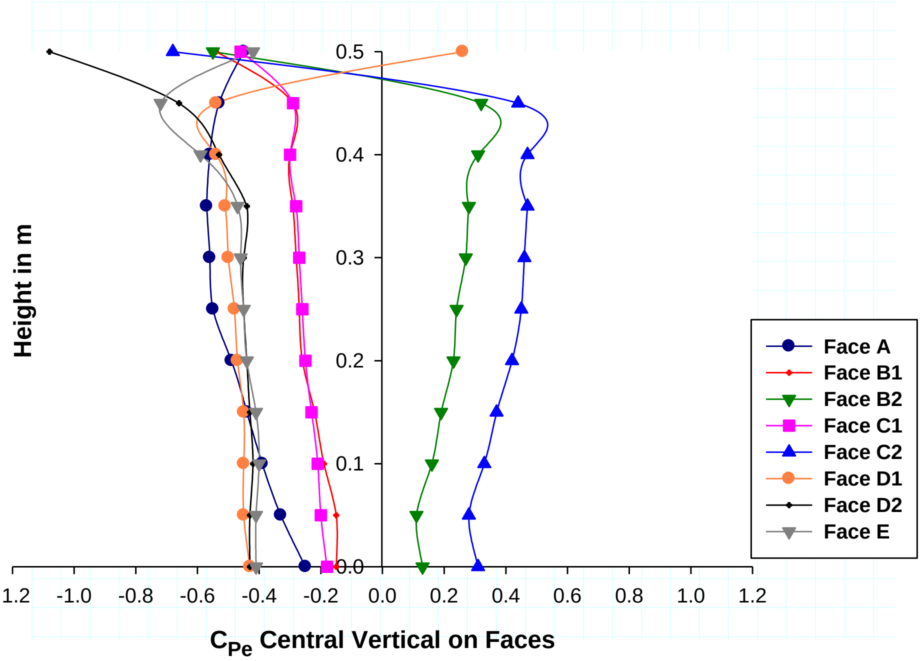

Figure 5. 96: C_{Pe} Along Central Vertical Line on Faces Diamond Shape Model 90° Wind Angle

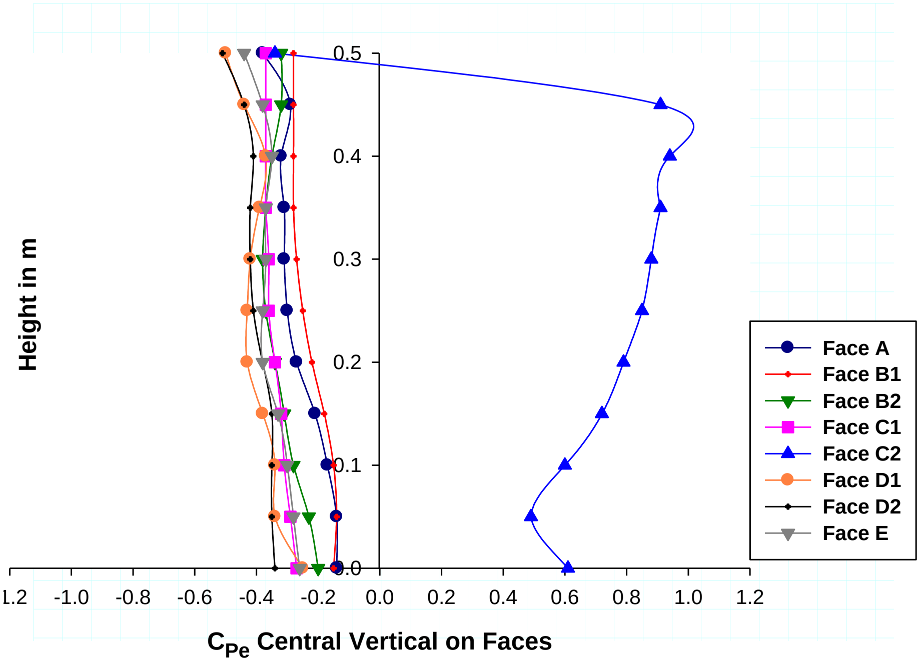

Figure 5. 97: C_{Pe} Along Central Vertical Line on Faces Diamond Shape Model 120° Wind Angle

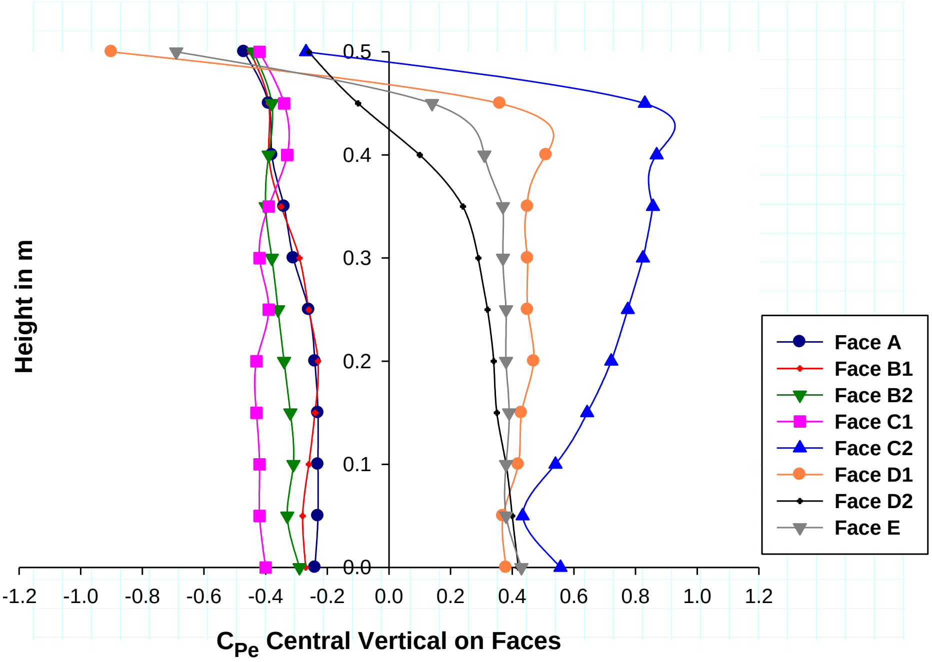

Figure 5. 98: C_{Pe} Along Central Vertical Line on Faces Diamond Shape Model 150° Wind Angle

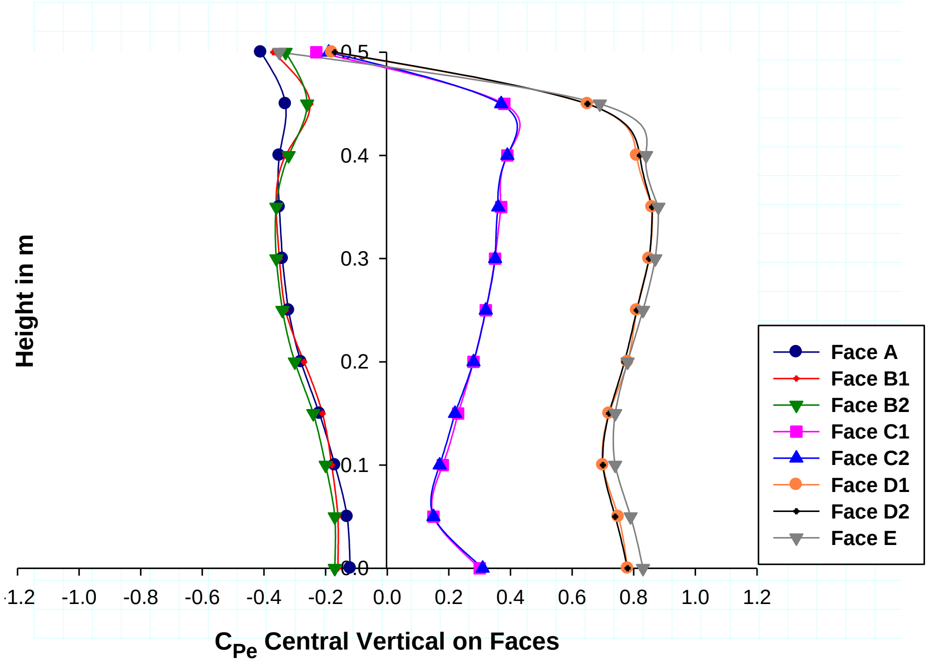

Figure 5. 99: C_{Pe} Along Central Vertical Line on Faces Diamond Shape Model 180° Wind Angle

5.4 WRENCH C-SHAPE

Wrench plan shaped model is symmetrical about one axis in plan. Study for this model has been conducted for different wind angle of attacks from 0° to 180° @ 15° interval. Wind has been varied in a clockwise direction. However due to space restrictions discussion for 0° to 180° @ 30° has been done. The surface pressure generated around the model has been studied and discussed in terms of coefficient of pressure on the faces. It will be interesting to know the behavior of pressure generated on faces falling within the recessed cavity (inner faces of the model). Illustration of flow pattern around the model and velocity vector diagrams have been provided to understand flow separation, reattachment of flow, creation of wakes and vortices. Velocity vectors depict relative flow direction and speed around the model. The pressure on each of the inner faces have been found almost similar for a particular wind incident angle.

5.4.1 C_{Pe} Contour 0° Wind Angle

At 0° angle of wind attack distribution of pressure coefficient on faces are similar on symmetrical faces. Flow separation is taking place before it strikes orthogonally on face A. As expected, the pressure contour on face A is similar to that on windward face of a rectangular model. Pattern of pressure contour is parabolic in nature and symmetrical about the vertical center line. The area average C_{Pe} on the face is 0.67.

On the inclined faces B1 and B2 high gradient of vertical contour isobars are seen with positive value of C_{Pe} towards windward side and negative C_{Pe} towards lee side from where wind detachment is taking place with high speed.

Side faces C1 and C2 are under suction. High turbulence and formation of eddies are expected towards the upwind side as the C_{Pe} values are maximum negative. Being the symmetrical faces the values of C_{Pe} on the faces should have been similar. However, some differences in the values are observed. It is due to three-dimensional anisotropic behavior of wind. Though, pattern of isobars is vertical in most part of the faces, inclined isobars at the top and bottom corners both are appearing towards the lee side. It could be the effect of backwash past the inclined face D1 and D2 respectively.

Face D1 and D2 are under wake (Figure 5.106). Negative pressure gradient is high on these faces towards the windward side up to middle width of the face after which the gradient decreases with minimum value of suction towards the lee side.

Face E1 and E2 are facing backwash but unlike in rectangular model the pattern of pressure contours is not concentric on the faces due to recessed opening on one side and inclined face D1 and D2 respectively on another side. Negative flow from the wake tends to contour the surface from the recessed opening towards the respective outer side of the faces i.e., towards the meeting edges with D1 and D2 respectively (Figure 5.99). However, suction is increasing from bottom to top of the faces. Area average C_{Pe} on the faces are -0.29 each. High concentration of suction is seen at the top outer side of the faces suggesting outflow of wind from the faces.

Face F1 and F2, though side faces, and are under wake, backwash seems to be surfing along the face width towards the cavity opening creating suction throughout the face with an upwash. At top of the faces high concentration of suction is seen from where the flow is merging with the flow from the roof recirculation cavity.

Faces G1 and G2 are inside the cavity and almost horizontal isobars of suction with minor gradient of reduction towards top is seen on the faces. Similar are the cases with other faces (H1, H2; I1, I2 and J1, J2) inside the cavity. The pattern of isobars and C_{Pe} values on these faces are similar.

Roof top is under negative pressure throughout. The pattern of contours is similar to the shape itself with high concentration of negative pressure (minimum C_{Pe} = -1.28) near top of windward face A.

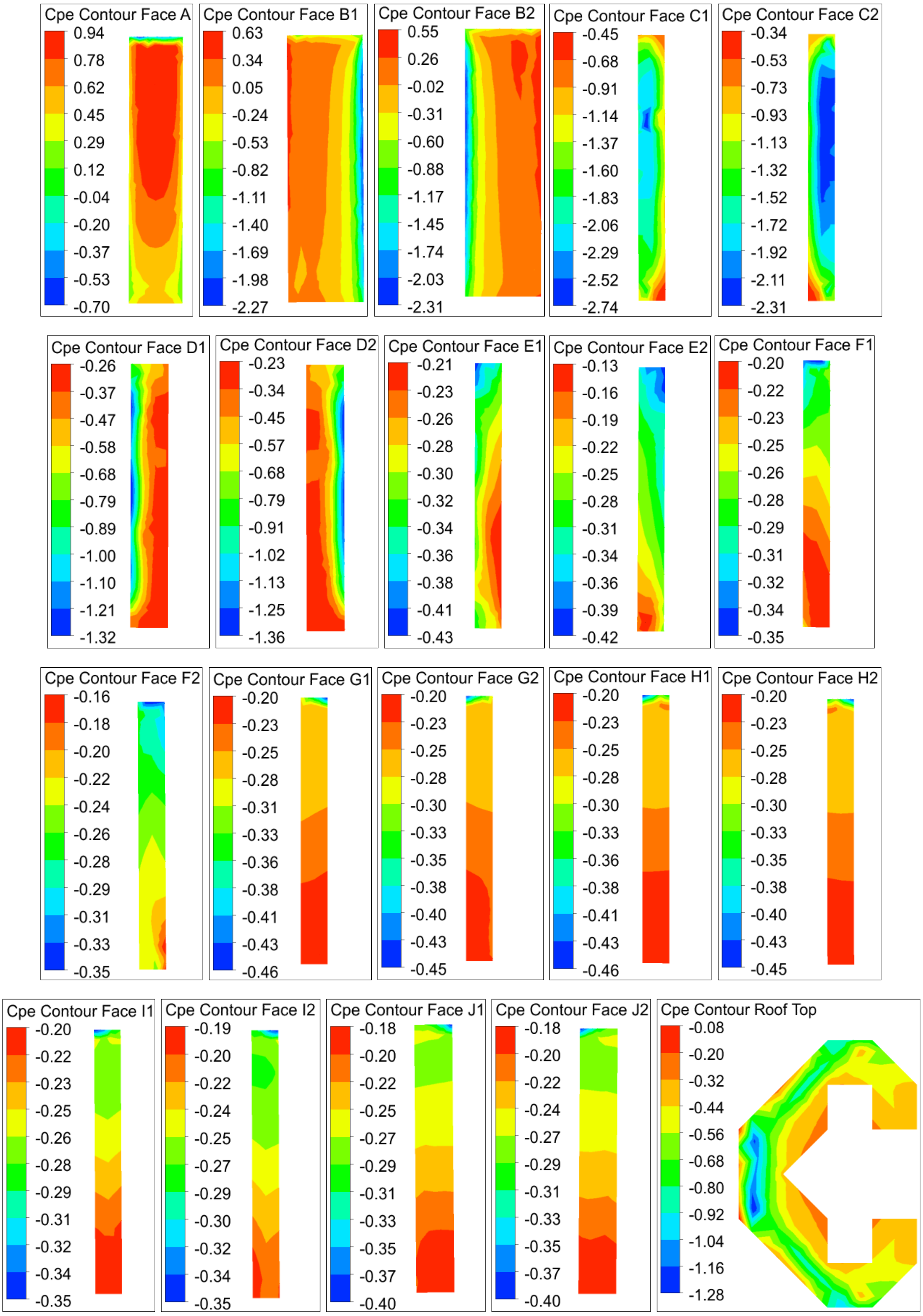

Figure 5. 100: C_{Pe} Contour on Faces & Roof Wrench Shape Model 0° Wind Angle

Table 5. 5: Area Average C_{Pe} on Faces Wrench Shape Model

Face	Wind Angle of Incidence						
	0°	30°	60°	90°	120°	150°	180°
Face A	0.67	0.22	-0.54	-0.77	-0.42	-0.34	-0.30
Face B1	-0.15	-0.66	-0.51	-0.23	-0.25	-0.39	-0.42
Face B2	-0.15	0.52	0.59	0.08	-0.49	-0.60	-0.42
Face C1	-1.70	-0.69	-0.23	-0.19	-0.31	-0.85	-1.57
Face C2	-1.70	-1.15	-0.11	0.72	0.20	-1.10	-1.57
Face D1	-0.53	-0.30	-0.21	-0.28	-0.68	-1.14	-0.51
Face D2	-0.53	-0.77	-1.05	-0.21	0.68	0.44	-0.51
Face E1	-0.29	-0.24	-0.30	-0.29	-0.40	-0.08	0.57
Face E2	-0.29	-0.31	-0.74	-1.12	-0.11	0.62	0.57
Face F1	-0.25	-0.31	-0.38	-0.15	0.30	0.59	0.60
Face F2	-0.25	-0.26	-0.36	-0.44	-0.14	0.29	0.60
Face G1	-0.25	-0.28	-0.35	-0.28	0.01	0.47	0.67
Face G2	-0.25	-0.28	-0.35	-0.26	0.06	0.46	0.67
Face H1	-0.24	-0.28	-0.35	-0.26	0.05	0.51	0.68
Face H2	-0.24	-0.28	-0.35	-0.26	0.06	0.46	0.68
Face I1	-0.24	-0.28	-0.35	-0.26	0.08	0.55	0.68
Face I2	-0.24	-0.27	-0.35	-0.27	0.03	0.41	0.68
Face J1	-0.24	-0.27	-0.35	-0.26	0.08	0.55	0.74
Face J2	-0.24	-0.27	-0.35	-0.26	0.06	0.50	0.74
Roof							
Top	-0.56	-0.56	-0.53	-0.48	-0.39	-0.54	-0.57

5.4.2 C_{Pe} Contour 30° Wind Angle

As the wind incidence angle moves to 30° in clockwise direction and impinges on the confluence of faces AB2, there is no symmetrical behaviour of distribution of pressure on the faces. Positive pressure, half parabolic in nature exists on face A and B2 both with suction at the far ends of the faces from where separation of flow is taking place. The area average C_{Pe} on face A is reduced to 0.22 compared to 0.67 at 0° wind angle of attack. However, on face B2 it is changed from -0.15 to 0.52.

On face B1 suction exists. The pattern of pressure isobars is almost vertical. High negative pressure is seen towards the upwind side, improving near the middle, remaining almost similar in most part of the middle and again reducing towards the lee side. This indicates high turbulence and formation of eddies at the edges on face B1.

On face C1 suction exists on the face with vertical pressure isobars, high suction towards the near end reducing towards the far end, but, a bit inclined due to wake effect from face D1. On face C2 high suction is seen towards the near end covering more than half the width. At the center vortex shedding is apparently observed.

Face D1 is under wake (Figure 5.109) and area average suction coefficient of pressure on the face is -0.30. The pressure isobars are inclined on the face. Vertical pressure pattern exists on face D2 with low suction from the rear end till the middle of the face with high gradient. After the middle width it is gradual towards the upwind edge. For this angle of wind attack, maximum suction area average C_{Pe} = -0.77 exists on this face.

Though faces E1 and E2 are submerged in the wake region, pattern of pressure contours is different due to their relative location with respect to wake. The area average C_{Pe} on the faces are respectively -0.24 and -0.31.

Almost vertical suction isobar in the middle of face F1 of greater magnitude than near the edges appear. Least fluctuation in C_{Pe} values on the face is found. On face F2 upwash from wake is observed. Area average C_{Pe} on face F1 and F2 are -0.31 and -0.26 respectively.

Inside the cavity faces G1, G2, H1, H2, I1, I2, J1 and J2 flow is generating almost equal area average C_{Pe} of -0.28/-0.27. Pattern on the faces is slightly different due to backwash coupled with recirculation of air within the cavity.

On the roof top, again, the overall pressure is suction improving from the near end to far end. Spot of high concentration of suction is seen near top of confluence of face AB2.

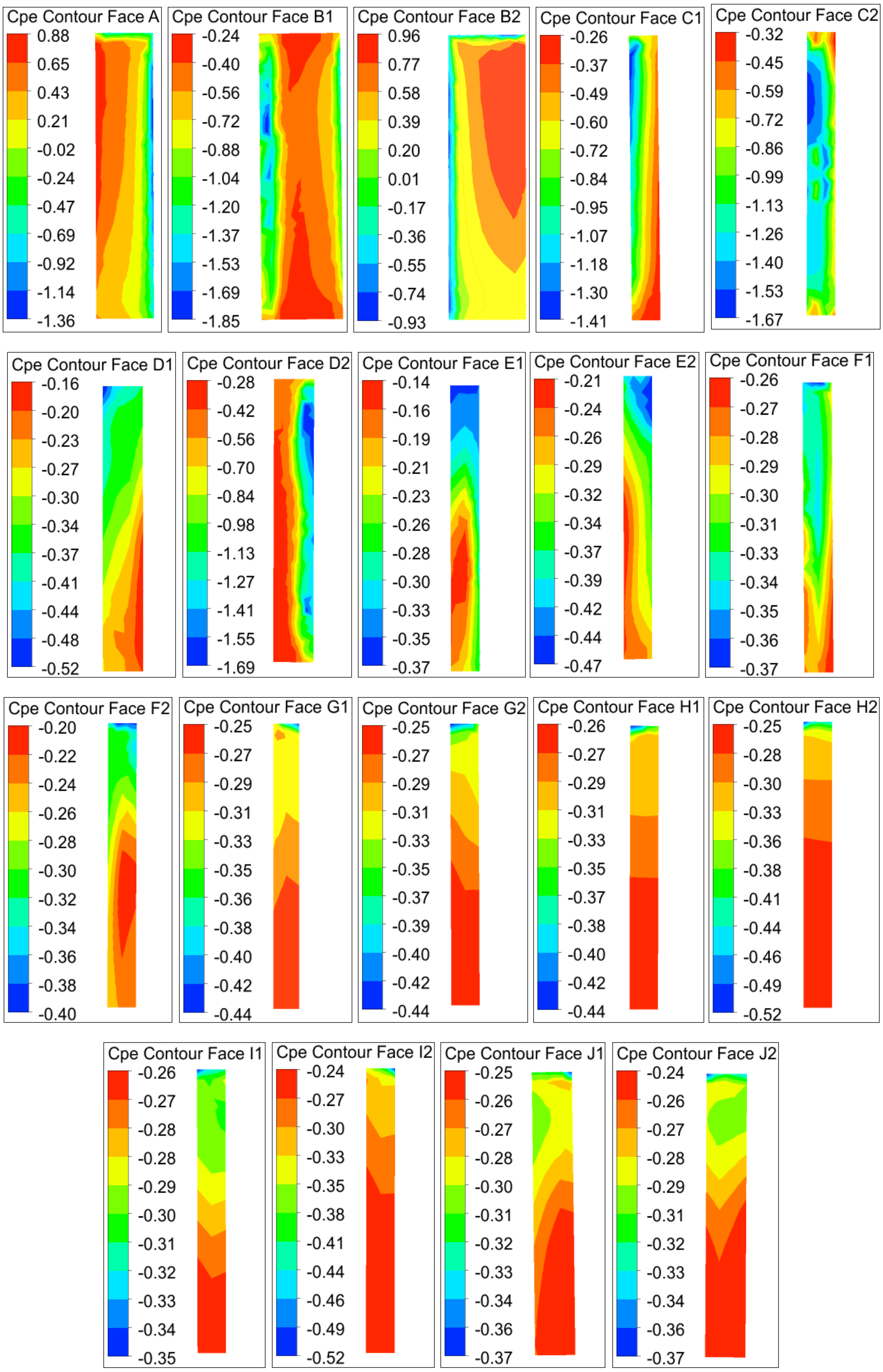

Figure 5. 100: C_{Pe} Contour on Faces & Roof Wrench Shape Model 30° Wind Angle (Contd.)

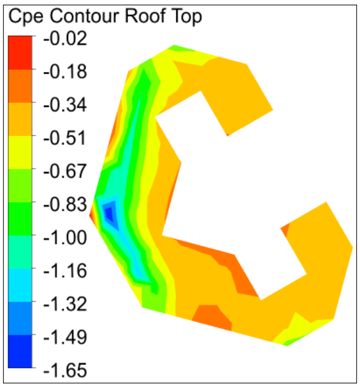

Figure 5. 101: C_{Pe} Contour on Faces & Roof Wrench Shape Model 30° Wind Angle

5.4.3 C_{Pe} Contour 60° Wind Angle

As the angle of wind incidence increases from 30° to 60, the severity position of attack of wind on face B2 changes. It shifts towards face C2. As such, half parabolic pressure pattern concentrated towards face C2 is formed.

A portion of face C2 towards the near end is also having positive pressure. However, at the far end on face C2 negative pressure exists owing to flow detachment from there. Gradient of pressure coefficient is high on face C2 with maximum positive = 0.86 and maximum negative = -0.98. Area average C_{Pe} on face C2 is -0.11, least on all faces for this angle of wind attack.

On face A minimum suction exists in the middle increasing towards both ends with high gradient of vertical isobars. A major part of face B1 is immersed in low suction due to backwash from wake on lee side. But, towards the upwind side high suction is observed at the confluence of face AB2 due to flow separation.

Face C1 is under wake (Figure 5.112) but, due to the fact that it is inclined with respect to backflow the contour patterns are showing inclined isobars.

Face D1 is also under wake. Area average C_{Pe} on face D1 is -0.21. Pattern of pressure contour on face D2 is vertical due to creation of shear layer on the surface as wind is surfing past the face after getting detached from the windward edge of face D2 and is imparting high suction gradient of pressure on the face. High turbulence and formation of eddies are suspected on the face near the middle height towards the upwind side. Vortex shedding at top and bottom towards the lee side appears on face D2. Area average C_{Pe} = -1.05 on face D2 is maximum negative for all faces at this angle of wind attack.

Negative velocity from backwash is surfing past face E1 form its outer edge towards the cavity opening creating inclined isobars at the bottom gradually becoming vertical along height. Suction is more towards the cavity opening. On face E2 high gradient of suction exists. Area average C_{Pe} on the face is -0.74.

All the inner faces are under suction of almost similar magnitude. Shear layer formation and vortex shedding is seen on face F1with vertical isobars. Face H2 and I2 are subjected to similar suction on most part of the faces due to circulation of backwash within the small cavity between these two faces. Face J1 and J2 are having same minimum and maximum C_{Pe} value of -0.42 and -0.31 respectively.

On the roof top overall pressure is suction. Concentration of high suction strip near the top of face B2 exists on the roof.

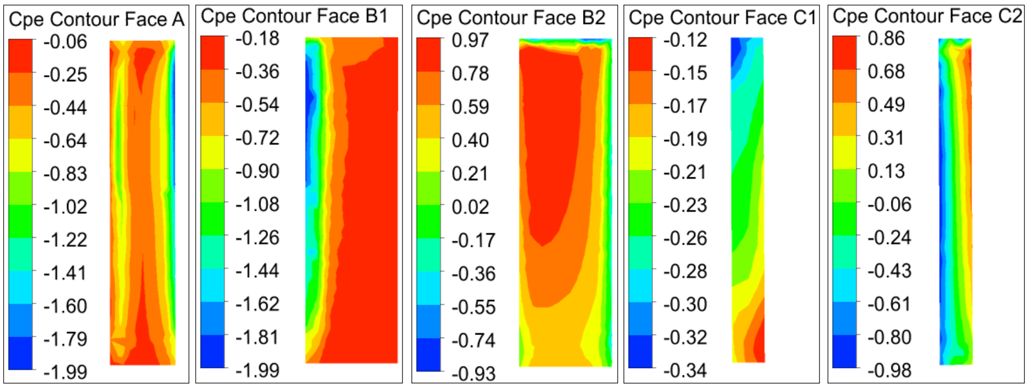

Figure 5. 101: C_{Pe} Contour on Faces & Roof Wrench Shape Model 60° Wind Angle (Contd.)

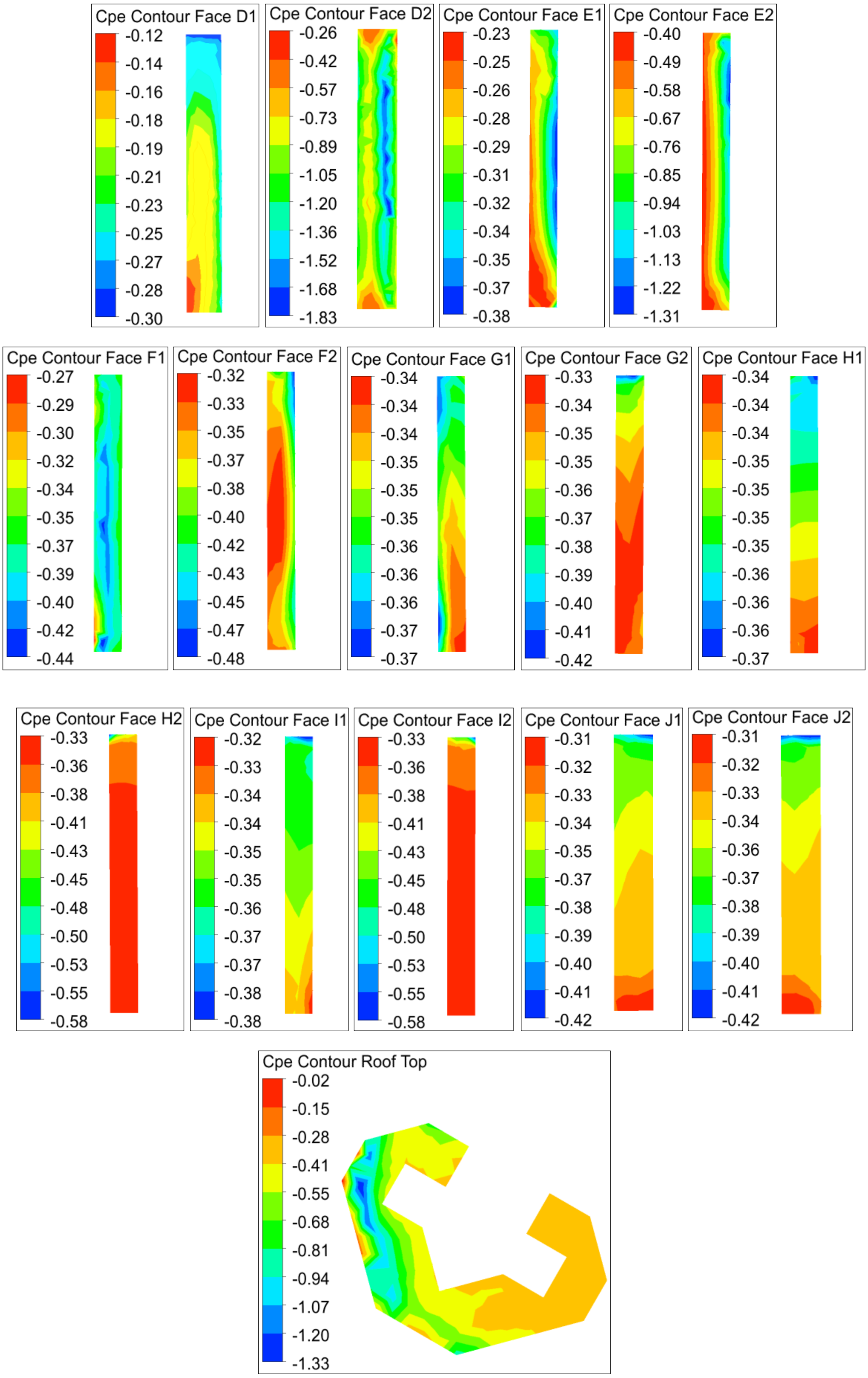

Figure 5. 102: C_{Pe} Contour on Faces & Roof Wrench Shape Model 60° Wind Angle

5.4.4 C_{Pe} Contour 90° Wind Angle

At 90° wind incidence angle face C2 is facing the severity of wind due to direct exposure of wind. Inclined faces B2 and D2 are also facing the impact of wind towards their near end edges. Separation is taking place from far end edges of face B2 and D2. As such, face C2 is under positive pressure increasing in height due to atmospheric boundary layer flow. However, the pattern of pressure contours on the face is not parabolic and concentric about the vertical centre line, but, triangular owing to the effect of inclined dissimilar faces B2 and D2. It is shifted more towards face B2 as wind tends to flow past face B2 more rapidly than that past face D2 (Figure 5.115).

High gradient of vertical isobars exists on face B2 and D2 with positive pressure towards the windward side and negative pressure towards the downwind side. Even though the gradient of pressure is high on the faces, area average C_{Pe} on face B2 is 0.08 and that on face D2 is -0.21.

Face A is the side face and pressure pattern on the face is vertical. High gradient of suction exists towards the near end edge till the middle width after which suction stabilizes. Face F2 is also the side face and similar pattern of vertical pressure isobars as that on face A is observed on the face with high turbulence towards the windward side due to detachment of flow.

Face B1 is under wake. Since it is inclined and not orthogonal to the backwash, flow of wind from the wake is surfing along the width of the face towards the confluence of face AB1, conflicting with the sidewash from face A and creating eddies at the confluence.

Gradual upwash from the wake is noticed on face C1 with area average C_{Pe} = -0.19. Face D1 is partially under the influence of backwash and partially under sidewash due to its inclined orientation. Accordingly, towards the lee side the pressure pattern on the face is being governed by backwash, suction being increased in trapezoidal formation along height. Towards the windward side pressure pattern is vertical.

Pattern of isobars on face E1 and E2 is vertical being the side faces. On face E1 suction exists towards the lee side but, towards the windward side positive vertical isobars are observed due to impact of direct wind at the edge. On face E2 highest suction (area average C_{Pe} = -1.12) exists.

Within the recessed cavity flow is highly complex with a swirling motion created within the larger cavity and the smaller cavities between G1H1I1 and G2H2I2 both. Flow is hitting at the outer edge of face F1 creating positive pressure there and enters into the cavity. Finally, flow is taking exit from the cavity from face F2 (Figure 5.117). This implies the reason for different area average C_{Pe} on face F1 and F2 to be -0.15 and -0.44 respectively. Pattern of pressure isobars on face F1 and F2 are vertical.

On other faces inside the cavity minor variation of pressure coefficients on the faces are observed with almost same area average C_{Pe} on the faces in the range of -0.26 to -0.28.

On the roof top slight positive pressure above face F1 is seen. Rest area of roof is under suction with two distinct concentrations of high suction above face C2.

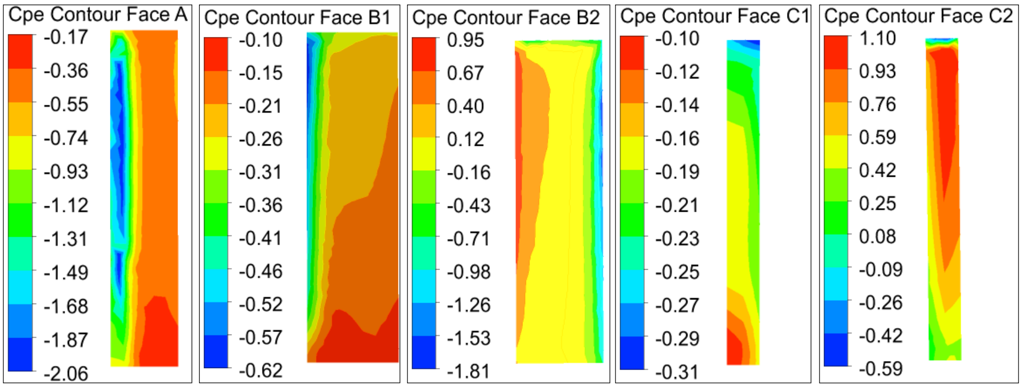

Figure 5. 102: C_{Pe} Contour on Faces & Roof Wrench Shape Model 90° Wind Angle (Contd.)

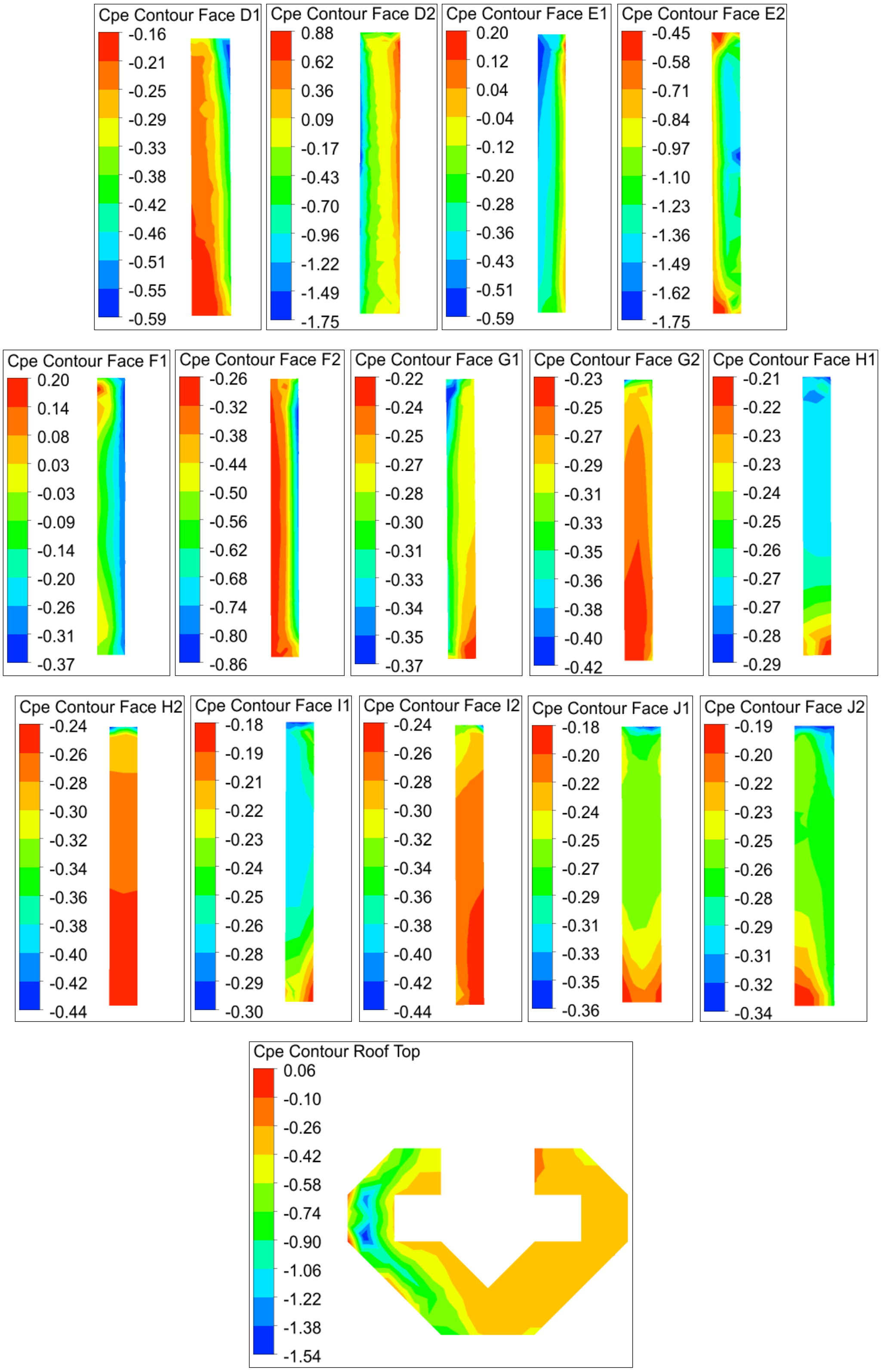

Figure 5. 103: C_{Pe} Contour on Faces & Roof Wrench Shape Model 90° Wind Angle

5.4.5 C_{Pe} Contour 120° Wind Angle

At 120° of wind incidence, skewed wind is impinging on face D2 and positive pressure exists on this face. Positive pressure also exists on face C2 near the meeting edge of face D2 and C2 due to its inclined orientation. At another edge of face C2 suction occurs as flow is detaching from this edge. The pressure isobars are vertical with high gradient (maximum C_{Pe} = 1.07 and minimum C_{Pe} = -0.54).

On face B2 suction of low magnitude exists in the middle width increasing towards the edges. Formation of small eddies in the middle 2/3rd height of the model are apparent towards the near end due to separation of flow at that end.

Face A is subjected to side wash at the near end and backwash at the far end as shown by the contour patterns.

Face B1 and C1 are under wake and are subjected to upwash. The area average C_{Pe} on the faces are -0.25 and -0.31 respectively. At the top corner on face C1 towards the confluence of C1D1 concentration of high suction is observed.

Face D1 is partially facing sidewash towards the near end and backwash towards the far end. Wind seems to be spiraling from the bottom due to backwash and forming high turbulence zone at the top half towards the near end from where wind separation is taking place. The gradient of pressure is high on the surface.

Pressure contour on face E1 suggests that it is influenced by direct impact of wind towards its upwind side with a maximum C_{Pe} = 0.84 whereas towards the far end from where wind detachment is taking place a negative pressure of C_{Pe} = -1.43 exists. Thus, a high gradient of pressure exists on face E1.

Face F1 is partially exposed to wind towards its outer side. Near top on the face positive pressure to the tune of maximum C_{Pe} = 0.84 is observed. The area average C_{Pe} on the face is 0.3.

Other cavity region faces from G1 to J1 and F2 to J2 the area average coefficient of pressure on the faces are positive, though of less magnitude (between 0.01 to 0.08). The pressure patterns on the faces are different on the faces due to complex flow within the cavity but overall pressure is gradual from positive at the bottom to negative at the top. This suggests that wind is contouring inside the cavity in the lower heights and then flowing into the cavity from the top.

On roof top least area average C_{Pe} = -0.39 for all wind angle of attacks exists. Concentration of local high negative pressure is seen above Face E1 and C2.

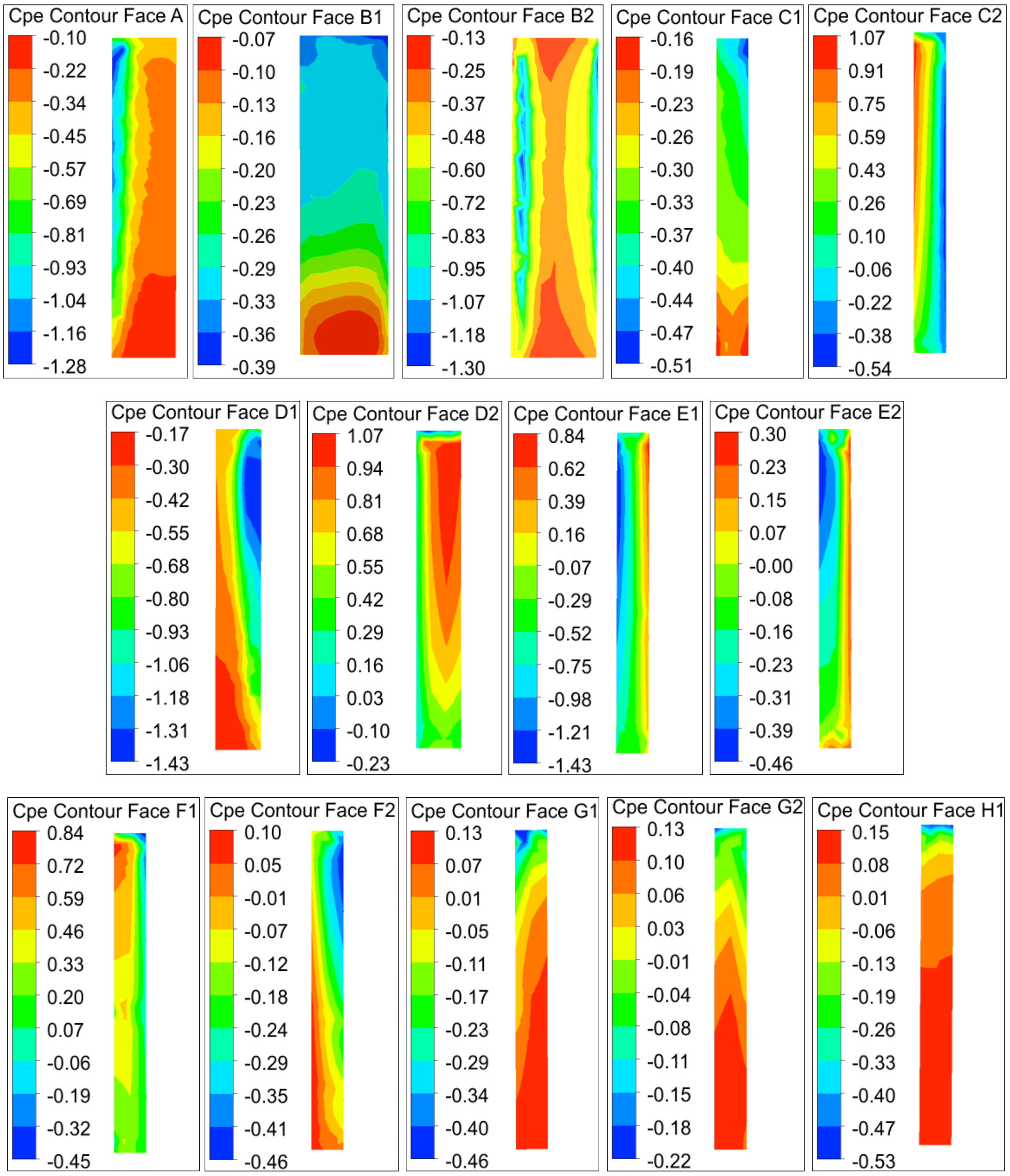

Figure 5. 103: C_{Pe} Contour on Faces & Roof Wrench Shape Model 120° Wind Angle (Contd.)

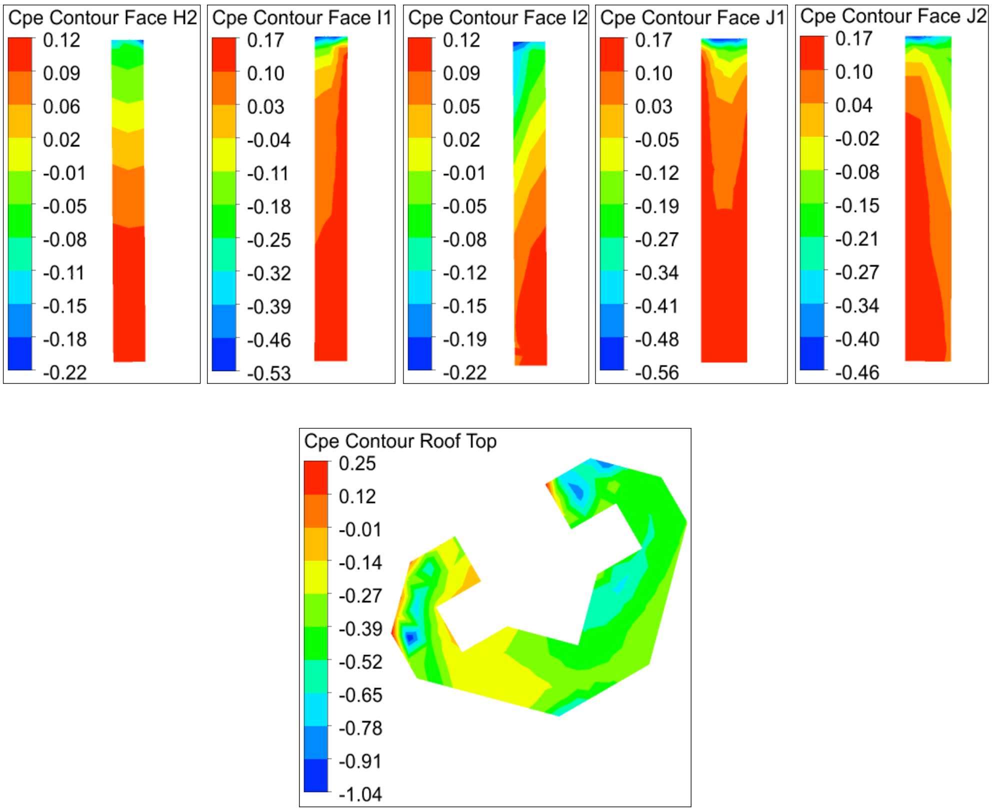

Figure 5. 104: C_{Pe} Contour on Faces & Roof Wrench Shape Model 120° Wind Angle

5.4.6 C_{Pe} Contour 150° Wind Angle

At this angle of wind attack faces A, B1 and B2 are under shadowed region of wind and hence suction exist on the faces. On face A gradual upwash is observed. On face B1, though maximum suction and minimum suction C_{Pe} on the face is similar to that on face A, pressure contours are twisting with formation of vortex shedding at top and bottom towards the confluence of face B1C1. Face B2 is under the influence of both, side wash and backwash. Towards the near end suction at the upper half height is seen to be very high (C_{Pe} = -2.01) with formation of high gradient isobars. However, towards the far end upwash from the wake develops almost similar suction on the face.

Wind impact is taking place at the edge of face D2 and E2 creating half parabolic pressure contours on the faces near the confluence of edges. The area average C_{Pe} on face D2 and E2 are 0.44 and 0.62 respectively. After deviating from the far end edge of face D2 wind is shearing past the face C2 (Figure 5.121) and separating from its far end. High gradient of suction from C_{Pe} = -0.01 to -1.82 is observed on the face with a vertical isobar. Formation of high turbulence eddies is seen near the upper height towards the edge from where wind detachment is taking place. Area average C_{Pe} on the face is -1.10.

On face D1 after separation at the confluence of face D1E1 wind is shearing past the face due to its inclined orientation. The pressure isobars are almost vertical with high gradient and nearly symmetrical from both edges. Near the center of the face high suction (C_{Pe} = -1.80) is observed. Vortex shedding at top and bottom both towards its far end is seen. Area average C_{Pe} on face D1 is -1.14, highest on all faces for this angle of attack exists.

Face C1 is inclined with respect to wind direction and is observing side wash at its near end and backwash at its far end i.e., lee side. High suction in the middle 1/3rd height towards the upwind side is observed. Area average C_{Pe} on the face is -0.85.

On face E1 minimum suction area average (C_{Pe} = -0.08) pressure coefficients among all the faces exists on face E1. However, the minimum and maximum coefficient of pressure on the face are -1.10 and 1.07 respectively. The face is susceptible to cladding designs. The pressure isobars are diagonal with maximum suction at the bottom towards the downwind side probably due to mixed response of separation of wind and ground surface wind generated from the upwind vortex. Positive pressure on the upper part towards upwind side is seen in a triangular formation.

On inner face F1, as it is exposed to direct wind, positive pressure increasing in height due to atmospheric boundary layer flow is observed with C_{Pe} = 0.59. After impinging on face F1 wind is entering into the recessed cavity and is creating positive pressure on internal faces.

It is observed that, except face F2, positive pressure of similar strength is developed on the internal faces up to half or more height due to circulation of wind within the cavity. On the upper height of the faces pressure is gradually reducing from positive to negative towards roof top from where wind is escaping.

On face F2 least positive C_{Pe} = 0.29 among the inner faces is developed. A gradual reduction in pressure along height is seen on face F2 with a suction concentration towards the top outer side of the face.

On the roof top huge area of high suction and creation of roof top recirculation zone is observed above face I1, J1, J2 and I2 which can be treated to be sensitive for roof structures. A small pinch of portion above the outer side of face F1 and inner side of face F2 on the roof top positive pressure exists.

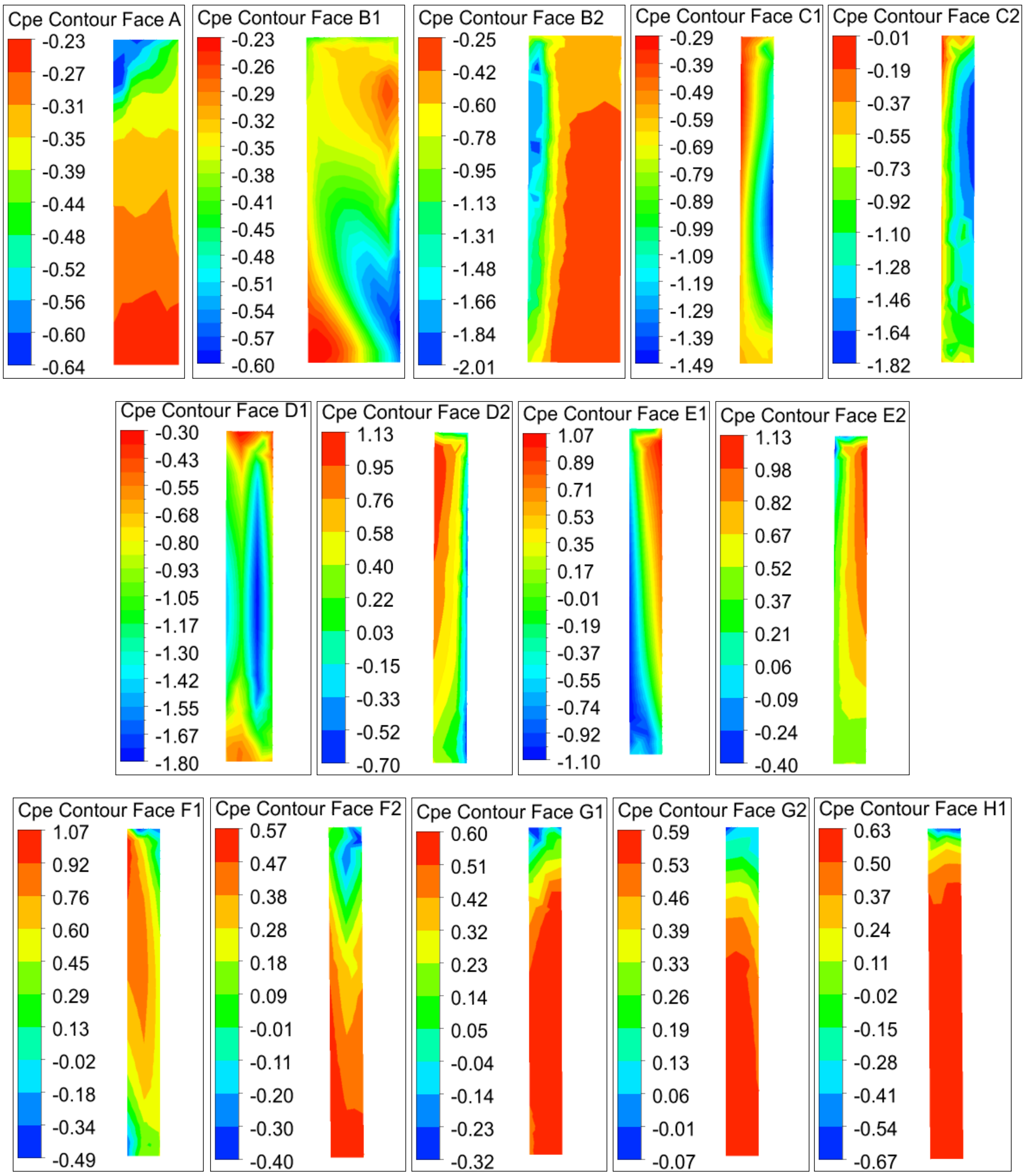

Figure 5. 104: C_{Pe} Contour on Faces & Roof Wrench Shape Model 150° Wind Angle (Contd.)

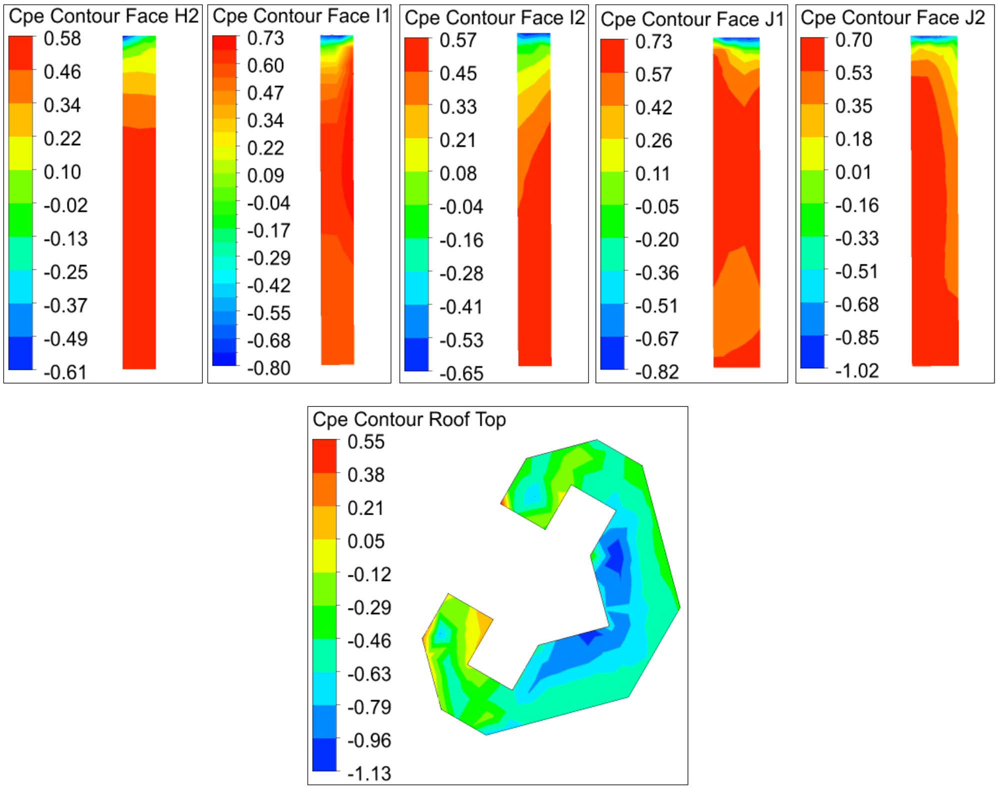

Figure 5. 105: C_{Pe} Contour on Faces & Roof Wrench Shape Model 150° Wind Angle

5.4.7 C_{Pe} Contour 180° Wind Angle

Figure 5.105 shows the pressure contours at 180° wind angle of attack. Faces E1 and E2 and inner faces J1 and J2 are exposed to direct wind and having positive pressure. Positive pressure isobars triangular is shape on the upper height of the face E1 and E2 are seen. In the lower portion effect of upwind vortex creates suction on the faces. Area average C_{Pe} on face E1 and E2 is 0.57 each. Owing to the symmetry of the model along the wind direction, pressure on similar and opposite faces are mirror image of each other.

Faces J1 and J2 are having highest positive C_{Pe} = 0.74 each among the faces experiencing positive pressure. After hitting faces J1 and J2, it is reflecting and circulating within the two small cavities (Figure 5.124) created between faces G1H1I1 at one side and G2H2I2 on another side. Flow within the cavity seems to be highly complex due to combined effect of stagnation, upwash, downwash, circulation of flow within the cavity and creation of ground level upwind vortex (Figure 5.133). As a result, positive pressure on most part of the lower height on the inner faces G1 to I1 and G2 to I2 of similar magnitude is developed. However, due to exist of flow from roof, negative pressure is observed on the upper portion of the faces and at the bottom suction is seen due to effect of downwash from faces J1 and J2. The area average coefficient of pressure on the faces are of similar magnitude (0.67/0.68). Faces F1 and F2 are, though side faces, also experiencing positive pressure. However, the coefficient of pressure (0.60 each) on the faces are least among the inner faces.

Face D1 and D2 are inclined surfaces and partially exposed to direct wind. Towards the upwind side positive pressure isobars in a triangular formation are seen. Pressure is increasing along height. Flow separation is taking place from the confluence of face C1D1 at one side and C2D2 at another side. As such, the lee side of face D1 and D2 are experiencing negative pressure. High gradient of pressure exists on the faces. Area average suction coefficient of the faces are -0.51 each.

Face C1 and C2 are side faces and are facing the effect of side wash. Vertical isobars are observed with high suction towards the near end edge reducing towards lee side. High gradient of pressure exists on the faces. Area average suction coefficient on the faces is maximum (-1.56/-1.57) comparative to other faces experiencing suction.

Face A, B1 and B2 are under wake. On face B1 and B2 combined effect of backwash and side wash are observed due to their inclined surface. Towards the windward side high suction exists on the faces and reduces sharply. On most part of the faces suction pressure of similar magnitude is seen. Area average C_{Pe} on the faces are -0.42 each.

Face A are completely submerged into wake. Flow from wake is hitting at the middle of the face from where upwash and downwash is developed reducing the suction further towards upper height and ground. Area average value of C_{Pe} is -0.30 on the face.

On the roof top highest suction area average C_{Pe} = -0.57 among all the wind angles of attack exists at this angle of wind attack. Two distinct suction concentration is seen one each above the confluence of face I1J1 and I1J2. At a portion positive pressure also exist near the confluence of face F1G1 and F2G2. For this angle of wind attack variation of C_{Pe} is decisive for roof top structures; minimum being -1.37 and maximum being 0.35.

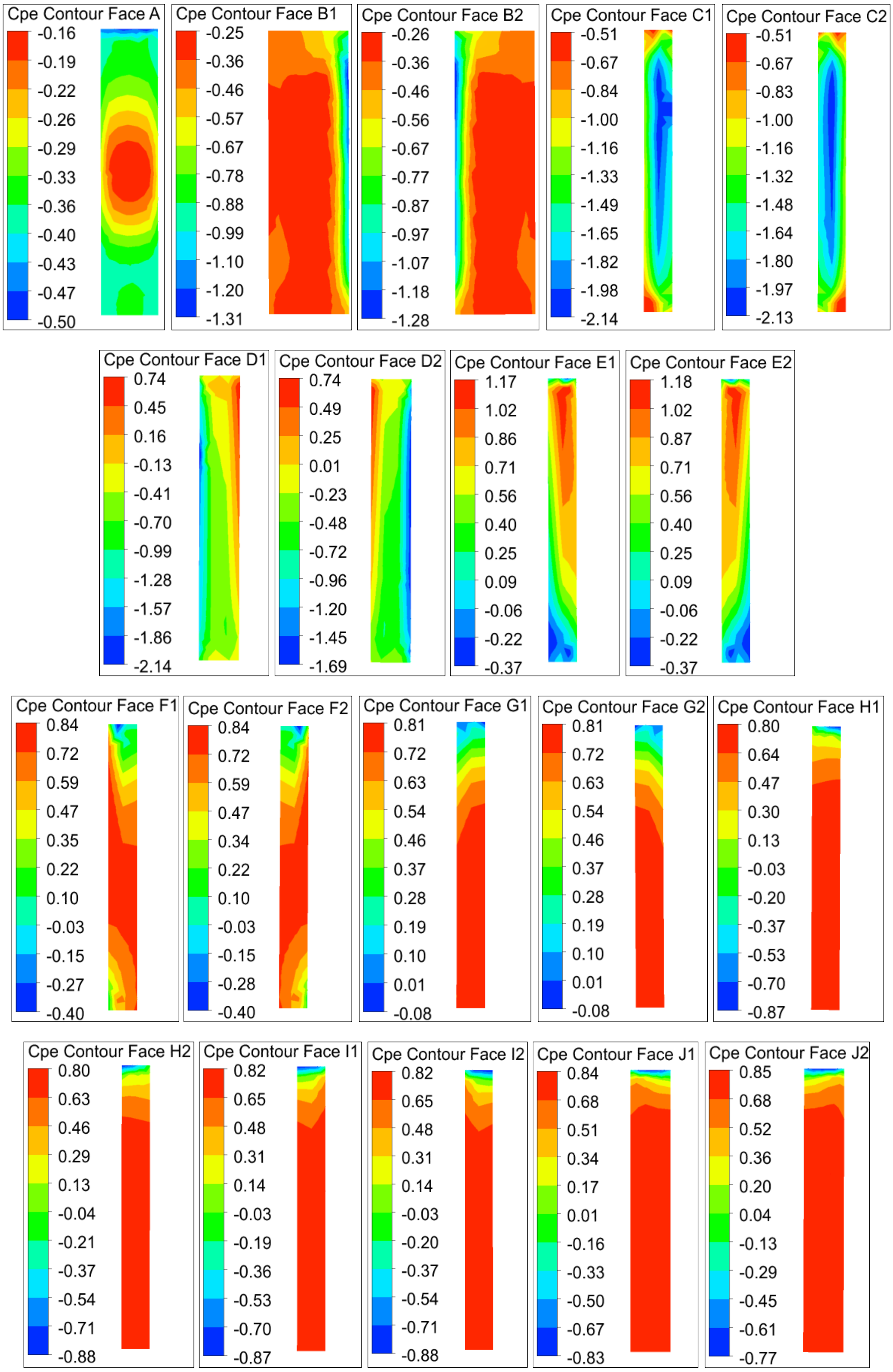

Figure 5. 105: C_{Pe} Contour on Faces & Roof Wrench Shape Model 180° Wind Angle (Contd.)

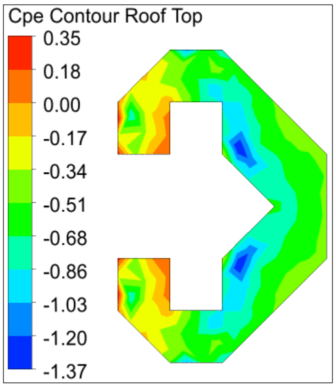

Figure 5. 106: C_{Pe} Contour on Faces & Roof Wrench Shape Model 180° Wind Angle

5.4.8 Wind Flow Pattern

Streamlines of wind flow patterns for all the discussed wind angles from 0° to 180° @ 30° have been shown in Figure 5.106, 5.109, 5.112, 5.115, 5.118, 5.121 & 5.124 at different heights of the model viz Z = 0.165 m, Z = 0.250 m and Z = 0.335 m and Figure 5.107, 5.110, 5.113, 5.116, 5.119, 1.122 & 5.125 show the velocity contours at the same heights for different wind incidence angles. Velocity vector diagrams at different heights for varied wind angles are shown in Figure 5.108,5.111, 5.114, 5.117, 5.120, 5.123 & 5.126.

The importance of these picture in understanding the effect of wind flow in pressure distribution around model envelope and their characteristics has already been discussed in para 4.1 and 4.2.5.

Flow separation and formation of vortices can be seen from the flow patterns. Besides the vortices formed behind the model, small vortices within the recessed cavity and the cutout region enclosed by faces G1H1I1 and G2H2I2 are formed for some of the wind angles. Secondary vortices within the recessed cavity are also formed for certain wind angle of attack. Flow patterns are different in shape, intensity and strength for different wind angles and for different levels of heights. Since coefficient of pressure is a mathematical representation of impact or velocity pressure of wind striking on the surfaces, it largely depends upon the variation of flow field around the model. For different wind angle of incidence, the flow field around the model is different. It is also different at different levels of height of the model. Hence, different pressure distributions on same faces of the model are expected to occur. Pattern of pressure distribution on different faces can this be corelated with the flow pattern and the velocity contours. Positive pressure on faces occurred due to effect of direct wind force. Negative pressure occurred on faces due to suction force acting on the surfaces. Similarities in pressure coefficient on faces occurred due to equal and opposite faces and the wind flow equally affecting the faces due to symmetrical wind flow pattern. In case of unsymmetrical flow pattern, the pressure on faces is dissimilar.

It can be observed also that the distance between the streamlines is not constant. In general, where separation between the streamlines moves apart, flow is expected to slows down. Before striking the model, the streamlines are moving apart which indicates reduction in velocity of the flow. Where the streamlines come closure, it indicates speeding up of fluid greater than the free stream speed. Downstream of the model where reattachment of flow occurs, the flow stream recovers the free stream value. Largest velocity change occurs from where detachment of flow from the model is taking place. Beyond a distance far away from the model in the upper and lower part of the diagram, flow is deflected but the distance between the streamlines changes little and the corresponding flow stream change is relatively small.

For 0° and 180° wind incidence angles two vortices are formed behind the model. At 0° wind incidence angle the intensity and strength of vortices are increasing with height. However, the size and of wake is decreasing with height. At Z = 335 mm the streamlines of wake are denser compared to Z =165 mm and Z = 250 mm indicating higher suction velocity at Z = 335 mm height of the model in wind direction. But, at 180° wind incidence angle suction velocity at Z = 250 mm seems to be lower than those at Z = 165 mm and Z = 335 mm along the wind direction as the spacing between the streamlines are larger comparative to other heights. At both the angles no circulation of air is observed within the larger cavity region. However, within the smaller cavity regions, circulation of air exists.

At 30° and 60° wind angles two dissimilar wake vortices behind the model is formed. Circulation of flow within the larger cavity and within the smaller cavities as well are seen. At Z = 250 mm deceleration of flow field in the direction of wind appears to exist as indicated by the larger spacing of streamlines.

At 90° wind angle the size of the wake behind the model is smaller than those found on other angles of wind attack. Is shows smooth and streamlined transition of flow past the model. The drag at this angle of wind attack is expected to be minimum than those on other wind angles. Secondary vortex within only one smaller cavity between the cut faces G1 H1 I1 are seen. A larger secondary vortex within the recessed cavity is also seen.

At 120° wind angle of attack, wake streamlines are reducing in size from bottom to top. Two distinct vortices, almost similar, in the wake region behind the model are formed for this angle of wind attack. Secondary vortex within the larger cavity and one smaller cavity within the cut faces G1 H1 I1 are also observed. Horizontal flow in the wind direction seems to be decelerating at mid height of the model.

At 150° wind angle of attack vortices are largely different in size and formation along the height. Secondary vortex within the larger cavity and one smaller cavity within the cut faces G1 H1 I1 are also seen.

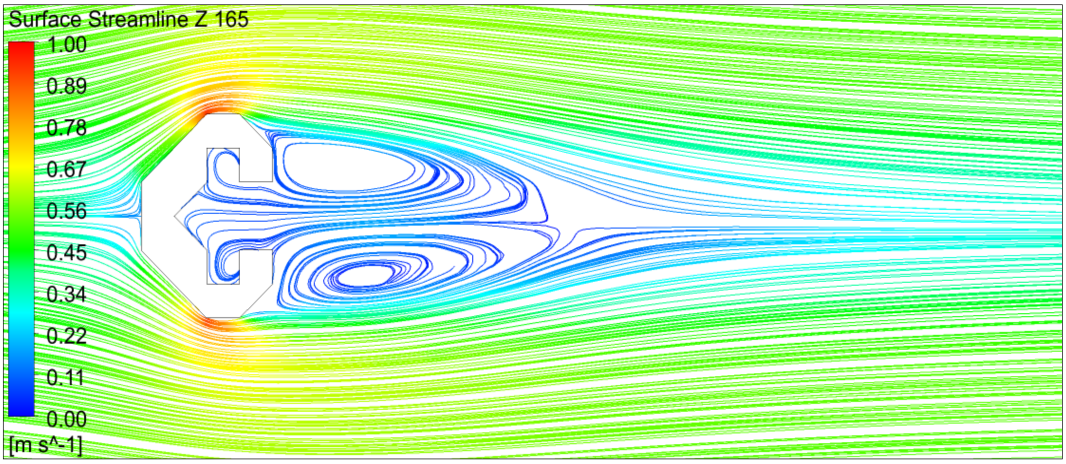

(a) Surface Streamline at Height Z = 165 mm

Figure 5. 106: Surface Streamline Wrench Shape Model 0° Wind Angle (Contd.)

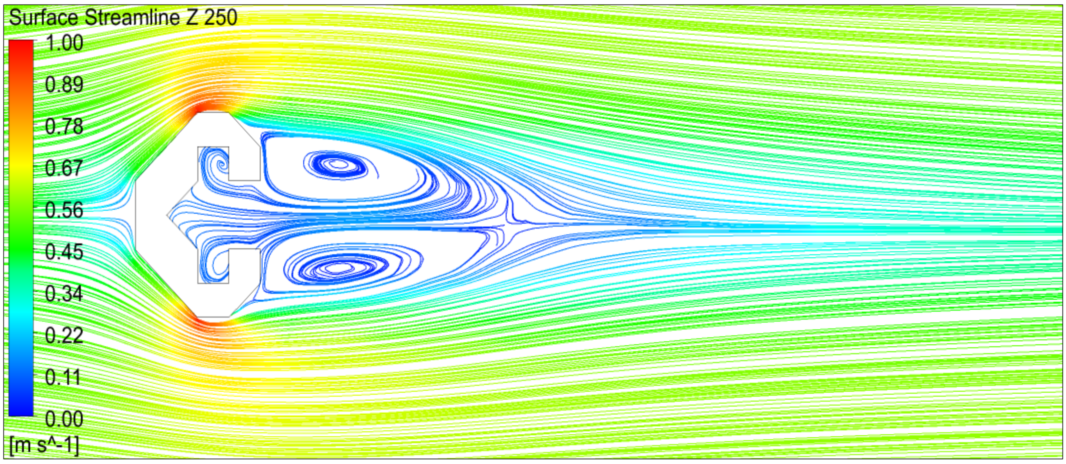

(b) Surface Streamline at Height Z = 250 mm

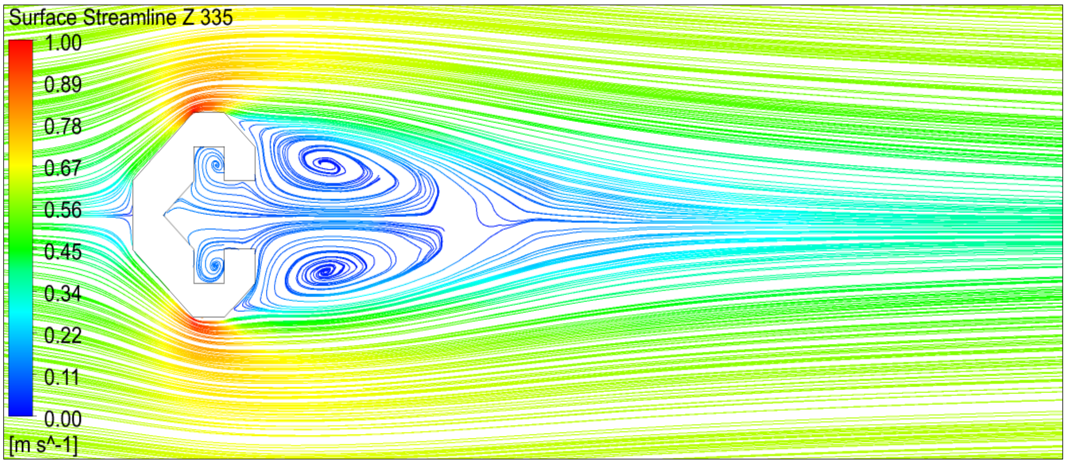

(c) Surface Streamline at Height Z = 335 mm

Figure 5. 107: Surface Streamline Wrench Shape Model 0° Wind Angle

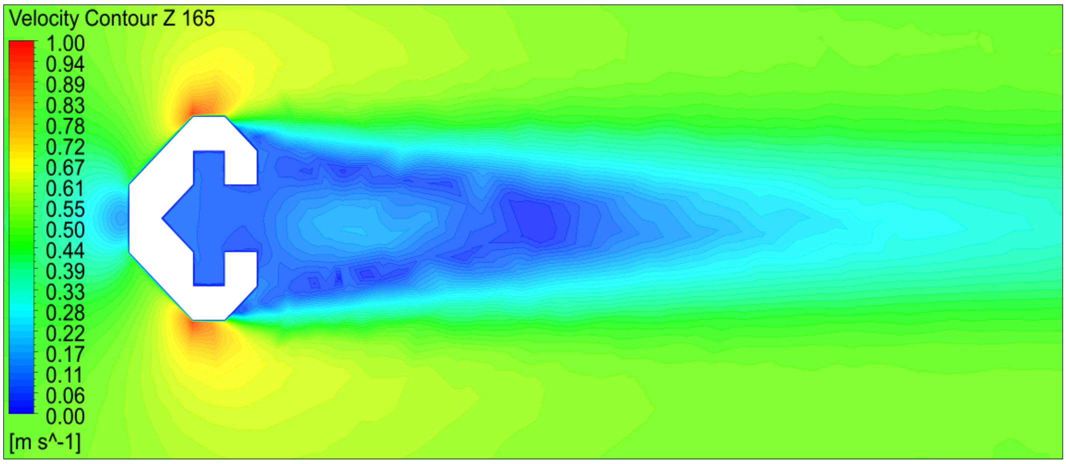

(a) Velocity Contour at Height Z = 165 mm

Figure 5. 107: Velocity Contour Wrench Shape Model 0° Wind Angle (Contd.)

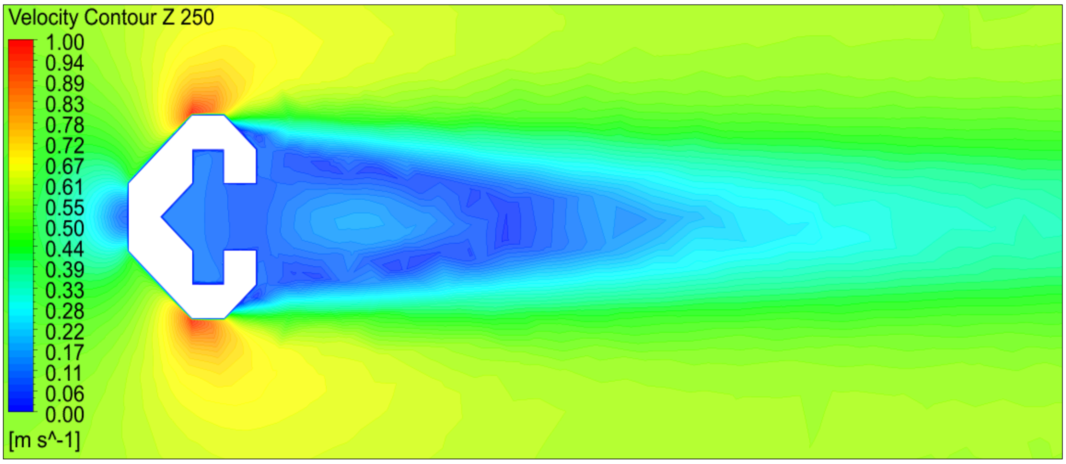

(b) Velocity Contour at Height Z = 250 mm

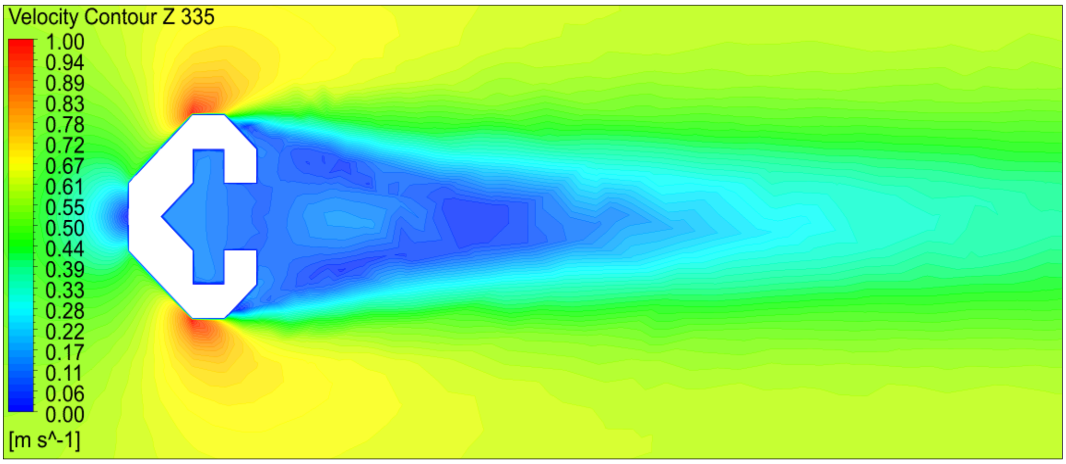

(c) Velocity Contour at Height Z = 335 mm

Figure 5. 108: Velocity Contour Wrench Shape Model 0° Wind Angle

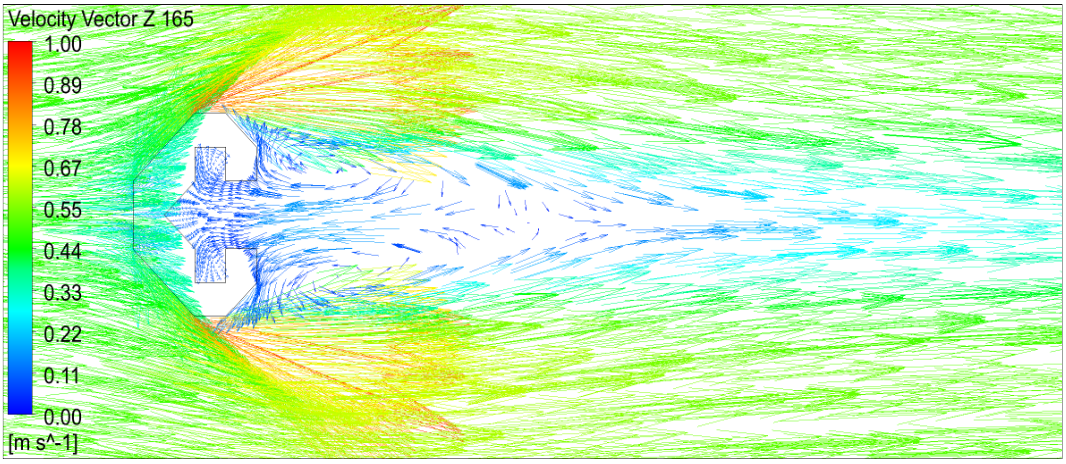

(a) Velocity Vector at Height Z = 165 mm

Figure 5. 108: Velocity Vector Faces Wrench Shape Model 0° Wind Angle (Contd.)

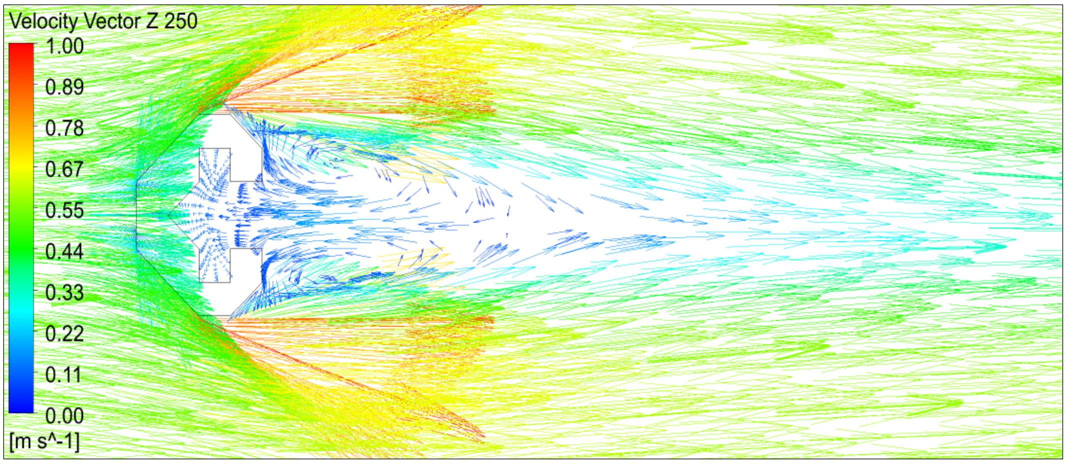

(b) Velocity Vector at Height Z = 250 mm

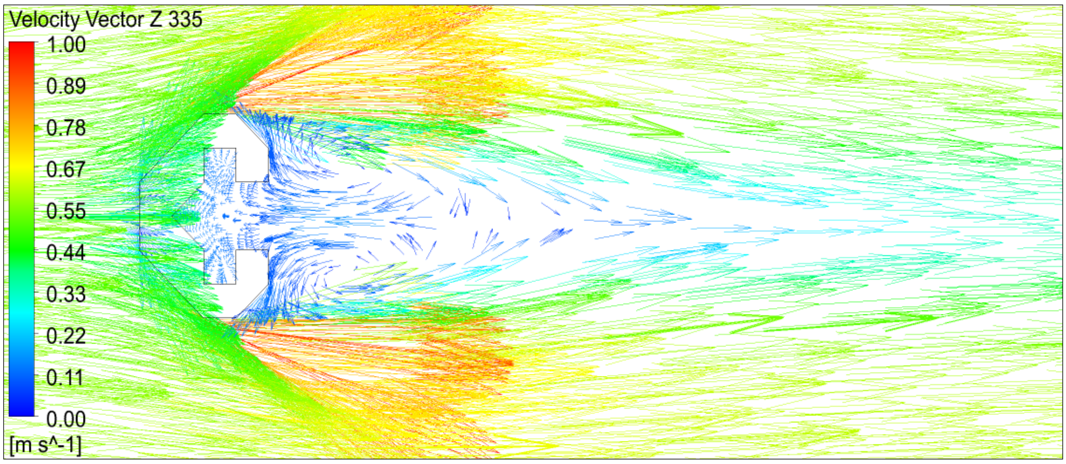

(c) Velocity Vector at Height Z = 335 mm

Figure 5. 109: Velocity Vector Faces Wrench Shape Model 0° Wind Angle

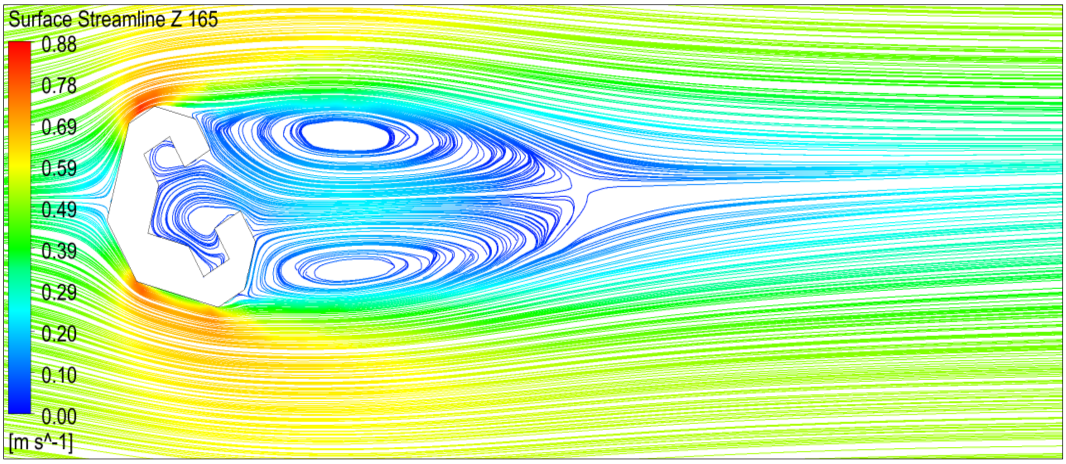

(a) Surface Streamline at Height Z = 165 mm

Figure 5. 109: Surface Streamline Wrench Shape Model 30° Wind Angle (Contd.)

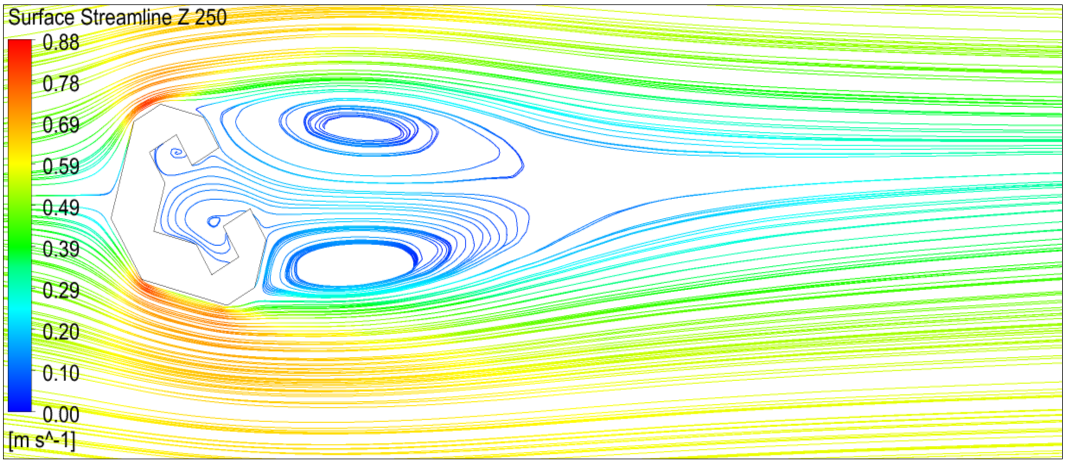

(b) Surface Streamline at Height Z = 250 mm

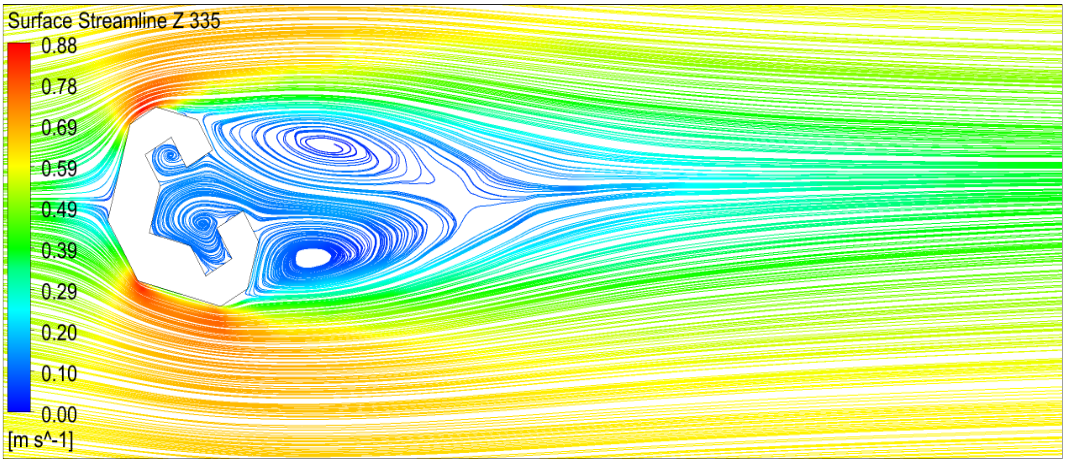

(c) Surface Streamline at Height Z = 335 mm

Figure 5. 110: Surface Streamline Wrench Shape Model 30° Wind Angle

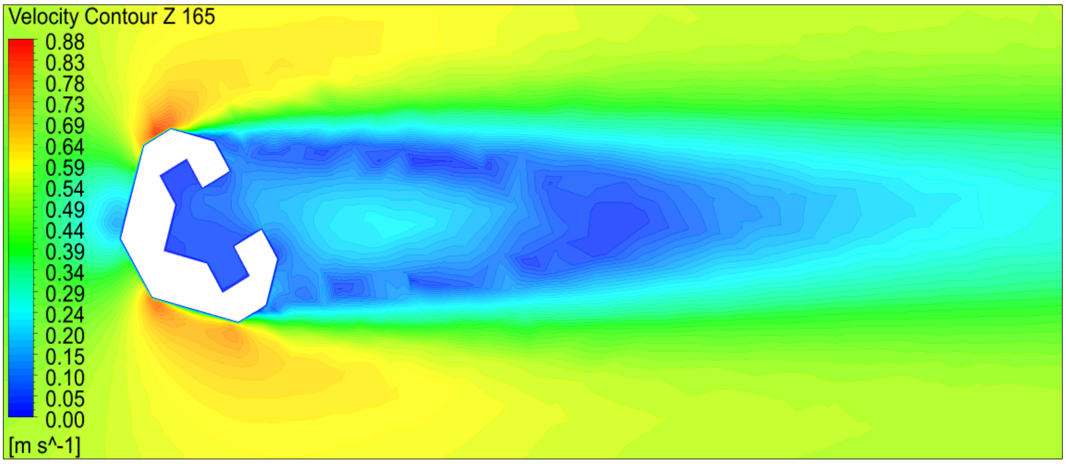

(a) Velocity Contour at Height Z = 165 mm

Figure 5. 110: Velocity Contour Wrench Shape Model 30° Wind Angle (Contd.)

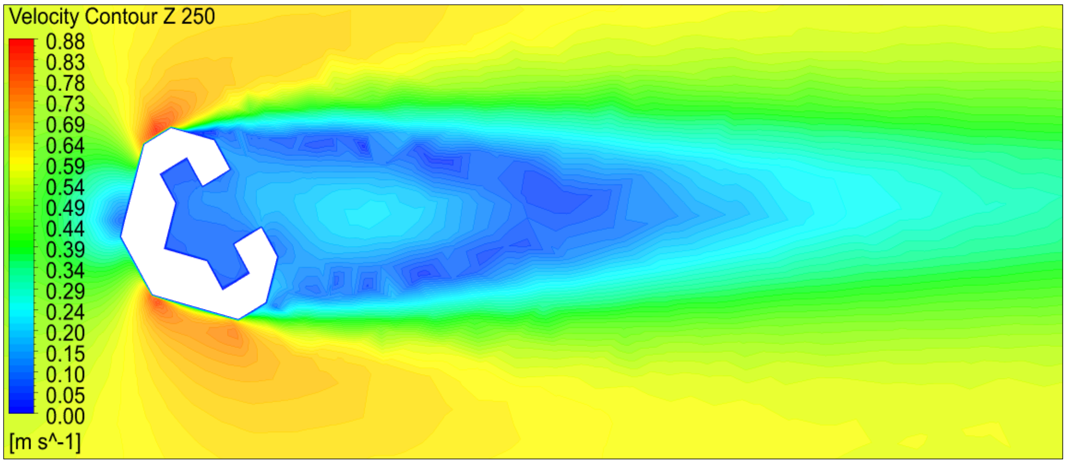

(b) Velocity Contour at Height Z = 250 mm

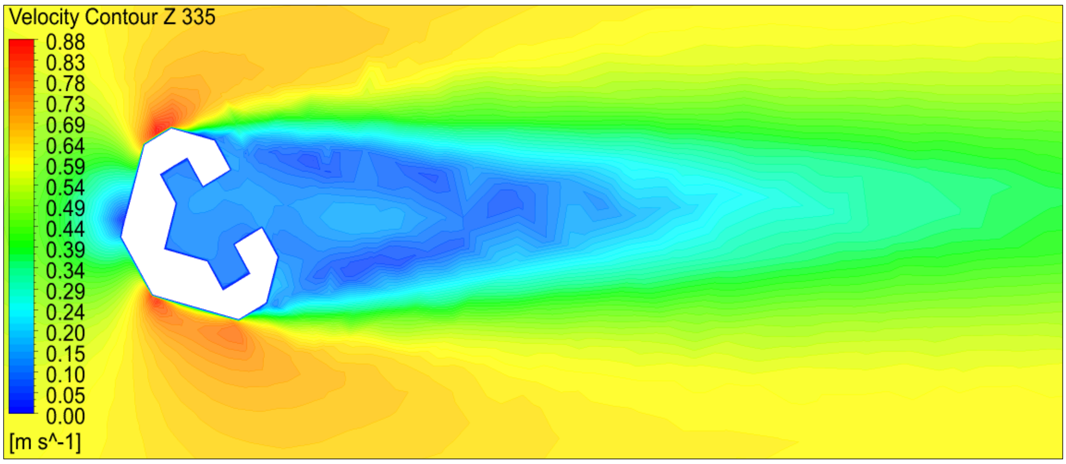

(c) Velocity Contour at Height Z = 335 mm

Figure 5. 111: Velocity Contour Wrench Shape Model 30° Wind Angle

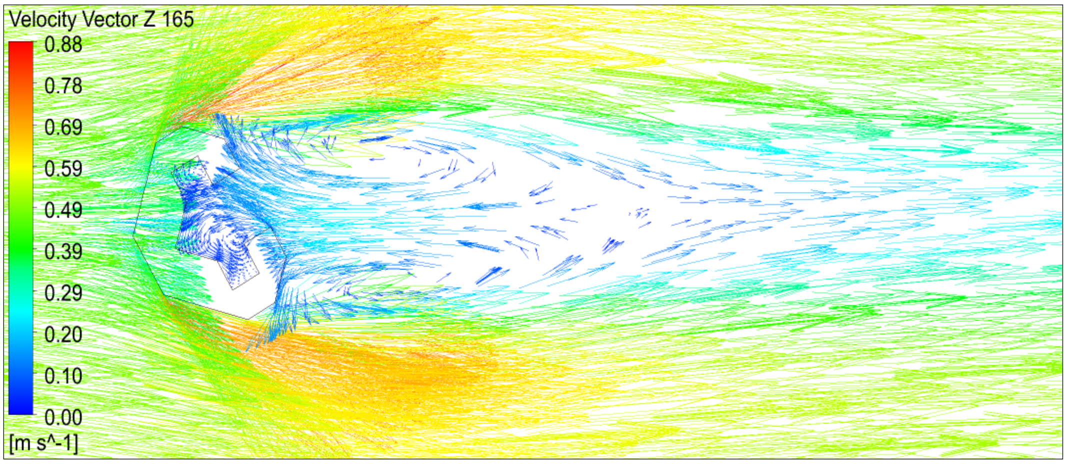

(a) Velocity Vector at Height Z = 165 mm

Figure 5. 111: Velocity Vector Wrench Shape Model 30° Wind Angle (Contd.)

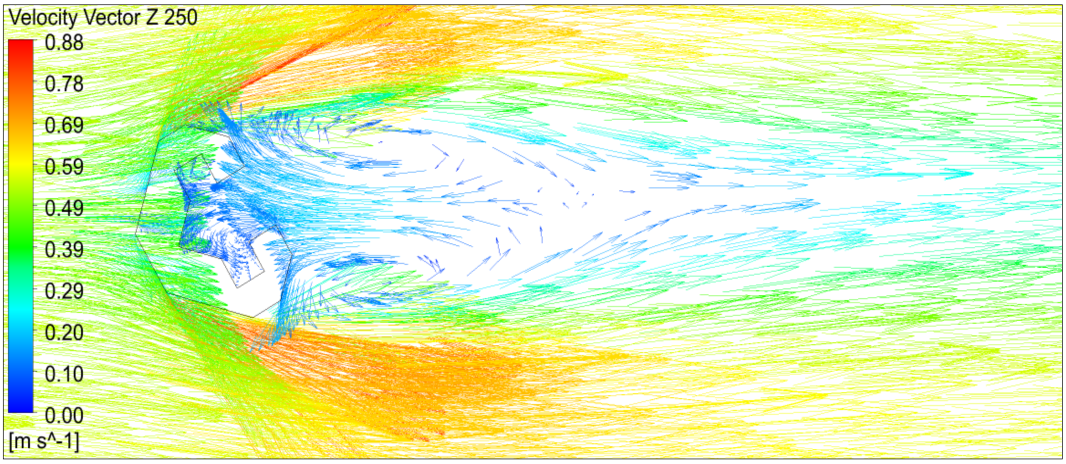

(b) Velocity Vector at Height Z = 250 mm

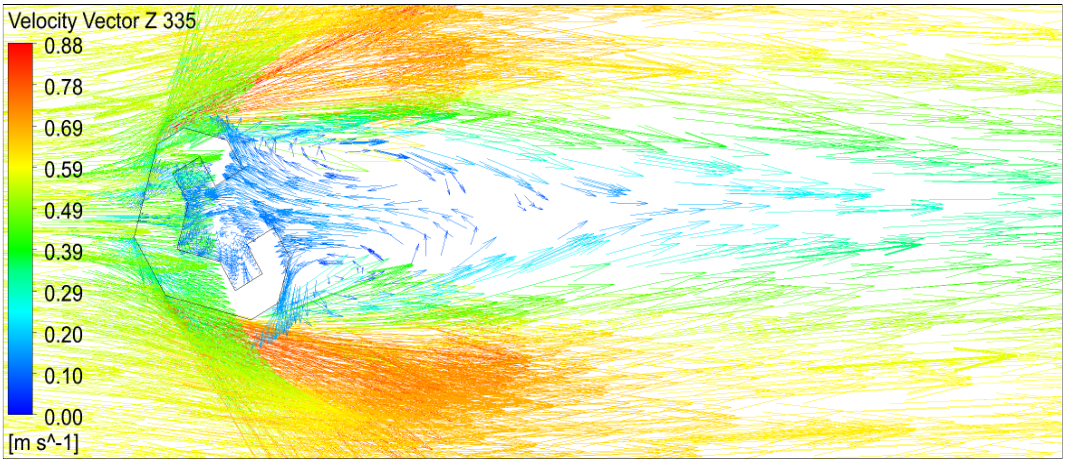

(c) Velocity Vector at Height Z = 335 mm

Figure 5. 112: Velocity Vector Wrench Shape Model 30° Wind Angle

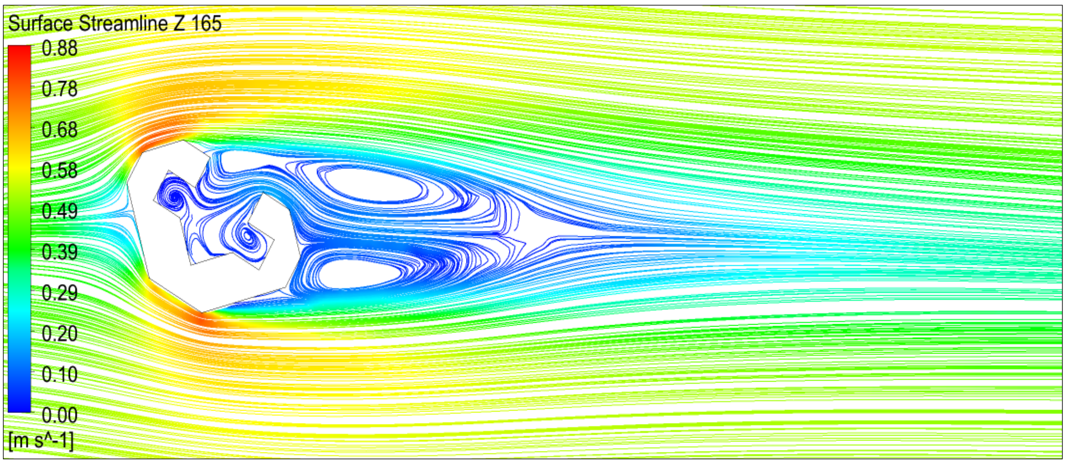

(a) Surface Streamline at Height Z = 165 mm

Figure 5. 112: Surface Streamline Wrench Shape Model 60° Wind Angle (Contd.)

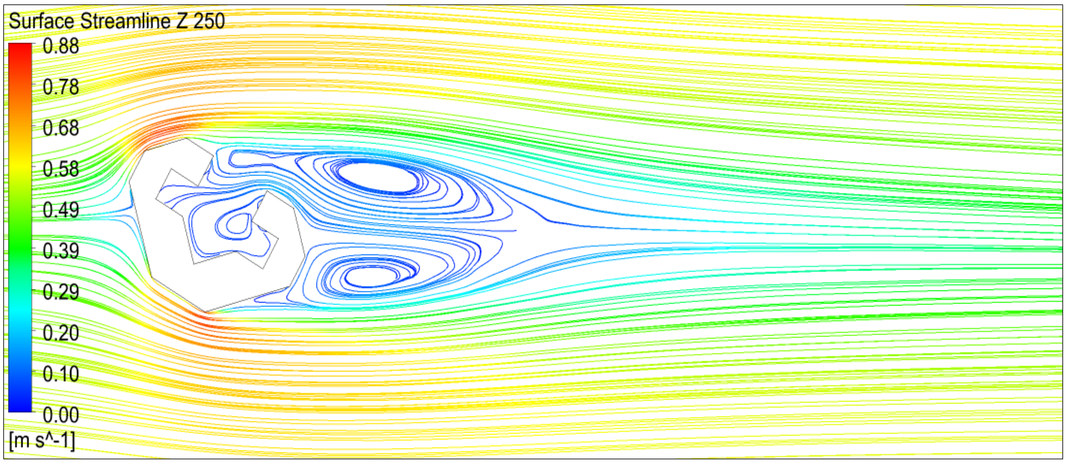

(b) Surface Streamline at Height Z = 250 mm

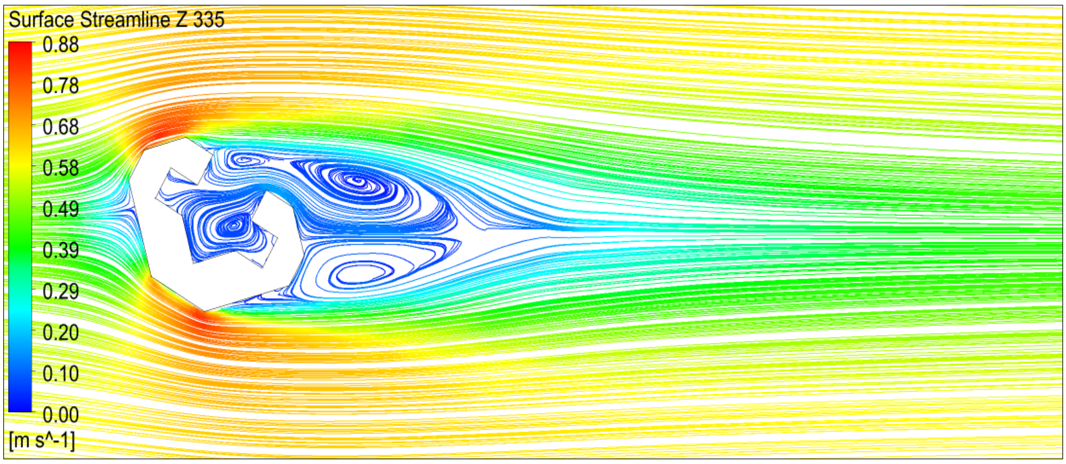

(c) Surface Streamline at Height Z = 335 mm

Figure 5. 113: Surface Streamline Wrench Shape Model 60° Wind Angle

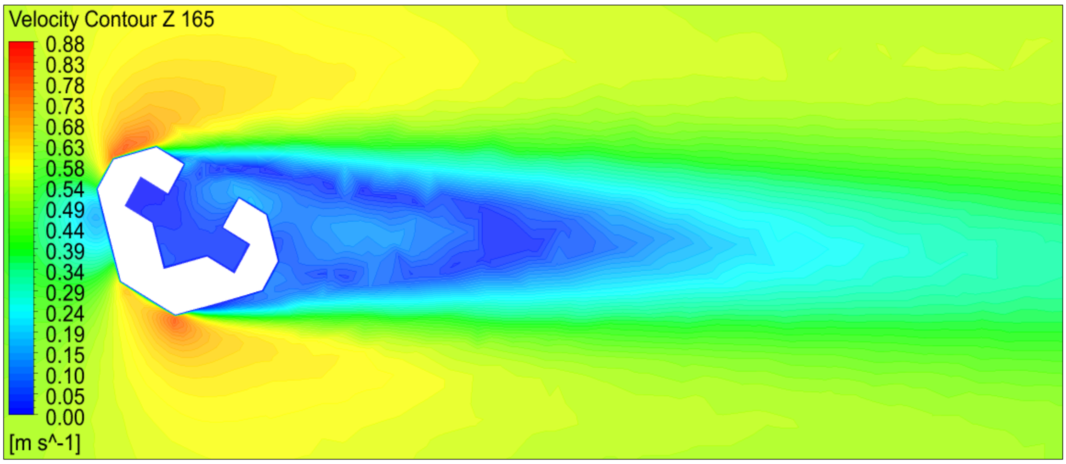

(a) Velocity Contour at Height Z = 165 mm

Figure 5. 113: Velocity Contour Wrench Shape Model 60° Wind Angle (Contd.)

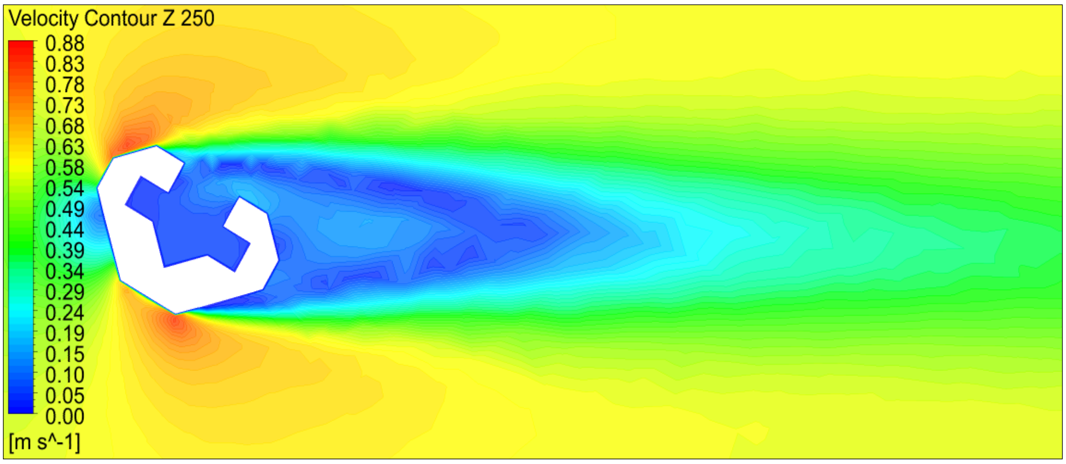

(b) Velocity Contour at Height Z = 250 mm

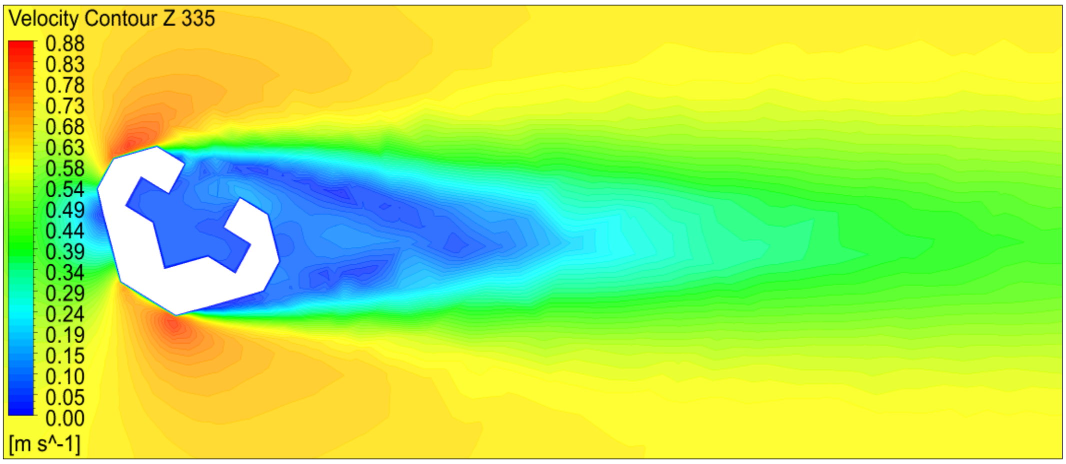

(c) Velocity Contour at Height Z = 335 mm

Figure 5. 114: Velocity Contour Wrench Shape Model 60° Wind Angle

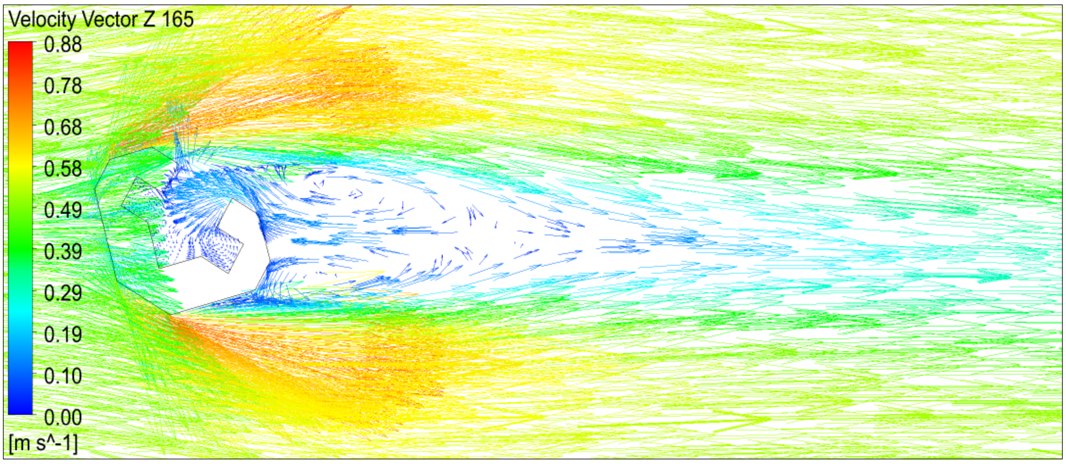

(a) Velocity Vector at Height Z = 165 mm

Figure 5. 114: Velocity Contour Wrench Shape Model 60° Wind Angle (Contd.)

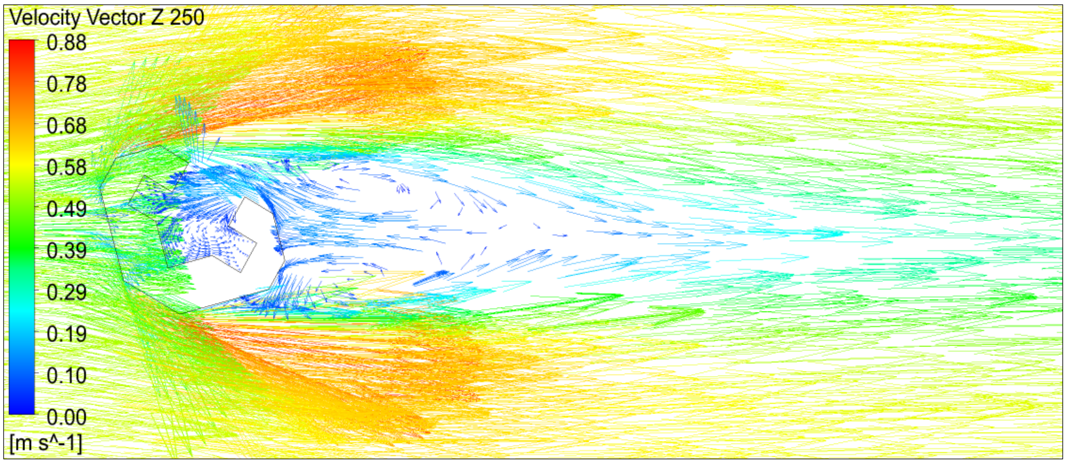

(b) Velocity Vector at Height Z = 250 mm

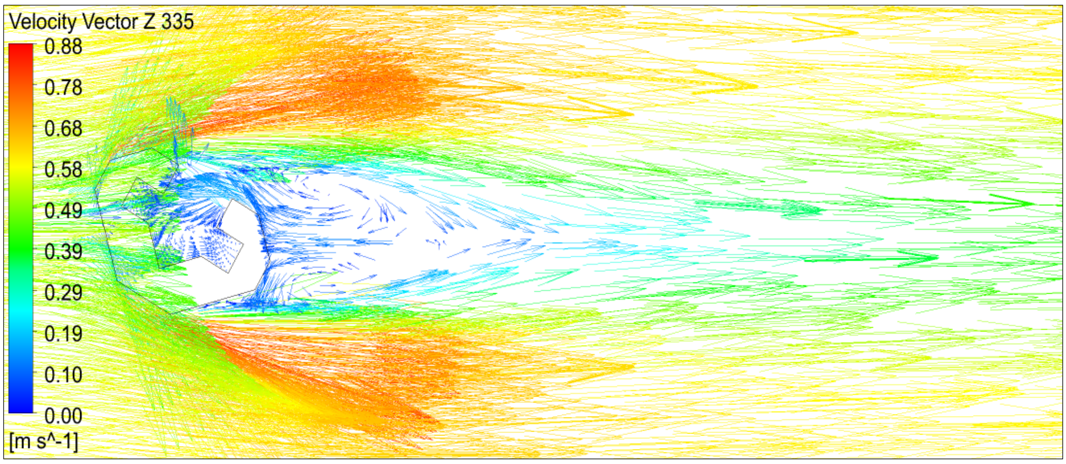

(c) Velocity Vector at Height Z = 335 mm

Figure 5. 115: Velocity Contour Wrench Shape Model 60° Wind Angle

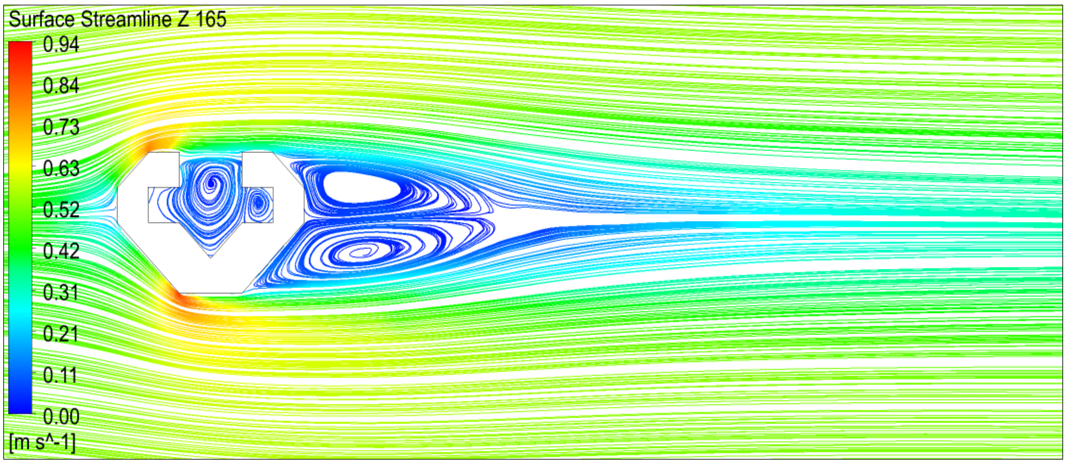

(a) Surface Streamline at Height Z = 165 mm

Figure 5. 115: Surface Streamline Wrench Shape Model 90° Wind Angle (Contd.)

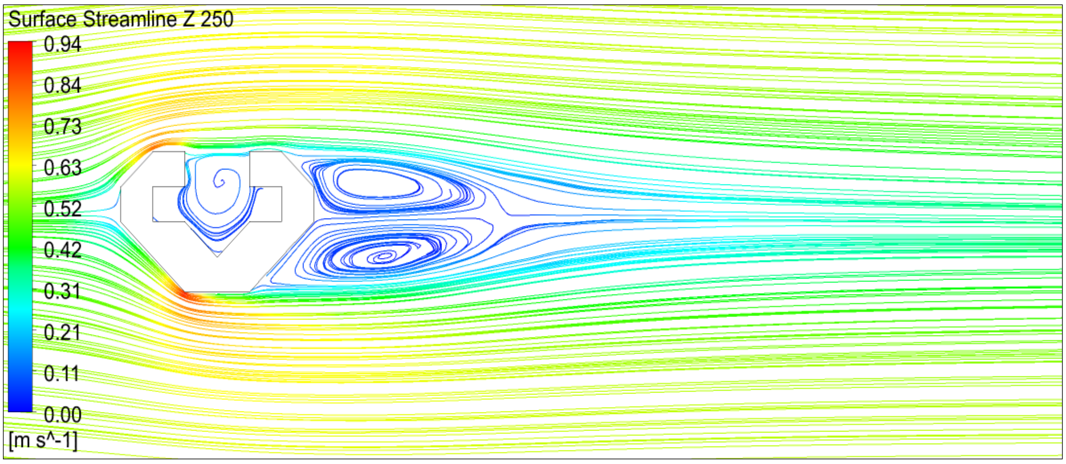

(b) Surface Streamline at Height Z = 250 mm

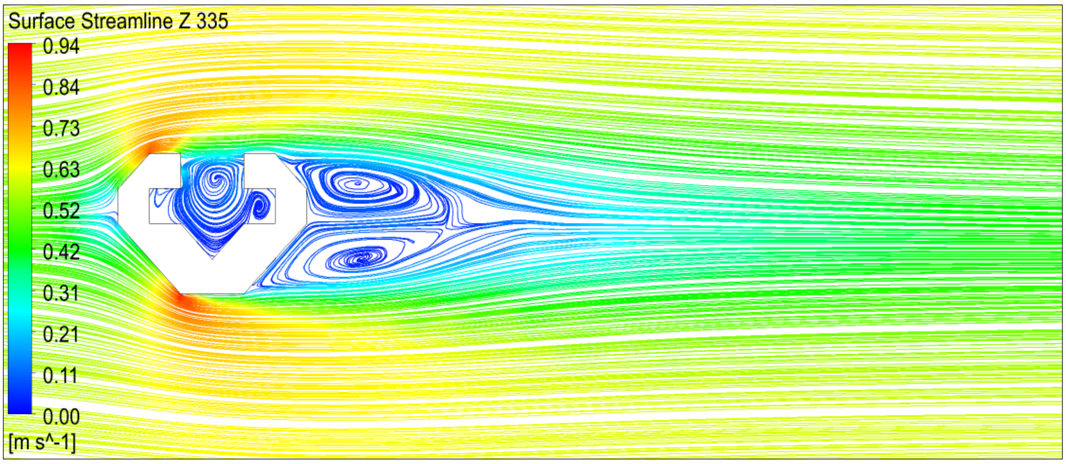

(c) Surface Streamline at Height Z = 335 mm

Figure 5. 116: Surface Streamline Wrench Shape Model 90° Wind Angle

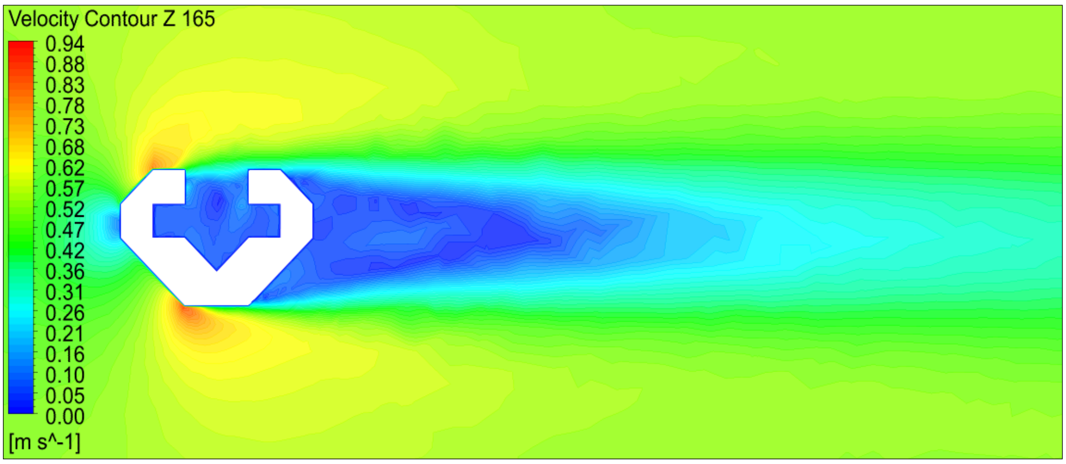

(a) Velocity Contour at Height Z = 165 mm

Figure 5. 116: Velocity Contour Wrench Shape Model 90° Wind Angle (Contd.)

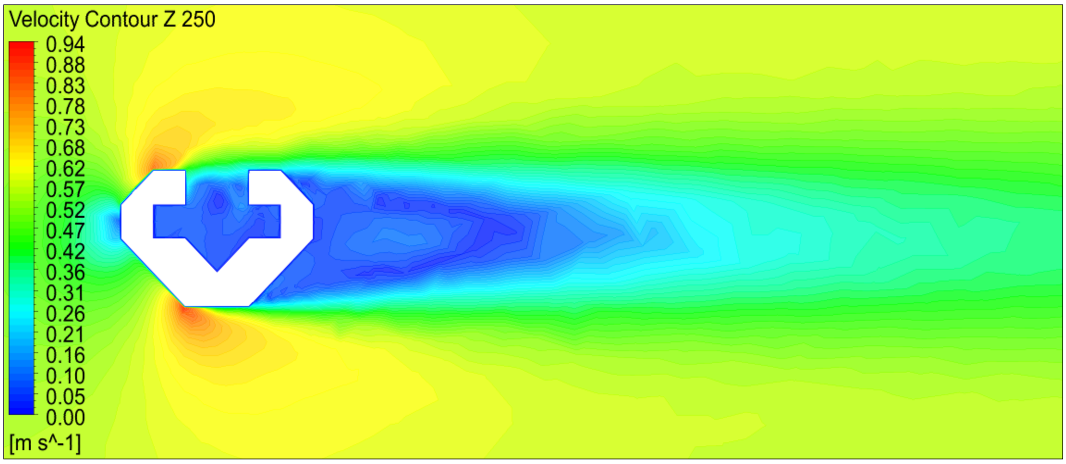

(b) Velocity Contour at Height Z = 250 mm

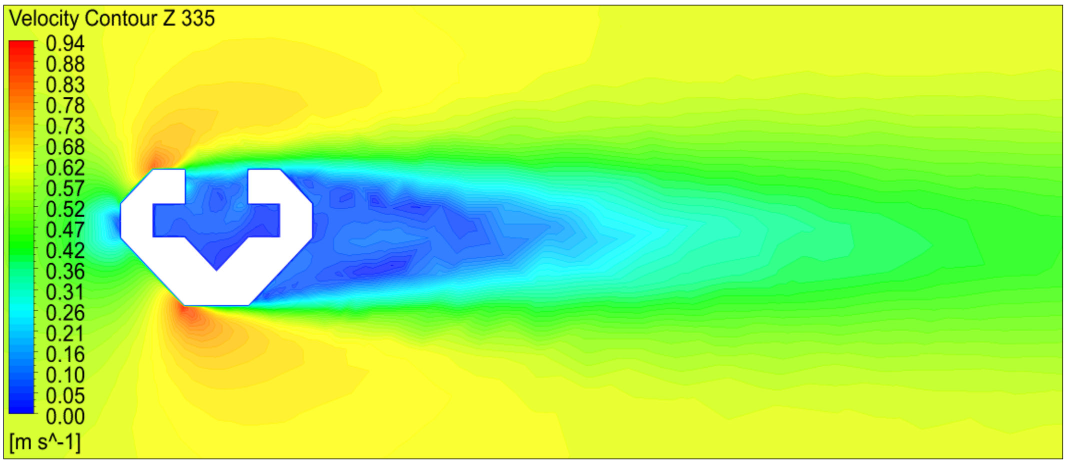

(c) Velocity Contour at Height Z = 335 mm

Figure 5. 117: Velocity Contour Wrench Shape Model 90° Wind Angle

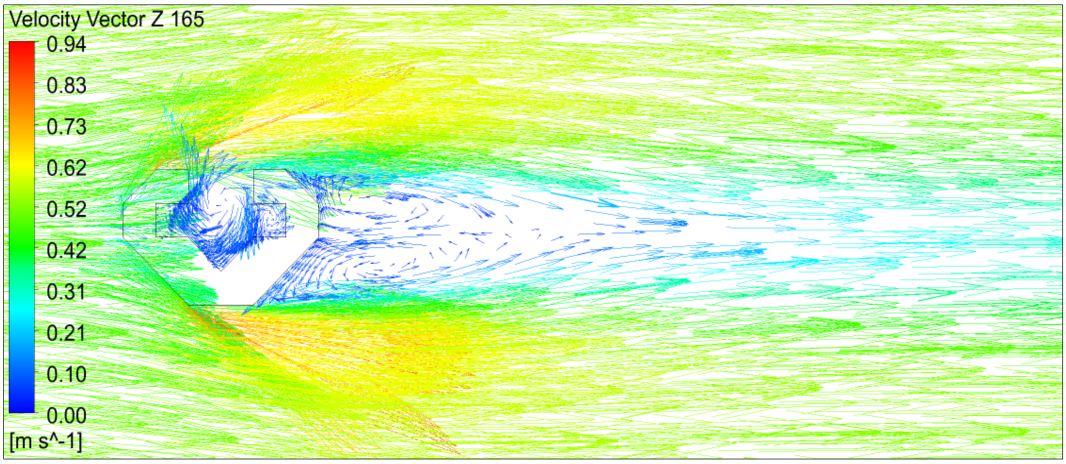

(a) Velocity Vector at Height Z = 165 mm

Figure 5. 117: Velocity Vector Wrench Shape Model 90° Wind Angle (Contd.)

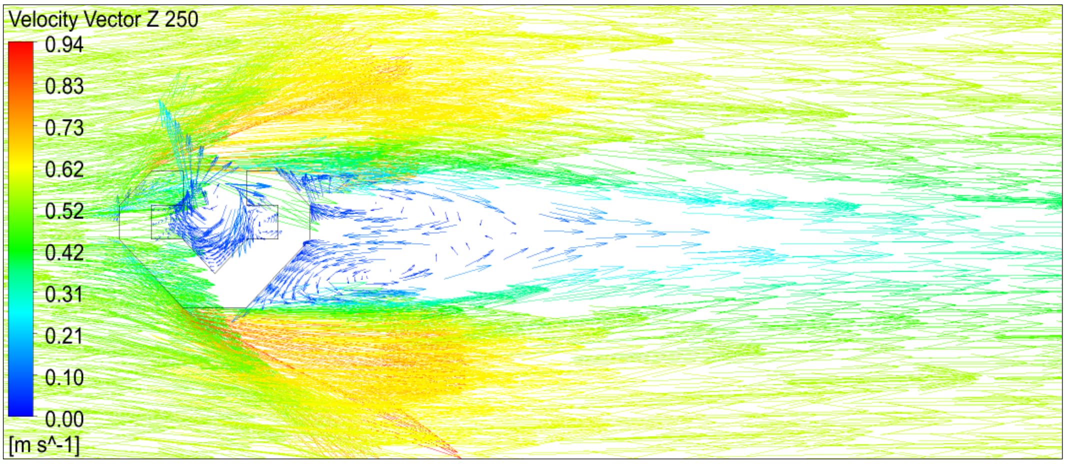

(b) Velocity Vector at Height Z = 250 mm

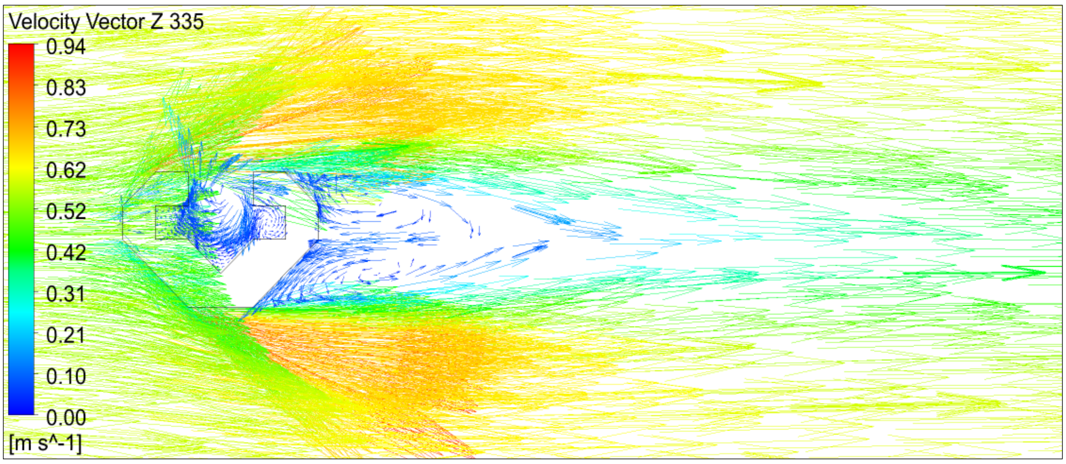

(c) Velocity Vector at Height Z = 335 mm

Figure 5. 118: Velocity Vector Wrench Shape Model 90° Wind Angle

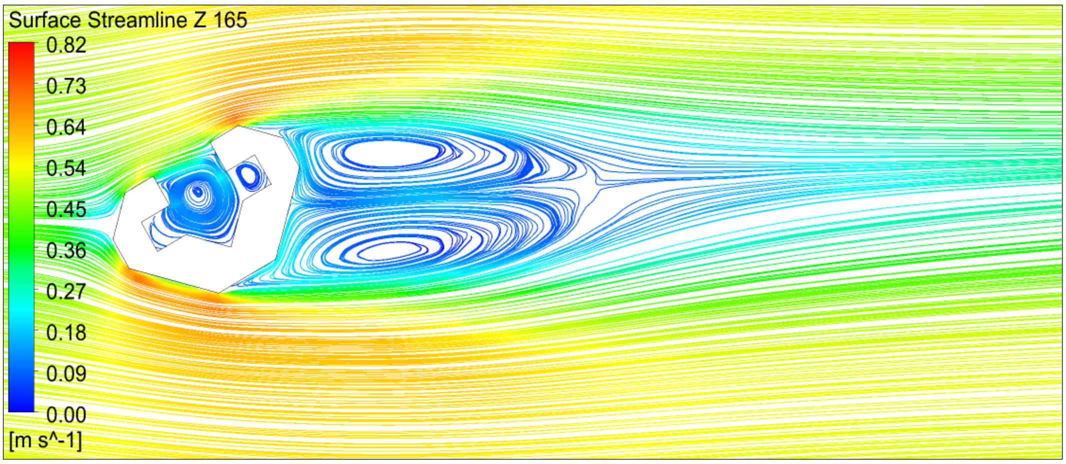

(a) Surface Streamline at Height Z = 165 mm

Figure 5. 118: Surface Streamline Wrench Shape Model 120° Wind Angle (Contd.)

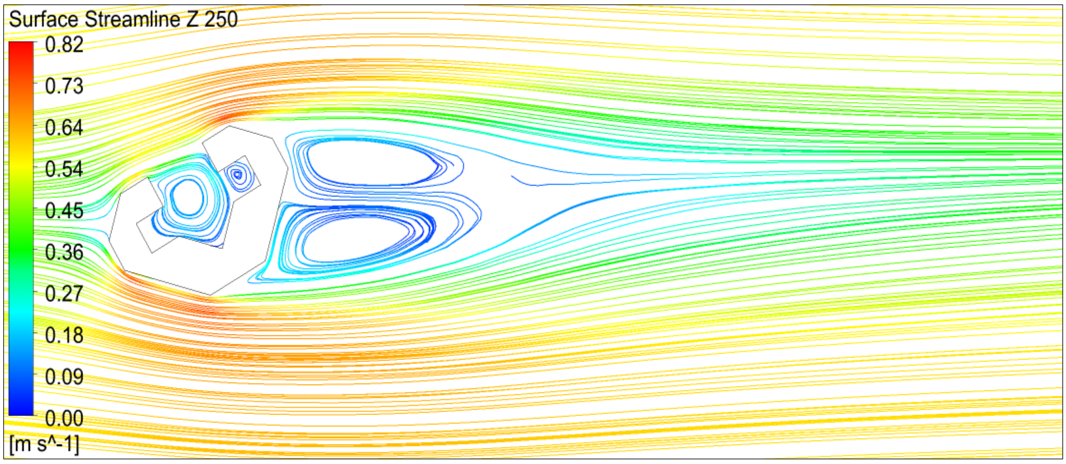

(b) *Surface Streamline at Height Z = 250 mm*

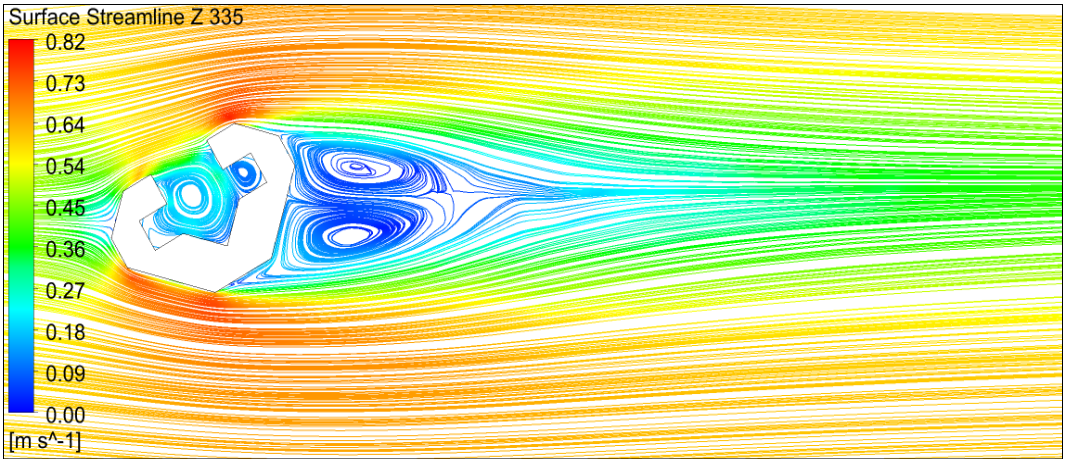

(c) *Surface Streamline at Height Z = 335 mm*

Figure 5. 119: Surface Streamline Wrench Shape Model 120° Wind Angle

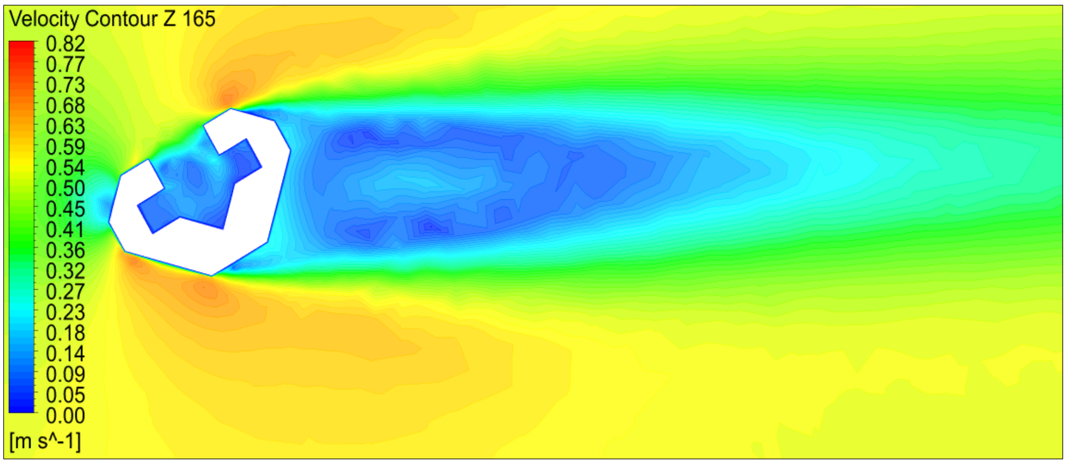

(a) *Velocity Contour at Height Z = 165 mm*

Figure 5. 119: Velocity Contour Wrench Shape Model 120° Wind Angle (Contd.)

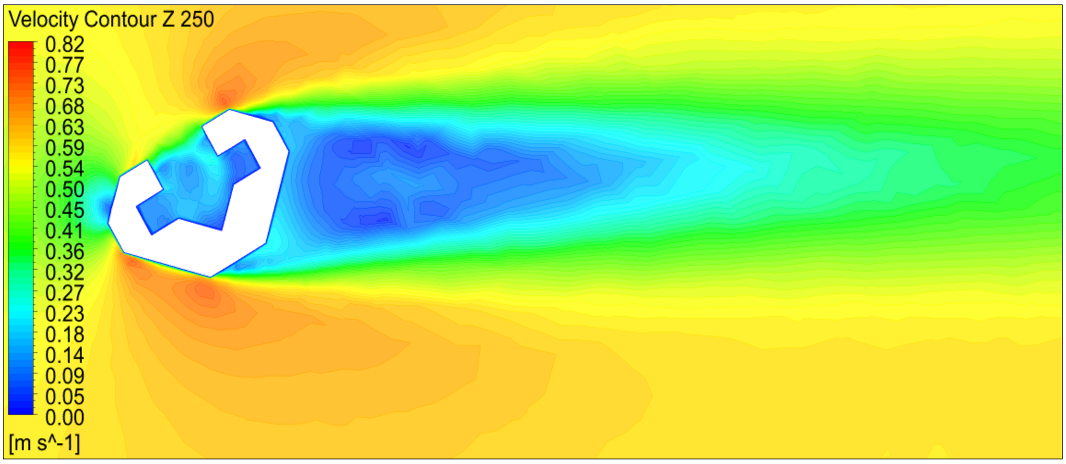

(b) Velocity Contour at Height Z = 250 mm

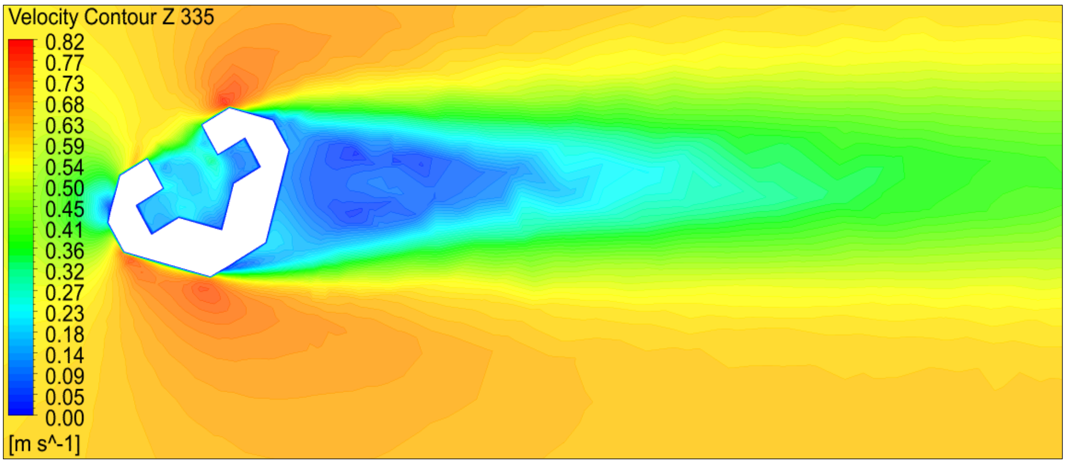

(c) Velocity Contour at Height Z = 335 mm

Figure 5. 120: Velocity Contour Wrench Shape Model 120° Wind Angle

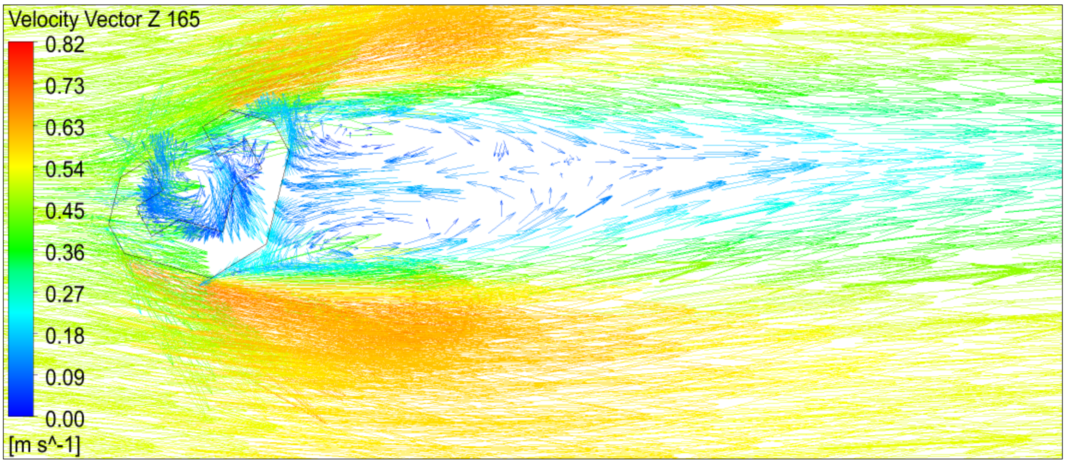

(a) Velocity Vector at Height Z = 165 mm

Figure 5. 120: Velocity Vector Wrench Shape Model 120° Wind Angle (Contd.)

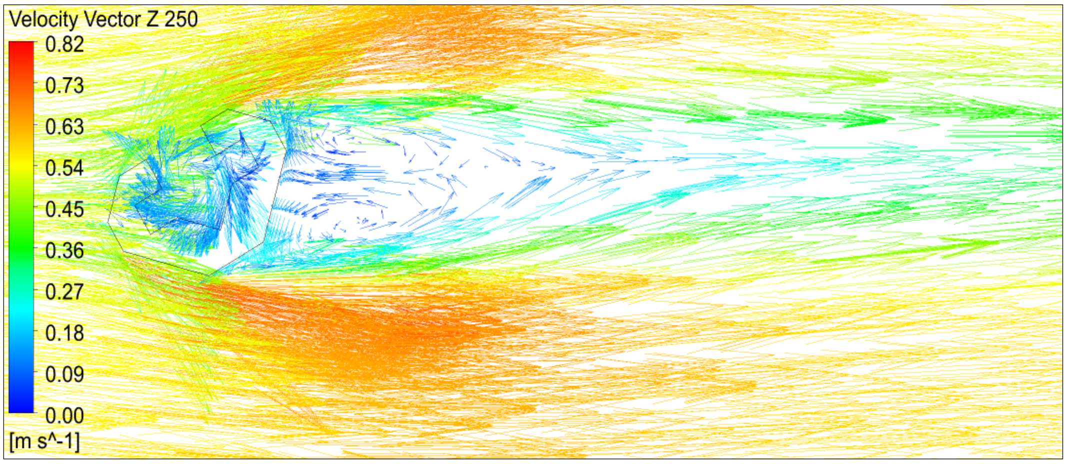

(b) Velocity Vector at Height Z = 250 mm

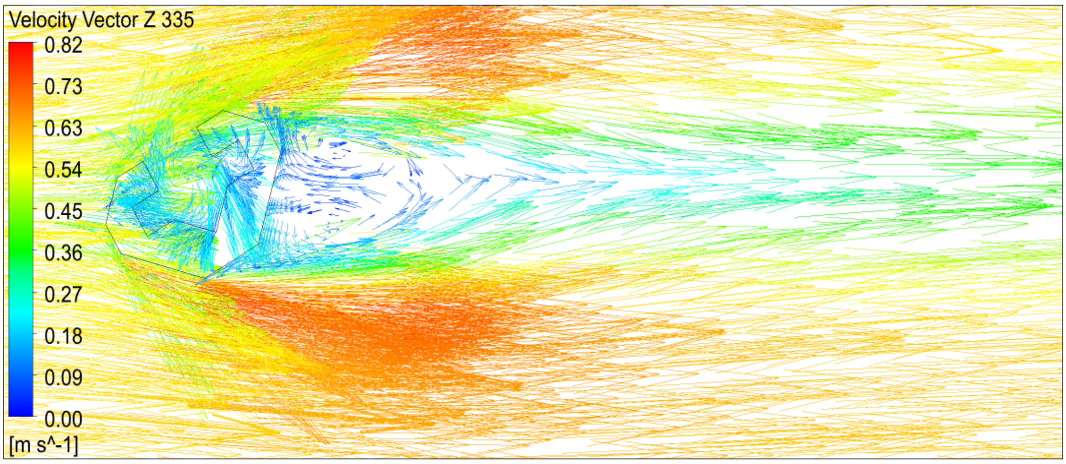

(c) Velocity Vector at Height Z = 335 mm

Figure 5. 121: Velocity Vector Wrench Shape Model 120° Wind Angle

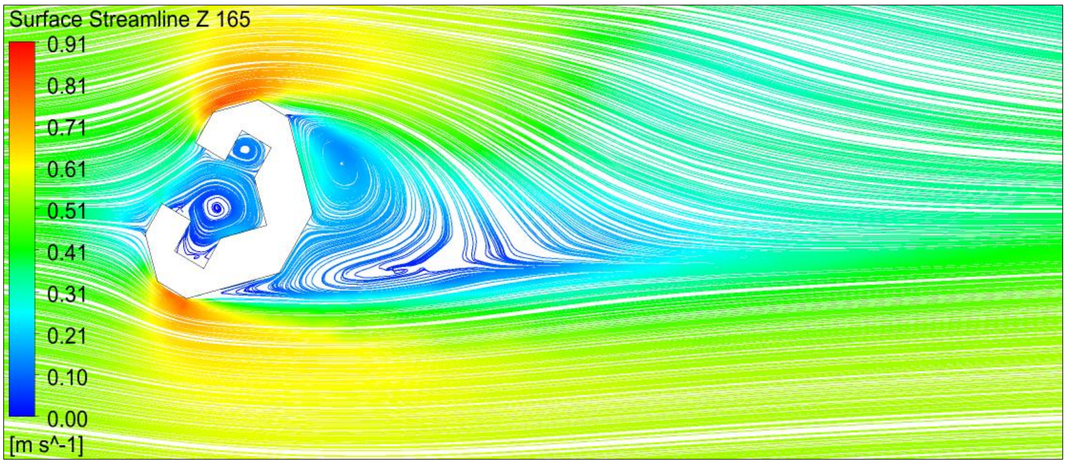

(a) Surface Streamline at Height Z = 165 mm

Figure 5. 121: Surface Streamline Wrench Shape Model 150° Wind Angle (Contd.)

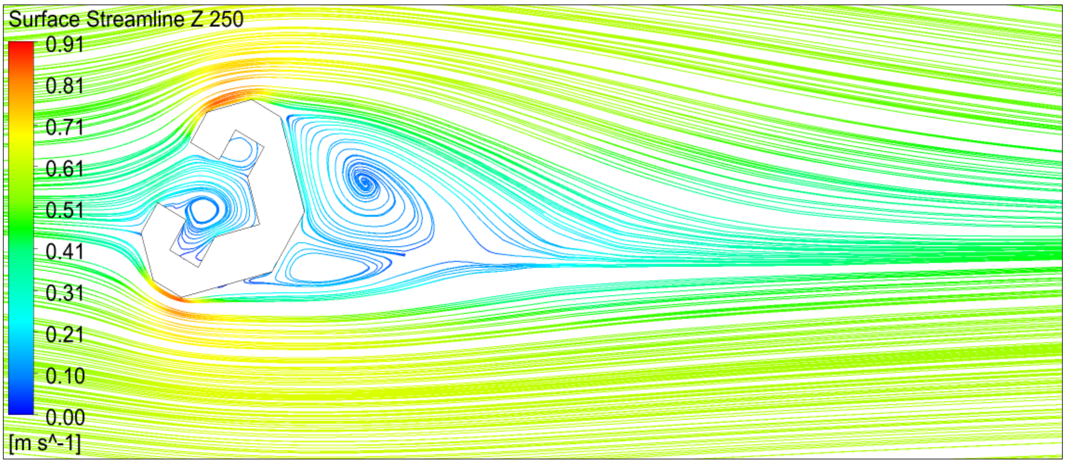

(b) Surface Streamline at Height Z = 335 mm

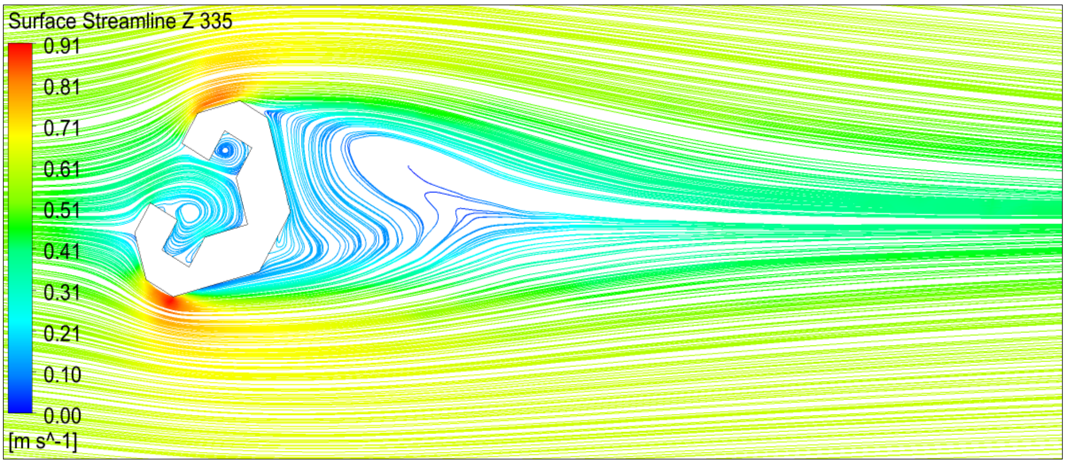

(c) Surface Streamline at Height Z = 335 mm

Figure 5. 122: Surface Streamline Wrench Shape Model 150° Wind Angle

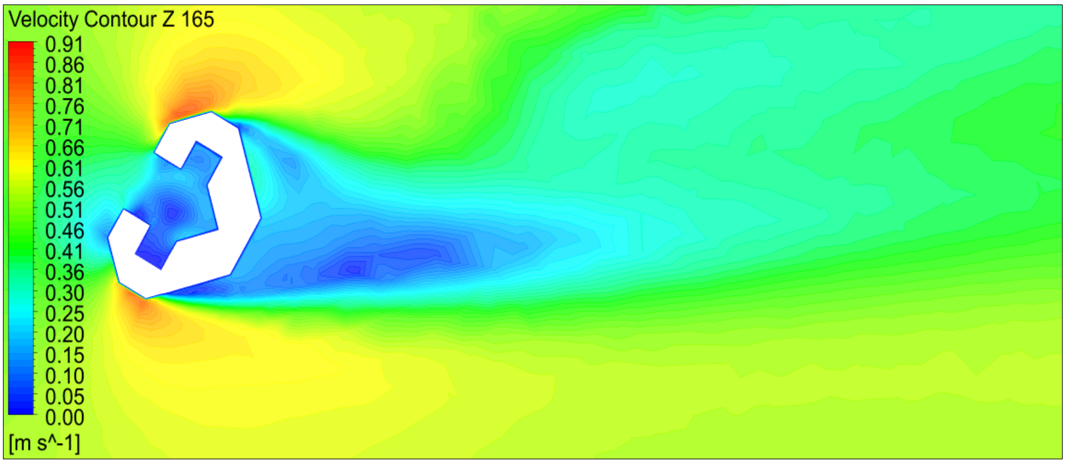

(a) Velocity Contour at Height Z = 165 mm

Figure 5. 122: Velocity Contour Wrench Shape Model 150° Wind Angle (Contd.)

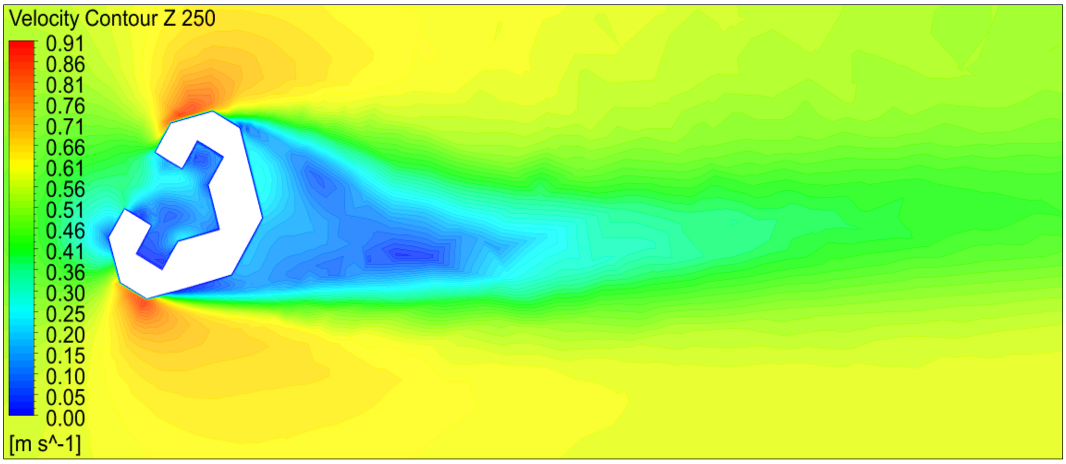

(b) Velocity Contour at Height Z = 250 mm

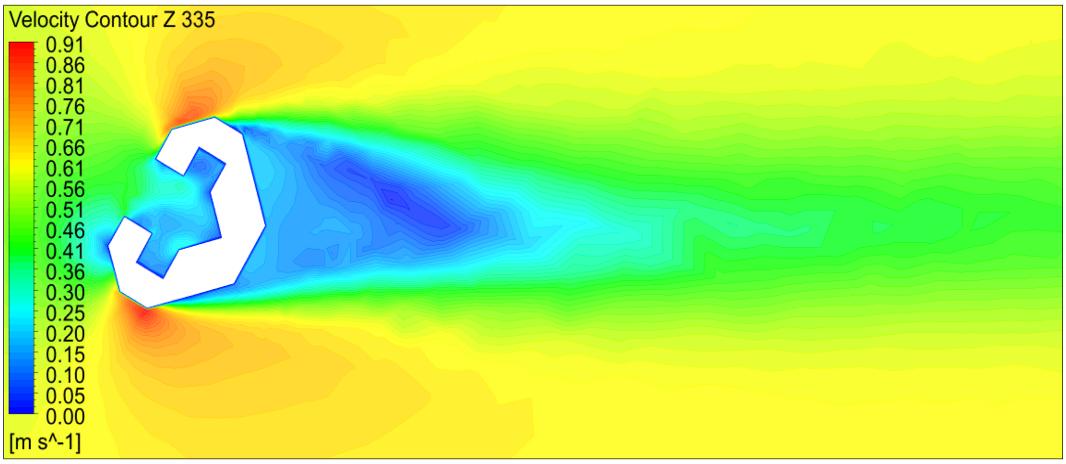

(c) Velocity Contour at Height Z = 335 mm

Figure 5. 123: Velocity Contour Wrench Shape Model 150° Wind Angle

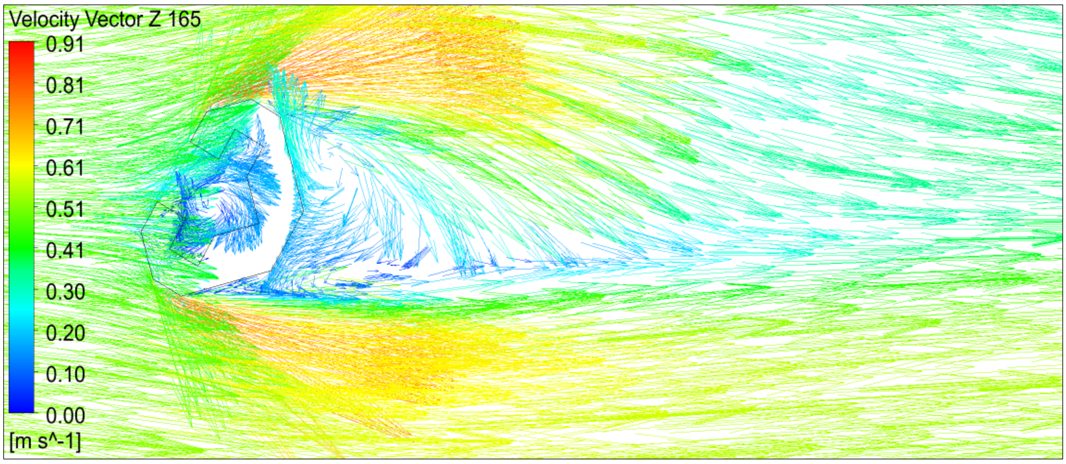

(a) Velocity Vector at Height Z = 165 mm

Figure 5. 123: Velocity Vector Wrench Shape Model 150° Wind Angle (Contd.)

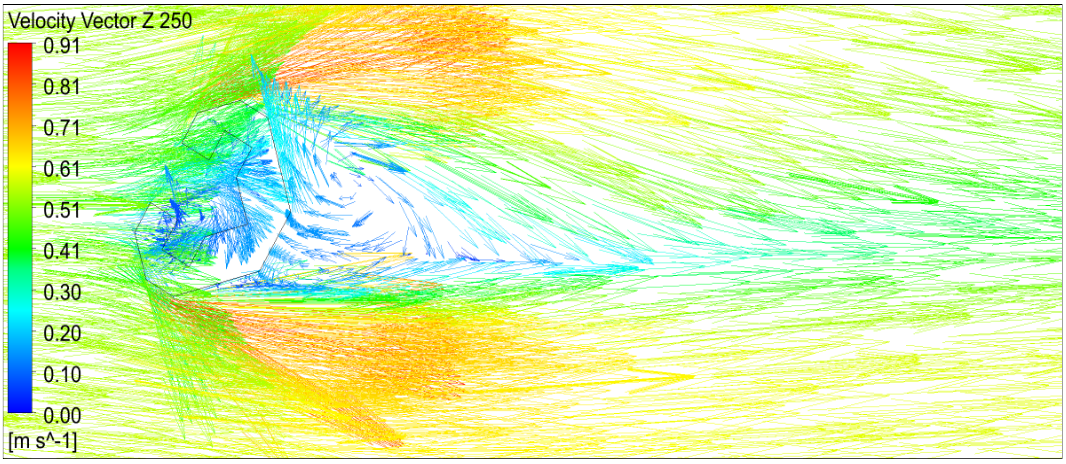

(b) Velocity Vector at Height Z = 250 mm

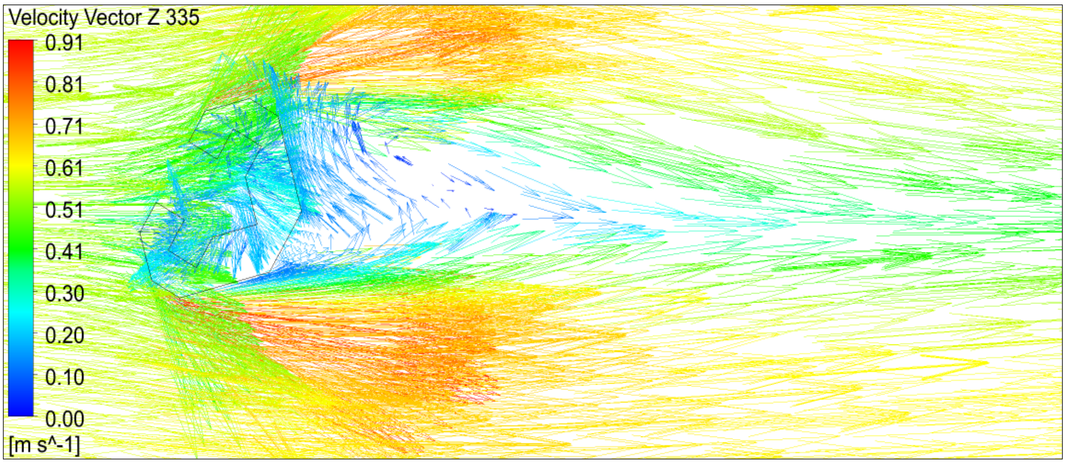

(c) Velocity Vector at Height Z = 335 mm

Figure 5. 124: Velocity Vector Wrench Shape Model 150° Wind Angle

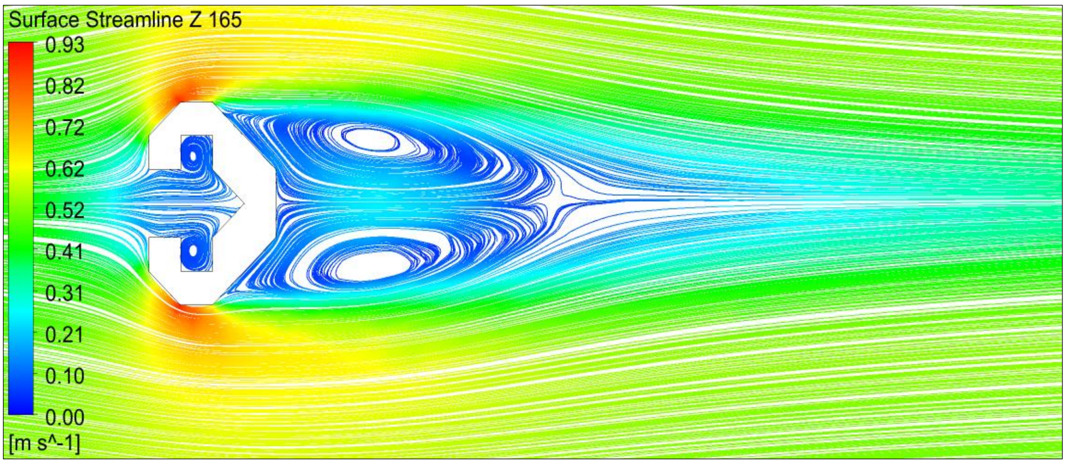

(a) Surface Streamline at Height Z = 165 mm

Figure 5. 124: Surface Streamline Wrench Shape Model 180° Wind Angle (Contd.)

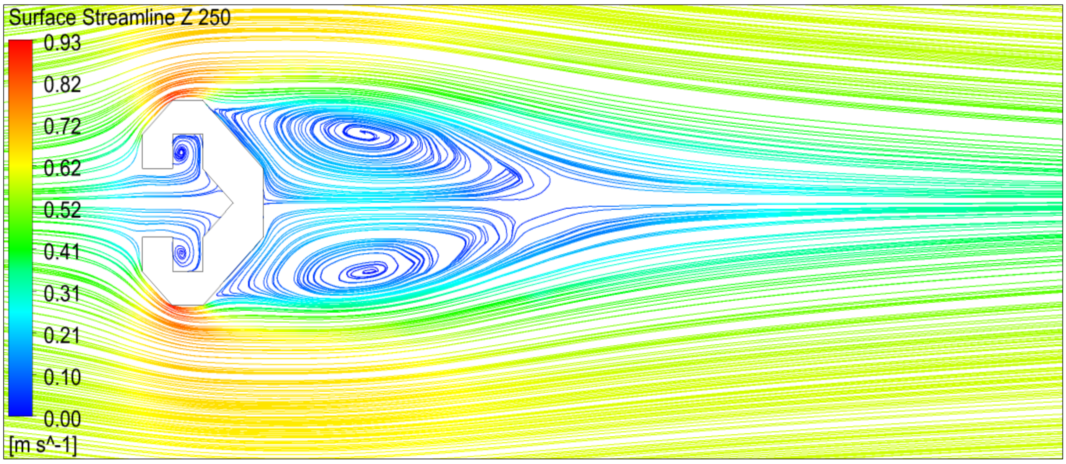

(b) Surface Streamline at Height Z = 250 mm

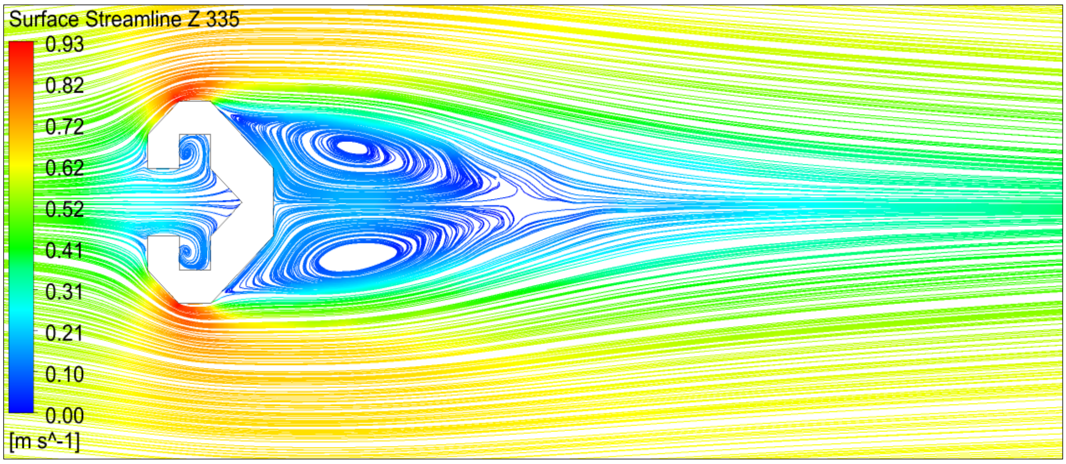

(c) Surface Streamline at Height Z = 335 mm

Figure 5. 125: Surface Streamline Wrench Shape Model 180° Wind Angle

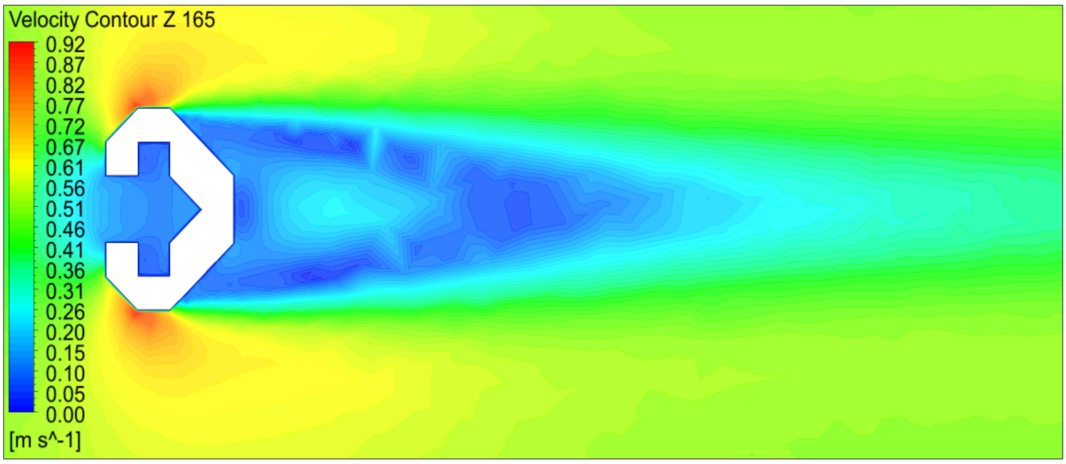

(a) Velocity Contour at Height Z = 165 mm

Figure 5. 125: Velocity Contour Wrench Shape Model 180° Wind Angle (Contd.)

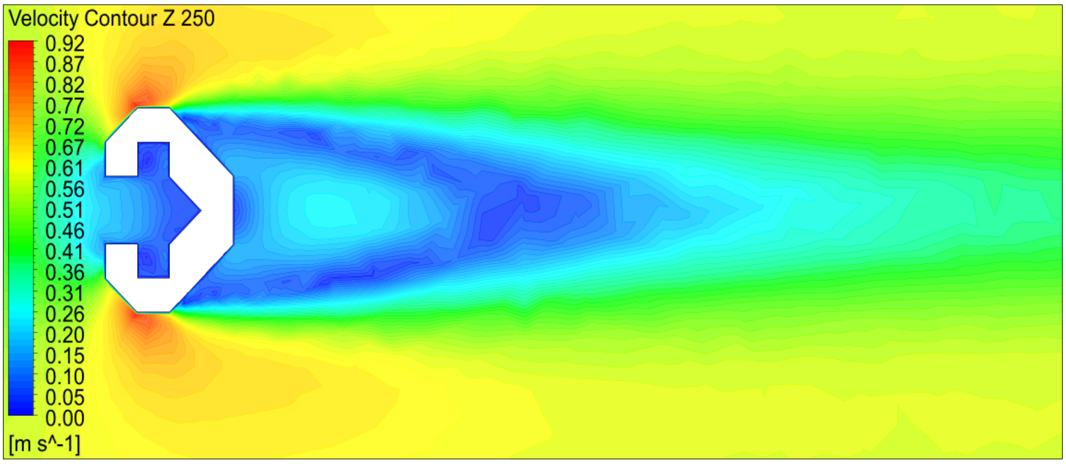

(b) Velocity Contour at Height Z = 250 mm

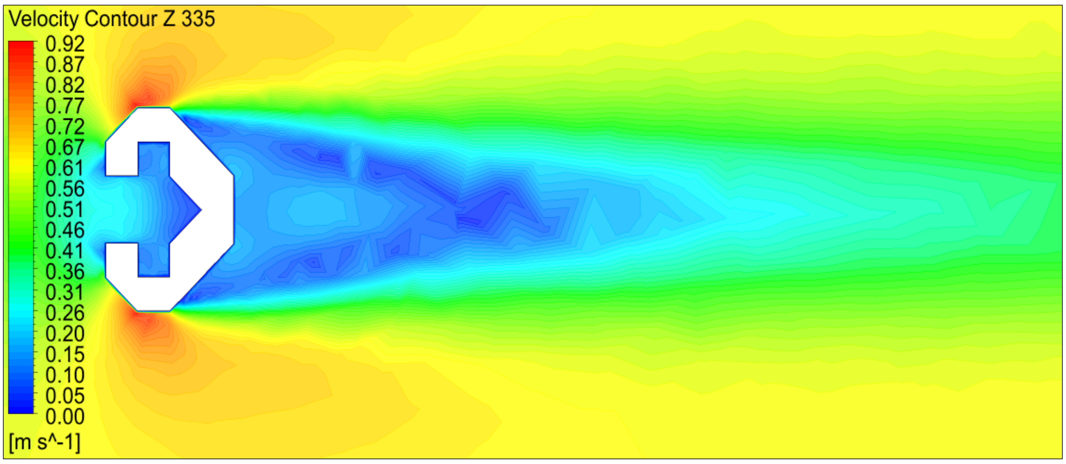

(c) Velocity Contour at Height Z = 335 mm

Figure 5. 126: Velocity Contour Wrench Shape Model 180° Wind Angle

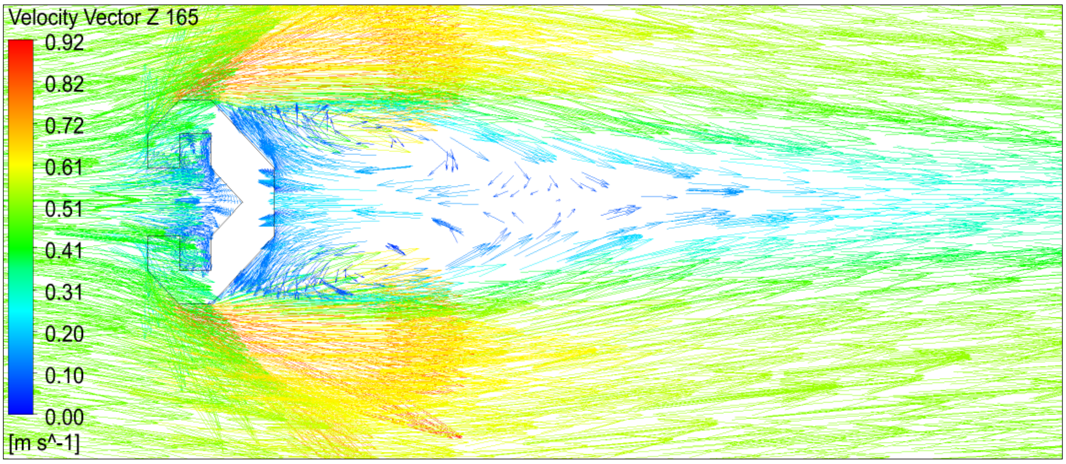

(a) Velocity Vector at Height Z = 165 mm

Figure 5. 126: Velocity Vector Wrench Shape Model 180° Wind Angle (Contd.)

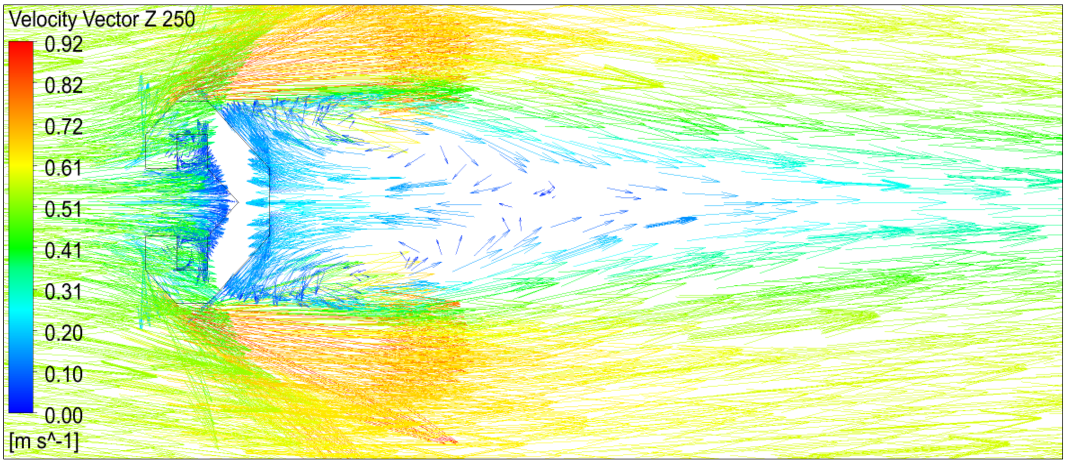

(b) Velocity Vector at Height Z = 250 mm

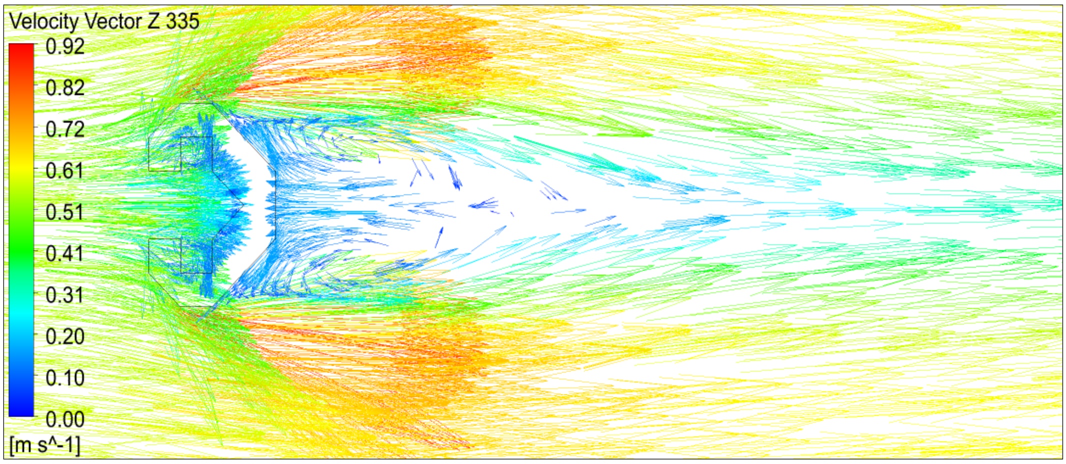

(c) Velocity Vector at Height Z = 335 mm

Figure 5. 127: Velocity Vector Wrench Shape Model 180° Wind Angle

5.4.9 Velocity Streamline Along Wind Direction on Central Vertical Plane

The streamlines showing the flow directions on cross section through central vertical plane of the model along the wind direction for different wind incidence angles are shown in Figure 5.127, 5.128, 5.129, 5.130, 5.131, 5.132 & 5.133 respectively. The recirculation of flow behind the model and formation of vorticity, the upwind vortex at ground level, upwash, downwash and stagnation zones on the windward faces and recirculation cavity formed at the roof level can be seen. It can be visualized that the effects are different for different angles of wind attack.

For 0° to 60° wind angle vorticity behind the model is observed at roof levels. From 90° to 180° wind angles, it is shifting towards the ground. At 180° it is shifted towards the model as well. Secondary vortex at ground behind the model is also seen at 180° wind angle.

The formation of roof level recirculation zone at 0° wind angle is remarkable. Formation of this zone is progressively less intensified till 90° wind angle and then increasing again. At 180° wind angle huge formation of shear layer is seen above the roof. It is an important phenomenon so far as the dispersion of exhaust gases, smokes etc. is concerned as the flow is escaping from the roof cavity in most of the cases of wind angles.

At 90° and 120° wind incidence angle the ground level upwind vortex is less intensified and closer to the model. At 180° wind angle its location is farther away from the model and the strength and intensity of the upwind vortex are supplemented as the stagnated wind, entrapped within the recessed cavity, moves upstream at ground level.

At 60° wind angle large spacing in the streamlines at mid height of the model is seen suggesting slower speed of backwash stream at this height. At 90° wind angle spacing between the streamlines towards the wake region is more. It indicates deceleration of flow stream.

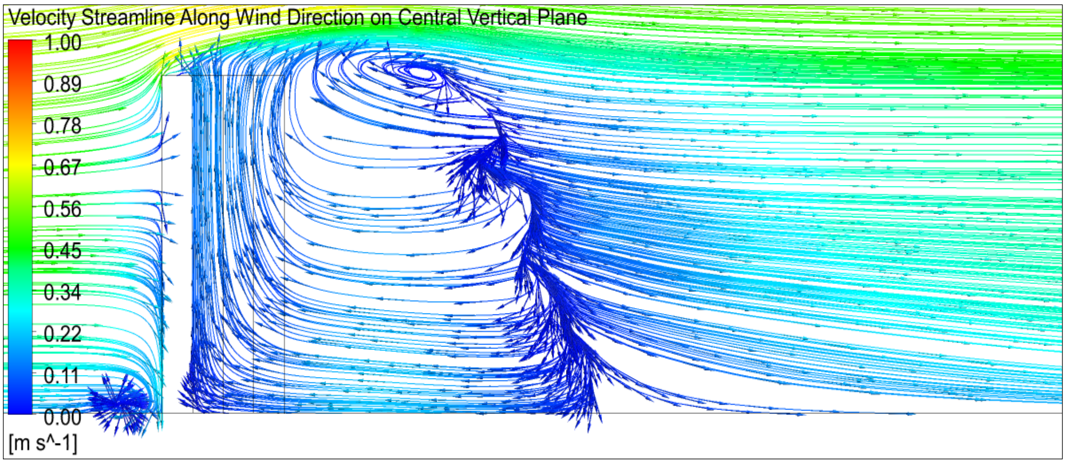

Figure 5. 128: Velocity Streamline Along the Wind Direction on Central Vertical Plane Wrench Shape Model 0° Wind Angle

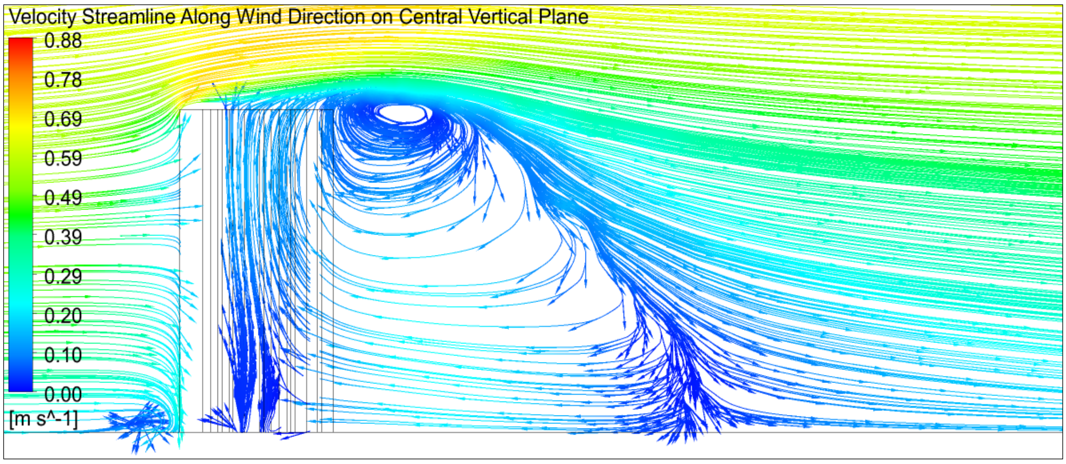

Figure 5. 129: Velocity Streamline Along the Wind Direction on Central Vertical Plane Wrench Shape Model 30° Wind Angle

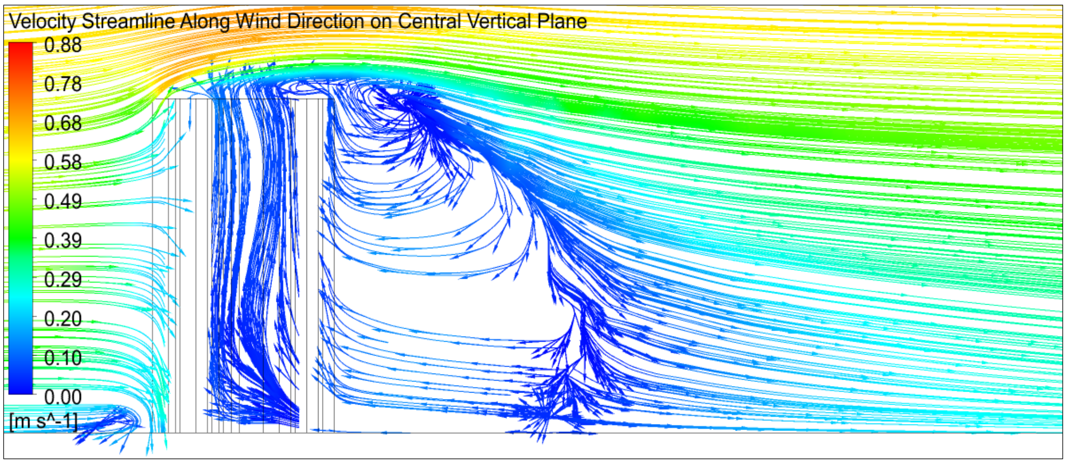

Figure 5. 130: Velocity Streamline Along the Wind Direction on Central Vertical Plane Wrench Shape Model 60° Wind Angle

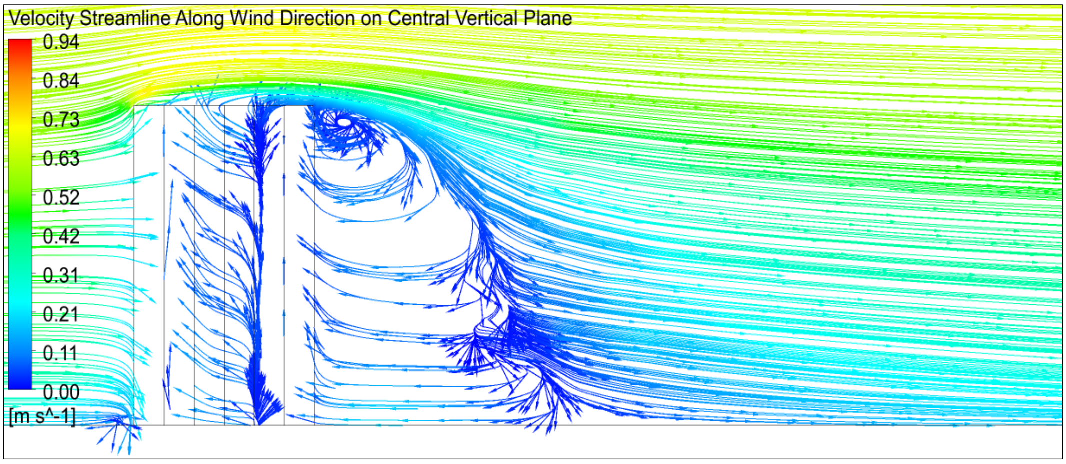

Figure 5. 131: Velocity Streamline Along the Wind Direction on Central Vertical Plane Wrench Shape Model 90° Wind Angle

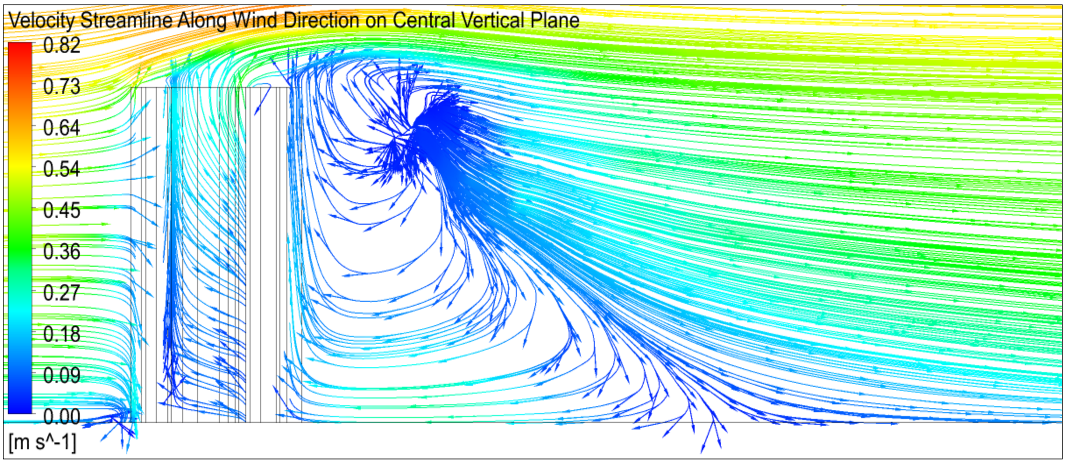

Figure 5. 132: Velocity Streamline Along the Wind Direction on Central Vertical Plane Wrench Shape Model 120° Wind Angle

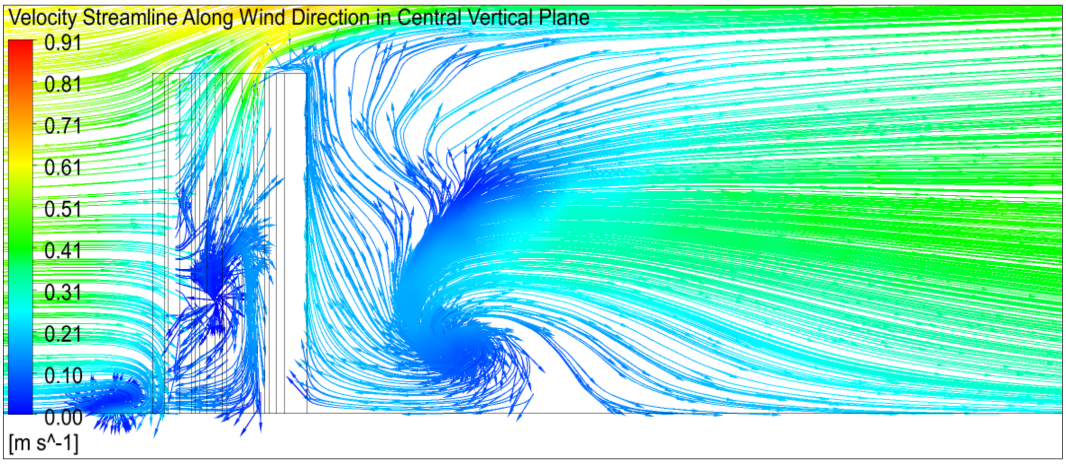

Figure 5. 133: Velocity Streamline Along the Wind Direction on Central Vertical Plane Wrench Shape Model 150° Wind Angle

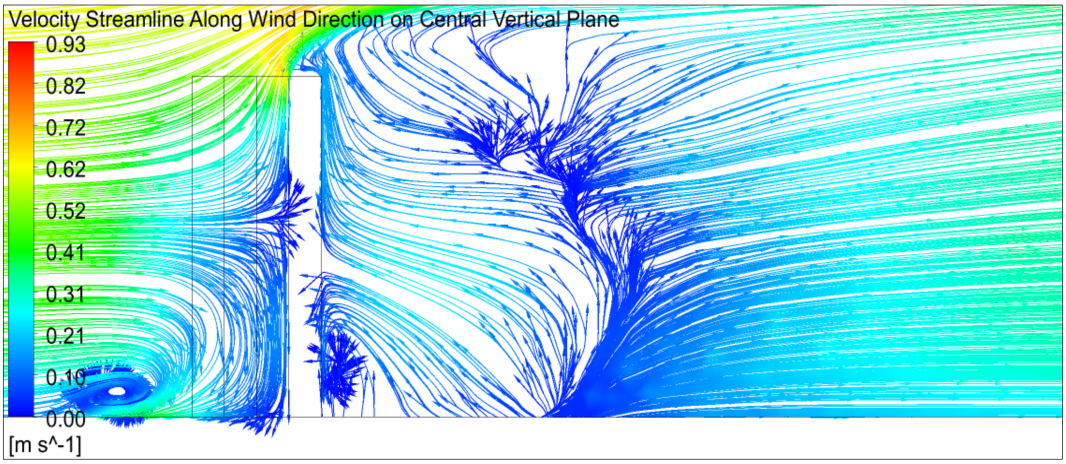

Figure 5. 134: Velocity Streamline Along the Wind Direction on Central Vertical Plane Wrench Shape Model 180° Wind Angle

5.4.10 C_{Pe} Along Building Perimeter

Graphical plot representing the variation of C_{Pe} on the building façade at three different heights Z = 0.165 m (about 1/3rd height of the model), Z = 0.25 m (1/2 height of the model) and Z = 0.335 m (about 2/3rd height of the model) for different wind angles of attack from 0° to 180° @ 30° have been shown in Figure 5.134, 5.135, 5.136, 5.137, 5.138, 5.139 & 5.140 respectively. This graphical representation provides us overall scenario of positive and suction pressure along the perimeter of the model and also the pressure gradient on the faces. For all the wind angles the maximum positive coefficient of pressure almost reaching the value of 1. As explained earlier, small variations in C_{Pe} on the faces shows formation of local eddies whereas, huge rise in the values suggests formation of pressure region on the surface. Sudden decrease in C_{Pe} values show shear layer formation at the place.

It can be visualized that for 0° wind angle positive pressure on face A and partly on face B1 and B2 exists. Rest all faces are under suction. On faces B1, C1, B2 and C2 high gradient of pressure exist.

At 30° angle of attack positive pressure exists on major portion of face A and B2. Maximum fluctuation in C_{Pe} values also exist on these faces.

At 60° wind angle positive pressure on most part of faces B2 and C2 is present. Whereas pressure gradient is maximum on faces A, B1 and C2.

At 90° face C2 is bearing positive pressure. In some part of faces B2 and D2 positive pressure also exists. High fluctuations in C_{Pe} values are seen on face B2 and D2.

For 120° wind angle face D2 is under positive pressure. In some portion of face C2 and F1 also positive pressure exists. All the internal faces do have positive pressure as well. High gradient of pressure is present on face E1 and C2.

Positive pressure on faces E1, E2, D2 and all the internal faces are seen for 150° wind incidence angle. Gradient of pressure is high on face E1 and D2. At 180° wind incidence, face E1, E2 and all the internal faces are under positive pressure. High gradient pf pressure exists on face D1 and D2.

The location where maximum suction exist is vital for design of cladding units. The detailed suction C_{Pe} values for different angle of wind incidence on the corners or faces are shown in Table 5.6. It is quite evident that maximum suction (-2.24) occurs on the corners B1C1 and B2C2 for 0° wind angle of attack which shall govern the design of cladding units for this shape and size of the wrenched plan shaped building. However, if the cladding design is done considering the coefficient on face-to-face basis and preparing appropriate block pressure diagram for the faces, it will be economically cheaper at the same time the building will be safer against failure of cladding design.

Table 5. 6: Maximum Suction in Terms of C_{Pe} For Cladding Design

AoA	Location	Z		
		0.165 m	0.250 m	0.335 m
0°	Corner B1C1	-2.02	-2.22	-2.24
	Corner B2C2	-2.02	-2.22	-2.24
30°	Face B1	-1.44	-1.64	-1.80
	Corner D2C2	-1.39	-1.37	-1.54
60°	Face B1	-1.45	-1.60	-1.62
	Face D2	-1.52	-1.62	-1.60
90°	Face A	-2.04	-1.93	-1.99
	Face E2	-1.28	-1.39	-1.43
120°	Corner AB2	-0.92	-1.02	-1.06
	Corner D1E1	-0.97	-1.15	-1.35
150°	Face B2	-1.39	-1.73	-1.91
	Face D1	-1.72	-1.80	-1.69
180°	Face C1	-1.96	-2.02	-2.09
	Face C2	-1.96	-2.02	-2.09

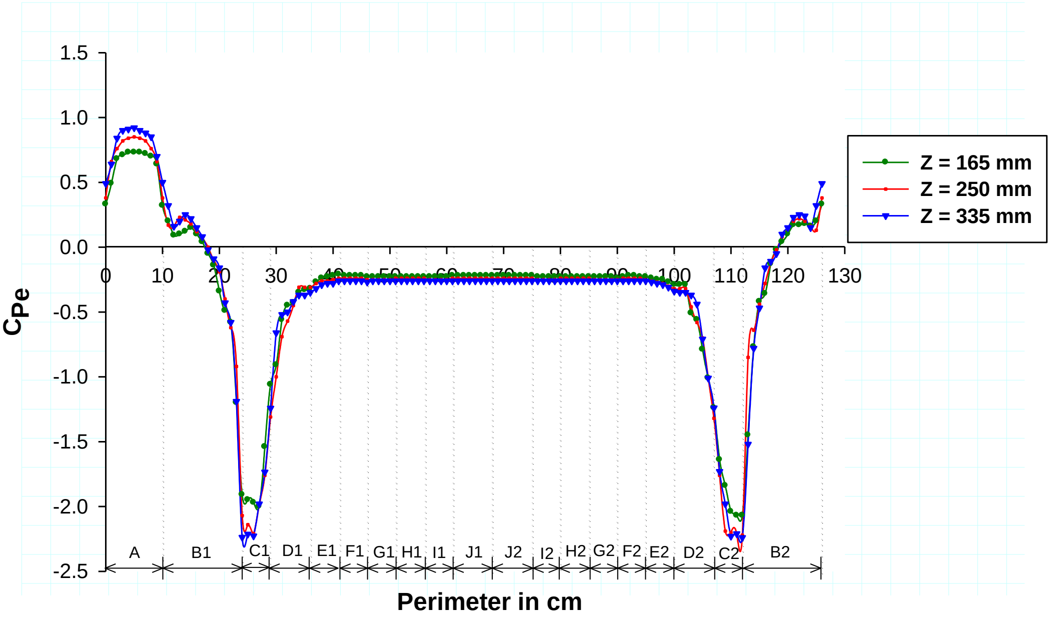

Figure 5. 135: C_{Pe} Along Perimeter Wrench Shape Model 0° Wind Angle

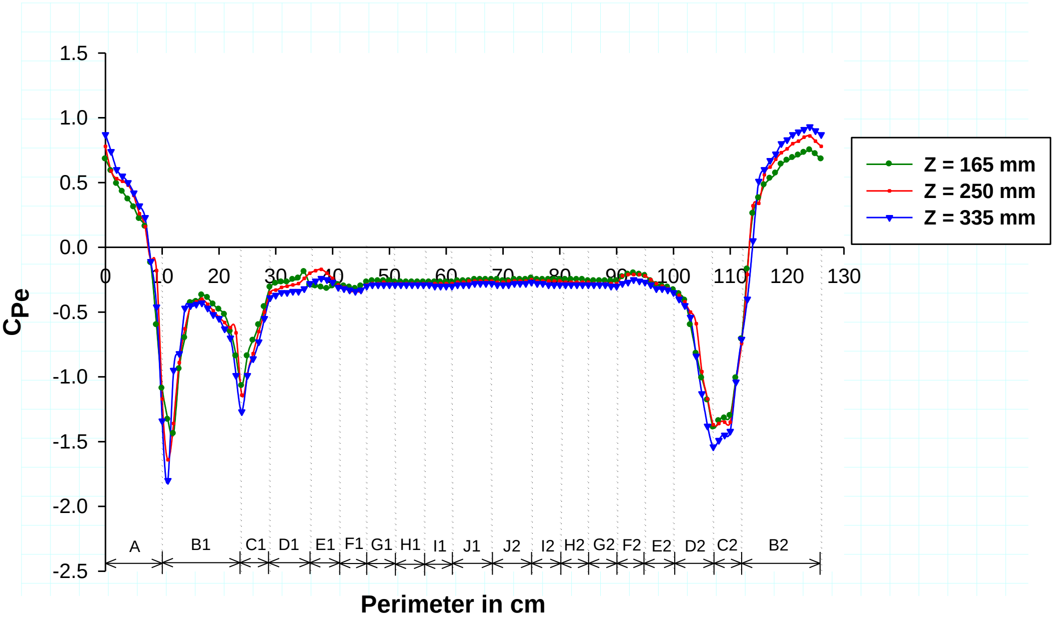

Figure 5. 136: C_{Pe} Along Perimeter Wrench Shape Model 30° Wind Angle

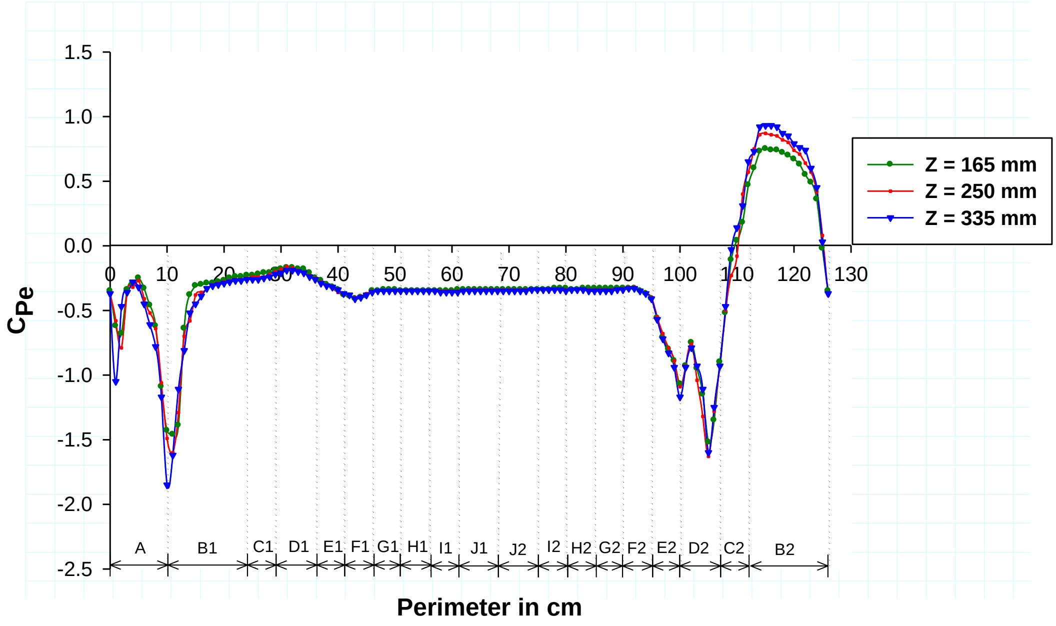

Figure 5. 137: C_{Pe} Along Perimeter Wrench Shape Model 60° Wind Angle

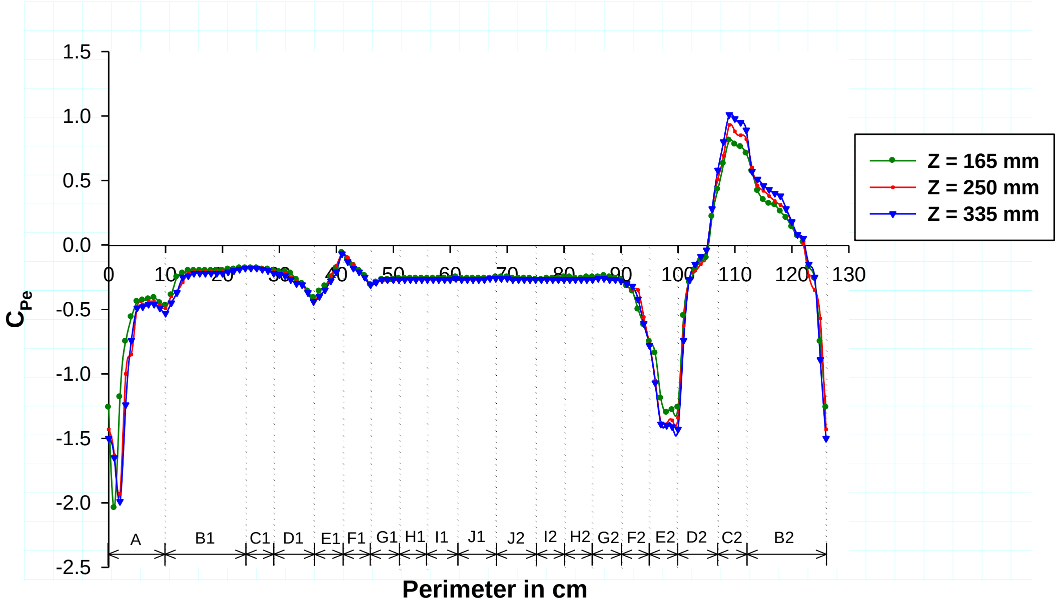

Figure 5. 138: C_{Pe} Along Perimeter Wrench Shape Model 90° Wind Angle

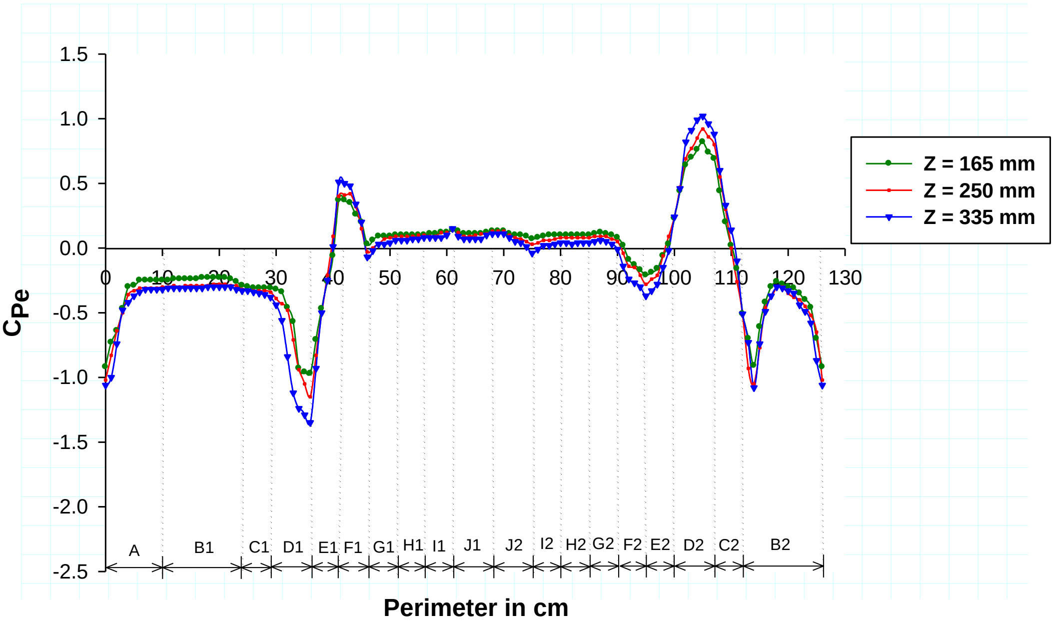

Figure 5. 139: C_{Pe} Along Perimeter Wrench Shape Model 120° Wind Angle

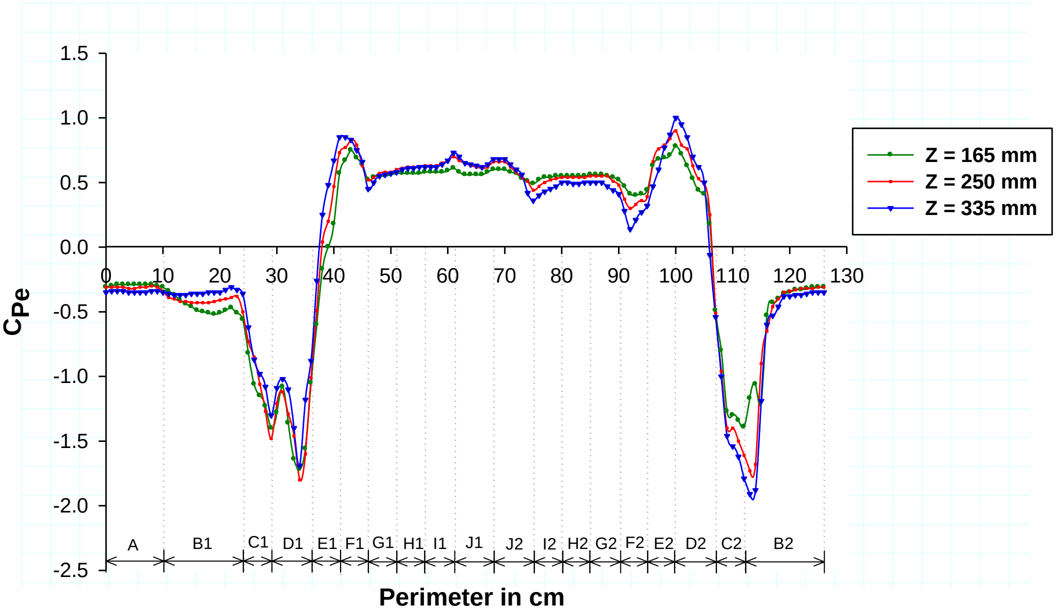

Figure 5. 140: C_{Pe} Along Perimeter Wrench Shape Model 150° Wind Angle

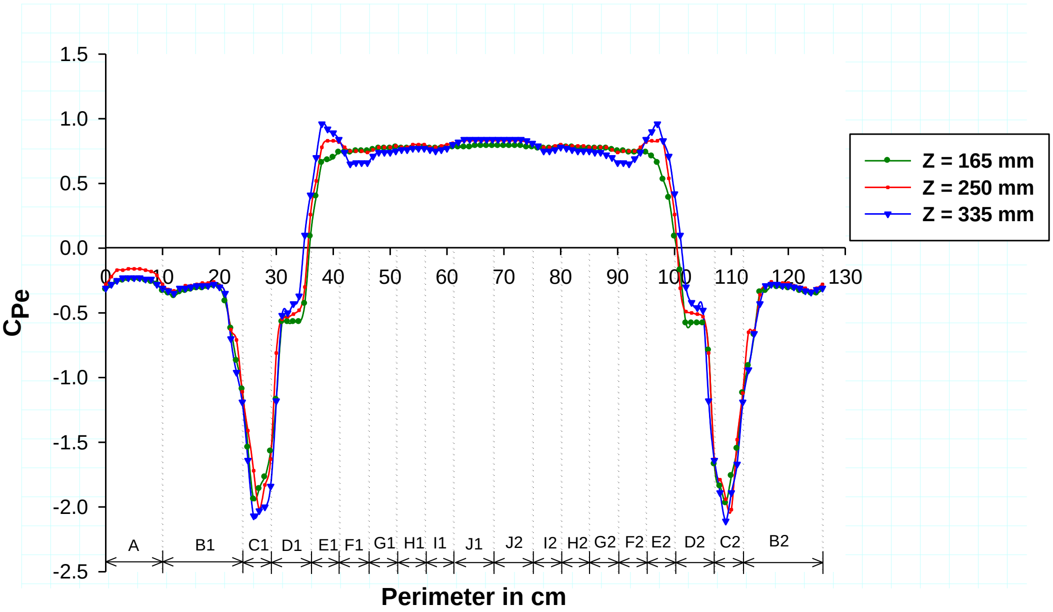

Figure 5. 141: C_{Pe} Along Perimeter Wrench Shape Model 180° Wind Angle

5.4.11 C_{Pe} Along Central Vertical Line on Faces

Variation of pressure coefficient along the central vertical line on faces are shown in Figure 5.141, 5.142, 5.143, 5.144, 5.145, 5.146 & 5.147 for different angle of wind incidence. The variation of pressure coefficient along the centre line on faces gives the flawless pattern of pressure coefficients throughout the height on faces. It also depicts fine picture of the change in flow pattern along the height of the faces. It is observed that in most cases where positive pressure exists on the face due to direct impingement of wind, the maximum value of C_{Pe} along the central vertical line is nearly 1.0. Also, it has been pointed out earlier that symmetrically opposite faces show mirror image of the C_{Pe} values along the line.

At 0° wind incidence angle face A is facing the wind orthogonally and the maximum positive C_{Pe} is nearly 1.0. It occurs at 0.45 m height of the model from where sudden change in C_{Pe} from positive to negative is taking place as the flow is leaving from roof height. Positive coefficient of pressure is also occurring on inclined faces B1 and B2 along the central vertical line. High fluctuation of suction pressure exists on symmetrical faces C1 and C2. In the middle height of the faces suction is high. Other outer faces have mild suction of uniform nature along the height. Inner faces are under suction which is increasing along height. Small fluctuations in C_{Pe} values are also observed along the height on inner faces.

At 30° wind incidence angle face A and B2 are exposed to direct wind. Rest all outer faces are under suction. Highest suction is shown on face C2 in the middle height of the face. Fluctuation in C_{Pe} along the height of face D2 is huge. On all the inner faces the behaviour of central vertical C_{Pe} line is similar to that which exists at 0° wind angle of attack except that on faces F1 and F2. On face F1 suction is more than that on face F2.

At 60° wind angle of attack only face B2 is under the influence of direct wind. Positive pressure occurs on face C2 between height 0.35 m to 0.475 m. Face D2 is suffering with high fluctuating negative pressure. On the inner faces complex gradient of suction along the height is observed. Moreover, increased value of suction in comparison to other previous angles exists on the faces. Face F1 is under high suction.

For 90° wind angle from the behaviour of C_{Pe} central vertical line it is obvious that this face is exposed orthogonally to wind whereas, face B2, though exposed to direct wind but the impact of wind on the face is slanted. Face E2 is subjected to maximum suction among all the inner faces. Huge fluctuation of suction in the middle height exists on inner face F1 and F2. Face F2 is on more suction compared to face F1.

At 120° angle of wind incidence both faces D2 and C2 are directly exposed to wind. At the lower 0.05 m height of face E2 mild positivity in C_{Pe} values exist. Suction is increasing along height on face D1 first with high gradient up to 0.2 m height of the model, then gradually up to 0.4 m from where it sharply reduces towards roof. Among the inner faces, face F2 is under increasing suction along height. Rest faces are under positive pressure of similar value except face F1 which seems to be showing direct exposure to wind. Moreover, pressure on the face is sharply changing to negative towards roof between the height from 0.35 m to 0.45 m. Since the C_{Pe} graph along the perimeter has been drawn for height up to 0.335 m this aspect in not visible there.

Maximum difference in coefficient of pressure between the outer faces are observed at 150° angle of wind attack. Face D2 and E2 are under positive pressure due to exposure of direct wind. On face E2 huge variation from suction at ground to positive pressure till 0.25 m height of the model and again sharp suction towards roof exists on the face. Inner faces except face F1 and F2 are having almost constant positive C_{Pe} values up to height of 0.15 m. From there pressure is reducing and sharply moves to suction towards roof. On face F1 positive pressure is low at ground, increasing along height and sharply moving to suction at roof height due to separation of flow. On face F2 fluctuations from positive to negative from 0.35 m (approx.) is visible. From the point of view of a designer, this wind incidence angle seems to be important as large differences of C_{Pe} values on the faces, especially on the outer faces are observed.

At 180° of wind attack the central vertical C_{Pe} graph on face E1 and E2 exhibit that they are exposed to direct wind. The model, being symmetrical along the direction of wind, C_{Pe} on similar and opposite faces are almost overlapping on one another. Except face E1 and E2 other outer faces are under suction. Massive suction is revealed on face C1 and C2 which is also present on the faces for 0° wind angle but with huge fluctuation along height. Positive pressure of similar growth along height on the inner faces do exist.

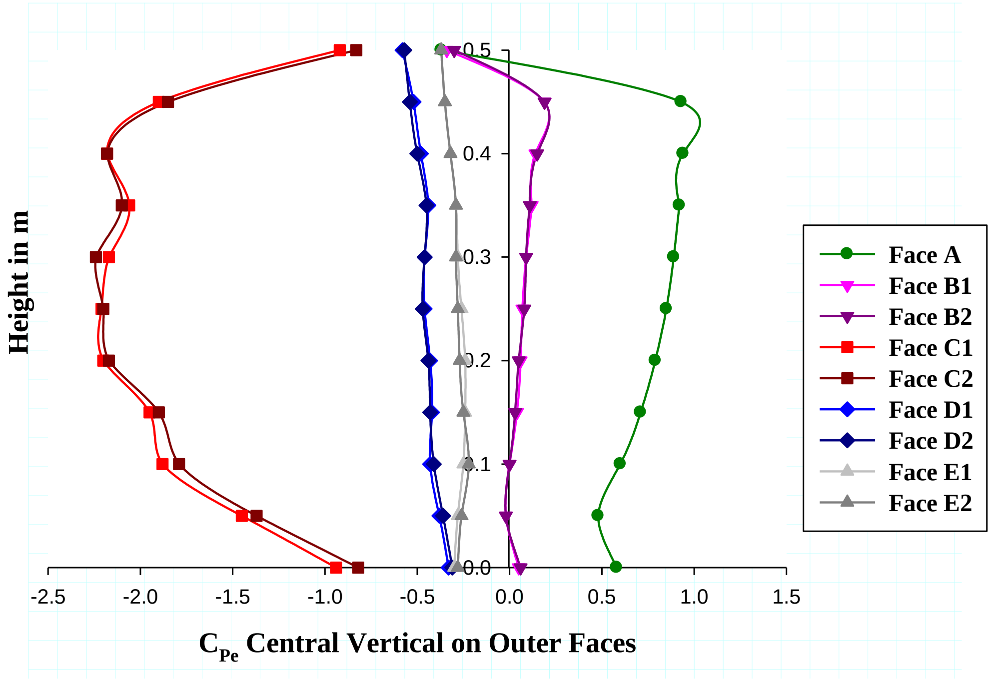

(a): C_{Pe} Along Central Vertical Line on Outer Faces Wrench Shape Model 0° Wind Angle

Figure 5. 141: C_{Pe} Along Central Vertical Line on Faces Wrench Shape Model 0° Wind Angle

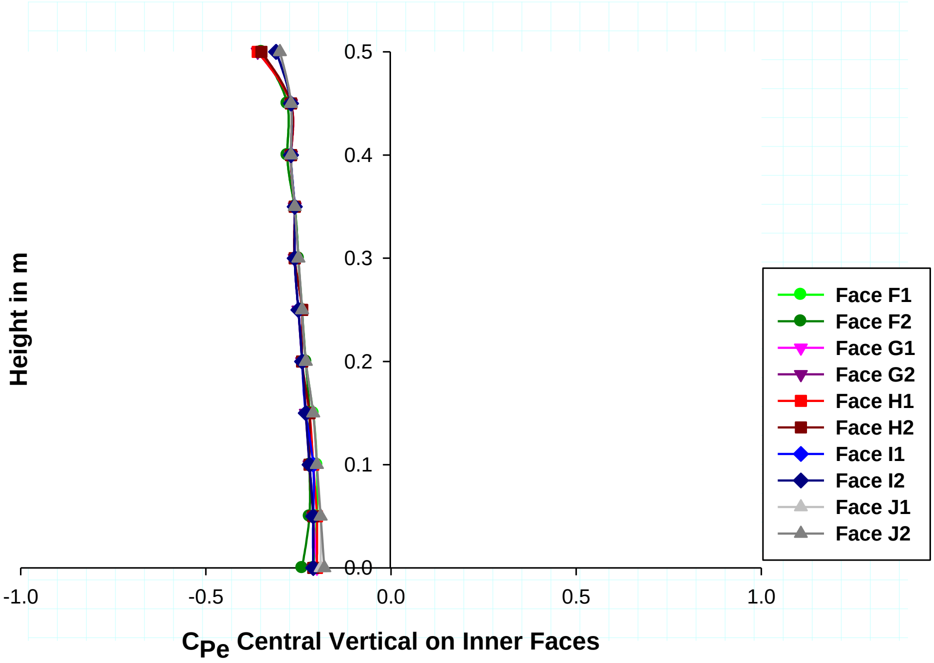

(b): C_{Pe} Along Central Vertical Line on Inner Faces Wrench Shape Model 0° Wind Angle

Figure 5. 1421: C_{Pe} Along Central Vertical Line on Faces Wrench Shape Model 0° Wind Angle

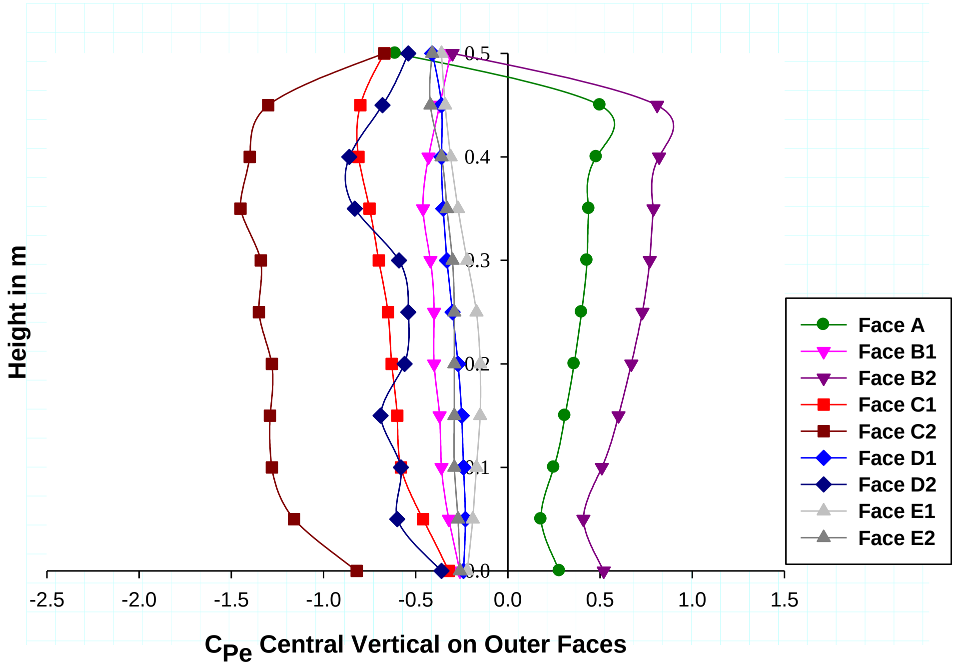

(a): C_{Pe} *Along Central Vertical Line on Outer Faces Wrench Shape Model 30° Wind Angle*

Figure 5. 142: C_{Pe} *Along Central Vertical Line on Faces Wrench Shape Model 30° Wind Angle*

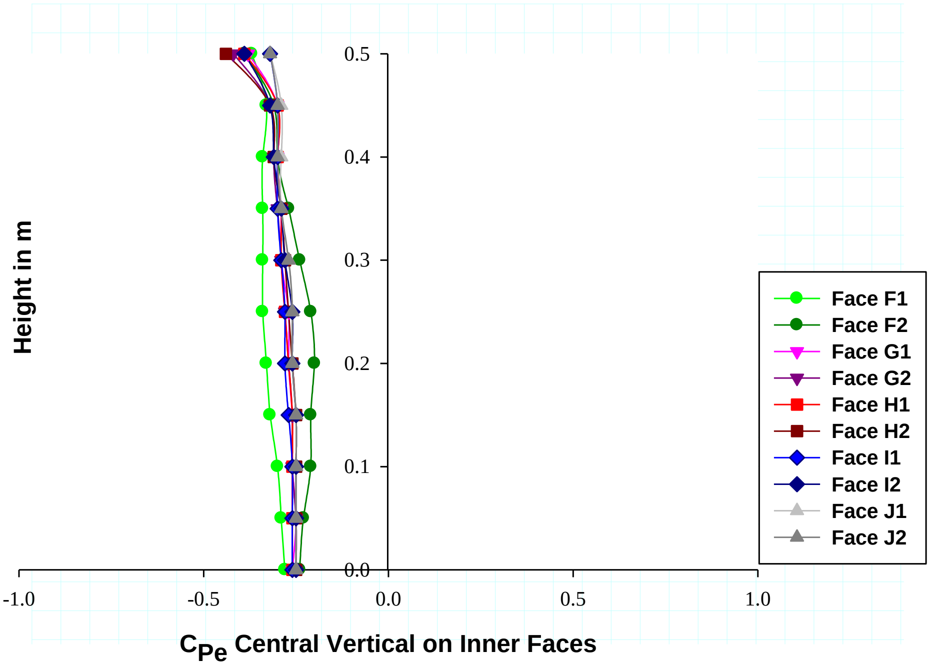

(b): C_{Pe} *Along Central Vertical Line on Inner Faces Wrench Shape Model 30° Wind Angle*

Figure 5. 142: C_{Pe} *Along Central Vertical Line on Faces Wrench Shape Model 30° Wind Angle*

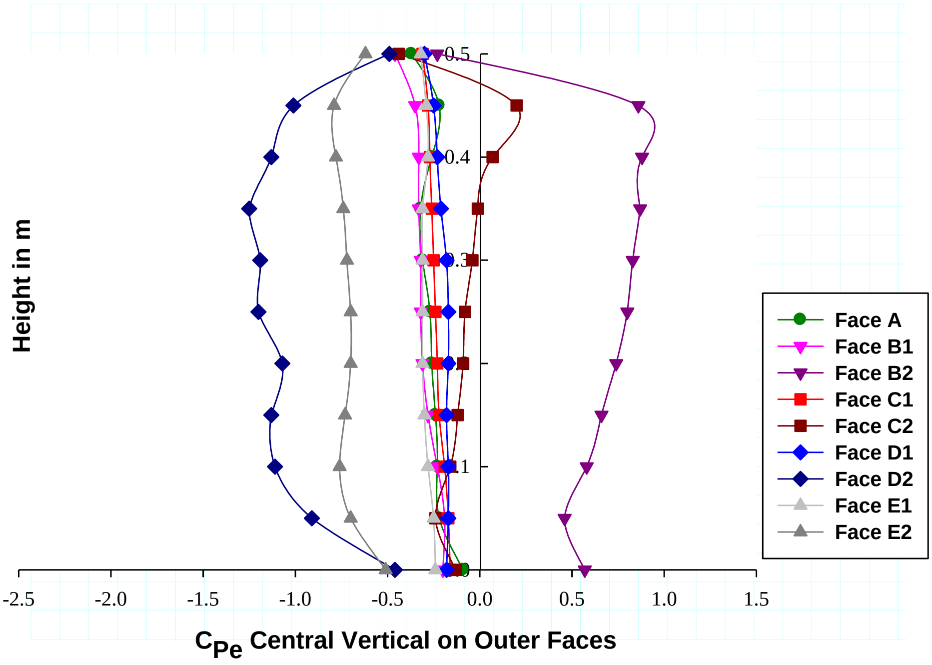

(a): C_{Pe} *Along Central Vertical Line on Outer Faces Wrench Shape Model 60° Wind Angle*

Figure 5.143: C_{Pe} *Along Central Vertical Line on Faces Wrench Shape Model 60° Wind Angle*

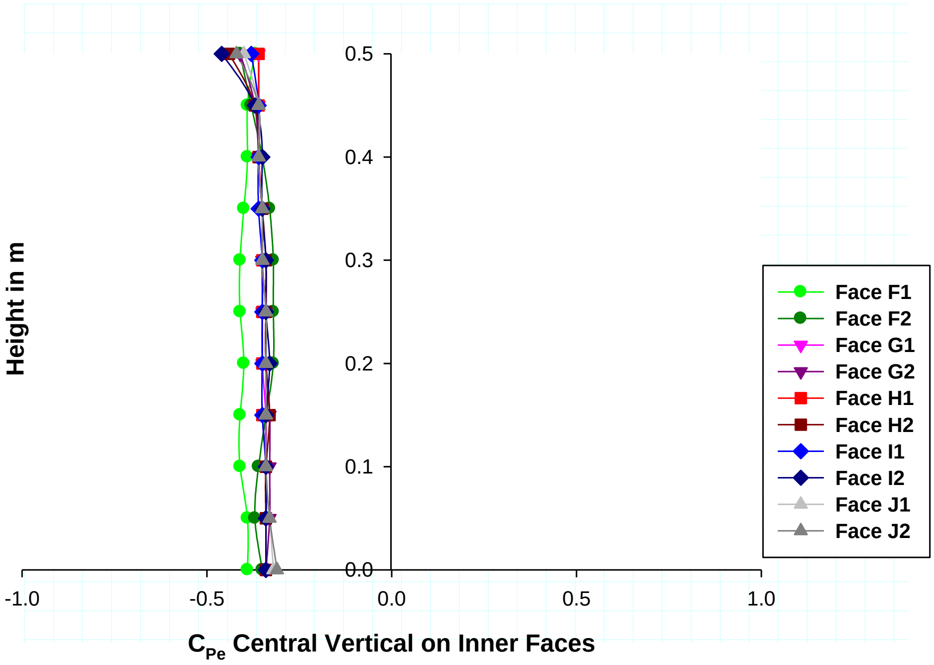

(b): C_{Pe} *Along Central Vertical Line on Inner Faces Wrench Shape Model 60° Wind Angle*

Figure 5. 143: C_{Pe} *Along Central Vertical Line on Faces Wrench Shape Model 60° Wind Angle*

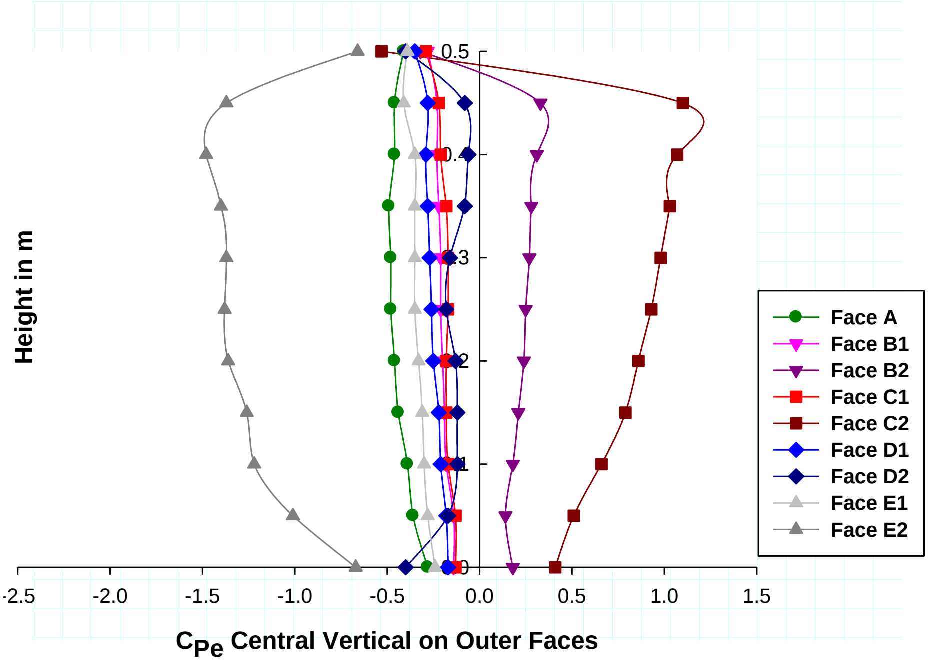

(a): C_{Pe} *Along Central Vertical Line on Outer Faces Wrench Shape Model 90° Wind Angle*

Figure 5. 144: C_{Pe} *Along Central Vertical Line on Faces Wrench Shape Model 90° Wind Angle*

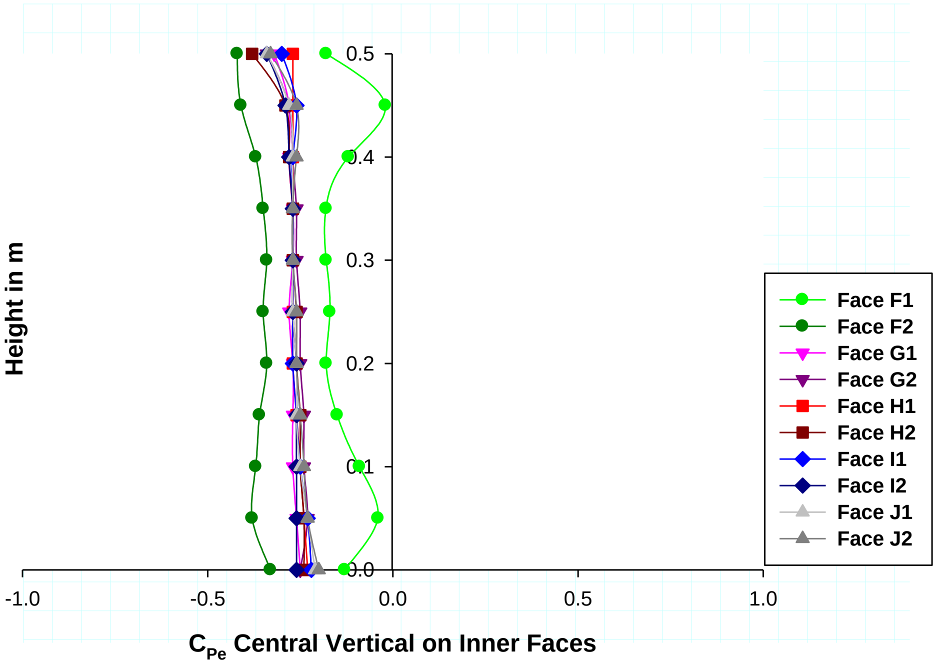

(b): C$_{Pe}$ *Along Central Vertical Line on Inner Faces Wrench Shape Model 90° Wind Angle*

Figure 5. 144: C$_{Pe}$ *Along Central Vertical Line on Faces Wrench Shape Model 90° Wind Angle*

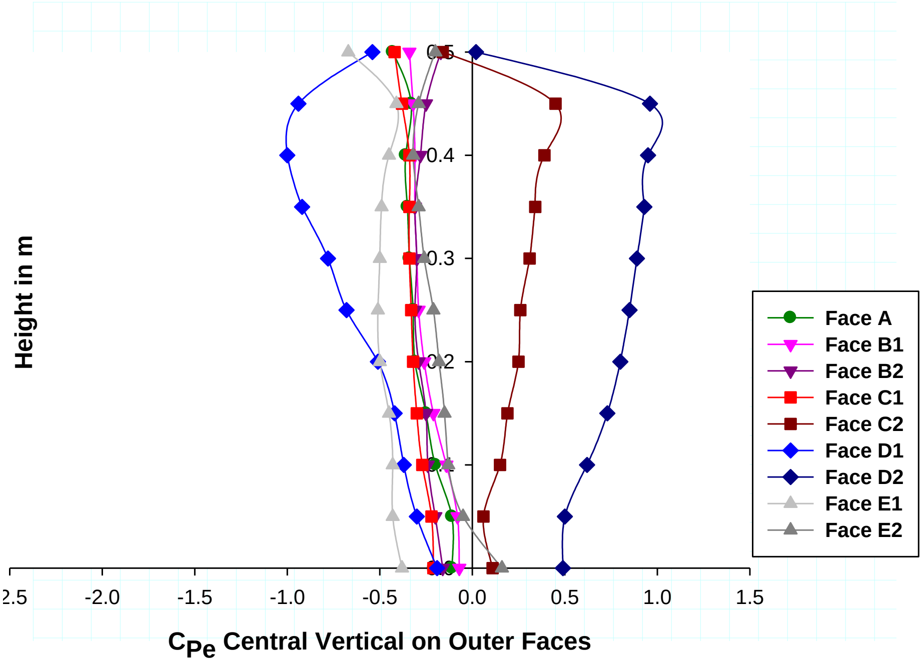

(a): C$_{Pe}$ *Along Central Vertical Line on Outer Faces Wrench Shape Model 120° Wind Angle*

Figure 5. 145: C$_{Pe}$ *Along Central Vertical Line on Faces Wrench Shape Model 120° Wind Angle*

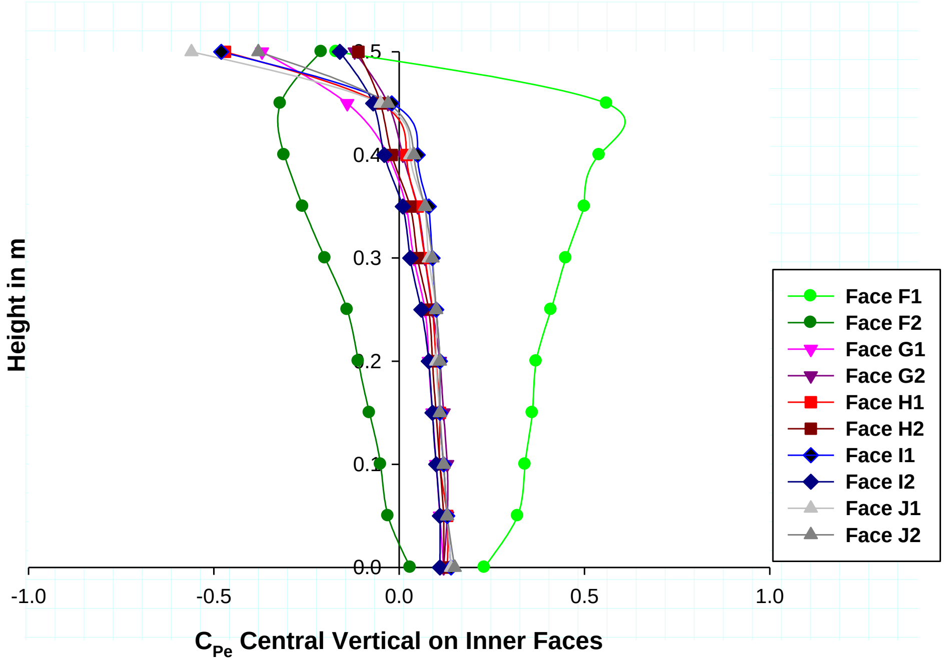

(b): C$_{Pe}$ *Along Central Vertical Line on Inner Faces Wrench Shape Model 120° Wind Angle*

Figure 5. 145: C$_{Pe}$ *Along Central Vertical Line on Faces Wrench Shape Model 120° Wind Angle*

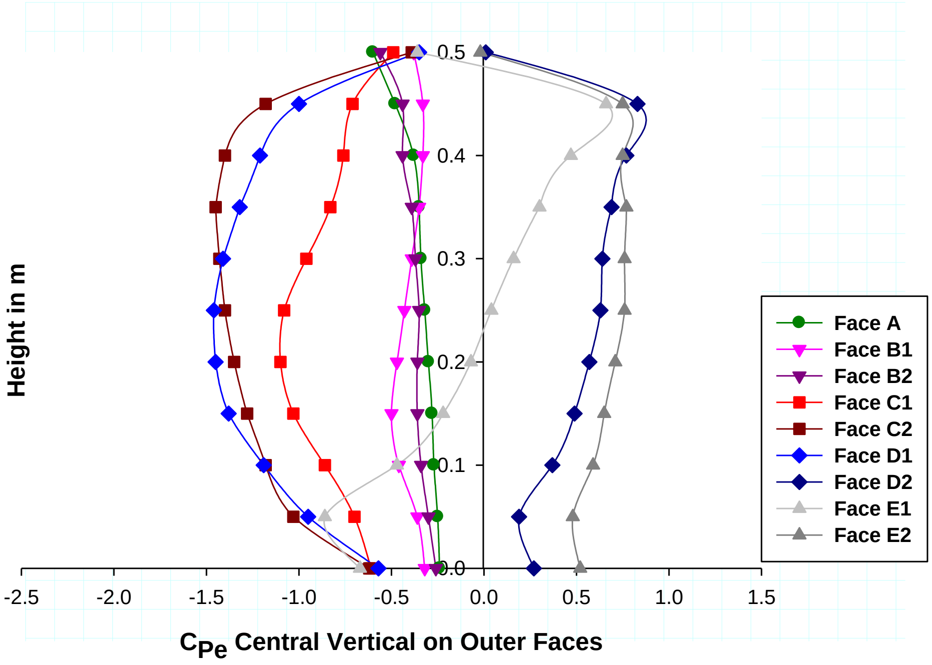

(a): C$_{Pe}$ *Along Central Vertical Line on Outer Faces Wrench Shape Model 150° Wind Angle*

Figure 5. 146: C$_{Pe}$ Along Central Vertical Line on Faces Wrench Shape Model 150° Wind Angle

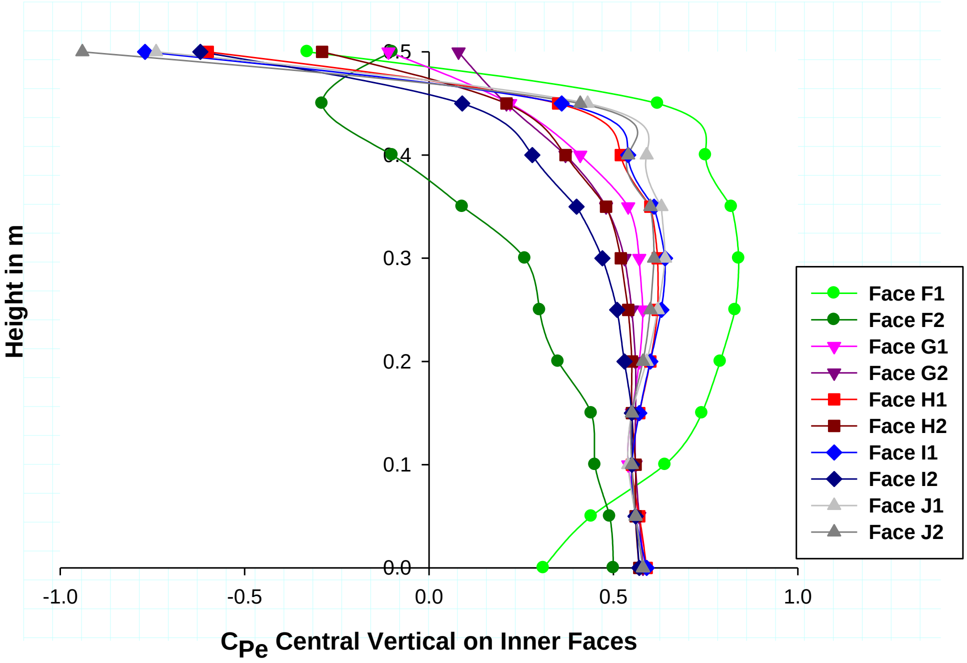

(b): C_{Pe} Along Central Vertical Line on Inner Faces Wrench Shape Model 150° Wind Angle

Figure 5. 146: C_{Pe} Along Central Vertical Line on Faces Wrench Shape Model 150° Wind Angle

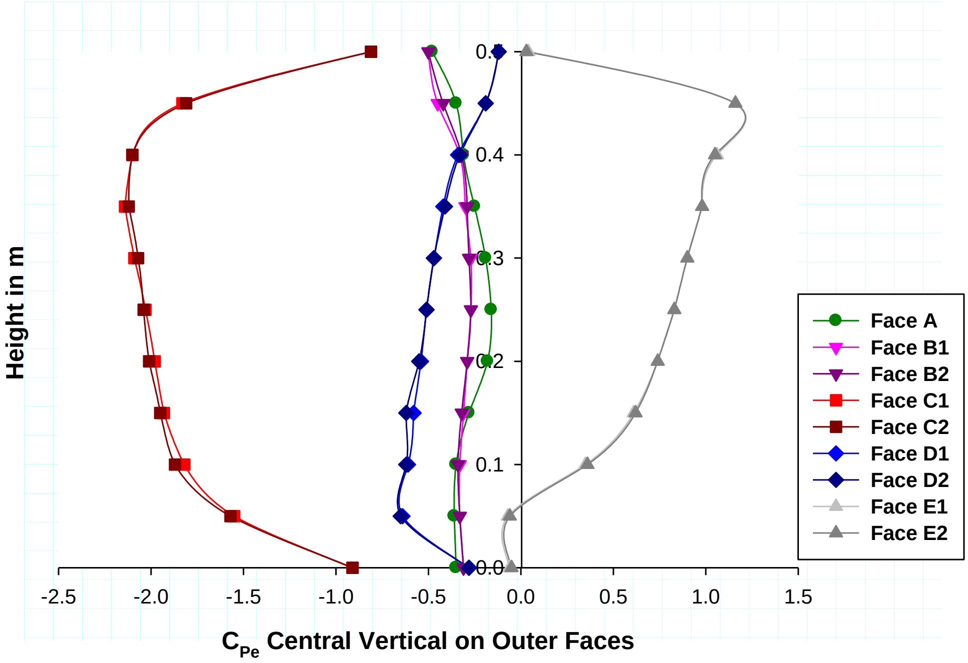

(a): C_{Pe} Along Central Vertical Line on Outer Faces Wrench Shape Model 180° Wind Angle

Figure 5. 147: C_{Pe} Along Central Vertical Line on Faces Wrench Shape Model 180° Wind

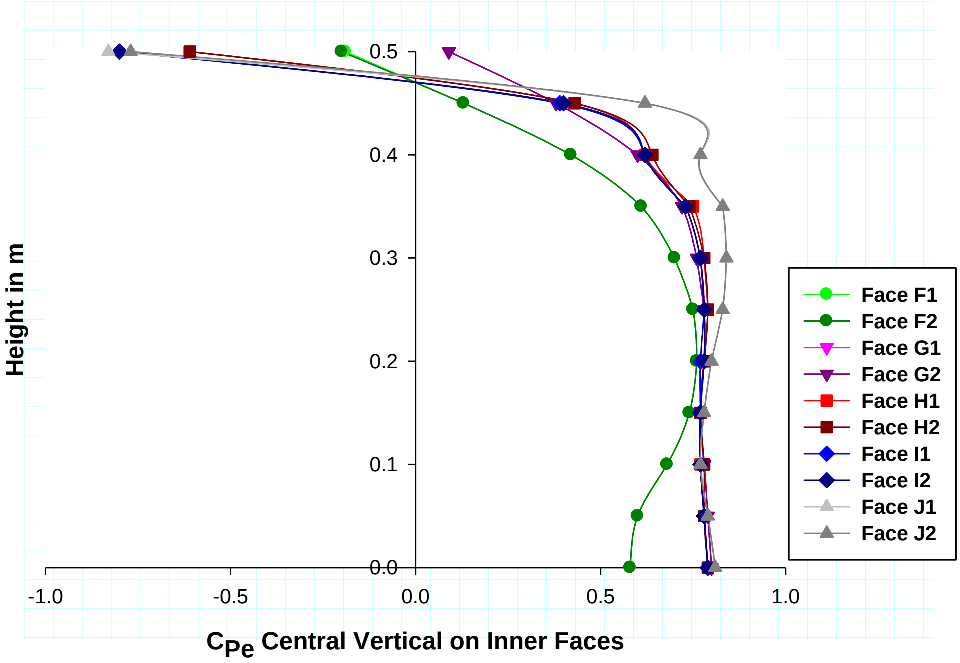

(b): C_{Pe} *Along Central Vertical Line on Inner Faces Wrench Shape Model 180° Wind Angle*

Figure 5. 147: C_{Pe} *Along Central Vertical Line on Faces Wrench Shape Model 180° Wind Angle*

CHAPTER 6 STRUCTURAL PARAMETERS

6.1 GENERAL

As discussed earlier in chapter 3 that ANSYS (CFX) has the ability to provide wind induced base shear $(F_x \& F_y)$, base moment $(M_x \& M_y)$ and torsion moment (M_Z) of the simulated model directly from its function calculator. The primary concern with the mean velocity of wind on building is two-fold. First the turbulence of the natural wind approaching the building and second the local turbulence provoked in the wind by the building envelope when wind strikes on it. Since, the N-S equations of flow in $k - \varepsilon$ turbulence model uses RANS equations, the first state of turbulence/gustiness has been incorporated as time independent mean velocity of flow at the inlet. The details of development of the local turbulence provoked by the building envelope on the values of forces and moments has been taken into account in the present study. In simple words the shear force developed on the faces including the roof surfaces have been taken into account along with that developed due to impact/velocity pressure of striking wind. The comparison of these forces and moments have been discussed in two categories. The plan shapes symmetric about both axes and model plan shapes symmetric about one axis are discussed separately to have an overall assessment of these issues with respect to one another in both categories. In the present study wind axes and body axes coincide with each other for all wind incidence angle. So, base shear force in x-direction (F_x) and drag force will be the same. Similarly base shear force in y-direction (F_y) and lift force will be the same. Bending and twisting moments have been reckoned at centroid of cross-section.

For models symmetrical about both axes study has been conducted for extended angle of wind attack from 0° to 90° and for models symmetrical about one axis, from 0° to 180° in clockwise direction which are sufficient to understand the impact of wind on the models for all wind directions. The forces and moments have been represented in terms of dimensionless coefficients defined in Equations 6.1 to 6.5.

Force coefficient of the whole building along x-direction i.e., in wind direction (coefficient of drag):

$$C_{fx} = \frac{F_x}{(0.5\rho u_H^2)L_x H} \qquad (Eq. 6.1)$$

Force coefficient of the whole building along y-direction i.e., across wind direction (coefficient of lift):

$$C_{fy} = \frac{F_y}{(0.5\rho u_H^2)L_y H} \qquad (Eq. 6.2)$$

Overturning Moment coefficient of the whole building about x-direction (direction of wind):

$$C_{mx} = \frac{M_x}{(0.5\rho u_H^2)(L_y H)(0.5H)} \qquad (Eq. 6.3)$$

Overturning Moment coefficient of the whole building about y-direction (across wind direction):

$$C_{my} = \frac{M_y}{(0.5\rho u_H^2)(L_x H)(0.5H)} \qquad (Eq. 6.4)$$

Torsional coefficient of the whole building about z-direction:

$$C_{tm} = \frac{M_z}{(0.5\rho u_H^2)(L_x L_y)(H)} \qquad (Eq. 6.5)$$

Where,

F_x = Total force (base shear) on the model along wind direction.

F_y = Total force (base shear) on the model across wind direction.

M_x = Total moment (base moment) along x-direction.

M_y = Total moment (base moment) along y-direction.

M_z = Total moment (torsional moment) along z-direction.

ρ = Density of wind taken in the simulation (= 1.225 kg/m^3).

u_H = Wind velocity at roof top (= 0.63 m/s).

L_x = Projected length of the model orthogonal to the wind direction.

L_y = Projected length of the model in the wind direction.

H = Height of the model (= 0.5 m)

6.2 MODELS WITH SYMMETRY ABOUT BOTH AXES

6.2.1 Force Coefficient Along Wind Direction (Drag Coefficient)

Figure 6.1 shows the variation of C_{fx} for rectangular, plus and octagonal plan shape models due to varied wind incidence angles. It is observed that for all the wind angles C_{fx} in rectangular model is higher than those in plus shape and octagonal models. The maximum and minimum coefficient of drag in rectangular model is at 0° and 75° respectively. In plus shape model, maximum is at 0° & 90° and, minimum is at 30° and 60°. In case of octagonal model, the maximum occurs at 75° and minimum at 15° wind incidence angle. In octagonal model least variation of C_{fx} due to change in wind incidence angle is observed compared to rectangular and plus models.

6.2.2 Force Coefficient Across Wind Direction (Lift Coefficient)

Figure 6.2 shows the variation of C_{fy} in the three models due to various wind angle of attack. It is observed that irrespective of the sign (+ve or -ve) maximum value of C_{fy} in rectangular model occurs at 15° and the minimum occurs at 0°, 60° & 90° wind angle of attack. In plus shape model the maximum is again at 15° and minimum occurs only at 30° wind incidence angle. In octagonal model the maximum and minimum C_{fy} value is observed to be at 60° & 0° wind angle respectively.

6.2.3 Bending Moment Coefficient

Variation of moment coefficients along x direction (C_{mx}) for rectangular, plus and octagonal shape models for different wind incidence angles has been shown in Figure 6.3. It can be visualized that the pattern of variation is similar to that of C_{fy} for the respective models. However, the values are different and the maximum and minimum C_{mx} exists at the same wind incidence angle as that of the values of C_{fy} of the respective model. Similar is the case with C_{my}, the variation pattern of which are similar to that of C_{fx} but with different maximum and minimum values (Figure 6.4).

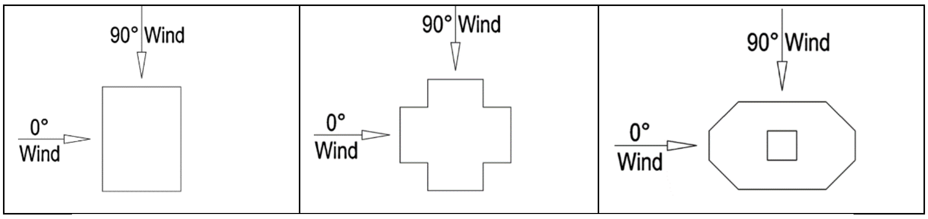

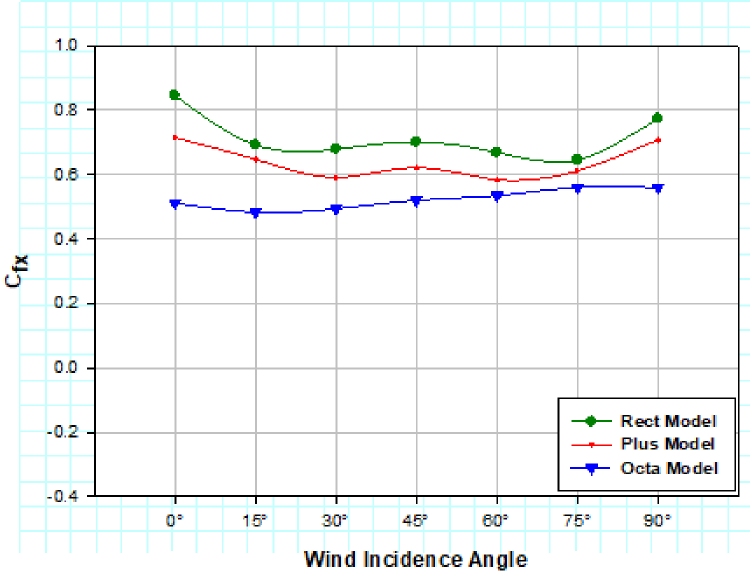

Figure 6. 1: Base Shear Coefficient Along Wind Direction (Drag Coefficient)

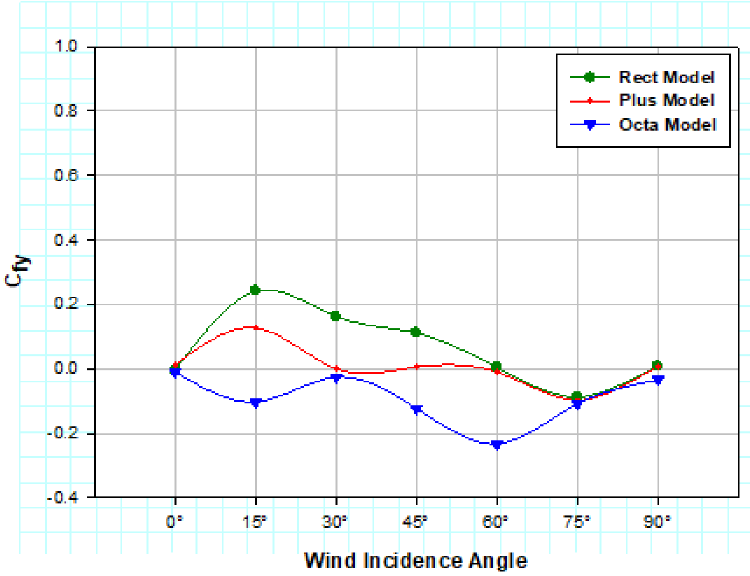

Figure 6. 2: Base Shear Coefficient Across Wind Direction (Lift Coefficient)

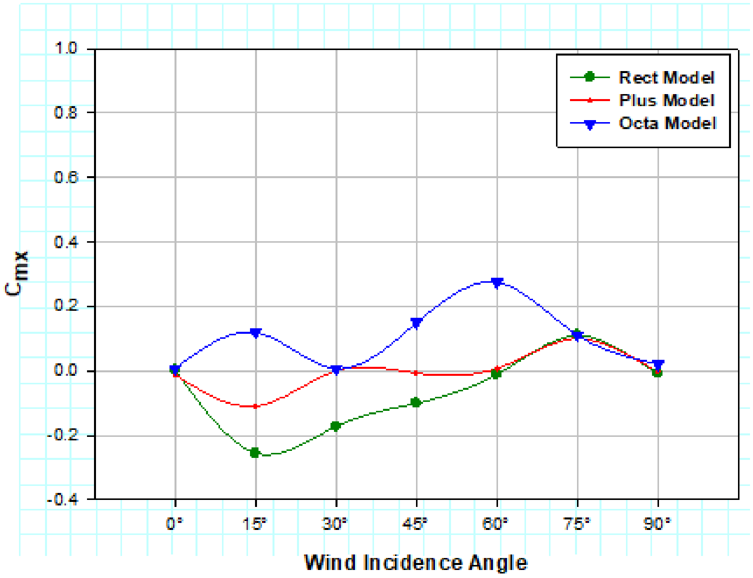

Figure 6. 3: Base Moment Coefficient Along X-Direction

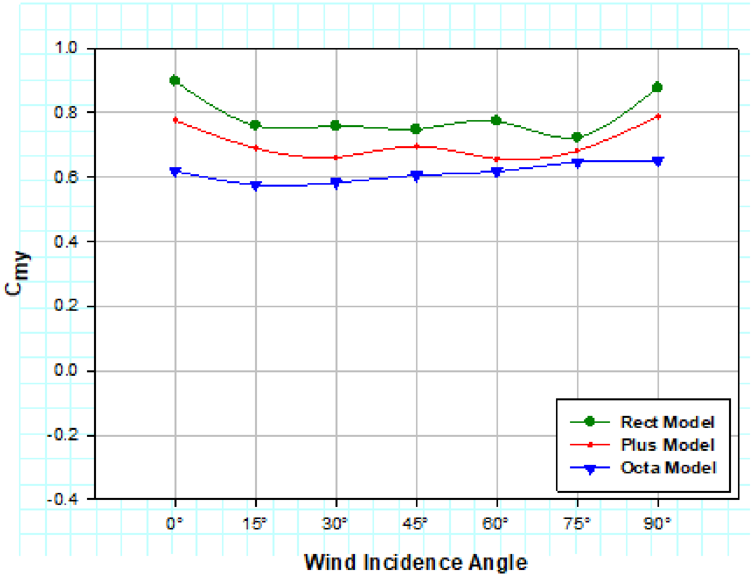

Figure 6. 4: Base Moment Coefficient Along Y-Direction

6.2.4 Twisting Moment Coefficient

Figure 6.5 shows the torsional moment coefficient (C_{tm}) for the three models. It is observed that the plus shape model does not develop torsional moment due to variation of wind angle of attack. But the octagonal model has been affected the most due to torsional moment, the maximum occurring at 45° wind incidence angle. At 0° and 90°

wind the octagonal model is unaffected by torsion. The maximum C_{tm} in rectangular model is observed to be at 15° and the minimum at 0°, 60° & 90° wind incidence angle.

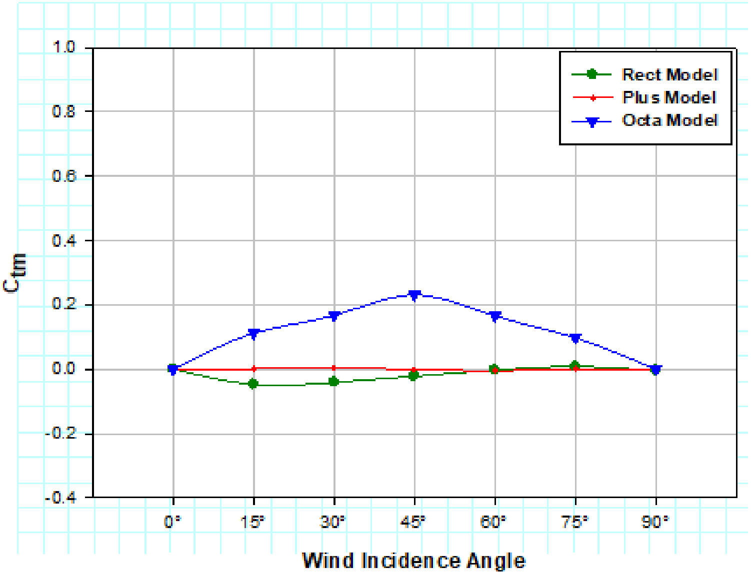

Figure 6. 5: Twisting Moment Coefficient Along Z-Direction

6.3 MODELS WITH SYMMETRY ABOUT ONE AXIS

6.3.1 Force Coefficient Along Wind Direction (Drag Coefficient)

Figure 6.6 shows the variation of C_{fx} for L shape, diamond shape and wrench shape models due to varied wind incidence angles. It is observed that fluctuation of C_{fx} values in diamond shape model is more than those in L shape and wrench shape models. Least variation is seen on the wrench shape model. Not as much of fluctuation is seen in wrench shape model. The maximum and minimum coefficient of drag in L shape model is at 0° and 60° respectively. Fluctuation of C_{fx} values in L shape model is more from 0° to 90° wind incidence angle whereas, from 105° onwards it is almost similar. The maximum coefficient of drag in diamond shape lies between 135° and 150° angle of wind incidence and the minimum occurs at 165°. In wrench shape model the maximum and minimum C_{fx} are at 150° and 75° wind angle of attack respectively.

6.3.2 Force Coefficient Across Direction (Lift Coefficient)

Figure 6.7 shows the variation of C_{fy} in the three models due to various wind angle of attack. It is observed that irrespective of the sign (+ve or -ve) maximum value of C_{fy} in L shape model occurs at 90° and the minimum occurs at 135° wind angle of attack. No major difference is seen between 120° and 150°. In diamond shape model the maximum is at 165° and minimum occurs at 0° & 90° wind incidence angle. In wrench shape model the maximum and minimum C_{fy} value is observed to be at 150° & 75° wind angle respectively.

6.3.3 Bending Moment Coefficients

Variation of moment coefficients along x direction (C_{mx}) for L shape, diamond shape and wrench shape models for different wind incidence angles has been shown in Figure 6.8. It can be visualized that the pattern of variation is similar to that of C_{fy} for the respective models. However, the values are different and the maximum and minimum C_{mx} exists at the same wind incidence angle as that of the values of C_{fy} of the respective model. Similar is the case with C_{my}, the variation pattern of which are similar to that of C_{fx} but with different maximum and minimum values (Figure 6.9).

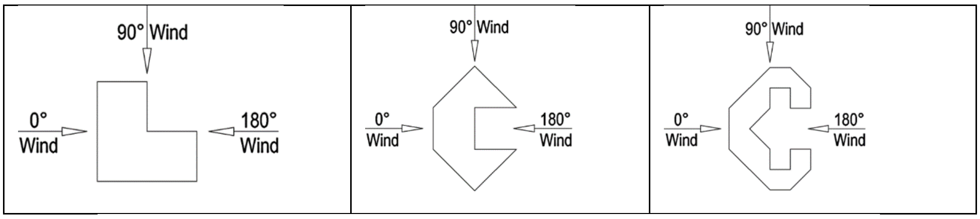

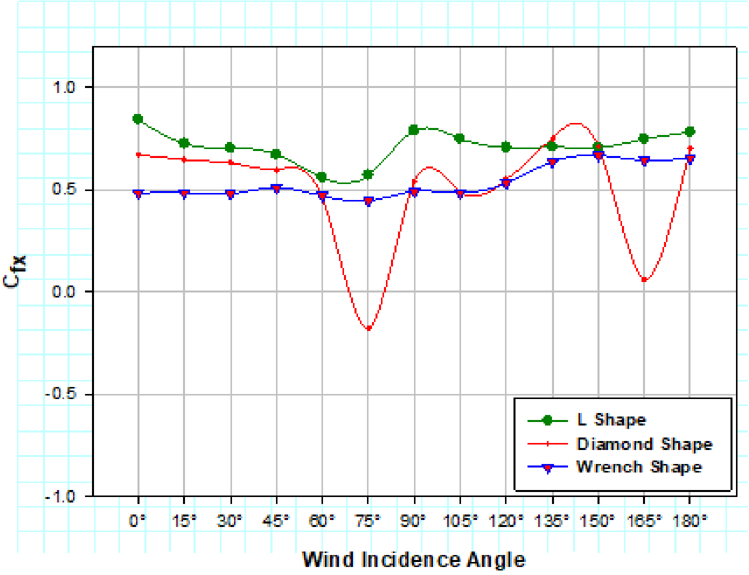

Figure 6. 6: Base Shear Coefficient Along Wind Direction (Drag Coefficient)

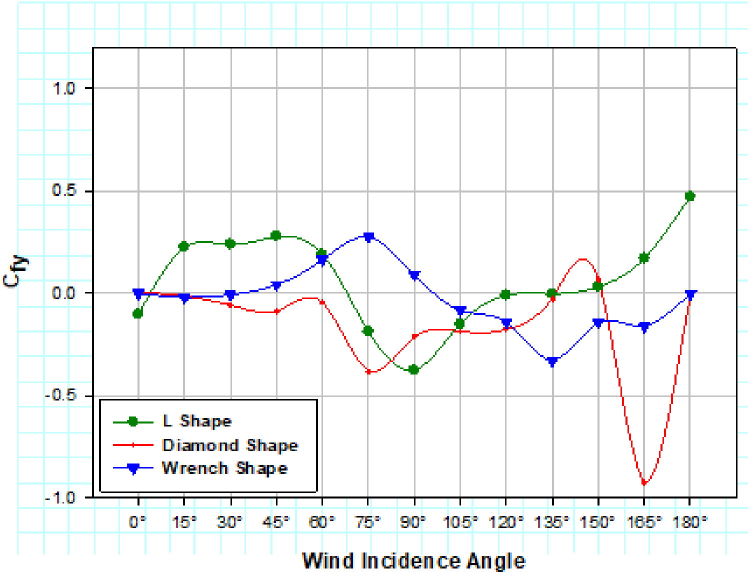

Figure 6. 7: Base Shear Coefficient Across Wind Direction (Lift Coefficient)

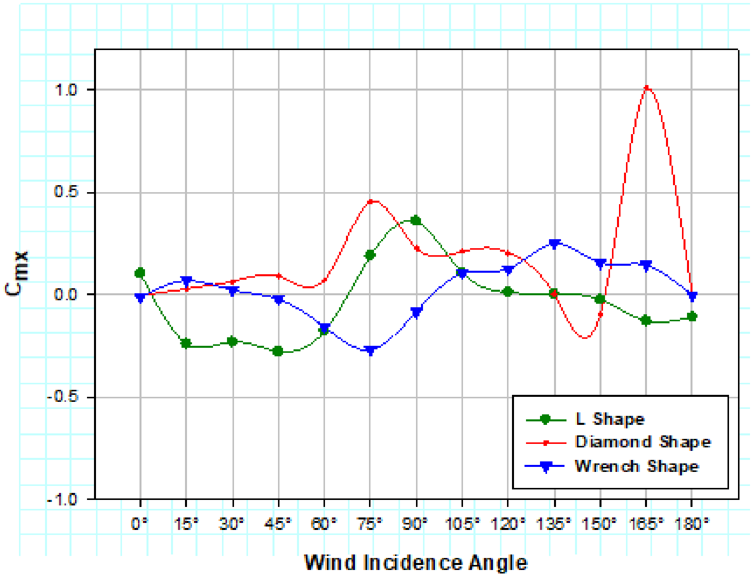

Figure 6. 8: Base Moment Coefficient Along Wind Direction

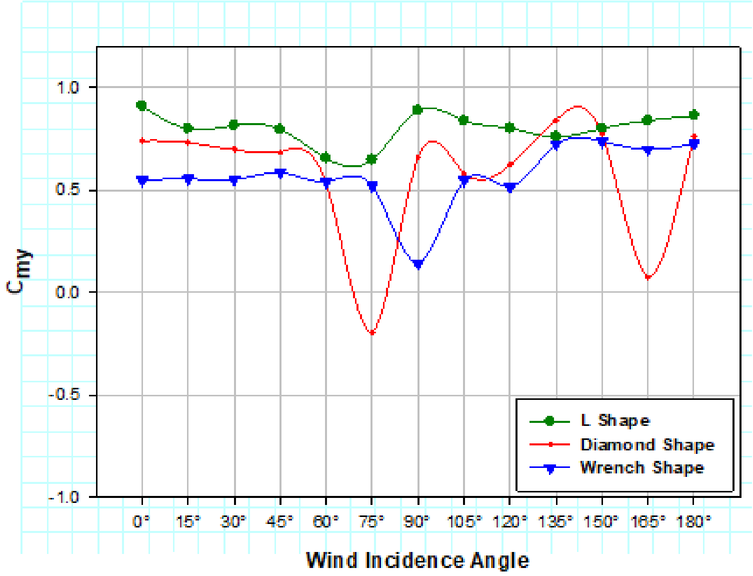

Figure 6. 9: Base Moment Coefficient Across Wind Direction

6.3.4 Twisting Moment Coefficient

Figure 6.10 shows the twisting moment coefficient (C_{tm}) for the three models. It is observed that fluctuation in torsional moments in all the three models are varying and changing sign quite largely. In the L shape model, the maximum and minimum C_{tm} values, irrespective of sigh (+ve or-ve), is attained at 180° and 135" wind angle of attack respectively. Whereas, in diamond shape model the maximum values occur at 45° and minimum at 0° and 180" wind angle where no torsional moment exists. In wrench model also no torsional moment exists at 0° and 180° wind incidence angle and the maximum exists for 75° wind angle.

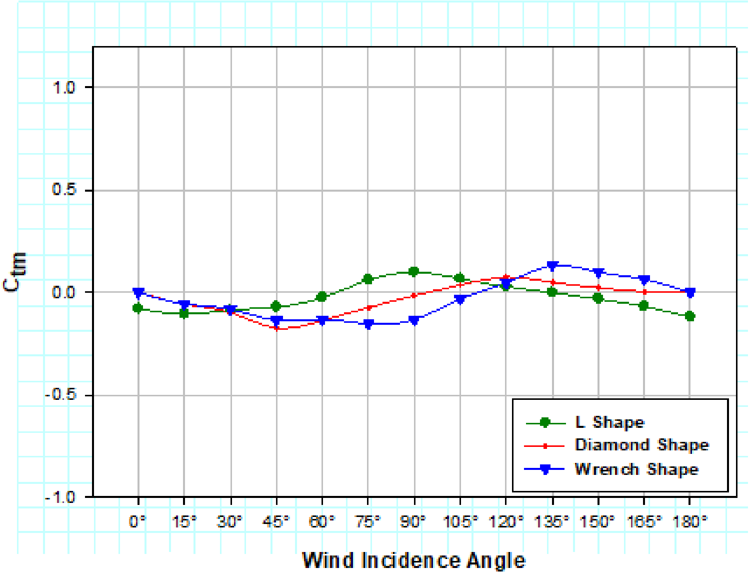

Figure 6. 10: Twisting Moment Coefficient About Z-Direction

CHAPTER 7 CONCLUSIONS

7.1 GENERAL

In the preceding chapters this thesis covers study conducted to examine the response of different edge configured tall buildings due to change in cross section having equal plan area of 300 sqm and height 50 m and variation of wind structural parameters based on numerical study. Detailed study is made to investigate the effects of change in wind direction on the wind loads and local pressure distributions for cladding/glazing units. The following conclusion can be drawn from this study:

7.2 PRESSURE MEASUREMENT - MODELS SYMMETRICAL ABOUT BOTH AXES

7.2.1 Rectangular Model

1. For orthogonal wind directions (0° and 90° wind incidence angles) isobars of pressure coefficient are parabolic and symmetrical about central vertical line of the windward face and increasing with height due to exponential increase in flow velocity owing to atmospheric boundary layer effect.
2. Pressure coefficients towards the edges of the windward face are suction in nature due to flow separation and reversal of flow.
3. Upwash from the roof edge of windward face causes pressure near the roof height to reduce and become negative at the roof edge.
4. Side faces and downwind face are experiencing suction pressure. Suction on the side faces is more on the near end edge and reduces towards the far end edges. Due to low velocity and high turbulence leeward face is experiencing almost uniform suction.
5. On the roof negative pressure zone is developed immediately after the separation of flow from the windward top edge and suction is reducing from the leading edges of windward side to lee side.
6. Wind flow direction has significant effects on the pressure distribution at all faces. Orthogonal wind directions are most critical directions for pressure and suction

on the faces. However, on roof top area average coefficient of suction pressure is maximum at 30° wind angle.

7.2.2 Plus Shape Model

1. When wind impinges perpendicular to the leading windward face, pressure coefficients are positive on the windward face as well as on the recessed faces (cut corner faces) on windward side. Suction occurs on the side faces and the lee face including the cut corner faces.
2. Maximum positive pressure coefficient for orthogonal wind directions on the windward face is lower than those on the rectangular model. However, at 30° and 60° wind angle area average pressure coefficient is a little higher on the respective recessed face on which wind is impinging directly, as flow tends to be entrapped within the recessed faces.
3. Similarly maximum suction coefficient for orthogonal wind directions on the side and lee faces are lower than those on the rectangular model.
4. Pressure or suction on the faces is changing widely due to change in wind directions.
5. On roof top suction pressure exists for all wind angles and the values of suction pressure does not change much due to change in wind directions.
6. Suction pressure on roof top for all wind angles are much lower than those on the rectangular roof top.

7.2.3 Octagonal-Oval Model

At 0° wind angle breadth of the model is less than depth of the octagonal-oval model whereas, in rectangular model breadth of the model is more than depth of the model. For 90° wind incidence angle they are vice-versa. Hence comparison of pressure coefficient on octagonal-oval shaped model for 0° wind angle is made with those at 90° wind angle and vice-versa.

1. For 0° wind incidence angle the coefficient of pressure on windward face on octagonal-oval shaped is higher than that on rectangular model; but for 90° wind angle it is lower.

2. However, value of suction coefficient on the lee face is on lesser side in both the cases.
3. For 0° wind angle suction coefficient on the parallel side faces of octagonal-oval model are almost similar as those on the side faces in rectangular model. But, for 90° wind angle the value of suction coefficient on the parallel side faces of octagonal-oval model is more than double when compared with those on rectangular model. Long after body and short after body effect in flow reattachment is responsible for this result.
4. On the inner faces of the central opening similar suction coefficient occur on all faces for the respective wind incidence angles. However, the values of suction coefficient increase with increase in wind angle from 0° to 90°.
5. At roof top suction coefficient is maximum at 75° wind angle.

7.3 PRESSURE MEASUREMENT - MODELS SYMMETRICAL ABOUT ONE AXIS

7.3.1 L-Shape Model

1. When wind is impinging on the larger face orthogonally, pattern of pressure isobars on the windward face and the larger face (side face) orientated parallel to the wind direction are very similar to that of the rectangular model in the windward region. But on other faces pressure patterns are different.
2. When one of the re-entrant wing faces is orthogonal to the impact of wind and another is parallel, positive pressure is developed on the face on which wind is impinging perpendicularly. But pressure distribution is not symmetrical about the vertical center line of the face. It is shifted towards the free end from where separation of wind is taking place. On another wing face, the orientation of which is parallel to the wind direction is also subjected to positive pressure despite being a side face unlike in the rectangular model where suction occurs on the side faces.
3. Maximum area average suction coefficient on roof is at 120° angle of wind attack. Fixing roof structures at this orientation of the building is crucial for stability due to wind load.
4. For wind incident angles ranging 0° to 60° the re-entrant wing faces experience

homogeneous suction pressure. Upon further increase of the wind incident angles between 90° to 180°, the pressure on the re-entrant wing faces increases due to stagnation of air. This is the unique characteristic of L shape buildings which plays an important role in design of cladding systems on re-entrant faces. The height of the building and the relative length dimensions of the wing faces play an important role in producing pressure on the wing faces.

7.3.2 C- Diamond Shape Model

1. Suction pressure in recessed faces for different wind incidence angles are almost constant for less than 60° wind angle as flow tends to skip past the recess gap leaving stagnant flow in the recessed cavity. The recessed faces are subjected to uniform suction pressure field at 60° wind incidence angle. Further changes in angle of wind incidence, pressure field within the recessed cavity turns out to be positive at 150° wind angle.
2. At 90° wind angle average suction on the surface of face A is maximum for all faces and for all wind directions.
3. On roof surface the average suction is maximum at 30° orientation of the building.
4. At 150° wind angle local high suction pressure on roof is developed above the face after lee side of recessed cavity unlike in other cases where local high suction is developed above the face on which wind is striking first.
5. Maximum positive pressure is developed on face E falling within the recessed cavity at 180° angle of wind attack.

7.3.3 C- Wrench Shape Model

1. Highest suction on roof for all wind angles of attack exists at 180° of wind attack. Suction concentration on large area of roof exists at this angle of wind attack with a high gradient of suction. As such, for design of roof structures this angle of wind attack is decisive.
2. Uniform suction pressure field within the recessed cavity exists up to 90° angle of wind attack unlike in the diamond C-shape in which suction pressure field is constant up to 60° wind angle. Almost equal suction pressure exists on the

recessed cavity faces at the respective angle of wind. The pressure field gradually shifts to positive from 150° angle of wind attack.

3. At 0° angle of wind attack high gradient of pressure from positive to negative exists on the inclined faces C1 and C2. Similarly, at 150° wind angle of attack, high gradient of pressure exists on face D1 and E1. For cladding design these faces are crucial for the respective angle of wind attacks.
4. At 120° the pressure field within the recessed cavity is almost negligible. On roof surface suction is minimum for this angle of wind.

7.4 FORCE COEFFICIENTS - MODELS SYMMETRICAL ABOUT BOTH AXES

In the present study wind axes and body axes coincide with each other as model is rotated in anticlockwise direction to change the steps in wind incidence angle in clockwise direction. So, base shear force in x-direction (F_x) and drag force will be the same. Similarly base shear force in y-direction (F_y) and lift force will be the same as shown in figure 7.1 below. Bending and twisting moments have been reckoned at centroid of cross-section.

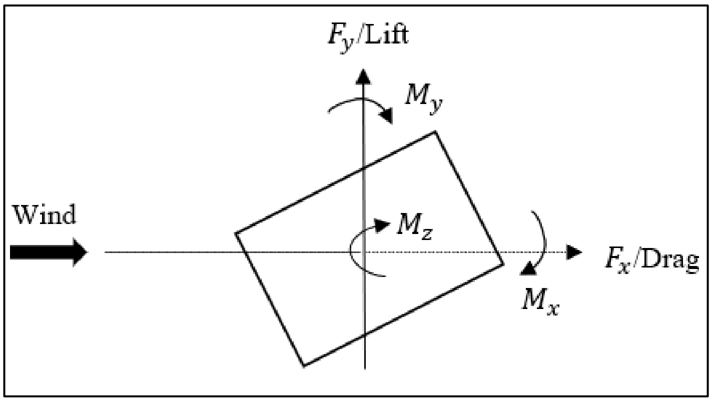

Figure 7. 1: Schematic Diagram for Structural Parameters

7.4.1 Rectangular Model

1. Base Shear Coefficient (C_{fx}) is maximum 0° wind Angle and minimum at 75° wind angle.
2. Base Shear Coefficient (C_{fy}) is maximum at 15° wind angle and minimum at 0° wind angle.

3. Overturning Moment Coefficient (C_{my}) is maximum at 0° wind angle and minimum at 75° wind angle.
4. Overturning Moment Coefficient (C_{mx}) is maximum at 15° wind angle and minimum at 0° wind angle.
5. Twisting moment coefficient (C_{tm}) is maximum at 15° wind angle.

7.4.2 Plus Shape Model

When compared with the similar identity with rectangular model

1. Maximum base shear coefficient (C_{fx}) is increased by 23.94% and it occurs at 75° wind angle.
2. Maximum overturning moment coefficient (C_{my}) is reduced by 12.19% and it occurs at both 0° and 90° wind angle.
3. Maximum twisting moment coefficient (C_{tm}) is almost nil for all wind angles.

7.4.3 Octagonal-Oval Model

When compared with the similar identity with rectangular model

1. Maximum base shear coefficient (C_{fx}) is reduced by 31.03% and it occurs at 60° wind angle.
2. Maximum overturning moment coefficient (C_{my}) is reduced by 24.58% and it also occurs at 60° wind angle
3. Maximum twisting moment coefficient (C_{tm}) is 0.23 at 45° wind angle.

7.5 FORCE COEFFICIENTS – MODELS SYMMETRICAL ABOUT ONE AXIS

7.5.1 L-Shape Model

When compared with the similar identity with rectangular model

1. Maximum base shear coefficient (C_{fx}) is increased by 31.15% and it occurs at 75° wind angle.

2. Maximum overturning moment coefficient (C_{my}) is increased by 6.72% and it occurs at 90° wind angle.
3. Maximum twisting moment coefficient (C_{tm}) is 0.12 and it occurs at 180° wind angle.

7.5.2 Diamond C-Shape Model

When compared with the similar identity with rectangular model

1. Maximum base shear coefficient (C_{fx}) is increased by 9.37% and it occurs at 165° wind angle.
2. Maximum overturning moment coefficient (C_{my}) is also increased by 12.67% and it occurs at the same wind angle (165°).
3. Maximum twisting moment coefficient (C_{tm}) is 0.17 and it occurs at 45° wind angle.

7.5.3 Wrench C-Shape Model

When compared with the similar identity with rectangular model

1. Maximum base shear coefficient (C_{fx}) is increased by 36.91% and it occurs at 135° wind angle.
2. Maximum overturning moment coefficient (C_{my}) is decreased by 14.64% and it also occurs at the same wind angle (135°).
3. Maximum twisting moment coefficient (C_{tm}) is 0.15 and it occurs at 75° wind angle.

7.6 COMPARISION BETWEEN MODELS

1. Among the symmetrical model’s structural response of octagonal model is the best for economic reason as the drag coefficient and overturning moment coefficients are minimum for all wind direction comparative to rectangular and plus models. The central opening in the octagonal model may be utilized as service core area. However, land orientation for 45° prevailing wind conditions should be avoided as twisting moment coefficient is higher at this wind angle.

2. Among the unsymmetrical models C-Diamond shape and C-Wrench shape models are the worst so far as ventilation is concerned as surface pressures on the recessed faces are found to be constant due to reflection of flow among the faces for most orientations of wind flow. If mechanical ventilation is provided these models can be used.
3. Among the C-Diamond and C-Wrench models, C-Diamond shape model may be preferred over C-Wrench shape model as the maximum drag and maximum overturning moment coefficient in C-Diamond shape is less comparative to C-Wrench model. However, overturning moment coefficient is marginally more.
4. For roof structures such as water tank, solar panels, hydroponic farming, mobile towers, hoardings etc. Rectangular model was observed to be most vulnerable as suction at roof is higher than other models.
5. The strength and intensity of ground level upwind vortex in Diamond and Wrench models at 180° wind angle was observed to be higher than other models.

7.7 RECOMMENDATIONS FOR FUTURE STUDY

Based on the present study future investigations may be carried on the following area:

1. Effect of aerodynamics modifications (rounded, chamfered etc.) on wind pressure distribution and response on building shapes taken in the present study.
2. Effect of opening (balconies, courtyard etc.) on wind pressure distribution and response on the building shapes taken in the present study.
3. Effect of increase in height of buildings on pressure distribution and response on the building shapes taken in the present study can also be investigated and documented.
4. Dynamic response analysis of the buildings based on time varying wind data may also be conducted.

REFERENCES

[1] “Model Building Bye Laws 2016”.

[2] The Council on Tall Buildings and Urban Habitat (CTBUH), “CTBUH Height Criteria for Measuring & Defining Tall Buildings.” https://www.ctbuh.org

[3] W. D. Baines, “Effect of Velocity Distribution on Wind Loads and flow patterns Building,” Proceedings of Conference “Wind effect on buildings and structures” National Physical Laboratory 26-28 June 1963. P 198-225.

[4] Dryden Huge L. and Hill George C., “Wind Pressures on Structures,” Scientific Papers of the Bureau of Standards, vol. 20, pp. 697–732, 1925.

[5] B. S. Taranath, Wind and Earthquake Resistant Buildings. New York: Marcel Dekker, 2004.

[6] Davenport AG, “Response of six building shapes to turbulent wind,” Phil Trans Roy Soc London Ser A. Math Phys Sci, vol. 269, no. 1199, pp. 385–394, 1971, doi: 10.1098/rsta.1971.0039.

[7] P. A. Bailey and K. C. S. Kwok, “Interference Excitation of Twin Tall Buildings,” 1985.

[8] K. C. S. Kwok and P. A. Bailey, “Aerodynamic Devices for Tall Buildings and Structures,” J Eng Mech, vol. 113, no. 3, pp. 349–365, Mar. 1987, doi: 10.1061/(ASCE)0733-9399(1987)113:3(349).

[9] T. Balendra, G. K. Nathan, and K. H. Kang, “A Deterministic Model for Wind Induced Oscillations of Slender Vertical Structures,” in Computational Mechanics *’88*, S. N. Atluri and G. Yagawa, Eds., Berlin, Heidelberg: Springer Berlin Heidelberg, 1988, pp. 935–936.

[10] M. Dionne and A. G. Davenport, “A simple relationship between the gust response factor and fatigue damage,” Journal of Wind Engineering and Industrial Aerodynamics, vol. 30, no. 1–3, pp. 45–54, Aug. 1988, doi: 10.1016/0167-6105(88)90070-0.

[11] R. Dutton and N. Isyumov, “Reduction of tall building motion by aerodynamic treatments,” Journal of Wind Engineering and Industrial Aerodynamics, vol. 36, no. PART 2, pp. 739–747, Jan. 1990, doi: 10.1016/0167-6105(90)90071-J.

[12] H. Hayashida and Y. Iwasa, “Aerodynamic shape effects of tall building for vortex induced vibration,” Journal of Wind Engineering and Industrial Aerodynamics, vol. 33, no. 1–2, pp. 237–242, Mar. 1990, doi: 10.1016/0167-6105(90)90039-F.

[13] H. Hayashida, Y. Mataki, and Y. Iwasa, “Aerodynamic damping effects of tall building for a vortex induced vibration,” Journal of Wind Engineering and

Industrial Aerodynamics, vol. 43, no. 1–3, pp. 1973–1983, Jan. 1992, doi: 10.1016/0167-6105(92)90621-G.

[14] J. E. Cermak and L. S. Cochran, “Physical modelling of the atmospheric surface layer,” 1992.

[15] Beneke D.L. and Kwok K. C. S., “Aerodynamic Effect of Wind Induced Torsion on Tall Buildings,” Journal of Wind Engineering and industrial Aerodynamics, vol. 50, no. Elsevier, pp. 271–280, 1993.

[16] W. J. Zhang, K. C. S. Kwok, and Y. L. Xu, “Aeroelastic torsional behaviour of tall buildings in wakes,” Journal of Wind Engineering and Industrial Aerodynamics, vol. 51, no. 2, pp. 229–248, Feb. 1994, doi: 10.1016/0167-6105(94)90006-X.

[17] Z. Yin Wang, E. J. Plate, M. Rau, and R. Keiser, “Scale effects in wind tunnel modelling,” ELSEVIER, 1996.

[18] H. Kawai, “Effect of corner modifications on aeroelastic instabilities of tall buildings,” Journal of Wind Engineering and Industrial Aerodynamics, vol. 74–76, pp. 719–729, Apr. 1998, doi: 10.1016/S0167-6105(98)00065-8.

[19] Q. S. Li, J. Q. Fang, A. P. Jeary, C. K. Wong, and D. K. Liu, “Evaluation of wind eeects on a supertall building based on full-scale measurements,” 2000.

[20] Y.-M. Kim and K.-P. You, “Dynamic responses of a tapered tall building to wind loads,” Journal of Wind Engineering and Industrial Aerodynamics, vol. 90, pp. 1771–1782, 2002.

[21] Y. Zhou, T. Kijewski, and A. Kareem, “Along-Wind Load Effects on Tall Buildings: Comparative Study of Major International Codes and Standards,” Journal of Structural Engineering, vol. 128, no. 6, pp. 788–796, Jun. 2002, doi: 10.1061/(ASCE)0733-9445(2002)128:6(788).

[22] S. Thepmongkorn, G. S. Wood, and K. C. S. Kwok, “Interference effects on wind-induced coupled motion of a tall building,” Journal of Wind Engineering and Industrial Aerodynamics, vol. 90, no. 12–15, pp. 1807–1815, Dec. 2002, doi: 10.1016/S0167-6105(02)00289-1.

[23] Y. Zhou, T. Kijewski, and A. Kareem, “Aerodynamic Loads on Tall Buildings: Interactive Database,” Journal of Structural Engineering, vol. 129, no. 3, pp. 394–404, Mar. 2003, doi: 10.1061/(ASCE)0733-9445(2003)129:3(394).

[24] M. Gu and Y. Quan, “Across-wind loads of typical tall buildings,” Journal of Wind Engineering and Industrial Aerodynamics, vol. 92, no. 13, pp. 1147–1165, Nov. 2004, doi: 10.1016/J.JWEIA.2004.06.004.

[25] N. Lin, C. Letchford, Y. Tamura, B. Liang, and O. Nakamura, “Characteristics of wind forces acting on tall buildings,” Journal of Wind Engineering and Industrial Aerodynamics, vol. 93, no. 3, pp. 217–242, Mar. 2005, doi: 10.1016/j.jweia.2004.12.001.

[26] S. Liang, Q. S. Li, L. Zou, and J. R. Wu, “Simplified formulas for evaluation of across-wind dynamic responses of rectangular tall buildings,” *Wind and Structures*, vol. 8, no. 3, pp. 197–212, Jun. 2005, doi: 10.12989/was.2005.8.3.197.

[27] J. Lim and B. Bienkiewicz, “Wind-induced response of structurally coupled twin tall buildings,” Wind and Structures, vol. 10, no. 4, pp. 383–398, Aug. 2007, doi: 10.12989/was.2007.10.4.383.

[28] J. G. Zhao and K. M. Lam, “Interference effects in a group of tall buildings closely arranged in an L- or T-shaped pattern,” Wind and Structures, vol. 11, no. 1, pp. 1–18, Feb. 2008, doi: 10.12989/WAS.2008.11.1.001.

[29] J. Y. Fu, Q. S. Li, J. R. Wu, Y. Q. Xiao, and L. L. Song, “Field measurements of boundary layer wind characteristics and wind-induced responses of super-tall buildings,” Journal of Wind Engineering and Industrial Aerodynamics, vol. 96, no. 8–9, pp. 1332–1358, Aug. 2008, doi: 10.1016/j.jweia.2008.03.004.

[30] Y. Kim and J. Kanda, “Characteristics of aerodynamic forces and pressures on square plan buildings with height variations,” Journal of Wind Engineering and Industrial Aerodynamics, vol. 98, no. 8–9, pp. 449–465, Aug. 2010, doi: 10.1016/J.JWEIA.2010.02.004.

[31] G. Ming and Q. Yong, “Across-wind loads and effects of super-tall buildings and structures,” Sci China Technol Sci, vol. 54, no. 10, pp. 2531–2541, Oct. 2011, doi: 10.1007/s11431-011-4543-5.

[32] K. M. Lam, J. G. Zhao, and M. Y. H. Leung, “Wind-induced loading and dynamic responses of a row of tall buildings under strong interference,” Journal of Wind Engineering and Industrial Aerodynamics, vol. 99, no. 5, pp. 573–583, 2011, doi: 10.1016/j.jweia.2011.02.006.

[33] Z. N. Xie and M. Gu, “Simplified formulas for evaluation of wind-induced interference effects among three tall buildings,” Journal of Wind Engineering and Industrial Aerodynamics, vol. 95, no. 1, pp. 31–52, Jan. 2007, doi: 10.1016/j.jweia.2006.05.003.

[34] Y. Hui, Y. Tamura, and A. Yoshida, “Mutual interference effects between two high-rise building models with different shapes on local peak pressure coefficients,” Journal of Wind Engineering and Industrial Aerodynamics, vol. 104–106, pp. 98–108, May 2012, doi: 10.1016/J. JWEIA.2012.04.004.

[35] J. A. Amin and A. K. Ahuja, “Experimental study of wind-induced pressures on buildings of various geometries,” 2011. [Online]. Available: www.ijest-ng.com

[36] Amin J.A and Ahuja A.K, “Experimental Study of Wind-induced Pressure on Buildings of Various Geometries,” Industrial Journal of Engineering Science and Technology, vol. 3, no. 5, pp. 1–19, 2011.

[37] J. A. Amin and A. K. Ahuja, “Mean interference effects between two buildings: Effects of close proximity,” Structural Design of Tall and Special Buildings, vol. 20, no. 7, pp. 832–852, Nov. 2011, doi: 10.1002/tal.564.

[38] Y. Hui, A. Yoshida, and Y. Tamura, “Interference effect on local peak pressure between two high-rise buildings with rectangular shape,” in The Seventh International Colloquium on Bluff Body Aerodynamics and Applications (BBAA7), Shanghai, China, 2012.

[39] S. Y. Wong and K. M. Lam, “Effect of recessed cavities on wind-induced loading and dynamic responses of a tall building,” Journal of Wind Engineering and Industrial Aerodynamics, vol. 114, pp. 72–82, Mar. 2013, doi: 10.1016/J.JWEIA.2012.12.013.

[40] Tanaka H, Tamura Y, Ohtake K, Nakai M, Kim YC, and Bandi E K, “Experimental Investigation of Aerodynamic Forces and Wind Pressure Acting on Tall Buildings with Various Unconventional Configuration,” Journal of Wind Engineering and Industrial Aerodynamics, vol. 107–108, pp. 179–191, 2013.

[41] Ritu Raj and Ahuja. A.K, “Wind Loads on Cross Shape Tall Buildings,” JAIR, vol. 2, no. 2, 2013.

[42] Amin J.A and Ahuja A.K, “Effects of Side Ratio on Wind Induced Pressure Distribution on Rectangular Buildings,” Hindawi Publishing Corporation, J Struct, pp. 1–12, 2013. doi: dx.doi.org/10.1155/2013/176739.

[43] J. A. Amin and A. K. Ahuja, “Effects of Side Ratio on Wind-Induced Pressure Distribution on Rectangular Buildings,” Journal of Structures, vol. 2013, pp. 1–12, Aug. 2013, doi: 10.1155/2013/176739.

[44] Y. Li, Q. S. Li, and K. L. Ju, “Experimental investigation of the wind pressure distribution and wind interference effects on a typical tall building,” in Advanced Materials Research, 2013, pp. 444–451. doi: 10.4028/www.scientific.net/AMR.639-640.444.

[45] Y. Hui, A. Yoshida, and Y. Tamura, “Interference effects between two rectangular-section high-rise buildings on local peak pressure coefficients,” J Fluids Struct, vol. 37, pp. 120–133, Feb. 2013, doi: 10.1016/j.jfluidstructs.2012.11.007.

[46] E. Kumar Bandi, H. Tanaka, Y. Chul Kim, K. Ohtake, A. Yoshida, and Y. Tamura, “High-Rise Buildings Peak Pressures Acting on Tall Buildings with Various Configurations,” 2013. [Online]. Available: www.ctbuh-korea.org/ijhrb/index.php

[47] J. Yi and Q. S. Li, “Wind tunnel and full-scale study of wind effects on a super-tall building,” J Fluids Struct, vol. 58, pp. 236–253, Oct. 2015, doi: 10.1016/j.jfluidstructs.2015.08.005.

[48] X. F. Yu, Z. N. Xie, J. B. Zhu, and M. Gu, “Interference effects on wind pressure distribution between two high-rise buildings,” Journal of Wind Engineering and Industrial Aerodynamics, vol. 142, pp. 188–197, Jul. 2015, doi: 10.1016/j.jweia.2015.04.008.

[49] D. K. Kwon, A. Kareem, R. Stansel, and B. R. Ellingwood, “Wind load factors for dynamically sensitive structures with uncertainties,” Eng Struct, vol. 103, pp. 53–62, Nov. 2015, doi: 10.1016/j.engstruct.2015.08.031.

[50] R. Ahlawat and A. K. Ahuja, “Wind Loads on ‘T’ Plan Shape Tall Buildings,” Journal of Academia and Industrial Research (JAIR), vol. 4, no. 1, 2015.

[51] R. K. Goliya, N. K. Samaiya, G. R. Sabareesh, and A. Gupta, “Current Status of Interference Effect Studies on Tall Buildings,” International Journal of Civil Engineering Research, vol. 7, no. 2, pp. 105–115, 2016, doi: 10.3850/978-981-07-8012-8.

[52] R. Pundhir and N. Barde, “Study of Wind Pressure on Tall Building Due to Change in Relative Position of Interfering Building,” 2016. [Online]. Available: http://www.ripublication.com

[53] B. S. Chauhan and A. K. Ahuja, “Height Effect of Interfering Buildings on Wind Pressure Distribution on Rectangular Plan Tall Buildings,” in 9 th Asia-Pacific Conference on Wind Engineering, Auckland, New Zealand, 2017, pp. 1–4.

[54] B. Chauhan and A. Ahuja, “Effect of Height and Orientation of Interfering Buildings on Wind Loads on Tall Buildings”. ISEC Press, 2017.

[55] S. K. Nagar, R. Raj, and N. Dev, “Experimental study of wind-induced pressures on tall buildings of different shapes,” Wind and Structure, vol. 31, no. 5, pp. 441–453, 2020.

[56] M. Gu, X. Wang, and Y. Quan, “Wind tunnel test study on effects of chamfered corners on the aerodynamic characteristics of 2D rectangular prisms,” Journal of Wind Engineering and Industrial Aerodynamics, vol. 204, p. 104305, Sep. 2020, doi: 10.1016/J.JWEIA.2020.104305.

[57] A. C. Khanduri, T. Stathopoulos, and C. Bedard, “Generalization of wind-induced interference effects for two buildings,” Wind and Structures, vol. 3, no. 4, pp. 255–266, Dec. 2000, doi: 10.12989/was.2000.3.4.255.

[58] G. Lamberti, L. Amerio, G. Pomaranzi, A. Zasso, and C. Gorlé, “Comparison of high-resolution pressure measurements on a high-rise building in a closed and open-section wind tunnel,” Journal of Wind Engineering and Industrial Aerodynamics, vol. 204, p. 104247, Sep. 2020, doi: 10.1016/J.JWEIA.2020.104247.

[59] D. Li, B. Liu, X. Zhou, and Z. Wang, “Size effects of area extreme pressure for large-scale cladding,” Structures, vol. 29, pp. 408–415, Feb. 2021, doi: 10.1016/J.ISTRUC.2020.11.027.

[60] S. Pal, R. Raj, and S. Anbukumar, “Bilateral interference of wind loads induced on duplicate building models of various shapes,” Latin American Journal of Solids and Structures, vol. 18, no. 5, 2021, doi: 10.1590/1679-78256595.

[61] S. Pal, R. Raj, and S. Anbukumar, “Comparative study of wind induced mutual interference effects on square and fish-plan shape tall buildings,” Sādhanā, vol. 46, no. 2, p. 86, 2021, doi: 10.1007/s12046-021-01592-6.

[62] M. Franek and M. Macák, “Effects of Interference on Local Peak Pressures Between Two Buildings with an Elliptical Cross-Section,” Slovak Journal of Civil Engineering, vol. 29, no. 1, pp. 35–41, Mar. 2021, doi: 10.2478/sjce-2021-0006.

[63] S. Kumar Nagar, R. Raj, and N. Dev, “Proximity effects between two plus-plan shaped high-rise buildings on mean and RMS pressure coefficients,” Scientia Iranica, pp. 1–28, 2021.

[64] I. P. Castro A N and D. A. G. Robins, “The flow around a surface-mounted cube in uniform and turbulent streams,” 1977.

[65] M. S. Germi and H. E. Kalehsar, “Numerical investigation of interference effects on the critical wind velocity of tall buildings,” Structures, Elsevier, vol. 30, pp. 239–252, 2021.

[66] P. J. Richards and R. P. Hoxey, “Appropriate boundary conditions for computational wind engineering models using the k-Ɛ turbulence model,” 1993.

[67] Y. Q. Zhang, A. H. Huber, S. P. S. Arya, and W. H. Snyder, “Numerical simulation to determine the effects of incident wind shear and turbulence level on the flow around a building,” Journal of Wind Engineering and Industrial Aerodynamics, vol. 46 & 47, pp. 129–134, 1993.

[68] Stathopoulos T, “Numerical Simulation of Wind-induced Pressure on Buildings of Various Geometries,” J. Wind Engg. Indus. Aerodynamic, vol. 46 & 47, pp. 419–430, 1993.

[69] N. Bazeos and D. E. Beskos, “Torsional moments on buildings subjected to wind loads,” Eng Anal Bound Elem, vol. 18, no. 4, pp. 305–310, Dec. 1996, doi: 10.1016/S0955-7997(96)00040-9.

[70] I. R. Cowan, I. P. Castro, and A. G. Robins, “Numerical considerations for simulations of flow and dispersion around buildings,” Journal of Wind Engineering and Industrial Aerodynamics, vol. 67 & 68, pp. 535–545, 1997.

[71] Y. Tominaga, A. Mochida, and R. Yoshie, “AIJ Guideline for Practical Applications of CFD to Wind Environment around Buildings,” in The Forth International Symposiumon Computational Wind Engineering (CWE 2006), Yokohama, 2006, pp. 1–5. [Online]. Available: https://www.researchgate.net/publication/266884529

[72] S. Reiter, “Validation Process for CFD Simulations of Wind Around Buildings-2008,” in European Built Environment CAE Conference, 2008, pp. 1–18.

[73] C. C. K. Cheng, K. M. Lam, and A. Y. T. Leung, “Wind flow in the recessed cavities of a tall building,” in The Seventh Asia-Pacific Conference on Wind Engineering, Taipei, 2009.

[74] H. Montazeri, B. Blocken, W. D. Janssen, and T. van Hooff, “CFD analysis of wind comfort on high-rise building balconies: validation and application,” in Seventh International Colloquium on Bluff Body Aerodynamics and Applications (BBAA7) , 2012, pp. 1674–1681.

[75] R. K. Pradeep, V. Ehsan, and S. Azadeh, "Computation Fluid Dynamics Approach for Highrise Buildings," Centre for Earthquake Engineering, IIIT Hyderabad, A3C-12, Report No. IIIT/TR/2013/-1, Hyderabad, pp. 1–9, 2013.

[76] Chakraborty S and Dalui S K, "Numerical Study of Surface Pressure on Square Plan Shape Tall Building," in Symposium on sustainable infrastructure development (SID), Feb. 2013, pp. 252–258.

[77] Kheyari P and Dalui S.K, "Estimation of Wind Load on a Tall Building Under Interference Effect," Jordon J Civil Eng, vol. 9, no. 1, pp. 84–101, 2014.

[78] B. Bhattacharyya, E. Zurich, and S. K. Dalui, "Comparative study between regular and irregular plan shaped tall building under wind excitation by numerical technique," 2014, doi: 10.13140/2.1.1689.9202.

[79] S. K. Verma, A. K. Roy, S. Lather, and M. Sood, "CFD Simulation for Wind Load on Octagonal Tall Buildings," International Journal of Engineering Trends and Technology (IJETT), vol. 24, no. 4, 2015, [Online]. Available: http://www.ijettjournal.org

[80] R. Paul and S. K. Dalui, "Wind effects on 'Z' plan-shaped tall building: a case study," International Journal of Advanced Structural Engineering, vol. 8, no. 3, pp. 319–335, Sep. 2016, doi: 10.1007/s40091-016-0134-9.

[81] R. Kar and S. K. Dalui, "Wind interference effect on an octagonal plan shaped tall building due to square plan shaped tall buildings," International Journal of Advanced Structural Engineering (IJASE), vol. 8, no. 1, pp. 73–86, 2016, doi: 10.1007/s40091-016-0115-z.

[82] S. Kumar Dalui and R. Paul, "The Effects of Position of Limbs on a Rectangular Plan Shaped Tall Building under Wind," in World congress on Advances in Civil, Environmental and Material research (ACEM16), 2016, pp. 1–17.

[83] D. Kumar and S. K. Dalui, "Effect of internal angles between limbs of cross plan shaped tall building under wind load," Wind and Structures, An International Journal, vol. 24, no. 2, pp. 95–118, Feb. 2017, doi: 10.12989/was.2017.24.2.095.

[84] A. Mukherjee and A. K. Bairagi, "Wind Pressure and Velocity Pattern Around 'N' Plan Shape Tall Building- A Case Study," in Asian J. Civil Eng, 2017, pp. 1241–1258.

[85] A. Kumar Bairagi and K. Dalui, "Comparison of Pressure Coefficient Between Square and Setback Tall Building due to Wind Load," in 11th Structural Engineering Convention, 2018, pp. 1–6. [Online]. Available: https://www.researchgate.net/publication/329786479

[86] M. Mallick, A. Mohanta, A. Kumar, and V. Raj, "Modelling of Wind Pressure Coefficients on C-Shaped Building Models," Modelling and Simulation in Engineering, vol. 2018, pp. 1–13, 2018, doi: 10.1155/2018/6524945.

[87] P. Sanyal and S. K. Dalui, "Effects of courtyard and opening on a rectangular plan shaped tall building under wind load," International Journal of Advanced

Structural Engineering, vol. 10, no. 2, pp. 169–188, Jun. 2018, doi: 10.1007/s40091-018-0190-4.

[88] G. W. Alminhana, A. L. Braun, and A. M. Loredo-Souza, "A numerical study on the aerodynamic performance of building cross-sections using corner modifications," Latin American Journal of Solids and Structures, vol. 15, no. 7, Jun. 2018, doi: 10.1590/1679-78254871.

[89] B. S. Chauhan and A. K. Ahuja, "Response of Tall Building Subjected to Wind Loads Under Interference Condition," International Journal of Civil Engineering and Technology (IJCIET), vol. 11, no. 2, pp. 156–163, 2020, [Online]. Available: http://www.iaeme.com/ijciet/issues.asp

[90] N. Tomasello, F. Valenti, G. Cascone, and S. M. C. Porto, "Development of a CFD model to simulate natural ventilation in a semi-open free-stall barn for dairy cows," *Buildings*, vol. 9, no. 8, Aug. 2019, doi: 10.3390/buildings9080183.

[91] A. K. Bairagi and S. K. Dalui, "Forecasting of wind induced pressure on setback building using artificial neural network," Periodica Polytechnica Civil Engineering, vol. 64, no. 3, pp. 751–763, Sep. 2020, doi: 10.3311/PPci.15769.

[92] P. Sanyal and S. K. Dalui, "Effect of corner modifications on Y' plan shaped tall building under wind load," Wind and Structures, An International Journal, vol. 30, no. 3, pp. 245–260, 2020, doi: 10.12989/was.2020.30.3.245.

[93] P. Sanyal and S. K. Dalui, "Comparison of aerodynamic coefficients of various types of Y-plan-shaped tall buildings," Asian Journal of Civil Engineering, vol. 21, no. 7, pp. 1109–1127, Nov. 2020, doi: 10.1007/s42107-020-00265-9.

[94] R. Raj, S. Jha, S. Singh, and S. Choudhary, "Response Analysis of Plus Shaped Tall Building with Different Bracing Systems Under Wind Load," International Journal of Advanced Research in Engineering and Technology (IJARET), vol. 11, no. 3, pp. 371–380, 2020.

[95] Ritu Raj, Rana T, Anchalia, and Khola U, "Numerical Study of Wind Excited Action on H Plan-Shaped Tall Building," International Journal of Emerging Technologies, vol. 11, no. 3, pp. 591–605, 2020.

[96] A. K. Bairagi and S. K. Dalui, "Wind environment around the setback building models," Build Simul, vol. 14, no. 5, pp. 1525–1541, Oct. 2021, doi: 10.1007/s12273-020-0758-3.

[97] S. D. S. K.; B. S. Mandal, "Wind induced response of corner modified 'U' plan shaped tall building," KoreaScience, vol. 32, no. 6, pp. 521–537, 2021.

[98] P. Sanyal and S. K. Dalui, "Effects of internal angle between limbs of 'Y' plan shaped tall building under wind load," Journal of Building Engineering, vol. 33, pp. 1–14, 2021.

[99] P. Sanyal and S. K. Dalui, "Effects of side ratio for 'Y' plan shaped tall building under wind load," Build Simul, vol. 14, no. 4, pp. 1221–1236, Aug. 2021, doi: 10.1007/s12273-020-0731-1.

[100] S. Kato, S. Murakami, T. Takahashi, and T. Gyobu, “Chained analysis of wind tunnel test and CFD on cross ventilation of large-scale market building.”

[101] M. G. Gomes, A. Moret Rodrigues, and P. Mendes, “Experimental and numerical study of wind pressures on irregular-plan shapes,” Journal of Wind Engineering and Industrial Aerodynamics, vol. 93, no. 10, pp. 741–756, 2005, doi: 10.1016/j.jweia.2005.08.008.

[102] P. Mendis, T. Ngo, N. Haritos, A. Hira, B. Samali, and J. Cheung, “Wind Loading on Tall Buildings,” *EJSE:* loading on structures, vol. 7, pp. 51–54, 2007.

[103] K. M. Lam, M. Y. H. Leung, and J. G. Zhao, “Interference effects on wind loading of a row of closely spaced tall buildings,” Journal of Wind Engineering and Industrial Aerodynamics, vol. 96, no. 5, pp. 562–583, May 2008, doi: 10.1016/J.JWEIA.2008.01.010.

[104] S. Mukherjee, S. Chakraborty, S. K. Dalui, and A. K. Ahuja, “Wind induced pressure on ‘Y’ plan shape tall building,” Wind and Structures, An International Journal, vol. 19, no. 5, pp. 523–540, Nov. 2014, doi: 10.12989/was.2014.19.5.523.

[105] B. Bhattacharyya and S. K. Dalui, “Along and across wind effects on irregular plan shaped tall building,” in Advances in Structural Engineering: Dynamics, Volume Two, Springer India, 2015, pp. 1445–1460. doi: 10.1007/978-81-322-2193-7_111.

[106] G. W. Alminhana, A. L. Braun, and A. M. Loredo-Souza, “A numerical-experimental investigation on the aerodynamic performance of CAARC building models with geometric modifications,” Journal of Wind Engineering and Industrial Aerodynamics, vol. 180, pp. 34–48, Sep. 2018, doi: 10.1016/j.jweia.2018.07.001.

[107] B. Bhattacharyya and S. K. Dalui, “Investigation of mean wind pressures on ‘E’ plan shaped tall building,” Wind and Structures, An International Journal, vol. 26, no. 2, pp. 99–114, Feb. 2018, doi: 10.12989/was.2018.26.2.099.

[108] B. Biswarup and D. S. Kumar, “Experimental and Numerical Study of Wind-Pressure Distribution on Irregular-Plan-Shaped Building,” Journal of Structural Engineering, vol. 146, no. 7, p. 04020137, Jul. 2020, doi: 10.1061/(ASCE)ST.1943-541X.0002686.

[109] Y. Zhang, Z. Gu, and C. W. Yu, “Review on numerical simulation of airflow and pollutant dispersion in urban street canyons under natural background wind condition,” Aerosol and Air Quality Research, vol. 18, no. 3. AAGR Aerosol and Air Quality Research, pp. 780–789, Mar. 01, 2018. doi: 10.4209/aaqr.2017.09.0303.

[110] ANSYS Inc, *ANSYS CFX-Solver Theory Guide*. 2009. [Online]. Available: http://www.ansys.com

[111] Revuz J, Hargeaves D. M, and Owen J.S., “On the Domain Size for the Steady State CFD Modelling of a Tall Building,” Wind Structure, vol. 15, no. 4, pp. 313–329, 2012.

[112] J. Franke et al, “Impact of wind and storm on city life and built environment,” Recommendation on the use of CFD in Wind Engineering. In: COST action C14, vol. Version 1.0, pp. 1–12, 2004.

[113] ANSYS Lecture 7, “Introduction to ANSYS Meshing,” 15.0 Release., 2015.

LIST OF PUBLICATIONS

1. Arun Kumar, and Ritu Raj. 2021. “Study of pressure distribution on an irregular octagonal plan oval-shape building using CFD.” Civil Engineering Journal (Iran), 7 (10): 1787–1805. Salehan Institute of Higher Education. https://doi.org/10.28991/cej-2021-03091760.
2. Arun Kumar and Ritu Raj, “CFD Study of Flow Characteristics and Pressure Distribution on Re-Entrant Wing Faces of L-Shape Buildings,” Civil Engineering and Architecture, vol. 10, no. 1, pp. 289–304, Jan. 2022, https://doi.org/10.13189/cea.2022.100125.
3. Arun Kumar; Rahul Kumar Meena; Deepak Sharma and Ritu Raj. 24 Oct 2023. “Structural Parameters of Wrench – C shape Buildings using CFD” International Journal of Construction Management, https://doi.org/10.1080/15623599.2023.2271218
4. Arun Kumar; Rahul Kumar Meena; Ritu Raj; Mohammad Iqbal Khan; Jamal M. Khatib “CFD Study of pressure Distribution on Recessed Faces of Diamond C-Shaped Building” Building Journal by MDPI (ISSN2075-5309) accepted on 3rd Nov 2023 for publication.
5. Arun Kumar, Rahul Kumar Meena, Ritu Raj, Mohammad Iqbal Khan, Jamal M. Khatib “Wind Effects on Re-entrant Wing Faces of Plus Plan Shape Building” in Building Journal by MDPI, Manuscript ID: buildings-2734245 7th Nov 2023.

Papers presented in International Conferences.

1. Arun Kumar and Ritu Raj, “Application of Neural Networks in Pavement Performance Studies” paper presented in International Conference on Advances in Construction Materials and Structure (ACMS - 2018) held between 7th and 8th March 2018. Organized by IIT Roorkee.

2. Arun Kumar and Ritu Raj, “Effect of edge configuration on rectangular and plus plan shape buildings having same plan area (300 sq m) and height (50 m)”, paper presentation in International Conference on Recent Developments in Sustainable Infrastructure: Research & Practices (ICRDSI 2020) held between 18th to 21st Dec

2020, organized by KIIT, Bhubaneswar. Published in eBook ISBN 978-981-16-8433-3.

3. Arun Kumar and Ritu Raj, “Effect of Edge Configuration on Pressure Distribution of an Irregular Octagonal Plan Oval-Shape Building Using CFD” paper presentation in international conference on Advancement in Construction Technology and Management (ACTM 2021) held on 11th – 12th March 2021, organized by College of Engineering, Pune.